

# UCLA

## UCLA Electronic Theses and Dissertations

### Title

Engineering Multifunctional Mesoporous Silica Nanoparticles for Stimuli-Responsive Drug Delivery and Bioimaging

### Permalink

<https://escholarship.org/uc/item/1630x8km>

### Author

Cheng, Chi-An

### Publication Date

2020

### Copyright Information

This work is made available under the terms of a Creative Commons Attribution-NonCommercial-NoDerivatives License, available at <https://creativecommons.org/licenses/by-nc-nd/4.0/>

Peer reviewed|Thesis/dissertation

UNIVERSITY OF CALIFORNIA

Los Angeles

Engineering Multifunctional Mesoporous Silica Nanoparticles  
for Stimuli-Responsive Drug Delivery and Bioimaging

A dissertation submitted in partial satisfaction of the  
requirements for the degree Doctor of Philosophy  
in Bioengineering

by

Chi-An Cheng

2020

© Copyright by

Chi-An Cheng

2020

## ABSTRACT OF THE DISSERTATION

Engineering Multifunctional Mesoporous Silica Nanoparticles  
for Stimuli-Responsive Drug Delivery and Bioimaging

by

Chi-An Cheng

Doctor of Philosophy in Bioengineering

University of California, Los Angeles, 2020

Professor Benjamin M. Wu, Co-Chair

Professor Jeffrey I. Zink, Co-Chair

This dissertation makes contributions to the fields of formulation and delivery of anticancer drugs, antibiotics, and imaging agents, primarily focused on engineering mesoporous silica nanoparticles (MSNs) for stimuli-responsive drug delivery. The strategies and techniques developed in this dissertation will be especially useful for achieving precision medicine or personalized medicine, which is defined as the “right drug, right dosage at right timing to right patient”. Although various emerging approaches for personalized disease treatment that take individual variability into account have been developed, the necessity of delivering the desired therapeutics at the desired time to the specific site of the disease and with accurate dosage remains a challenge. Here we first review the previously reported stimuli-responsive MSNs controlled by supramolecular nanomachines for antibiotic and drug delivery. In the second part of the

dissertation, we report novel MSNs-based nanoparticles engineered to be responsive to noninvasive stimuli, such as alternating magnetic field (AMF) or high-intensity focused ultrasound (HIFU). AMF-responsive drug delivery demonstrates the controlled therapeutic efficacy for pancreatic cancer cells *in vitro* by adjusting different lengths of AMF exposure time. The HIFU-responsive MSNs provide a promising platform for magnetic resonance imaging (MRI)-guided HIFU (MRgHIFU)-stimulated cargo delivery. The change of  $T_1$  reports on the amount of released cargo which is imageable by MRI *ex vivo*. Both AMF-and MRgHIFU-stimulation strategies offer the potential for the spatial, temporal, and dosage control of drug delivery. In the last part, we develop an approach to achieve both high loading and high release amount of a water-insoluble antibiotic clofazimine (CFZ) carried by MSNs by using acetophenone (AP) as a chaperone molecule, solving the water insolubility problem faced when treating multidrug-resistant tuberculosis. The treatment of *Mycobacterium tuberculosis* infected macrophages with optimized CFZ-loaded MSNs shows good therapeutic efficacy *in vitro*. Finally, we develop a hollow mesoporous silica nanoparticle (HMSN) formulated near infrared (NIR) fluorophore IR-140, to realize a novel biocompatible shortwave infrared (SWIR) optical imaging contrast agent for bioimaging with a higher tissue penetration depth. The J-aggregates of IR-140 stabilized inside HMSNs showed the potential to overcome the stability, toxicity, and brightness challenges faced by common SWIR contrast agents.

The dissertation of Chi-An Cheng is approved.

Hsian-Rong Tseng

Holden H. Wu

Benjamin M. Wu, Committee Co-Chair

Jeffrey I. Zink, Committee Co-Chair

University of California, Los Angeles

2020

*To my beloved parents and husband*

## TABLE OF CONTENTS

Abstract .....	ii
Committee Page .....	iv
List of Schemes.....	x
List of Figures .....	xi
List of Tables .....	xxiii
Acknowledgements .....	xxiv
Vita .....	xxx
CHAPTER 1 Introduction	
1.1 Background of Stimuli-Responsive Nanomachines and Caps for Drug Delivery .....	1
1.2 Introduction of The Dissertation .....	4
1.3 Figures .....	7
1.4 References .....	8
CHAPTER 2 Supramolecular Nanomachines as Stimuli-Responsive Gatekeepers on Mesoporous Silica Nanoparticles for Antibiotic and Cancer Drug Delivery	
2.1 Abstract .....	11
2.2 Introduction .....	12
2.3 Supramolecular Nanovalves for Stimuli Responsive Cargo Delivery .....	15
2.4 Supramolecular Snap-Tops for Stimuli Responsive Cargo Delivery .....	33
2.5 Nanopistons and Their Use as Size-Selective Caps .....	35
2.6 Summary .....	36
2.7 Acknowledgment .....	37



2.8	Figures and Tables .....	38
2.9	References .....	58
CHAPTER 3 Spatial, Temporal, and Dose Control of Drug Delivery using Noninvasive Magnetic Stimulation		
3.1	Abstract .....	64
3.2	Introduction .....	65
3.3	Synthesis and Characterization of MnFe <sub>2</sub> O <sub>4</sub> @CoFe <sub>2</sub> O <sub>4</sub> Nanoparticles .....	69
3.4	Synthesis and Characterization of Mag@MSNs-APTS Core@Shell Nanoparticles .....	71
3.5	Synthesis and Characterization of Mag@MSNs-APTS, Mag@MSNs-ACVA, and Mag@MSNs-AMA Core@Shell Nanoparticles .....	72
3.6	Thermal Responsiveness of the Gatekeeper and Bulk Heating- Triggered Cargo Release .....	75
3.7	Alternating Magnetic Field-Triggered Cargo Release .....	77
3.8	Alternating Magnetic Field-Triggered Release of Doxorubicin .....	80
3.9	<i>In Vitro</i> Studies of Cytotoxicity and Stability of the Drug-Delivery System .....	81
3.10	<i>In Vitro</i> Cellular Killing Studies .....	81
3.11	Significance for Potential Biomedical Applications .....	83
3.12	Summary .....	84
3.13	Methods .....	86
3.14	Acknowledgment .....	98
3.15	Scheme and Figures .....	99
3.16	References .....	116
CHAPTER 4 A Responsive Mesoporous Silica Nanoparticle Platform for Magnetic Resonance Imaging-Guided High-Intensity Focused Ultrasound- Stimulated Cargo Delivery with Controllable Location, Time, and Dose		
4.1	Abstract .....	123
4.2	Introduction .....	124

4.3	Design of Ultrasound-Responsive MSNs .....	127
4.4	Gd(DTPA) <sup>2-</sup> Loading, PEG Capping, and PEG Cap Stability at Body Temperature .....	130
4.5	Proof-of-Concept: Ultrasound-Stimulated Release of Gd(DTPA) <sup>2-</sup> ..	132
4.6	MRI-Guided HIFU-Stimulated Release of Gd(DTPA) <sup>2-</sup> and MRI Contrast Change .....	133
4.7	Mechanisms of HIFU-Stimulated Gd(DTPA) <sup>2-</sup> Release .....	137
4.8	Dose and Temporal Control of Released Gd(DTPA) <sup>2-</sup> by MRgHIFU Stimulation Time and Power Level .....	138
4.9	Three-Dimensional Spatial Control of Released Gd-(DTPA) <sup>2-</sup> at the Focal Point of MRgHIFU Stimulation .....	140
4.10	<i>Ex Vivo</i> MRgHIFU-Stimulated Gd(DTPA) <sup>2-</sup> Release and MRI Contrast Change .....	141
4.11	Significance for Potential Biomedical Applications .....	142
4.12	Summary .....	143
4.13	Methods .....	144
4.14	Acknowledgment .....	153
4.15	Scheme, Figures and Tables .....	154
4.16	References .....	178

CHAPTER 5 Facile Strategy Enabling Both High Loading and High Release Amounts of the Water-Insoluble Drug Clofazimine Using Mesoporous Silica Nanoparticles

5.1	Abstract .....	187
5.2	Introduction .....	187
5.3	Synthesis and Characterization of MSNs .....	190
5.4	CFZ Solubility Enhancement .....	191
5.5	CFZ Loading by Using Different Nonaqueous Solvents: AP and DMSO .....	195
5.6	CFZ Release to Aqueous Solution by Using Different Nonaqueous Solvents: AP and DMSO .....	197
5.7	Effect of the CFZ Loading Concentration on CFZ Release .....	198
5.8	Effect of the CFZ Loading Concentration on AP Release .....	199

5.9	Effect of External AP on CFZ Release .....	201
5.10	Antibacterial Effect of AP-Assisted CFZ Delivery by MSNs .....	202
5.11	Summary .....	204
5.12	Methods .....	205
5.13	Acknowledgment .....	210
5.14	Figures and Tables .....	211
5.15	References .....	225
CHAPTER 6	Shortwave Infrared Imaging with J-aggregates Stabilized in Hollow Mesoporous Silica Nanoparticles	
6.1	Abstract .....	230
6.2	Introduction .....	231
6.3	Result and Discussion .....	233
6.4	Summary .....	236
6.5	Methods .....	237
6.6	Acknowledgment .....	262
6.7	Schemes, Figures and Tables .....	263
6.8	References .....	289

## LIST OF SCHEMES

Scheme 3.1	(a) Schematic illustration of the synthesis of azo snap-top core@shell mesoporous silica nanoparticles and triggered release under an alternating magnetic field. (b) Scheme of the conjugation and capping of 3-aminopropyltriethoxysilane (APTS), 4,4'-azobis(4-cyanovaleric acid) (ACVA), 1-adamantylamine (AMA), and $\beta$ -cyclodextrin ( $\beta$ -CD) on the surface of core@shell nanoparticles .....	99
Scheme 4.1	Scheme of the synthesis and HIFU-stimulated release of $\text{Gd}(\text{DTPA})^{2-}$ from PEGylated mesoporous silica nanoparticles (MSNs-PEG). After HIFU stimulation, PEG undergoes bond cleavage and vibration to release $\text{Gd}(\text{DTPA})^{2-}$ .....	154
Scheme 6.1	Synthesis of hollow mesoporous silica nanoparticles (HMSNs) .....	263
Scheme 6.2	Synthesis of IR-140-loaded HMSN-PEG. (A) Overall synthesis starting from Stöber spheres. (B) Detailed schematic of conjugation of polyethylene glycol (PEG) to the surface of HMSN-APTS .....	264

## LIST OF FIGURES

Figure 1.1	TEM images of (A) typical mesoporous silica nanoparticles, (B) large pore silica nanoparticles, and (C) core@shell nanoparticles.....	7
Figure 1.2	Sketch of the three major modes of operation of pore uncapping. (1) Reusable valve where a bulky cyclic molecule has a binding constant to the attached thread-like “stalk” that decreases when stimulated. (2) Reversible valve where the bulky cyclic molecule has a binding constant at a position close to the pore opening that decreases allowing it to slide away from the pore opening but not leave the stalk. (3) A bulky molecule is chemically bonded to the pore opening and the bond is broken when stimulated.....	7
Figure 2.1	(A) A pseudorotaxane on a solid silica support. (B) Graphical representations of operation of nanovalves gating the pore openings on silica particles. (C) Graphical representations of the surface attachment of bistable rotaxanes to silica particles along with a cycle for loading and release of guest molecules....	38
Figure 2.2	The loading of rhodamine B (RhB) molecules, capping of CB[6] rings, and release of RhB by raising the pH using alkyne-functionalized mesoporous silica nanoparticles MCM-41 .....	40
Figure 2.3	Design and preparation of viologen threads (stalk component) and CB[6] (cap) on MSNs that operate under pH-control .....	40
Figure 2.4	Scheme of the synthesis of the mechanized nanoparticles and their operation under oscillating magnetic fields (OMFs) .....	41
Figure 2.5	External heating of Au@MSN@Valve causes dissociation of CB[6] caps from the stalks and release of the cargo molecules from the pores .....	42
Figure 2.6	Depiction of a cross section of a hollow nanoparticle illustrating the wormlike pores connecting the interior to the surrounding solution .....	42
Figure 2.7	Light activation of a pH nanovalve containing a photoacid attached adjacent	

	to an acid-stimulated aniline/ $\alpha$ -CD valve.....	43
Figure 2.8	Depiction of the fully assembled Tf-nanovalue-modified MSN system and its pH-responsive cargo release .....	43
Figure 2.9	(A) Steps of stalk synthesis, cargo loading, capping, and release. (B) Cap dissociation from protonated stalk by low pH. (C) TEM image of the capped MSN .....	44
Figure 2.10	Moxifloxacin-loaded MSNs functionalized with pH-responsive capping system were uptaken into lysosomal compartments in a macrophage. The pH-responsive cap was opened and moxifloxacin was released to kill the intracellular <i>Francisella tularensis</i> .....	45
Figure 2.11	Synthesis of 4-(3-triethoxysilylpropylureido)azobenzene (TSUA)- and (E)-4-((4-(benzylcarbamoyl)phenyl)diazenyl) benzoic acid (BPDB)-modified MCM-41 and two approaches to the operation and function of the azobenzene-modified MCM-41 NPs carrying nanovalves .....	46
Figure 2.12	Cartoon of the red-light-responsive drug delivery system constructed by MSNs modified with mAzo/ $\beta$ -CD supramolecular valves .....	47
Figure 2.13	Design and preparation of ferrocene-based mechanized nanoparticles, which operate under redox or pH control according to the nature of the ring capping the pores .....	47
Figure 2.14	Schematic illustration of the NIR light- or external heating-triggered cargo release from SC[4]A-QAS nanovalves modified AuNR@MSN .....	48
Figure 2.15	Diagram of pillar[5]arenes derivative based MSN drug delivery system and its cargo release triggered by either pH or competitive binding .....	48
Figure 2.16	Design and pH-dependent operation of mechanized nanoparticles .....	49
Figure 2.17	Size illustration of (A) various cargo molecules and (B) azobenzene stalks. (C) Schematic illustration of the fully assembled rotaxane nanovalue and	

	operation .....	50
Figure 2.18	Synthesis and operation of the thermal-sensitive supramolecular platform activable by an oscillating magnetic field .....	51
Figure 2.19	(A) The structure of a weblike megagate using MG-2 as the capping molecule and the relative sizes of the pore, the dextran cargo, and the smaller FDS cargo. (B) Schematic representation of the cyclodextrin attachment onto the silica modified with aldehyde through imine formation. (C) The capping of megagate by MG-1 prevents the dextran from escaping, while FDS can freely diffuse out from the pore. Addition of acid allows the release of dextran.....	52
Figure 2.20	Schematic representation of the self-amplifying chemical sensing process .....	53
Figure 2.21	Synthesis and activation of an enzyme-responsive snap-top system .....	53
Figure 2.22	Synthesis of the alkyne-terminated stopper and assembly of disulfide-based snap-top nanocarriers .....	54
Figure 2.23	Preparation and structure of MSN-GFLGR <sub>7</sub> RGDS/ $\alpha$ -CD snap-top .....	55
Figure 2.24	Schematic illustration of rhodamine B/benzidine inserted in the cavity of $\beta$ -CD and acting like a piston due to the pH change, which makes cargo release ..	55
Figure 2.25	Schematic illustration of the dual-cargo release process. The first cargo release is achieved by lowering of pH and is followed by the second cargo release triggered by the presence of the reducing agent mercaptoethanol.....	56
Figure 3.1	(a) Schematic illustration of the synthesis of MnFe <sub>2</sub> O <sub>4</sub> @CoFe <sub>2</sub> O <sub>4</sub> nanoparticles by a seed-mediated thermal decomposition method. (b) Corresponding transmission electron microscope (TEM) images and (c) diameter distributions of MnFe <sub>2</sub> O <sub>4</sub> and MnFe <sub>2</sub> O <sub>4</sub> @CoFe <sub>2</sub> O <sub>4</sub> nanoparticles after each step .....	100
Figure 3.2	(a) TEM image and (b) size distribution of 11.4 nm MnFe <sub>2</sub> O <sub>4</sub> @CoFe <sub>2</sub> O <sub>4</sub> nanoparticles. (c) Field dependent magnetization curve of MnFe <sub>2</sub> O <sub>4</sub> @CoFe <sub>2</sub> O <sub>4</sub> nanoparticles at 300 K. (d) Time- and concentration-	

	dependent temperature increase profiles of toluene solution containing MnFe <sub>2</sub> O <sub>4</sub> @CoFe <sub>2</sub> O <sub>4</sub> nanoparticles triggered by an alternating magnetic field (AMF) .....	101
Figure 3.3	High angle X-ray diffraction pattern of MnFe <sub>2</sub> O <sub>4</sub> @CoFe <sub>2</sub> O <sub>4</sub> nanoparticles ...	102
Figure 3.4	(a) Fourier-transform Infrared (FT-IR) spectrum and (b) thermogravimetric analysis (TGA) of MnFe <sub>2</sub> O <sub>4</sub> @CoFe <sub>2</sub> O <sub>4</sub> nanoparticles .....	103
Figure 3.5	(a) TEM image of core@shell nanoparticles (Mag@MSNs-APTS). (b) Nitrogen adsorption/desorption isotherms of Mag@MSNs-APTS at 77 K .....	104
Figure 3.6	Size distribution of 55.0 nm Mag@MSNs-APTS core@shell nanoparticles ...	105
Figure 3.7	Dynamic light scattering diameter distribution of Mag@MSNs-APTS in deionized H <sub>2</sub> O at room temperature .....	105
Figure 3.8	(a) Zeta potential values, (b) FT-IR, and (c) TGA of Mag@MSNs, Mag@MSNs-APTS, Mag@MSNs-ACVA, and Mag@MSNs-AMA, respectively. (d) TEM image of Mag@MSNs-AMA. (e) N <sub>2</sub> adsorption/desorption isotherms of Mag@MSNs-AMA at 77 K .....	106
Figure 3.9	(a) The cleavage of C-N bonds caused by bulk heating for 10 min. (b) Zeta potential values of Mag@MSNs-ACVA after 10 min of bulk heating in D.I. water. (c) The release of fluorescein from Mag@MSN- caused by bulk heating trigger in water bath at 37 °C, 60 °C, or 80 °C. (d) Release efficiency of fluorescein from Mag@MSNs- after bulk heating at 23, 37, 60, or 80 °C trigger for 10 min .....	107
Figure 3.10	Time dependent release efficiency of fluorescein from Mag@MSN- caused by bulk heating trigger in water bath at 37, 60, and 80 °C .....	108
Figure 3.11	(a) Dose control of cargo release from Mag@MSNs- by adjusting the AMF “ON” time. (b-f) Time-dependent release profiles of fluorescein through various time periods of magnetic actuation under AMF. (g) Release efficiencies of fluorescein at plateau and the solution temperatures after the	



	various time periods of AMF trigger .....	109
Figure 3.12	TEM images of fluorescein-loaded Mag@MSN-AMA-CD after 10 min exposure of the AMF trigger .....	110
Figure 3.13	(a) The cleavage of C-N bonds caused by 10 min of AMF trigger. (b) Zeta potential values of Mag@MSNs-ACVA before and after 10 min of AMF trigger in D.I. water .....	111
Figure 3.14	Time dependent release profile of fluorescein from Mag@MSNs- through magnetic actuation under AMF for 3 min for 3 cycles .....	112
Figure 3.15	(a) UV-Vis spectra of Mag@MSNs-AMA-CD and doxorubicin (DOX)-loaded Mag@MSNs-AMA-CD in PBS. (b-d) Time-dependent release profiles of DOX from Mag@MSNs- in PBS through various time periods of magnetic actuation under AMF .....	113
Figure 3.16	(a) Cytotoxicity of Mag@MSNs-AMA-CD to PANC-1 determined by a CCK-8 assay. (b) Cytotoxicity of DOX-loaded Mag@MSNs-AMA-CD. (c) Cytotoxicity of DOX-loaded Mag@MSNs-AMA-CD after 4 h treatment and 12 h grow in the regular culture medium .....	114
Figure 3.17	(a) <i>In vitro</i> cellular killing effect of DOX-loaded Mag@MSNs-AMA-CD after AMF exposure. (b) The viability of PANC-1 after treatment by Mag@MSNs-AMA-CD or DOX-loaded Mag@MSNs-AMA-CD. (c) Fluorescence microscope images of PANC-1 cells (ii) after 4 h treatment by DOX-loaded Mag@MSNs-AMA-CD and (iii) followed by 10 min of AMF exposure. Cells without the treatment by nanoparticles is shown in (i) .....	115
Figure 4.1	Size distribution of $91.6 \pm 15.1$ nm MSNs .....	155
Figure 4.2	Characterizations of MSNs, MSNs-APTS, and MSNs-PEG .....	156
Figure 4.3	Pore diameter distribution of MSNs, MSNs-APTS, MSNs-PEG, and Gd(DTPA) <sup>2-</sup> -loaded MSNs-PEG .....	157
Figure 4.4	The colloidal stability of MSNs-PEG and MSNs-APTS in PBS after being	

	kept undisturbed for 30 min, 1 day, and 3 days at room temperature .....	157
Figure 4.5	Ultrasound-stimulated Gd(DTPA) <sup>2-</sup> release using a probe sonicator .....	158
Figure 4.6	TEM image of MSNs-PEG after 30 min of probe sonication .....	159
Figure 4.7	(a-b) Set-up of the MRgHIFU system. (c) Top view of the HIFU transducer without cooling water and cap .....	160
Figure 4.8	HIFU-stimulated Gd(DTPA) <sup>2-</sup> release in a tissue-mimicking agarose phantom and the resulting observable MRI contrast changes .....	161
Figure 4.9	The percentage of T <sub>1</sub> -weighted image intensity changes of the MRgHIFU-stimulated water-dispersed Gd(DTPA) <sup>2-</sup> -loaded MSNs-PEG, unstimulated water-dispersed Gd(DTPA) <sup>2-</sup> -loaded MSNs-PEG, unstimulated Gd(DTPA) <sup>2-</sup> -loaded MSNs-PEG mixed in methylcellulose (2.5 wt %) and concentrated milk (v/v = 1/1), the mixture of methylcellulose (2.5 wt %) and concentration milk (v/v = 1/1), and agarose phantom background .....	162
Figure 4.10	(a) Schematic illustration showing the shortening and lengthening effect of loaded and released Gd(DTPA) <sup>2-</sup> on T <sub>1</sub> relaxation time. (b) T <sub>1</sub> relaxivity (r <sub>1</sub> ) values of free Gd(DTPA) <sup>2-</sup> , and Gd(DTPA) <sup>2-</sup> -loaded MSNs-PEG before and after HIFU stimulation (3 cycles of 1 min, 74 W) .....	163
Figure 4.11	(a) r <sub>1</sub> values of free Gd(DTPA) <sup>2-</sup> , and Gd(DTPA) <sup>2-</sup> -loaded MSNs-PEG without and with 30 min of ultrasound stimulation by the probe sonicator. (b) T <sub>1</sub> -weighted images of each sample in (a) at different Gd(III) concentrations .....	164
Figure 4.12	(a) r <sub>1</sub> and (b) r <sub>2</sub> values of Gd(DTPA) <sup>2-</sup> with or without HIFU stimulation (3 cycles of 1 min, 74 W) .....	165
Figure 4.13	(a) r <sub>1</sub> and (b) r <sub>2</sub> values of Gd(DTPA) <sup>2-</sup> with or without 30 min of probe sonication.....	165
Figure 4.14	(a) Temperature increase profiles of Gd(DTPA) <sup>2-</sup> -loaded MSNs-PEG in deionized H <sub>2</sub> O and in methylcellulose gel/milk mixture during the HIFU stimulation (74 W) measured by dynamic MRI temperature mapping. (b)	

	MALDI-TOF spectra of PEG ( $M_n$ 2,000 Da) without HIFU stimulation, after 3 cycles of 1 min HIFU stimulation, and 2 cycles of 5 min HIFU stimulation ...	166
Figure 4.15	The colloidal stability of HIFU-stimulated MSNs-PEG and unstimulated MSNs-PEG in deionized H <sub>2</sub> O after being kept undisturbed for 30 min .....	167
Figure 4.16	Dose control of released Gd(DTPA) <sup>2-</sup> and MRI contrast enhancement with different HIFU stimulation parameters .....	168
Figure 4.17	Ultrasound-stimulated Gd(DTPA) <sup>2-</sup> release using the probe sonicator and the resulting T <sub>1</sub> changes .....	169
Figure 4.18	The percentage of T <sub>1</sub> -weighted image intensity changes of the methylcellulose gel/milk-mixed Gd(DTPA) <sup>2-</sup> -loaded MSNs-PEG (a) after 1, 3, 5, or 10 min of HIFU stimulation (74 W); (b) after 3 min of HIFU stimulation at electrical power levels of 9 W, 74 W, or 290 W. (c) Time-dependent T <sub>1</sub> -weighted image intensity of Gd(DTPA) <sup>2-</sup> -loaded MSNs-PEG with multiple HIFU stimulations (3 cycles of 1 min, 74 W) .....	169
Figure 4.19	TEM image of MSNs-PEG after 3 min of HIFU stimulation .....	170
Figure 4.20	3-D control of the MRgHIFU focal point and stimulated cargo release. (a) The axial, sagittal and coronal cross sections of the sample well of interest in the agarose phantom. (b) The color-coded $\Delta$ T <sub>1</sub> -weighted images in three orientations .....	171
Figure 4.21	<i>Ex vivo</i> MRgHIFU-stimulated Gd(DTPA) <sup>2-</sup> release and the controllable MRI contrast changes. (a) T <sub>1</sub> -weighted image before HIFU stimulation of the chicken breast tissue injected with methylcellulose gel containing Gd(DTPA) <sup>2-</sup> -loaded MSNs-PEG. The color-coded $\Delta$ T <sub>1</sub> -weighted images of the HIFU-stimulated sample, unstimulated sample, and tissue background after each cycle of HIFU stimulation (3 min, 2.5 MHz, 8 W) are shown. (b) The percentage of T <sub>1</sub> -weighted image intensity changes of the background, unstimulated sample, and HIFU-stimulated sample after each cycle of HIFU stimulation .....	172

Figure 4.22	<i>Ex vivo</i> MRgHIFU-stimulated Gd(DTPA) <sup>2-</sup> release and the controllable MRI contrast changes in three-dimensional space. The T <sub>1</sub> -weighted image of the chicken breast before the HIFU stimulation was shown in (a) axial, (b) sagittal, and (c) coronal orientations. The color-coded Δ T <sub>1</sub> -weighted images, acquired by subtracting the T <sub>1</sub> -weighted images before from the one after 3 cycles of HIFU stimulation, were shown in three-dimensional space .....	173
Figure 4.23	<i>Ex vivo</i> MRgHIFU control experiment. (a) A piece of chicken breast tissue was injected with methylcellulose gel only. (b) The percentage of T <sub>1</sub> -weighted image intensity changes of the tissue background and the HIFU-stimulated gel after each cycle of HIFU stimulation (3 min, 2.5 MHz, 8 W). (c) Color-coded Δ T <sub>1</sub> -weighted images of the chicken tissue after each cycle of HIFU stimulation .....	174
Figure 4.24	Preparation of the agarose phantom .....	175
Figure 5.1	Chaperone-assisted delivery strategy for water-insoluble clofazimine drugs ...	211
Figure 5.2	Characterization of MSNs .....	212
Figure 5.3	Clofazimine (CFZ) solubility enhancement in the presence of various hydrotropes .....	213
Figure 5.4	CFZ solubility enhancement in the presence of different concentrations of acetophenone (AP) in H <sub>2</sub> O .....	214
Figure 5.5	Conventional method and chaperone-assisted method for water-insoluble CFZ loading and release .....	215
Figure 5.6	UV-Vis spectra of CFZ in AP as a function of concentration, calibration curve of CFZ in AP at room temperature, and photograph of CFZ dissolved in AP ...	216
Figure 5.7	UV-Vis spectra of time-dependent CFZ release in buffer solution by using (a) dimethyl sulfoxide (DMSO) or (b) AP as loading solvents .....	217
Figure 5.8	UV-Vis spectra, calibration curve of CFZ in buffer solution at room	

	temperature, and photograph of CFZ dissolved in buffer solution .....	218
Figure 5.9	Time-dependent release capacity of (a) CFZ and (c) AP and release efficiency of (b) CFZ and (d) AP in buffer solution .....	219
Figure 5.10	(a) Concentration dependent UV-Vis spectra and (b) calibration curve of AP in ethanol buffer solution .....	220
Figure 5.11	Time-dependent release efficiency of CFZ in buffer solution with or without the addition of AP to the buffer solution.....	221
Figure 5.12	(a) Schematic illustration of applying chaperone-assisted CFZ delivery strategy to selectively killing <i>M. tuberculosis</i> in macrophage. (b) AP/CFZ loaded MSNs kill <i>M. tuberculosis in vitro</i> in macrophage cultures. <i>M. tuberculosis</i> -infected THP-1 macrophages were untreated, treated with MSN loaded with AP (AP-MSN), treated with MSN loaded with CFZ and AP (AP/CFZ-MSN), or treated with CFZ dissolved in a mixture of DMSO and H <sub>2</sub> O (CFZ/DMSO) for 4 days .....	222
Figure 6.1	(A) Regions of the electromagnetic spectrum employed for optical imaging. (B) J-aggregation and characteristic photophysical properties. (C) IR-140. (D) Work reported herein: the stabilization of IR-140 J aggregates in hollow mesoporous silica nanoparticles (HMSNs) to result in biocompatible shortwave infrared (SWIR)-emissive contrast agents .....	265
Figure 6.2	TEM images of (A) Stöber silica spheres, (B) dSiO <sub>2</sub> @MSNs, and (C) HMSNs	266
Figure 6.3	(A) Schematic of loading IR-140 into HMSNs. (B) Washing conditions facilitate J-aggregation. Ten mg/mL HMSNs were combined with 10 mM IR-140 in DMSO and washed with PBS with and without sonication. Pre-wash spectrum, diluted 1:350 is shown. Loading control for solid, non-porous Stöber spheres is shown. (C/D) TEM images of HMSNs with (D) and without (C) IR-140 treatment .....	267
Figure 6.4	UV/Vis/NIR spectra of HMSNs or dSiO <sub>2</sub> @MSNs containing IR-140. The	

	loading concentrations of IR-140 were (A) 20 mM and (B) 5 mM .....	268
Figure 6.5	Control experiment with Stöber silica spheres. (A) The zeta potential of Stöber silica spheres (black), and Stöber silica spheres-APTS (red) in D.I. water at room temperature. (B/C/D) UV/Vis/NIR spectra of Stöber silica spheres or Stöber silica spheres-APTS containing IR-140. The loading concentrations of IR-140 were (B) 20 mM, (C) 10 mM, or (D) 5 mM .....	269
Figure 6.6	UV/Vis/NIR spectra of IR-140 loaded HMSNs, Stöber silica spheres, Stöber silica spheres-APTS, or dSiO <sub>2</sub> @MSNs .....	270
Figure 6.7	The loading capacity of IR-140 in HMSNs or HMSNs-APTS at different IR-140 loading concentrations .....	271
Figure 6.8	Nitrogen adsorption /desorption isotherms of (A) HMSNs, (C) HMSNs-APTS, and (E) dSiO <sub>2</sub> @MSNs. Pore diameter distributions of (B) HMSNs, (D) HMSNs-APTS, and (F) dSiO <sub>2</sub> @MSNs .....	272
Figure 6.9	TEM images of HMSNs with (C) and without (A) IR-140 treatment. (B) As a control, HMSNs were washed with PBS but without the loading of IR-140. (D) Mixture of HMSNs with and without IR-140 treatment .....	273
Figure 6.10	UV/Vis/NIR spectra of HMSNs-APTS containing IR-140 for dye loading concentrations of 20 mM, 10 mM, or 5 mM in PBS, after washing the particles with PBS .....	274
Figure 6.11	The dynamic light scattering size distribution of HMSNs-APTS, HMSNs-APTS containing IR-140, and HMSNs-PEG containing IR-140 in PBS .....	275
Figure 6.12	The zeta potential of HMSNs, HMSNs-APTS, HMSNs-APTS containing IR-140, and HMSNs-PEG containing IR-140 in D.I. water .....	276
Figure 6.13	(A) Normalized absorption and emission of IR-140 J-aggregate in HMSNs-PEG, J-aggregate in solution, and monomer. (B) Emission (1000–1700 nm) of IR-140 monomer, J-aggregate in solution and J-aggregate in HMSNs-PEG	

	upon 980 nm excitation. (C) Normalized relative absorption of IR-140 J-aggregate in 35% DMSO/0.9% NaCl in water and in HMSNs-PEG in PBS on day zero and day 1 or 14. (D) Photostability under laser irradiation (97 mW/cm <sup>2</sup> ) at 980 nm for IR-140 J-aggregate in HMSNs-PEG and IR-140 J-aggregate in 35% DMSO/0.9% NaCl in water, and at 785 nm for monomer in DMSO .....	277
Figure 6.14	UV/Vis/NIR characterization of IR-140 J-aggregate formation in solution at 0.01 mg/mL in (A) DMSO/water (B) DMSO/1xPBS and (C) DMSO/0.9% NaCl in water .....	278
Figure 6.15	Emission of monomer and J-aggregate states of IR-140 under 980 nm excitation. (A) Absorbance traces of samples used in vial images in B and in Figure 4.13B, baseline corrected to 521 nm. (B) Images of IR-140 monomer in DMSO, IR-140 J-aggregate in solution and J-aggregate in HMSNs-PEG under 980 nm irradiation ( $99 \pm 3 \text{ mWcm}^{-1}$ ) .....	279
Figure 6.16	Stability of J-aggregates over time, displayed as the normalized, relative absorbance remaining for IR-140 in HMSNs-PEG after 14 days, and IR-140 in solution after 1 day .....	280
Figure 6.17	Photostability of J-aggregates in the presence and absence of oxygen. (A) Raw data of IR-140 J-aggregate in 35 % DMSO/0.9% NaCl at 0.01 mg/mL under 980 nm irradiation with 79 mWcm <sup>-2</sup> power density. (B) Raw data of HMSNs-PEG loaded with IR-140 at 1.0 mg/mL in 1x PBS under 980 nm irradiation with 101 mWcm <sup>-2</sup> power density .....	281
Figure 6.18	Cytotoxicity study of IR-140 loaded HMSNs-PEG examined by a CCK-8 assay .....	282
Figure 6.19	Whole-mouse imaging at 16 fps (980 nm, 91 mW/cm <sup>2</sup> excitation; 1000–1700 nm collection) upon i.v. delivery of IR-140 HMSNs-PEG. Background subtracted stills were averaged over 5 frames at 3 s (A), 8 s (B), 25 s (C), and 120 s (D) post injection .....	283

Figure 6.20	Images from the front (A/C) and left side (B/D) of a nude mouse directly after vascular clearance (>2 m post injection) (A/B), and after 50 minutes (C/D), showing uptake of IR-140 loaded HMSNs-PEG in the liver and spleen .....	284
Figure 6.21	HMSN or HMSN-APTS used in this work .....	285
Figure 6.22	Absorption coefficient of IR-140 monomer in DMSO .....	285
Figure 6.23	Uncorrected absorption coefficient of IR-140 J-aggregate in 35% DMSO/0.9% NaCl in water .....	286
Figure 6.24	Corrected absorption coefficient of IR-140 J-aggregate in 35% DMSO/0.9% NaCl in water .....	286
Figure 6.25	Solvent corrected integrated fluorescence intensity versus absorbance plots for (A) IR-26 and (B) IR-140 J-aggregate, also corrected for reabsorption .....	287
Figure 6.26	Photobleaching data plotted as the $\ln[A]$ vs time and the corresponding linear fits .....	287



## LIST OF TABLES

Table 2.1	Cell lines used in studies with supramolecular nanomachines .....	57
Table 2.2	Animal models used in studies with supramolecular nanomachines .....	57
Table 4.1	Brunauer-Emmett-Teller (BET) surface area, total pore volume, and average pore diameter of MSNs, MSNs-APTS, MSNs-PEG, and Gd(DTPA) <sup>2-</sup> -loaded MSNs-PEG analyzed from the N <sub>2</sub> adsorption/desorption isotherms .....	176
Table 4.2	Summary of the Gd(DTPA) <sup>2-</sup> release efficiency and temperature increase using various HIFU parameters (power levels and stimulation times) .....	177
Table 5.1	Chemical structures of possible hydrotropes for clofazimine (CFZ) and their water solubilities .....	223
Table 5.2	Summary of the amount of loaded CFZ and acetophenone (AP) in mesoporous silica nanoparticles (MSNs) (nmole/mg) and the mole ratio of AP/CFZ loaded in MSNs .....	224
Table 6.1	Photophysical characterization of IR-140 .....	288
Table 6.2	Photobleaching rates of IR-140 .....	288
Table 6.3	Photobleaching rates and values used in calculations and corrections .....	288

## ACKNOWLEDGEMENTS

Pursuing a doctorate degree in the United States has always been in my career vision since childhood, challenging but very beautiful. I am glad that my passion for growing into a Renaissance Woman let me pretty much enjoy the life of asking questions as a bioengineer and approaching questions as a chemist, even if stepping into the world of engineering is kind of beyond my expectation. Here, I would like to take special privilege to acknowledge people who helped me fulfill my vision, supported me through difficulties, and whom I shared my good times and bad times with.

First, I would like to deeply thank my Ph.D. advisor, Prof. Jeffrey Zink, for being such a supportive and hands-off P.I. He has always been so considerate and encourageable so that I was able to confidently take a leap of faith in things that interested me. His passion toward science has inspired me greatly. “The happiest people have jobs that don’t feel like work. That’s why we scientists work on Saturdays, because it’s fun.” This is what he said when asked to give advice for students, and the fact that I was able to work happily in lab on Saturdays and even till late nights is just a good example of being stimulated by his excitement for science. He always did his best to prepare us for every opportunities. Although I could not remember exactly what he told me in the end of one personal meeting that he squeezed time out to go through my slide deck before I left for a postdoc onsite interview, I would never forget what he would like to convey to me— “It is your turn now. Take your best shot!” I would also like to show my sincere gratitude to my committee co-chair, Prof. Benjamin Wu, for his continuous support and consideration. I look forward to our spicy hotpot meeting in Boston.

I enjoy and appreciate the pleasant and productive collaborations across disciplines with Prof. Marcus Horwitz, Prof. Oliver Bruns, Prof. Yung-Ya Lin, Prof. Caius Radu, and particularly, Prof. Holden Wu and Prof. Ellen Sletten. Without their guidance and support, I would not have finished my Ph.D. studies and dissertation at this moment. I was fond of all the meetings we had— we stirred up innovative ideas, we brought solutions according to people’s expertise, and we excitingly presented data thirsting for feedback from the groups. Working on more than ten projects in four and a half years would not have been possible without talented scientists and students from their labs— Dr. Le Zhang, we could not have our “costly” magnetic resonance imaging-guided high-intensity focused ultrasound for drug delivery work completed and published in *J. Am. Chem. Soc.* without his expertise and hard work; Emily (Maly) Cosco, a clever organic chemist and photophysician, from whom I experienced and learned the beauty of photophysics, without her knowledge and efforts we could not publish our first collaborative work in *J. Am. Chem. Soc.*; Dr. Bai-Yu Lee and Dr. Daniel Clemens, whose expertise in bacteria encouraged me to deeply explore real life problems and our collaborative work has turned out to be my first paper in the United States. I would also like to thank other collaborators, including Shyam Ramakrishnan and Jakob Lingg for their supportive animal work in our shortwave infrared imaging study in Germany; Dr. Sayoni Ray and Dr. Zhao Li, for their efforts in our study of magnetic heating-triggered cargo release using liposomes; Dr. Soumya Poddar and Roy Pan, for their work in our finally completed potent drug delivery project; Daniel Estabrook and John Chapman, for their hard work on our ongoing fluoruous-emulsions project.

I am so thankful to have worked with such great colleagues in the Zink lab. I would especially

like to acknowledge Dr. Bastian Ruehle and Dr. Philippe Saint-Cricq-Riviere, who have led me to the research journey when I first joined the Zink group. Their insightful ideas and taking time to teach me the fundamentals of different techniques have allowed me to quickly go deep into the most important scientific questions. I would like to thank all my labmates, including Prof. Kun Nie, Prof. Changli Zhang, Prof. Sandra Sanchez-Salcedo, Dr. Wen-Yen Huang, Dr. Zilu Li, Dr. Jonathan Brosmer, Dr. Sheba Plamthottam, Dr. Navnita Kumar, Dr. Yao Cai, Dr. Qilin Yu, Dr. Yijun Xie, Dr. Chia-Jung Yu, Ruining Wang, Fang-Chu Lin, Tian Deng, and Jaime Fidel Ruiz-Robles. Special acknowledgment goes to my husband, Dr. Wei Chen, who is also my mentor and partner in both life and work. Thank you to Wei for all his support, and for always listening to me when I talked about ups and downs throughout all these years. It is just so wonderful to discuss on how to improve the drug loading capacity of nanoparticles with my significant other at home while doing dishes or even while lying on the couch watching TV. Nothing could be more pleasant than achieving goals together with him.

My life in Los Angeles would not be so eventful without friends and seniors whom I shared sweet memories with, including Dr. Cheng-Wei Lin, Wai H. Mak, Dr. Yu-Jen (Alex) Jan, and Dr. Po-Hung Hsieh, Dr. Yan-Kai Tzeng, Dr. Yiliu Wang, Prof. Yi-Hsin Liu, Prof. Si-Han Wu, Prof. Yi-Ping Chen, Monica Sandoval Perez, Yasuyuki Kato, Dr. Eugene Kung, Dr. Chi-Ping Liu, Sin-Kuan Lee, Yu-Chieh Wu and Dr. Jer-Yu Jeng. A special acknowledgment goes to Prof. Hsian-Rong Tseng, for being such a good role model and for patiently and continuously mentoring me. I would never forget his expectation and all his efforts to help me become a better me. I appreciate Dr. Linya Wang for leading me into the world of event organization and management, where we

amazingly attracted 300 people coming from around the world to attend our SoCal Taiwanese Biotechnology Symposium. I would like to show my sincere gratitude to Mr. Yang-Chan Chang and Ms. Zoe Hsu from Science and Technology Division of Taipei Economic and Cultural Office in Los Angeles, for giving me so many wonderful opportunities to host VVIP in different events and connect with amazing people. I would like to thank my oldest and dearest friends Abby and her husband Spencer and boy Melvin, Janice, Natasha, Xiaoling, Yi-Ling, Ru-Fang and his husband Lantis, Grape, and Ming-Ching, for all the fun conversations and for always standing by my side. I could not have survived without them.

Finally, I would like to deeply thank my parents for their support throughout my entire life and for fostering my curiosity and creativity. Their encouragement along the way makes me dream big with no worries.

Part of Chapter 1 (Section 1.1), is reprinted and adapted with permission from (Kumar, N.; Chen, W.; Cheng, C. A.; Deng, T.; Wang, R.; Zink, J. I. “Stimuli-Responsive Nanomachines and Caps for Drug Delivery” *Enzymes* **2018**, *43*, 31–65). Copyright 2018 Elsevier. Co-author contributions: Kumar, N., Chen, W., Cheng, C. A.; Deng, T., Wang, R., and Zink, J. I. reviewed the literature and drafted the manuscript of this book chapter. Jeffrey I. Zink was the P.I.

Chapter 2 is reprinted and adapted with permission from (Cheng, C. A.; Deng, T.; Lin, F. C.; Cai, Y.; Zink, J. I. “Supramolecular Nanomachines as Stimuli-Responsive Gatekeepers on Mesoporous Silica Nanoparticles for Antibiotic and Cancer Drug Delivery” *Theranostics* **2019**, *9*, 3341–3364. Copyright 2019 Ivyspring. Co-author contributions: Cheng C. A., Deng T., Lin F. C. and Cai Y. reviewed the literature and drafted the manuscript of this review article. Jeffrey I. Zink

was the P.I.

Chapter 3 is reprinted and adapted with permission from (Chen, W.; Cheng, C. A.; Zink, J. I. “Spatial, Temporal, and Dose Control of Drug Delivery using Noninvasive Magnetic Stimulation” *ACS Nano* **2019**, *13*, 1292-1308) Copyright 2019 American Chemical Society. Co-author contributions: Chen W. and Cheng C. A. designed and performed all the experiments. Jeffrey I. Zink was the P.I.

Chapter 4 is reprinted and adapted with permission from (Cheng, C. A.; Chen, W.; Zhang, L.; Wu, H. H.; Zink, J. I. “A Responsive Mesoporous Silica Nanoparticle Platform for Magnetic Resonance Imaging-Guided High-Intensity Focused Ultrasound-Stimulated Cargo Delivery with Controllable Location, Time, and Dose” *J. Am. Chem. Soc.* **2019**, *141*, 17670–17684. Copyright 2019 American Chemical Society. Co-author contributions: Cheng C. A. and Chen W. designed and performed the synthesis and characterization of material, and all the chemistry related studies. Zhang L. performed the magnetic resonance imaging-guided high intensity focused ultrasound experiments experiments. Holden H. Wu and Jeffrey I. Zink were the P.Is.

Chapter 5 is reprinted and adapted with permission from (Chen, W.; Cheng, C. A.; Lee, B. Y.; Clemens, D. L.; Huang, W. Y.; Horwitz, M. A.; Zink J. I. “Facile Strategy Enabling Both High Loading and High Release Amounts of the Water-Insoluble Drug Clofazimine Using Mesoporous Silica Nanoparticles” *ACS Applied Materials & Interfaces* **2018**, *10*, 31870-31881) Copyright 2018 American Chemical Society. Co-author contributions: Chen W., Cheng C. A., and Huang W. Y. designed and performed the synthesis and characterization of material, and all the chemistry related studies. Lee B. Y., and Clemens D. L. performed the cells and bacteria studies. Marcus A.

Horwitz, and Jeffrey I. Zink were the P.Is.

Chapter 6 is reprinted and adapted with permission from (Chen, W.; Cheng, C. A.; Cosco, E. D.; Ramakrishnan, S.; Lingg, J. G. P.; Bruns, O. T.; Zink, J. I.; Sletten, E. M. “Shortwave Infrared Imaging with J-aggregates Stabilized in Hollow Mesoporous Silica Nanoparticles” *J. Am. Chem. Soc.* **2019**, *141*, 12475–12480) Copyright 2019 American Chemical Society. Co-author contributions: Chen W., Cheng C. A., and Cosco E. D. performed the synthesis and characterization of materials, and photophysics. Cheng C. A. performed the cell studies. Cosco E. D., Ramakrishnan S., and Lingg J. G. P. performed the shortwave infrared imaging and animal studies. Oliver T. Bruns, Jeffrey I. Zink, and Ellen M. Sletten were the P.Is. The texts of introduction, result and discussion were mainly organized and written by Professor Ellen M. Sletten when preparing the manuscript for publication.

## VITA

- 2015 – 2020 Graduate Student with Prof. Jeffrey I. Zink  
University of California, Los Angeles  
Los Angeles, California
- 2019 – 2020 Dissertation Year Fellowship (DYF)  
University of California, Los Angeles  
Los Angeles, California
- 2019 Research Showcase Travel Award for Fall 2019 ACS National Meeting  
University of California, Los Angeles  
Los Angeles, California
- 2013 – 2014 Patent engineer  
Jianq Chyun IP Group  
Taipei, Taiwan
- 2009 – 2012 Research assistant with Prof. Huan-Cheng Chang  
Academia Sinica  
Taipei, Taiwan
- 2011 Dean's Award of College of Science (to top 10 % graduates)  
National Taiwan University  
Taipei, Taiwan
- 2009 – 2011 Master student with Prof. Huan-Cheng Chang  
National Taiwan University  
Taipei, Taiwan
- 2009 Dean's Award of College of Science (to top 10 % graduates)  
National Taiwan University  
Taipei, Taiwan
- 2005 – 2009 Bachelor of Science with Prof. Huan-Tsung Chang  
National Taiwan University  
Taipei, Taiwan



2005 – 2009 Academic Excellence Awards (to top 5 % students, for four semesters)  
National Taiwan University  
Taipei, Taiwan

2008 Outstanding Teaching Assistant  
National Taiwan University  
Taipei, Taiwan

Selected Publications # equal contribution

8. **Cheng, C. A.**#; Chen, W.#; Zhang, L.; Wu, H.; Zink, J. I. A Responsive Mesoporous Silica Nanoparticle Platform for Magnetic Resonance Imaging-Guided High-Intensity Focused Ultrasound-Stimulated Cargo Delivery with Controllable Location, Time, and Dose, *J. Am. Chem. Soc.* **2019**, *141*, 17670–17684.
7. Chen, W.#; **Cheng, C.A.**#; Cosco, E.D.#; Ramakrishnan, S.; Lingg, J.G.P.; Bruns, O.T.; Zink, J.I.; Sletten, E.M., “Shortwave Infrared Imaging with J-aggregates Stabilized in Hollow Mesoporous Silica Nanoparticles.” *J. Am. Chem. Soc.* **2019**, *141*, 12475–12480.
6. **Cheng, C. A.**; Deng, T.; Lin, F. C.; Cai, Y.; Zink, J. I. Supramolecular Nanomachines as Stimuli-Responsive Gatekeepers on Nanoparticles for Antibiotic and Cancer Drug Delivery, *Theranostics* **2019**, *9*, 3341–3364. (Selected as back cover)
5. Ray, S.; **Cheng, C. A.**; Chen, W.; Li, Z. Zink, J. I., Lin, Y. Y. Magnetic Heating Stimulated Cargo Release with Dose Control using Multifunctional MR and Thermosensitive Liposome, *Nanotheranostics* **2019**, *3*, 166–178. (Selected as front cover)
4. Chen, W.#; **Cheng, C.A.**#; Zink, J.I., “Spatial, Temporal, and Dose Control of Drug Delivery Using Noninvasive Magnetic Stimulation.” *ACS Nano* **2019**, *13*, 1292–1308.
3. Chen, W.#; **Cheng, C.A.**#; Lee, B.Y.; Clemens, D.L.; Huang, W.Y.; Horwitz, M.A.; Zink, J.I., “Facile Strategy Enabling Both High Loading and High Release Amounts of the Water-Insoluble Drug Clofazimine Using Mesoporous Silica Nanoparticles.” *ACS Appl. Mater. Interfaces* **2018**, *7*, 31870–31881.
2. Wu, T. J.; Tzeng, Y. K.; Chang, W. W.; **Cheng, C. A.**; Kuo. Y.; Chien, C. H.; Chang, H. C.; Yu, J. Tracking the Engraftment and Regenerative Capabilities of Transplanted Lung Stem Cells Using Fluorescent Nanodiamonds, *Nature Nanotechnology* **2013**, *8*, 682–689.
1. Fang, C. Y.#; V, V.#; **Cheng, C. A.**#; Yeh, S. H.; Chang, C. F.; Li, C. L.; Chang, H. C. The Exocytosis of Fluorescent Nanodiamond and Its Use as a Long-Term Cell Tracker, *Small* **2011**, *7*, 3363–3370.

# CHAPTER 1

## Introduction

This introduction consists of two parts. In section 1.1, I provide a background of the field adapted and reprinted with permission from a review book chapter (Navnita Kumar, Wei Chen, **Chi-An Cheng**, Tian Deng, Ruining Wang, Jeffrey I. Zink *Enzymes* **2018**, *43*, 31–65). Copyright 2018 Elsevier. Co-author contributions: Kumar, N., Chen, W., Cheng, C. A.; Deng, T., and Wang, R. reviewed the literature and drafted the manuscript of this book chapter. Jeffrey I. Zink was the P.I.

In section 1.2, I introduce and give an overview of the research work in Chapter 3 to 6 of my dissertation.

### 1.1 Background of Stimuli-Responsive Nanomachines and Caps for Drug Delivery

Major objectives in nanomedicine and nanotherapy include: the ability to trap therapeutic molecules inside of nano-carriers; carry therapeutics to the site of the disease with no leakage; release high local concentrations of drug; release only on demand—either autonomous or external; and kill the cancer or an infectious organism. In this section we focus on mesoporous silica nanoparticles (MSNs) as the nano-carriers and nanomachines or related capping agents to trap, carry and release therapeutic molecules. Localized release of high concentrations of therapeutics produce low concentrations when diluted in the total volume of blood and reduce off-target side effects. Nanomachines that carry out the stimuli-responsive local release of drugs consist of a solid support (the MSN) and moving parts (molecules that undergo large amplitude motion) that respond to either external spatial and temporal control, or to internal chemical stimuli specific to the site of the disease.

The MSNs that are the backbone of the drug delivery platforms are the result of two key discoveries: the sol–gel synthesis of silica and self-assembling surfactant templates of the pores.

Silica,  $\text{SiO}_2$ , is one of the most abundant minerals on earth. A solution-based synthesis was first reported in 1847 by Ebelmen who discovered that alkoxysilanes formed an amorphous form of silica when exposed to moisture.<sup>1</sup> This reaction is now known as a sol–gel synthesis.<sup>2</sup> The initially formed gel can be dried to produce a xerogel under mild conditions, and organic or biomolecules that are dissolved in the initial solution can be trapped in the forming glass.<sup>3</sup> Trapped enzymes can be stabilized in the amorphous glass, retain their enzymatic reactive properties, and be used as biosensors.<sup>4,5</sup>

The second key discovery, independently discovered by several groups, was that liquid crystalline phases of surfactant molecules can be used as templates to form highly structured pores in sol–gel glass. The structure that is primarily discussed in this section involves rod-shaped surfactant structures that are encapsulated in glass and upon removal by extraction or calcination leave behind empty tubular pores. The most famous example involved a cetylammmonium halide template (CTAB) that was first reported in the patent literature in 1971, independently reported in 1990, then again in 1991 by Beck *et al.* and now known as “MCM41”.<sup>6-8</sup> The as-synthesized materials were multi-sized aggregates, but further refinements by many groups ultimately led to controllable synthesis of both nanofilms<sup>9-13</sup> and nanospheres. The latter structures containing mesopores (between 2 and 8 nm) are shown in **Figure 1.1** and discussed in this section.

MSNs have remarkable properties. Typical particles discussed in this section are spheres about 100nm in diameter with tubular pores about 2.5 nm in diameter. One gram of particles has a surface area of about 1000  $\text{m}^2$  and a pore volume of about 1  $\text{cm}^3$ . Because typical anticancer drugs have a density of about 1  $\text{g}/\text{cm}^3$ , the carrying capacity can be 100 wt% (although this upper limit is rarely achieved because of imperfect molecular packing).

Are mesostructured silica nanoparticles safe? The answer is generally yes. It is beyond the scope of this discussion to go into detail, but it is important to note that “not all silica is created

equal”; some forms such as “fumed” silica made at very high temperatures have very different properties from those of solution-based sol–gel silica.<sup>2,14</sup> Many *in vivo* studies have been carried out with the latter with no adverse effects from the nanoparticles. It is also important to note that silica dissolves in water; ocean water contains enough silicic acid that diatoms form biomineralized silica structures. Silica is excreted by mammals in the feces and urine.

Methods of chemically derivatizing silica surfaces are well established and can be applied to MSNs. The molecules to be attached can be added to the initial preparation solution (co-synthesis) or after formation of the MSNs (post-synthesis grafting). Pure MSNs aggregate in aqueous solution, but chemically attaching charged molecules to the outer surfaces stabilizes colloidal suspensions. Fluorescent molecules are attached in order to use the particles for imaging applications; biomolecules are attached to actively target cancer cells.

The diverse capping systems can be broadly categorized into three main groups as seen in **Figure 1.2**. Reusable caps are based on reversible binding constants of a bulky capping molecule. Completely reversible caps work on the principle of reversal of affinity of a bulky ring shaped molecule threaded on a stalk containing two or more binding sites after stimulation. Irreversible caps function *via* chemical bond cleavage of the bulky capping molecule, thus permanently detaching them from the nanomachines. Caps based on supramolecular systems such as rotaxanes and pseudorotaxanes that consist of a long chain-like molecule threaded through a cyclic molecule are discussed in Chapter 2.

Stimuli-responsive drug delivery in general, and nanomachines in particular, require a biocompatible stimulus and/or power supply. How can the delivery system be activated when the particles are deep in the body? Two categories of stimuli are being used: external and autonomous. External activation has the desirable property of being under control by the operator; it can be turned on or off as desired and it can be localized to the site of the disease. Examples using external

activation by alternating magnetic fields (AMFs) and high-intensity focused ultrasound (HIFU) will be discussed respectively in Chapter 3 and Chapter 4 of this dissertation. One can be used depending on the need—AMFs penetrate tissue better than HIFU without suffering from blockage by bone and air; HIFU obtains a more precise spatial focus on the order of 10 mm<sup>3</sup>. The second category, autonomous activation, takes advantage of chemical properties that are as specific as possible to the site of the disease. The most widely used properties include pH change (from pH 7.4 in blood to 6 or below in tumors or lysosomes of cells), redox change (antioxidants such as glutathione in the cytosols of cells), enzymes over expressed by tumor cells or antigens, or antibodies specific to tumor cells. These subjects have been reviewed extensively.<sup>15-24</sup> In Chapter 2, the design, synthesis and operation of several stimuli-responsive supramolecular caps for therapeutic or imaging applications are discussed.<sup>25</sup>

## **1.2 Introduction of The Dissertation**

The research included in this dissertation makes the most of the MSN's preeminent properties and focus on biomedical applications, primarily stimuli-responsive drug delivery and bioimaging, aiming to provide alternative approaches to achieving precision medicine. We exploited the high surface area and large pore volume of MSNs to carry and deliver large amounts of anticancer drugs, antibiotics, and imaging agents. We functionalized the surface of MSNs for different purposes based on their easy surface functionalization. Of particular importance, MSN's low toxicity allowed us to fearlessly introduce them to bio-systems. The questions I am specifically interested in during my PhD research include: (1) how to precisely deliver drugs at the desired time to the specific site of the disease and with accurate dosage; (2) how to deliver water-insoluble drugs to improve the treatment to specific diseases; (3) how to create a new shortwave infrared (SWIR) optical imaging contrast agent that is easy to deliver and use (good stability and water solubility,

biocompatible). The following paragraphs provide a brief introduction of the work in each chapter that is able to address the above questions.

In Chapter 3, I discussed the first approach to controlling the drug release location, time, and dose.<sup>26</sup> We synthesized monodispersed superparamagnetic nanoparticles with a high magnetization and high specific loss power that efficiently generates localized heating under an AMF. We engineered core@shell nanoparticles that have mesoporous silica shell “drug containers” around the magnetic core with a thermos-responsive cap. Released drug dosage as well as killing of cancer cells were shown controllable by the AMF exposure time. On the basis of the inherent nature of AMF, the AMF-stimulated drug delivery offers the potential to noninvasively and precisely control the location, time and dosage of the released drugs, avoiding the risk of overheating the surrounding tissues.

In Chapter 4, I discussed the second approach that used magnetic resonance imaging-guided high-intensity focused ultrasound (MRgHIFU) to precisely control the drug release location, time, and dose.<sup>27</sup> Compared to AMF, HIFU has a more precise energy-focusing ability which may be favored to treat rather delicate tissue. We engineered MSNs with a widely used polymer, polyethylene glycol (PEG), which we found to be ultrasound-sensitive. *Via* the guidance of MRI, the cargo release was shown pinpointed at the HIFU focal point in three-dimensional space. Cargo released amount and the correlated MRI contrast change were shown controllable by the HIFU stimulation time. This technology was demonstrated *ex vivo*, opening up an opportunity for future image-guided theranostic applications.

In Chapter 5, I presented a “chaperone-assisted” delivery strategy to approach the problem of water-insoluble drug delivery.<sup>28</sup> Acetophenone (AP) was found as the promising chaperone that helped improve both loading and release of clofazimine (CFZ), an antibiotic used to treat tuberculosis, using MSNs.<sup>28</sup> The antibacterial effect to the intracellular *M. tuberculosis* using this

delivery strategy further validate their potential use in biomedical applications. This is the first work that examines an appropriate chaperone for CFZ and to actually integrate the strategy with nanoparticles. This novel “chaperone-assisted” delivery strategy could also be applied to other hydrophobic drugs with their suitable loading solvents (chaperone), broadening the type of diseases to be treated with this approach.

In Chapter 6, I presented a design of a new SWIR optical imaging contrast agent that fulfilled the need of good stability, good water solubility as well as biocompatibility.<sup>29</sup> We employed the photophysical consequences including bathochromically-shifted absorption and emission spectra caused by J-aggregation to reach SWIR region, a compelling region of the electromagnetic spectrum. The J-aggregates of a near infrared (NIR) fluorophore IR-140 inside PEG conjugated hollow mesoporous silica nanoparticles (HMSNs-PEG) are stable for multiple weeks in phosphate-buffered saline and enable high resolution imaging *in vivo* with 980 nm excitation. The use of this new SWIR optical imaging contrast agent has the potential to overcome the stability, toxicity, and brightness challenges faced by normal SWIR contrast agents.

### 1.3 Figures

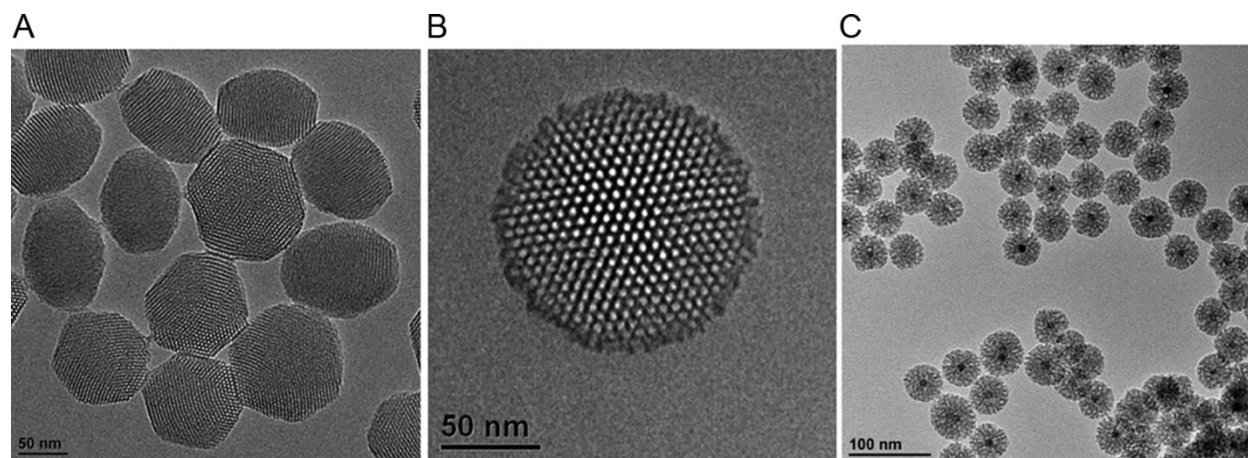


**Figure 1.1.** TEM images of (A) typical mesoporous silica nanoparticles, (B) large pore silica nanoparticles, and (C) core@shell nanoparticles.

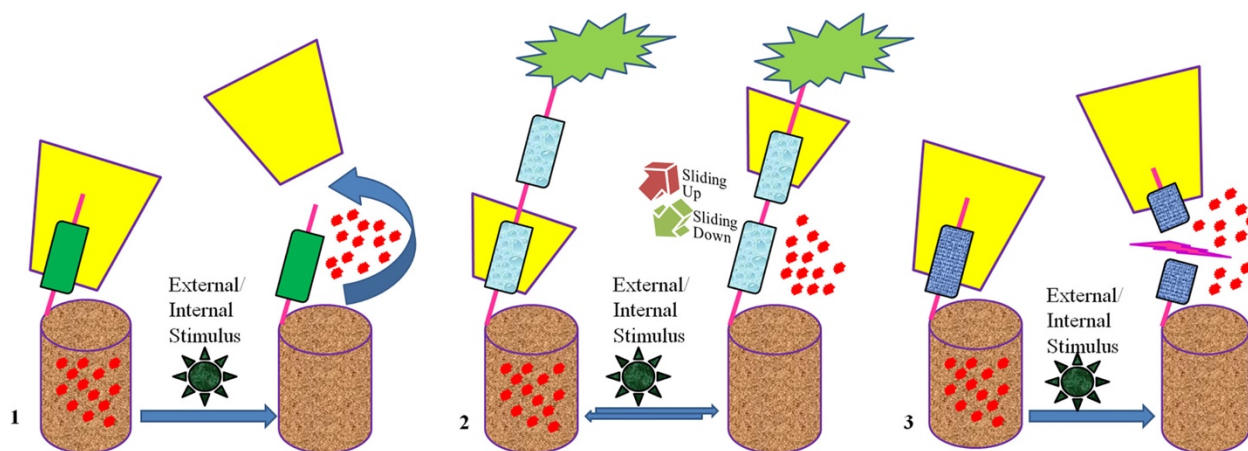


**Figure 1.2.** Sketch of the three major modes of operation of pore uncapping. (1) Reusable valve where a bulky cyclic molecule has a binding constant to the attached thread-like “stalk” that decreases when stimulated. (2) Reversible valve where the bulky cyclic molecule has a binding constant at a position close to the pore opening that decreases allowing it to slide away from the pore opening but not leave the stalk. (3) A bulky molecule is chemically bonded to the pore opening and the bond is broken when stimulated.



## 1.4 References

- (1) M. Ebelmen, Sur la production artificielle de l'hydrophane, *Comptes Rend. de l'Acad des Sciences* 69 (1847) 527.
- (2) C. J. Brinker, G. W. Scherer, *Sol-Gel Science*, Academic Press, New York, 1990.
- (3) L. Ellerby, C. Nishida, F. Nishida, S. Yamanaka, B. Dunn, J. Valentine, J. I. Zink, Encapsulation of proteins in transparent porous silicate glasses prepared by the sol-gel method, *Science* 255 (1992) 1113–1115.
- (4) K. E. Chung, E. H. Lan, M. S. Davidson, B. S. Dunn, J. S. Valentine, J. I. Zink, Measurement of dissolved oxygen in water using glass-encapsulated myoglobin, *Anal. Chem.* 67 (1995) 1505–1509.
- (5) B. C. Dave, B. Dunn, J. S. Valentine, J. I. Zink, Sol-gel encapsulation methods for biosensors, *Anal. Chem.* 66 (2008) 1120A–1127A.
- (6) J. S. Beck, C. T.-W. Chu, I. D. Johnson, C. T. Kresge, M. E. Leonowicz, W. J. Roth, J. W. Vartuli, Synthetic porous crystalline material: its synthesis and use WO Patent 91/1130, 1991.
- (7) T. Yanagisawa, T. Shimizu, K. Kuroda, C. Kato, The preparation of alkyltriethylammonium-kaneinite complexes and their conversion to microporous materials, *Bull. Chem. Soc. Jpn.* 63 (1990) 988–992.
- (8) V. Chiola, J. E. Ritsko, C. D. Vanderpool, Process for producing low bulk density silica, U.S. Patent 3, 1971, pp. 556–725.
- (9) M. H. Huang, B. S. Dunn, J. I. Zink, In situ luminescence probing of the chemical and structural changes during formation of dip-coated lamellar phase sodium dodecyl sulfate sol-gel thin films, *J. Am. Chem. Soc.* 122 (2000) 3739–3745.
- (10) F. Nishida, J. M. McKiernan, B. Dunn, J. I. Zink, In situ fluorescence probing of the chemical changes during sol-gel thin film formation, *J. Am. Ceram. Soc.* 78 (1995) 1640–1648.
- (11) M. H. Huang, B. S. Dunn, H. Soyez, J. I. Zink, In situ probing by fluorescence spectroscopy of the formation of continuous highly-ordered lamellar-phase mesostructured thin films, *Langmuir* 14 (1998) 7331–7333.
- (12) B. C. Dave, H. Soyez, J. M. Miller, B. Dunn, J. S. Valentine, J. I. Zink, Synthesis of protein-doped sol-gel SiO<sub>2</sub> thin films: evidence for rotational mobility of encapsulated cytochrome c, *Chem. Mater.* 7 (1995) 1431–1434.
- (13) Y. Lu, R. Ganguli, C. A. Drewien, M. T. Anderson, C. J. Brinker, W. Gong, Y. Guo, H. Soyez, B. Dunn, M. H. Huang, J. I. Zink, Continuous formation of supported cubic and hexagonal mesoporous films by sol-gel dip-coating, *Nature* 389 (1997) 364–368.
- (14) D. Tarn, C. E. Ashley, M. Xue, E. C. Carnes, J. I. Zink, C. J. Brinker, Mesoporous silica nanoparticle nano-carriers: biofunctionality and biocompatibility, *Acc. Chem. Res.* 46 (2013) 792–801.

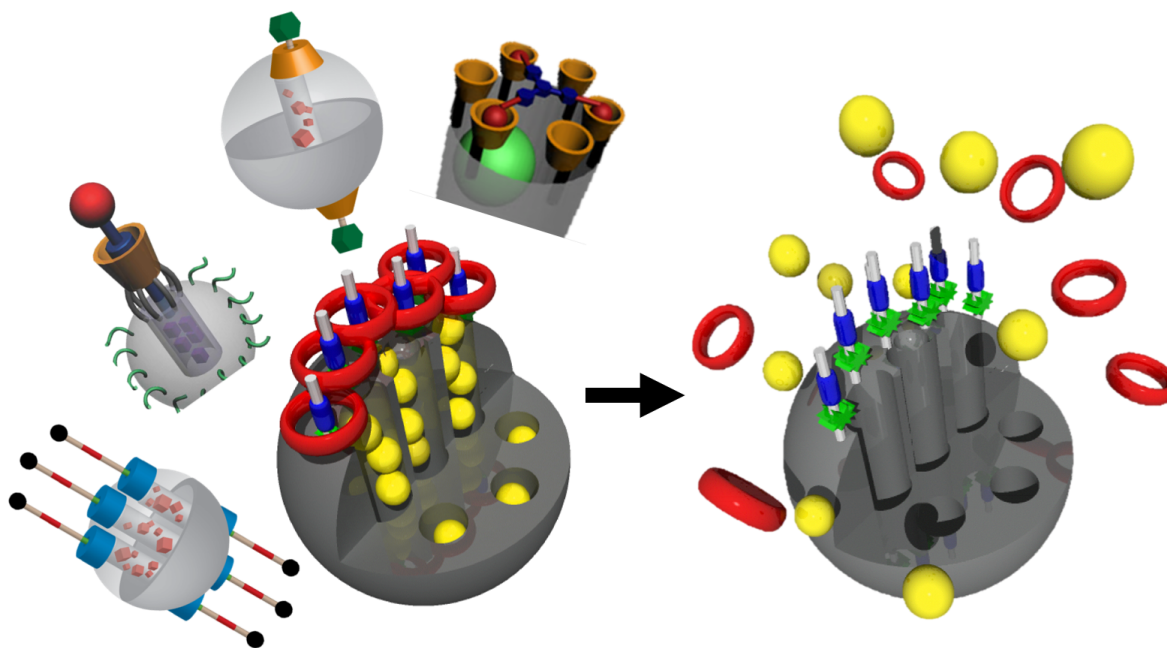
- (15) B. Rühle, P. Saint-Cricq, J. I. Zink, Externally controlled nanomachines on mesoporous silica nanoparticles for biomedical applications, *Chemphyschem* 17 (2016) 1769–1779.
- (16) F. Peng, Y. Su, Y. Zhong, C. Fan, S.-T. Lee, Y. He, Silicon nanomaterials platform for bioimaging, biosensing, and cancer therapy, *Acc. Chem. Res.* 47 (2014) 612–623.
- (17) V. Biju, Chemical modifications and bioconjugate reactions of nanomaterials for sensing, imaging, drug delivery and therapy, *Chem. Soc. Rev.* 43 (2014) 744–764.
- (18) Z. Tao, Mesoporous silica-based nanodevices for biological applications, *RSC Adv.* 4 (2014) 18961–18980.
- (19) C. Argyo, V. Weiss, C. Bräuchle, T. Bein, Multifunctional mesoporous silica nanoparticles as a universal platform for drug delivery, *Chem. Mater.* 26 (2013) 435–451.
- (20) Y. Chen, H. Chen, J. Shi, In vivo bio-safety evaluations and diagnostic/therapeutic applications of chemically designed mesoporous silica nanoparticles, *Adv. Mater.* 25 (2013) 3144–3176.
- (21) J. L. Vivero-Escoto, R. C. Huxford-Phillips, W. Lin, Silica-based nanoprobe for biomedical imaging and theranostic applications, *Chem. Soc. Rev.* 41 (2012) 2673–2685.
- (22) Z. Li, J. C. Barnes, A. Bosoy, J. F. Stoddart, J. I. Zink, Mesoporous silica nanoparticles in biomedical applications, *Chem. Soc. Rev.* 41 (2012) 2590–2605.
- (23) J. E. Lee, N. Lee, T. Kim, J. Kim, T. Hyeon, Multifunctional mesoporous silica nanocomposite nanoparticles for theranostic applications, *Acc. Chem. Res.* 44 (2011) 893–902.
- (24) M.W. Ambrogio, C. R. Thomas, Y.-L. Zhao, J. I. Zink, J. F. Stoddart, Mechanized silica nanoparticles: a new frontier in theranostic nanomedicine, *Acc. Chem. Res.* 44 (2011) 903–913.
- (25) C.-A. Cheng, T. Deng, F.-C. Lin, Y. Cai, J. I. Zink, Supramolecular nanomachines as stimuli-responsive gatekeepers on mesoporous silica nanoparticles for antibiotic and cancer drug delivery, *Theranostics* 9 (2019) 3341–3364.
- (26) W. Chen, C.-A. Cheng, J. I. Zink, Spatial, temporal, and dose control of drug delivery using noninvasive magnetic stimulation, *ACS Nano* 13 (2019) 1292–1308.
- (27) C.-A. Cheng, W. Chen, L. Zhang, H. H. Wu, J. I. Zink, A responsive mesoporous silica nanoparticle platform for magnetic resonance imaging-guided high-intensity focused ultrasound-stimulated cargo delivery with controllable location, time, and dose, *J. Am. Chem. Soc.* 141 (2019) 17670–17684.
- (28) W. Chen, C.-A. Cheng, B.-Y. Lee, D. L. Clemens, W.-Y. Huang, M. A. Horwitz, J. I. Zink, *ACS Applied Materials & Interfaces* 10 (2018) 31870–31881.
- (29) W. Chen, C.-A. Cheng, E. D. Cosco, S. Ramakrishnan, J. G. P. Lingg, O. T. Bruns, J. I. Zink, E. M. Sletten, *J. Am. Chem. Soc.* 141 (2019) 12475–12480.

## CHAPTER 2

# Supramolecular Nanomachines as Stimuli-Responsive Gatekeepers on Mesoporous Silica Nanoparticles for Antibiotic and Cancer Drug Delivery

This chapter of the dissertation was adapted and reprinted with permission from Chi-An Cheng, Tian Deng, Fang-Chu Lin, Yao Cai, Jeffrey I. Zink *Theranostics* **2019**, 9, 3341–3364. Copyright 2019 Ivyspring. Co-author contributions: Cheng C. A., Deng T., Lin F. C. and Cai Y. reviewed the literature and drafted the manuscript of this review article. Jeffrey I. Zink was the P.I.

### Table of Content Figure



## 2.1 Abstract

Major objectives in nanomedicine and nanotherapy include the ability to trap therapeutic molecules inside of nano-carriers, carry therapeutics to the site of the disease with no leakage, release high local concentrations of drug, release only on demand – either autonomous or external, and kill the cancer or an infectious organism. This review will focus on mesoporous silica nanoparticle carriers with a large internal pore volume suitable for carrying anticancer and antibiotic drugs, and supramolecular components that function as caps that can both trap and release the drugs on-command.

Caps that are especially relevant to this review are rotaxanes and pseudorotaxanes that consist of a long chain-like molecule threaded through a cyclic molecule. Under certain conditions discussed throughout this review, the cyclic molecule can be attracted to one end of the rotaxane and in the presence of a stimulus can slide to the other end. When the thread is attached near the pore opening on MSNs, the sliding cyclic molecule can block the pore when it is near the particle or open it when it slides away.

The design, synthesis and operation of supramolecular systems that act as stimuli-responsive pore capping devices that trap and release molecules for therapeutic or imaging applications are discussed. Uncapping can either be irreversible because the cap comes off, or reversible when the cyclic molecule is prevented from sliding off by a steric barrier. In the latter case the amount of cargo released (the dose) can be controlled. These nanomachines act as valves.

Examples of supramolecular systems stimulated by chemical signals (pH, redox, enzymes, antibodies) or by external physical signals (light, heat, magnetism, ultrasound) are presented. Many of the systems have been studied *in vitro* proving that they are taken up by cancer cells and release drugs and kill the cells when stimulated. Some have been studied in mouse models; after IV injection they shrink tumors or kill intracellular pathogens after stimulation. Supramolecular

constructs offer fascinating, highly controllable and biologically compatible platforms for drug delivery.

## 2.2 Introduction

Supramolecular constructs on mesoporous silica nanoparticles (MSNs) for drug delivery, the subject of this review, resulted from the convergence of two fields: sol-gel synthesis of metal oxide solids,<sup>1</sup> and organic syntheses of supramolecular rotaxanes and pseudorotaxanes.<sup>2</sup> The primary current goal is to use porous sol-gel nanomaterials to carry cargo molecules such as drugs, and supramolecular constructs to hold the cargo in place until stimulated to release it on command. Success in this venture would result in the decrease in off-target effects of the drugs by carrying them with no leakage to the site of the disease, and releasing high local concentrations of them where and when desired.

Sol-gel chemistry had a resurgence in popularity a decade ago because it is a solution-based synthesis for making metal oxide solids. Silica (silicon dioxide) was one of the favorites because of its optical transparency, the ability to synthesize the glass around organic and biomolecules (including enzymes),<sup>3-6</sup> the ability to use molds to make monoliths in desired shapes, and the ability to synthesize films<sup>7-9</sup> fibers and nanoparticles in amazing varieties of shapes and sizes.

Especially interesting was the syntheses of glass around liquid crystalline phases of surfactant molecules to template mesoporous glass. After the hydrolysis and condensation of the precursor molecules tetraalkoxysilanes around rod-shaped two-dimensional hexagonal phases of cetyltrimmonium chloride, the templating surfactant was removed by solvent extraction or calcination to make silica materials with uniform sized and well-ordered pores. This procedure was patented and the material named MSM-41 even though the same material had been patented 16 years earlier<sup>10</sup> and rediscovered prior to the second patent. Further research led to controllable

synthesis of nanospheres. Typical MSNs discussed in this review are spheres about 100 nm in diameter with tubular pores about 2.5 nm in diameter. The size of supramolecular nanomachines should be comparable to that of the pores of MSNs in order to trap the cargo inside. The majority of supramolecular nanomachines discussed in this article are capable of capping pores of this size (2.5 nm). The biocompatibility of these materials has been reviewed<sup>11,12</sup> and many examples of in vitro and in vivo studies are shown in this review (**Tables 2.1 and 2.2**). One gram of particles has a surface area of about 1000 m<sup>2</sup> and a pore volume of about 1 cm<sup>3</sup>. Because typical anticancer drugs have a density of about 1 g/cm<sup>3</sup>, the carrying capacity can be 100 wt% (although this upper limit is rarely achieved because of imperfect molecular packing).

During the same period, supramolecular organic molecule-based structures were being synthesized. Especially relevant to this review are the now famous rotaxanes consisting of a long chain-like molecule threaded through a cyclic molecule (known as a pseudo-rotaxane).<sup>2</sup> When large “blocking” molecules were attached to the ends of the chain, the cyclic molecule could not slide off and was held in place by “mechanical bonds”. Under certain conditions discussed throughout this review, the cyclic molecule could be attracted to one end of the rotaxane and in the presence of a stimulus could slide to the other end. The bonding of one end of this organic structure to mesoporous sol-gel glass was the key to unlock and open the door to an amazing variety of drug-delivery vehicles.

The ground-breaking paper that reported the system is shown in **Figure 2.1A**.<sup>13</sup> A thread containing a dioxynaphthalene was attached to a silica surface and a cyclic ring molecule containing two bipyridinium units was threaded on to it. Chemical reduction of the ring weakened the attraction to the thread thus releasing the ring. Oxidation caused it to re-attach, and the threading/dethreading was monitored by the quenching and reappearance of the naphthalene fluorescence. This rotaxane system worked on the solid support.

The next advance was the attachment of the organic component to the regions around the pore openings on silica particles (**Figure 2.1B**).<sup>14</sup> Ir(PPY)<sub>3</sub> was chosen as the cargo molecule because it is brightly fluorescent and stable in the presence of the oxidizing and reducing agents required to trigger the trapping and release. When the paraquat was attracted to the dioxynaphthalene near the pore opening, the cargo molecules were trapped in the pore. When the reducing agent CNBH<sup>3-</sup> was added, the pseudorotaxane disassembled releasing the fluorophore into the solution. The fluorescence of the naphthalene component that had been partially quenched by the paraquat increased in intensity. This supramolecular nanovalve is an example of a molecular machine consisting of a solid framework with movable parts capable of doing work.

Continuing studies further refined and enhanced the new nanomachine. A more complicated stalk containing two different binding sites for the paraquat enabled the system to be switched back and forth as a result of sequential oxidation and reduction steps (**Figure 2.1C**).<sup>15</sup> One end of the stalk was attached to the pore openings on the silica and a bulky group was attached on the other end to prevent escape of the ring. This rotaxane was the first example of a truly reversible nanovalve. The positioning of the rotaxane on the particle was refined,<sup>16</sup> and the system was reconfigured such that it could be stimulated by light energy via a photoredox transducers.<sup>17,18</sup>

The focus of these pioneering studies was to prove that the rotaxane actually moved when attached to a silica surface, and then to prove that it could actually trap molecules in pores and release them on command. When it became clear that the supramolecular concept of a controllable cap on a pore was a reality, attention turned to potential applications. A challenging one was to improve on nanomaterials as drug delivery vehicles. Liposomes were being used, but drug release from them was not controllable. Rotaxane caps are, but they only operated in non-aqueous media. Attention turned to water-based supramolecular systems, and the results of those investigations, including operation in vitro and in vivo, are described in this review and summarized in **Table 2.1**

and 2.2, respectively.

## **2.3 Supramolecular Nanovalves for Stimuli Responsive Cargo Delivery**

Macrocyclic molecules such as cucurbit[n]urils ( $n=5-10$ , CB[n]), cyclodextrins (CDs), crown ethers, and pillararenes tend to form inclusion complexes with guests and can be dissociated reversibly or irreversibly in response to external stimuli in aqueous solution. Therefore, these families of polymacrocycles have been used as the biologically friendly rings on the nanovalves for drug delivery applications.<sup>19</sup> In this section, two categories of supramolecular capping systems will be discussed based on their reversibility of capping and uncapping. First, pseudorotaxane nanovalves are discussed. In the closed position the cyclic molecules are on a binding site on the stalks that is close to the pore openings. Upon activation they slide away from and off of the stalk. The system is reusable because the cyclic molecules can be rethreaded, but they are irreversible because in biological conditions the cyclic molecules diffuse away from the particles and have such low concentrations that the rate of rebinding is very low. Next, reversible rotaxane nanovalves are discussed. These nanovalves, in contrast, are reversible because a bulky group at the end of the stalk prevents the cyclic molecules from leaving the stalk. At the end of this section, we will also describe “inactive supramolecular systems”. Different from the pseudorotaxane and rotaxane nanovalves, the active parts of this inactive system are not the supramolecular inclusion complexes, but bond breaking between the bulky inclusion complexes and the nanoparticles occurs.

### **2.3.1 Irreversible Pseudorotaxane Based Nanovalves**

#### **2.3.1.1 Cucurbit[n]urils**

CB[n] are pumpkin-shaped cyclic methylene-bridged glycoluril oligomers that were named cucurbituril because of their resemblance to pumpkins, the most prominent member of the



*cucurbitaceae* plant family.<sup>20,21</sup> CB[n] analogues have a common depth (9.1 Å), but their widths and volumes vary. Their shape of the narrower portals to the entry with the wider cavity produces significant steric barriers to guest association and dissociation.<sup>22</sup> To have biological applications, water solubility is an essential property. The three members of the cucurbiturils CB[5], CB[6], and CB[7] possess modest solubility in water. Among these CB[n] analogues, CB[6] was the first and the most widely studied cucurbituril, with greater than a one hundred year history.

#### *CB[6] Rings and Bisammonium Stalks*

Angelos *et al.* synthesized pseudorotaxanes consisting of CB[6] rings and bisammonium stalks bonded to mesoporous silica nanoparticles (MSNs) (**Figure 2.2**).<sup>23</sup> Alkyne-functionalized MSNs were synthesized and the particles were loaded with rhodamine B (RhB) cargo molecules by soaking the MSNs in a RhB solution (0.5 mM) for 5 h at room temperature. Then an excess of CB[6] was added to the above mixture and thus capping the pore. The release of RhB was carried out by raising the pH. The binding of CB[6] with the bisammonium stalks is pH-dependent; at neutral and acidic pH the CB[6] rings encircle the stalks tightly and thus block the pores. At basic pH, deprotonation of the stalks switch off the ion-dipole interactions between the CB[6] rings and the stalks resulting in dethreading of CB[6]. The subsequent release of the RhB cargo was monitored as a function of time by fluorescence spectroscopy.

#### *CB[6] Rings and Dialkyl-4,4-bipyridinium (Viologen) Stalks*

Khashab *et al.* designed another pH-controlled CB[6] - based pseudorotaxane nanoparticle system.<sup>24</sup> In this case, dialkyl-4,4-bipyridinium (viologen) dicationic guests form highly stable inclusion complexes with CB[6] hosts, giving rise to a well-known [2]pseudorotaxane (**Figure 2.3**). The internal cavity of CB[6] forms strong complexes with the alkyl chains in the stalk by means of hydrophobic interactions and electrostatic interactions between the positive charge on

viologen and carbonyl oxygens on CB[6]. Under acidic conditions (pH 4), the carboxylate end group becomes protonated attracting the CB[6] macrocycle away from the pore towards the end of the stalk and thus releases the cargo.

#### *CB[6] Rings and N-(6-aminohexyl) Aminomethyltriethoxysilane Stalks*

The CB[6] valve can be stimulated by means other than pH. Thomas *et al.* expanded the use of CB[6] by constructing a thermosensitive nanovalve that is operable by oscillating magnetic fields (OMFs) (**Figure 2.4**).<sup>25</sup> This system was also the first study exploring the possibility of OMF-triggered cargo release. The carrier, a core-shell nanoparticle with a superparamagnetic iron oxide core and a mesoporous silica shell, was synthesized by phase-transferring the iron oxide nanoparticle into the water phase and forming an outer silica shell. The resulted core-shell MSN was then grafted with N-(6-aminohexyl) aminomethyltriethoxysilane (stalk) by refluxing the nanoparticles with the stalks in toluene overnight. RhB and doxorubicin (DOX) were used as the cargos. The loading of the cargo was done by soaking the stalk-mechanized core-shell MSNs in RhB or DOX solution overnight. Finally, the cargo-loaded nanoparticles were capped with CB[6] rings and the whole system was ready to use. The hydrophobic cavity of CB[6] encircles the alkyl chain of the stalk through non-covalent London force, ion-dipole interactions and hydrogen bonding. The binding constant between CB[6] ring and the stalk decrease at high temperature, thus slipping off the cap and allowing the cargo to diffuse out. The authors not only demonstrated the release of RhB and DOX under OMFs, but they also showed that internal heat generated from the iron oxide core and not bulk heating actuated the CB[6]/stalk pseudorotaxane complex.

The thermo-sensitive valve-controlled particles were taken up by MDA-MB-231 breast cancer cells and released DOX on-command in the cells. After being taken up by the cells, the mechanized nanoparticles showed minimal DOX release. Upon exposure to OMFs, the local

heating generated from the superparamagnetic core initiated the release of DOX from the silica pores and induced cell apoptosis.

Croissant *et al.* demonstrated that this thermo-sensitive nanovalve was operable by plasmonic heating (**Figure 2.5**).<sup>26</sup> The authors developed a novel one-pot method to synthesize the carrier, a core/shell structure with a 20 nm gold core and a 150 nm mesoporous silica shell (designated as Au@MSN). In this method, the authors used autoreduction of tetrachloroaurate ions in the presence of cetyltrimethylammonium bromide (CTAB), which is the template of mesopore formation. The Au@MSNs were mechanized with the stalks, loaded with RhB cargos, and finally capped with CB[6] rings. The nanovalves were activated through the localized heat generated from plasmonic heating of the Au core. Similar to the magnetic heating, the local temperature rise is useful for spatially controlled drug delivery.

#### *CB[7] Rings and Cinnamamide Stalks*

Another CB[n] analogue, CB[7], was found to possess a suitable cavity and form stable host-guest complexes with trans-cinnamamide derivatives.<sup>20,27,28</sup> This CB[7]-cinnamamide complex is responsive to UV light (300 nm).<sup>29</sup> After UV irradiation, a trans- to cis- conformational change of cinnamamide is induced, leading to dissociation caused by a change in the steric hindrance. Utilizing this property, CB[7]-cinnamamide pseudorotaxane has been developed as a light-switchable supramolecular nanovalve on MSNs [30]. The outer surface of the MSNs was first functionalized with 3-aminopropyl groups. Amino modified nanoparticles were reacted with cinnamoyl chloride, and then the pores of the functionalized MSNs were loaded with RhB. Finally, pores were capped with CB[7], which forms stable inclusion complexes with the grafted cinnamamide moieties. The authors showed that 300 nm UV light induced the release of the entrapped RhB due to the trans- to cis- conformational change of cinnamamide which dethreaded

the inclusion complex. The authors also showed that by using pulsed UV irradiation, a “ladder” controlled-release profile of RhB could be achieved, which could potentially control the dose of the released drugs for further applications.

### 2.3.1.2 Cyclodextrins

#### *$\alpha$ -CD Rings and Anilinoalkane Stalks*

Alpha cyclodextrin ( $\alpha$ -CD) molecules have been shown to have strong binding for benzene and benzene derivatives. The binding affinity between  $\alpha$ -CD and the anilinoalkane group decreases after protonation of the aniline when the pH is lowered causing dissociation to occur. Du and coworkers<sup>31</sup> designed a pH-responsive nanovalve based on  $\alpha$ -CD and anilinoalkane stalks on hollow MSNs (**Figure 2.6**). Three different linkers were attached on the particles' surfaces and the cargo, fluorescent Hoechst 33342, was loaded into pores.  $\alpha$ -CD was added to MSN as the capping agent. To optimize the length of the linker control of the pore openings, N-phenylaminomethyltriethoxysilane (PhAMTES) and N-phenylaminopropyltrimethoxysilane (PhAPTMS) were both tested. The amine group on PhAMTES was one carbon from silica, whereas that of PhAPTMS was three carbons away. To tune the trigger pH that opened the nanovalves, p-anisidine with higher pKa than that of aniline was linked to 3-iodopropyltrimethoxysilane (IPTMS) and used as the third linker. The release profiles of the three nanovalves were obtained by monitoring the emission intensity of cargos in aqueous solution after acidification. The trigger pH is governed by the pKa of aniline nitrogen: the release profiles of the three nanovalves were similar if triggered by pH 3.5 or 5, but only the nanovalve with IPTMS can be triggered at biorelevant pH 6. This nanovalve was an early example of a pH controlled pseudorotaxane nanovalve system in aqueous solution, and the study systematically explored the effects of stalk length and pH conditions on the cargo release profiles.

Dong and coworkers<sup>32</sup> studied the effects of polymer coatings around MSNs on the aniline based pseudorotaxane nanovalves' properties. Surface coatings of low molecular weight polyethylene imine (PEI) carry and protect siRNA, and it was of interest to determine if the nanovalves would function properly for drug delivery underneath such a coating. For the initial study, 1.8 kDa PEI was coated by electrostatic interaction and hydrogen bonding on 120 nm MSNs with pH sensitive nanovalves that open at pH 3.5. The second model consists of polyethylene imine-polyethylene glycol (PEI-PEG)-coated 50 nm MSNs. The release profiles of fully assembled MSNs with both polymer coating and nanovalves were similar to those of MSNs with only nanovalves, which indicated that the polymer coating did not stop cargo release.

Guardado-Alvarez and coworkers<sup>33</sup> reported a light responsive nanovalve based on  $\alpha$ -CD on a stalk containing an aniline derivative and a photoacid, 6,8-dihydroxy-1,3-pyrenedisulfonic acid (**Figure 2.7**). The latter was covalently bonded to an MSN's surface next to a pH responsive nanovalve, and when it was photoexcited at 408 nm, it transferred protons to adjacent stalks. Protonation of the aniline nitrogen caused the  $\alpha$ -CD to dissociate due to decreased binding affinity. Propidium iodide (PI) was used as the cargo and was monitored by fluorescence intensity excited at 448 nm. The release profile showed that there was little premature release at neutral pH, and an increase in fluorescence intensity in solution after irradiation. The pH of the bulk solution stayed neutral but the local pH on MSN surface became acidic. No release was observed when the solution surrounding the MSN was buffered at pH 8 because the buffer prevented acidification. In addition, no release was observed when the system was irradiated at 514 nm, a wavelength that was not absorbed by the photoacid. By turning on and off the pump laser, the amount of release was controllable.

Hwang *et al.* further refined the pH-responsive aniline/ $\alpha$ -CD inclusion complex toward *in vitro* and *in vivo* applications by attaching a targeting protein, transferrin (Tf), to the surface of the

particle (**Figure 2.8**).<sup>34</sup> It was important to determine if the valve would still operate under a protein coating and if the system would actively target receptors on cancer cells. The authors put fluorescent imaging molecules in the pores and targeting proteins and pH-sensitive aniline/ $\alpha$ -CD nanovalves on the same MSN. At neutral pH, the pseudorotaxane was stable and able to seal cargo inside the pores of MSNs. However, the binding constant between the stalk and  $\alpha$ -CD decreased when the phenyl amine was protonated ( $pK_a \approx 6$ ) in acidic environment, and thus dethreaded the  $\alpha$ -CD and released the cargo. Because transferrin was also bonded onto the nanoparticles, the authors first optimized the relative surface coverages of the nanovalves and transferrin in order to be able to deliver the maximum amount of cargo controlled by the valves and also obtain the maximum amount of cell targeting with the transferrin. Dox was used as the anticancer drug for both *in vitro* and *in vivo* studies.

*In vitro* testing with human pancreatic cancer cells (MiaPaCa-2) showed an enhanced delivery of Dox and cell killing effect. The *in vivo* study was done using SCID mice with xenografts of MiaPaCa-2. Animals were treated by IV injection with saline solution, free Dox, unloaded nanovalve-modified MSNs, nanovalve-modified MSNs loaded with Dox, and Tf-nanovalve-modified MSNs loaded with Dox. The average body weights of those treated mice without DOX were unchanged. The results of the hematology and serology examinations also showed the safety of these nanoparticles to the mice. The tumors in the control group and unloaded nanovalve-modified MSN group kept growing. However, significant tumor growth inhibition was found in the mice treated with Dox-loaded nanovalve-modified MSNs, showing the effective delivery of Dox by the nanoparticles inside the tumor. There was almost no difference in growth inhibition between targeted and untargeted particles, which may be explained by a protein corona that blocks the transferrin protein from being sensed by the Tf receptors of cancer cells.<sup>35</sup>

### *β-CD Rings and Benzimidazole Stalks*

Xue, *et al.*<sup>36</sup> reported a different pH responsive pseudorotaxane nanovalve based on a benzimidazole stalk and a β-cyclodextrin (β-CD) ring, and studied its autonomous drug release *in vitro* (**Figure 2.9**). A series of benzimidazole derivatives were tested, and methyl-1*H*-benzimidazole (MBI) was chosen as the stalk because of the pH range for protonation. It forms noncovalent bonding interactions with β-CD at pH 7.4, and protonates at lower pH (pH 6 or less) leading to weaker binding and release β-CD. THP-1 and KB-31 cell lines were chosen for *in vitro* study. After MBI was attached on the MSN surface, cargo was loaded followed by β-CD capping. Hoechst dye was first used to verify the delivery performance, and it showed little premature release at pH 7 and rapid release at pH 6 and lower. Then DOX was loaded for *in vitro* study. The release of DOX was slower compared to that of the dye and incomplete due to electrostatic interactions between the positively charged DOX and the negatively charged pore walls of the MSNs. To mitigate these charge effects, positively charged ammonium groups were co-condensed on the MSN, and rapid triggered release was observed. This system was tested in cell culture media to study the biological influence on the delivery system and it was fully functional under culture media conditions.

Finally, the action of the MSNs were studied *in vitro*. FITC-labeled MSN was first used to demonstrate that MSN was taken up by cells in acidic lysosomes. Using confocal microscopy, it was shown that more than 80% FITC-labeled MSN was colocalized with TRITC-labeled anti-LAMP-1 antibody labeled lysosomes in both cell lines. Then the release of Hoechst dye was studied in both cell lines. At 1 and 3 hours there was no release, but after 6 h, acidification caused the dye to be released to the nuclei of both THP-1 and KB-31. In the NH<sub>4</sub>Cl treated cells, where the pH of lysosomes was increased to pH 6, the Hoechst staining was not found in nuclei. The release of DOX was studied in KB-31. After taken up by cell, the MSNs released DOX and led to

apoptotic cell death. However, in the NH<sub>4</sub>Cl treated cells where acidification was suppressed, little cell death was observed.

### *Pseudorotaxane Nanovalves for Treatment of Infectious Diseases*

Two of the pH -activated cyclodextrin capped nanovalves described above, the one with the anilinoalkane stalk and the other with the benzimidazole stalk, were used to treat intracellular bacterial infectious disease. Mononuclear phagocytes, primarily monocytes and tissue macrophages, are known as professional phagocytes because of their reputation for avidly ingesting and killing bacteria. However, one class of pathogens, known as intracellular parasites, intentionally induce their uptake by macrophages with the aim of hijacking host cell machinery towards their own end – survival and intracellular replication. The two pseudorotaxane nanovalves were used to kill *Francisella tularensis* (Ft), the agent of tularemia. This bacterium is referred to by the US government as a Tier 1 Select Agent because of especially high concern that they may be intentionally employed in a bioterrorist attack.

Li *et al.*<sup>37</sup> optimized pH-responsive nanovalves functionalized MSN to deliver moxifloxacin (MXF) for Ft infection treatment both *in vitro* and *in vivo* (**Figure 2.10**). Two pH-responsive nanovalves were chosen: one consisted of anilinoalkane (ANA) stalks and  $\alpha$ -CD caps, and the other was composed of 1-methyl-1H-benzimidazole (MBI) and  $\beta$ -CD caps. Both stalks become protonated at pH 6 and lower, thus the caps dissociated and cargo released in lysosomes. The MSNs were optimized in the following aspects: charge of pore wall, efficiency of stalk attachment, concentration and pH of loading solution, loading duration and MSN washing after loading.

MSN uptake by macrophages was first tested *in vitro*. A large amount of uptaken rhodamine-labeled MSN was observed in both the monocyte-derived macrophages and the differentiated THP-1 cells. To investigate the efficacy in killing Ft, MXF loaded MSN with ANA/ $\alpha$ -CD (MXF-



MSN-ANA) or MBI/  $\beta$ -CD (MXF-MSN-MBI) and control MSN without MXF loading were used to treat infected THP-1 for one day. Ft was killed by both MXF-MSN-ANA and MXF-MSN-MBI while the bacteria grew with control MSN or no treatment. Compared at the same concentration, MXF-MSN-MBI killed more Ft than MXF-MSN-ANA.

MXF-MSN-MBI was tested *in vivo*. Mice were infected with Ft and suffered severe weight loss without treatment. However, mice treated with MXF-MSN maintained their weight. Also, without treatment, Ft grew rapidly, but intravenously administered MXF-MSN-MBI decreased the number of bacteria in lung by 4.0 logs. MXF-MSN-MBI was more effective than 2 to 4 times higher dose of free MXF killing Ft in lung.

#### *$\beta$ -CD Rings and Azobenzene Derivatives*

Most of the pseudorotaxane nanovalves discussed up to this point were stimulated by pH changes that switched stalks from hydrophobic to hydrophilic and thus decreased the binding constants to the hydrophobic interiors of cyclodextrins. The pH changes from that of blood to that of lysosomes caused autonomous cargo release and the use of transducers such as photoacids enable light activation. A different way of releasing cyclodextrin and drugs involves molecular geometry changes and accompanying polarity changes.

Azobenzene derivatives undergo photo-induced reversible trans-cis isomerization when the molecules are irradiated with UV or blue light.<sup>38-40</sup> Azobenzene derivatives can be grafted on the interior pore walls of MSNs and the back-and-forth wagging motion in the pores can trap and release cargo molecules. This type of nanomachine has been called an impeller.<sup>41-44</sup> Azobenzene derivatives can also be grafted on the outside surface of MSNs and bind cyclodextrin when in the trans- conformation and dethread in the cis- conformation, serving as photosensitive gatekeepers, to control and regulate cargo release from MSNs. For example, Ferris *et al.* attached two types of

azobenzene derivatives prepared from 4-(3-triethoxysilylpropylureido)azobenzene and (E)-4-((4-(benzylcarbamoyl)phenyl)diazenyl) benzoic acid to the outer surface of MSNs (**Figure 2.11**).<sup>45</sup> Those azobenzene derivatives bind  $\beta$ -CD in their trans- form and then the  $\beta$ -CD caps were released when the azobenzene derivatives photoisomerize to the cis- conformation after irradiation with UV light. The authors showed that RhB was released after the UV light actuation.

Compared with UV light, red and near-infrared (NIR) light in the therapeutic window (600-1000 nm) are preferable for biomedical applications due to better tissue penetrability and decreased photodamage to biological systems. Tetra-ortho-methoxy-substituted azobenzene (mAzO) can undergo trans-to-cis isomerization when irradiated with red light. Wang *et al.* attached mAzO and  $\beta$ -CD on the surface of MSNs as the capping systems to control release of DOX by using red light (625 nm) (**Figure 2.12**).<sup>46</sup> To show the photo-responsiveness of this capping systems in deep tissue, drug release was investigated by placing a piece of pork tissue (2 mm thick) between the light source and the sample. Although a lower release rate and amount were observed compared with that without tissue, red light irradiation at low power (60 mW/cm<sup>2</sup>, 360 min) still induced DOX release (23%) after passing through the tissue.

#### *Electrochemical and Redox Activation of Pseudorotaxane Valves*

Khashab and coworkers<sup>47</sup> reported a ferrocene and  $\beta$ -CD/ cucurbit[7]uril (CB7) based nanovalve that was responsive to redox and pH changes (**Figure 2.13**). Ferrocenedicarboxylic acid was coupled to amine-functionalized surface of MSN, and RhB dye was loaded as the cargo. Then  $\beta$ -CD or CB7 was capped by host-guest interaction. At pH 2, CB7 was bound to protonated ferrocenedicarboxylic acid, and when pH increased to 10, ferrocene dianion was formed and the binding affinity to CB7 was decreased. This mechanism was supported by NMR spectroscopy and cyclic voltammetry. The release profile of CB7 was tested: limited leakage was observed before

trigger, and the emission intensity of the released RhB increased immediately after trigger. The  $\beta$ -CD cap was more sensitive to the electrochemical oxidation trigger and had minimal activation from pH modulation.

### 2.3.1.3 Calix[n]arenes

A third type of macrocyclic rings in supramolecular chemistry, in addition to cyclodextrins and cucurbit[n]urils, are the calix[n]arenes. They are made up of phenol units linked by methylene bridges. Although calix[n]arenes have been incorporated with mesoporous silica materials, only a few studies have used calix[n]arenes as stimulus-responsive nanovalves for controlled cargo release compared with cyclodextrins and cucurbit[n]urils. Among different analogues of calix[n]arenes, sulfonato-calix[n]arenes (designated as SC[n]A) are water-soluble and have been reported to be biocompatible.

#### *Calix[n]arenes Rings and Acetylcholine Stalks*

Yang *et al.* reported a supramolecular valve based on sulfonatocalix[4]arene (SC[4]A) that demonstrated NIR light-triggered cargo release (**Figure 2.14**).<sup>48</sup> Mesoporous silica-coated gold nanorods (AuNR@MSNs) were synthesized followed by grafting acetylcholine stalks onto the nanoparticles. RhB as a model drug was loaded in the mesopores. SC[4]A was then added to encircle the stalks on the surface of AuNR@MSNs *via* host-guest complexation to form the supramolecular switches. Plasmonic heating generated from AuNR cores upon NIR light stimulation decreased the SC[4]A ring-stalk binding affinity, and thus dissociated the SC[4]A rings from the stalks and released the cargos. The release of RhB was monitored by UV-vis absorption spectroscopy. “Ladder” release profile generated by using periodic ON/OFF NIR laser irradiation showed the ability to control the dose.

#### 2.3.1.4 Crown Ethers

Crown ethers have been used to construct stable complexes with alkali and transition-metal cations *via* electrostatic interactions.<sup>49</sup> The complexes can be perturbed by pH and ultrasonic waves,<sup>50,51</sup> where the changes in pH may weaken the electrostatic interactions and hydrogen bonding, and the gain of energy from ultrasound may lead to the dissociation of metal cations from crown ethers. These properties make the crown ether/metal cation complexes candidates for supramolecular nanovalves. By conjugating crown ethers onto the pores entry of MSNs, the loaded cargos can be entrapped in the presence of capping agents (*i.e.*, metal cations) and be released upon triggered by pH and ultrasonic waves.

Leung *et al.* developed Fe<sub>3</sub>O<sub>4</sub>@SiO<sub>2</sub> core-shell nanoparticles capped with crown ethers for ultrasound and pH-responsive drug release.<sup>52</sup> The core-shell structure was prepared by coating Fe<sub>3</sub>O<sub>4</sub> nanoparticles with a mesoporous silica shell using modified hydrothermal sol-gel reactions. The mesoporous silica shell was functionalized with APTES and then coupled to dibenzo-crown ethers through amide linkages. Then DOX was loaded and the pores of the core-shell nanoparticles were capped with Na<sup>+</sup> and Cs<sup>+</sup> ions through the formation of complexes with the crown ethers on the outer surface. DOX controlled release was tested in PBS at pH 4 or pH 7.4. The results showed that DOX release was triggered at pH 4 in combination with ultrasound. This is because the pores were uncapped by lowering pH in the presence of ultrasound which broke up the interaction between the metal cations and crown ether's ethylene glycol chains. MTT assays confirmed that the crown ether/metal cation complexes capped nanoparticles were biocompatible to L929 cells (a murine aneuploidy fibrosarcoma cell line). Reasonable cellular uptake of the nanoparticles in L929 cells was observed from MRI analysis.

### 2.3.1.5 Pillararenes

Pillararenes are synthetic macrocycles that were first synthesized in 2008 and subsequently attracted attention in drug delivery research.<sup>53</sup> A supramolecular construct incorporated in an MSN based drug delivery system was reported by Sun, *et al.* in 2013.<sup>54</sup> A pyridinium compound that is positively charged at neutral pH was attached to MSN surface as a stalk (**Figure 2.15**). Negatively charged carboxylatopillar[5]arene (CP[5]A) was used as a cap and held in place by the electrostatic attraction to the stalk. When the pH was decreased below 5, CP[5]A was protonated which weakened its interaction with stalk and led to uncapping. Methyl viologen salts can also trigger uncapping because of its higher binding affinity with CP[5]A.

Huang *et al.* utilized phosphonated pillar[5]arenes (PPA[5]) as capping agents in an MSN based drug delivery system.<sup>55</sup> Specific ion pairing between hydrated phosphonates on PPA[5] and quaternary ammoniums on stalks capped the pores tightly. When PPA[5] was protonated, the host-guest interaction between cap and stalk weakened, leading to cargo release. Competitive binding by  $Zn^{2+}$  ions also caused decapping and cargo release. Additionally, when gold nanorods (GNRs) were embedded inside MSNs and irradiated with near-infrared (NIR) radiation, the photothermal increase in temperature weakened host-guest interaction.

The PPA[5] gated GNR@MSNs were studied *in vitro* using human A549 lung carcinoma cell line. The empty particles showed no cytotoxicity. When the particles were loaded with DOX, cell apoptosis was observed and was increased with the NIR trigger due to the synergistic effect of photothermo-chemotherapy.

### 2.3.2 Reversible Rotaxane Based Nanovalves

Rotaxane supramolecular systems that can uncap and recap the pores of MSNs reversibly (without loss of the cap from the stalk) are discussed in this section. After assembling the complex

formed by nanocap and stalk on the surface of the nanoparticle, the “closed” state of the stalk with the region of highest affinity brings the nanocap close enough to the particle surface to prevent cargo leakage. The “open” state starts when binding between the nanocap and the stalk is no longer favorable, where the nanocap slides along the stalk away from the surface of the nanoparticle until reaching an end-terminating stopper group. The objective of putting the end-terminating stopper group is to prevent the nanocap from unthreading completely so that the above “closed” and “open” states can be switched reversibly. A variation on this theme is to position two binding sites on the stalk with the strongest binder nearest the pore opening. When the binding of the cap to the strong site is turned off, the ring slides to the weaker binding site and stops. When the strong binding is turned on again, the cap slides back. This motif resembles the action of a rotaxane but the blocking of cap release is caused by the second binding site and not a physical steric blocking group.

#### *CB[6] Rings and Trisammonium Stalks*

Angelos *et al.* have designed a completely reversible valve based on CB[6] and trisammonium stalks (**Figure 2.16**).<sup>56</sup> Propidium iodide (PI) cargo was loaded by soaking the stalk-attached nanoparticles in the PI solution overnight so that the dye molecules can diffuse into the empty nanopores. To complete the valve, CB[6] was added to the mixture to form an inclusion complex composed of the CB[6] rings and the trisammonium stalks. The beauty of this system is that it operates like a “dialed-in” clock system to selectively release the cargo at both low and high pH. At neutral pH, the two nitrogen atoms separated by four carbon atoms are protonated, therefore, through ion–dipole binding interactions between both portals of the macrocycle, the CB[6] ring is pulled down to sit close to and thus block the nanopores. When pH is low (~ 5), the anilinium nitrogen atom separated by six carbon atoms from the ammonium nitrogen is protonated thus moving the CB[6] ring to the distal hexamethylenediammonium station and releasing PI. The

binding constant of CB[6] is strongest with nitrogens separated by the six carbons. At high pH (~10), all three nitrogen atoms on the stalk are deprotonated thus dethreading the CB[6] ring and releasing PI. These mechanized nanoparticles are highly dispersible in water, making this system a good candidate for the biological applications whose goal is to kill cells at both low and high pH.

#### *$\alpha$ -CD Rings and Azobenzene Derivatives*

Tarn *et al.* developed two azobenzene-based rotaxane nanovalves with reversibility in response to blue light (403 nm) irradiation (**Figure 2.17**).<sup>57</sup> These nanovalves were synthesized as follows. First, p-nitrobenzoic acid was reacted with glucose to give 4,4'-azobenzenecarboxylic acid. Then, 4,4'-azobenzenecarboxylic acid was reacted with N-hydroxysuccinimide to conjugate at one end with two adamantane-based molecules of different lengths, respectively. Next, the resulting azobenzene-containing molecules were complexed with  $\alpha$ -CD to form the  $\alpha$ -CD/azobenzene pseudorotaxanes. Finally, those pseudorotaxanes of different lengths were attached to aminopropyltriethoxysilane (APTES) modified-MSNs, yielding the ready-to-use nanocarriers. It is notable that the authors completed all the nanovalve attachment including stalks and nanocaps before loading cargos instead of *vice versa*. The method of loading cargos was by suspending the nanovalves in organic solvents under UV light irradiation to destabilize hydrophobic interactions between  $\alpha$ -CD and the azobenzene moiety. To cap the pores after cargo loading, the particles were suspended in water in the dark to allow rebinding of the  $\alpha$ -CD to azobenzene. Three fluorescent dyes with size between 1 and 2 nm, alizarin red S, PI, and Hoechst 33342, were chosen as the cargo molecules. The authors demonstrated that the two stalks of different lengths allowed the selective loading and release of those dyes based on the size. The adamantane functional group was selected as the stopper for two reasons: it is bulky enough (diameter of 0.5 nm) to prevent  $\alpha$ -CD from unthreading; its binding affinity (binding constants of  $100 \text{ M}^{-1}$  [58]) with  $\alpha$ -CD is lower

than trans-azobenzene with  $\alpha$ -CD so that competitive binding is limited. In this way,  $\alpha$ -CD will either bind trans-azobenzene (“closed” state) or forms a metastable adamantane/ $\alpha$ -CD state that holds the nanocap away from the pore openings (“open” state) when cis-azobenzene is formed by photoexcitation. The reversibility of the designed nanomachines was demonstrated by sequential fluorescence spectra. When the near-UV light was turned off, the fluorescence intensity leveled off until the stimulus was reapplied.

### 2.3.3 Inactive Supramolecular Systems

In addition to the supramolecular systems discussed above, there are other types of mechanisms involving bulky host-guest supramolecules that are not themselves serving as the active parts. These types of systems are called “inactive supramolecular systems”. They typically use a bulky inclusion complex with a labile bond linked to the particle. The whole supermolecular complex is removed intact by bond cleavage through heat,<sup>59</sup> photo-redox,<sup>60</sup> or pH<sup>61</sup> at a location between the inclusion complex and nanoparticles.

#### *Activation Using Thermal-Sensitive Bonds*

Very recently, Chen *et al.* developed a  $\beta$ -CD-adamantane cap held on to the superparamagnetic core@silica shell nanoparticles by a thermo labile bond on 4,4'-azobis(4-cyanovaleric acid) (ACVA).<sup>62</sup> This bond was cleaved by the localized heat generated from the superparamagnetic core by oscillating magnetic field (OMF) actuation (**Figure 2.18**). The authors first demonstrated that the release amount of fluorescein cargos was adjustable by controlling the OMF exposure time. *In vitro* drug release study was conducted to deliver DOX to PANC-1 cells. A positive correlation between the viability of the cells treated with DOX-loaded Mag@MSNs-AMA-CD and the OMF trigger time showed that dose control was achieved. Cells treated with nanoparticles without DOX under 10 min of OMF exposure didn't show any adverse effect,



confirming that the heat generated from OMF interacting with the superparamagnetic core was not harmful to the cells.

### *Megagates and Supramolecular Amplifiers*

A unique use of the adamantane/ $\beta$ -CD interaction is formation of megagates over the large (6.5 nm) pores of SBA-15 silica. Xue, *et al.* designed and synthesized pH-responsive “weblike” megagates to cover the bigger pores with the goal trapping cargo molecules (**Figure 2.19**).<sup>61</sup> Two types of megagates, MG-1 and MG-2, were designed to cap and block larger and relatively smaller molecules, respectively. The extended structure of MG-1, which has a diameter of about 5.5 nm, was synthesized by linking a 1,3,5-triphenylbenzene core to three adamantane arms through triethylene glycol chains. MG-1 sufficiently prevents leakage of 4 nm dextran from the nanoparticle. To be able to reduce the gap between adamantane moieties for storing a smaller fluorescein disodium salt (FDS) cargo, hexaalkyne was chosen to be the core of MG-2 to generate a megagate with twice as many adamantane moieties as MG-1. To attach the megagate to the silica, ammine-modified  $\beta$ -CD stalks were grafted on the surface of SBA-15 through imine formation. Then, the adamantane arms form inclusion complexes with the  $\beta$ -CD and block the pores. FDS can diffuse freely out of the pore when a megagate is capped by MG-1, while dextran can only escape from the pore when the gate is opened due to the cleavage of imine bonds in the stalks at low pH.

Xue, *et al.* employed this megagate system to construct an enzyme-encapsulated MSN based chemical amplifier (**Figure 2.20**).<sup>63</sup> In this study, the pH-responsive MG-2 enables substrate size-selectivity and thus controls the substrate access toward the encapsulated porcine liver esterase (PLE) in the MSN pores. PLE substrates 4-acetozycinnamic acid (ACA) and 5-carboxy-fluorescein diacetate (CFDA) were chosen due to their different sizes. The CFDA molecules are

too big to pass through the megagate; only the small ACA analytes are able to diffuse in and out of the gaps between the adamantane moieties. ACA analytes undergo hydrolysis reactions after they interact with the hydrolase enzymes in the pores, generating acetic acid to actuate the megagate and allowing CFDA molecules to diffuse into the pore. Hydrolysis of CFDA produces a fluorescent product. The catalytic amplification process then occurs due to the subsequent gate opening of the neighboring pores resulted from the additional hydrolysis of CFDA, and the process is monitored by increase in the fluorescence signal.

## 2.4 Supramolecular Snap-Tops for Stimuli Responsive Cargo Delivery

A “snap-top” rotaxane is a supramolecule composed of a cyclic molecule on a stalk and a large “stopper” molecule attached to the end of the stalk to keep the cyclic molecule in place. The closed system is snapped open when the bulky stopper is removed thus allowing the cyclic molecule to move away from the pore. Patel *et al.* reported an enzyme-responsive snap-top nanovalve based on [2]rotaxane and  $\alpha$ -CD (**Figure 2.21**).<sup>64</sup> MSNs were first modified with APTES to introduce amine groups which were then alkylated with tri(ethylene glycol)monoazide monotosylate units. Next, the cargo loading step was performed followed by the incubation with  $\alpha$ -CD at 5°C for 24 h. At low temperature,  $\alpha$ -CD threaded onto the tri(ethylene glycol) chains and effectively blocked the nanopores. The azide terminals of the cargo-loaded particles were then attached to adamantyl ester stopper molecules through Cu(I)-catalyzed azide-alkyne “click”cycloaddition. In this design, porcine liver esterase (PLE) catalyzed hydrolysis of the adamantyl ester stopper, allowing  $\alpha$ -CD to dethread and release the cargo molecules from the pores. RhB was used as a model drug and the result from luminescence spectroscopy showed that rhodamine B was released only after adding PLE.

Ambrogio *et al.* reported another snap-top system in which stalks with disulfide bonds were encircled by CB[6] or  $\alpha$ -CD rings and bulky adamantyl groups at the terminal acted as the stoppers (**Figure 2.22**).<sup>65</sup> The stalks were grafted onto MSNs through the reaction between azide-terminated diethylene glycol monotosylates and amino groups of APTES on the surface of MSNs. Then, nanoparticles were loaded with RhB followed by adding either CB[6] or  $\alpha$ -CD to thread the stalks. The entire snap-top system was completed by click chemistry between the azide group at the end of the stalks with propargyl ethers that contained disulfide linkages and bulky adamantyl groups at the end. The two snap-top systems showed no leakage but released rhodamine B upon the addition of dithiothreitol (DTT) and 2-mercaptoethanol (ME) which reduced the disulfide bonds, removed the adamantyl stoppers, and thus uncapped the pores of the CB[6] or  $\alpha$ -CD-capped nanoparticles, respectively.

Another example of supramolecular snap-tops was designed by He *et al.* (**Figure 2.23**).<sup>66</sup> In this design, an alkoxy silane and  $\alpha$ -CD was also used as a stalk and a nanocap, then serial peptide sequences were attached as the stopper molecule. The stopper, Gly-Phe-Leu-Gly (GFLG), can be hydrolyzed by cathepsin B, which is an overexpressed protease in various tumors. Almost 60% and 80% of the loaded DOX was released from the nanoparticles in the presence of cathepsin B at pH 7.4 and 5.0, respectively. Cervical cancer cells (HeLa) and a normal cell line of African green monkey SV40-transformed kidney fibroblast cells (COS7) were used to evaluate the targeting and drug release ability of DOX-loaded MSN-GFLGR<sub>7</sub>RGDS/ $\alpha$ -CD nanoparticles. These nanoparticles were shown not only to be efficiently taken up by tumor cells *via* integrins receptor-mediated targeting, but also can specifically release DOX into tumor cells *via* enzymatic digestion of GFLG peptide.

## 2.5 Nanopistons and Their Use as Size-Selective Caps

A supramolecular nanopiston can serve as a gate to control cargo release. The piston consists of a molecule that moves in or out of a cavity provided by a ring (such as  $\beta$ -CD) that is immobilized around the opening of the pores. In this section, combination of a nanopiston with an inactive supramolecular system that allows sequential release of small molecules by the first stimulus and larger molecules by a second different stimulus is discussed.

Zhao *et al.* designed and fabricated a MSN-based nanopiston (**Figure 2.24**).<sup>64</sup> This pH-mediated dual cargo delivery system consisted of  $\beta$ -CD which is covalently linked around the portal of the nanopores of MSNs and a RhB/benzidine compound that is inserted into the cavity of  $\beta$ -CD and moves in and out like a piston. It can control the trapping and release of the cargo molecules in response to pH changes. At neutral conditions, small cargos are trapped in the pore of MSNs and the RhB/benzidine plug blocks the  $\beta$ -CD gate tightly. As the pH value of the system decreased from 7 to 4, the protonated RhB/benzidine plug left the cavities of  $\beta$ -CDs and the small cargo was released by diffusing through the cavities of  $\beta$ -CD.

A similar design can be used for dual-cargo delivery that can sequentially deliver two different sizes of cargos on-command. It has the potential to achieve combination drug therapy. Wang *et al.* functionalized MSN surfaces with  $\beta$ -CD, which served as a gate to store large Hoechst 33342 molecules (**Figure 2.25**).<sup>68</sup> The second smaller cargo, p-coumaric acid (CA), was loaded by diffusing it through the cavities of the  $\beta$ -CD into the pores of MSNs. Methyl orange (MO) was then added into the system to form a complex with the  $\beta$ -CD and plug the  $\beta$ -CD rings. Upon lowering the pH to 3.5, the formation constant between  $\beta$ -CD and MO decreased. The removal of the protonated MO molecules from the  $\beta$ -CD cavities was followed by the release of the small CA cargo while the larger Hoechst 33342 were still blocked by the  $\beta$ -CD rings. Release of Hoechst 33342 was then triggered by introducing a reducing agent 2-mercaptoethanol that cleaved the

disulfide bonds that linked the  $\beta$ -CD rings covalently onto the MSN surfaces. Removal of the  $\beta$ -CD rings released Hoechst 33342.

## 2.6 Summary

In keeping with the theme of this special issue of Theranostics, this review focused on supramolecular systems that carry out on-command, stimulated drug delivery. The review emphasized the mesoporous silica nanoparticles that have demonstrated efficacy *in vitro* and *in vivo*. There are of course very many other capping methods in addition to pseudorotaxanes and rotaxanes, and also many different types of nanoparticles have been studied.<sup>53,69-74</sup> Mesoporous silica forms a type of “hard” inorganic particle that is structurally stable for drug delivery.<sup>75,76</sup> For biomedical applications other important types of hard nanoparticles include those made from amorphous silica, gold, iron oxide, quantum dots and nanodiamonds.<sup>77-81</sup> Important types of “soft” nanomaterials include liposomes (the most successful in biomedical applications to date), polymers and dendrimers. Hybrid organic/inorganic particles have also been examined; particles made from organosilanes and lipid bilayer-coated silica are examples closely related to those discussed in this review. Many innovative capping systems on nanoparticles have also been used including thermal- and pH-sensitive polymers, and DNA to name a few. Supramolecular capping systems are fascinating, versatile, highly controllable, reversible, and biologically compatible. As is the case with other drug delivery systems, it is a long and costly road to clinical trials and eventual use in the clinic,<sup>82</sup> but all of the above properties make supramolecular capping systems together on mesoporous silica nanoparticles worthy of the attention that they are being given. Because of the importance of the biomedical applications, imaginative chemists, biologists, medical doctors, physicists and engineers will develop innovative new functional and controllable

nanomaterials that will eventually advance to the clinic and help mankind.

## **2.7 Acknowledgment**

The authors gratefully acknowledge financial support through the years by the National Science Foundation, the National Institutes of Health, and the Defense Threat Reduction Agency. Manuscript writing was supported in part by the Zink Research and Student Support Fund.

## 2.8 Figures and Tables

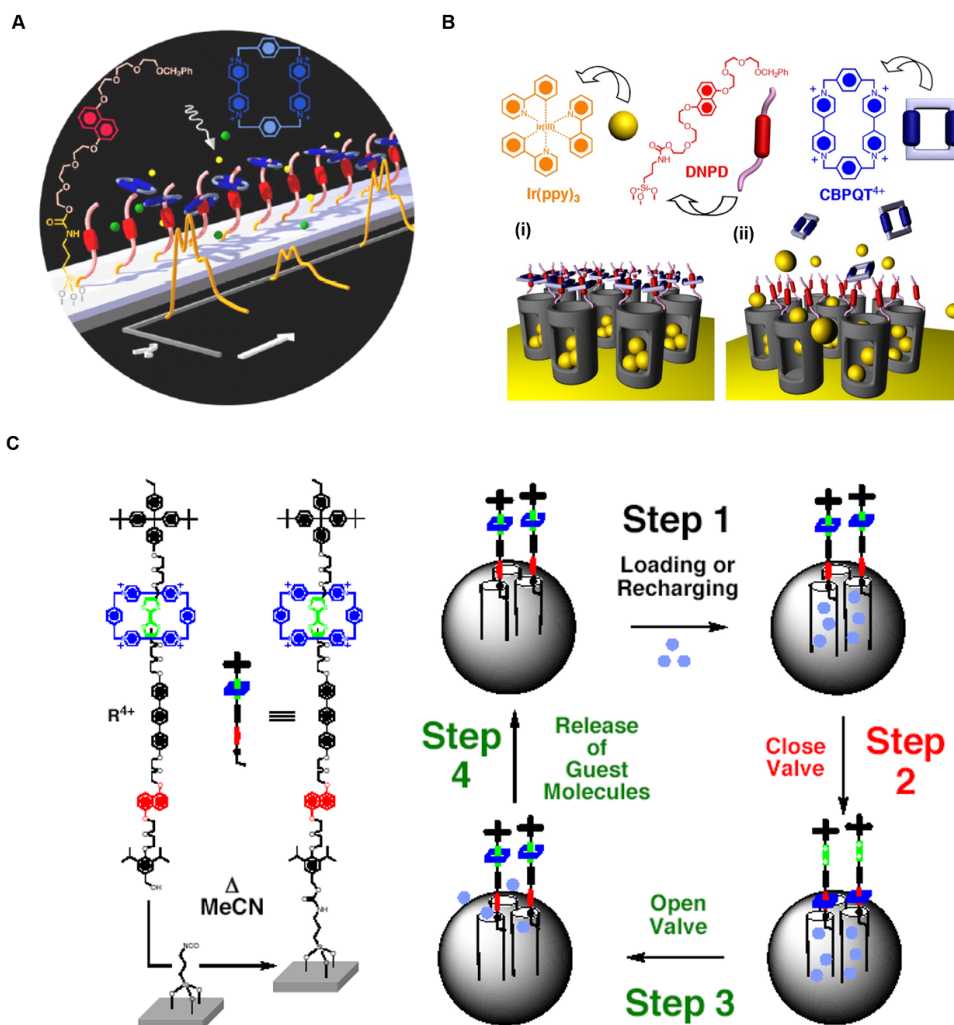


**Figure 2.1.** (A) A pseudorotaxane on a solid silica support. Reprinted with permission from Ref. 13, copyright (2001) Angew. Chemie - Int. Ed. (B) Graphical representations of operation of nanovalves gating the pore openings on silica particles. (i) The orifices of the nanopores (diameter 2 nm) are covered with pseudorotaxanes (formed between DNPd and CBPQT<sup>4+</sup>) which trap the luminescent Ir(ppy)<sub>3</sub> molecules inside the nanopores. (ii) Upon their reduction, the CBPQT<sup>2+</sup> bisradical dications are released and allow the Ir(ppy)<sub>3</sub> to escape. Reprinted with permission from Ref. 14, copyright (2004) J. Am. Chem. Soc. (C) Graphical representations of the surface attachment of bistable rotaxanes to silica particles along with a cycle for loading and release of guest molecules. Left: The structural formula of the bistable [2]rotaxane R<sup>4+</sup> and the procedure used for tethering R<sup>4+</sup> to the surface of mesoporous silica particles. Right: The

proposed mechanism for the operation of the nanovalve. The moving part of the molecular valve is a CBPQT<sup>4+</sup> ring (blue), which shuttles between a TTF station (green) and a DNP station (red) under redox control. The openings of the cylindrical pores on the silica are blocked by the CBPQT<sup>4+</sup> ring when the valve is closed. Guest molecules (turquoise spheres) are loaded in Step 1 by diffusion into the open pores when the CBPQT<sup>4+</sup> ring is located on the TTF station. The valve is closed in Step 2 by oxidation of the TTF unit to its dication, causing the CBPQT<sup>4+</sup> ring to move to the DNP station, which is much closer to the openings of the pores. The valve can be opened (Step 3) by adding ascorbic acid to reduce the TTF dication back to its neutral state, whereupon the CBPQT<sup>4+</sup> ring moves back from the DNP station to be relocated around the much more  $\pi$  electron-rich TTF station, releasing the guest molecules in Step 4. The valve is ready for recharging (*i.e.*, returning to Step 1). Thus, the valve can be closed and opened reversibly. The silica particles are not drawn to scale, and only a few of the ordered pores are shown. Reprinted from Ref. 15, copyright (2005) Proc. Natl. Acad. Sci.



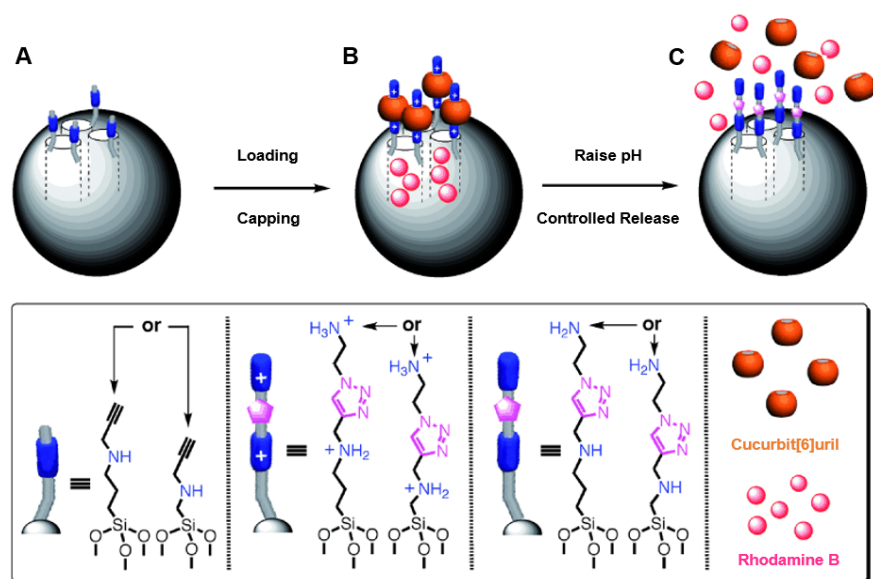


**Figure 2.2.** The alkyne-functionalized mesoporous silica nanoparticles MCM-41 are loaded (A→B) with rhodamine B (RhB) molecules, and capped (A→B) with CB[6] during the CB[6]-catalyzed alkyne-azide 1,3-dipolar cycloadditions. RhB molecules are released (B→C) by switching off the ion–dipole interactions between the CB[6] rings and the bisammonium stalks by raising the pH and deprotonating the amines. Reprinted with permission from Ref. 23, copyright (2008) *Angew. Chemie - Int. Ed.*

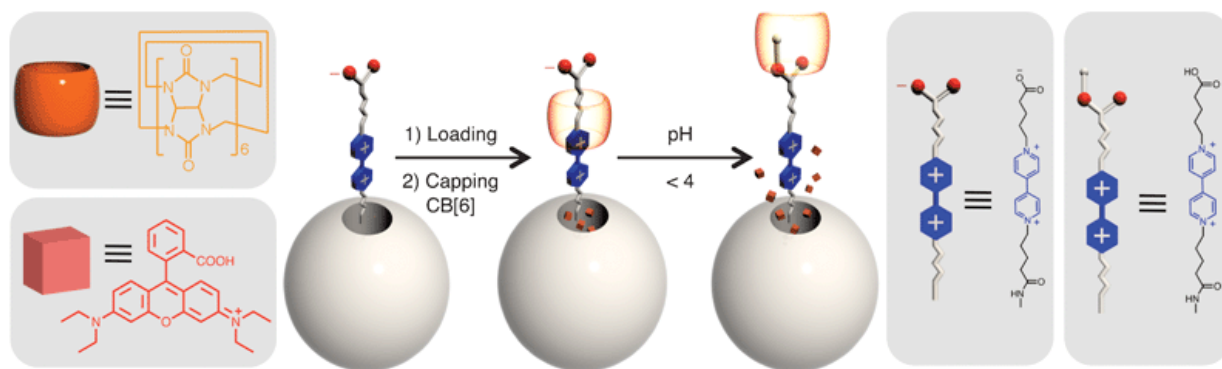


**Figure 2.3.** Design and preparation of viologen threads (stalk component) and CB[6] (cap) on MSNs that operate under pH-control. Reprinted with permission from Ref. 24, copyright (2009) *Chem. Commun.*

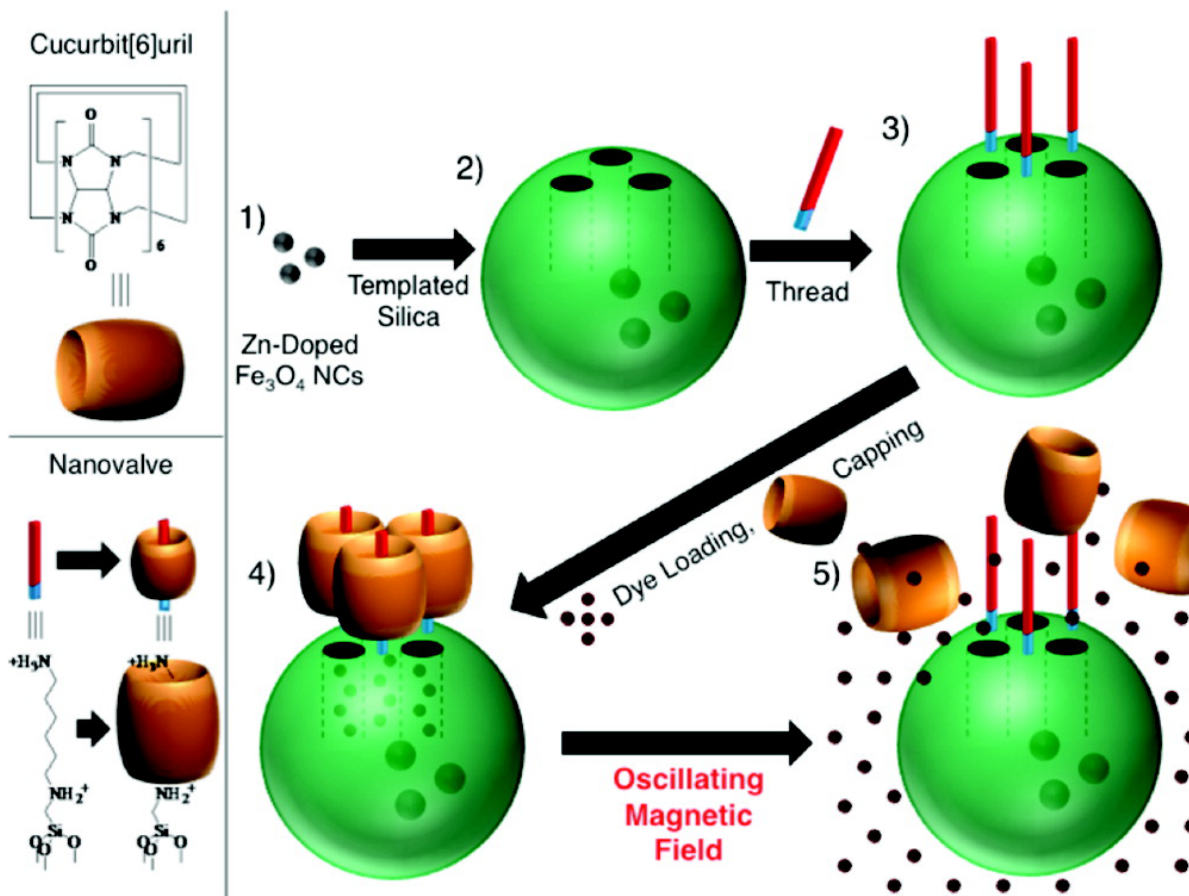


**Figure 2.4.** Scheme of the synthesis of the mechanized nanoparticles and their operation under oscillating magnetic fields (OMFs). (1) Supraparamagnetic nanoparticles are synthetically positioned at the core of MSNs; (2) the molecular machine is then attached to the nanoparticle's surface; (3) the drug is loaded into the particle and (4) the pores are capped to complete the system. (5) Drug release is realized using remote heating via an OMF. Reprinted with permission from Ref. 25, copyright (2010) J. Am. Chem. Soc.

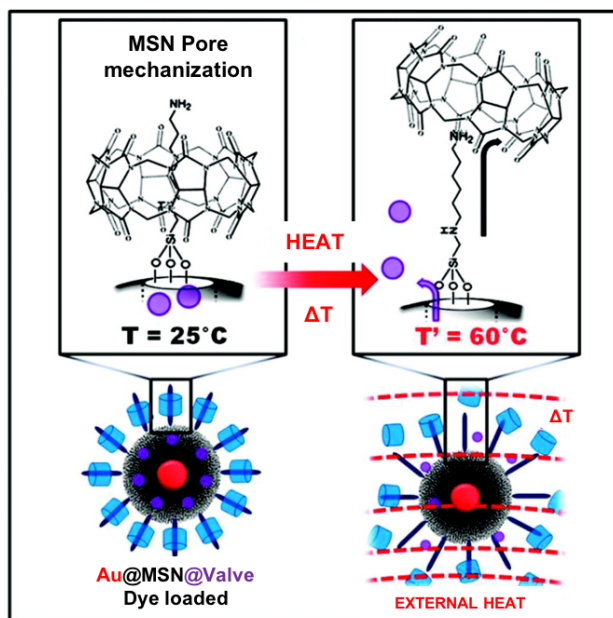


**Figure 2.5.** External heating of a suspension of Au@MSN@Valve to 60 °C causes dissociation of the CB[6] caps from the stalks and release of the cargo molecules from the pores. Reprinted with permission from Ref. 26, copyright (2012) J. Am. Chem. Soc.

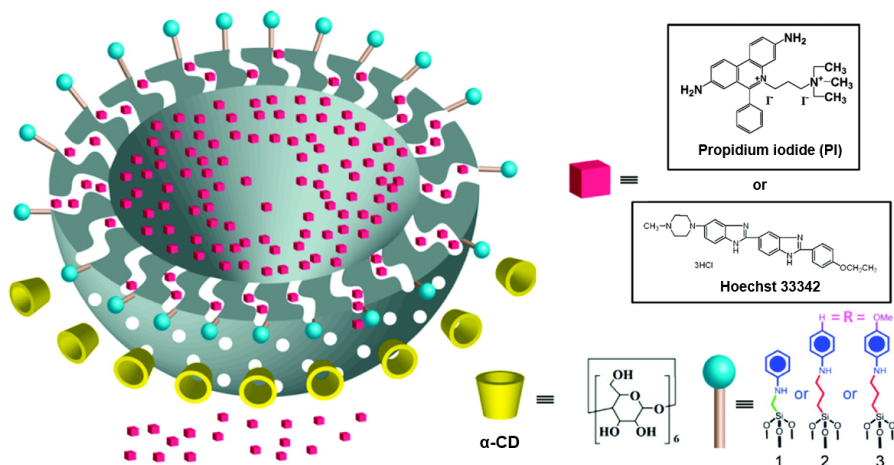


**Figure 2.6.** Depiction of a cross section of a hollow nanoparticle illustrating the wormlike pores connecting the interior to the surrounding solution. The stalks and the  $\alpha$ -CD rings that control the pore openings are also shown. Reprinted with permission from Ref. 31, copyright (2009) J. Am. Chem. Soc.

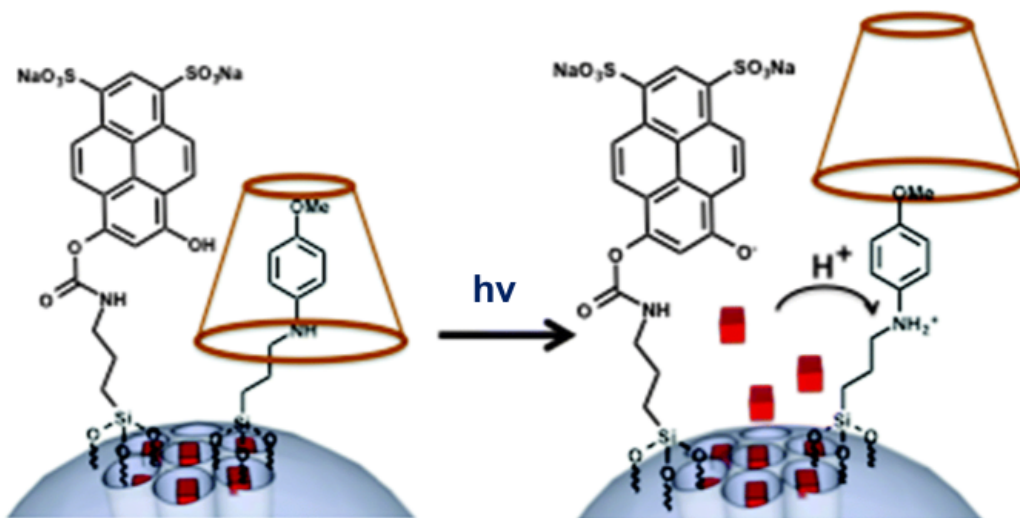


**Figure 2.7.** Light activation of a pH nanovalve. A photoacid is attached adjacent to an acid-stimulated aniline/ $\alpha$ -CD valve. Photoexcitation of the photoacid causes protonation of the stalk and releases the cap and cargo. Reprinted with permission from Ref. 33, copyright (2014) Chem. Commun.

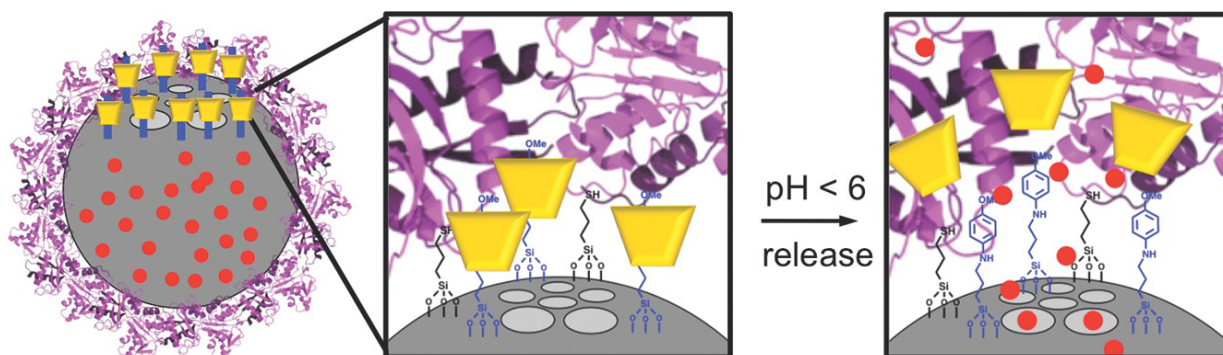


**Figure 2.8.** Depiction of the fully assembled Tf-nanovalve-modified MSN system. The operation of the aniline/ $\alpha$ -CD valve was not inhibited by the Tf coating. Reprinted with permission from Ref. 34, copyright (2015) Small.

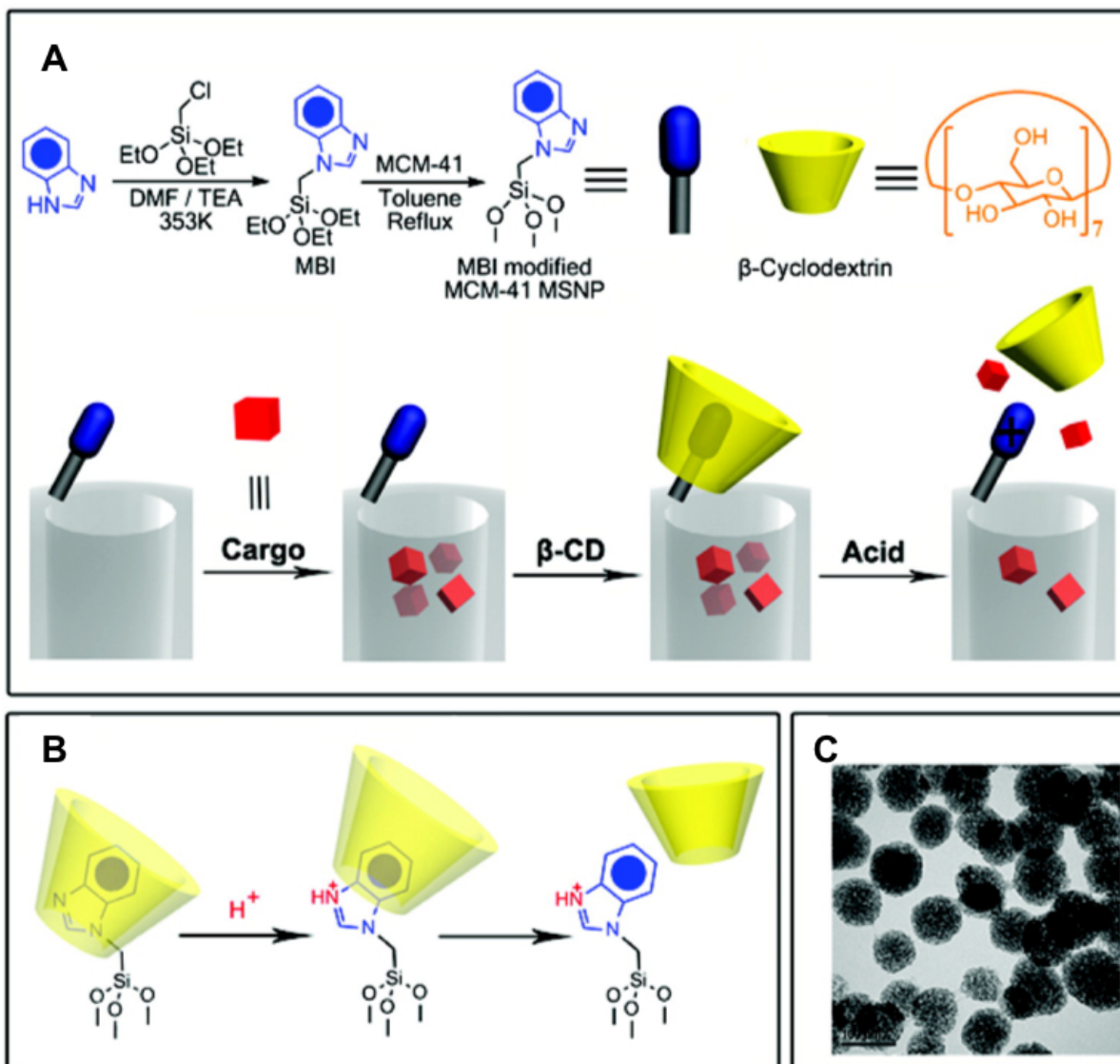


**Figure 2.9.** (A) Steps of stalk synthesis, cargo loading, capping, and release. (B) Cap dissociation from protonated stalk after pH decreases below 6. (C) TEM image of the capped MSN. Reprinted with permission from Ref. 36, copyright (2010) J. Am. Chem. Soc.

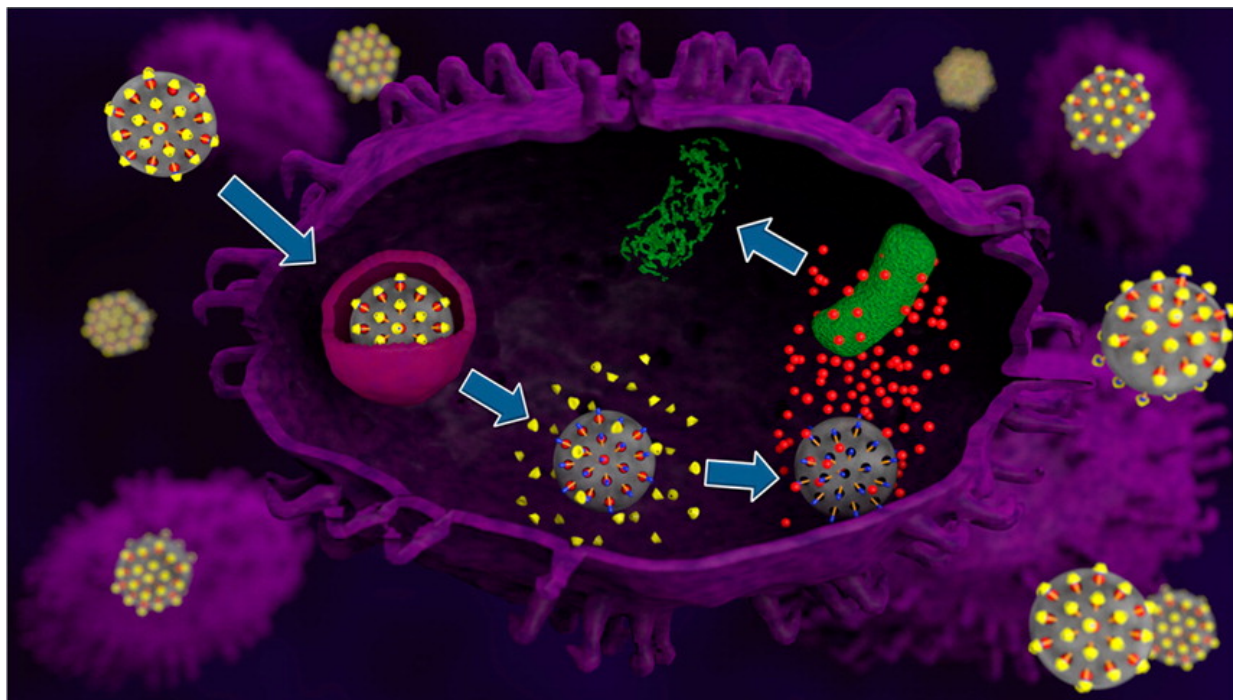


**Figure 2.10.** Moxifloxacin-loaded MSNs functionalized with pH-responsive capping system were uptaken into lysosomal compartments in a macrophage. The pH-responsive cap was opened and moxifloxacin was released to kill the intracellular *Francisella tularensis*. Reprinted with permission from Ref. 37, copyright (2015) ACS Nano.

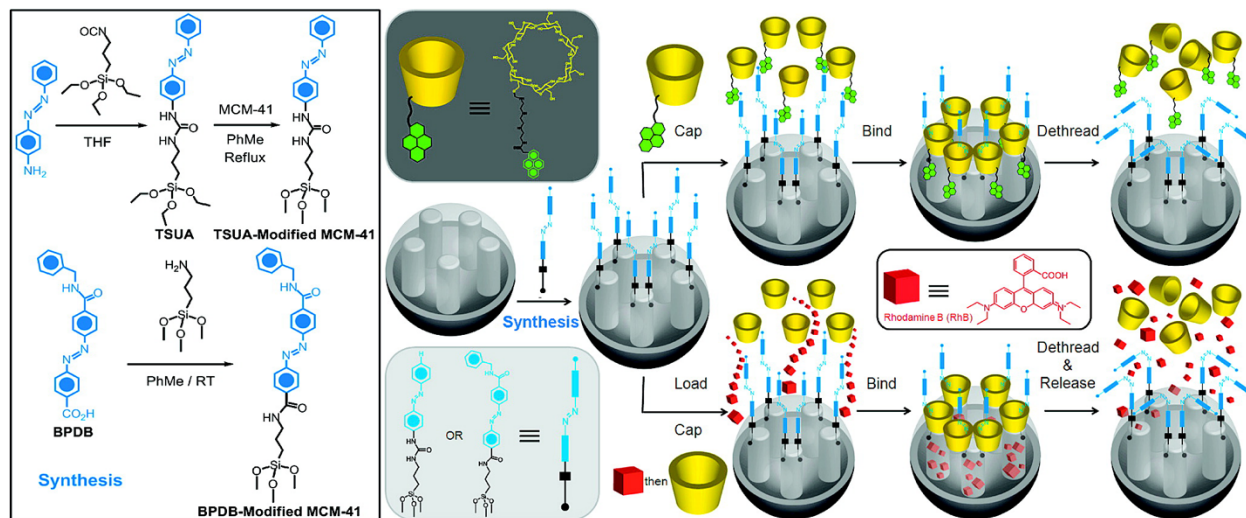


**Figure 2.11.** Synthesis of 4-(3-triethoxysilylpropylureido)azobenzene (TSUA)- and (E)-4-((4-(benzylcarbamoyl)phenyl)diazenyl) benzoic acid (BPDB)-modified MCM-41. Two approaches to the operation and function of the azobenzene-modified MCM-41 NPs carrying nanovalves. Py- $\beta$ -CD or  $\beta$ -CD threads onto the trans- azobenzene stalks to seal the nanopores. Upon irradiation (351 nm), the isomerization of trans-to-cis azobenzene units leads to the dissociation of Py- $\beta$ -CD or  $\beta$ -CD rings from the stalks, thus opening the gates to the nanopores and releasing the cargo. Reprinted with permission from Ref. 45, copyright (2009) J. Am. Chem. Soc.

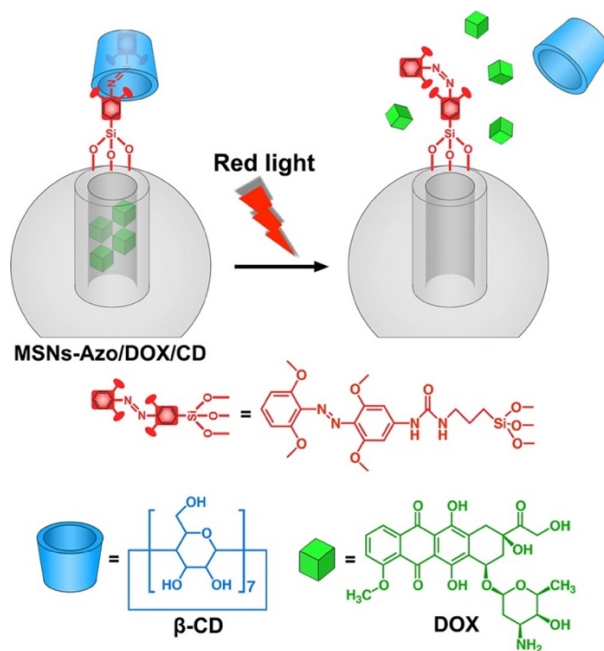


**Figure 2.12.** Cartoon of the red-light-responsive drug delivery system constructed by MSNs modified with mAzo/ $\beta$ -CD supramolecular valves. Reprinted with permission from Ref. 46, copyright (2016) Langmuir.

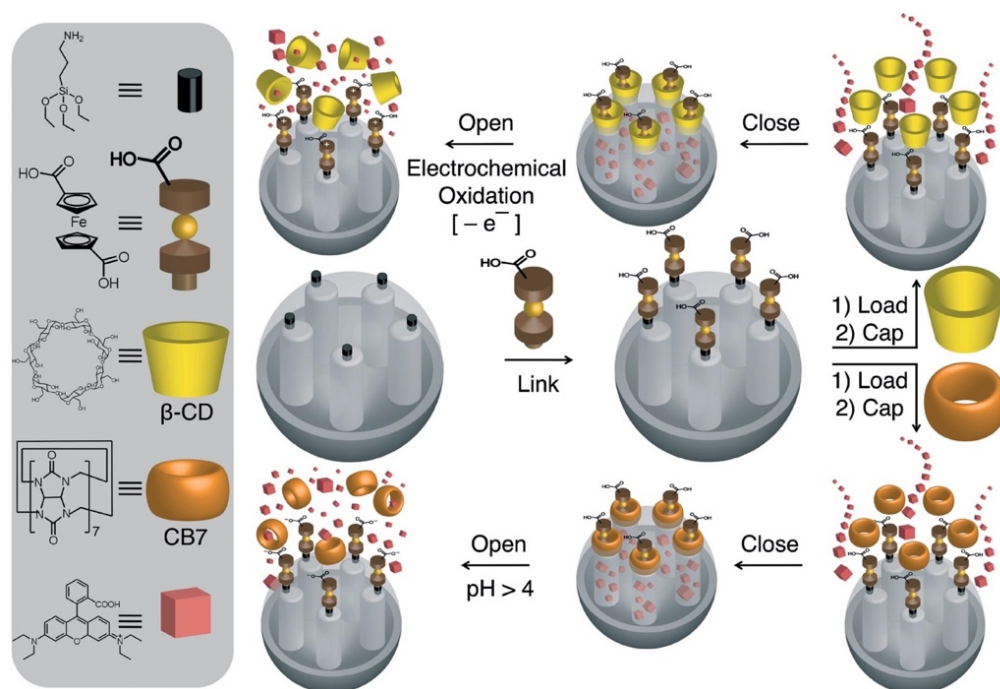


**Figure 2.13.** Design and preparation of ferrocene-based mechanized nanoparticles, which operate under redox or pH control according to the nature of the ring ( $\beta$ -CD in the top route and CB7 in the bottom route) capping the pores. Reprinted with permission from Ref. 47, copyright (2009) European J. Org. Chem.



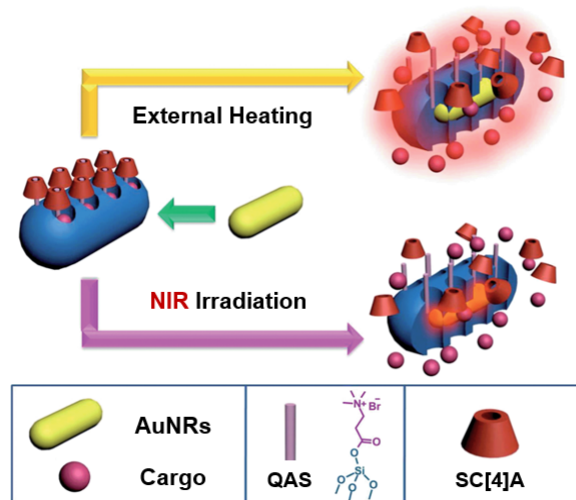


**Figure 2.14.** Schematic representation of SC[4]A-QAS nanovalves based on AuNR@MSN. The nanovalves can be operated by either NIR light irradiation or external heating to regulate the release of RhB. Reprinted with permission from Ref. 48, copyright (2014) Chem. Sci.

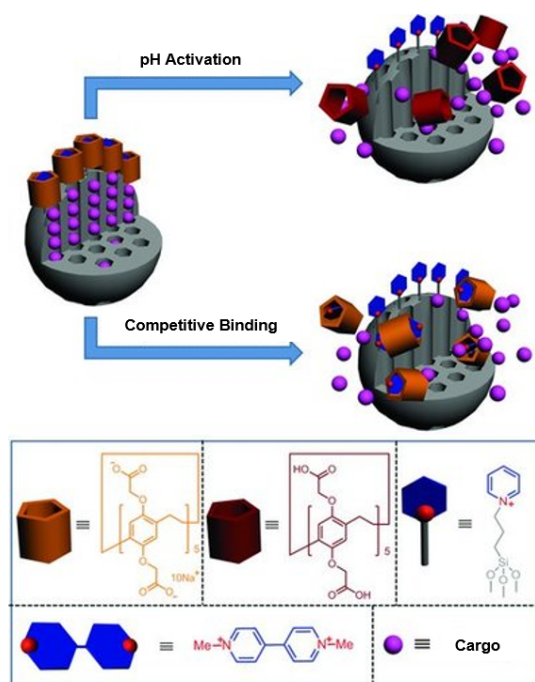


**Figure 2.15.** Diagram of pillar[5]arenes derivative based MSN drug delivery system. It can be triggered by both pH and competitive binding. Rhodamine B (RhB), calcein, and doxorubicin hydrochloride (DOX) were used as cargos. Reprinted with permission from Ref. 54, copyright (2013) Small.

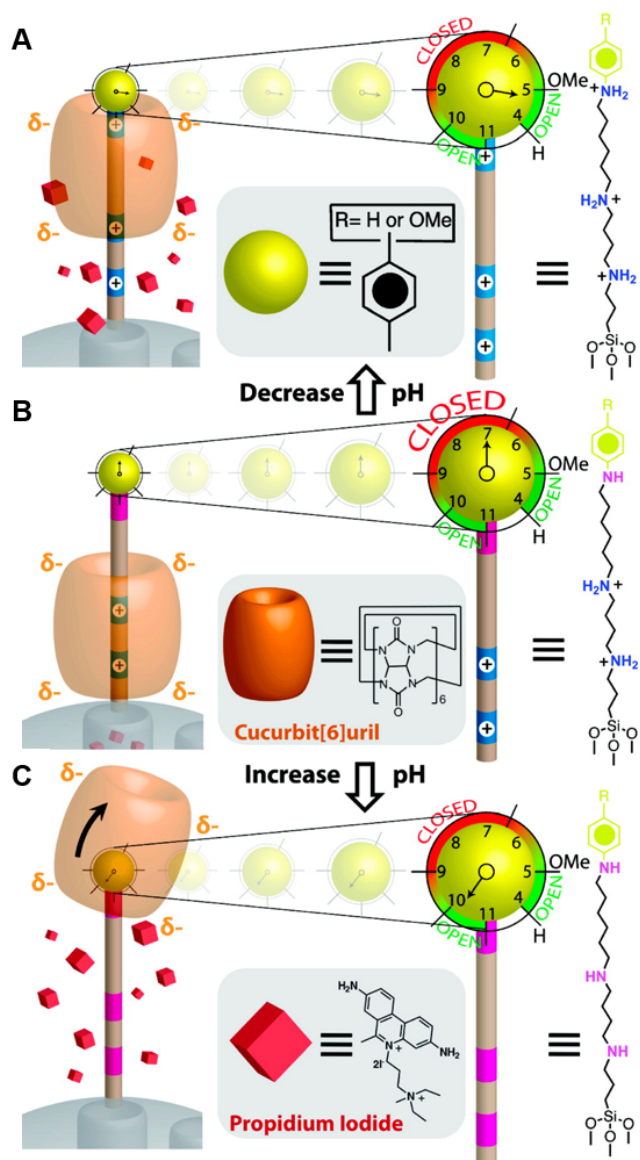


**Figure 2.16.** Design and pH-dependent operation of mechanized nanoparticles. (A) When pH is lowered such that the anilinium nitrogen atom is protonated, the CB[6] ring shuttles to the distal hexamethylenediammonium station, and PI is released. (B) At neutral pH, the CB[6] ring sits on the tetramethylenediammonium recognition unit, blocking the nanopores. (C) When the pH is raised, all of the nitrogen atoms on the stalk are deprotonated resulting in dethreading of the CB[6] ring. The system is designed such that the pH-response can be fine-tuned by changing the functional group R to modulate the pKa of the anilinium nitrogen atom. Reprinted with permission from Ref. 56, copyright (2009) J. Am. Chem. Soc.

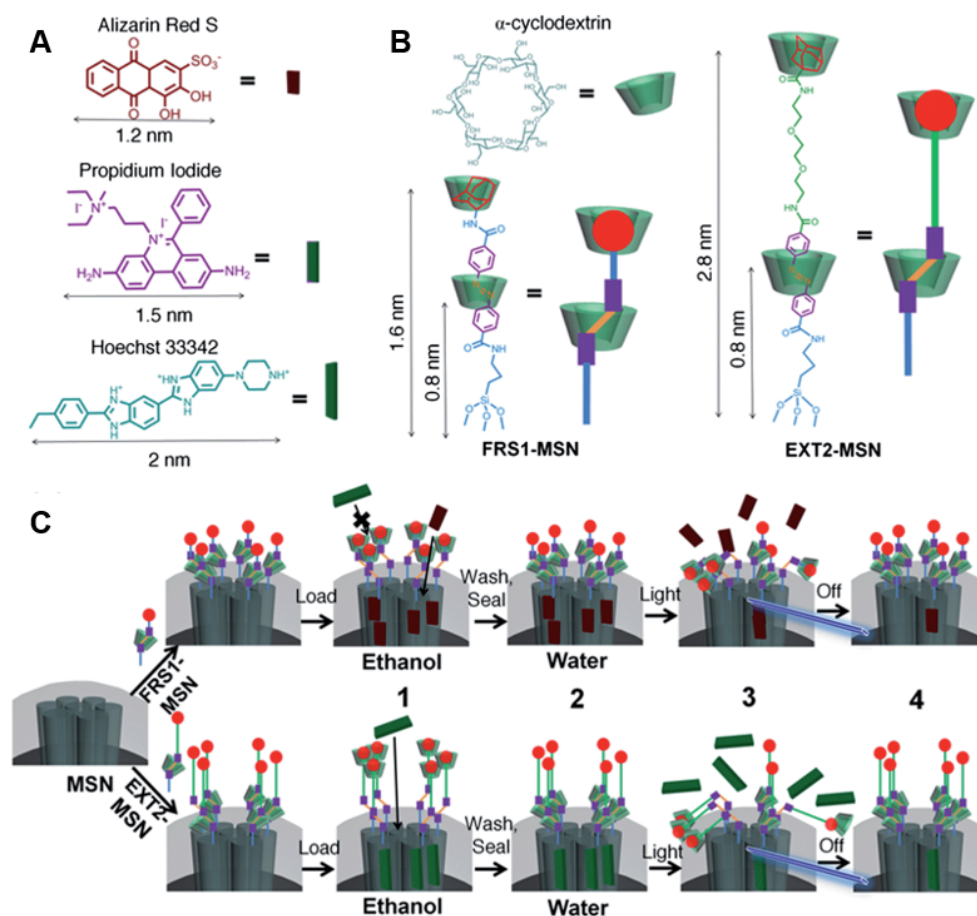


**Figure 2.17.** (A) Size illustration of various cargo molecules and (B) azobenzene stalks FRS1-MSN and EXT2-MSN. Because of the shorter stalk length, FRS1-MSN is limited to loading cargo molecules  $<2$  nm. Hoechst 33342 and propidium iodide dyes remain excluded from FRS1-MSN as a result of their size. However, EXT2-MSN is observed to load all three of the listed fluorophores. (C) Schematic illustration of the fully assembled rotaxane nanovalve and operation. (1) After synthesis, the nanovalves are suspended in an organic solvent, which destabilizes hydrophobic interactions between the  $\alpha$ -cyclodextrin and azobenzene moiety and allows for cargo loading. (2) Upon solvent exchange to water, rebinding of the cyclodextrin to azobenzene seals in the loaded cargo. (3) Irradiation with light induces isomerization to cis-azobenzene, forcing cyclodextrin to move to the end of the stalk, and allowing cargo to release. (4) Upon removal of the light stimulus, thermal relaxation of cis-azobenzene to its more stable trans isomer allows rebinding of the cyclodextrin and seals in the remaining cargo. Reprinted with permission from Ref. 57, copyright (2014) Nanoscale.

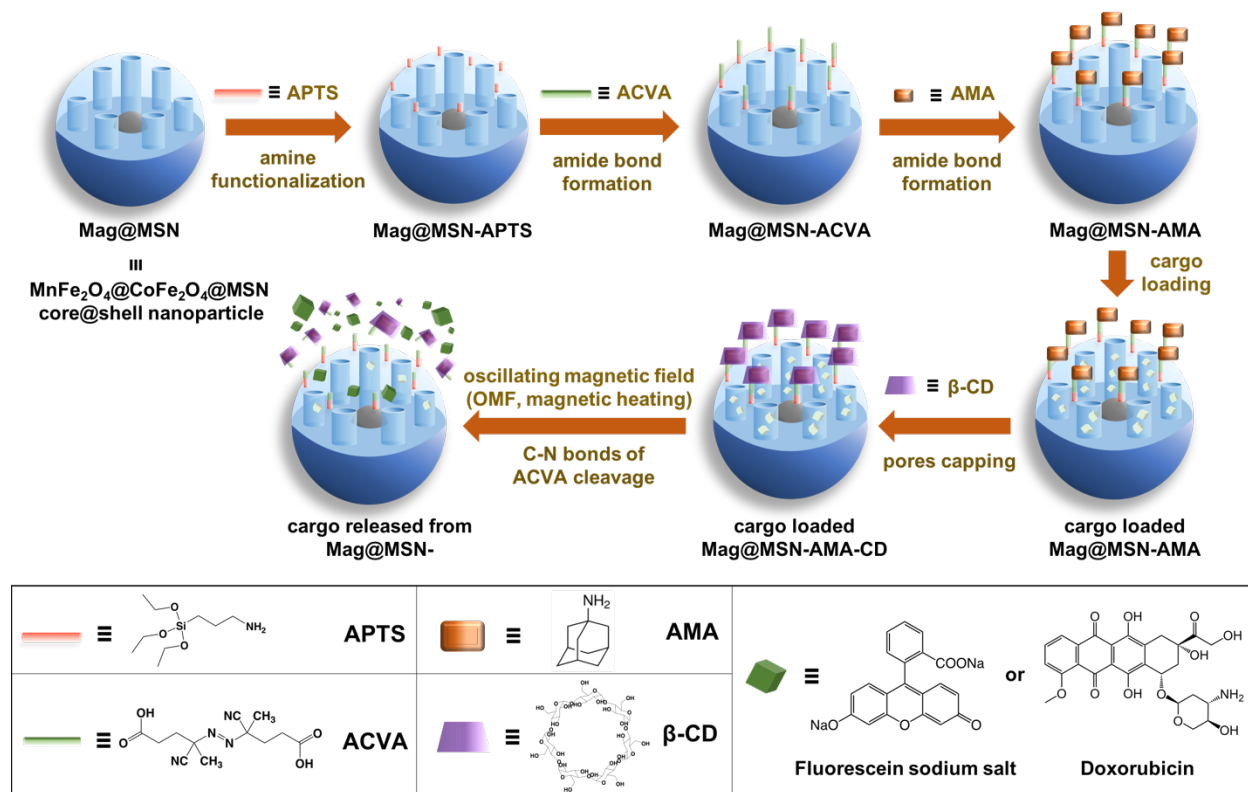


**Figure 2.18.** Synthesis and operation of the thermal-sensitive supramolecular platform activable by an oscillating magnetic field. Adapted with permission from Ref. 62, copyright (2019) ACS Nano.

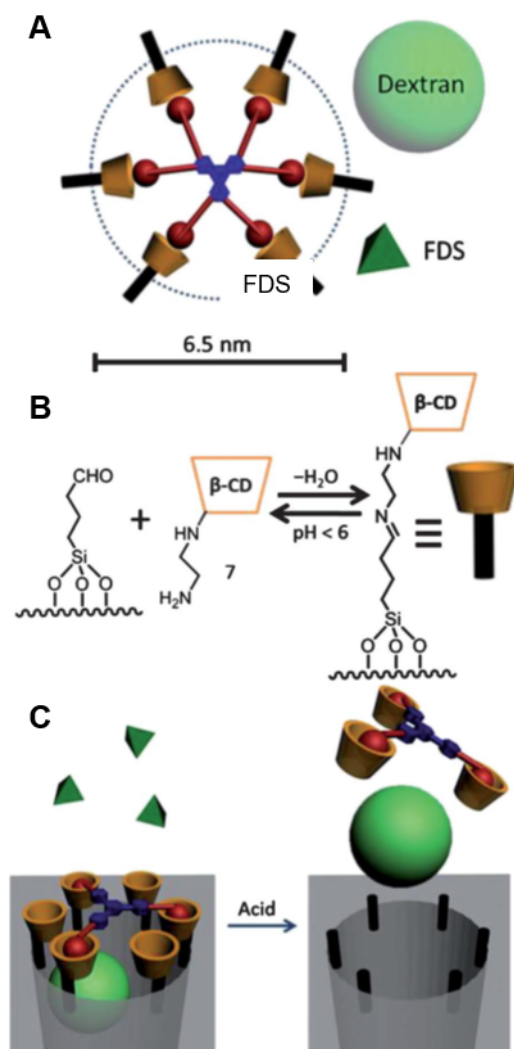


**Figure 2.19.** (A) The structure of a weblike megagate using MG-2 as the capping molecule. The relative sizes of the pore (dashed circle), the dextran cargo (the light green ball), and the smaller FDS cargo (the dark green pyramid) are shown. (B) Schematic representation of the cyclodextrin attachment onto the silica modified with aldehyde through imine formation. (C) The capping of megagate by MG-1 prevents the dextran from escaping, while FDS can freely diffuse out from the pore. Addition of acid allows the release of dextran. Reprinted with permission from Ref. 61, copyright (2012) Nanoscale.

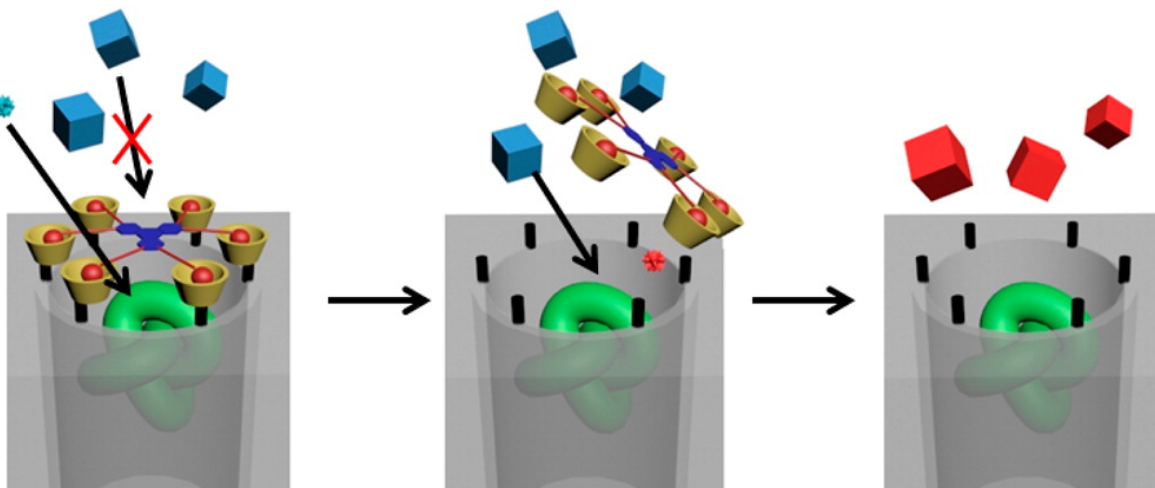


**Figure 2.20.** Schematic representation of the self-amplifying chemical sensing process. The megagate selectively allows only the small analyte molecule (blue ball) to diffuse into the pore to actuate megagate. Upon the opening of the gate, the substrate (blue cubes) is able to access the enzyme to initiate a catalytic production of fluorescent molecules. Reprinted with permission from Ref. 63, copyright (2013) J. Am. Chem. Soc.

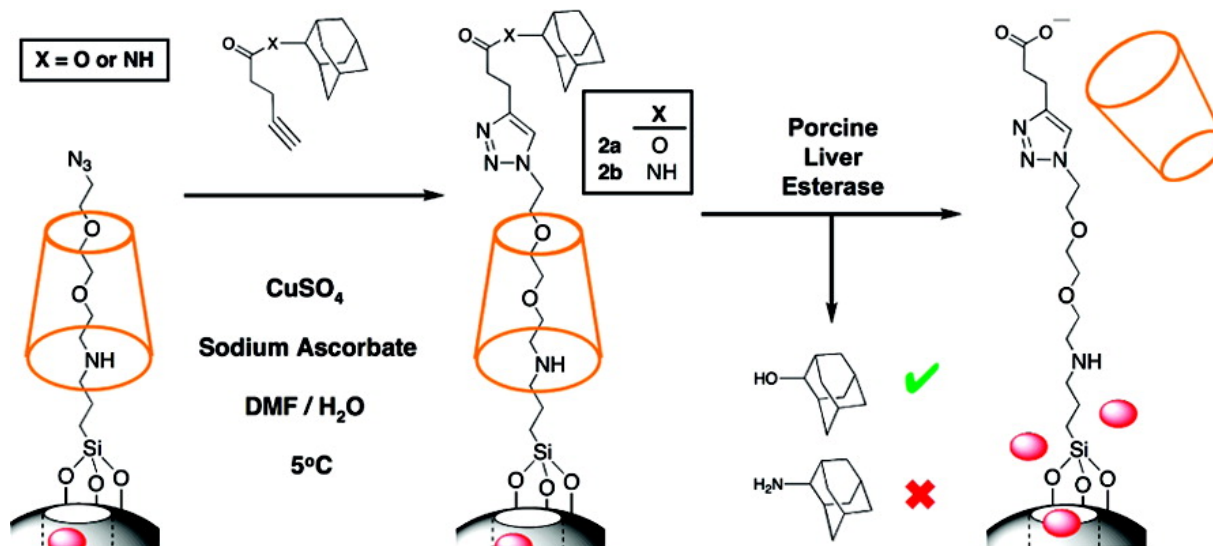


**Figure 2.21.** Synthesis and activation of an enzyme-responsive snap-top system. Reprinted with permission from Ref. 64, copyright (2008) J. Am. Chem. Soc.

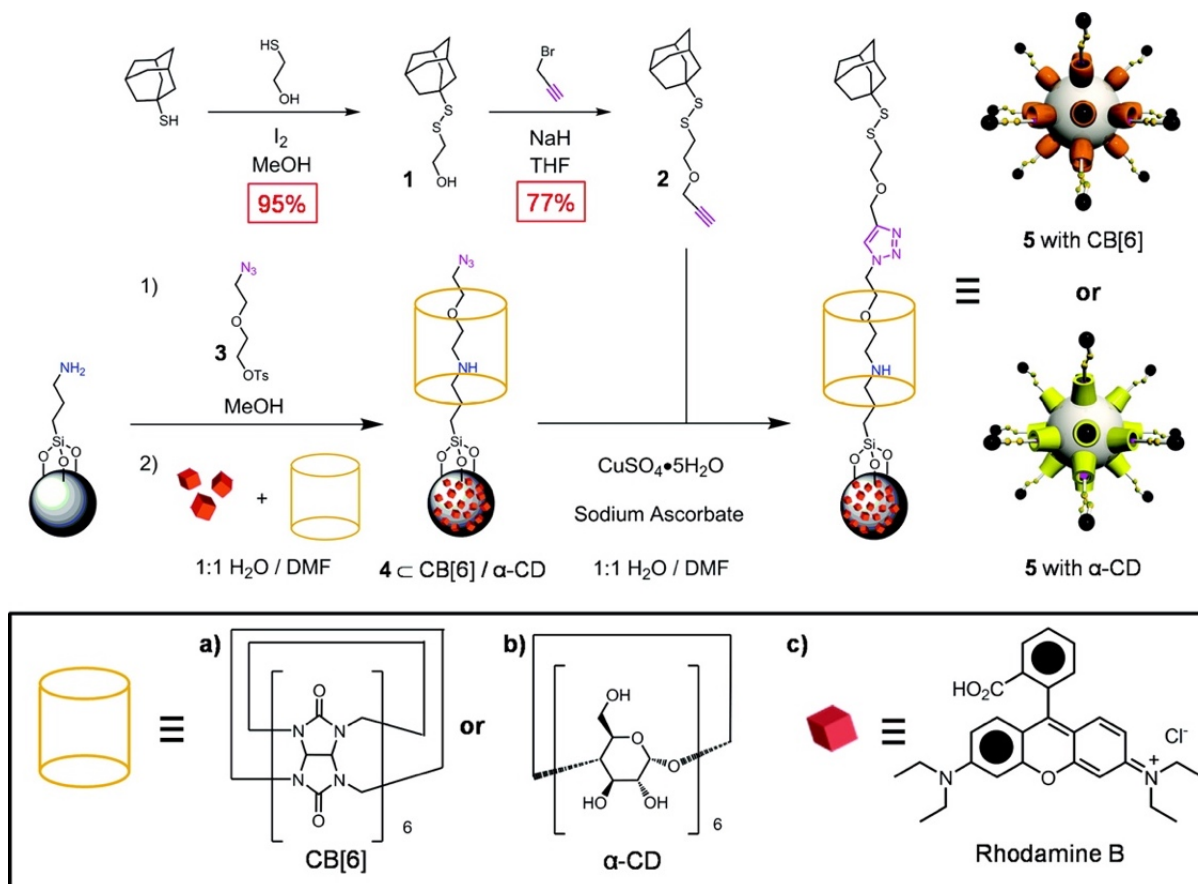


**Figure 2.22.** Synthesis of the alkyne-terminated stopper and assembly of disulfide-based snap-top nanocarriers. The nanocarriers studied utilize  $\text{CB}[6]$  or  $\alpha$ -CD as the capping agent and Rhodamine B as the cargo. Reprinted with permission from Ref. 65, copyright (2010) Org. Lett.

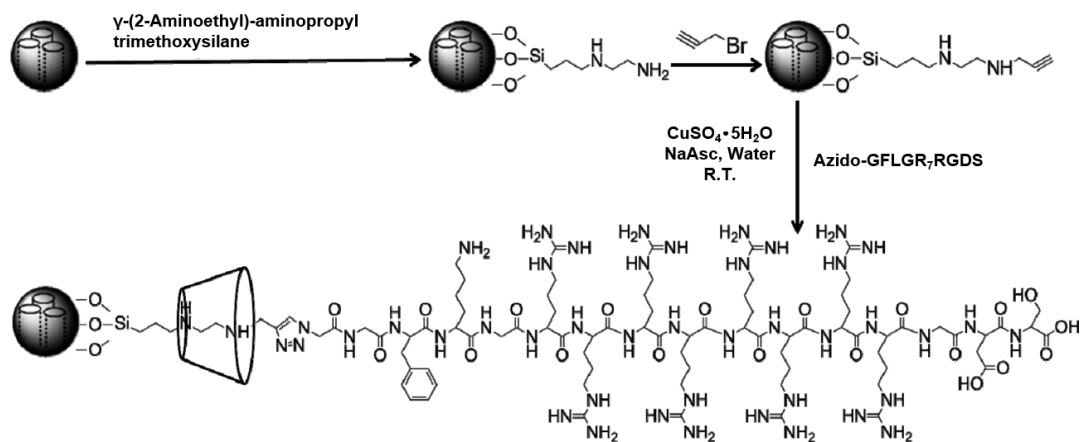


**Figure 2.23.** Preparation and structure of MSN-GFLGR<sub>7</sub>RGDS/ $\alpha$ -CD snap-top. Reprinted with permission from Ref. 66, copyright (2015) ACS Appl. Mater. Interfaces.

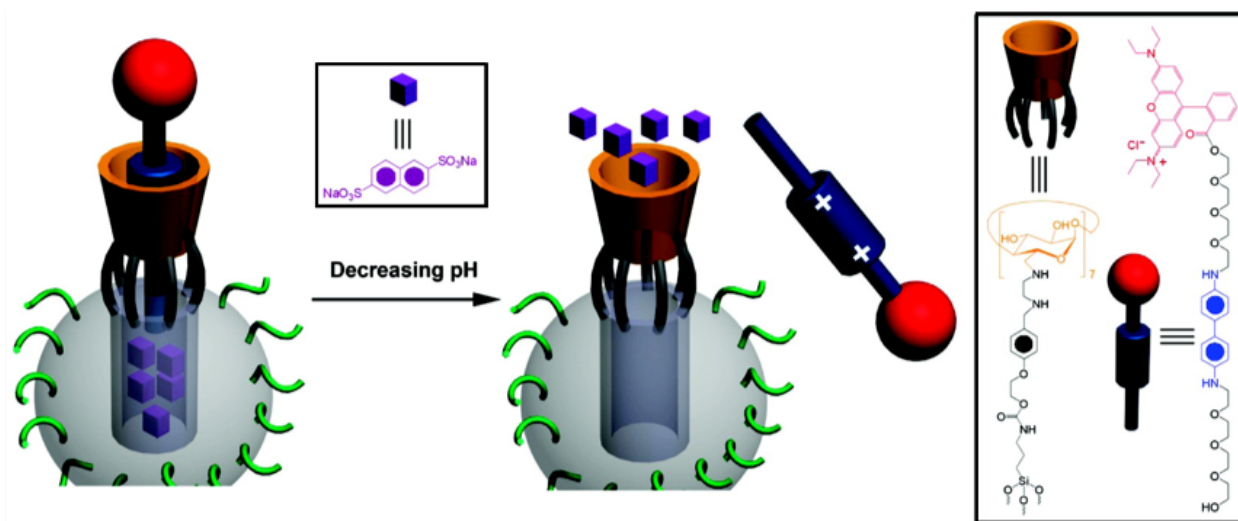


**Figure 2.24.** Schematic illustration of rhodamine B/benzidine inserted in the cavity of  $\beta$ -CD and acting like a piston due to the pH change, which makes cargo release. An ideal mode is to have one nanopore functionalized with one  $\beta$ -CD ring, as shown in the figure. Reprinted with permission from Ref. 67, copyright (2010) J. Am. Chem. Soc.



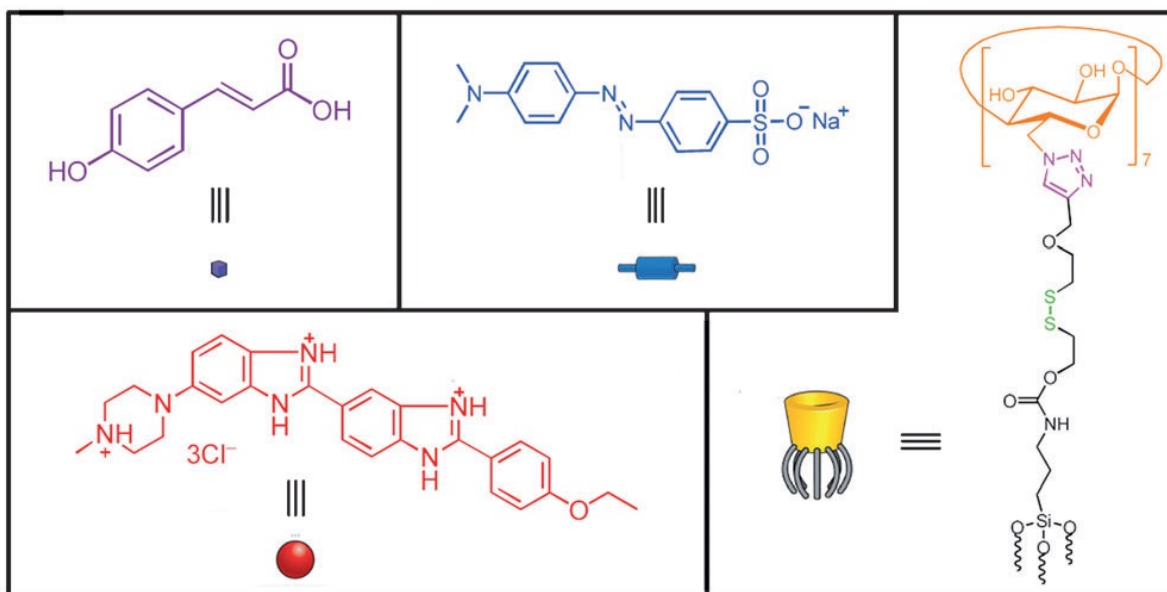
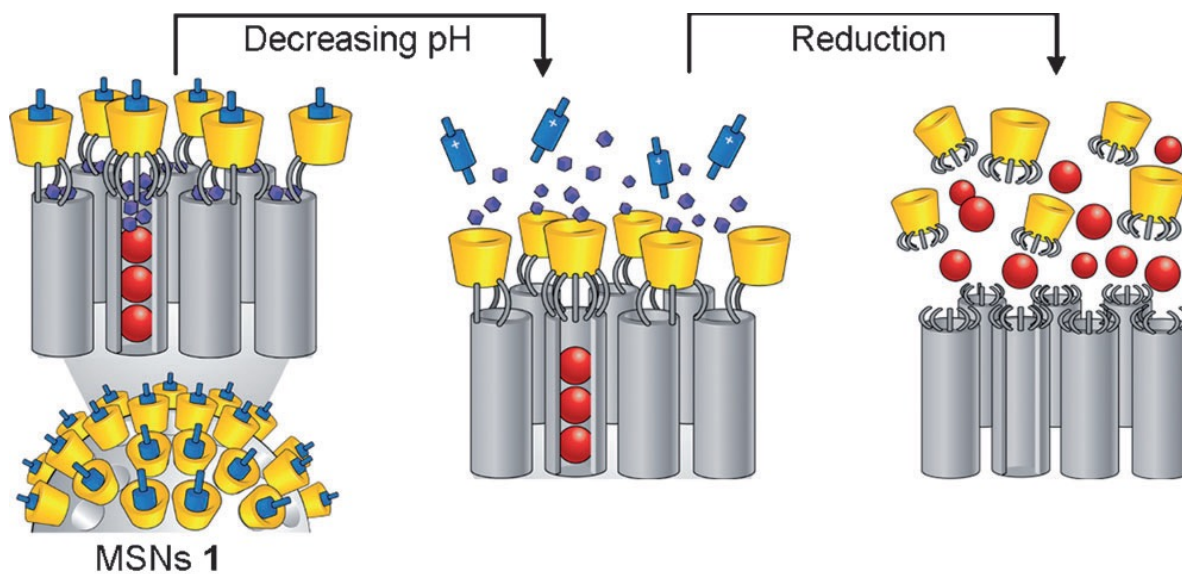


**Figure 2.25.** Schematic illustration of the dual-cargo release process. The first cargo release is achieved by lowering of pH and is followed by the second cargo release triggered by the presence of the reducing agent mercaptoethanol. Reprinted with permission from Ref. 68, copyright (2012) Angew. Chemie - Int. Ed.

**Table 2.1.** Cell lines used in studies with supramolecular nanomachines

Cell line	Description	Drug delivered	Reference
MDA-MB-231	human breast cancer cells	doxorubicin	25
MiaPaCa-2	human pancreatic cancer cells	doxorubicin	34
THP-1 and KB-31	THP-1: human differentiated leukemia monocytes KB-31: human squamous carcinoma cells	doxorubicin	36
MDM and THP-1	MDM: human monocyte-derived macrophages THP-1: human differentiated leukemia monocytes (macrophage-like cells)	moxifloxacin	37
L929	murine aneuploidy fibrosarcoma cells	-	52
A549	adenocarcinomic human alveolar basal epithelial cells	doxorubicin	53
PANC-1	human pancreatic cancer cells	doxorubicin	62
HeLa and COS7	HeLa: human cervical cancer cells COS7: African green monkey SV40-transformed kidney fibroblast cells	doxorubicin	66

**Table 2.2.** Animal models used in studies with supramolecular nanomachines

Animal model	Description	Drug delivered	References
mice	MiaPaCa-2 xenografts	doxorubicin	34
mice	<i>Francisella tularensis</i> infection	moxifloxacin	37

## 2.9 References

- (1) Brinker CJ, Scherer GW. Sol-gel science the physics and chemistry of sol-gel processing. San Diego, USA: Academic Press; **1990**.
- (2) Stoddart JF. Mechanically interlocked molecules (MIMs)-molecular shuttles, switches, and machines (Nobel Lecture). *Angew Chem Int Ed*. **2017**; *56*: 11094-125.
- (3) Dunn B, Miller JM, Dave BC, Valentine JS, Zink JI. Strategies for encapsulating biomolecules in sol-gel matrices. *Acta Mater*. **1998**; *46*: 737-41.
- (4) Dave BC, Soyeyz H, Miller JM, Dunn B, Valentine JS, Zink JI. Synthesis of protein-doped sol-gel SiO<sub>2</sub> thin films: evidence for rotational mobility of encapsulated cytochrome c. *Chem Mater*. **1995**; *7*: 1431-4.
- (5) Chung KE, Lan EH, Davidson MS, Dunn BS, Valentine JS, Zink JI. Measurement of dissolved oxygen in water using glass-encapsulated myoglobin. *Anal Chem*. **1995**; *67*: 1505-9.
- (6) Miller JM, Dunn B, Valentine JS, Zink JI. Synthesis conditions for encapsulating cytochrome c and catalase in SiO<sub>2</sub> sol-gel materials. *J Non-Cryst Solids* **1996**; *202*: 279-89.
- (7) Huang MH, Dunn BS, Zink JI. In situ luminescence probing of the chemical and structural changes during formation of dip-coated lamellar phase sodium dodecyl sulfate sol-gel thin films. *J Am Chem Soc*. **2000**; *122*: 3739-45.
- (8) Nishida F, McKiernan JM, Dunn BS, Zink JI, Brinker CJ, Hurd AJ. In situ fluorescence probing of the chemical changes during sol-gel thin film formation. *J Am Ceram Soc*. **1995**; *78*: 1640-48.
- (9) Klichko Y, Liong M, Choi E, Angelos S, Nel AE, Stoddart JF, et al. Mesostructured silica for optical functionality, nanomachines, and drug delivery. *J Am Ceram Soc*. **2009**; *92*: 2-10.
- (10) Chiola V, Ritsko JE, Vanderpool CD. Process for producing low-bulk density silica. U.S. Patent. **1971**; *3*: 556-725.
- (11) Lindén M. Biodistribution and excretion of intravenously injected mesoporous silica nanoparticles: implications for drug delivery efficiency and safety. In: Tamanoi F, Ed. *The Enzymes*. Oxford, UK: Elsevier; **2018**: 155-80.
- (12) Croissant JG, Brinker CJ. Biodegradable silica-based nanoparticles: dissolution kinetics and selective bond cleavage. In: Tamanoi F, Ed. *The Enzymes*. Oxford, UK: Elsevier; **2018**: 181-214.
- (13) Chia S, Cao J, Stoddart JF, Zink JI. Working supramolecular machines trapped in glass and mounted on a film surface. *Angew Chem Int Ed*. **2001**; *40*: 2447-51.
- (14) Hernandez R, Tseng HR, Wong JW, Stoddart JF, Zink JI. An operational supramolecular nanovalve. *J Am Chem Soc*. **2004**; *126*: 3370-1.
- (15) Flood AH, Liu Y, Tseng HR, Zink JI, Stoddart JF, Celestre PC, et al. A reversible molecular valve. *Proc Natl Acad Sci*. **2005**; *102*: 10029-34.

- (16) Nguyen TD, Liu Y, Saha S, Leung KCF, Stoddart JF, Zink JI. Design and optimization of molecular nanovalves based on redox-switchable bistable rotaxanes. *J Am Chem Soc.* **2007**; *129*: 626-34.
- (17) Saha S, Johansson E, Flood AH, Tseng HR, Zink JI, Stoddart JF. A photoactive molecular triad as a nanoscale power supply for a supramolecular machine. *Chem Eur J.* **2005**; *11*: 6846-58.
- (18) Nguyen TD, Leung, KCF, Liong M, Liu Y, Stoddart JF, Zink JI. Versatile supramolecular nanovalves reconfigured for light activation. *Adv Funct Mater.* **2007**; *17*: 2101-10.
- (19) Ambrogio MW, Thomas CR, Zhao YL, Zink JI, Stoddart JF. Mechanized silica nanoparticles: a new frontier in theranostic nanomedicine. *Acc Chem Res.* **2011**; *44*: 903-13.
- (20) Lagona J, Mukhopadhyay P, Chakrabarti S, Isaacs L. The cucurbit[n]uril family. *Angew Chem Int Ed.* **2005**; *44*: 4844-70.
- (21) Freeman WA, Mock WL, Shih NY. Cucurbituril. *J Am Chem Soc.* **1981**; *103*: 7367-8.
- (22) Márquez C, Hudgins RR, Nau WM. Mechanism of host-guest complexation by cucurbituril. *J Am Chem Soc.* **2004**; *126*: 5806-16.
- (23) Angelos S, Yang YW, Patel K, Stoddart JF, Zink JI. pH-responsive supramolecular nanovalves based on cucurbit[6]uril pseudorotaxanes. *Angew Chem Int Ed.* **2008**; *47*: 2222-6.
- (24) Khashab NM, Belowich ME, Trabolsi A, Friedman DC, Valente C, Lau Y, et al. pH-responsive mechanised nanoparticles gated by semirotaxanes. *Chem Commun.* **2009**; 5371-3.
- (25) Thomas CR, Ferris DP, Lee JH, Choi E, Cho MH, Kim ES, et al. Noninvasive remote-controlled release of drug molecules in vitro using magnetic actuation of mechanized nanoparticles. *J Am Chem Soc.* **2010**; *132*: 10623-5.
- (26) Croissant J, Zink JI. Nanovalve-controlled cargo release activated by plasmonic heating. *J Am Chem Soc.* **2012**; *134*: 7628-31.
- (27) Kim K, Selvapalam N, Ko YH, Park KM, Kim D, Kim J. Functionalized cucurbiturils and their applications. *Chem Soc Rev.* **2007**; *36*: 267-79.
- (28) Nau WM, Ghale G, Hennig A, Bakirci H, Bailey DM. Substrate-selective supramolecular tandem assays: monitoring enzyme inhibition of arginase and diamine oxidase by fluorescent dye displacement from calixarene and cucurbituril macrocycles. *J Am Chem Soc.* **2009**; *131*: 11558-70.
- (29) Kim Y, Ko YH, Jung M, Selvapalam N, Kim K. A new photo-switchable “on-off” host-guest system. *Photochem Photobiol Sci.* **2011**; *10*: 1415-9.
- (30) Sun YL, Yang BJ, Zhang SXA, Yang YW. Cucurbit[7]uril pseudorotaxane-based photoresponsive supramolecular nanovalve. *Chem Eur J.* **2012**; *18*: 9212-6.
- (31) Du L, Liao S, Khatib HA, Stoddart JF, Zink JI. Controlled-access hollow mechanized silica nanocontainers. *J Am Chem Soc.* **2009**; *131*: 15136-42.
- (32) Dong J, Xue M, Zink JI. Functioning of nanovalves on polymer coated mesoporous silica nanoparticles. *Nanoscale.* **2013**; *5*: 10300-6.

- (33) Guardado-Alvarez TM, Russell MM, Zink JI. Nanovalve activation by surface-attached photoacids. *Chem Commun.* **2014**; *50*: 8388-90.
- (34) Hwang AA, Lu J, Tamanoi F, Zink JI. Functional nanovalves on protein-coated nanoparticles for in vitro and In vivo controlled drug delivery. *Small.* **2015**; *11*: 319-28.
- (35) Salvati A, Pitek AS, Monopoli MP, Prapainop K, Bombelli FB, Hristov DR, et al. Transferrin-functionalized nanoparticles lose their targeting capabilities when a biomolecule corona adsorbs on the surface. *Nat Nanotechnol.* **2013**; *8*: 137-43.
- (36) Meng H, Xue M, Xia T, Zhao YL, Tamanoi F, Stoddart JF, et al. Autonomous in vitro anticancer drug release from mesoporous silica nanoparticles by pH-sensitive nanovalves. *J Am Chem Soc.* **2010**; *132*: 12690-7.
- (37) Li Z, Clemens DL, Lee BY, Dillon BJ, Horwitz MA, Zink JI. Mesoporous silica nanoparticles with pH-sensitive nanovalves for delivery of moxifloxacin provide improved treatment of lethal pneumonic tularemia. *ACS Nano.* **2015**; *9*: 10778-89.
- (38) Yoshida N, Seiyama A, Fujimoto M. Stability and structure of the inclusion complexes of alkyl-substituted hydroxyphenylazo derivatives of sulfanilic acid with alpha-cyclodextrin and beta-cyclodextrin. *J Phys Chem.* **1990**; *94*: 4254-9.
- (39) Bortolus P, Monti S. Cis .Dblharw. Trans photoisomerization of azobenzene-cyclodextrin inclusion complexes. *J Phys Chem.* **1987**; *91*: 5046-50.
- (40) Inoue Y, Kuad P, Okumura Y, Takashima Y, Yamaguchi H, Harada A. Thermal and photochemical switching of conformation of poly(ethylene glycol)-substituted cyclodextrin with an azobenzene group at the chain end. *J Am Chem Soc.* **2007**; *129*: 6396-7.
- (41) Zhu Y, Fujiwara M. Installing dynamic molecular photomechanics in mesopores: a multifunctional controlled-release nanosystem. *Angew Chem Int Ed.* **2007**; *46*: 2241-4.
- (42) Angelos S, Choi E, Vögtle F, De Cola L, Zink JI. Photo-driven expulsion of molecules from mesostructured silica nanoparticles. *J Phys Chem C.* **2007**; *111*: 6589-92.
- (43) Lu J, Choi E, Tamanoi F, Zink JI. Light-activated nanoimpeller-controlled drug release in cancer cells. *Small.* **2008**; *4*: 421-6.
- (44) Lau YA, Henderson BL, Lu J, Ferris DP, Tamanoi F, Zink JI. Continuous spectroscopic measurements of photo-stimulated release of molecules by nanomachines in a single living cell. *Nanoscale.* **2012**; *4*: 3482-9.
- (45) Ferris DP, Zhao YL, Khashab NM, Khatib HA, Stoddart JF, Zink JI. Light-operated mechanized nanoparticles. *J Am Chem Soc.* **2009**; *131*: 1686-8.
- (46) Wang D, Wu S. Red-light-responsive supramolecular valves for photocontrolled drug release from mesoporous nanoparticles. *Langmuir.* **2016**; *32*: 632-6.
- (47) Khashab NM, Trabolsi A, Lau YA, Ambrogio MW, Friedman DC, Khatib HA, et al. Redox- and pH-controlled mechanized nanoparticles. *Eur J Org Chem.* **2009**; 1669-73.

- (48) Li H, Tan LL, Jia P, Li QL, Sun YL, Zhang J, et al. Near-infrared light-responsive supramolecular nanovalve based on mesoporous silica-coated gold nanorods. *Chem Sci.* **2014**; *5*: 2804-8.
- (49) Gokel GW, Leevy WM, Weber ME. Crown Ethers: Sensors for ions and molecular scaffolds for materials and biological models. *Chem Rev.* **2004**; *104*: 2723-50.
- (50) Wu Z, Ondruschka B, Stark A. Ultrasonic cleavage of thioethers. *J Phys Chem A.* **2005**; *109*: 3762-66.
- (51) Cai Y, Pan H, Xu R, Hu Q, Li N, Tang R. Ultrasonic controlled morphology transformation of hollow calcium phosphate nanospheres: a smart and biocompatible drug release system. *Chem Mater.* **2007**; *19*: 3081-83.
- (52) Lee SF, Zhu XM, Wang YX J, Xuan SH, You Q, Chan WH, et al. Ultrasound, pH, and magnetically responsive crown-ether-coated core/shell nanoparticles as drug encapsulation and release systems. *ACS Appl Mater Interfaces.* **2013**; *5*: 1566-74.
- (53) Song N, Yang YW. Molecular and supramolecular switches on mesoporous silica nanoparticles. *Chem Soc Rev.* **2015**; *44*: 3474-504.
- (54) Sun YL, Yang YW, Chen DX, Wang G, Zhou Y, Wang CY, et al. Mechanized silica nanoparticles based on pillar[5]arenes for on-command cargo release. *Small.* **2013**; *9*: 3224-9.
- (55) Huang X, Wu S, Ke X, Li X, Du X. Phosphonated pillar[5]arene-valved mesoporous silica drug delivery systems. *ACS Appl Mater Interfaces.* **2017**; *9*: 19638-45.
- (56) Angelos S, Khashab NM, Yang YW, Trabolsi A, Khatib HA, Stoddart JF, et al. pH clock-operated mechanized nanoparticles. *J Am Chem Soc.* **2009**; *131*: 12912-4.
- (57) Tarn D, Ferris DP, Barnes JC, Ambrogio MW, Stoddart JF, Zink JJ. A reversible light-operated nanovalve on mesoporous silica nanoparticles. *Nanoscale.* **2014**; *6*: 3335-43.
- (58) Falvey P, Lim CW, Darcy R, Revermann T, Karst U, Giesbers M, et al. Bilayer vesicles of amphiphilic cyclodextrins: host membranes that recognize guest molecules. *Chem Eur J.* **2005**; *11*: 1171-80.
- (59) Rühle B, Datz S, Argyo C, Bein T, Zink JJ. A molecular nanocap activated by superparamagnetic heating for externally stimulated cargo release. *Chem Commun.* **2016**; *52*: 1843-6.
- (60) Guardado-Alvarez TM, Devi LS, Vabre JM, Pecorelli TA, Schwartz BJ, Durand JO, et al. Photo-redox activated drug delivery systems operating under two photon excitation in the near-IR. *Nanoscale.* **2014**; *6*: 4652-8.
- (61) Xue M, Cao D, Stoddart JF, Zink JJ. Size-selective pH-operated megagates on mesoporous silica materials. *Nanoscale.* **2012**; *4*: 7569-74.
- (62) Chen W, Cheng CA, Zink JJ. Spatial, temporal, and dose control of drug delivery using non-invasive magnetic stimulation. *ACS Nano.* **2019**; *13*: 1292-1308.
- (63) Xue M, Zink JJ. An enzymatic chemical amplifier based on mechanized nanoparticles. *J Am Chem Soc.* **2013**; *135*: 17659-62.

- (64) Patel K, Angelos S, Dichtel WR, Coskun A, Yang YW, Zink JJ, et al. Enzyme-responsive snap-top covered silica nanocontainers. *J Am Chem Soc.* **2008**; *130*: 2382-3.
- (65) Ambrogio MW, Pecorelli TA, Patel K, Khashab NM, Trabolsi A, Khatib HA, et al. Snap-top nanocarriers. *Org Lett.* **2010**; *12*: 3304-7.
- (66) Cheng YJ, Luo GF, Zhu JY, Xu XD, Zeng X, Cheng DB, et al. Enzyme-induced and tumor-targeted drug delivery system based on multifunctional mesoporous silica nanoparticles. *ACS Appl Mater Interfaces.* **2015**; *7*: 9078-87.
- (67) Zhao YL, Li Z, Kabehie S, Botros YY, Stoddart JF, Zink JJ. pH-operated nanopistons on the surfaces of mesoporous silica nanoparticles. *J Am Chem Soc.* **2010**; *132*: 13016-25.
- (68) Wang C, Li Z, Cao D, Zhao YL, Gaines JW, Bozdemir OA, et al. Stimulated release of size-selected cargos in succession from mesoporous silica nanoparticles. *Angew Chem Int Ed.* **2012**; *57*: 5460-5.
- (69) Aznar E, Oroval M, Pascual L, Murguía JR, Martínez-Máñez R, Sancenón F. Gated materials for on-command release of guest molecules. *Chem Rev.* **2016**; *116*: 561-718.
- (70) Kumar N, Chen W, Cheng CA, Deng T, Wang R, Zink JJ. Stimuli-responsive nanomachines and caps for drug delivery. In: Tamanoi F, Ed. *The Enzymes*. Oxford, UK: Elsevier; **2018**: 31-65.
- (71) Argyo C, Weiss V, Bräuchle C, Bein T. Multifunctional mesoporous silica nanoparticles as a universal platform for drug delivery. *Chem Mater.* **2014**; *26*: 435-51.
- (72) Wen J, Yang K, Liu F, Li H, Xu Y, Sun S. Diverse gatekeepers for mesoporous silica nanoparticle based drug delivery systems. *Chem Soc Rev.* **2017**; *46*: 6024-45.
- (73) Yang YW. Towards biocompatible nanovalves based on mesoporous silica nanoparticles. *MedChemComm.* **2011**; *2*: 1033-49.
- (74) Coll C, Bernardos A, Martínez-Máñez R, Sancenón F. Gated silica mesoporous supports for controlled release and signaling applications. *Acc Chem Res.* **2013**; *46*: 339-49.
- (75) Chen W, Cheng CA, Lee BY, Clemens DL, Huang WY, Horwitz MA, et al. A facile strategy enabling both high loading and high release amounts of the water-insoluble drug clofazimine using mesoporous silica nanoparticles. *ACS Appl Mater Interfaces.* **2018**; *10*: 31870-81.
- (76) Zhao N, Lin X, Zhang Q, Ji Z, Xu FJ. Redox-triggered gatekeeper-enveloped starlike hollow silica nanoparticles for intelligent delivery systems. *Small.* **2015**; *11*: 6467-79.
- (77) Wu TJ, Tzeng YK, Chang WW, Cheng CA, Kuo Y, Chien CH, et al. Tracking the engraftment and regenerative capabilities of transplanted lung stem cells using fluorescent nanodiamonds. *Nat. Nanotechnol.* **2013**; *8*: 682-9.
- (78) Fang CY, Vijayanthimala V, Cheng CA, Yeh SH, Chang CF, Li CL, et al. The exocytosis of fluorescent nanodiamond and its use as a long-term cell tracker. *Small.* **2011**; *7*: 3363-70.
- (79) Hui YY, Cheng CA, Chen OY, Chang HC. Bioimaging and quantum sensing using NV centers in diamond nanoparticles. In Yang N, Jiang X, Pang DW, Eds. *Carbon Nanoparticles and Nanostructures*. Cham, Switzerland: Springer International Publishing; **2016**: 109-37.

- (80) Chen X, Zhang Q, Li J, Yang M, Zhao N, Xu FJ. Rattle-structured rough nanocapsules with in-situ-formed gold nanorod cores for complementary gene/chemo/photothermal therapy. *ACS Nano*. **2018**; *12*: 5646-56.
- (81) Duan S, Yang Y, Zhang C, Zhao N, Xu FJ. NIR-responsive polycationic gatekeeper-cloaked heteronanoparticles for multimodal imaging-guided triple-combination therapy of cancer. *Small*. **2017**; *13*: 1603133.
- (82) Faria M, Björnmalm M, Thurecht KJ, Kent SJ, Parton RG, Kavallaris M, et al. Minimum information reporting in bio–nano experimental literature. *Nat Nanotechnol*. **2018**; *13*: 777-85.

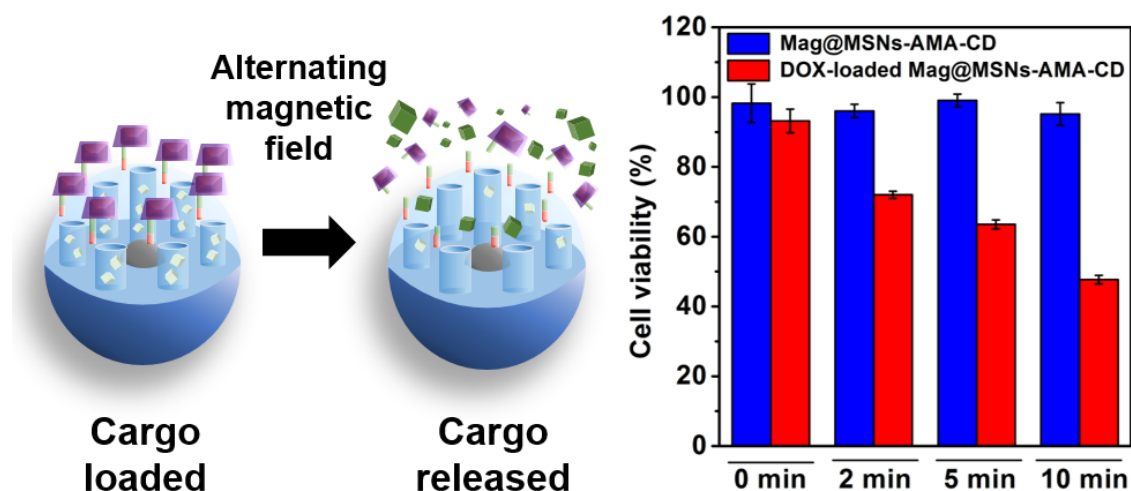


## CHAPTER 3

# Spatial, Temporal, and Dose Control of Drug Delivery using Noninvasive Magnetic Stimulation

This chapter of the dissertation was adapted and reprinted with permission from Wei Chen#, **Chi-An Cheng**#, Jeffrey I. Zink *ACS Nano* **2019**, *13*, 1292-1308. Copyright 2019 American Chemical Society. Co-author contributions: Chen W.# and Cheng C. A.# (co-first authors) designed and performed all the experiments. Jeffrey I. Zink was the P.I.

### Table of Content Figure



### 3.1 Abstract

Noninvasive stimuli-responsive drug delivery using magnetic fields in conjunction with superparamagnetic nanoparticles offers the potential for the spatial and temporal control of drug release. When hyperthermia is not desired and control of the dosage is required, it is necessary to design a platform in which local heating on the nanoscale releases the therapeutic cargo without the bulk heating of the surrounding medium. In this study, we report a design using a stimuli-

responsive nanoparticle platform to control the dosage of the cargo released by an alternating magnetic field (AMF) actuation. A core@shell structure with a superparamagnetic doped iron oxide ( $\text{MnFe}_2\text{O}_4@\text{CoFe}_2\text{O}_4$ ) nanoparticle core in a mesoporous silica shell was synthesized. The core used here has a high saturation magnetization value and a high specific loss power for heat generation under an AMF. The mesoporous shell has a high cargo-carrying capacity. A thermoresponsive molecular-based gatekeeper containing an aliphatic azo group was modified on the core@shell nanoparticles to regulate the cargo release. The mesoporous structure of the silica shell remained intact after exposure to an AMF, showing that the release of cargo is due to the removal of the gatekeepers instead of the destruction of the structure. Most importantly, we demonstrated that the amount of cargo released could be adjusted by the AMF exposure time. By applying multiple sequential exposures of AMF, we were able to release the cargo step-wise and increase the total amount of released cargo. *In vitro* studies showed that the death of pancreatic cancer cells treated by drug-loaded nanoparticles was controlled by different lengths of AMF exposure time due to different amount of drugs released from the carriers. The strategy developed here holds great promise for achieving the dosage, temporal, and spatial control of therapeutics delivery without the risk of overheating the particles' surroundings.

### **3.2 Introduction**

Precision medicine, defined as “right drug, right dosage at right timing to right patient”, is a rapidly developing and popular global trend for cancer treatment.<sup>1</sup> This emerging approach takes the individual variability into account for personalized disease treatment regimen design.<sup>1</sup> However, the necessity to deliver the desired therapeutic, at the desired time, to the specific site of the disease, and with accurate dosage of therapeutics remains a challenge.<sup>2</sup> Over the past decade, many examples of stimuli-responsive drug delivery platforms responsive to internal cellular

stimuli (such as pH change,<sup>3-6</sup> redox potential,<sup>7,8</sup> enzymes<sup>9</sup> or biomolecules<sup>10,11</sup>) and external stimuli (such as light,<sup>12-15</sup> heat,<sup>16-23</sup> or ultrasound<sup>24,25</sup>) have been developed for cancer treatment because they offer the ability to both enhance the therapeutic efficacy at the target sites and reduce the premature release of drug molecules thus reducing off-target side effects. Delivery of the accurate dosage is a key feature in chemotherapy.<sup>26-28</sup> The dosage of the therapeutics should be in the optimal range called therapeutic window, where the dosages exceed the threshold concentration and can treat disease effectively, while below the concentration which is significantly toxic to normal cells.<sup>29</sup> In view of this, after getting information from genetic databases to find out the right drug to the right patients, the next challenge is to deliver the right dosage of therapeutics in a spatio-temporal controlled manner to the desired lesion location.<sup>2,30</sup> However, important limitations of the above stimuli-responsive drug delivery exist: the platforms responsive to pH change, redox potential, and enzyme cannot precisely control the delivery time, the delivery location, and the delivery dosage; the light responsive platforms have the most focused spatial control (on the order of mm<sup>3</sup>) but suffer from the limited penetration depth in tissue; the heat responsive platforms create a risk of inducing tumor metastasis when hyperthermia occurs;<sup>31-35</sup> and ultrasound suffers from blockage by bone and air even though under ideal condition can attain the spatial focus on the order of 10 mm<sup>3</sup>.<sup>36</sup>

Non-invasive magnetic fields in conjunction with superparamagnetic nanoparticles offer a possible solution to overcome these limitations. Magnetic fields are harmless, are localized with dimensions governed by the size of the magnetic coil (on the order of cm<sup>3</sup>), and can be turned on and off under precise control. Superparamagnetic nanoparticles have been investigated extensively for a wide variety of biomedical applications including magnetic resonance imaging (MRI) contrast enhancement,<sup>37,38</sup> hyperthermia therapy,<sup>39</sup> and drug delivery.<sup>22,40-42</sup> Among them, drug delivery triggered by heat generated when magnetic nanoparticles are exposed to an alternating

magnetic field (AMF) actuation is an emerging approach to externally and non-invasively triggered drug release.<sup>43-49</sup> AMF actuation of drug delivery has the following benefits: (1) the release of drugs can be spatially and temporally controlled, offering the advantages for delivering a high local concentration of therapeutics to the lesion site and reducing off-site drug delivery from the carriers, (2) no penetration depth limitation of the magnetic field, enabling the actuation be initiated in the deep animal body without the concern of light scattering or absorption by tissues,<sup>22,50-52</sup> and (3) less restriction on the type of tissues being treated compared with ultrasound stimulation that is strongly attenuated by air and bone structures.<sup>36</sup> In hyperthermia therapy, when the blood is congested locally during heating, more energy will be provided for the tumor growth.<sup>31-35,53</sup> In this case, the original tumor cells suffering from necrosis, starvation or suffocation due to insufficient internal blood supply may be rescued, thus accelerating tumor cell metastasis.<sup>31-35</sup> Therefore, it is critical to monitor the temperature while doing AMF actuation, in order to prevent the bulk solution from being overheated.

Only a limited amount of drugs can be carried on and released from the surface of a magnetic nanoparticle. To increase the amount of drugs that can be delivered, polymers,<sup>54</sup> dendrimers,<sup>55,56</sup> and lipid bilayers,<sup>57</sup> have been attached to magnetic nanoparticles to enhance the payload of drugs. Mesoporous silica has aroused much attention during the past decade due to its high surface area and large pore volume for cargo loading and delivery.<sup>58-66</sup> Additionally, the stability, high biocompatibility, high cellular internalization efficiency, and easy surface functionalization of mesoporous silica makes it a strong candidate for use as a coating of superparamagnetic nanoparticles in a drug delivery platform.<sup>17,18,67-70</sup>

To achieve the controllable drug delivery under the magnetic field actuation, various thermal responsive gatekeepers have been developed during the past several years. Thomas *et al.* designed the first nanovalve for magnetic triggered release study based on MSNs, in which cucurbit[6]uril

was used as a cap that released the cargo when the supramolecular interaction between the cap and the stalk on the surface of MSNs was decreased.<sup>41</sup> Thermo-sensitive polymers such as azo-functionalized polyethylene glycol,<sup>17</sup> poly(*N*-isopropylacrylamide),<sup>21</sup> and poly[(ethylene glycol)-co-(*L*-lactide)]<sup>23</sup> polymer have also been used as the capping agents to prevent premature release. In this work, we reported small molecular-based gatekeeper that is responsive to the heat generated by a superparamagnetic core in an AMF.

The nanoplatform consists of 4,4'-azobis(4-cyanovaleric acid) (ACVA), an aliphatic azo-containing compound which can be irreversibly cleaved by heat and ultrasound,<sup>43,71</sup> that was attached on the surface of core@shell nanoparticles consisting of a manganese and cobalt doped iron oxide magnetic nanoparticle cores and a mesoporous silica shell (**Scheme 3.1**). Adamantane molecules were conjugated to ACVA through an amide bond coupling reaction. After loading the cargo in the pores of core@shell nanoparticles, bulky  $\beta$ -cyclodextrin ( $\beta$ -CD) was used to bind with the adamantane forming a well-known supramolecular host-guest complex with a high association equilibrium constant ( $5.2 \times 10^4 \text{ M}^{-1}$ ).<sup>7,14,72-79</sup> The pores of core@shell nanoparticles were blocked by this bulky complex and the cargo inside was prevented from being released prematurely. We demonstrate that this small molecular-based gatekeeper can be triggered by magnetic heating with minimal bulk heating. In addition, we demonstrate that the exposure time to the AMF controlled the dosage of the released cargo. We quantify the cargo release efficiency while simultaneously monitoring the temperature of the bulk solution, and obtain both dosage and temporal controlled release with no dangerous bulk heating. This proof-of-concept of precision on command drug delivery establishes the opportunities to enhance the treatment efficacy, reduce the side effect of chemotherapy and at the same time avoid the risk of inducing tumor metastasis generated by hyperthermia.

### 3.3. Synthesis and Characterization of MnFe<sub>2</sub>O<sub>4</sub>@CoFe<sub>2</sub>O<sub>4</sub> Nanoparticles

To achieve superior magnetic heating efficacy, we synthesized MnFe<sub>2</sub>O<sub>4</sub>@CoFe<sub>2</sub>O<sub>4</sub> nanoparticles with a magnetically soft MnFe<sub>2</sub>O<sub>4</sub> core, and a magnetically hard CoFe<sub>2</sub>O<sub>4</sub> shell using a seed-mediated method (**Figure 3.1a**).<sup>39</sup> First, 6.3 nm MnFe<sub>2</sub>O<sub>4</sub> nanoparticles were synthesized by a thermal decomposition method.<sup>37,38,80</sup> The larger MnFe<sub>2</sub>O<sub>4</sub> nanoparticles (8.2 nm) were then obtained by using the synthesized 6.3 nm MnFe<sub>2</sub>O<sub>4</sub> nanoparticles as the seeds. Next, the CoFe<sub>2</sub>O<sub>4</sub> shell layer was grown on the surface of the synthesized 8.2 nm MnFe<sub>2</sub>O<sub>4</sub> nanoparticles to form 10.1 or 11.4 nm MnFe<sub>2</sub>O<sub>4</sub>@CoFe<sub>2</sub>O<sub>4</sub> nanoparticles (**Figure 3.1bc**). Both the MnFe<sub>2</sub>O<sub>4</sub> (6.3 and 8.2 nm) and the MnFe<sub>2</sub>O<sub>4</sub>@CoFe<sub>2</sub>O<sub>4</sub> (10.1 and 11.4 nm) nanoparticles have uniform size distributions as measured by transmission electron microscopy (TEM) (**Figure 3.1bc** and **Figure 3.2ab**). From the corresponding diffraction peaks in high angle X-ray diffraction patterns (**Figure 3.3**), the 11.4 nm core@shell MnFe<sub>2</sub>O<sub>4</sub>@CoFe<sub>2</sub>O<sub>4</sub> nanoparticles possess the typical spinel structure.<sup>81</sup>

To quantify field dependent magnetization of MnFe<sub>2</sub>O<sub>4</sub>@CoFe<sub>2</sub>O<sub>4</sub> at 300 K, a superconducting quantum interference device (SQUID) was used. The saturated magnetization of 11.4 nm MnFe<sub>2</sub>O<sub>4</sub>@CoFe<sub>2</sub>O<sub>4</sub> is 105 emu/g (**Figure 3.2c**), higher than that of Fe<sub>3</sub>O<sub>4</sub> nanoparticles (80 emu/g).<sup>82</sup> The higher magnetization of the MnFe<sub>2</sub>O<sub>4</sub>@CoFe<sub>2</sub>O<sub>4</sub> produces a greater magnetic heating efficiency compared with Fe<sub>3</sub>O<sub>4</sub> under an AMF (*vide infra*). The tiny hysteresis loop (**Figure 3.2c**) shows almost no coercive force which validates the superparamagnetic property of MnFe<sub>2</sub>O<sub>4</sub>@CoFe<sub>2</sub>O<sub>4</sub> nanoparticles.

To further confirm the nanoparticle identity, both Fourier transform-infrared (FT-IR) spectroscopy and thermogravimetric analysis (TGA) were conducted. In the FT-IR spectrum (**Figure 3.4a**), the three peaks at 2851, 2921, and 2955 cm<sup>-1</sup> arise from the CH<sub>2</sub> symmetric and antisymmetric stretches in oleic acid and oleylamine and confirm that the surface of MnFe<sub>2</sub>O<sub>4</sub>@CoFe<sub>2</sub>O<sub>4</sub> nanoparticles is covered with oleic acid and oleylamine. The TGA results

show that the amount of oleic acid and oleylamine on the surface of MnFe<sub>2</sub>O<sub>4</sub>@CoFe<sub>2</sub>O<sub>4</sub> nanoparticles is 13 wt% (**Figure 3.4b**). Due to the abundant capping agents with long hydrocarbon chains, the MnFe<sub>2</sub>O<sub>4</sub>@CoFe<sub>2</sub>O<sub>4</sub> nanoparticles can be well suspended in hexane (**Figure 3.2c**).

To investigate the heat generation efficiency of 11.4 nm MnFe<sub>2</sub>O<sub>4</sub>@CoFe<sub>2</sub>O<sub>4</sub> nanoparticles, the specific loss power (SLP) was quantified. The SLP of MnFe<sub>2</sub>O<sub>4</sub>@CoFe<sub>2</sub>O<sub>4</sub> was calculated using equation (1), where  $C$  is the volumetric heat capacity of solvent,  $V_s$  is the sample volume,  $m$  is the mass of MnFe<sub>2</sub>O<sub>4</sub>@CoFe<sub>2</sub>O<sub>4</sub>, and  $dT/dt$  is the initial slope of the time-dependent temperature increase curve.

$$\text{Specific loss power} = \frac{CV_s}{m} \frac{dT}{dt} \quad (1)$$

MnFe<sub>2</sub>O<sub>4</sub>@CoFe<sub>2</sub>O<sub>4</sub> nanoparticles were dispersed in toluene and an AMF (375 kHz, 5kW) was applied for heat generation. Time- and concentration-dependent temperature increase profiles (**Figure 3.2d**) show that the solution temperature abruptly increased upon the application of AMF trigger. The temperature of the toluene solution containing nanoparticles finally achieved 44, 55, and 67 °C after 6 min magnetic actuation at the concentrations of MnFe<sub>2</sub>O<sub>4</sub>@CoFe<sub>2</sub>O<sub>4</sub> are 0.5, 1, and 2.5 mg/mL, respectively. The SLP of the MnFe<sub>2</sub>O<sub>4</sub>@CoFe<sub>2</sub>O<sub>4</sub> nanoparticles was calculated to be 1510.8 W/g (equation 2), 5 times higher than that of 20 nm Fe<sub>3</sub>O<sub>4</sub> nanoparticles (302.2 W/g) (equation 3).<sup>83</sup> This superior heating performance of MnFe<sub>2</sub>O<sub>4</sub>@CoFe<sub>2</sub>O<sub>4</sub> nanoparticles under the AMF shows its potential of serving as an efficacious heat source for thermal-triggered drug release.

For MnFe<sub>2</sub>O<sub>4</sub>@CoFe<sub>2</sub>O<sub>4</sub>:

$$\begin{aligned} \text{Specific loss power} &= \frac{CV_s dT}{m dt} \quad (1) \\ &= \frac{1.5108 (J mL^{-1} K^{-1}) \times 1 (mL)}{1 \times 10^{-3} (g)} \times \frac{1 (K)}{1 (s)} \\ &= 1510.8 Wg^{-1}_{(Fe+Mn+Co)} \quad (2) \end{aligned}$$

For Fe<sub>3</sub>O<sub>4</sub>:

$$\begin{aligned} \text{Specific loss power} &= \frac{CV_s dT}{m dt} \quad (1) \\ &= \frac{1.5108 (J mL^{-1} K^{-1}) \times 1 (mL)}{1 \times 10^{-3} (g)} \times \frac{1 (K)}{5 (s)} \\ &= 302.2 Wg^{-1}_{(Fe)} \quad (3) \end{aligned}$$

### 3.4 Synthesis and Characterization of Mag@MSNs-APTS Core@Shell Nanoparticles

To construct nanoparticles with cargo-carrying capability, we synthesized nanoparticles with a mesoporous silica shell around the superparamagnetic core. The coating was achieved by hydrolysis and condensation of tetraethyl orthosilicate (TEOS) in the presence of hexadecyltrimethylammonium bromide (CTAB) surfactant templates in basic solution.<sup>84</sup> The resulting nanoparticles are designated as Mag@MSNs (Mag denotes magnetic MnFe<sub>2</sub>O<sub>4</sub>@CoFe<sub>2</sub>O<sub>4</sub> and MSNs denotes mesoporous silica nanoparticles).

In order to attach thermal sensitive caps, the surface of the mesoporous silica shell was functionalized with amine groups by hydrolysis and condensation reactions of 3-(aminopropyl)triethoxysilane (APTS). The modified nanoparticles are designated as Mag@MSNs-APTS. By using TEM, the average diameter of Mag@MSNs-APTS core@shell nanoparticles is 55 nm and their shell thickness is 22 nm with obvious mesoporous structure



(**Figure 3.5a** and **Figure 3.6**). From the dynamic light scattering (DLS) diameter distribution (**Figure 3.7**), the average diameter of Mag@MSNs-APTS is 105.6 nm at room temperature, showing that the nanoparticles are well dispersed in water.

N<sub>2</sub> adsorption-desorption isotherms and pore diameter distribution were used to further characterize the pores of Mag@MSNs-APTS core@shell nanoparticles. The Brunauer-Emmett-Teller (BET) surface area, Barrett-Joyner-Halenda (BJH) average pore diameter, and total pore volume of Mag@MSNs-APTS are 653.4 m<sup>2</sup>/g, 2.8 nm, and 1.06 cm<sup>3</sup>/g, respectively (**Figure 3.5b**). In addition, the high surface area and pore volume of Mag@MSNs-APTS – the desired properties of MSNs – suggest that cargos such as small molecules can be loaded inside the pores of Mag@MSNs-APTS (vide infra), allowing those cargos to be efficiently carried and delivered by the nanoparticles.

### **3.5 Synthesis and Characterization of Mag@MSNs-APTS, Mag@MSNs-ACVA and Mag@MSNs-AMA Core@Shell Nanoparticles**

Particles for magnetically stimulated release need not only cargo-carrying capability but also a stimulus-responsive capping mechanism. To introduce the latter functionality to the nanoparticles, the surface of the core@shell nanoparticles were conjugated with a thermolabile gatekeeper 4,4'-azobis(4-cyanovaleric acid) (ACVA).<sup>43,71</sup> ACVA was chemically bonded to Mag@MSNs-APTS using 1-ethyl-3-(3-diethylaminopropyl) carbodiimide (EDC) and *N*-hydroxysuccinimide (NHS) coupling agents.<sup>85</sup> The carboxylic acid on ACVA formed an amide bond with the primary amine of APTS, and the resulting particles were designated as Mag@MSNs-ACVA (**Scheme 3.1b**). Subsequently, 1-adamantylamine (AMA) was conjugated on the surface of the nanoparticles through the same standard crosslinking method, with the terminal carboxylic acid of ACVA forming another amide bond with the primary amine of AMA. The

nanoparticles modified with AMA were designated as Mag@MSNs-AMA (**Scheme 3.1b**).

The successful attachment of APTS, ACVA, and AMA on the surface of Mag@MSNs was confirmed by zeta potential measurements, FT-IR, and TGA after each step. The zeta potential of Mag@MSNs, Mag@MSNs-APTS, Mag@MSNs-ACVA, and Mag@MSNs-AMA were measured in deionized water at room temperature (**Figure 3.8a**). The zeta potential value of Mag@MSNs-APTS was +46.2 mV, much more positive than that of Mag@MSNs (-26.1 mV), showing abundant primary amines on the surface of Mag@MSNs-APTS. Mag@MSNs-ACVA has a negative zeta potential value of -21.0 mV. This significant decrease in the zeta potential value indicates that ACVA molecules with carboxylates on both ends were successfully attached to the surface of Mag@MSNs-APTS, with one end stretching out from the surface of Mag@MSNs-ACVA available for further AMA conjugation. Mag@MSNs-AMA with the nearly neutral zeta potential value of -0.45 mV confirms the conjugation of the amine on AMA to the free carboxylate on the surface of Mag@MSNs-ACVA, leaving the uncharged functional group on AMA stretching out from the surface of the particles (**Scheme 3.1b**).

FT-IR spectroscopy was used to characterize surface functional groups after each conjugation step (**Figure 3.8b**). The appearance of two bands in the IR spectrum of Mag@MSNs-APTS due to N-H stretching vibrations at  $\nu = 3628 \text{ cm}^{-1}$  and  $\nu = 3648 \text{ cm}^{-1}$  shows the presence of primary amines attached to the surface of Mag@MSNs-APTS. The successful conjugation of ACVA to the surface of Mag@MSNs-APTS through secondary amide bond formation was confirmed by a new characteristic amide absorption (amide II) at  $\nu = 1550 \text{ cm}^{-1}$ . Additionally, a nitrile absorption appears at  $\nu = 2253 \text{ cm}^{-1}$  (nitrile stretching) from ACVA also supports the successful conjugation of ACVA on the Mag@MSNs-APTS. This is also supported by newly emerging absorptions at  $\nu = 1719 \text{ cm}^{-1}$  (C=O stretching),  $\nu = 1451 \text{ cm}^{-1}$  (C-H bending), and three absorption peaks at  $\nu = 2904 \text{ cm}^{-1}$ ,  $\nu = 2934 \text{ cm}^{-1}$ , and  $\nu = 2981 \text{ cm}^{-1}$  (C-H stretching) from ACVA. Finally, the

conjugation of AMA on the surface of Mag@MSNs-ACVA is confirmed by the appearance of the absorption at  $\nu = 1474 \text{ cm}^{-1}$  (C-H bending) from AMA.

TGA was used to determine the weight of organic moieties on the particles (**Figure 3.8c**). The weight loss of Mag@MSNs, Mag@MSNs-APTS, Mag@MSNs-ACVA, and Mag@MSNs-AMA after heating to 550 °C in air were 6 %, 8 %, 11 %, and 13 %, respectively. The increase in weight loss after each conjugation indicates that the weight of APTS, ACVA, and AMA modified on the surface of core@shell nanoparticles were 2 %, 3 %, and 2 %, respectively. The results from zeta potential measurements, FT-IR, and TGA show that APTS, ACVA, and AMA were successfully and sequentially attached on the surface of Mag@MSNs.

To confirm that the morphology and mesoporous structure of core@shell nanoparticles remains intact after surface modification, we conducted TEM and N<sub>2</sub> adsorption-desorption isotherms analysis of the core@shell nanoparticles after ACVA and AMA conjugation. By TEM, Mag@MSNs-AMA (**Figure 3.8d**) is 55 nm in size with obvious mesoporous structure, very similar to that of Mag@MSNs-APTS (**Figure 3.5a**), indicating that the particles were not damaged after the surface functionalization. The BET surface area, total pore volume, and BJH average pore diameter of Mag@MSNs-AMA are 593.5 m<sup>2</sup>/g, 0.96 cm<sup>3</sup>/g, and 2.8 nm, respectively (**Figure 3.8e**). Similar to Mag@MSNs-APTS (**Figure 3.5b**), Mag@MSNs-AMA preserves the characteristics of mesoporous structure – high surface area and large pore volume – enabling efficient loading and delivery of cargos. AMA and thermolabile ACVA are mainly attached to the outer surface rather than to the inner pore wall of the core@shell nanoparticles, as evidenced by the unchanged average pore diameter of Mag@MSNs-AMA and Mag@MSNs-APTS. Those thermal sensitive gatekeepers selectively bonded on the outer surface of the core@shell nanoparticles can effectively bind to  $\beta$ -cyclodextrin ( $\beta$ -CD) that blocks the pore openings to prevent cargos from leakage, and act as a thermal-sensitive switch to release the cargos on-demand.

### 3.6 Thermal Responsiveness of the Gatekeeper and Bulk Heating-Triggered Cargo Release

To investigate the thermal responsiveness of the gatekeeper, we first demonstrated the cleavage of the gatekeeper triggered by increasing the temperature of the surrounding water. Sample tubes containing Mag@MSNs-ACVA dispersed in deionized water (0.5 mg/mL) were placed for 10 min in the hot water baths heated by a hot plate set at 37 °C, 60 °C, and 80 °C (called bulk heating) (**Figure 3.9c**). The cleavage of C-N bonds of ACVA was confirmed by the zeta potential measurement. After Mag@MSNs-ACVA was heated at 37 °C, 60 °C, and 80 °C for 10 min, the zeta potential values were -20.0 mV, -6.7 mV, and 0.3 mV, respectively (**Figure 3.9ab**). The sample heated at 37 °C shows very similar zeta potential value compared to that of the control without heating (-21.0 mV), showing that the gatekeepers were stable at physiological temperature and the C-N bonds were intact. However, when the temperature increased, the C-N bonds were cleaved, producing fragments of 4-cyanopentanoic acid and nitrogen (**Figure 3.9a**). The removal of the carboxylate group after cleavage explains why the zeta potential becomes increasing after heating.

The bulk heating-triggered cargo release was studied using fluorescein as a model molecule due to its stability and size similar to that of many anticancer drugs (1.5 nm), *e.g.*, doxorubicin or paclitaxel. Fluorescein molecules were loaded in Mag@MSNs-AMA by soaking the particles in 3 mM of the fluorescein solution for 24 h. To trap fluorescein in the pores of core@shell nanoparticles, the pores were capped by bulky  $\beta$ -CD, which strongly binds to AMA on the surface of the nanoparticles and forms a non-covalent supramolecular bond with adamantane.<sup>72,73,86</sup> The particles capped by  $\beta$ -CD were designated as Mag@MSNs-AMA-CD. Fluorescein loaded Mag@MSNs-AMA-CD were washed thoroughly with deionized water to remove the untrapped fluorescein molecules.

To trigger the release of fluorescein, the bulk heating was performed in hot water baths at

various temperatures according to the following procedure (**Figure 3.9c**). Sample tubes containing fluorescein loaded Mag@MSNs-AMA-CD dispersed in deionized water (0.5 mg/mL) were placed in water baths set at 37 °C, 60 °C, and 80 °C for 10 min. To monitor the fluorescein released from Mag@MSNs-AMA-CD, the samples after heating were spun down and aliquots of the supernatants were collected for fluorescence measurements. An unheated sample at room temperature (23 °C) served as the control. The release efficiency is defined as (mass of released fluorescein/mass of loaded fluorescein) x 100 %. Only slight release (less than 3%) of fluorescein from Mag@MSNs-AMA-CD at 23 °C and 37 °C after 10 min heating was observed (**Figure 3.9d**), indicating that the CD cap blocked the pore opening of the particles tightly and minimized premature leakage. The release efficiency of fluorescein strongly increased to 39 % upon heating at 60 °C for 10 min. When the samples were heated in a hot water bath at a higher temperature (80 °C), more than half (55 % release efficiency) of the fluorescein was released after 10 min heating. In addition, after 3 cycles of 10 min heating at 80 °C, almost all fluorescein (near 100 % release efficiency) was released after 3 cycles of 10 min heating (**Figure 3.10**). To determine the long-term release profile of fluorescein, the samples heated at 37 °C, 60 °C, and 80 °C were performed with 9, 9, and 4 such heating/monitoring cycles. The time period between each heating cycle is also 10 min. The cumulative release of fluorescein gradually increased with heating time and finally reached 78 % after 9 cycles of 10 min heating at 60 °C (**Figure 3.10**). On the contrary, the release efficiency of fluorescein after 9 cycles of 10 min heating at 37 °C is only 24 %, which is much lower than that from 60 °C heating, and is close to the control group at 23 °C (19 %). This implies that the CD cap was constructed successfully on the surface of the Mag@MSNs so that little premature leakage was observed either at room temperature or physiological temperature. Most importantly, the cargo release amount and cargo releasing rate can be controlled simply by tuning the temperature of the water bath.

### 3.7 Alternating Magnetic Field-Triggered Cargo Release

Two types of release studies were conducted by using another heat source – an alternating magnetic field (AMF) – which can induce localized heating (here called magnetic heating): (a) a single exposure to AMF for different lengths of time, and (b) multiple sequential exposures each for the same length of time. Fluorescein loaded Mag@MSNs-AMA-CD particles were dispersed in deionized water (0.5 mg/mL) at room temperature. To confirm the tightness of the gatekeeper, release of fluorescein before triggering with magnetic heating was monitored by spinning down the nanoparticles and collecting aliquots of the supernatants for fluorescence measurements. After monitoring the release every 20 min over a period of 40 min at room temperature, the sample was placed in a water-cooled five-turn copper coil generating an AMF at a power of 5 kW and a frequency of 375 kHz (**Figure 3.11a**). Exposure times were 1, 2, 3, 5, or 10 min, followed again by monitoring the release. To have enough time for dye to diffuse out from the pores, monitoring cycles were performed every 10 min at room temperature until the maximum release of fluorescein was achieved. Only slight leakage (less than 5 %) of fluorescein was observed in the first 40 min at room temperature before exposure to an AMF, showing the effectiveness of the gatekeeper to prevent premature leakage of the dye (**Figure 3.11b-f**). The release efficiency of fluorescein was 10 % immediately after 1 min of the AMF trigger, showing that some caps were successfully removed by the magnetic heating. The amount of released fluorescein gradually increased over time at room temperature until it leveled off (total release efficiency of 23.6 %) at 70 min post-AMF trigger (**Figure 3.11b**). After the caps are removed, it takes time for fluorescein molecules to diffuse out from the pores of nanoparticles and reach equilibrium at the end. To correlate the release efficiency of fluorescein with the AMF trigger exposure time, the samples were exposed to the AMF for longer actuation times of 2, 3, 5, and 10 min. Similar time-dependent release profiles were observed in all cases: (i) the burst of release during magnetic heating, (ii) the gradual

increase in the release at room temperature, and (iii) the plateau reached 80 min post-AMF trigger (**Figure 3.11b-f**). Even though the initial rise in release during the burst stage (i) was not obviously increased as a function of the longer magnetic heating time, the cumulative release efficiencies of fluorescein at plateau were significantly enhanced, reaching 41.9 %, 56.5 %, 65.3 %, and 75.9 % with 2, 3, 5, and 10 min of heating time, respectively. This suggested that the number of caps removed from the surface of nanoparticles is directly correlated with the AMF trigger time.

To know whether the removal of the cap is a result of localized internal heating from the magnetic core under the AMF or an increase in the ambient temperature, we simultaneously monitored the temperature of the solution containing Mag@MSNs-AMA-CD immediately after 1, 2, 3, 5, and 10 min of AMF actuation. Less than 6 degrees of temperature increase was observed, where the temperatures were found to be 24, 24, 26, 27, and 29 °C after 1, 2, 3, 5, and 10 min of AMF actuation (**Figure 3.11g**), respectively. Even the highest temperature of the solution after exposing to AMF was below 30 °C, indicating that the release of fluorescein was not triggered by bulk heating from the surrounding solution. Instead, the fairly high local temperature (that can be above 65 °C)<sup>83</sup> achieved internally from the magnetic core was the main heat source to cleave the thermolabile ACVA, which will undergo thermolysis over 60 °C.<sup>17,71</sup>

To confirm that the mesoporous structure of silica particles can withstand the temperature of localized magnetic heating, the structure of Mag@MSNs-AMA-CD after 10 min of the AMF actuation was analyzed by TEM. The TEM image (**Figure 3.12**) shows that the mesoporous silica structure was intact without any damage and the diameters of the particles didn't change after exposing to the internal heating from the inner magnetic core. The cleavage of the C-N bonds was supported by the change in the zeta potential of the Mag@MSN-ACVA particle from -21.0 mV before exposure to -1.8 mV after 10 min of exposure (**Figure 3.13**). The results confirm that the release of fluorescein molecules from Mag@MSNs-AMA-CD is through the removal of the

thermal-sensitive gatekeepers on the surface rather than the destruction of the mesoporous structure of silica particles.

The second type of release study was performed with multiple sequential exposures of AMF to achieve the maximal release of fluorescein. To confirm the tightness of the gatekeeper, the release of fluorescein before each trigger was monitored by fluorescence spectroscopy every 10 min. Only slight leakage (less than 10 %) of fluorescein was observed in the first 30 min at room temperature before exposure to the first cycle of AMF actuation. Three cycles of AMF actuation for 3 min followed by 70 min of the monitoring at room temperature were carried out. The temperature of the solution right after each AMF exposure was measured to be 26 °C, 26 °C, and 26 °C, respectively, only 3 degrees higher than that before each AMF exposure. The minimal temperature increase indicates that the observed release was not triggered by the bulk heating from the surrounding solution but by the higher local temperature achieved internally from the magnetic core. The release efficiency at plateau where fluorescein molecules achieved equilibrium after the first cycle was 60 % (**Figure 3.14**), which is similar to the release efficiency of fluorescein after 3 min of AMF actuation shown in **Figure 3.11d** (56.5 %). Subsequently, the second cycle of AMF actuation was applied and the release efficiency increased to approximate 80 % compared to the background. The second heating cycle caused an additional 20 % more fluorescein can be released. However, when the third cycle of AMF actuation was applied, no increase in the release of fluorescein was observed. This implies two possibilities: (1) part of the caps still block the pore openings after the trigger, and/or (2) even after the caps are fully removed, some fluorescein molecules adhere to the pores of Mag@MSNs-AMA-CD. Stepwise time-dependent release profile triggered by multiple cycles of AMF actuation was observed in three stages which is similar to **Figure 3.11b-f**. Based on this stepwise release profile, we can control the release of desired amount of fluorescein in the specific time period.



### 3.8 Alternating Magnetic Field-Triggered Release of Doxorubicin

In preparation for *in vitro* cancer cell studies, we investigated the loading and AMF release of doxorubicin (DOX), a widely used anticancer drug. DOX was loaded in Mag@MSNs-AMA by soaking the particles in a 2.6 mM DOX solution for 24 h followed by the capping by  $\beta$ -CD. The loading capacity of DOX in Mag@MSNs-AMA-CD was calculated to be 4 % after the DOX-loaded Mag@MSNs-AMA-CD was thoroughly washed with deionized water and PBS to remove the untrapped DOX molecules. The absorption peak at 503 nm of UV-vis spectrum (**Figure 3.15a**) provides spectroscopic evidence that DOX was loaded in Mag@MSNs-AMA-CD.

To prove that the dosage of released DOX from Mag@MSNs-AMA-CD could be controlled after being triggered by different durations of AMF exposure, sample tubes containing DOX-loaded Mag@MSNs-AMA-CD in PBS were placed in the center of the coil with 2, 5, or 10 min of exposure time. Before the AMF exposure, the release of DOX was monitored every 30 min over a period of 60 min at room temperature. Only slight leakage (less than 5 %) of DOX was observed in the first 60 min at room temperature before the AMF exposure. After the AMF exposure, the release of DOX was monitored every 30 min over a period of 3 h followed by every 2 h over a period of 6 h. The released DOX gradually increased over time at room temperature until it leveled off at 540 min post AMF exposure. The cumulative release efficiencies of DOX reach 35.6 %, 45.6 %, and 53.1 % with 2, 5, and 10 min of AMF exposure, respectively (**Figure 3.15b-d**). The temperature of the solution after the AMF exposure was measured to be 24, 26, and 28 °C, respectively. The minimal temperature increase shows that the release of DOX was not triggered by bulk heating from the surrounding solution but by the localized high temperature from the magnetic core. The results demonstrated that the release of DOX can be triggered by an AMF and that the dosage of the DOX released from the nanocarriers can be controlled by different lengths of the AMF exposure.

### 3.9 *In vitro* Studies of Cytotoxicity and Stability of Drug Delivery System

*In vitro* cytotoxicity studies were carried out to evaluate the potential biological applications of the drug delivery system. A pancreatic cancer cell line (PANC-1) was used to evaluate the cytotoxicity of Mag@MSNs-AMA-CD by a colorimetric cell counting kit-8 (CCK-8) assay. The cell viabilities of PANC-1 after 20 h and 70 h incubation at various nanoparticle concentrations are shown in **Figure 3.16a**. No significant decrease in cell viability was detected even at a very high particle concentration (200  $\mu\text{g/mL}$ ) at both 20 h and 70 h. The Mag@MSNs-AMA-CD particles we developed are not toxic and are suitable to be used as drug delivery carriers.

To test the stability of the gatekeepers of Mag@MSNs-AMA-CD *in vitro*, PANC-1 cells were treated with DOX-loaded Mag@MSNs-AMA-CD at various concentrations. The results show that no significant cell viability decrease was observed after 4 h incubation (**Figure 3.16b**). The minimal cytotoxicity proves the tightness of the gatekeepers which prevent the leakage of DOX from the nanocarriers in a biological environment at 37 °C. In addition, the proliferation of PANC-1 (**Figure 3.16c**) was not hindered in a 12 h growth in Dulbecco's modified Eagle's medium (DMEM) supplemented with 10 % fetal bovine serum (FBS) after 4 h treatment by DOX-loaded Mag@MSNs-AMA-CD. These results demonstrate that the drug delivery system prevents the leakage of DOX and thus minimizes the cytotoxicity before activation, and that the proliferation of the PANC-1 was not hindered.

### 3.10 *In vitro* Cellular Killing Studies

*In vitro* cellular killing by DOX-loaded Mag@MSNs-AMA-CD after AMF exposure was studied. PANC-1 cells were treated with DOX-loaded Mag@MSNs-AMA-CD for 4 h followed by the AMF exposure for 2, 5, and 10 min (**Figure 3.17a**). The cell viabilities of the control groups including without the treatment by nanoparticles, and treatment by Mag@MSNs-AMA-CD

without DOX were also investigated. **Figure 3.17b** shows that without the treatment by Mag@MSNs-AMA-CD, the exposure of the cells to AMF (2, 5, and 10 min) did not kill the PANC-1 cells. The results corroborated that the magnetic field was harmless to cells and is a safe stimulus for the drug delivery. No decrease of PANC-1 cell viability was observed after the 4 h incubation with 50  $\mu\text{g}/\text{mL}$  Mag@MSNs-AMA-CD followed by exposure to various lengths of AMF (2, 5, and 10 min). The results indicate that the localized heating generated from Mag@MSNs-AMA-CD during the AMF exposure was not harmful to the cells, and was desirable because killing by hyperthermia did not occur.

The effects of the release of DOX from Mag@MSNs-AMA-CD in PANC-1 cells triggered by the AMF were studied. The PANC-1 cells were incubated with 50  $\mu\text{g}/\text{mL}$  DOX-loaded Mag@MSNs-AMA-CD followed by various lengths of exposure to AMF (2, 5, and 10 min). The results show that the viabilities of PANC-1 were 72 %, 63 %, and 47 % after 2, 5, and 10 min of AMF exposure, respectively (**Figure 3.17b**), which demonstrates that the loss of cell viabilities was correlated with the lengths of AMF exposure time. As AMF exposure time was increased, the dosage of released DOX from the nanocarriers increased and thus killed more PANC-1 cells. The results demonstrate that not only the release of DOX from Mag@MSNs-AMA-CD in cellular environment can be remotely triggered by an AMF, but also that the dosage of the released DOX is controlled by the lengths of AMF exposure and thus different levels of cell killing can be achieved.

Uptake of DOX-loaded Mag@MSNs-AMA-CD by PANC-1 cells and the release of DOX from the nanocarriers in PANC-1 cells after the exposure of the AMF were verified by fluorescence microscope images. PANC-1 cells were treated with 50  $\mu\text{g}/\text{mL}$  DOX-loaded Mag@MSNs-AMA-CD for 4 h. Before the AMF trigger, the red fluorescence derived from DOX was located around the nuclei but not overlapped with blue fluorescence derived from the nucleus stained by Hoechst

33342 dye ((ii) in **Figure 3.17c**), compared with that of control group (without the treatment of nanoparticles, (i) in **Figure 3.17c**). The results indicate that before the exposure to AMF, DOX was not released from the Mag@MSNs-AMA-CD nanoparticles taken up by the PANC-1 cells. However, after the AMF exposure, some of the red fluorescence derived from DOX overlapped with the blue fluorescence of the Hoechst-stained nuclei ((iii) in **Figure 3.17c**). This result demonstrates that DOX was released from Mag@MSNs-AMA-CD in PANC-1 cells after the exposure of the AMF, and thus stained the nuclei and caused cell death.

### **3.11 Significance for Potential Biomedical Applications**

To reduce the side-effects of drugs, release of therapeutics within a specific time, to a targeted location, and with a controlled dosage has always been a goal for drug delivery applications. Although many proof-of-concept stimulated release of drugs have been studied, a majority of them are responsive to internal stimuli such as pH,<sup>3,87</sup> redox,<sup>7,8</sup> or enzymes,<sup>9</sup> and it is almost impossible to precisely control the amount of therapeutics released from the carriers. Even though several studies have reported the externally triggered release of drugs *via* magnetic fields, none of them quantified the release efficiency of the cargos, making it hard to estimate the amount of cargo released upon trigger, nor did they test the tunable dosage released by changing the trigger duration under the magnetic field. In this work, we successfully demonstrated that the release efficiency (hence, the release amount) of fluorescein and DOX can be well controlled by manipulating the AMF trigger time (**Figure 3.11g**). Additionally, with the AMF as an external stimulus, the particles with therapeutics can be delivered and released to the target site on-demand. For those treatments to some disease requiring multiple dosing such as multiple dose insulin injection therapy, the common way is to inject therapeutics several times daily. With the drug delivery strategy developed in this study, by simply applying multiple sequential exposure of AMF, the therapeutics

could be released stepwise *in situ* with the desired amount in the specific time period, and finally reach the required amount in its therapeutic window. The designed controllable drug delivery provides alternative method to those therapies required multiple injection, and at the same time reduces the off-target side effects in chemotherapy.

In addition to chemotherapy, high temperatures (hyperthermia) can also damage and kill cancer cells, usually with minimal injury to normal tissues. Although hyperthermia is a promising way to kill cancer cells, a number of challenges must be overcome including: (1) increasing probability of tumor metastasis,<sup>31-35</sup> (2) difficulty in accurate temperature measurement inside a tumor, (3) problems of keeping an area at a constant temperature without affecting nearby tissues, and (4) body tissue's heterogeneity in response to heat.<sup>31</sup> Even using local hyperthermia for which energy (such as microwave, radiofrequency, or ultrasound) must be delivered to a small volume (*e.g.* a tumor) does not solve all the problems stated above. On the other hand, the internal heat source generated by applying AMF to magnetic cores only heats up a small local area (within a range of magnetic core) as compared to area affected by microwave, radiofrequency, and ultrasound. Thus, this magnetic heating method in combination with drug delivery provides an alternative approach of cancer treatment that has the potential to overcome the challenges faced with traditional chemotherapy and hyperthermia, and is especially beneficial to the case where thermal ablation or necrosis is undesired.

### **3.12 Summary**

In summary, monodisperse manganese and cobalt doped iron oxide ( $\text{MnFe}_2\text{O}_4@ \text{CoFe}_2\text{O}_4$ ) nanoparticles with a high magnetization (105 emu/g) and high specific loss power (1510.8 W/g) were synthesized. The high magnetization of these superparamagnetic nanoparticles provides efficient magnetic heating under an alternating magnetic field (AMF), thus holding great promise

for magnetic heating triggered drug delivery. To increase the amount of drug over that available using the nanoparticles themselves, mesoporous silica shell “containers” are synthesized around the magnetic core, forming a core@shell structure with 55 nm in diameter. The spatial, temporal, and dose control of drug release was achieved using a thermal-responsive gatekeeper containing a thermal-labile molecule 4,4'-azobis(4-cyanovaleric acid), and a host guest complexation formed by adamantylamine and  $\beta$ -cyclodextrin. This gatekeeper was stable at physiological temperature, while at the higher temperature (60 or 80 °C) the gatekeeper was cleaved. When the fluorescein loaded gatekeeper modified nanoparticles were heated for 10 min in 60 or 80 °C water baths, 39 % or 55 % respectively of fluorescein was released. However, when the AMF was applied, the magnetic core served as a heat source, and the localized heating generated from the core led to more efficient fluorescein release (75.9 % of the highest) with the temperature rise of the bulk solution no more than 5 degrees. Most importantly, in this study we demonstrated externally-controlled dosage of fluorescein or doxorubicin (DOX) by controlling the AMF exposure time. Multiple sequential exposure of AMF allows cargo release in a stepwise manner. *In vitro* studies show that the drug delivery system is biocompatible. DOX-loaded nanoparticles did not cause a decrease in cell viability in the absence of AMF stimulation, but the viabilities of the pancreatic cancer cells decreased by 28 %, 37 %, and 53 % as the AMF exposure time increased from 2, 5 to 10 min. Taken together, the thermal-responsive drug delivery actuated by AMF offers the potential of becoming an emerging chemotherapy that non-invasively and precisely control the dosage of drugs, and avoiding the risk generated when overheating the bulk solution.

### 3.13 Methods

#### 3.13.1 Materials and Chemicals

Iron(III) acetylacetonate ( $\text{Fe}(\text{acac})_3$ , 97%), Manganese(II) acetylacetonate ( $\text{Mn}(\text{acac})_2$ , 21%-23% Mn), cobalt(II) acetylacetonate ( $\text{Co}(\text{acac})_2$ , 97%), 1,2-dodecanediol (90%), oleic acid (90%), oleylamine (70%), benzyl ether (98%), hexane (98.5+%), chloroform (99.5+%), hexadecyltrimethylammonium bromide (CTAB, 99+%), tetraethyl orthosilicate (TEOS, 98%), (3-aminopropyl)triethoxysilane (APTS, 99%), 4,4'-azobis(4-cyanovaleric acid) (ACVA, 98+%) 1-adamantylamine (AMA, 97%),  $\beta$ -cyclodextrin ( $\beta$ -CD, 97+%), ammonium nitrate ( $\text{NH}_4\text{NO}_3$ , 98+%), 1-Ethyl-3-(3-dimethylaminopropyl) carbodiimide (EDC, 98+%), *N*-hydroxysuccinimide (NHS, 98%), phosphate-buffered saline (PBS, 10X), bisBenzimide H 33342 trihydrochloride (Hoechst 33342, 98+%), and fluorescein sodium salt were purchased from Sigma-Aldrich. Doxorubicin hydrochloride (DOX-HCl) was purchased from Cayman Chemical. Dimethyl sulfoxide (DMSO, 99.9+%), sodium hydroxide (NaOH, 97+%), hydrochloric acid (HCl, 36.5%-38%, trace metal grade), and nitric acid ( $\text{HNO}_3$ , 67%-70%, trace metal grade) were purchased from Fisher Scientific. Dulbecco's modified Eagle's medium (DMEM) with high glucose, fetal bovine serum (FBS), antibiotics (10,000 U/mL penicillin, 10,000  $\mu\text{g}/\text{mL}$  streptomycin, and 29.2 mg/mL L-glutamine), Dulbecco's phosphate-buffered saline (DPBS), and trypsin-ethylenediaminetetraacetic acid (trypsin-EDTA) (0.05 %) were purchased from Gibco. Cell counting kit-8 (CCK-8) was purchased from Dojindo Molecular Technologies, Inc. Paraformaldehyde solution (4 % in PBS) was purchased from USB Corporation. Ethanol (200 proof) was purchased from Decon Laboratories, Inc. All chemicals were used without further purification.

### 3.13.2 Characterization

The size and morphology of nanoparticles were investigated by transmission electron microscopy (TEM, Tecnai T12) with an operating voltage of 120 kV.  $\text{MnFe}_2\text{O}_4@\text{CoFe}_2\text{O}_4$  or Mag@MSN core@shell nanoparticles were dispersed in hexane or ethanol at a low concentration (0.2 mg/mL). The suspension (10  $\mu\text{L}$ ) of the nanoparticles was dropped onto the carbon-coated copper grid and dried at room temperature. The X-ray diffraction pattern of the powder was obtained by a PANalytical, X'Per PRO diffractometer with Cu  $K_\alpha$  radiation ( $\lambda = 1.5418 \text{ \AA}$ ); the operating voltage and current were 45 kV and 40 mA, respectively. The field-dependent magnetization of  $\text{MnFe}_2\text{O}_4@\text{CoFe}_2\text{O}_4$  was measured using a superconducting quantum interference device (SQUID) Quantum Design MPMS7 magnetometer at 300 K. The iron/manganese/cobalt ratio of the  $\text{MnFe}_2\text{O}_4@\text{CoFe}_2\text{O}_4$  nanoparticles was quantitatively determined by ICP-OES using a Shimadzu ICPE-9000 instrument. Typically, 2 mg of  $\text{MnFe}_2\text{O}_4@\text{CoFe}_2\text{O}_4$  powder was dissolved in 0.5 mL of hydrochloric acid solution. The solution was diluted with 2 %  $\text{HNO}_3$  for quantitative measurement. The calibration curves for iron, manganese, and cobalt were created from 0 ppm to 10 ppm. The surface area, pore volume, and pore size of Mag@MSN core@shell nanoparticles were determined by  $\text{N}_2$  adsorption-desorption isotherm measurements at 77 K (Autosorb-iQ, Quantachrome Instruments). Mag@MSN core@shell was degassed at 110  $^\circ\text{C}$  for 12 h before the measurement. The surface area and pore size distribution of Mag@MSN core@shell were determined by Brunauer-Emmett-Teller (BET) and Barrett-Joyner-Halenda (BJH) methods. The dynamic light scattering (DLS) size and zeta potential values were determined by a laser particle analyzer LPA-3100 at room temperature. The functional groups on the surface of Mag@MSN core@shell were characterized by Fourier transform infrared spectroscopy (FTIR, JASCO FT/IR-420) spectrometer in the range of 4000–400  $\text{cm}^{-1}$ . Thermogravimetric analysis (TGA) was performed on a Perkin-Elmer Pyris Diamond



TG/DTA machine under air flow. About 10 mg of Mag@MSN core@shell were loaded in aluminum pans and the data were recorded from 50 °C to 550 °C at a scan rate of 10 °C/min. An empty aluminum pan was used as the reference. The loading capacities of fluorescein or DOX were determined by UV-Vis Spectroscopy (Cary 5000). The absorbance of the peaks at 477 nm (fluorescein) or 503 nm (DOX) was used for quantification, respectively. The release of fluorescein or DOX was measured by an Acton Spectra Pro 2300i CCD cooled with liquid nitrogen. Fluorescein or DOX were excited by a CUBE 445-40C laser (Coherent Inc.) at a wavelength of 448 nm and a power of 4 mW (fluorescein) or 2 mW (DOX).

### **3.13.3 Synthesis of Magnetic MnFe<sub>2</sub>O<sub>4</sub>@CoFe<sub>2</sub>O<sub>4</sub> Nanoparticles**

Synthesis of 6.3 nm MnFe<sub>2</sub>O<sub>4</sub> nanoparticles: MnFe<sub>2</sub>O<sub>4</sub> nanoparticles were synthesized following a previously reported method with a slight modification.<sup>37,38</sup> Two mmol of Fe(acac)<sub>3</sub>, 1 mmol of Mn(acac)<sub>2</sub>, 10 mmol of 1,2-dodecanediol, 6 mmol of oleic acid, and 6 mmol of oleylamine were dissolved in 20 mL of benzyl ether in a three-neck flask. The reaction was heated to 200 °C under the flow of nitrogen with vigorously stirring and kept at that temperature for 1 h. The reaction mixture was then heated up and refluxed for 1 h (298 °C). Afterwards, the resulting solution containing MnFe<sub>2</sub>O<sub>4</sub> nanoparticles was cooled to room temperature. The nanoparticles were precipitated by adding 40 mL of ethanol and further separated by centrifugation (7830 rpm, 10 min). Finally, MnFe<sub>2</sub>O<sub>4</sub> nanoparticles were dispersed in 10 mL of hexane with 50 μL of oleic acid and 50 μL of oleylamine.

Synthesis of 8.2 nm MnFe<sub>2</sub>O<sub>4</sub> nanoparticles: The larger MnFe<sub>2</sub>O<sub>4</sub> nanoparticles were synthesized by growing MnFe<sub>2</sub>O<sub>4</sub> on the MnFe<sub>2</sub>O<sub>4</sub> nanoparticles prepared previously. Generally, two mmol of Fe(acac)<sub>3</sub>, 1 mmol of Mn(acac)<sub>2</sub>, 10 mmol of 1,2-dodecanediol, 2 mmol of oleic acid, and 2 mmol of oleylamine were dissolved in 20 mL of benzyl ether in a 100 mL three-neck flask.

The  $\text{MnFe}_2\text{O}_4$  nanoparticles (90 mg) obtained previously in 10 mL of hexane were added to the reaction mixture. The reaction mixture was heated to 90 °C and kept at that temperature for 30 min to remove hexane. Then the reaction mixture was heated to 200 °C under the flow of nitrogen with vigorously stirring. After 1 h, the reaction mixture was heated to 298 °C and refluxed for 1 h. The nanoparticles were precipitated by adding 40 mL of ethanol and further separated by centrifugation. Finally, the  $\text{MnFe}_2\text{O}_4$  nanoparticles were re-dispersed in 10 mL of hexane with 50  $\mu\text{L}$  of oleic acid and 50  $\mu\text{L}$  of oleylamine.

Synthesis of 10.1 nm  $\text{MnFe}_2\text{O}_4@\text{CoFe}_2\text{O}_4$  nanoparticles: To coat  $\text{CoFe}_2\text{O}_4$  on the surface of  $\text{MnFe}_2\text{O}_4$  nanoparticles, two mmol of  $\text{Fe}(\text{acac})_3$ , 1 mmol of  $\text{Co}(\text{acac})_2$ , 10 mmol of 1,2-dodecanediol, 2 mmol of oleic acid, and 2 mmol of oleylamine were dissolved in 20 mL of benzyl ether in a 100 mL three-neck flask.  $\text{MnFe}_2\text{O}_4$  (8.2 nm) nanoparticles (180 mg) obtained previously in 10 mL of hexane were added to the reaction mixture. The synthetic procedure and reaction temperature were the same as that of the 8.2 nm  $\text{MnFe}_2\text{O}_4$  nanoparticles synthesis. Finally,  $\text{MnFe}_2\text{O}_4@\text{CoFe}_2\text{O}_4$  nanoparticles (10.1 nm) were re-dispersed in 10 mL of hexane with 50  $\mu\text{L}$  of oleic acid and 50  $\mu\text{L}$  of oleylamine.

Synthesis of 11.4 nm  $\text{MnFe}_2\text{O}_4@\text{CoFe}_2\text{O}_4$  nanoparticles: To coat  $\text{CoFe}_2\text{O}_4$  on the surface of  $\text{MnFe}_2\text{O}_4@\text{CoFe}_2\text{O}_4$  (10.1 nm) nanoparticles to obtain the larger nanoparticles, two mmol of  $\text{Fe}(\text{acac})_3$ , 1 mmol of  $\text{Co}(\text{acac})_2$ , 10 mmol of 1,2-dodecanediol, 2 mmol of oleic acid, and 2 mmol of oleylamine were dissolved in 20 mL of benzyl ether in a 100 mL three-neck flask.  $\text{MnFe}_2\text{O}_4@\text{CoFe}_2\text{O}_4$  (10.1 nm) nanoparticles (270 mg) obtained previously in 10 mL of hexane were added to the reaction mixture. The synthetic procedure and reaction temperature were the same as that of 10.1 nm  $\text{MnFe}_2\text{O}_4@\text{CoFe}_2\text{O}_4$  nanoparticle synthesis. Finally,  $\text{MnFe}_2\text{O}_4@\text{CoFe}_2\text{O}_4$  nanoparticles (11.4 nm) were re-dispersed in 10 mL of hexane with 50  $\mu\text{L}$  of oleic acid and 50  $\mu\text{L}$  of oleylamine for further use.

### 3.13.4 Measurement of Specific Loss Power

Measurement of the heat generation from 11.4 nm MnFe<sub>2</sub>O<sub>4</sub>@CoFe<sub>2</sub>O<sub>4</sub> nanoparticles was performed using a magnetic hyperthermia system (MSI Automation, Inc.) The diameter of the five-turn copper coil was 50 mm. The alternating frequency, induction power, and magnetic field strength were 375 kHz, 5 kW, and 20 kAm<sup>-1</sup>, respectively. The MnFe<sub>2</sub>O<sub>4</sub>@CoFe<sub>2</sub>O<sub>4</sub> nanoparticles were dispersed in toluene in a 2 mL of glass sample vial and the concentrations were 2.5, 1, or 0.5 mg/mL. The temperature of the solution was recorded after the exposure to the AMF as a function of time. The specific loss power of MnFe<sub>2</sub>O<sub>4</sub>@CoFe<sub>2</sub>O<sub>4</sub> was calculated using equation (1), where  $C$  is the volumetric heat capacity of solvent,  $V_s$  is the sample volume,  $m$  is the mass of MnFe<sub>2</sub>O<sub>4</sub>@CoFe<sub>2</sub>O<sub>4</sub>, and  $dT/dt$  is the initial slope of the time-dependent temperature increase curve.

$$\text{Specific loss power} = \frac{CV_s}{m} \frac{dT}{dt} \quad (1)$$

### 3.13.5 Synthesis of APTS-Functionalized MnFe<sub>2</sub>O<sub>4</sub>@CoFe<sub>2</sub>O<sub>4</sub>@Mesoporous Silica (Mag@MSNs-APTS) Core@Shell nanoparticles

MnFe<sub>2</sub>O<sub>4</sub>@CoFe<sub>2</sub>O<sub>4</sub> nanoparticles (11.4 nm, 2.5 mg) were dispersed in 0.2 mL of chloroform. 2 mL of CTAB aqueous solution (40 mg of CTAB, 54 mM) was added to the MnFe<sub>2</sub>O<sub>4</sub>@CoFe<sub>2</sub>O<sub>4</sub> colloidal solution, and the mixture was sonicated for 10 min with a fully sealed cover to generate oil-in-water emulsion. The emulsion was then sonicated for 1 h to evaporate chloroform. The clear well-dispersed MnFe<sub>2</sub>O<sub>4</sub>@CoFe<sub>2</sub>O<sub>4</sub> colloidal aqueous solution (2 mL) was obtained and designated as MnFe<sub>2</sub>O<sub>4</sub>@CoFe<sub>2</sub>O<sub>4</sub>@CTAB. Meanwhile, 40 mg of CTAB was dissolved in 18 mL of water with 120  $\mu$ L of NaOH solution (2 M) in a 100 mL flask. Then, the previous 2 mL of MnFe<sub>2</sub>O<sub>4</sub>@CoFe<sub>2</sub>O<sub>4</sub>@CTAB colloidal solution was added to the reaction solution with vigorously stirring, and the temperature of the solution was brought up to 70 °C. To coat mesoporous silica shell on the surface of MnFe<sub>2</sub>O<sub>4</sub>@CoFe<sub>2</sub>O<sub>4</sub>@CTAB, 200  $\mu$ L of TEOS and 1.2 mL of ethyl acetate

were added dropwise into the solution. After stirring for 2 h, 40  $\mu\text{L}$  of APTS was added dropwise into the solution and stirred for another 2 h to generate amine functionalized  $\text{MnFe}_2\text{O}_4@\text{CoFe}_2\text{O}_4@\text{MSNs}$  ( $\text{Mag}@MSNs\text{-APTS}$ , Mag denotes magnetic). Afterwards, the solution was cooled to room temperature and  $\text{Mag}@MSNs\text{-APTS}$  was centrifuged and washed 3 times with ethanol. Subsequently,  $\text{Mag}@MSNs\text{-APTS}$  was dispersed in 20 mL of ethanol containing 120 mg of  $\text{NH}_4\text{NO}_3$  and the reaction was stirred at 60  $^\circ\text{C}$  for 1 h to remove the surfactants. The surfactant removal procedures were repeated twice and  $\text{Mag}@MSNs\text{-APTS}$  was washed several times with D.I. water and ethanol to obtain the surfactant-free  $\text{Mag}@MSNs\text{-APTS}$ .

### **3.13.6 Synthesis of ACVA Functionalized $\text{Mag}@MSNs\text{-APTS}$ ( $\text{Mag}@MSNs\text{-ACVA}$ )**

The conjugation of 4,4'-azobis(4-cyanovaleric acid) (ACVA) on the surface of  $\text{Mag}@MSNs\text{-APTS}$  was carried out by using an amide bond coupling reaction. At first, the carboxylic acid of ACVA (20 mg) was activated by 40 mg of EDC and 20 mg of NHS in 4 mL of DMSO. To crosslink the activated ACVA to the primary amine of APTS, after 30 min activation at room temperature, 20 mg of  $\text{Mag}@MSNs\text{-APTS}$  dispersed in 4 mL of DMSO were added dropwise to the activated ACVA in DMSO and stirred for 24 h. The ACVA functionalized  $\text{Mag}@MSNs\text{-APTS}$  ( $\text{Mag}@MSNs\text{-ACVA}$ ) was washed, centrifuged, and re-suspended in DMSO 3 times to remove the excess ACVA, EDC, and NHS.

### **3.13.7 Synthesis of AMA Functionalized $\text{Mag}@MSNs\text{-ACVA}$ ( $\text{Mag}@MSNs\text{-AMA}$ )**

The conjugation of 1-adamantylamine (AMA) on the surface of  $\text{Mag}@MSNs\text{-ACVA}$  was carried out through amide bond formation between the carboxylic acid group of ACVA and the primary amine of AMA. Typically, the carboxylic acid groups of  $\text{Mag}@MSNs\text{-ACVA}$  (20 mg) were activated by 40 mg of EDC and 20 mg of NHS in 4 mL of DMSO. To crosslink ACVA to AMA, after 30 min activation at room temperature, 20 mg of AMA dissolved in 4 mL of DMSO

was added to the activated Mag@MSNs-ACVA in DMSO and stirred for 24 h. Finally, AMA functionalized Mag@MSNs-ACVA (Mag@MSNs-AMA) was washed, centrifuged, and re-suspended in DMSO 3 times to remove the excess AMA, EDC, and NHS.

### **3.13.8 Loading of Fluorescein or DOX in Mag@MSNs-AMA and Snap-Top Attachment (Mag@MSNs-AMA-CD)**

The loading of fluorescein or DOX was carried out by using water as the solvent. In general, 1 mg of Mag@MSNs-AMA was dispersed in 1 mL of D.I. water with 3 mM fluorescein or 2.6 mM DOX. After stirring for 24 h, 16 mg of the  $\beta$ -CD capping agent was added to the solution to prevent fluorescein or DOX from being released. The sample was designated as Mag@MSNs-AMA-CD. After mixing for 48 h, the fluorescein or DOX-loaded Mag@MSNs-AMA-CD was centrifuged and washed with water 5 times (fluorescein) or with water 7 times followed by PBS 2 times (DOX) to remove the free fluorescein or DOX molecules. The final product was suspended in 2 mL of D.I. water for the water bath heating or magnetic heating triggered release experiments.

### **3.13.9 Triggered Release of Fluorescein from Mag@MSNs-AMA-CD by Water Bath Heating**

0.5 mg of fluorescein loaded Mag@MSNs-AMA-CD was dispersed in 1 mL of water in an Eppendorf tube. Water baths at 37, 60, or 80 °C were prepared. The samples were heated in the 37, 60, or 80 °C water baths for 10 min per heating cycle (heating on = 10 min). After each heating cycle, the solution was centrifuged and 20  $\mu$ L of supernatant was collected and diluted. The released fluorescein molecules were then monitored by fluorescence spectroscopy, followed by another heating cycle. The time period between each heating cycle was 10 min (heating off = 10 min). In total, 9 such heating/monitoring cycles were performed for the samples in both the 37 °C and the 60 °C water baths; 4 such heating/monitoring cycles were performed for the sample in the 80 °C water bath. For comparison, the supernatant of the sample in the air at room temperature (23

°C) was collected and the released fluorescein was monitored at the same time with the samples heated in water baths. The intensity of the fluorescein released from Mag@MSNs-AMA-CD was integrated from 510 nm to 520 nm.

#### **3.13.10 Triggered Release of Fluorescein or DOX from Mag@MSNs-AMA-CD by Single Cycle of Magnetic Heating**

0.5 mg of fluorescein or DOX-loaded Mag@MSNs-AMA-CD was dispersed in 1 mL of water in an Eppendorf tube. Before being triggered by magnetic heating, the fluorescein or DOX loaded nanoparticle solution at room temperature was centrifuged and 20  $\mu$ L of supernatant was collected every 20 min (fluorescein) or 30 min (DOX) and measured by fluorescence spectroscopy. After monitoring the release every 20 min over a period of 40 min (fluorescein) or every 30 min over a period of 60 min (DOX) at room temperature, the sample was exposed to an alternating magnetic field (AMF) in the center of a water-cooled five-turn copper coil (5 cm height and diameter) at a power of 5 kW and a frequency of 375 kHz for 1, 2, 3, 5, and 10 min, respectively, followed by monitoring the release of fluorescein or DOX. After that, several monitoring cycles were performed every 10 min (fluorescein), or every 30 min over a period of 180 min followed by every 2 h over a period of 6 h (DOX) until the release of fluorescein or DOX leveled off. The intensities of the fluorescein or DOX released from Mag@MSNs-AMA-CD was integrated from 510 nm to 520 nm or 580 nm to 605 nm, respectively.

#### **3.13.11 Triggered Release of Fluorescein from Mag@MSNs-AMA-CD by Sequential Cycles of Magnetic Heating**

0.5 mg of fluorescein loaded Mag@MSNs-AMA-CD was dispersed in 1 mL of water in an Eppendorf tube. Before being triggered by magnetic heating, the fluorescein loaded nanoparticle solution at room temperature was centrifuged and 20  $\mu$ L of supernatant was collected every 10

min and measured by fluorescence spectroscopy. After monitoring the release every 10 min over a period of 30 min at room temperature, the sample was exposed to an AMF in the center of a water-cooled five-turn copper coil (5 cm height and diameter) at a power of 5 kW and a frequency of 375 kHz for 3 min, followed by monitoring the release of fluorescein. Several monitoring cycles were performed every 10 min until the release of fluorescein leveled off, followed by another AMF heating for 3 min. In total, 3 such heating/monitoring series were performed to achieve the maximum release of fluorescein. The intensity of the fluorescein released from Mag@MSNs-AMA-CD was integrated from 510 nm to 520 nm.

#### **3.13.12 Zeta Potential Value Measurement of Mag@MSNs-ACVA after Bulk or Magnetic Heating**

0.5 mg of Mag@MSNs-ACVA was dispersed in 1 mL of water in an Eppendorf tube. For bulk heating treatment, the Eppendorf tubes containing the samples were put in a hot water bath at 37, 60, or 80 °C for 10 min. Afterwards, the solution was centrifuged and the nanoparticles were washed and redispersed in D.I. water. For magnetic heating treatment, the Eppendorf tube containing the sample was exposed to an AMF at a power of 5 kW and a frequency of 375 kHz for 10 min. Similarly, after the treatment, the solution was centrifuged and the nanoparticles were washed and redispersed in D.I. water. The zeta potential values of the samples after bulk heating or magnetic heating treatment were measured.

#### **3.13.13 Loading Capacity Analysis of Fluorescein or DOX**

After loaded with 3 mM fluorescein or 2.6 mM DOX and capped with  $\beta$ -CD, Mag@MSNs-AMA-CD were washed with water 5 times (fluorescein) or washed with water 7 times followed by PBS 2 times (DOX). The supernatants collected during each washing step were collected and their absorption spectra were measured by UV-Vis spectroscopy. To calculate the amount of fluorescein or DOX loaded in Mag@MSNs-AMA-CD, the amount of fluorescein or DOX

removed during all the washing steps was subtracted from the total amount of fluorescein or DOX in the initial loading solution. The loading capacities of fluorescein or DOX were calculated using the maximum absorbance at 491 nm (fluorescein) or 503 nm (DOX) and the following definition of loading capacity: (mass of loaded fluorescein or DOX / mass of particles) x 100%.

#### **3.13.14 Release Efficiency Analysis of Fluorescein or DOX**

To determine the release efficiency of fluorescein, 0.5 mg of fluorescein or DOX-loaded Mag@MSNs-AMA-CD in 1 mL of water was put in a hot water bath at 90 °C. The fluorescein or DOX released from the nanoparticles was separated from the nanoparticles by centrifugation and recorded by spectrophotometry. The intensities of the fluorescein or DOX released from Mag@MSNs-AMA-CD were integrated from 510 nm to 520 nm or 580 nm to 605 nm, respectively. The fluorescence intensities corresponding to the fluorescein or DOX released after being heated at 90 °C for 50 min was set as the 100% release. The release efficiencies of fluorescein or DOX is defined as (mass of released cargo/mass of loaded cargo) x 100%.

#### **3.13.15 Cell Culture**

Human pancreatic cancer cells (PANC-1) were cultured in T-75 flasks (Corning) with vented caps in a high glucose Dulbecco's modified Eagle's medium (DMEM) supplemented with 10 % fetal bovine serum (FBS), and 1 % antibiotics (100 U/mL penicillin and 100 µg/mL streptomycin) in a humidity-controlled incubator at 37 °C with 5 % CO<sub>2</sub>. In all culture conditions, the PANC-1 culture media were daily changed and the cells were harvested by trypsinization with 0.05 % trypsin-ethylenediaminetetraacetic acid (EDTA) for passaging every 2-3 days.

#### **3.13.16 *In Vitro* Cytotoxicity**

The viabilities of PANC-1 after the treatment of Mag@MSNs-AMA-CD and DOX-loaded Mag@MSNs-AMA-CD were examined by using a cell counting kit-8 (CCK-8) assay. The cells



were seeded in 96-well plates at a density of  $5 \times 10^3$  cells per well in 200  $\mu\text{L}$  of Dulbecco's modified Eagle's medium (DMEM) supplemented with 10% FBS and 1% antibiotics in a humidity-controlled incubator at 37 °C for 24 h attachment. After the attachment, the medium was removed and the cells were incubated in 200  $\mu\text{L}$  of fresh DMEM containing 0, 2, 5, 10, 15, 20, and 40  $\mu\text{g}$  of Mag@MSNs-AMA-CD (*i.e.* 0, 10, 25, 50, 75, 100, and 200  $\mu\text{g}/\text{mL}$ ) for 20 or 70 h in an incubator at 37 °C. After incubation, the medium was removed and the treated cells were washed twice with DPBS. To measure the cell viability, 100  $\mu\text{L}$  of DMEM and 10  $\mu\text{L}$  of CCK-8 cellular cytotoxicity reagent were added to each well. Then, the plates were put in the incubator for 2 h at 37 °C. To measure the number of the viable cells in each condition, a plate reader (Tecan M1000) was used to measure the absorbance at 450 nm and 650 nm (as the reference). The DMEM medium (100  $\mu\text{L}$ ) mixed with CCK-8 reagent (10  $\mu\text{L}$ ) served as a background control.

### **3.13.17 *In Vitro* Drug Delivery Triggered by an AMF and Cellular Cytotoxicity**

PANC-1 cells were seeded in 8-well chamber slides at a density of  $2.5 \times 10^4$  cells per well in 500  $\mu\text{L}$  of DMEM supplemented with 10% FBS and 1% antibiotics in a humidity-controlled incubator at 37 °C for 24 h attachment. After the attachment, the medium was removed and the cells were incubated in 300  $\mu\text{L}$  of fresh DMEM containing 15  $\mu\text{g}$  of DOX-loaded Mag@MSNs-AMA-CD (50  $\mu\text{g}/\text{mL}$ ) for 4 h in an incubator at 37 °C. The control groups including cells not treated by nanoparticles and those treated with Mag@MSNs-AMA-CD (50  $\mu\text{g}/\text{mL}$ ) without DOX were also investigated. After 4 h incubation, the medium was removed and the treated cells were washed twice with DPBS (500  $\mu\text{L}$  x 2).

The chamber slides containing the treated or untreated PANC-1 cells in 500  $\mu\text{L}$  of medium were exposed to an AMF in the center of a water-cooled five-turn copper coil at a power of 5 kW and a frequency of 375 kHz for 2, 5, and 10 min, respectively. After the AMF treatment, the cells

were further incubated in an incubator at 37 °C for 12 h. To measure the cell viability after the treatment, the medium was removed and 200 µL of DMEM and 20 µL of CCK-8 reagent were added to each well. Afterwards, the chamber slides were put in the incubator for 2 h at 37 °C. Finally, 100 µL of the reaction solution was transferred to a 96-well plate and the viability was measured by a plate reader described above.

### **3.13.18 Fluorescence Microscope Images of PANC-1 Cells after Treatment**

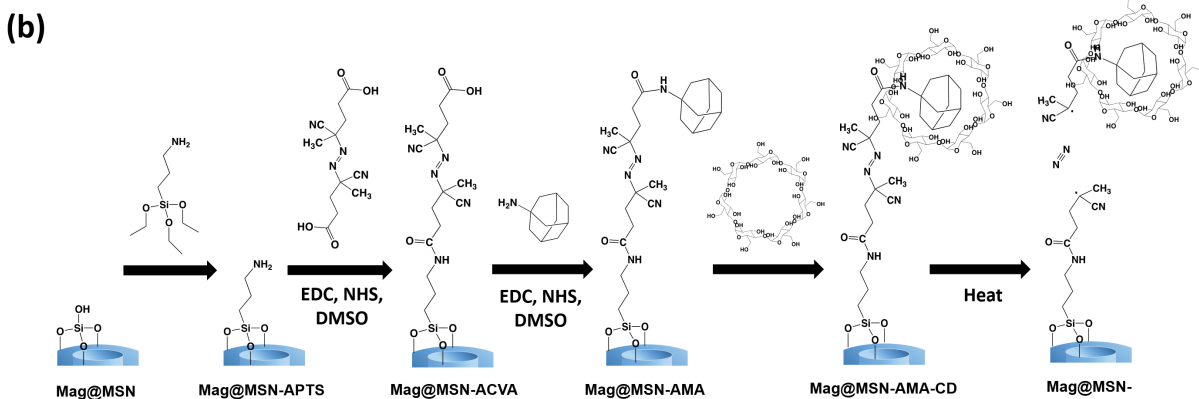
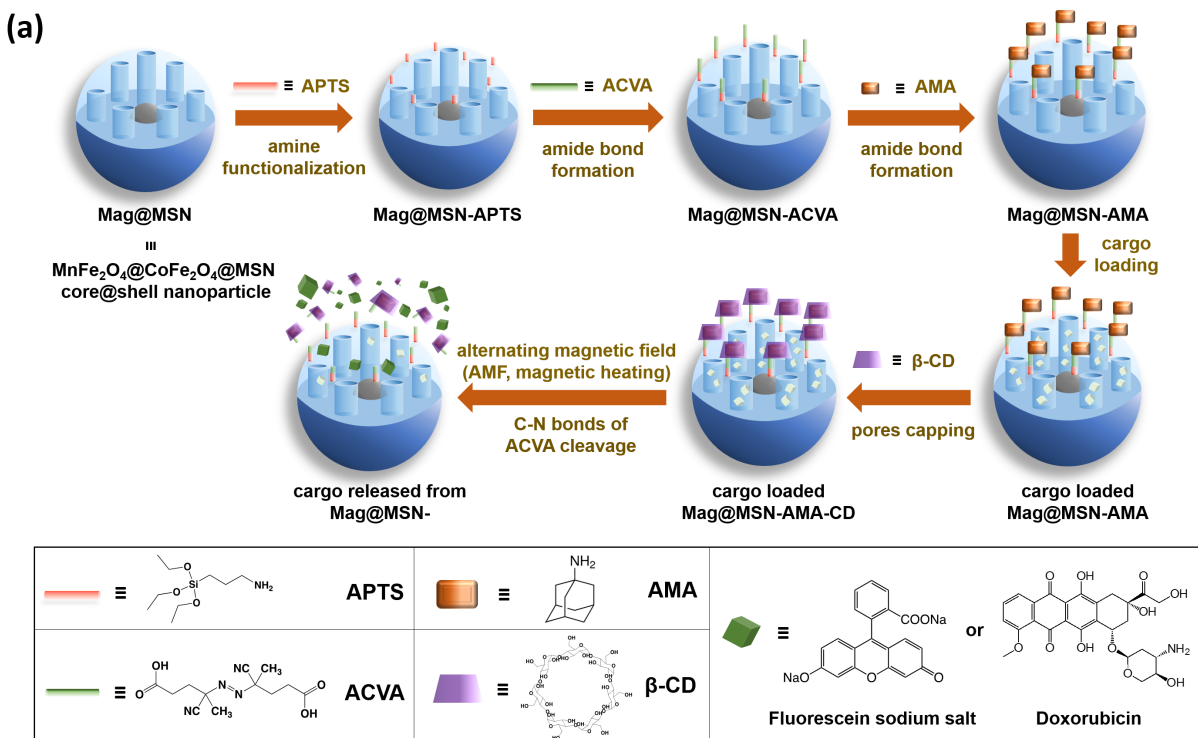
PANC-1 cells were seeded in 8-well chamber slides at a density of  $2.5 \times 10^4$  cells per well in 500 µL of DMEM supplemented with 10% FBS and 1% antibiotics in a humidity-controlled incubator at 37 °C for 24 h attachment. After the attachment, the medium was removed and the cells were incubated in 300 µL of fresh DMEM containing 15 µg of DOX-loaded Mag@MSNs-AMA-CD (50 µg/mL) for 4 h in an incubator at 37 °C followed by washing with DPBS 2 times (500 µL x 2). The control group including cells not treated by nanoparticles was also investigated. After the washing, the chamber slides containing the treated or untreated PANC-1 cells in 500 µL of medium were exposed to an AMF in the center of a water-cooled five-turn copper coil at a power of 5 kW and a frequency of 375 kHz for 10 min. After the AMF treatment, the cells were further incubated in an incubator at 37 °C for 12 h followed by washing with DPBS 3 times (500 µL x 3) and fixed with 4 % paraformaldehyde in PBS for 20 min. Then, the fixed cells were washed with DPBS 3 times (500 µL x 3) with slightly shake. Afterwards, the nuclei of the cells were stained with Hoechst 33342 (500 µL, 5 µg/mL) for 20 min followed by washing with DPBS 5 times (500 µL x 5). Finally, the stained cells covered by mounting medium cover glass before being visualized under a Zeiss fluorescence microscope.

### **3.14 Acknowledgment**

We gratefully acknowledge financial support by the Zink Student Research Support Fund.

We thank Dr. Yao Cai for discussing the experimental procedures of cell studies.

### 3.15 Scheme and Figures



**Scheme 3.1.** (a) Schematic illustration of the synthesis of azo snap-top core@shell mesoporous silica nanoparticles and triggered release under an alternating magnetic field. (b) Scheme of the conjugation and capping of APTS, ACVA, AMA, and  $\beta$ -CD on the surface of core@shell nanoparticles (EDC = 1-ethyl-3-(3-dimethylaminopropyl) carbodiimide; NHS = *N*-hydroxysuccinimide; DMSO = dimethyl sulfoxide). After the trigger with heat, the cleavage of C-N bonds of ACVA makes the bulky  $\beta$ -CD and AMA complexation leave from the surface, and the cargo could thus be released from Mag@MSN-.

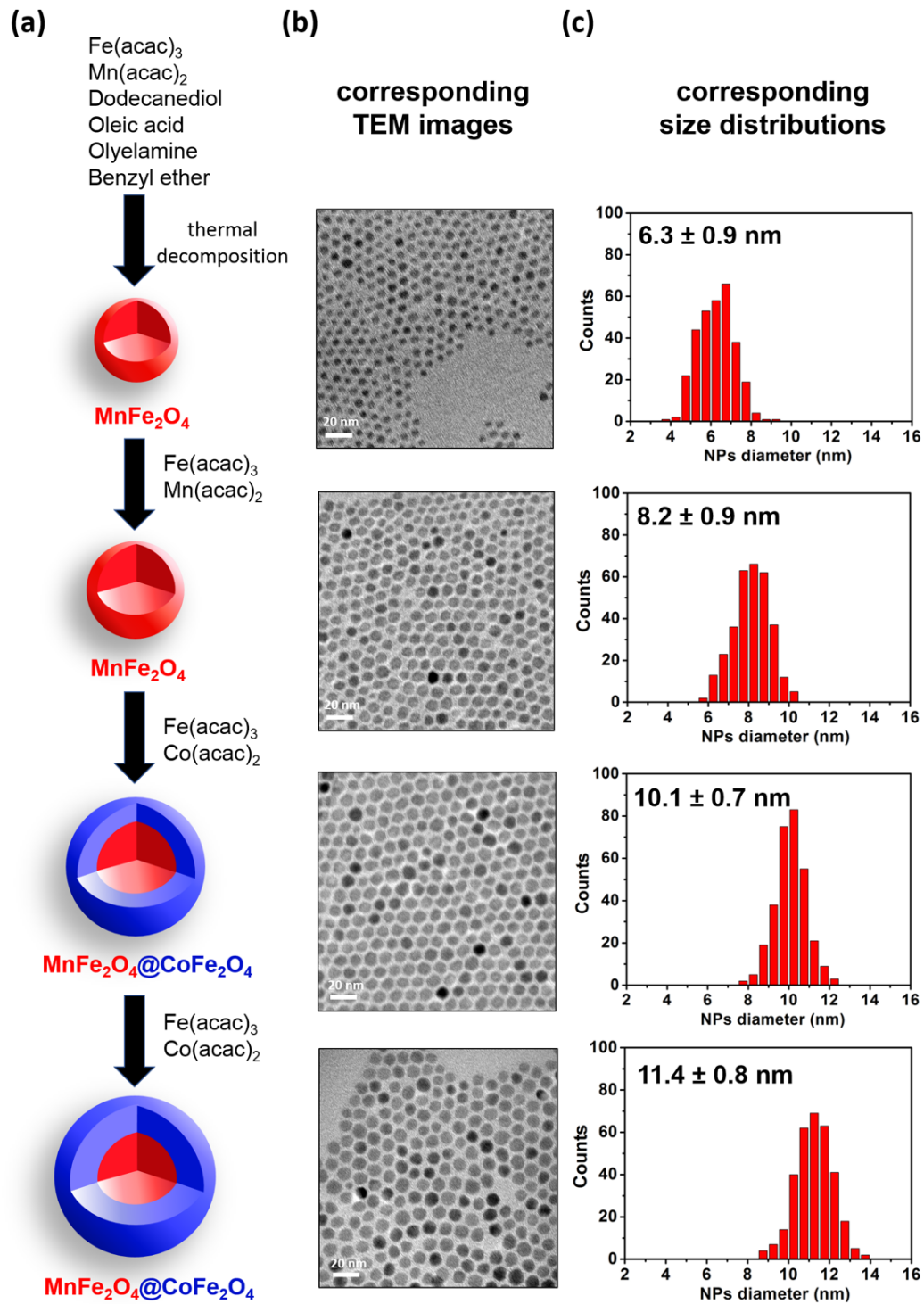


**Figure 3.1.** (a) Schematic illustration of the synthesis of MnFe<sub>2</sub>O<sub>4</sub>@CoFe<sub>2</sub>O<sub>4</sub> nanoparticles by a seed-mediated thermal decomposition method. (b) Corresponding TEM images and (c) diameter distributions of MnFe<sub>2</sub>O<sub>4</sub> and MnFe<sub>2</sub>O<sub>4</sub>@CoFe<sub>2</sub>O<sub>4</sub> nanoparticles after each step.

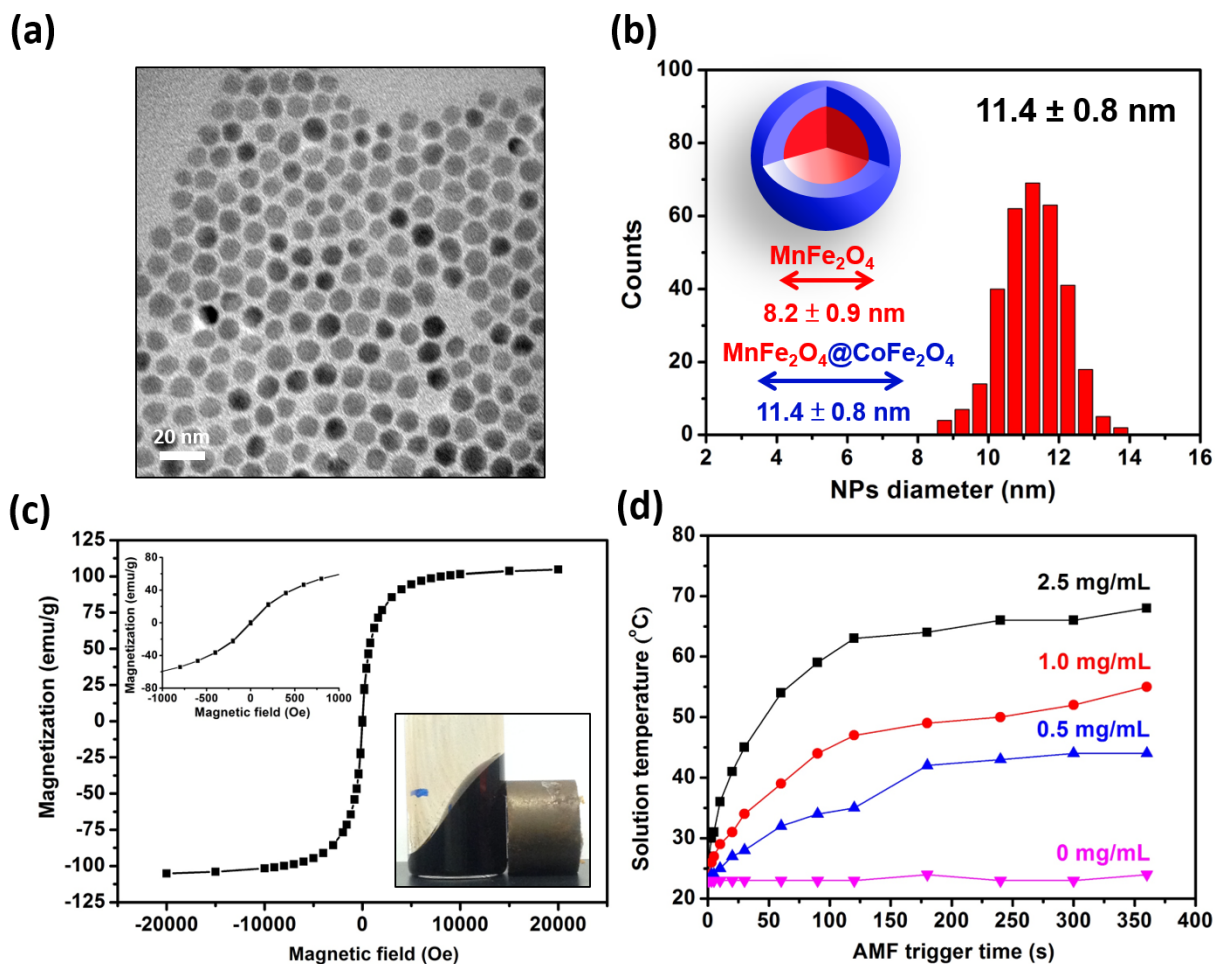


**Figure 3.2.** (a) TEM image and (b) size distribution of 11.4 nm  $\text{MnFe}_2\text{O}_4@\text{CoFe}_2\text{O}_4$  nanoparticles. Inset shows the schematic illustration of magnetic core@shell  $\text{MnFe}_2\text{O}_4@\text{CoFe}_2\text{O}_4$  structure. (c) Field dependent magnetization curve of  $\text{MnFe}_2\text{O}_4@\text{CoFe}_2\text{O}_4$  nanoparticles at 300 K. Inset shows small scale of field dependent magnetization curves and  $\text{MnFe}_2\text{O}_4@\text{CoFe}_2\text{O}_4$  nanoparticles in hexane were attracted by a magnet. (d) Time- and concentration-dependent temperature increase profiles of toluene solution containing  $\text{MnFe}_2\text{O}_4@\text{CoFe}_2\text{O}_4$  nanoparticles triggered by an AMF.

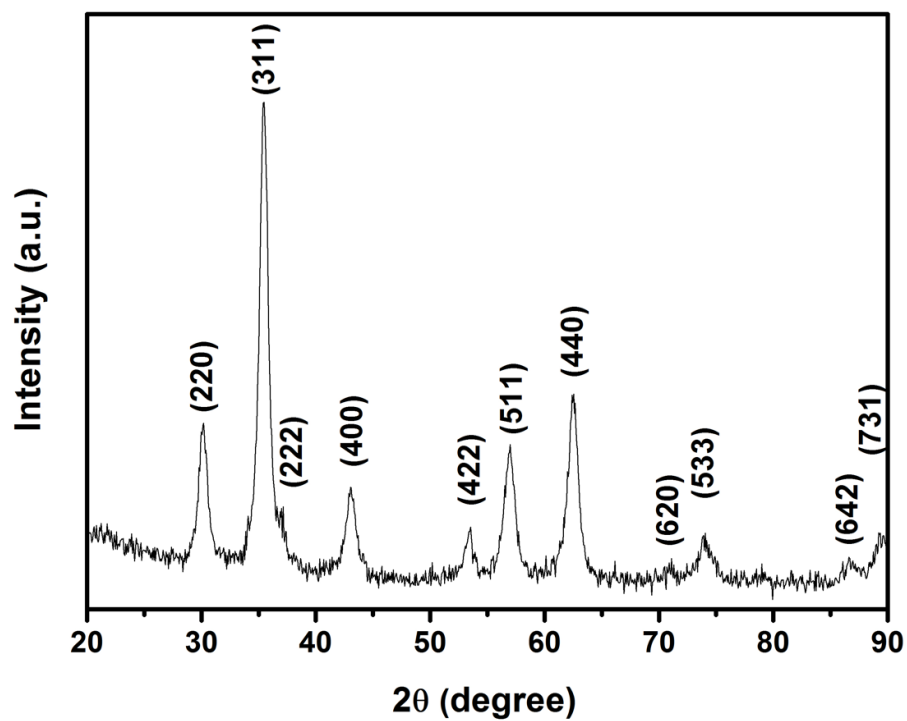
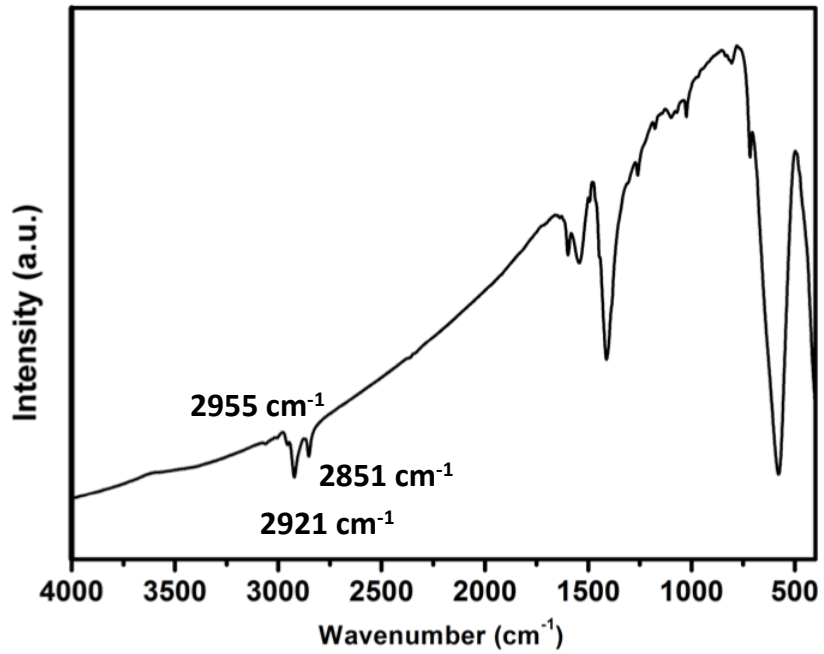


**Figure 3.3.** High angle X-ray diffraction pattern of  $\text{MnFe}_2\text{O}_4@\text{CoFe}_2\text{O}_4$  nanoparticles.

(a)



(b)

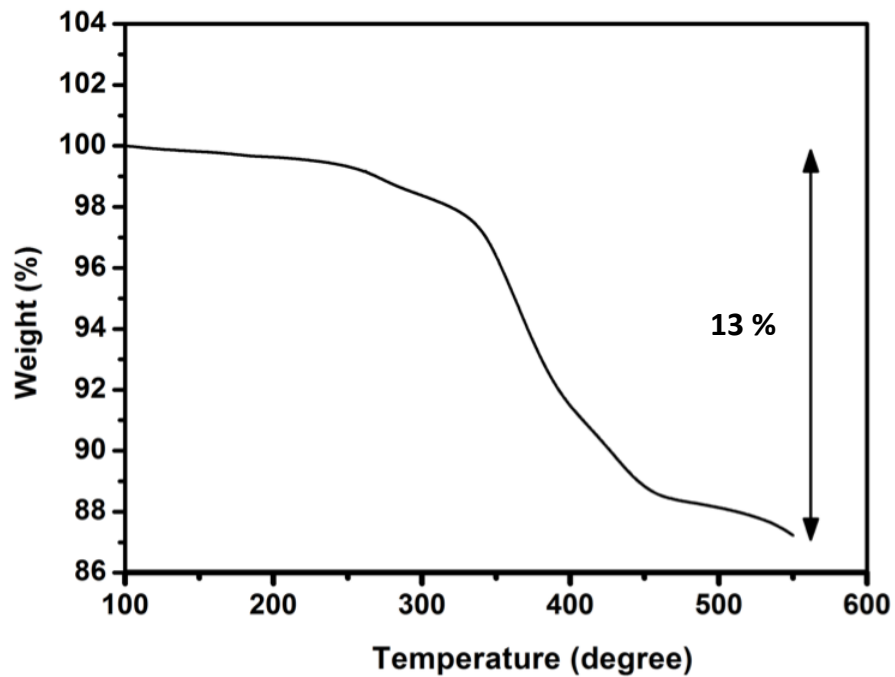


**Figure 3.4.** (a) Fourier-transform Infrared (FTIR) spectrum and (b) thermogravimetric analysis (TGA) of MnFe<sub>2</sub>O<sub>4</sub>@CoFe<sub>2</sub>O<sub>4</sub> nanoparticles.



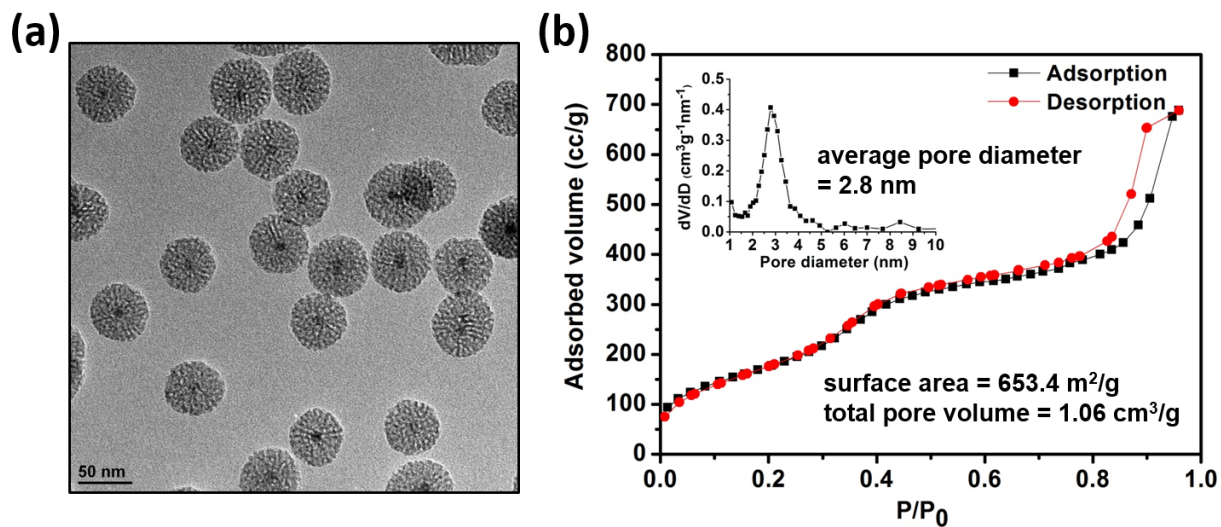


**Figure 3.5.** (a) TEM image of APTS functionalized core@shell nanoparticles (Mag@MSNs-APTS). (b) Nitrogen adsorption/desorption isotherms of Mag@MSNs-APTS at 77 K. The BET surface area and pore volume are 653.4 m<sup>2</sup>/g, and 1.06 cm<sup>3</sup>/g, respectively. Inset shows the pore diameter distribution of Mag@MSNs-APTS. The average pore diameter is 2.8 nm.

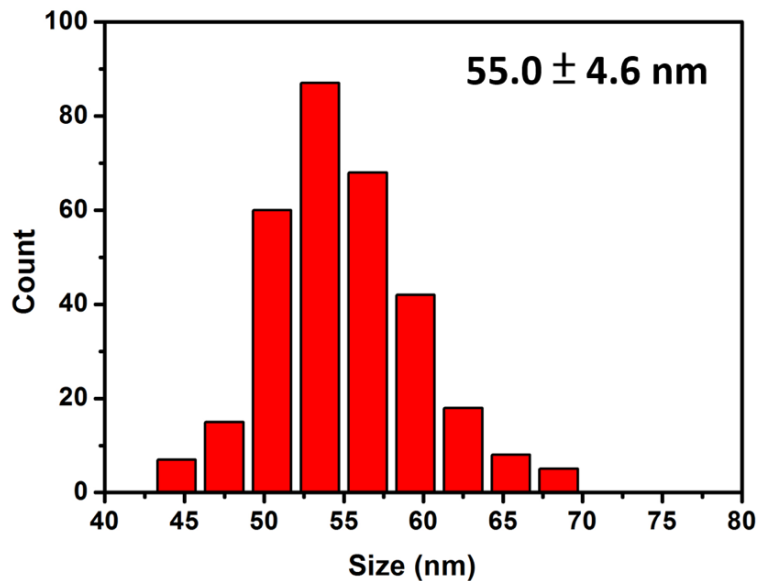


**Figure 3.6.** Size distribution of 55.0 nm Mag@MSNs-APTS core@shell nanoparticles.

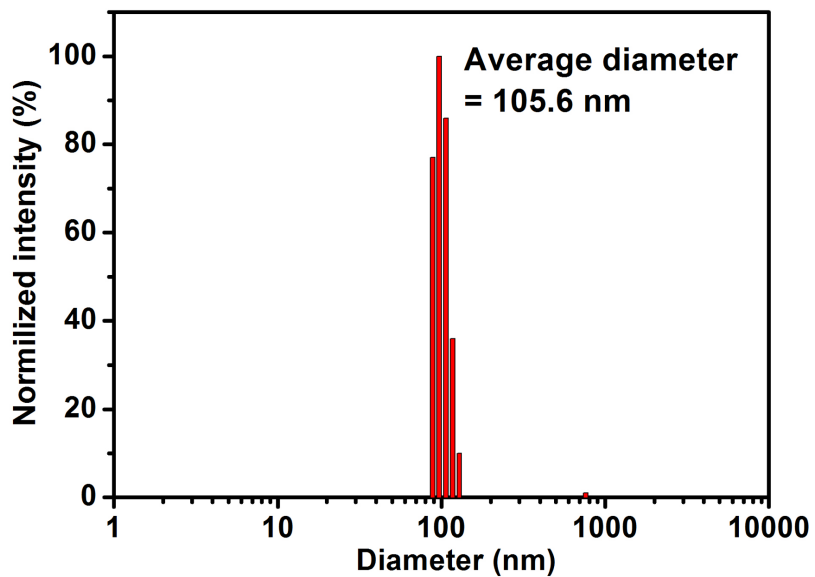


**Figure 3.7.** Dynamic light scattering diameter distribution of Mag@MSNs-APTS in deionized H<sub>2</sub>O at room temperature.

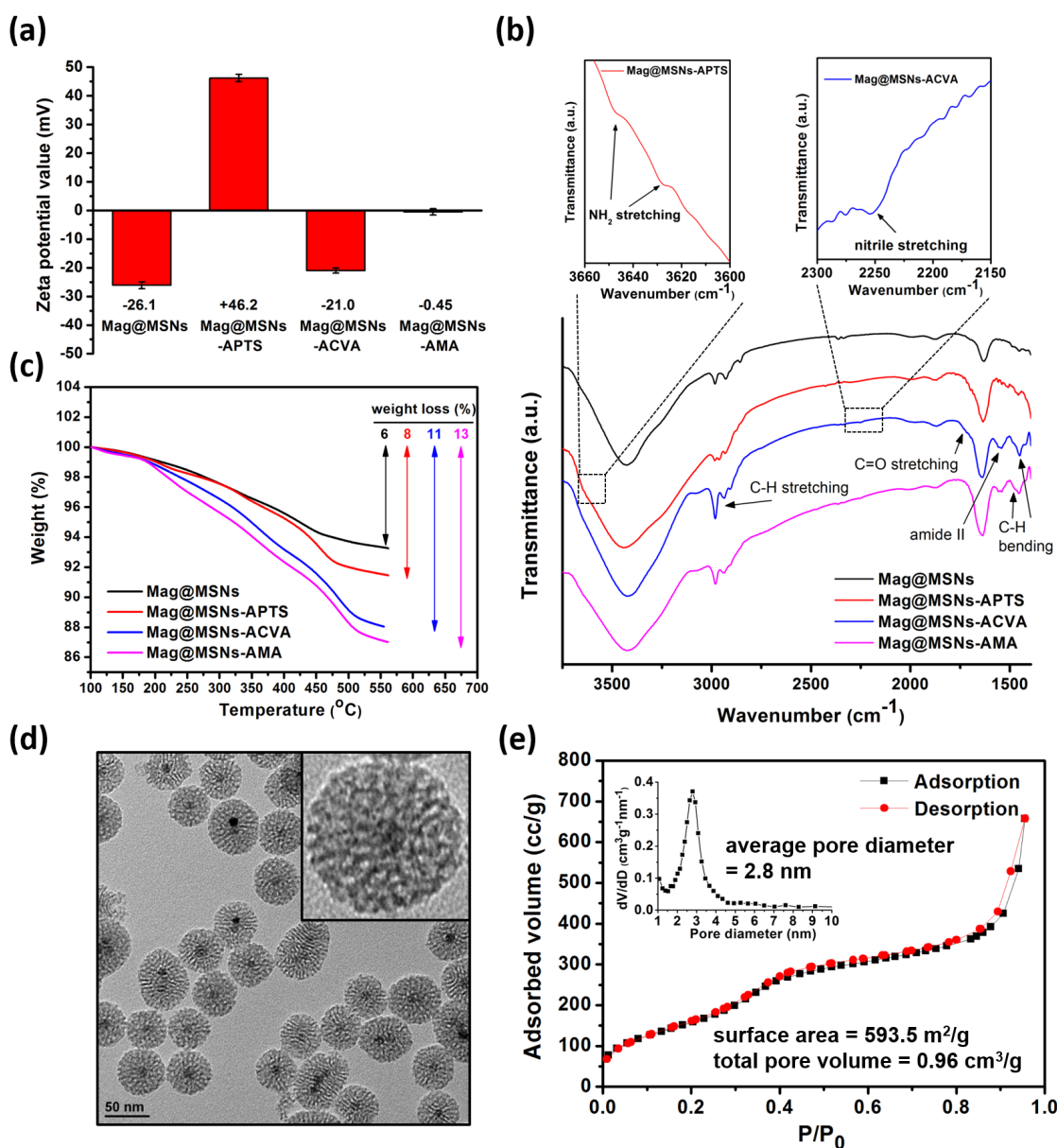


**Figure 3.8.** (a) Zeta potential values, (b) Fourier transform infrared spectroscopy (FT-IR), and (c) thermogravimetric analysis (TGA) of Mag@MSNs, Mag@MSNs-APTS, Mag@MSNs-ACVA, and Mag@MSNs-AMA, respectively. (d) TEM image of Mag@MSNs-AMA. Inset shows the enlarged Mag@MSNs-AMA. (e) N<sub>2</sub> adsorption/desorption isotherms of Mag@MSNs-AMA at 77 K. Inset shows the pore diameter distribution of Mag@MSNs-AMA. The BET surface area, pore volume, and average pore diameter are 593.5  $\text{m}^2/\text{g}$ , 0.96  $\text{cm}^3/\text{g}$ , and 2.8 nm, respectively.

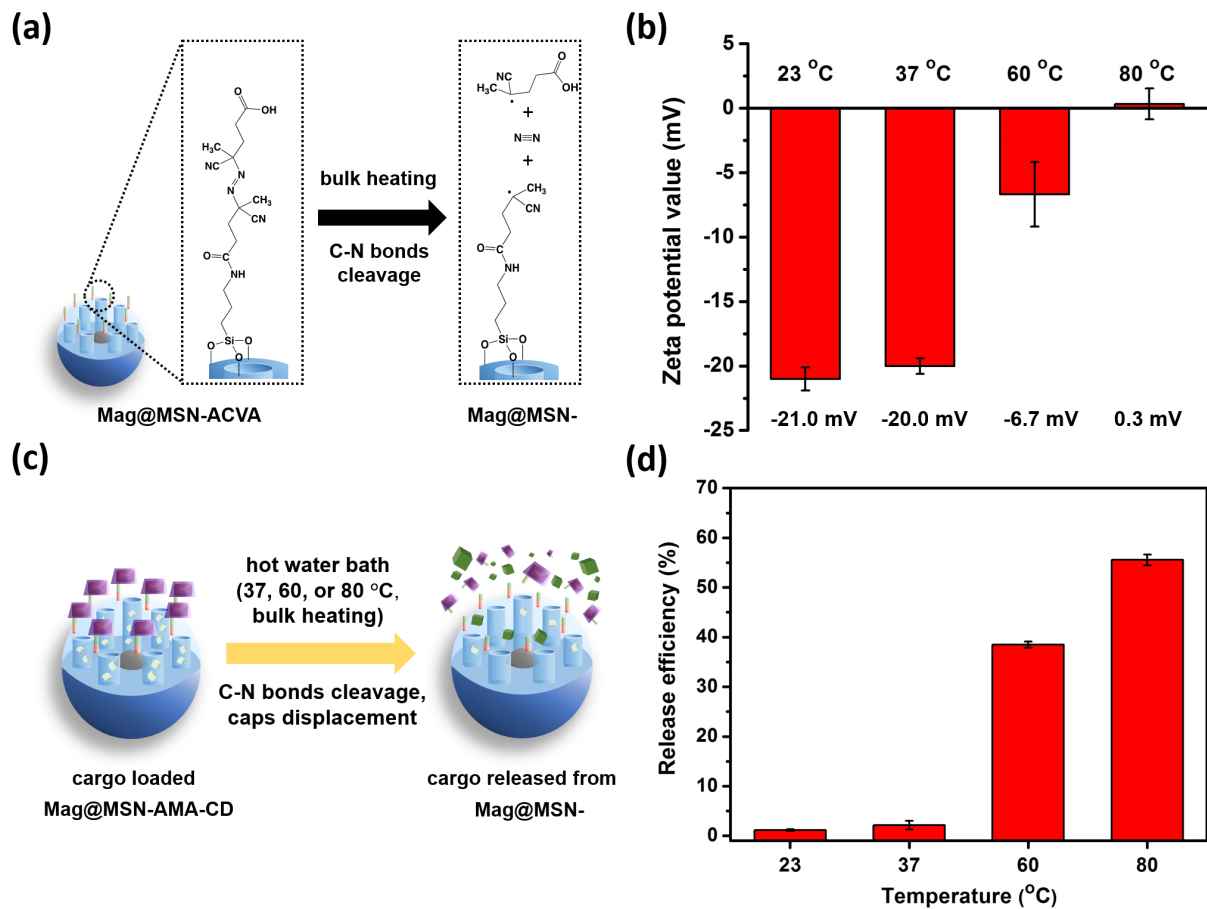


**Figure 3.9.** (a) The cleavage of C-N bonds caused by bulk heating for 10 min. (b) Zeta potential values of Mag@MSNs-ACVA after 10 min of bulk heating in D.I. water. The concentration of Mag@MSNs-ACVA in D.I. water is 0.5 mg/mL. (c) The release of fluorescein from Mag@MSN- caused by bulk heating trigger in water bath at 37 °C, 60 °C, or 80 °C. The sample stayed at room temperature (23 °C) was also recorded as a control. (d) Release efficiency of fluorescein from Mag@MSNs- after the bulk heating at 23 °C, 37 °C, 60 °C, or 80 °C trigger for 10 min (N = 3).

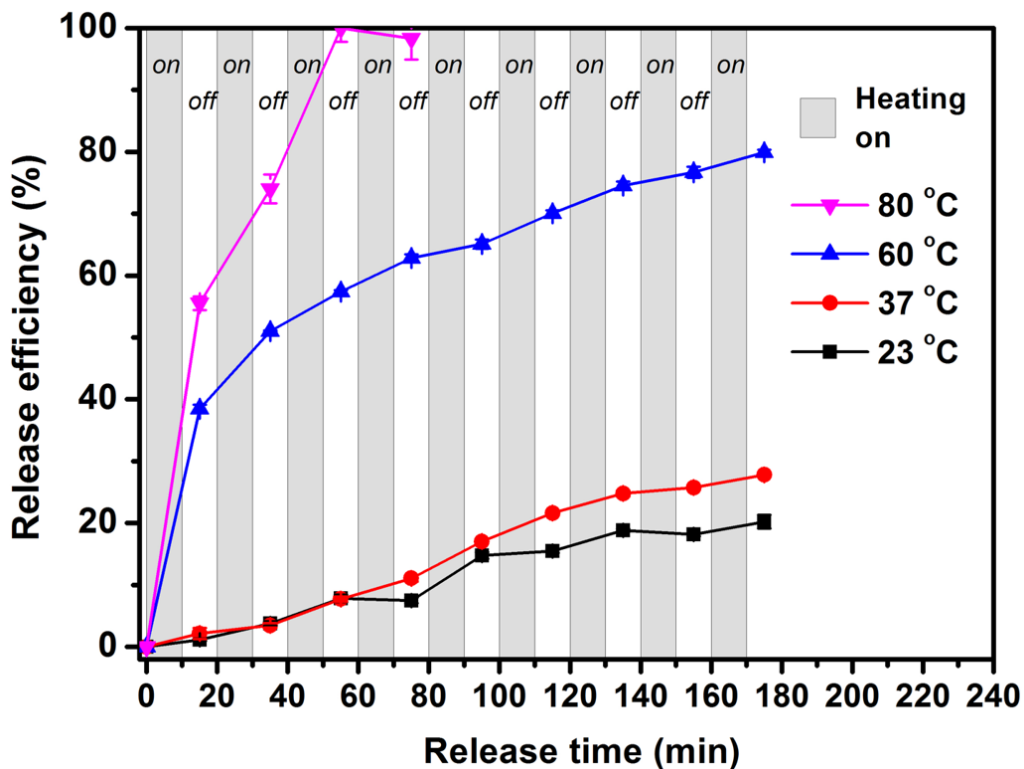


**Figure 3.10.** Time dependent release efficiency of fluorescein from Mag@MSN- caused by bulk heating trigger in water bath at 37 °C, 60 °C, and 80 °C. The sample stayed at room temperature (23 °C) was also recorded as a control.

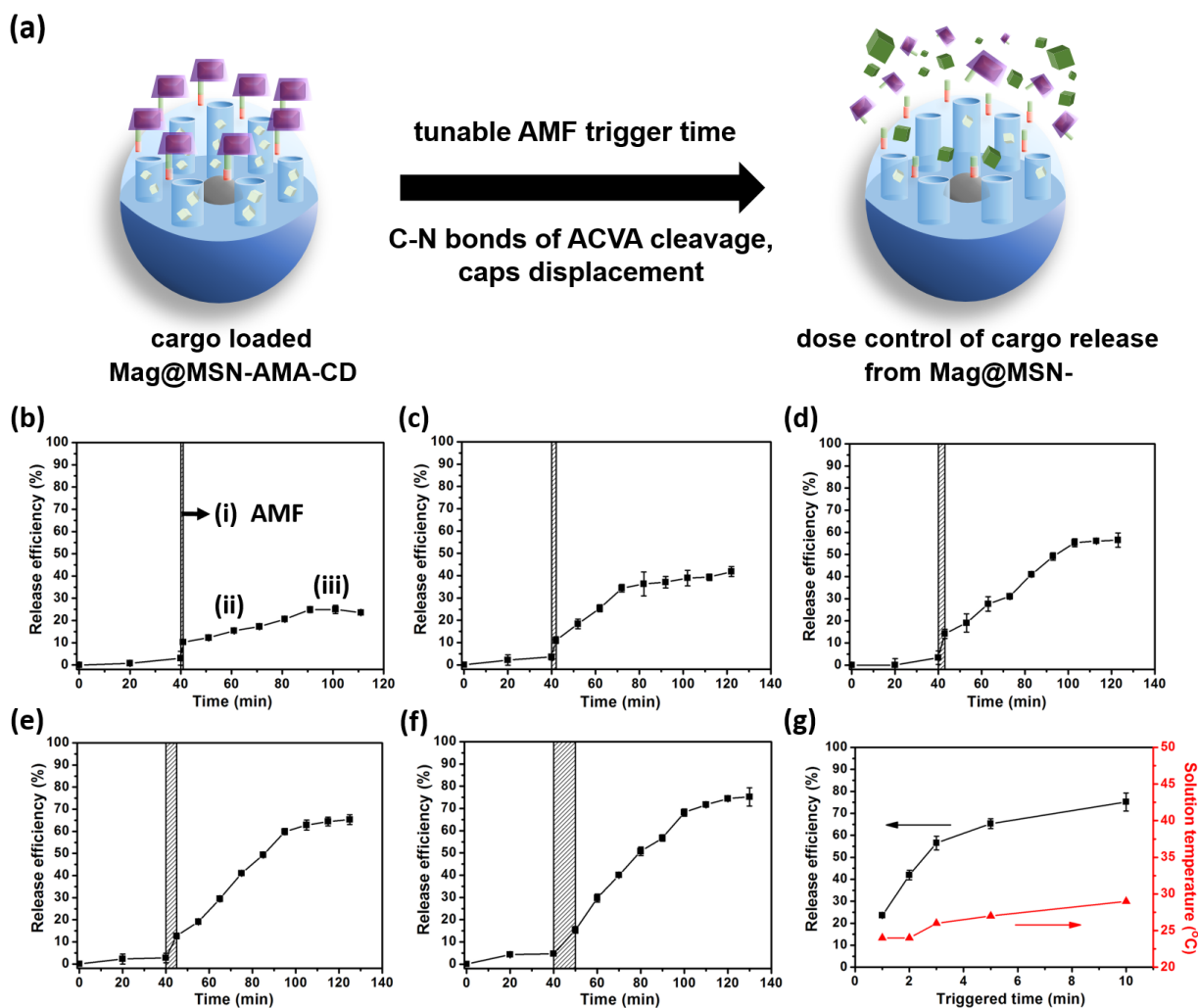


**Figure 3.11.** (a) Dose control of cargo release from Mag@MSNs- by adjusting the AMF “ON” time. Time-dependent release profile of fluorescein from Mag@MSNs- through magnetic actuation under AMF for (b) 1, (c) 2, (d) 3, (e) 5, and (f) 10 min, respectively. (g) The release efficiency of fluorescein at plateau and the solution temperature after the various time periods of trigger under AMF (N = 3).

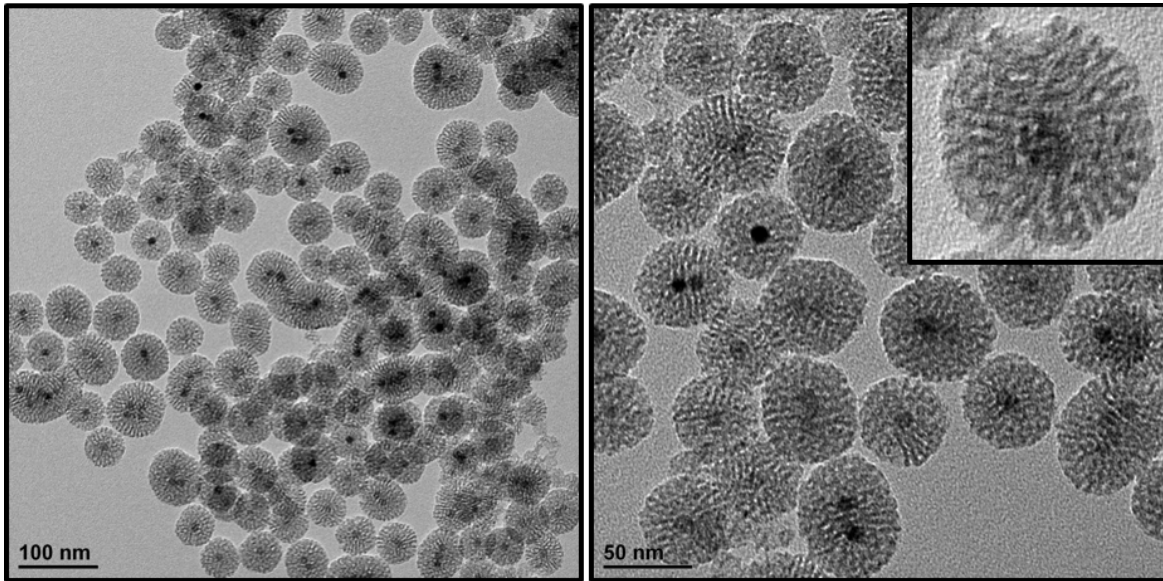


**Figure 3.12.** TEM images of fluorescein-loaded Mag@MSN-AMA-CD after 10 min exposure of the AMF trigger.

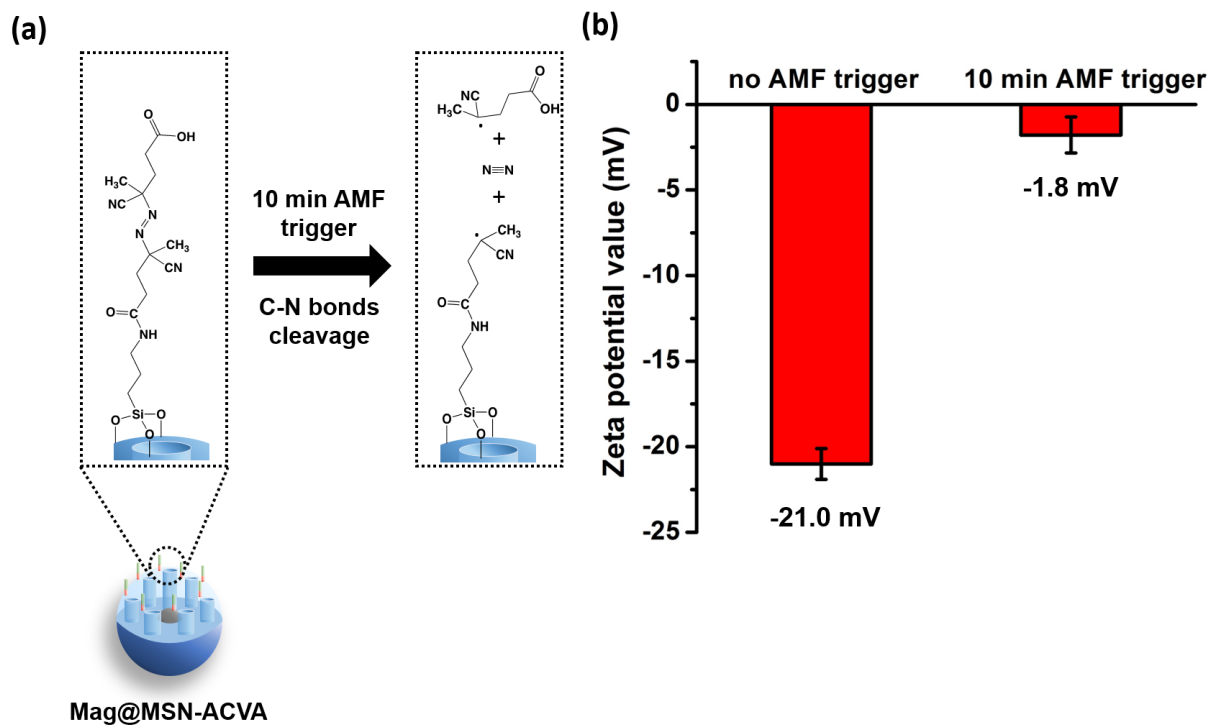


**Figure 3.13.** (a) The cleavage of C-N bonds caused by 10 min of AMF trigger. (b) Zeta potential values of Mag@MSNs-ACVA before and after 10 min of AMF trigger in D.I. water. The concentration of Mag@MSNs-ACVA in D.I. water is 0.5 mg/mL.



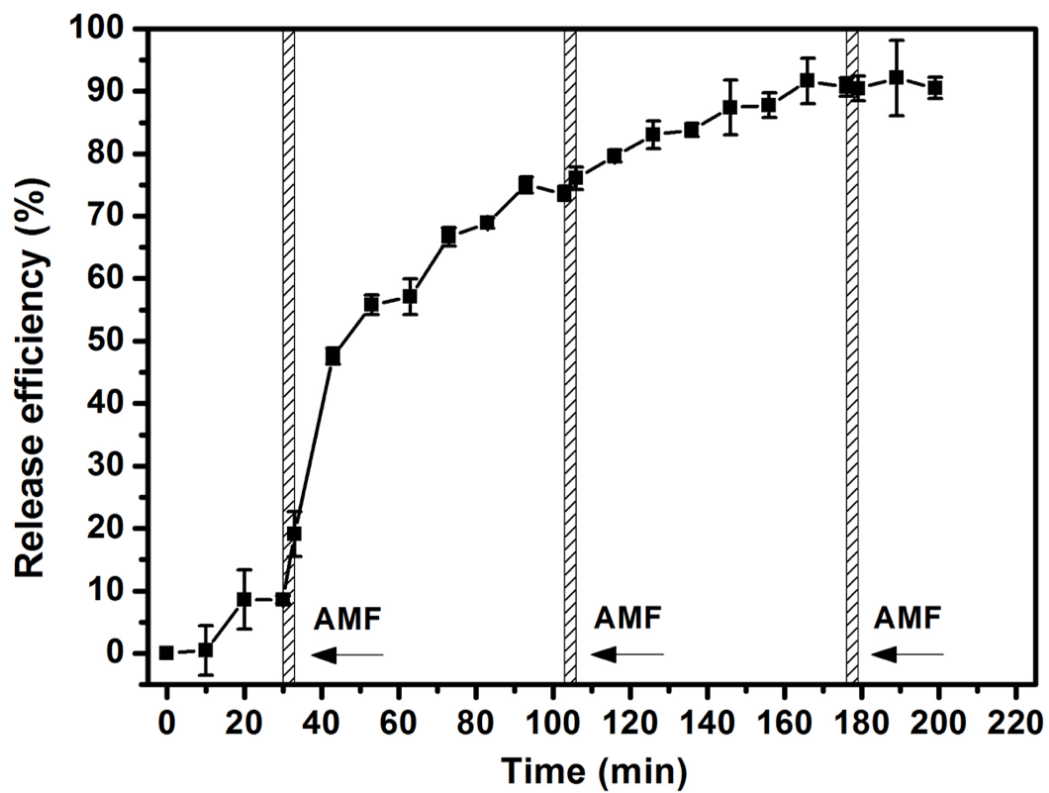


**Figure 3.14.** Time dependent release profile of fluorescein from Mag@MSNs- through magnetic actuation under AMF for 3 min for 3 cycles (N = 3). The temperature of the solution right after each exposure was measured to be 26 °C, 3 degrees higher than that before each AMF exposure.

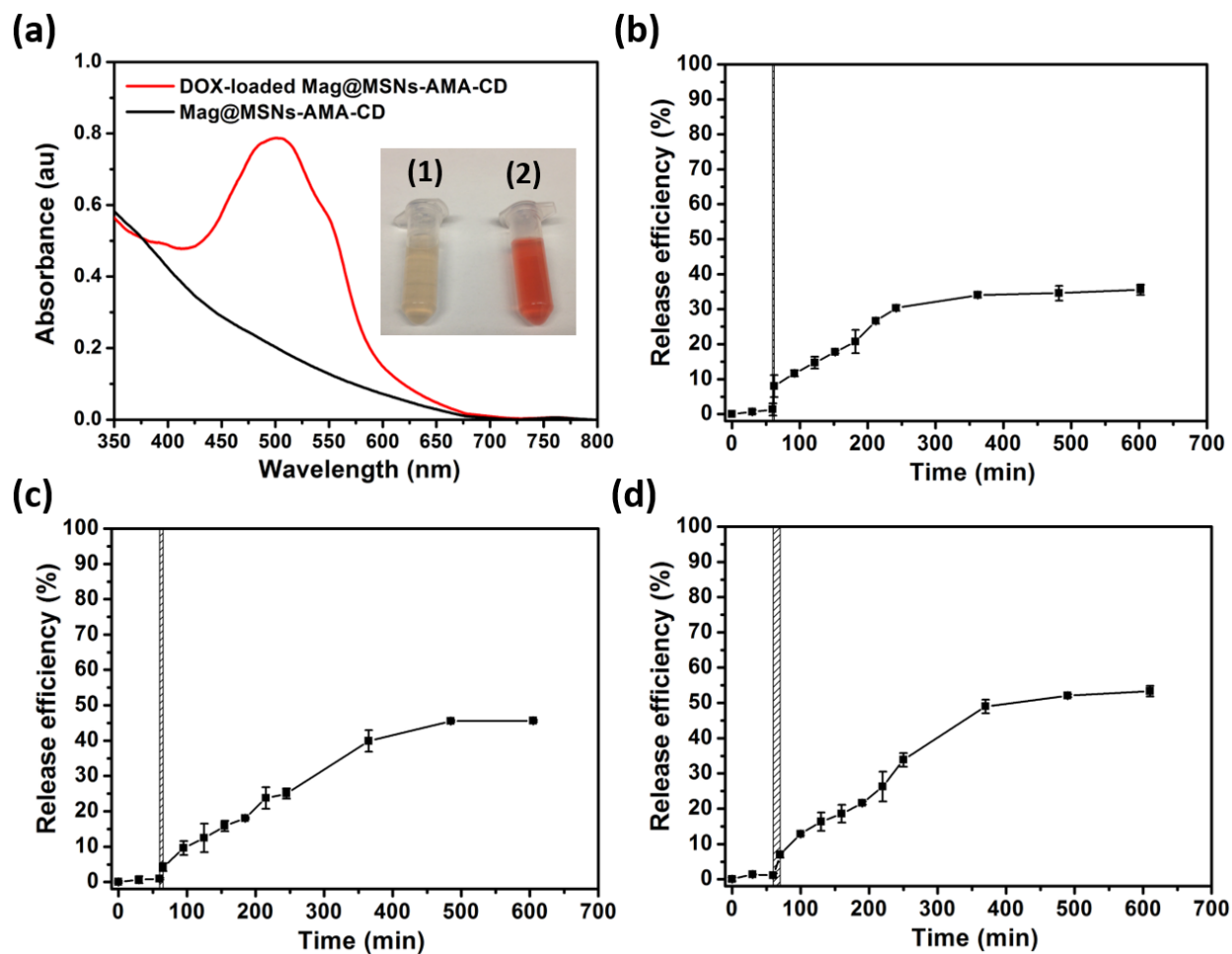


**Figure 3.15.** (a) UV-Vis spectra of Mag@MSNs-AMA-CD and DOX-loaded Mag@MSNs-AMA-CD in PBS. Inset shows the photograph of tubes containing (1) Mag@MSNs-AMA-CD and (2) DOX-loaded Mag@MSNs-AMA-CD in PBS. Time-dependent release profile of DOX from Mag@MSNs- in PBS through magnetic actuation under AMF for (b) 2, (c) 5, and (d) 10 min, respectively (N=3). The concentration of DOX-loaded Mag@MSNs-AMA-CD in PBS for each release study was 0.5 mg/mL.

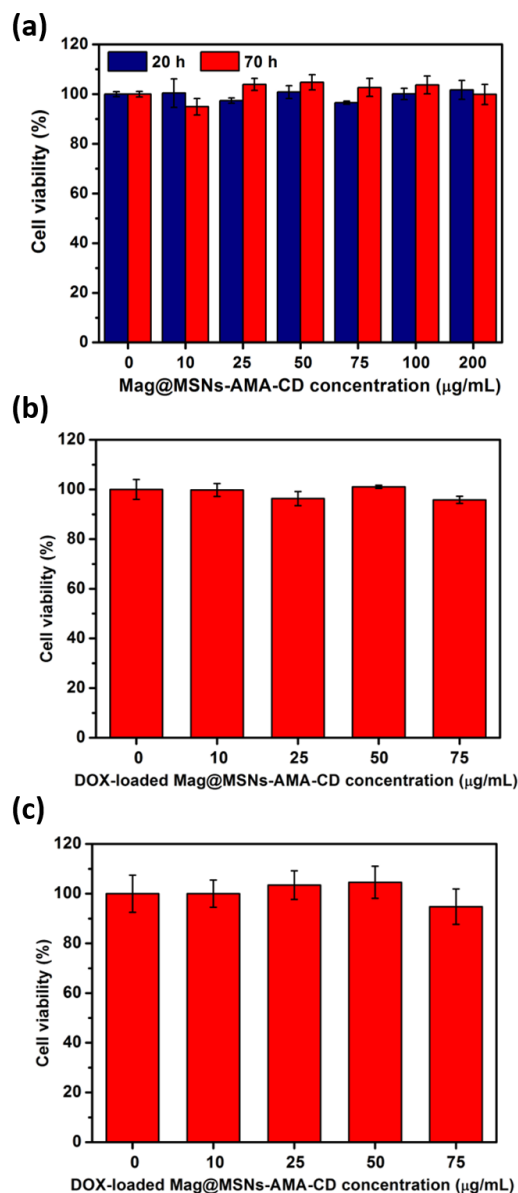


**Figure 3.16.** (a) Cytotoxicity of Mag@MSNs-AMA-CD. PANC-1 was incubated with Mag@MSNs-AMA-CD at various nanoparticle concentrations for 20 and 70 h, and the viability was determined by a CCK-8 assay and normalized to the control without Mag@MSNs-AMA-CD treatment. Data are means  $\pm$  SD of three independent experiments. (b) Cytotoxicity of DOX-loaded Mag@MSNs-AMA-CD. PANC-1 was incubated with DOX-loaded Mag@MSNs-AMA-CD at various concentrations for 4 h. The viability was determined by a CCK-8 assay and normalized to the control without DOX-loaded Mag@MSNs-AMA-CD nanoparticle treatment. Data are means  $\pm$  SD of three independent experiments. (c) After the 4 h treatment of DOX-loaded Mag@MSNs-AMA-CD, cells were allowed to grow in the regular culture medium for 12 h, and the viability was determined by a CCK-8 assay and normalized to the control without DOX-loaded Mag@MSNs-AMA-CD treatment. Data are means  $\pm$  SD of three independent experiments.

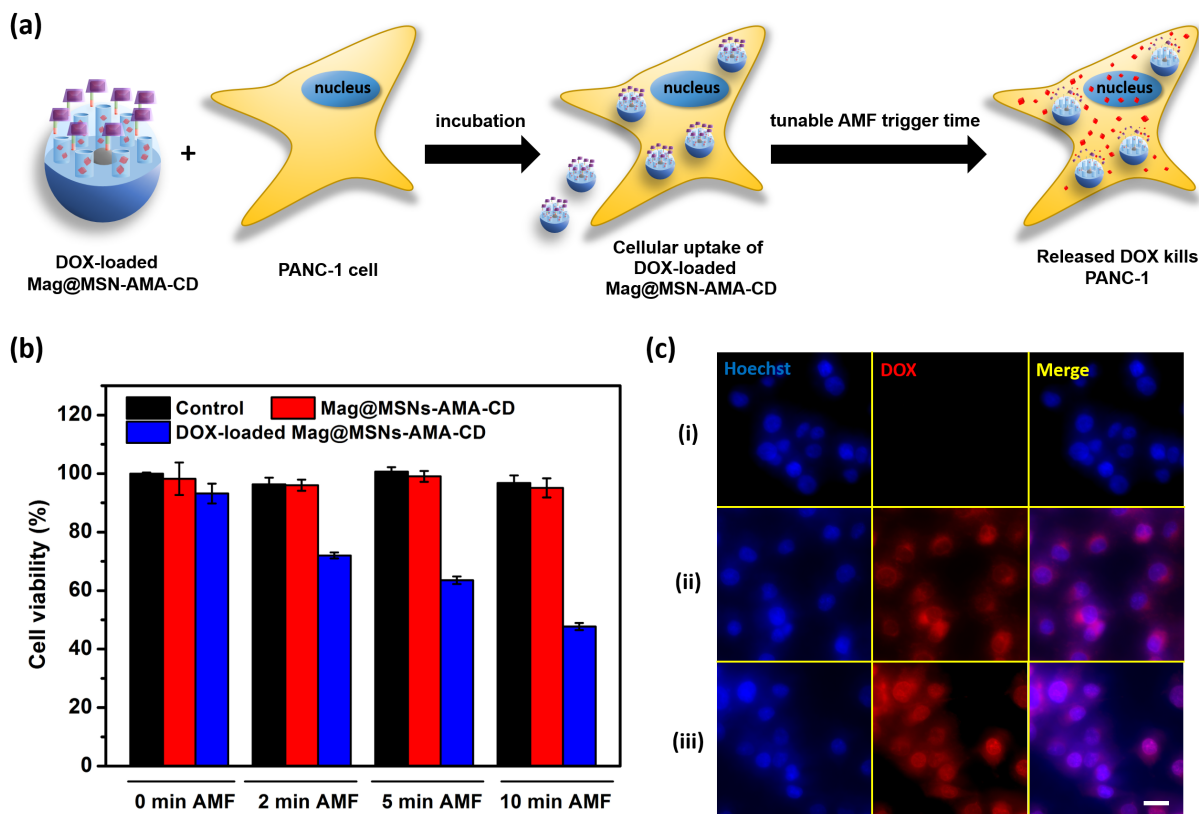


**Figure 3.17.** (a) *In vitro* cellular killing effect of DOX-loaded Mag@MSNs-AMA-CD after AMF exposure. PANC-1 cells were treated with DOX-loaded Mag@MSNs-AMA-CD followed by various lengths of AMF exposure. (b) The viability of PANC-1 after treatment by Mag@MSNs-AMA-CD, or DOX-loaded Mag@MSNs-AMA-CD. The control is cells without treatment by nanoparticles. The cells were treated for 4 h at a concentration of 50  $\mu\text{g}/\text{mL}$  followed by 2, 5, or 10 min of AMF exposure. The cells were allowed to grow in the regular culture medium for 12 h, and the viability was determined by a CCK-8 assay. Data are means  $\pm$  SD of four independent experiments. The viable cells in each sample were determined by the absorbance at 450 nm and 650 nm (as a reference). (c) Fluorescence microscope images of PANC-1 cells (ii) after 4 h treatment by DOX-loaded Mag@MSNs-AMA-CD, and (iii) after 4 h incubation with DOX-loaded Mag@MSNs-AMA-CD followed by 10 min of AMF exposure. The control group (i) is cells without the treatment by nanoparticles. Panels from left to right: cells of PANC-1 with the blue-emitting nucleus stained by Hoechst 33342; red emission from DOX; and the merged images. Scale bar is 20  $\mu\text{m}$ .

### 3.16 References

- (1) Collins, F. S.; Varmus, H. A New Initiative on Precision Medicine. *N. Engl. J. Med.* **2015**, *372*, 793–795.
- (2) Peck, R. W. Precision Medicine Is Not Just Genomics: The Right Dose for Every Patient. *Annu. Rev. Pharmacol. Toxicol.* **2018**, *58*, 105–122.
- (3) Li, Z.; Clemens, D. L.; Lee, B. Y.; Dillon, B. J.; Horwitz, M. A.; Zink, J. I. Mesoporous Silica Nanoparticles with pH-Sensitive Nanovalves for Delivery of Moxifloxacin Provide Improved Treatment of Lethal Pneumonic Tularemia. *ACS Nano* **2015**, *9*, 10778–10789.
- (4) Felber, A. E.; Dufresne, M. H.; Leroux, J. C. pH-Sensitive Vesicles, Polymeric Micelles, and Nanospheres Prepared with Polycarboxylates. *Adv. Drug Deliv. Rev.* **2012**, *64*, 979–992.
- (5) Liu, J.; Huang, Y.; Kumar, A.; Tan, A.; Jin, S.; Mozhi, A.; Liang, X. J. pH-Sensitive Nano-Systems for Drug Delivery in Cancer Therapy. *Biotechnol. Adv.* **2014**, *32*, 693–710.
- (6) Gao, W.; Chan, J.; Farokhzad, O. C. pH-Responsive Nanoparticles for Drug Delivery. *Mol. Pharm.* **2010**, *7*, 1913–1920.
- (7) Lee, B. Y.; Li, Z.; Clemens, D. L.; Dillon, B. J.; Hwang, A. A.; Zink, J. I.; Horwitz, M. A. Redox-Triggered Release of Moxifloxacin from Mesoporous Silica Nanoparticles Functionalized with Disulfide Snap-Tops Enhances Efficacy Against Pneumonic Tularemia in Mice. *Small* **2016**, *12*, 3690–3702.
- (8) Remant, R. B.; Chandrashekar, V.; Cheng, B.; Chen, H.; Peña, M. M. O.; Zhang, J.; Montgomery, J.; Xu, P. Redox Potential Ultrasensitive Nanoparticle for the Targeted Delivery of Camptothecin to HER2-Positive Cancer Cells. *Mol. Pharm.* **2014**, *11*, 1897–1905.
- (9) Renoux, B.; Raes, F.; Legigan, T.; Péraudeau, E.; Eddhif, B.; Poinot, P.; Tranoy-Opalinski, I.; Alsarraf, J.; Koniev, O.; Kolodych, S.; Lerondel, S.; Le Pape, A.; Clarhaut, J.; Papot, S. Targeting the Tumour Microenvironment with an Enzyme-Responsive Drug Delivery System for the Efficient Therapy of Breast and Pancreatic Cancers. *Chem. Sci.* **2017**, *8*, 3427–3433.
- (10) Ruehle, B.; Clemens, D. L.; Lee, B.-Y.; Horwitz, M. A.; Zink, J. I. A Pathogen-Specific Cargo Delivery Platform Based on Mesoporous Silica Nanoparticles. *J. Am. Chem. Soc.* **2017**, *139*, 6663–6668.
- (11) Mo, R.; Jiang, T.; Disanto, R.; Tai, W.; Gu, Z. ATP-Triggered Anticancer Drug Delivery. *Nat. Commun.* **2014**, *5*, 3364.
- (12) Li, H.; Tan, L. L.; Jia, P.; Li, Q. L.; Sun, Y. L.; Zhang, J.; Ning, Y. Q.; Yu, J.; Yang, Y. W. Near-Infrared Light-Responsive Supramolecular Nanovalve Based on Mesoporous Silica-Coated Gold Nanorods. *Chem. Sci.* **2014**, *5*, 2804–2808.
- (13) Guardado-Alvarez, T. M.; Sudha Devi, L.; Russell, M. M.; Schwartz, B. J.; Zink, J. I. Activation of Snap-Top Capped Mesoporous Silica Nanocontainers Using Two Near-Infrared Photons. *J. Am.*

- Chem. Soc.* **2013**, *135*, 14000–14003.
- (14) Tarn, D.; Ferris, D. P.; Barnes, J. C.; Ambrogio, M. W.; Stoddart, J. F.; Zink, J. I. A Reversible Light-Operated Nanovalve on Mesoporous Silica Nanoparticles. *Nanoscale* **2014**, *6*, 3335–3343.
- (15) Qiu, M.; Wang, D.; Liang, W.; Liu, L.; Zhang, Y.; Chen, X.; Sang, D. K.; Xing, C.; Li, Z.; Dong, B.; Xing, F.; Fan, D.; Bao, S.; Zhang, H.; Cao, Y. Novel Concept of the Smart NIR-Light-Controlled Drug Release of Black Phosphorus Nanostructure for Cancer Therapy. *Proc. Natl. Acad. Sci. USA* **2018**, *115*, 501–506.
- (16) Rühle, B.; Datz, S.; Argyo, C.; Bein, T.; Zink, J. I. A Molecular Nanocap Activated by Superparamagnetic Heating for Externally Stimulated Cargo Release. *Chem. Commun.* **2016**, *52*, 1843–1846.
- (17) Saint-Cricq, P.; Deshayes, S.; Zink, J. I.; Kasko, A. M. Magnetic Field Activated Drug Delivery Using Thermodegradable Azo-Functionalised PEG-Coated Core-Shell Mesoporous Silica Nanoparticles. *Nanoscale* **2015**, *7*, 13168–13172.
- (18) Thomas, C. R.; Ferris, D. P.; Lee, J.; Choi, E.; Cho, M. H.; Kim, E. S.; Stoddart, J. F.; Shin, J.; Cheon, J.; Zink, J. I. Noninvasive Remote Controlled Release of Drug Molecules *in Vitro* Using Magnetic Actuation of Mechanised Nanoparticles. *J. Am. Chem. Soc.* **2010**, *132*, 10623–10625.
- (19) Zhu, Y.; Tao, C. DNA-Capped Fe<sub>3</sub>O<sub>4</sub>/SiO<sub>2</sub> Magnetic Mesoporous Silica Nanoparticles for Potential Controlled Drug Release and Hyperthermia. *RSC Adv.* **2015**, *5*, 22365–22372.
- (20) Ruiz-Hernández, E.; Baeza, A.; Vallet-Regí, M. Smart Drug Delivery through DNA/Magnetic Nanoparticle Gates. *ACS Nano* **2011**, *5*, 1259–1266.
- (21) Baeza, A.; Guisasola, E.; Ruiz-Hernández, E.; Vallet-Regí, M. Magnetically Triggered Multidrug Release by Rybrid Mesoporous Silica Nanoparticles. *Chem. Mater.* **2012**, *24*, 517–524.
- (22) Guisasola, E.; Asín, L.; Beola, L.; De La Fuente, J. M.; Baeza, A.; Vallet Regí, M. Beyond Traditional Hyperthermia. *In Vivo* Cancer Treatment with Magnetic-Responsive Mesoporous Silica Nanocarriers. *ACS Appl. Mater. Interfaces* **2018**, *10*, 12518–12525.
- (23) Guo, W.; Yang, C.; Lin, H.; Qu, F. P(EO-Co-LLA) Functionalized Fe<sub>3</sub>O<sub>4</sub>@mSiO<sub>2</sub> Nanocomposites for Thermo/pH Responsive Drug Controlled Release and Hyperthermia. *Dalton Trans.* **2014**, *43*, 18056–18065.
- (24) Paris, J. L.; Cabanas, M. V.; Manzano, M.; Vallet-Regí, M. Polymer-Grafted Mesoporous Silica Nanoparticles as Ultrasound-Responsive Drug Carriers. *ACS Nano* **2015**, *9*, 11023–11033.
- (25) De Smet, M.; Heijman, E.; Langereis, S.; Hijnen, N. M.; Grüll, H. Magnetic Resonance Imaging of High Intensity Focused Ultrasound Mediated Drug Delivery from Temperature-Sensitive Liposomes: An *in Vivo* Proof-of-Concept Study. *J. Control. Release* **2011**, *150*, 102–110.
- (26) Peck, R. W. The Right Dose for Every Patient: A Key Step for Precision Medicine. *Nat. Rev. Drug Discov.* **2016**, *15*, 145–146.
- (27) Tucker, G. T. Personalized Drug Dosage – Closing the Loop. *Pharm. Res.* **2017**, *34*, 1539–1543.

- (28) Hawcutt, D. B.; Cooney, L.; Oni, L.; Pirmohamed, M. Precision Dosing in Children. *Expert Rev. Precis. Med. Drug Dev.* **2016**, *1*, 69–78.
- (29) Gonzalez, D.; Rao, G. G.; Bailey, S. C.; Brouwer, K. L. R.; Cao, Y.; Crona, D. J.; Kashuba, A. D. M.; Lee, C. R.; Morbitzer, K.; Patterson, J. H.; Wiltshire, T.; Easter, J.; Savage, S. W.; Powell, J. R. Precision Dosing: Public Health Need, Proposed Framework, and Anticipated Impact. *Clin. Transl. Sci.* **2017**, *10*, 443–454.
- (30) Wicki, A.; Witzigmann, D.; Balasubramanian, V.; Huwyler, J. Nanomedicine in Cancer Therapy: Challenges, Opportunities, and Clinical Applications. *J. Control. Release* **2015**, *200*, 138–157.
- (31) Hegyi, G.; Szigeti, G. P.; Szász, A. Hyperthermia *versus* Oncothermia: Cellular Effects in Complementary Cancer Therapy. *Evid. Based Complement. Alternat. Med.* **2013**, *2013*, 672873.
- (32) Hegewisch-Becker, S.; Braun, K.; Otte, M.; Corovic, A.; Atanackovic, D.; Nierhaus, A.; Hossfeld, D. K.; Pantel, K. Effects of Whole Body Hyperthermia (41.8 Degrees C) on the Frequency of Tumor Cells in the Peripheral Blood of Patients with Advanced Malignancies. *Clin. Cancer Res.* **2003**, *9*, 2079–2084.
- (33) Dickson, J. A.; Ellis, H. A. Stimulation of Tumour Cell Dissemination by Raised Temperature (42°C) in Rats with Transplanted Yoshida Tumours. *Nature* **1974**, *248*, 354–358.
- (34) Lord, P. F.; Kapp, D. S.; Morrow, D. Increased Skeletal Metastases of Spontaneous Canine Osteosarcoma after Fractionated Systemic Hyperthermia and Local X-Irradiation. *Cancer Res.* **1981**, *41*, 4331–4334.
- (35) Urano, M.; Epstein, R.; Rice, L.; Suit, H. D.; Chu, A. M. Effect of Whole-Body Hyperthermia on Cell Survival, Metastasis Frequency, and Host Immunity in Moderately and Weakly Immunogenic Murine Tumors. *Cancer Res.* **1983**, *43*, 1039–1043.
- (36) Klibanov, A. L.; Hossack, J. A. Ultrasound in Radiology: From Anatomic, Functional, Molecular Imaging to Drug Delivery and Image-Guided Therapy. *Invest. Radiol.* **2015**, *50*, 657–670.
- (37) Chen, W.; Lu, F.; Chen, C. C. V.; Mo, K. C.; Hung, Y.; Guo, Z. X.; Lin, C. H.; Lin, M. H.; Lin, Y. H.; Chang, C.; Mou, C. Y. Manganese-Enhanced MRI of Rat Brain Based on Slow Cerebral Delivery of Manganese(II) with Silica-Encapsulated Mn<sub>x</sub>Fe<sub>1-x</sub>O Nanoparticles. *NMR Biomed.* **2013**, *26*, 1176–1185.
- (38) Wu, S. H.; Lin, C. Y.; Hung, Y.; Chen, W.; Chang, C.; Mou, C. Y. PEGylated Silica Nanoparticles Encapsulating Multiple Magnetite Nanocrystals for High-Performance Microscopic Magnetic Resonance Angiography. *J. Biomed. Mater. Res. B.* **2011**, *99 B*, 81–88.
- (39) Lee, J. H.; Jang, J. T.; Choi, J. S.; Moon, S. H.; Noh, S. H.; Kim, J. W.; Kim, J. G.; Kim, I. S.; Park, K. I.; Cheon, J. Exchange-Coupled Magnetic Nanoparticles for Efficient Heat Induction. *Nat. Nanotechnol.* **2011**, *6*, 418–422.
- (40) Kumar, C. S. S. R.; Mohammad, F. Magnetic Nanomaterials for Hyperthermia-Based Therapy and Controlled Drug Delivery. *Adv. Drug Deliv. Rev.* **2011**, *63*, 789–808.

- (41) Thomas, C. R.; Ferris, D. P.; Lee, J. H.; Choi, E.; Cho, M. H.; Kim, E. S.; Stoddart, J. F.; Shin, J. S.; Cheon, J.; Zink, J. I. Noninvasive Remote-Controlled Release of Drug Molecules *in Vitro* Using Magnetic Actuation of Mechanized Nanoparticles. *J. Am. Chem. Soc.* **2010**, *132*, 10623–10625.
- (42) Guisasola, E.; Baeza, A.; Talelli, M.; Arcos, D. Magnetic-Responsive Release Controlled by Hot Spot Effect. *Langmuir* **2015**, *31*, 12777–12782.
- (43) Riedinger, A.; Guardia, P.; Curcio, A.; Garcia, M. A.; Cingolani, R.; Manna, L.; Pellegrino, T. Subnanometer Local Temperature Probing and Remotely Controlled Drug Release Based on Azo-Functionalized Iron Oxide Nanoparticles. *Nano Lett.* **2013**, *13*, 2399–2406.
- (44) Cazares-Cortes, E.; Espinosa, A.; Guigner, J. M.; Michel, A.; Griffete, N.; Wilhelm, C.; Ménager, C. Doxorubicin Intracellular Remote Release from Biocompatible Oligo(Ethylene Glycol) Methyl Ether Methacrylate-Based Magnetic Nanogels Triggered by Magnetic Hyperthermia. *ACS Appl. Mater. Interfaces* **2017**, *9*, 25775–25788.
- (45) Lee, J. H.; Chen, K. J.; Noh, S. H.; Garcia, M. A.; Wang, H.; Lin, W. Y.; Jeong, H.; Kong, B. J.; Stout, D. B.; Cheon, J.; Tseng, H. R. On-Demand Drug Release System for *in Vivo* Cancer Treatment through Self-Assembled Magnetic Nanoparticles. *Angew. Chem. Int. Ed.* **2013**, *52*, 4384–4388.
- (46) Noh, S. hyun; Moon, S. H.; Shin, T. H.; Lim, Y.; Cheon, J. Recent Advances of Magneto-Thermal Capabilities of Nanoparticles: From Design Principles to Biomedical Applications. *Nano Today* **2017**, *13*, 61–76.
- (47) Lee, N.; Yoo, D.; Ling, D.; Cho, M. H.; Hyeon, T.; Cheon, J. Iron Oxide Based Nanoparticles for Multimodal Imaging and Magneto-responsive Therapy. *Chem. Rev.* **2015**, *115*, 10637–10689.
- (48) Estelrich, J.; Escribano, E.; Queralt, J.; Busquets, M. A. Iron Oxide Nanoparticles for Magnetically-Guided and Magnetically-Responsive Drug Delivery. *Int. J. Mol. Sci.* **2015**, *16*, 8070–8101.
- (49) Mertz, D.; Sandre, O.; Bégin-Colin, S. Drug Releasing Nanoplatfoms Activated by Alternating Magnetic Fields. *Biochimica et Biophysica Acta* **2017**, *1861*, 1617–1641.
- (50) Gao, X.; Cui, Y.; Levenson, R. M.; Chung, L. W. K.; Nie, S. *In Vivo* Cancer Targeting and Imaging with Semiconductor Quantum Dots. *Nat. Biotechnol.* **2004**, *22*, 969–976.
- (51) Chopra, R.; Shaikh, S.; Chatzinoff, Y.; Munaweera, I.; Cheng, B.; Daly, S. M.; Xi, Y.; Bing, C.; Burns, D.; Greenberg, D. E. Employing High-Frequency Alternating Magnetic Fields for the Non-Invasive Treatment of Prosthetic Joint Infections. *Sci. Rep.* **2017**, *7*, 7520.
- (52) Schuerle, S.; Dudani, J. S.; Christiansen, M. G.; Anikeeva, P.; Bhatia, S. N. Magnetically Actuated Protease Sensors for *in Vivo* Tumor Profiling. *Nano Lett.* **2016**, *16*, 6303–6310.
- (53) Song, C. W. Effect of Local Hyperthermia on Blood Flow and Microenvironment: A Review. *Cancer Res.* **1984**, *44*, 4721–4730.
- (54) Ulbrich, K.; Holá, K.; Šubr, V.; Bakandritsos, A.; Tuček, J.; Zbořil, R. Targeted Drug Delivery with Polymers and Magnetic Nanoparticles: Covalent and Noncovalent Approaches, Release Control, and Clinical Studies. *Chem. Rev.* **2016**, *116*, 5338–5431.



- (55) Landarani-Isfahani, A.; Moghadam, M.; Mohammadi, S.; Royvaran, M.; Moshtael-Arani, N.; Rezaei, S.; Tangestaninejad, S.; Mirkhani, V.; Mohammadpoor-Baltork, I. Elegant pH-Responsive Nanovehicle for Drug Delivery Based on Triazine Dendrimer Modified Magnetic Nanoparticles. *Langmuir* **2017**, *33*, 8503–8515.
- (56) Chang, Y.; Liu, N.; Chen, L.; Meng, X.; Liu, Y.; Li, Y.; Wang, J. Synthesis and Characterization of DOX-Conjugated Dendrimer-Modified Magnetic Iron Oxide Conjugates for Magnetic Resonance Imaging, Targeting, and Drug Delivery. *J. Mater. Chem.* **2012**, *22*, 9594–9601.
- (57) Chen, Y.; Bose, A.; Bothun, G. D. Controlled Release from Bilayer-Decorated Magnetoliposomes via Electromagnetic Heating. *ACS Nano* **2010**, *4*, 3215–3221.
- (58) Tarn, D.; Ashley, C. E.; Xue, M.; Carnes, E. C.; Zink, J. I.; Brinker, C. J. Mesoporous Silica Nanoparticle Nanocarriers: Biofunctionality and Biocompatibility. *Acc. Chem. Res.* **2013**, *46*, 792–801.
- (59) Argyo, C.; Weiss, V.; Bräuchle, C.; Bein, T. Multifunctional Mesoporous Silica Nanoparticles as a Universal Platform for Drug Delivery. *Chem. Mater.* **2014**, *26*, 435–451.
- (60) Wu, S. H.; Mou, C. Y.; Lin, H. P. Synthesis of Mesoporous Silica Nanoparticles. *Chem. Soc. Rev.* **2013**, *42*, 3862–3875.
- (61) Guardado-Alvarez, T. M.; Chen, W.; Norton, A. E.; Russell, M. M.; Connick, W. B.; Zink, J. I. Analyte-Responsive Gated Hollow Mesoporous Silica Nanoparticles Exhibiting Inverse Functionality and an AND Logic Response. *Nanoscale* **2016**, *8*, 18296–18300.
- (62) Chen, W.; Tsai, P. H.; Hung, Y.; Chiou, S. H.; Mou, C. Y. Nonviral Cell Labeling and Differentiation Agent for Induced Pluripotent Stem Cells Based on Mesoporous Silica Nanoparticles. *ACS Nano* **2013**, *7*, 8423–8440.
- (63) Meng, H.; Wang, M.; Liu, H.; Liu, X.; Situ, A.; Wu, B.; Ji, Z.; Chang, C. H.; Nel, A. E. Use of a Lipid-Coated Mesoporous Silica Nanoparticle Platform for Synergistic Gemcitabine and Paclitaxel Delivery to Human Pancreatic Cancer in Mice. *ACS Nano* **2015**, *9*, 3540–3557.
- (64) Liu, X.; Situ, A.; Kang, Y.; Villabroza, K. R.; Liao, Y.; Chang, C. H.; Donahue, T.; Nel, A. E.; Meng, H. Irinotecan Delivery by Lipid-Coated Mesoporous Silica Nanoparticles Shows Improved Efficacy and Safety over Liposomes for Pancreatic Cancer. *ACS Nano* **2016**, *10*, 2702–2715.
- (65) Chen, W.; Cheng, C. A.; Lee, B. Y.; Clemens, D. L.; Huang, W. Y.; Horwitz, M. A.; Zink, J. I. Facile Strategy Enabling Both High Loading and High Release Amounts of the Water-Insoluble Drug Clofazimine Using Mesoporous Silica Nanoparticles. *ACS Appl. Mater. Interfaces* **2018**, *10*, 31870–31881.
- (66) Kumar, N.; Chen, W.; Cheng, C. A.; Deng, T.; Wang, R.; Zink, J. I. Stimuli-Responsive Nanomachines and Caps for Drug Delivery. *The Enzymes* **2018**, *43*, 31–65.
- (67) Chen, F.; Hong, H.; Zhang, Y.; Valdovinos, H. F.; Shi, S.; Kwon, G. S.; Theuer, C. P.; Barnhart, T. E.; Cai, W. *In Vivo* Tumor Targeting and Image-Guided Drug Delivery with Antibody-Conjugated,

- Radiolabeled Mesoporous Silica Nanoparticles. *ACS Nano* **2013**, *7*, 9027–9039.
- (68) Chou, C. C.; Chen, W.; Hung, Y.; Mou, C. Y. Molecular Elucidation of Biological Response to Mesoporous Silica Nanoparticles *in Vitro* and *in Vivo*. *ACS Appl. Mater. Interfaces* **2017**, *9*, 22235–22251.
- (69) Meng, H.; Xue, M.; Xia, T.; Ji, Z.; Tarn, D. Y.; Zink, J. I.; Nel, A. E. Use of Size and a Copolymer Design Feature to Improve the Biodistribution and the Enhanced Permeability and Retention Effect of Doxorubicin-Loaded Mesoporous Silica Nanoparticles in a Murine Xenograft Tumor Model. *ACS Nano* **2011**, *5*, 4131–4144.
- (70) Xia, T.; Kovichich, M.; Liong, M.; Meng, H.; Kabehie, S.; George, S.; Zink, J. I.; Nel, A. E. Polyethyleneimine Coating Enhances the Cellular Uptake of Mesoporous Silica Nanoparticles and Allows Safe Delivery of siRNA and DNA Constructs. *ACS Nano* **2009**, *3*, 3273–3286.
- (71) Berkowski, K. L.; Potisek, S. L.; Hickenboth, C. R.; Moore, J. S. Ultrasound-Induced Site-Specific Cleavage of Azo-Functionalized Poly(Ethylene Glycol). *Macromolecules* **2005**, *38*, 8975–8978.
- (72) Zhang, Q.; Wang, X.; Li, P. Z.; Nguyen, K. T.; Wang, X. J.; Luo, Z.; Zhang, H.; Tan, N. S.; Zhao, Y. Biocompatible, Uniform, and Redispersible Mesoporous Silica Nanoparticles for Cancer-Targeted Drug Delivery *in Vivo*. *Adv. Funct. Mater.* **2014**, *24*, 2450–2461.
- (73) Guardado-Alvarez, T. M.; Devi, L. S.; Vabre, J.-M.; Pecorelli, T. A.; Schwartz, B. J.; Durand, J.-O.; Mongin, O.; Blanchard-Desce, M.; Zink, J. I. Photo-Redox Activated Drug Delivery Systems Operating under Two Photon Excitation in the Near-IR. *Nanoscale* **2014**, *6*, 4652–4658.
- (74) Granadero, D.; Bordello, J.; Pérez-Alvite, M. J.; Novo, M.; Al-Soufi, W. Host-Guest Complexation Studied by Fluorescence Correlation Spectroscopy: Adamantane-Cyclodextrin Inclusion. *Int. J. Mol. Sci.* **2010**, *11*, 173–188.
- (75) Xue, M.; Zink, J. I. An Enzymatic Chemical Amplifier Based on Mechanized Nanoparticles. *J. Am. Chem. Soc.* **2013**, *135*, 17659–17662.
- (76) Zhang, Z.; Wang, L.; Wang, J.; Jiang, X.; Li, X.; Hu, Z.; Ji, Y.; Wu, X.; Chen, C. Mesoporous Silica-Coated Gold Nanorods as a Light-Mediated Multifunctional Theranostic Platform for Cancer Treatment. *Adv. Mater.* **2012**, *24*, 1418–1423.
- (77) Ma, X.; Zhao, Y. Biomedical Applications of Supramolecular Systems Based on Host-Guest Interactions. *Chem. Rev.* **2015**, *115*, 7794–7839.
- (78) Villalonga, R.; Cao, R.; Fragoso, A. Supramolecular Chemistry of Cyclodextrins in Enzyme Technology. *Chem. Rev.* **2007**, *107*, 3088–3116.
- (79) Zhang, R.; Li, L.; Feng, J.; Tong, L.; Wang, Q.; Tang, B. Versatile Triggered Release of Multiple Molecules from Cyclodextrin-Modified Gold-Gated Mesoporous Silica Nanocontainers. *ACS Appl. Mater. Interfaces* **2014**, *6*, 9932–9936.
- (80) Sun, S.; Zeng, H.; Robinson, D. B.; Raoux, S.; Rice, P. M.; Wang, S. X.; Li, G. Monodisperse  $MFe_2O_4$  (M=Fe, Co, Mn) Nanoparticles. *J. Am. Chem. Soc.* **2004**, *126*, 273–279.

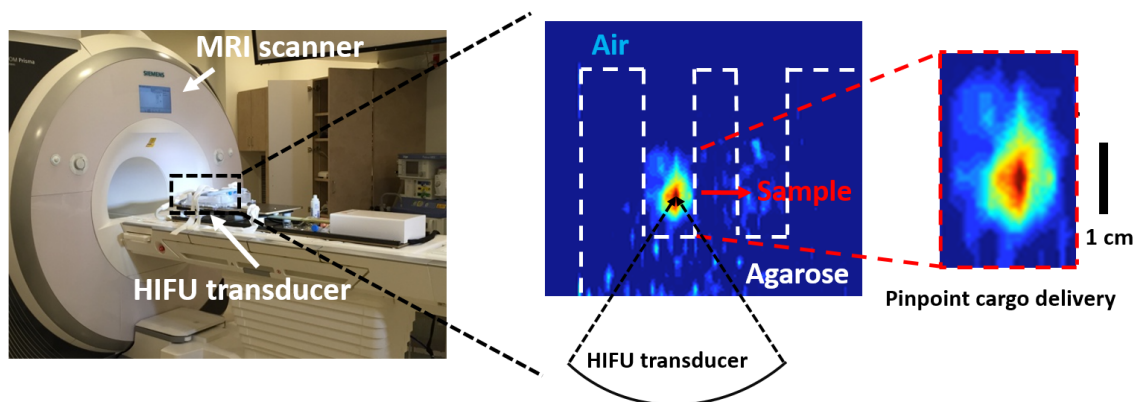
- (81) Jang, J. T.; Nah, H.; Lee, J. H.; Moon, S. H.; Kim, M. G.; Cheon, J. Critical Enhancements of MRI Contrast and Hyperthermic Effects by Dopant-Controlled Magnetic Nanoparticles. *Angew. Chem. Int. Ed.* **2009**, *48*, 1234–1238.
- (82) Lee, N.; Hyeon, T. Designed Synthesis of Uniformly Sized Iron Oxide Nanoparticles for Efficient Magnetic Resonance Imaging Contrast Agents. *Chem. Soc. Rev.* **2012**, *41*, 2575–2589.
- (83) Dong, J.; Zink, J. I. Taking the Temperature of the Interiors of Magnetically Heated Nanoparticles. *ACS Nano* **2014**, *8*, 5199–5207.
- (84) Liong, M.; Lu, J.; Kovoichich, M.; Xia, T.; Ruehm, S. G.; Nel, A. E.; Tamanoi, F.; Zink, J. I. Multifunctional Inorganic Nanoparticles for Imaging, Targeting, and Drug Delivery. *ACS Nano* **2008**, *2*, 889–896.
- (85) Jiang, H.; Xu, F. J. Biomolecule-Functionalized Polymer Brushes. *Chem. Soc. Rev.* **2013**, *42*, 3394–3426.
- (86) Paolino, M.; Ennen, F.; Lamponi, S.; Cernescu, M.; Voit, B.; Cappelli, A.; Appelhans, D.; Komber, H. Cyclodextrin-Adamantane Host-Guest Interactions on the Surface of Biocompatible Adamantyl-Modified Glycodendrimers. *Macromolecules* **2013**, *46*, 3215–3227.
- (87) Hwang, A. A.; Lee, B. Y.; Clemens, D. L.; Dillon, B. J.; Zink, J. I.; Horwitz, M. A. Tuberculosis: pH-Responsive Isoniazid-Loaded Nanoparticles Markedly Improve Tuberculosis Treatment in Mice. *Small* **2015**, *11*, 5066–5078.

## CHAPTER 4

# A Responsive Mesoporous Silica Nanoparticle Platform for Magnetic Resonance Imaging-Guided High-Intensity Focused Ultrasound-Stimulated Cargo Delivery with Controllable Location, Time, and Dose

This chapter of the dissertation was adapted and reprinted with permission from **Chi-An Cheng**<sup>#</sup>, Wei Chen<sup>#</sup>, Le Zhang, Holden H. Wu, Jeffrey I. Zink *J. Am. Chem. Soc.* **2019**, *141*, 17670–17684. Copyright 2019 American Chemical Society. Co-author contributions: Cheng C. A.<sup>#</sup> and Chen W.<sup>#</sup> (co-first authors) designed and performed the synthesis and characterization of material, and all the chemistry related studies. Zhang L. performed the magnetic resonance imaging-guided high intensity focused ultrasound experiments. Holden H. Wu and Jeffrey I. Zink were the P.Is.

### Table of Content Figure



### 4.1 Abstract

Magnetic resonance imaging (MRI) is an essential modality for clinical diagnosis, and MRI-guided high-intensity focused ultrasound (MRgHIFU) is a powerful technology for targeted therapy. Clinical applications of MRgHIFU primarily utilize hyperthermia and ablation to treat

cancerous tissue, but for drug delivery applications thermal damage is undesirable. A biofriendly MRgHIFU-responsive mesoporous silica nanoparticle (MSN) platform that is stimulated within a physiological safe temperature range has been developed, reducing the possibility of thermal damage to the surrounding healthy tissues. Biocompatible polyethylene glycol (PEG) was employed to cap the pores of MSNs, and the release of cargo molecules by HIFU occurs without substantial temperature increase ( $\sim 4$  °C). To visualize by MRI and measure the stimulated delivery in situ, a U.S. Food and Drug Administration (FDA)-approved gadolinium-based contrast agent, gadopentetate dimeglumine ( $\text{Gd}(\text{DTPA})^{2-}$ ), was used as the imageable cargo. Taking advantage of the three-dimensional (3-D) imaging and targeting capabilities of MRgHIFU, the release of  $\text{Gd}(\text{DTPA})^{2-}$  stimulated by HIFU was pinpointed at the HIFU focal point in 3-D space in a tissue-mimicking gel phantom. The amount of  $\text{Gd}(\text{DTPA})^{2-}$  released was controlled by HIFU stimulation times and power levels. A positive correlation between the amount of  $\text{Gd}(\text{DTPA})^{2-}$  released and  $T_1$  was found. The MRgHIFU-stimulated cargo release was further imaged in a sample of *ex vivo* animal tissue. With this technology, the biodistribution of the nanocarriers can be tracked and the MRgHIFU-stimulated cargo release can be pinpointed, opening up an opportunity for future image-guided theranostic applications.

## 4.2 Introduction

Noninvasive imaging is an essential technology for theranostics (*i.e.*, integrated diagnosis and therapy). Compared with modalities such as X-ray, computed tomography, ultrasound, positron emission tomography, or optical imaging, magnetic resonance imaging (MRI) provides an especially powerful suite of information that identifies and characterizes diseased tissues.<sup>1</sup> In addition, MRI does not involve ionizing radiation and achieves three-dimensional (3-D) anatomical coverage with flexible imaging orientations even for tissues deep in the body.

Accordingly, MRI is increasingly being used in clinical practice to guide therapies, such as hyperthermia and ablation using high-intensity focused ultrasound (HIFU)<sup>2,3</sup> or near-infrared laser light,<sup>4-6</sup> in conjunction with real-time MRI temperature measurement during the procedures.<sup>7</sup>

To date, MRI-guided HIFU (MRgHIFU) therapies for uterine fibroids, prostate tissue, essential tremor, tremor-dominated Parkinson's disease, and bone metastases have been approved by the U.S. Food and Drug Administration (FDA).<sup>8,9</sup> HIFU is a noninvasive technique with millimeter-sized energy-focusing ability and deep tissue penetration capability.<sup>8</sup> When ultrasound waves propagate in the body, both thermal and mechanical effects (*e.g.*, cavitation) occur.<sup>10</sup> A variety of HIFU-responsive nanoparticles that take advantage of these effects have been developed in order to enhance image contrast or to enable controlled release of encapsulated theranostic cargos at specific sites of interest.<sup>11-13</sup> Most of the well-developed HIFU-responsive drug carriers include heat-responsive thermosensitive liposomes.<sup>14-18</sup> Just recently, ThermoDox (lyso-thermosensitive liposomal doxorubicin) in combination with MRgHIFU-generated hyperthermia has received Institutional Review Board (IRB) approval to begin a Phase I study for the local treatment of the primary tumor in metastatic breast cancer.<sup>19</sup> As a source of localized hyperthermia, HIFU enhanced the delivery of doxorubicin carried by thermosensitive liposomes.<sup>14</sup>

Although chemotherapy combined with mild hyperthermia (39–42 °C) have synergistic effects that may increase anticancer efficacy,<sup>20,21</sup> the temperature window for effective hyperthermia is narrow,<sup>15,22,23</sup> and exceeding the window may induce tumor cell metastasis or vascular shutdown.<sup>24-26</sup> Even though the HIFU energy can be spatially focused, it may not always be possible to effectively increase the temperature in the targeted tissue because of heat dissipation by the blood flow in the body (*i.e.*, heat sink effect).

Another category of HIFU-responsive nanoparticles relies on ultrasound-associated mechanical forces.<sup>27</sup> Polymers were found to degrade faster and release incorporated cargos upon

ultrasound exposure.<sup>28</sup> A wide range of mechanically responsive cargo carriers<sup>29,30</sup> such as microbubbles,<sup>31,32</sup> micelles,<sup>33-35</sup> emulsions,<sup>36</sup> and polymeric nanoparticles<sup>37-40</sup> have been developed for drug delivery. However, most of the organic carriers formed via self-assembly are stable only above the critical micelle concentration (CMC) and are prone to disassembly when diluted in the biological environment.<sup>41</sup> Other factors such as shear stress, serum protein interactions, ionic strength, or pH may also lead to premature rupture of those drug carriers during circulation in the bloodstream and result in leakage of drugs before arriving at the target site.<sup>42-44</sup> In contrast, sturdy structures of particulate drugs may be too stable to release drugs at the target tissue.<sup>45</sup>

We have developed a new MRgHIFU-responsive platform based on mesoporous silica nanoparticles (MSNs). MSNs are rigid nanomaterials with precise size control of the particle diameter, high surface area and large pore volume for cargo loading and delivery,<sup>46-50</sup> high biocompatibility,<sup>51-53</sup> high cellular internalization efficiency, and easy surface functionalization.<sup>54-60</sup> Several ultrasound-responsive caps have thus been designed as the gatekeepers of cargo-loaded MSNs.<sup>61</sup> Most of the caps are thermally responsive polymers that require a temperature rise to undergo physical change (*e.g.*, phase transition or conformation change) in order to release cargos. Only a few examples of mechanically operable caps activated within a physiological temperature range or even at a lower temperature have been reported.<sup>62-66</sup> A copolymer cap including an ultrasound-labile tetrahydropyranyl moiety that is cleavable by laboratory ultrasound was shown to control the cargo release from MSNs, but the temperature during ultrasound stimulation was not closely examined.<sup>63,64</sup> In an effort to set the stage for clinical translation, biocompatible polyethylene glycol (PEG), one of the most widely used polymers in biomedical research, was chosen in this work to cap the pores of MSNs. PEG was shown to cleave because of mechanical forces generated by ultrasound,<sup>67</sup> so that cargos can be released primarily

in response to the mechanical effects of MRgHIFU without substantial temperature increase.

In this work, an FDA-approved gadolinium-based MRI contrast agent gadopentetate dimeglumine ( $\text{Gd}(\text{DTPA})^{2-}$ ) (Magnevist, Bayer) was used as the imageable cargo to demonstrate the performance of our proposed nanoparticle delivery system;  $\text{Gd}(\text{DTPA})^{2-}$  release causes an easily measurable MRI contrast change. Taking advantage of the 3-D capabilities of MRI and HIFU, the release of  $\text{Gd}(\text{DTPA})^{2-}$  from the nanoparticles was pinpointed at the HIFU focal point in 3-D space. The spatial- and temporal-control of  $\text{Gd}(\text{DTPA})^{2-}$  release was further demonstrated in *ex vivo* tissue, paving the way for *in vivo* studies in the future. Combining the advantages of mechanically responsive PEG and the focusing ability of MRgHIFU, HIFU-stimulated cargo delivery was achieved within a physiological temperature range, avoiding the need to substantially increase local temperature in areas with potential heat sink effects and reducing the possibility of thermal damage to the surrounding healthy tissues. With this technology, the biodistribution of the nanocarriers can be tracked by MRI and stimulated cargo release pinpointed by HIFU so as to have improved information for diagnosis or treatment of certain diseases (*e.g.*, cancer). In future studies, a drug (*e.g.*, anticancer chemotherapeutic agent) can be encapsulated together with an imaging agent (*e.g.*,  $\text{Gd}(\text{DTPA})^{2-}$ ), providing a new tool to achieve precision medicine—to deliver the precise dosage of drugs at a specific and controlled time and location.

### 4.3 Design of Ultrasound-Responsive MSNs

The nanoparticles that were designed to release cargo molecules by HIFU stimulation under MRI guidance have three main components: an MSN as the cargo carrier, MRI contrast agents as the cargo, and ultrasound-responsive PEG as the cap (**Scheme 4.1**). The FDA-approved contrast agent gadolinium-diethylenetriamine pentaacetic acid ( $\text{Gd}(\text{DTPA})^{2-}$ ) and its counterions meglumines (*i.e.*, gadopentetate dimeglumine: Magnevist) were chosen as the cargo. The PEG cap



is an FDA-approved polymer that has been clinically used for pharmaceutical formulations. PEGylated nanoparticles exhibit the stealth effect because their interactions with the reticuloendothelial system are reduced, thus prolonging their circulation time and enhancing their uptake in tumor tissues via the enhanced permeability and retention (EPR) effect.<sup>68-71</sup> PEG also improves the colloidal stability of the nanoparticles. In this design, conjugated PEG seals the pores of the MSNs and exposes them only when stimulated by HIFU, where vigorous vibration and/or cleavage of PEG<sup>67</sup> are induced. The entrapped Gd(DTPA)<sup>2-</sup> that is released by externally controlled HIFU stimulation causes T<sub>1</sub>-weighted MRI contrast changes. Therefore, MRI can be used to characterize the amount of HIFU-stimulated cargo release from the MSNs. Most importantly, this HIFU-stimulated cargo release does not require substantial heating, opening up an opportunity for drug delivery when temperature increase is not practical or not desired.

The MSN nanocarriers were synthesized by a sol-gel reaction in the presence of cationic surfactant templates by following published procedures.<sup>46,72</sup> The obtained nanoparticles were 91.6 ± 15.1 nm in diameter (**Figure 4.1**) and possessed an MCM-41 type structure (**Figure 4.2a**). To enable both the loading of Gd(DTPA)<sup>2-</sup> in the pores of MSNs and the conjugation of dicarboxylic acid-terminated PEG (HOOC-PEG-COOH) (average Mn = 2000 Da) on the surface of MSNs, the inner and outer surfaces of MSNs were functionalized with amine groups by postgrafting the silica surface with (3-aminopropyl)triethoxysilane (APTS) (designated as MSNs-APTS) (**Scheme 4.1**). Negatively charged Gd(DTPA)<sup>2-</sup> can interact electrostatically with those positively charged amine groups on the inner surfaces and thus increase its loading amount. On the outer surface, HOOC-PEG-COOH was conjugated to those amine groups by a standard 1-ethyl-3-(3-diethylaminopropyl) carbodiimide hydrochloride (EDC-HCl) and *N*-hydroxysulfosuccinimide sodium salt (sulfo-NHS) coupling reaction through amide bond formation (designated as MSNs-PEG). From transmission electron microscopy (TEM) images, the amine functionalization and PEGylation did not change

the morphology or mesoporous structures of the nanoparticles (**Figure 4.2a**). The amine functionalization and PEGylation to MSNs was confirmed by zeta potential (**Figure 4.2b**), Fourier transform-infrared spectroscopy (FT-IR) (**Figure 4.2c**), thermogravimetric analysis (TGA) (**Figure 4.2d**), N<sub>2</sub> adsorption–desorption isotherms (**Figures 4.2e, 4.3** and **Table 4.1**), and dynamic light scattering (DLS) measurements (**Figure 4.2f**) after each functionalization step. Characterization details are described in Section 4.13 Methods. The grafting amounts of APTS and PEG on the surface of MSNs were 3% and 18% of the total mass, respectively (**Figure 4.2d**). Compared with as-synthesized MSNs having 1045 m<sup>2</sup>/g in Brunauer–Emmett–Teller (BET) surface area, 1.04 cc/g in pore volume, and 2.9 nm average pore diameter, MSNs-APTS and MSNs-PEG showed smaller BET surface areas (595 and 108 m<sup>2</sup>/g, respectively), smaller total pore volumes (0.52 and 0.19 cc/g, respectively), and smaller average pore diameters (2.4 nm for MSNs-APTS and not available for MSNs-PEG) (**Table 4.1** and **Figure 4.3**). These decreases can be explained by the surface coverage of the nanoparticles and the blockage of the pore openings after the sequential grafting of APTS and PEG.<sup>73</sup> The increased DLS size of MSNs (282.1 ± 8.6 nm), MSNs-APTS (337.5 ± 5.7 nm), and MSNs-PEG (384.2 ± 4.1 nm) in deionized H<sub>2</sub>O provided additional evidence of successful amine functionalization and PEGylation (**Figure 4.2f**). The colloidal stability of the PEGylated nanoparticles was examined in phosphate-buffered saline (PBS) (pH 7.4). Before PEGylation, the DLS size of MSNs-APTS in PBS was markedly greater (959.2 ± 27.9 nm) than that in H<sub>2</sub>O, indicating serious aggregation in PBS due to its high ionic strength (**Figure 4.2f**).<sup>63</sup> However, after PEGylation, the DLS size of MSNs-PEG in PBS (356.6 ± 1.4 nm) was very similar to that in H<sub>2</sub>O (**Figure 4.2f**), showing good colloidal stability of MSNs-PEG in both solvents. The difference in their colloidal stabilities is clearly illustrated in **Figure 4.4**, where MSNs-PEG and MSNs-APTS in PBS were kept undisturbed for 30 min, 1 day, and 3 days at room temperature. Substantial aggregation of MSNs-APTS was observed within 30 min,

whereas MSNs-PEG remained well-suspended even after 3 days. The improved colloidal stability of PEGylated nanoparticles can be explained by the blocking of surface contact between nanoparticles by surface PEG and preventing aggregation of the nanoparticles by such steric repulsion.<sup>74</sup>

#### **4.4 Gd(DTPA)<sup>2-</sup> Loading, PEG Capping, and PEG Cap Stability at Body Temperature**

The loading of Gd-(DTPA)<sup>2-</sup> was carried out by soaking MSNs-APTS in a Gd(DTPA)<sup>2-</sup> solution (500 mM) and stirring overnight. The Gd-(DTPA)<sup>2-</sup>-loaded MSNs-APTS were then conjugated with HOOC-PEG-COOH ( $M_w = 2000$  Da) to seal the pores. The mixture reacted overnight and was washed thoroughly with deionized H<sub>2</sub>O to remove the unloaded or surface Gd-(DTPA)<sup>2-</sup>. To evaluate the loading capacity of Gd-(DTPA)<sup>2-</sup> in MSNs-PEG, Gd-(DTPA)<sup>2-</sup>-loaded MSNs-PEG was digested by aqua regia at 95 °C. The amount of Gd ions in the resulting powder was then dissolved by 2% HNO<sub>3</sub> and measured by inductively coupled plasma optical emission spectrometry (ICP-OES). The loading capacity of Gd-(DTPA)<sup>2-</sup>, defined as (mass of Gd-(DTPA)<sup>2-</sup> loaded in pores/mass of MSNs) × 100%, was calculated to be 24.1 ± 1.2%. This high loading of Gd-(DTPA)<sup>2-</sup> in the pores resulted in the decreased BET surface area and the decreased total pore volume (**Table 4.1**). Because of both the small size of Gd-(DTPA)<sup>2-</sup> molecules (*ca.* 0.8 nm) and the electrostatic interaction between the negatively charged Gd-(DTPA)<sup>2-</sup> and the positively charged pore walls, the Gd-(DTPA)<sup>2-</sup> may easily diffuse into the pores and stick to the pore wall. Another type of positively charged amine, N-trimethoxysilylpropyl-N,N,N-trimethylammonium (TA), was attached to the pore walls of MSNs (designated as MSNs-TA) to compare the loading of Gd-(DTPA)<sup>2-</sup> with that of MSNs-APTS. MSNs-TA showed lower loading capacity of Gd-(DTPA)<sup>2-</sup> (11.0 ± 0.5%), implying that the steric hindrance of the bulky trimethyl

groups in TA weakened the electrostatic interaction between the quaternary amine and Gd-(DTPA)<sup>2-</sup>

How to prevent the leakage of small Gd-(DTPA)<sup>2-</sup> molecules from the MSNs was the next challenge to overcome. To cover multiple pores, in our design, we conjugated both carboxylic acids of HOOC-PEG-COOH to amines on the surface of MSNs-APTS through stepwise conjugation method and formed U-shaped PEG caps. To confirm the formation of U-shaped PEG, its Gd-(DTPA)<sup>2-</sup> loading capacity after thorough washing was compared to that of the control group capped with monocarboxylic acid-terminated PEG, where the PEG can be attached to MSNs-APTS only at one end, leaving the other end extended into the solvent. As expected, the stretched form PEG cap showed lower Gd-(DTPA)<sup>2-</sup> loading capacity (18.4%), confirming that the stepwise conjugation method that attaches both ends of HOOC-PEG-COOH to MSNs-APTS improves the pore-capping capability. In addition to the geometry of PEG caps, the distance between PEG caps and the surface of MSNs-APTS was also another factor to optimize. Here, the capping capabilities of HOOC-PEGCOOH with higher molecular weight (Mn = 6500 Da and 25000 Da) were explored, with which the Gd-(DTPA)<sup>2-</sup> loading capacities were 19.0% and 19.1%, respectively. The lower Gd-(DTPA)<sup>2-</sup> loading capacities using these longer PEG caps compared to that of the shorter PEG (Mn = 2000 Da) may be attributed to the larger gap space between the U-shaped cap chain and the pore opening, allowing more Gd-(DTPA)<sup>2-</sup> molecules to diffuse out during the washing steps.

The stability of the PEG cap in aqueous solution at both room temperature (23 °C) and body temperature (37 °C) was examined. Gd-(DTPA)<sup>2-</sup>-loaded MSNs-PEG (3 mg/mL) was suspended in deionized H<sub>2</sub>O in Eppendorf tubes. Each tube was immersed in a water bath at room temperature (23 °C) or 37 °C for 2, 5, 8, 10, or 30 min. Negligible leakage of Gd-(DTPA)<sup>2-</sup> molecules was observed at room temperature (**Figure 4.5**). At 37 °C, only 3.8% of Gd-(DTPA)<sup>2-</sup> was released

over a period of 30 min, showing that PEG was tight enough to cap the pores and remained stable on the MSN's surface even at a physiological temperature.

#### 4.5 Proof-of-Concept: Ultrasound-Stimulated Release of Gd(DTPA)<sup>2-</sup>

To examine the ultrasound responsiveness of the PEG cap, a probe sonicator (VCX 130, Sonics & Materials, Inc., Newtown, CT) was used as an ultrasound source for a proof-of-concept experiment. Gd(DTPA)<sup>2-</sup>-loaded MSNs-PEG suspended in deionized H<sub>2</sub>O was stimulated with the probe sonicator (20 kHz, power density: 75 W/cm<sup>2</sup>) for 2, 5, 8, 10, or 30 min. The Gd(DTPA)<sup>2-</sup> release efficiency was defined as (mass of released Gd(DTPA)<sup>2-</sup>/mass of Gd(DTPA)<sup>2-</sup> loaded in pores) × 100%, where the mass of released Gd(DTPA)<sup>2-</sup> was quantified by ICP-OES. The amount of released Gd(DTPA)<sup>2-</sup> increased with the sonication time, where 30 min of sonication led to a release efficiency of 62% (**Figure 4.5**). This result confirms that ultrasonication uncapped the PEG-covered pores of MSNs and that the amount of released cargo was controllable by the sonication time. The temperatures of the samples measured with a thermometer immediately after sonication were 31, 42, 47, 49, and 51 °C after the 2, 5, 8, 10, and 30 min stimulation, respectively, by the probe sonicator. To measure the effect of only heat on the release, a control experiment was carried out using a water bath at 50 °C. Over a period of 30 min 24% of the Gd(DTPA)<sup>2-</sup> was released, which is less than half of that (62%) triggered with sonication and heating to a similar temperature (**Figure 4.5**). This result shows that although heat can cause partial release of Gd(DTPA)<sup>2-</sup> molecules, the released amount was relatively small because PEG is not degradable at 50 °C.<sup>75</sup> Mechanical effects of ultrasound, such as shock waves created during cavitation, induce PEG rupture<sup>67,76</sup> and thus efficiently release the entrapped cargo. Cavitation causes a rapid compression and rarefaction of the liquid. On a molecular level it causes a rapid motion of small molecules (*e.g.*, solvent molecules and Gd(DTPA)<sup>2-</sup>) that the polymer in the solvent cannot follow, thereby generating friction, increasing strain, and eventually leading to bond rupture.<sup>67,76</sup> The TEM

image of the nanoparticles after being exposed to ultrasound and high temperature (50 °C) for 30 min (**Figure 4.6**) shows that the mesoporous structure was intact. The release of  $\text{Gd}(\text{DTPA})^{2-}$  was primarily through opening of the pores stimulated by the rupture of the mechanically sensitive PEG gatekeeper rather than by the destruction of the mesoporous silica structure.

#### **4.6 MRI-Guided HIFU-Stimulated Release of $\text{Gd}(\text{DTPA})^{2-}$ and MRI Contrast Change**

The stimulated release experiments were carried out using a research HIFU system (Image Guided Therapy, Bordeaux, France) integrated with a whole-body 3 T MRI scanner (Prisma, Siemens Healthineers, Erlangen, Germany) (**Figure 4.7**). MRI was used to guide the HIFU stimulation, monitor the temperature during the stimulation, and pinpoint the release of  $\text{Gd}(\text{DTPA})^{2-}$  in real time. The HIFU transducer has a 128-element array with a frequency of 1 MHz and a peak electrical power output of 1200 W. The mechanical and electronic steering capabilities of the HIFU system can precisely steer the  $1 \times 1 \times 7 \text{ mm}^3$  cigarshaped HIFU focal point in three dimensions.

In the fields of MRI and ultrasound (including HIFU), it is customary to first use tissue-mimicking “phantoms” to evaluate feasibility, train operators, optimize protocols, and characterize technical performance of MRgHIFU technology before studying animal or human subjects.<sup>77-79</sup> Tissue-mimicking phantoms use materials designed to mimic pertinent properties of biological tissues and thus are used in preclinical research as an alternative to *ex vivo* tissues and organs. The advantages of using tissue-mimicking phantoms include superior availability and shelf life, high structural uniformity, and customizability. Several HIFU tissue-mimicking phantom formulations such as agar, gelatin, and polyacrylamide with additives to adjust their thermal and acoustic properties to be comparable to human soft tissues have been reported.<sup>77-84</sup> For example, the

acoustic attenuation and speed of sound of tissue-mimicking phantoms may be adjusted via the addition of silicon dioxide particles, concentrated milk, bovine serum albumin, corn syrup, glass beads, intralipid, graphite, or n-propanol.<sup>84-86</sup> Because of the similar convection and diffusion properties to that of extracellular space around tumor tissues,<sup>87</sup> agarose phantoms are commonly used for ultrasound-stimulated drug delivery studies.<sup>80,88,89</sup> For example, other researchers have used an agarose-based phantom with a thermosensitive indicator to study the spatial drug delivery profile using ultrasound-induced mild hyperthermia.<sup>80</sup> In addition to the above-mentioned phantoms, researchers in the community of MRI or ultrasound also commonly study nanoparticle samples in water or gel for initial demonstration of their new techniques.<sup>58,90,91</sup>

In this work, we followed the methodology in the community of MRI or ultrasound by using an agarose phantom as the sample holder to mimic aqueous tissues<sup>92,93</sup> and by placing nanoparticle samples in water for sample recycling and further quantification or in methylcellulose gel to mimic a tissue scaffold.<sup>90,94</sup> Concentrated milk was selected as the primary attenuation component in this work for its widespread availability, a high attenuation coefficient ( $\sim 0.8$  dB/cm/MHz) with a speed of sound that is typical of biological fluids (1547 m/s), and its previous uses in water-based phantoms.<sup>80,95</sup> The agarose phantom used in this work was 10 cm in diameter and contained sample wells that were 1.3 cm in diameter and 5 cm in height (**Figure 4.8a**). Agarose is sturdy and does not liquefy below 65 °C. The ultrasound waves penetrate through agarose without being absorbed because of its low acoustic attenuation coefficient.<sup>96</sup> The agarose phantom was placed on the HIFU transducer on the patient bed in the MRI scanner (**Figures 4.8a and 4.7a,b**). Two samples of water-suspended  $\text{Gd}(\text{DTPA})^{2-}$ -loaded MSNs-PEG, three samples of  $\text{Gd}(\text{DTPA})^{2-}$ -loaded MSNs-PEG mixed in methylcellulose (2.5 wt %) and concentrated milk (v/v = 1/1) (designated as gel/milk), and gel/milk itself were placed in the six sample wells in the agarose phantom. The phantom on the transducer was moved into the MRI scanner for further MRgHIFU experiments.

The aqueous suspension of Gd(DTPA)<sup>2-</sup>-loaded MSNs-PEG (sample 1) was stimulated with HIFU (3 cycles of 1 min, 74 W). T<sub>1</sub>-weighted turbo-spin-echo images of the entire agarose phantom were acquired before and after the HIFU stimulation, termed pre- and post-T<sub>1</sub>-weighted images, respectively. The post-T<sub>1</sub>-weighted image of sample 1 was darker than the pre-T<sub>1</sub>-weighted image (**Figure 4.8b**). To clearly depict the change in MR image intensity, T<sub>1</sub>-weighted images were processed by subtracting the post-T<sub>1</sub>-weighted image from the pre-T<sub>1</sub>-weighted image to generate the  $\Delta T_1$ -weighted image (**Figure 4.8b**). The HIFU-stimulated sample 1 exhibited a bright signal in the  $\Delta T_1$ -weighted image. The homogeneous brightness in the well was the result of diffusion of the released Gd(DTPA)<sup>2-</sup> in the well. The unstimulated control groups, including Gd(DTPA)<sup>2-</sup>-loaded MSNs-PEG in water (control 2), Gd(DTPA)<sup>2-</sup>-loaded MSNs-PEG in gel/milk (controls 3–5), and gel/milk itself (control 6), showed negligible changes between pre- and post-T<sub>1</sub>-weighted images as expected. The agarose phantom background (control 7) also showed no image change. In the entire 3-D  $\Delta T_1$ -weighted image of the agarose phantom containing the sample wells, only the HIFU-stimulated sample 1 strikingly showed an intense signal.

The amount of Gd(DTPA)<sup>2-</sup> released by HIFU stimulation was quantified by ICP-OES. HIFU-stimulated sample 1 had the released amount of Gd(DTPA)<sup>2-</sup> of 0.47  $\mu$ mole of Gd(DTPA)<sup>2-</sup>/mg of MSNs-PEG. The change in T<sub>1</sub>-weighted image intensity, evaluated as  $[(\text{pre-T}_1\text{-weighted image intensity} - \text{post-T}_1\text{-weighted image intensity})/\text{pre-T}_1\text{-weighted image intensity}] \times 100\%$ , was calculated to be 39% for the HIFU-stimulated sample 1 (**Figure 4.9**). This result confirmed that HIFU-stimulated Gd(DTPA)<sup>2-</sup> release occurred primarily in the well into which the HIFU was focused, with negligible effect on the other wells.

The above discussion emphasized the magnitude of the change in the T<sub>1</sub>-weighted image intensity. Initially it seemed surprising that Gd(DTPA)<sup>2-</sup> release caused a decrease in the intensity. However, the decrease in T<sub>1</sub>-weighted image intensity when the encapsulated Gd(DTPA)<sup>2-</sup> was



released from the pores of the nanoparticles can be explained by the Solomon–Bloembergen–Morgan theory that describes the parameters affecting  $T_1$  caused by a given Gd(III)-based contrast agent.<sup>97,98</sup>

According to the theory,  $T_1$  decreases when the rotational correlation time ( $\tau_r$ ) increases (*i.e.*, decreased rotation or tumbling rate of the Gd(III) contrast agent). Numerous studies have shown that Gd(III)-based contrast agents bonded to bulky proteins, nanoparticles, or peptides tumble more slowly and thus increase the contrast.<sup>99–101</sup> In the case of Gd(DTPA)<sup>2-</sup> loaded in the MSN's pores, electrostatic interactions with the positively charged pore wall of the bulky MSNs-PEG (**Figure 4.10a**) decreased the tumbling rate and thus enhanced  $r_1$  to  $8.6 \text{ s}^{-1}\text{mM}^{-1}$  (**Figure 4.10b**). After the HIFU stimulation (3 cycles of 1 min, 74 W), where 26% of the loaded Gd(DTPA)<sup>2-</sup> was released,  $r_1$  of Gd(DTPA)<sup>2-</sup>-loaded MSNs-PEG was reduced ( $6.9 \text{ s}^{-1}\text{mM}^{-1}$ ) compared to that before HIFU stimulation (**Figure 4.10b**), similar to what was found by ultrasound stimulation with a probe sonicator (**Figure 4.11a**;  $T_1$ -weighted images of each sample are shown in **Figure 4.11b**). No changes in either  $r_1$  or  $r_2$  of Gd(DTPA)<sup>2-</sup> itself were observed after HIFU or the probe sonicator stimulation under the same conditions (**Figures 4.12 and 4.13**), confirming that the structure of the Gd(DTPA)<sup>2-</sup> molecule was not changed by HIFU stimulation.

By using this nanoparticulated Gd(DTPA)<sup>2-</sup>, the total amount of Gd(DTPA)<sup>2-</sup> required to enhance  $T_1$ -weighted MR image contrast to the same level as that of free Gd(DTPA)<sup>2-</sup> can be reduced. This may be beneficial for avoiding accumulation of gadolinium-based contrast agents in the body over repeated contrast-enhanced examinations, which was described in a warning by the FDA in 2018.<sup>102</sup>

#### 4.7 Mechanisms of HIFU-Stimulated Gd(DTPA)<sup>2-</sup> Release

To study if the activation of the PEG cap by HIFU and the ensuing release of Gd(DTPA)<sup>2-</sup> was caused by heat, mechanical forces, or both, the temperature change caused by HIFU stimulation was measured. The increase in temperature was monitored by dynamic MRI temperature mapping acquired using a 2D gradient-echo protocol (TE= 20 ms, TR= 30 ms, spatial resolution of  $1 \times 1 \times 3 \text{ mm}^3$ , and temporal resolution of 2.8 s). The maximum temperature rise of water-suspended Gd(DTPA)<sup>2-</sup>-loaded MSNs-PEG was only 4 °C during the 1 min HIFU stimulation period, and the temperature returned to the starting temperature (20 °C room temperature) shortly after HIFU stopped (**Figure 4.14a**). The minimal temperature rise can be explained by the low sound attenuation coefficient of water; negligible sound energy was absorbed, and thus very little heat was generated during HIFU stimulation. Even at this low temperature (less than 24 °C), HIFU can stimulate 0.47 μmole of Gd(DTPA)<sup>2-</sup>/mg of MSNs-PEG release from the pores of MSNs-PEG. In contrast, the temperature rose by 11 °C after 1 min of HIFU stimulation of the sample mixed in the gel/milk mixture that has a higher sound attenuation coefficient (**Figure 4.14a**). Water therefore served as an ideal medium to demonstrate the mechanical sensitivity of PEG in the absence of appreciable temperature changes. The mechanical effects of HIFU allowed cargos to be released with minimal temperature increase, unlike the case where probe sonication was used (**Figure 4.5**).

To confirm the mechanical sensitivity of the polymer cap, PEG cleavage by HIFU at room temperature was examined by matrix-assisted laser desorption ionization-time-of-flight mass spectrometry (MALDI-TOF MS). The peaks from intact PEG were located around  $m/z = 2000$  (**Figure 4.14b**). After HIFU stimulation (3 cycles of 1 min, 1 MHz, 74 W), small peaks around  $m/z = 1000$  appeared. The signal intensity of those peaks increased with longer HIFU stimulation duration (2 cycles of 5 min). The intensity ratios of the fragment peaks around  $m/z = 1000$  to  $m/z$

= 2000 (defined as [the highest intensity of the peaks around  $m/z = 1000$ /the highest intensity of the peaks around  $m/z = 2000$ ]) were 0.11 (without HIFU), 0.20 (after 3 cycles of 1 min HIFU), and 0.71 (after 2 cycles of 5 min HIFU). The PEG cleavage was likely caused by HIFU-induced cavitation<sup>103,104</sup> and is consistent with previous studies showing that ultrasonic chain scission occurred around the center of the polymer chain.<sup>67,76</sup> PEG itself may also accelerate polymer degradation because hydrophilic PEG enhances the penetration of water and thus the rate of hydrolysis.<sup>67,76</sup> Further evidence of PEG degradation by HIFU was the decrease in colloidal stability of MSNs-PEG (**Figure 4.15**). Aggregation of the HIFU-stimulated nanoparticles implies that the PEG on the surface was degraded.

#### **4.8 Dose and Temporal Control of Released $\text{Gd}(\text{DTPA})^{2-}$ by MRgHIFU Stimulation**

##### **Time and Power Level**

The effects of exposure time and HIFU power levels on the amount of  $\text{Gd}(\text{DTPA})^{2-}$  released were measured based on the change of the  $T_1$ -weighted image intensity.  $\text{Gd}(\text{DTPA})^{2-}$ -loaded MSNs-PEG samples were dispersed in deionized  $\text{H}_2\text{O}$  and stimulated with HIFU at a fixed power level (74 W) for 3, 5, or 10 min. The  $T_1$ -weighted intensities decreased by 13%, 26%, and 35%, respectively (**Figure 4.16a**), and the corresponding  $\Delta T_1$ -weighted images increased in brightness with increasing HIFU stimulation time (**Figure 4.16c**). Similarly, the dependence of the  $\text{Gd}(\text{DTPA})^{2-}$  release on HIFU power levels was also measured. Three samples of water-suspended  $\text{Gd}(\text{DTPA})^{2-}$ -loaded MSNs-PEG were stimulated with HIFU for 3 min at power levels of 9, 74, and 290 W. The changes in  $T_1$ -weighted image intensity were 5%, 13%, and 60%, respectively (**Figure 4.16b**). The  $\Delta T_1$ -weighted image of the sample stimulated at 290 W showed strong signal changes (**Figure 4.16c**), which can be explained by strong cavitation and PEG fragmentation caused by such high acoustic intensity. The temperature increases during these HIFU stimulations

were monitored by dynamic MRI temperature mapping. During 3 min of HIFU stimulation at 74 W, the temperature increased by only 4 °C. The temperature increased by 7 °C during a 5 min exposure and by 10 °C during 10 min of exposure. For the 3 min stimulations at different power levels, the temperature increases were 1 °C at 9 W and 10 °C at 290 W.

The correlation between the amount of  $\text{Gd}(\text{DTPA})^{2-}$  released and  $T_1$  was quantified. The  $T_1$  relaxation times from the HIFU-stimulated samples in **Figure 4.16a,b** were measured by MRI  $T_1$  mapping, and the amount of  $\text{Gd}(\text{DTPA})^{2-}$  released was measured by ICP-OES. Increased  $\text{Gd}(\text{DTPA})^{2-}$  release from the pores of MSNs-PEG resulted in longer  $T_1$  relaxation times (**Figure 4.16d,e**). By adjusting the HIFU stimulation time or power level, the released amount of  $\text{Gd}(\text{DTPA})^{2-}$  could be controlled and monitored from the  $T_1$  relaxation time. **Table 4.2** summarizes the  $\text{Gd}(\text{DTPA})^{2-}$  release efficiency and temperature increase under various HIFU parameters (power levels and stimulation time). Similar results were found using probe sonication:  $T_1$  relaxation times increased with increasing duration of ultrasonication and thus higher release efficiency of  $\text{Gd}(\text{DTPA})^{2-}$  (**Figure 4.17**).

To demonstrate that HIFU can control the released dose of  $\text{Gd}(\text{DTPA})^{2-}$  over time,  $\text{Gd}(\text{DTPA})^{2-}$ -loaded MSNs-PEG samples were mixed in gel/milk and stimulated with HIFU for various durations and at different power levels. Again, the greater the HIFU stimulation times and power levels, the greater the decrease in  $T_1$ -weighted image intensity (**Figure 4.18a,b**). To control the release of  $\text{Gd}(\text{DTPA})^{2-}$  over time, multiple cycles of HIFU stimulations were performed (**Figure 4.18c**). After the first cycle of HIFU stimulation, the  $T_1$ -weighted image intensity decreased over a period of 30 min and leveled off. The second and third cycles of HIFU stimulation resulted in similar profiles. This sequence shows that the desired dose of released  $\text{Gd}(\text{DTPA})^{2-}$  can be achieved within a specific time window by adjusting the ON and OFF times of HIFU stimulation. The structure of the MSNs-PEG was intact after HIFU stimulation for 3 min (**Figure**

4.19), suggesting that the release of  $\text{Gd}(\text{DTPA})^{2-}$  was due to the opening of the pores gated by the mechanically sensitive PEG rather than by the destruction of the nanoparticle.

#### **4.9 Three-Dimensional Spatial Control of Released $\text{Gd}(\text{DTPA})^{2-}$ at the Focal Point of MRgHIFU Stimulation**

To visualize the 3-D precision with which the  $\text{Gd}(\text{DTPA})^{2-}$  cargo is released from the nanoparticles,  $\text{Gd}(\text{DTPA})^{2-}$ -loaded MSNs-PEG particles were mixed in a viscous gel to minimize diffusion of the  $\text{Gd}(\text{DTPA})^{2-}$  molecules after release. The particles were homogeneously mixed in 2.5 wt % methylcellulose, and the sample was transferred into sample wells ( $1.3 \times 1.3 \times 5 \text{ cm}^3$ ) molded in the agarose phantom. The well dimensions were large enough to allow the cigar-shaped HIFU focal point ( $1 \times 1 \times 7 \text{ mm}^3$ ) to be positioned well within the well's interior. The axial, coronal, and sagittal cross sections of the sample well of interest in the agarose phantom are shown in **Figure 4.20a**.

Considering the release studies in the previous sections, three cycles of 1 min HIFU stimulation (1 MHz, power level: 74 W) were chosen to activate the release of  $\text{Gd}(\text{DTPA})^{2-}$ . The MRI was acquired with a turbo-spin-echo inversion-recovery protocol shortly after the HIFU stimulation, and cross sections of the  $\Delta T_1$ -weighted images are shown in three orientations (**Figure 4.20b**). A clearly defined region of image signal change appeared. The cigar-shaped red spot, the position with maximal image intensity change, pinpoints the HIFU focal point which was near the center of the sample well. The change of image intensity away from the focal point sharply decreased, showing that the majority of the  $\text{Gd}(\text{DTPA})^{2-}$  was released at the focal point. The temperature increased 4 °C after the HIFU stimulation, again confirming that the release was primarily due to the mechanical responsiveness of the PEG cap.

#### 4.10 *Ex Vivo* MRgHIFU-Stimulated Gd(DTPA)<sup>2-</sup> Release and MRI Contrast Change

To demonstrate the potential of transferring our technology to preclinical and clinical *in vivo* studies in the future, 3-D spatial and dose-controlled cargo release in *ex vivo* chicken breast tissue samples was investigated. A  $3 \times 6 \text{ cm}^2$  piece of chicken breast was injected with methylcellulose gel containing Gd(DTPA)<sup>2-</sup>-loaded MSNs-PEG at two different locations and imaged before HIFU stimulation. The two injection sites were observable as bright regions in T<sub>1</sub>-weighted images (**Figure 4.21a**). A HIFU transducer with an 8-element annular array and similar size (25 mm in diameter) as the chicken breast was used for MRgHIFU. The HIFU focal point was  $0.7 \times 0.7 \times 3 \text{ mm}^3$  in size, and the peak electrical power output of the HIFU transducer was 200 W. One of the injection sites was stimulated with HIFU for 3 cycles of 3 min (2.5 MHz, 8 W). The color-coded  $\Delta T_1$ -weighted images and T<sub>1</sub>-weighted image intensity changes (%) of the HIFU-stimulated sample, the control sample without HIFU stimulation, and the chicken tissue background after each HIFU cycle are shown in panels a and b of **Figure 4.21**, respectively. The intensity changes of the HIFU-stimulated sample close to the focal point greatly increased with the number of HIFU cycles. After 3 cycles of HIFU stimulation, a clearly confined region of intensity change close to the HIFU focal point was observed in 3-D space (axial, coronal, and sagittal) (**Figure 4.22**). Negligible changes in T<sub>1</sub>-weighted image intensity were observed at the sample injection site without HIFU stimulation or in the background. These results confirm that MRgHIFU can achieve spatially selective stimulation for cargo release close to the HIFU focal point in *ex vivo* tissue. By using this technique, we can first visualize the presence of Gd(DTPA)<sup>2-</sup>-nanoparticles with MRI, stimulate with MRgHIFU at the focal point, and characterize the cargo release from the MRI contrast change.

A potentially challenging property of tissue is its acoustic energy-absorbing ability due to the abundance of proteins that may generate significant heat during HIFU stimulation and produce

overall image contrast changes caused by the temperature increase.<sup>105,106</sup> To examine if such temperature interference occurred, a control experiment was done by injecting methylcellulose gel into a  $3 \times 5 \text{ cm}^2$  sample of chicken breast. The gel injection site was stimulated by HIFU for 2 cycles of 3 min (2.5 MHz, 8 W). The temperature increase at the focal point measured by a 2D gradient-echo protocol was 10 °C. A negligible change in  $T_1$ -weighted image intensity was observed showing that the temperature interference was not a confounder (**Figure 4.23a–c**).

#### **4.11 Significance for Potential Biomedical Applications**

The phantom and *ex vivo* experiments open the door for further biomedical applications using the MRgHIFU-stimulated cargo release technology developed in this work. For future biomedical applications, drugs such as anticancer chemotherapeutics can be used as cargo. Combined with the use of MRgHIFU, a clinically available therapeutic modality, the MSNs-PEG drug delivery platform may lead to clinical applications such as cancer diagnosis and treatment. For example, we can identify the target tissues (*e.g.*, cancer) for treatment, confirm the delivery of cargo to the target tissues and avoid healthy tissues, and quantify the amount of cargo that has been released at the target tissues. If both a therapeutic and an imageable cargo such as a gadolinium-based contrast agent (*e.g.*, gadopentetate dimeglumine) are co-encapsulated in MSNs-PEG, the drug carriers can be monitored using MRI, and the drug release can be activated by MRgHIFU only when the drug carriers are observed at the tumor site. The drug release behavior can be observed *in situ* by MRI. The released dose of drugs may be calculated from the correlation between the released amount of gadolinium-based contrast agent with the change in  $T_1$ -weighted image intensity and/or  $T_1$  relaxation time as shown in this work. To achieve the required dosage in a desired therapeutic window, the released amount of therapeutics can be further controlled by adjusting HIFU parameters such as power level, stimulation duration, and number of stimulation cycles. The goal

of precision medicine, defined as giving a precise dosage of drugs in a specific location at a controlled time, could then be achieved.

Another advantage of this work is that only minimal to mild bulk heating is required to release cargos such as contrast agents and drugs. This is different from the ablation therapy widely investigated using HIFU and other thermally triggered drug delivery platforms. The predominantly mechanically triggered drug delivery strategy presented in this work may be especially beneficial for treating tissues in regions where it is impractical or undesirable to heat (*e.g.*, pancreatic or liver cancer near blood vessels and bile ducts).

#### **4.12 Summary**

In summary, this work showed that the combination of MRI-guided high-intensity focused ultrasound (MRgHIFU) and a polyethylene glycol (PEG)-capped mesoporous silica nanoparticle (MSN) platform can deliver cargos at a precisely predesignated localized spot monitored and visualized in real time by MRI. Both MRI and HIFU are clinically available and noninvasive, do not require ionizing radiation, and can access tissues deep in the body. The activation mechanism of the PEG cap does not require tissue-destructive heating. The MRgHIFU experiments carried out in a tissue-mimicking agarose phantom showed that when imageable cargo molecules ( $\text{Gd}(\text{DTPA})^{2-}$ , 24% of loading capacity) were released from the pores of MSNs-PEG, both the  $T_1$ -weighted image intensity and the  $T_1$  relaxivity ( $r_1$ ) decreased as predicted by the Solomon–Bloembergen–Morgan theory. The minimal to mild temperature increase during HIFU stimulation and verification of PEG bond cleavage after the stimulation confirmed that the mechanism of  $\text{Gd}(\text{DTPA})^{2-}$  release was mainly caused by mechanical forces of HIFU and not heat. The amount of  $\text{Gd}(\text{DTPA})^{2-}$  released was controllable by adjusting different durations and power levels of HIFU stimulation. A positive correlation between the release efficiency of  $\text{Gd}(\text{DTPA})^{2-}$  and  $T_1$



relaxation time was found: higher release efficiency of  $\text{Gd}(\text{DTPA})^{2-}$  led to longer  $T_1$ . 3-D MR images of the contrast intensity changes after HIFU stimulation allowed us to precisely pinpoint (with millimeter resolution) the location of  $\text{Gd}(\text{DTPA})^{2-}$  release that is chosen and controlled by the position of the HIFU focal point. The MRgHIFU-stimulated release study in *ex vivo* chicken breast tissue samples showed a sharply defined region where the  $T_1$ -weighted image intensity changed the most (14%) after HIFU stimulation (3 cycles of 1 min, 8 W). The technology in this work takes advantage of the powerful MRgHIFU platform as a clinical translation pathway and may enable new image-guided theranostic applications as a viable strategy for personalized therapy—delivering a precisely controlled dosage of drug to the specific diseased tissue location monitored by MRI in real time.

## 4.13 Methods

### 4.13.1 Materials and Chemicals

Hexadecyltrimethylammonium bromide (CTAB, 99+ %), tetraethyl orthosilicate (TEOS, 98%), (3-aminopropyl)triethoxysilane (APTS, 99%), ammonium nitrate ( $\text{NH}_4\text{NO}_3$ , 98+ %), 2-(N-morpholino)ethanesulfonic acid hydrate (MES hydrate, 99.5+ %), and methylcellulose (viscosity: 4000 cP) were purchased from Sigma-Aldrich. Ethanol (200 proof) was purchased from Decon Laboratories, Inc. Toluene (99.5+ %) was purchased from Macron Fine Chemicals. 1-Ethyl-3-(3-dimethylaminopropyl) carbodiimide hydrochloride (EDC-HCl, 99+ %) and *N*-hydroxysulfosuccinimide sodium salt (sulfo-NHS, 99+ %) were purchased from CovaChem. Magnevist was purchased from Bayer.  $\alpha,\omega$ -Bis-carboxy polyethylene glycol ( $\text{HOOC-PEG-COOH}$ ,  $M_w = 2000$  Da) was purchased from Iris Biotech GmbH. Hydrochloric acid ( $\text{HCl}$ , 36.5%–38%, trace metal grade), nitric acid ( $\text{HNO}_3$ , 67%–70%, trace metal grade), sodium hydroxide ( $\text{NaOH}$ , 97+ %), and agarose (low EEO) were purchased from Fisher Scientific. All chemicals were used

without further purification.

#### 4.13.2 Characterization

The morphology and diameters of nanoparticles were characterized by transmission electron microscopy (TEM, Tecnai T12) with an operating voltage of 120 kV. MSNs or MSNs-APTS were dispersed in ethanol at a low concentration (0.1 mg/mL). The suspension (10  $\mu$ L) of the nanoparticles was dropped onto a 200 mesh carbon-coated copper grid and dried at room temperature. The dynamic light-scattering (DLS) size and zeta potential values of nanoparticles were determined by a laser particle analyzer LPA-3100 at room temperature (23  $^{\circ}$ C). MSNs showed the characteristic zeta potential of  $-27.2$  mV in deionized H<sub>2</sub>O at pH 7, which was shifted to  $+37.9$  mV after APTS modification (**Figure 4.2b**). After PEGylation, the zeta potential dropped to  $+7.3$  mV, which was the result of charge screening by the formed amide bonds. The functional groups on the surface of MSNs were characterized by Fourier transform infrared spectroscopy (FT-IR, JASCO FT/IR-420) spectrometer in the range of  $4000$ – $400$   $\text{cm}^{-1}$ . The successful APTS modification was supported by the new absorption peaks at  $\nu = 1512$   $\text{cm}^{-1}$  (N–H bending) and the two bands at  $\nu = 3717$   $\text{cm}^{-1}$  and  $\nu = 3727$   $\text{cm}^{-1}$  (N–H stretching) in the FT-IR spectrum (**Figure 4.2c**). PEGylation was confirmed by the new absorption peak at  $\nu = 1555$   $\text{cm}^{-1}$  (amide II), supporting the formation of secondary amide bond. Stronger absorption peaks at  $\nu = 1464$   $\text{cm}^{-1}$  (C–H bending), and  $\nu = 2880$   $\text{cm}^{-1}$  and  $\nu = 2927$   $\text{cm}^{-1}$  (C–H stretching) of MSNs-PEG compared with MSNs-APTS also supported the successful PEGylation. Thermogravimetric analysis (TGA) was carried out using a PerkinElmer Pyris Diamond TG/DTA under air flow (200 mL/min). MSNs, MSNs-APTS, and MSNs-PEG (5–10 mg) were loaded in aluminum pans, and the data were recorded during a temperature scan from 30 to 550  $^{\circ}$ C at a scan rate of 10  $^{\circ}$ C/min. The plotted values are normalized to the weight at 100  $^{\circ}$ C. An empty aluminum pan was used as a reference.

The weight loss of MSNs, MSNs-APTS, and MSNs-PEG were 8%, 11%, and 29%, respectively, confirming the presence of organic matter in MSNs-APTS and MSNs-PEG (**Figure 4.2d**). The surface area, pore diameter, and pore volume of MSNs, MSNs-APTS, MSNs-PEG, or Gd(DTPA)<sup>2-</sup>-loaded MSNs-PEG were determined by N<sub>2</sub> adsorption–desorption isotherm measurement at 77 K (Autosorb-iQ, Quantachrome Instruments). Nanoparticles were degassed at 120 °C for 20 h before the measurement. The surface area and pore diameter distribution of the nanoparticles were determined by Brunauer–Emmett–Teller (BET) and Barrett–Joyner–Halenda (BJH) methods. The loading capacity and release efficiency of Gd(DTPA)<sup>2-</sup> from MSNs-PEG were quantified by inductively coupled plasma optical emission spectrometry (ICP-OES) using a Shimadzu ICPE-9000. The calibration curve was created from 0 to 10 ppm of gadolinium in 2% HNO<sub>3</sub>.

#### **4.13.3 Synthesis of Mesoporous Silica Nanoparticles (MSNs)**

Mesoporous silica nanoparticles were synthesized using a sol–gel reaction in the presence of cationic surfactant templates. In general, CTAB (250 mg) was dissolved in a mixture of 120 mL of deionized H<sub>2</sub>O and 875 μL of NaOH solution (2 M) in a 250 mL round-bottom flask with vigorous stirring. The solution was heated to 80 °C in an oil bath and kept at this temperature for 30 min followed by the dropwise addition of 1.25 mL of TEOS. The reaction was stirred for another 2 h for the formation of MSNs. Afterward, the solution was cooled to room temperature, centrifuged, and washed with ethanol three times to remove unreacted precursors and free surfactants.

#### **4.13.4 Synthesis of Amine-Functionalized MSNs (MSNs-APTS)**

To functionalize amine groups on the surface of MSNs, MSNs (180 mg) were dispersed in a mixture of 50 mL of anhydrous toluene and 150 μL of APTS. The reaction mixture was heated to

110 °C and refluxed for 12 h with vigorous stirring. After the reaction, APTS-modified MSNs (MSNs-APTS) were washed with ethanol two times. To remove the surfactant template, MSNs-APTS were dispersed in a mixture of 100 mL of ethanol and 2 g of NH<sub>4</sub>NO<sub>3</sub> in a 250 mL round-bottom flask. The reaction mixture was heated to 78 °C and refluxed for 1 h. The surfactant removal process by extraction was repeated twice. After the extraction, MSNs-APTS were centrifuged and further washed with deionized H<sub>2</sub>O and ethanol twice. Finally, MSNs-APTS were stored in ethanol for further usage.

#### 4.13.5 Gd(DTPA)<sup>2-</sup> Loading and PEG Capping

Before loading Gd(DTPA)<sup>2-</sup> in the mesopores of MSNs-APTS, MSNs-APTS were first washed with deionized H<sub>2</sub>O. The loading of Gd(DTPA)<sup>2-</sup> was carried out by soaking MSNs-APTS (20 mg) in 1 mL of gadopentetate dimeglumine solution (500 mM Gd(DTPA)<sup>2-</sup>). The solution was stirred overnight to let Gd(DTPA)<sup>2-</sup> diffuse into the pores of MSNs-APTS. The Gd(DTPA)<sup>2-</sup>-loaded MSNs-APTS were then conjugated with HOOC-PEG-COOH (M<sub>w</sub>= 2000 Da) to seal the pores. EDC-HCl (15.3 mg) and sulfo-NHS (8.7 mg) coupling agents were dissolved in 240 μL of MES solution (100 mM, pH= 6.0). So that both carboxylic acids on COOH-PEG-COOH could be activated, the PEG polymer (20 mg) dissolved in 200 μL of MES buffer solution was stepwise added into the solution of coupling agents every 10 min. Afterward, the activated PEG was stepwise added into the Gd(DTPA)<sup>2-</sup>-loaded MSNs-APTS solution every 10 min to enable both ends of the activated PEG to react with the primary amines on the surface of MSNs-APTS. The mixture was reacted overnight and then washed thoroughly with deionized H<sub>2</sub>O to remove the unloaded Gd(DTPA)<sup>2-</sup>, the excess EDC-HCl and sulfo-NHS, and PEG. The resulting PEG-capped nanoparticles are denoted as MSNs-PEG. Finally, Gd(DTPA)<sup>2-</sup>-loaded MSNs-PEG were stored in 10 mL of deionized H<sub>2</sub>O for further ultrasound-stimulated release studies.

#### **4.13.6 Ultrasound-Stimulated Release of Gd(DTPA)<sup>2-</sup> by a Probe Sonicator**

Gd(DTPA)<sup>2-</sup>-loaded MSNs-PEG solution (3 mg/mL) was prepared in deionized H<sub>2</sub>O in an Eppendorf tube. The tip of the probe sonicator (VCX 130, Sonics & Materials, Inc., Newtown, CT) was placed in the center of the solution. The ultrasound parameter was set with the frequency of 20 kHz and output power of 21 W (power density: 75 W/cm<sup>2</sup>). After various ultrasound stimulation time durations (2, 5, 8, 10, or 30 min) with the probe sonicator, the solution was centrifuged (14000 rpm, 10 min) to separate the particles and the supernatant containing released Gd(DTPA)<sup>2-</sup>. The supernatant and pellet were collected for further quantification of Gd(DTPA)<sup>2-</sup> loading capacity and release efficiency by ICP-OES.

#### **4.13.7 Quantification of Gd(DTPA)<sup>2-</sup> Loading Capacity and Gd-(DTPA)<sup>2-</sup> Release Efficiency after Ultrasound or HIFU Stimulation**

Gd(DTPA)<sup>2-</sup>-loaded MSNs-PEG solution stimulated by ultrasound or HIFU was centrifuged (7830 rpm, 15 min) to separate the pellet and the supernatant. The particle-containing pellet was dispersed in 10 mL of aqua regia at 95 °C for 12 h to be fully digested into powder. The resulting powder was then dissolved and diluted by 2% HNO<sub>3</sub>. The supernatant containing the released Gd(DTPA)<sup>2-</sup> was diluted by 2% HNO<sub>3</sub>. The concentration of Gd ions was measured by ICP-OES and quantified based on the Gd ion calibration curve (0, 0.01, 0.05, 0.1, 0.5, 1, 5, and 10 ppm). The definition of loading capacity is (mass of Gd(DTPA)<sup>2-</sup> loaded in pores/mass of MSNs-PEG) × 100%. The definition of release efficiency is (mass of released Gd(DTPA)<sup>2-</sup>/mass of Gd(DTPA)<sup>2-</sup> loaded in pores) × 100%.

#### **4.13.8 Preparation of Agarose Phantom**

An agarose gel “phantom” (*i.e.*, test object) was prepared and used as the sample holder for Gd(DTPA)<sup>2-</sup>-loaded MSNs-PEG during MRgHIFU experiments. The concentration of the agarose

used was 3.5 wt %. First, deionized H<sub>2</sub>O (500 mL) was added into a 1000 mL flask. Agarose powder (17.5 g) was then added slowly to the flask during vigorous stirring. The solution was heated to boiling and maintained at that temperature for 5 min. Subsequently, the hot solution was poured into a plastic container with a diameter of 10 cm and the sample wells were molded by glass test tubes with a diameter of 1.3 cm (**Figure 4.24**). Finally, the solution was cooled to 4 °C for the gel formation.

#### **4.13.9 Preparation of Methylcellulose Gel or Mixture of Methylcellulose Gel and Milk**

To prepare methylcellulose gel (2.5 wt %), methylcellulose powder (1.25 g) was slowly added to 15 mL of boiling water in a flask under vigorous stirring to dissolve the powder. After stirring for 3 min, 35 mL of room-temperature water was rapidly added to the solution and mixed until the mixture was homogeneous. The solution was then cooled at 4 °C overnight to complete the gelation process.

To prepare a mixture of methylcellulose gel (2.5 wt %) and milk (v/v = 1/1), methylcellulose (1.25 g) was slowly added to 15 mL of boiling water in a flask under vigorous stirring to dissolve the powder. After the mixture was stirred for 3 min, 10 mL of room-temperature water and 25 mL of concentrated milk were rapidly added to the solution and mixed until the mixture was homogeneous. The solution was then cooled at 4 °C overnight to complete the gelation process.

#### **4.13.10 MRI-Guided High-Intensity Focused Ultrasound (MRgHIFU)-Stimulated Release of Gd(DTPA)<sup>2-</sup>**

All MRgHIFU experiments were conducted using a research HIFU system (Image Guided Therapy, Bordeaux, France) integrated with a whole-body 3 T MRI scanner (Prisma, Siemens Healthineers, Erlangen, Germany). The HIFU system had a 128-element transducer array with a diameter of 9 cm, frequency of 1 MHz, a focal point of 1 × 1 × 7 mm<sup>3</sup> in size, and a peak electrical

power output of 1200 W. The electrical power output used ranged from 9 to 290 W. Gd(DTPA)<sup>2-</sup>-loaded MSNs-PEG dispersed in deionized H<sub>2</sub>O (1 mg/mL, 3 mL), methylcellulose gel (2.5 wt %, 3 mL), or methylcellulose gel (2.5 wt %)/milk mixture (v/v = 1/1) (3 mL) were placed in sample wells (1.3 × 1.3 × 5 cm<sup>3</sup>) in the agarose phantom (10 × 10 × 11.5 cm<sup>3</sup>). The agarose phantom was placed on top of the HIFU transducer, which was secured on the patient table of the 3 T MRI scanner. Through both mechanical and electronic steering of the HIFU transducer, the focal point was placed at the center of the sample well. The samples were stimulated by HIFU at a fixed electrical power level (74 W, power density: 7400 W/cm<sup>2</sup>) with different durations (3, 5, or 10 cycles of 1 min), or at different electrical power levels (9, 74, or 290 W, power density: 900, 7400, or 29000 W/cm<sup>2</sup>) for three cycles of 1 min. The cooling period between each cycle was 10 s. T<sub>1</sub>-weighted MR images were acquired before and after the HIFU stimulation using a 3D turbo-spin-echo protocol (see Section 4.13.11 T<sub>1</sub>-Weighted and T<sub>2</sub>-Weighted Images and T<sub>1</sub> and T<sub>2</sub> Mapping) to compare the image intensity. The ΔT<sub>1</sub>-weighted images were obtained by subtracting post-T<sub>1</sub>-weighted images from pre-T<sub>1</sub>-weighted images. The temperature of the solution during the HIFU stimulation was measured by a 2D gradient-echo MRI temperature mapping sequence every 1.8 s. To quantify the released amount of Gd(DTPA)<sup>2-</sup>, the HIFU-stimulated water-suspended samples were removed from the phantom and spun down to separate the pellet and supernatant. The particle-containing pellet was dispersed in 10 mL of aqua regia at 95 °C for 12 h to be fully digested into powder. The powder was then dissolved and diluted by 2% HNO<sub>3</sub>. The supernatant containing the released Gd(DTPA)<sup>2-</sup> was diluted by 2% HNO<sub>3</sub>. The concentration of Gd ions was measured by ICP-OES.

#### **4.13.11 T<sub>1</sub>-Weighted and T<sub>2</sub>-Weighted Images and T<sub>1</sub> and T<sub>2</sub> Mapping**

T<sub>1</sub>-weighted and T<sub>2</sub>-weighted images of water-suspended Gd(DTPA)<sup>2-</sup>-loaded MSNs-PEG

before and after the stimulation by a probe sonicator or MRgHIFU were acquired using a 3 T MRI scanner (Prisma, Siemens Healthineers, Erlangen, Germany) with gradient-echo or turbo-spin-echo (TSE) protocols respectively. The 1 mL samples with and without HIFU stimulation were mixed with 3 mL of methylcellulose (2.5 wt %) in 15 mL Falcon plastic tubes placed in a water bath. Acquisition parameters for gradient-echo T<sub>1</sub>-weighted images were as follows: field of view (FOV) = 350 × 350 × 60 mm<sup>3</sup>; matrix size = 256 × 256 × 20; echo time (TE) = 1.89 ms; repetition time (TR) = 20 ms; flip angle = 30°. Acquisition parameters for TSE T<sub>2</sub>-weighted images were the following: FOV = 350 × 350 × 60 mm<sup>3</sup>; matrix size = 256 × 256 × 20; TE = 118 ms; TR = 8 s; flip angle = 90°.

Parameters for the T<sub>1</sub> mapping protocol were as follows: inversion-recovery TSE sequence; FOV = 350 × 350 × 60 mm<sup>3</sup>; matrix size = 256 × 256 × 20; TE = 13 ms; TR = 8 s; inversion times (TIs) = 50, 100, 200, 300, 500, 750, 1000, 1500, 2500 ms; excitation pulse flip angle = 90°; inversion pulse flip angle = 180°. Parameters for the T<sub>2</sub> mapping protocol were the following: multiple-TE TSE sequence; FOV = 350 × 350 × 60 mm<sup>3</sup>; matrix size = 256 × 256 × 20; TEs = 12, 24, 35, 47, 59, 83, 94, 118 ms; TR = 8 s; excitation pulse flip angle = 90°; refocusing pulse flip angle = 180°. T<sub>1</sub> and T<sub>2</sub> were calculated using a monoexponential fitting algorithm as described below.

The standard inversion-recovery MR signal model was used to calculate T<sub>1</sub> maps. Images acquired with different inversion times (TIs) were fit pixel-wise to the equation  $M = M_0(1 - 2e^{-\tau/T_1})$ , where  $M_0$  is the magnetization at thermal equilibrium,  $M$  is the signal intensity of images acquired at TI =  $\tau$ . Similarly, the standard Car-Purcell-Meiboom-Gill (CPMG) signal model was used to calculate T<sub>2</sub> maps, where images acquired with different echo times (TEs) were fit pixel-wise to the equation  $M = M_0e^{-\tau/T_2}$ , with  $M_0$  being the magnetization at thermal equilibrium,  $M$  being the signal intensity of images acquired at TE =  $\tau$ .



#### **4.13.12 T<sub>1</sub> and T<sub>2</sub> Relaxivity (r<sub>1</sub> and r<sub>2</sub>) Measurement**

Different concentrations of Gd(DTPA)<sup>2-</sup>, G Gd(DTPA)<sup>2-</sup>-loaded MSNs-PEG, or ultrasound or HIFU-stimulated Gd(DTPA)<sup>2-</sup>-loaded MSNs-PEG were mixed with 2.5 wt % methylcellulose. T<sub>1</sub> and T<sub>2</sub> relaxation times were acquired by the 3 T MRI scanner using the above inversion–recovery TSE sequence and multiple-TE TSE sequence, respectively. r<sub>1</sub> or r<sub>2</sub> were calculated as the ratio of 1/T<sub>1</sub> or 1/T<sub>2</sub> to the concentration of Gd(III) determined by ICP-OES.

#### **4.13.13 Molecular Weight Measurement of PEG by Matrix-Assisted Laser Desorption/Ionization Time-of-Flight Mass Spectrometry (MALDI-TOF MS)**

HOOC-PEG-COOH (average M<sub>n</sub> = 2000 Da) dissolved in 3 mL of deionized H<sub>2</sub>O (3 mg/mL) was added to the sample well in the agarose phantom. HIFU stimulation was focused at the center of the sample solution. After being stimulated for three cycles of 1 min or two cycles of 5 min (1 MHz, 74 W), the samples were collected and diluted (1.8 mg/mL) for the MALDI-TOF measurement. Sodium trifluoroacetate in deionized H<sub>2</sub>O (10 mg/mL) was prepared as a cationizing agent. Dithranol dissolved in THF (20 mg/mL) was used as a matrix. PEG sample solution (5 μL), matrix solution (15 μL), and the cationizing agent (0.5 μL) were mixed well in an Eppendorf tube. A 1 μL portion of the mixture was spotted on a stainless steel target plate. Data were acquired in a reflection mode using a Bruker Ultraflex MALDI TOF/TOF mass spectrometer with the accelerating voltage at 25 kV.

#### **4.13.14 *Ex Vivo* MRgHIFU-Stimulated Gd(DTPA)<sup>2-</sup> Release and MRI Contrast Change**

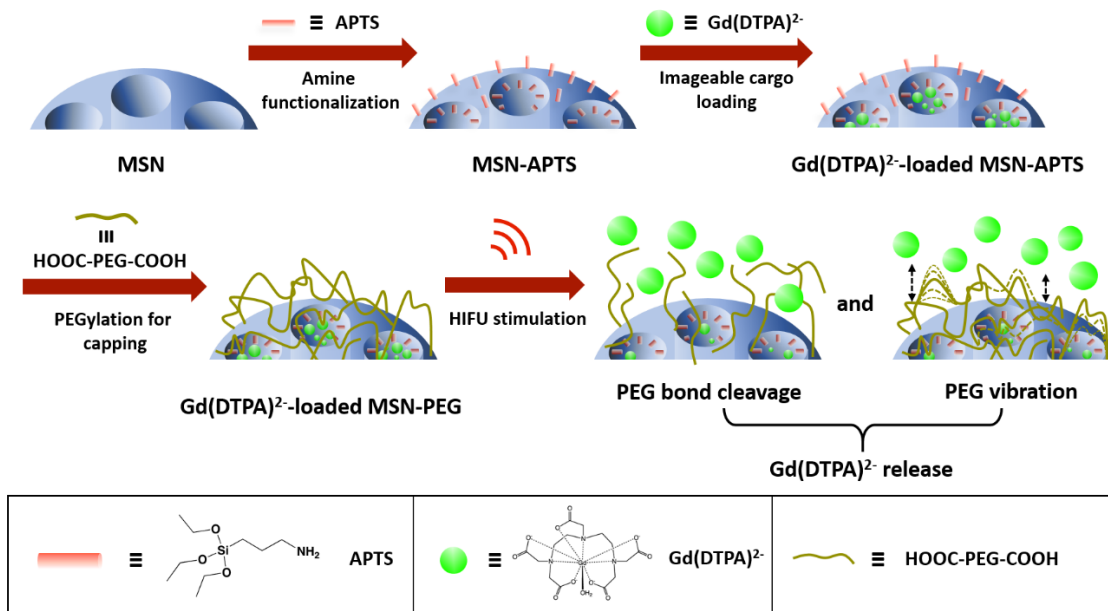
The *ex vivo* experiments were conducted using the research HIFU system (Image Guided Therapy, Bordeaux, France) integrated with the whole-body 3 T MRI scanner (Prisma, Siemens Healthineers, Erlangen, Germany). The same HIFU system also had an 8-element annular transducer array with a diameter of 25 mm, frequency of 2.5 MHz, a focal point 0.7 × 0.7 × 3 mm<sup>3</sup>

in size, and a peak electrical power output of 200 W. Gd(DTPA)<sup>2-</sup>-loaded MSNs-PEG (0.5 mg) dispersed in 2.5% methylcellulose gel (0.5 mL) were injected in a sample of boneless chicken breast tissue (3 × 6 cm<sup>2</sup>) that was about 1 cm thick. The HIFU transducer was placed under the chicken breast tissue sample and secured on the patient table of the 3 T MRI scanner. The HIFU focal point was positioned in the chicken breast tissue close to the sample injection site, and the sample was stimulated with HIFU for 3 cycles of 3 min (8 W). Control groups including the samples (0.5 mg of Gd(DTPA)<sup>2-</sup>-loaded MSNs-PEG in 0.5 mL of 2.5% methylcellulose gel) injected into chicken breast tissue without HIFU stimulation and 2.5% methylcellulose gel (0.5 mL) injected into chicken breast tissue with HIFU stimulation (2 cycles of 3 min) were also included. T<sub>1</sub>-weighted MR images were acquired before and after each HIFU stimulation cycle using the turbo-spin-echo protocol. The difference in T<sub>1</sub>-weighted image intensity was obtained by subtracting post-T<sub>1</sub>-weighted images from pre-T<sub>1</sub>-weighted images, resulting in ΔT<sub>1</sub>-weighted images. The temperatures of the chicken breast tissue during the HIFU stimulation were measured by a 2D gradient-echo MRI temperature mapping protocol before and right after the stimulation.

#### **4.14 Acknowledgment**

We gratefully acknowledge financial support by the UCLA Innovation Fund, UCLA Department of Radiological Sciences, and Zink Student Research Support Fund.

## 4.15 Scheme, Figures and Tables



**Scheme 4.1.** Scheme of the synthesis and HIFU-stimulated release of  $\text{Gd}(\text{DTPA})^{2-}$  from PEGylated mesoporous silica nanoparticles (MSNs-PEG). After HIFU stimulation, PEG undergoes bond cleavage and vibration to release  $\text{Gd}(\text{DTPA})^{2-}$ .

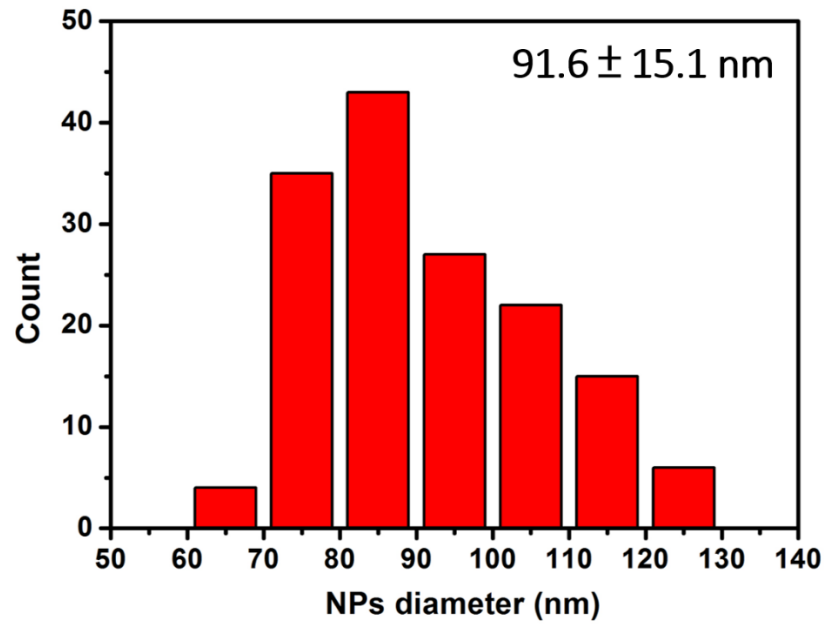


**Figure 4.1.** Size distribution of  $91.6 \pm 15.1$  nm mesoporous silica nanoparticles (MSNs).

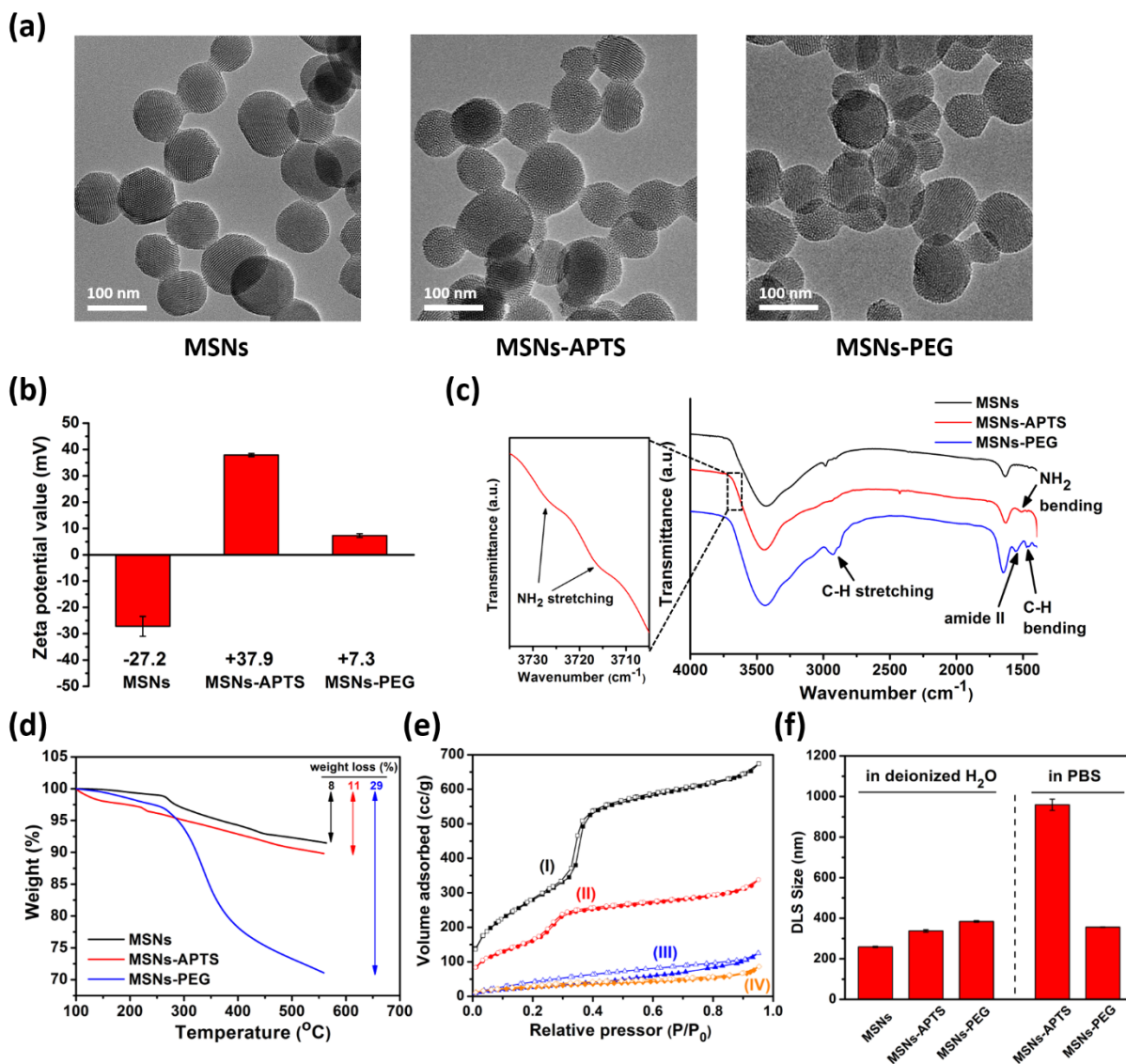


**Figure 4.2.** Characterizations of MSNs, MSNs-APTS, and MSNs-PEG. (a) TEM images of MSNs (left), MSNs-APTS (middle) and MSNs-PEG (right). (b) Zeta potential values, (c) FT-IR spectra, and (d) TGA results of MSNs, MSNs-APTS, and MSNs-PEG. (e)  $N_2$  adsorption/desorption isotherms of MSNs (curve (I)), MSNs-APTS (curve (II)), MSNs-PEG (curve (III)), and  $Gd(DTPA)^{2-}$ -loaded MSNs-PEG (curve (IV)). Solid: adsorption; hollow: desorption. (f) DLS size of MSNs, MSNs-APTS, and MSNs-PEG in deionized  $H_2O$ , and MSNs-APTS and MSNs-PEG in PBS, respectively.

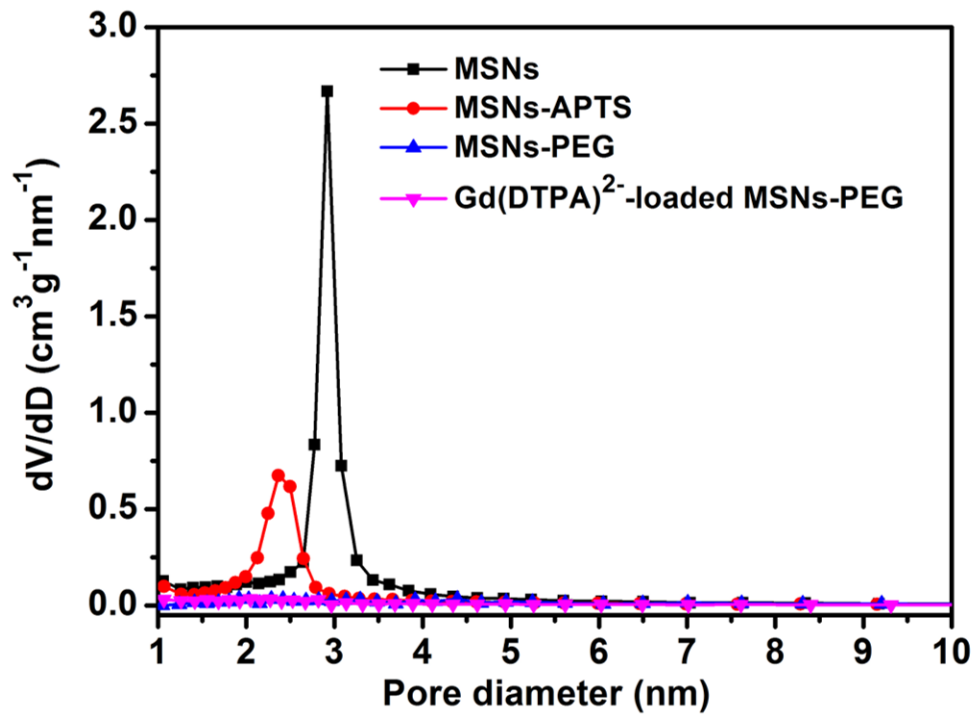


**Figure 4.3.** Pore diameter distribution of MSNs, MSNs-APTS, MSNs-PEG, and Gd(DTPA)<sup>2-</sup>-loaded MSNs-PEG measured at 77 K.

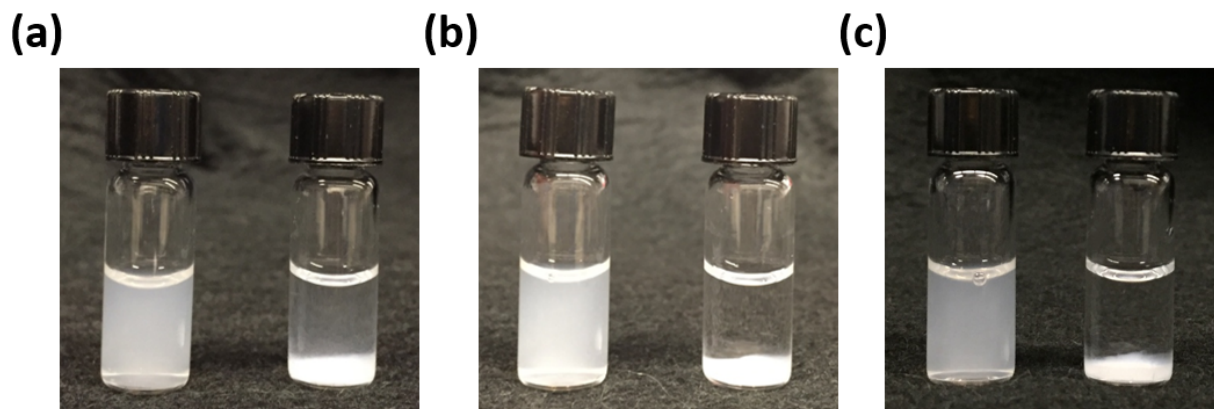


**Figure 4.4.** The colloidal stability of MSNs-PEG (left tube) and MSNs-APTS (right tube) in PBS after being kept undisturbed for (a) 30 min, (b) 1 day, and (c) 3 days at room temperature.

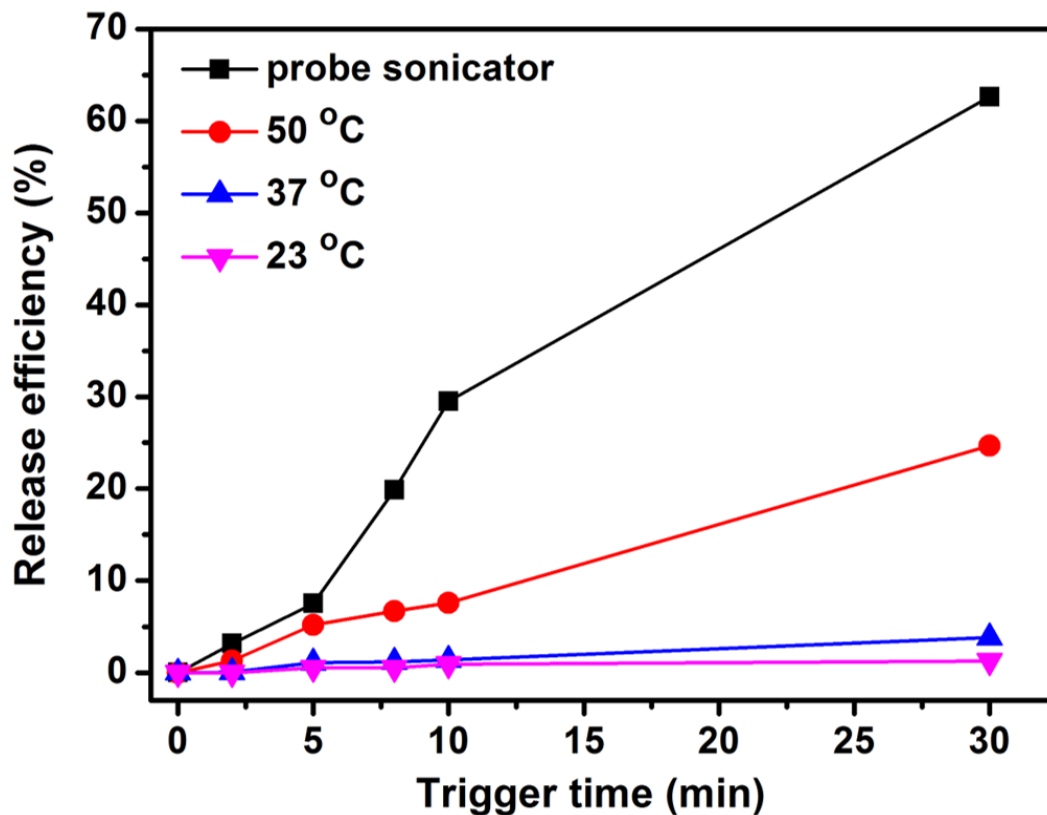


**Figure 4.5.** Ultrasound-stimulated  $\text{Gd}(\text{DTPA})^{2-}$  release using a probe sonicator. Time-dependent release profile of  $\text{Gd}(\text{DTPA})^{2-}$  from MSNs-PEG after probe sonication (black), or immersed in a 23 °C (pink), 37 °C (blue) or 50 °C (red) water bath. The loading capacity of  $\text{Gd}(\text{DTPA})^{2-}$  in MSNs-PEG was  $24.1 \pm 2.1$  %.

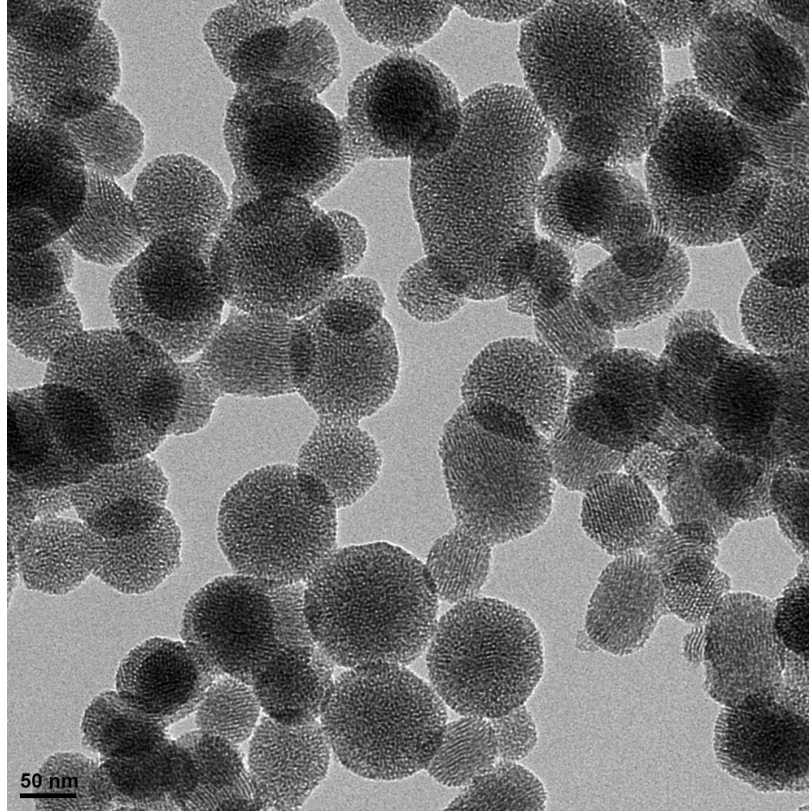


**Figure 4.6.** TEM image of MSNs-PEG after 30 min of probe sonication.



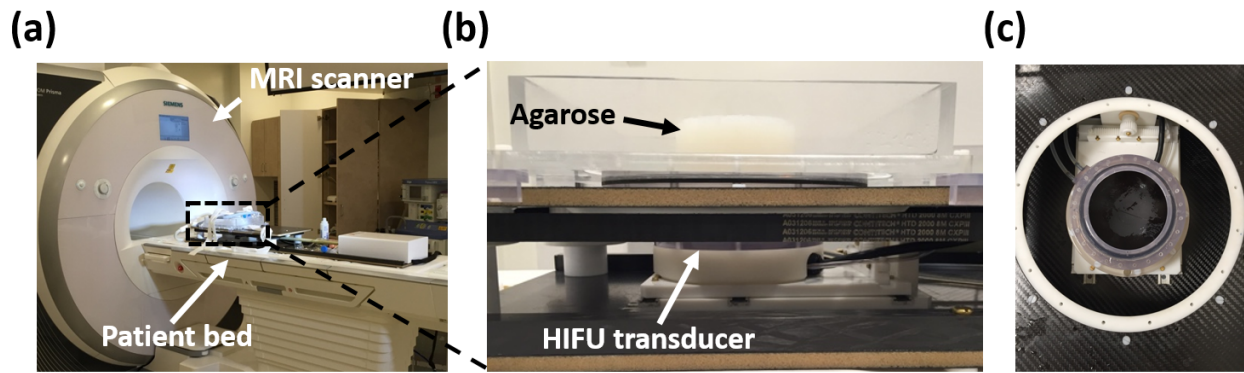


**Figure 4.7.** (a)(b) Set-up of the MRgHIFU system. The agarose phantom was placed on top of the water-cooled HIFU transducer, which was secured on the patient bed in a 3T whole-body MRI scanner. (c) Top view of the HIFU transducer without cooling water and cap.

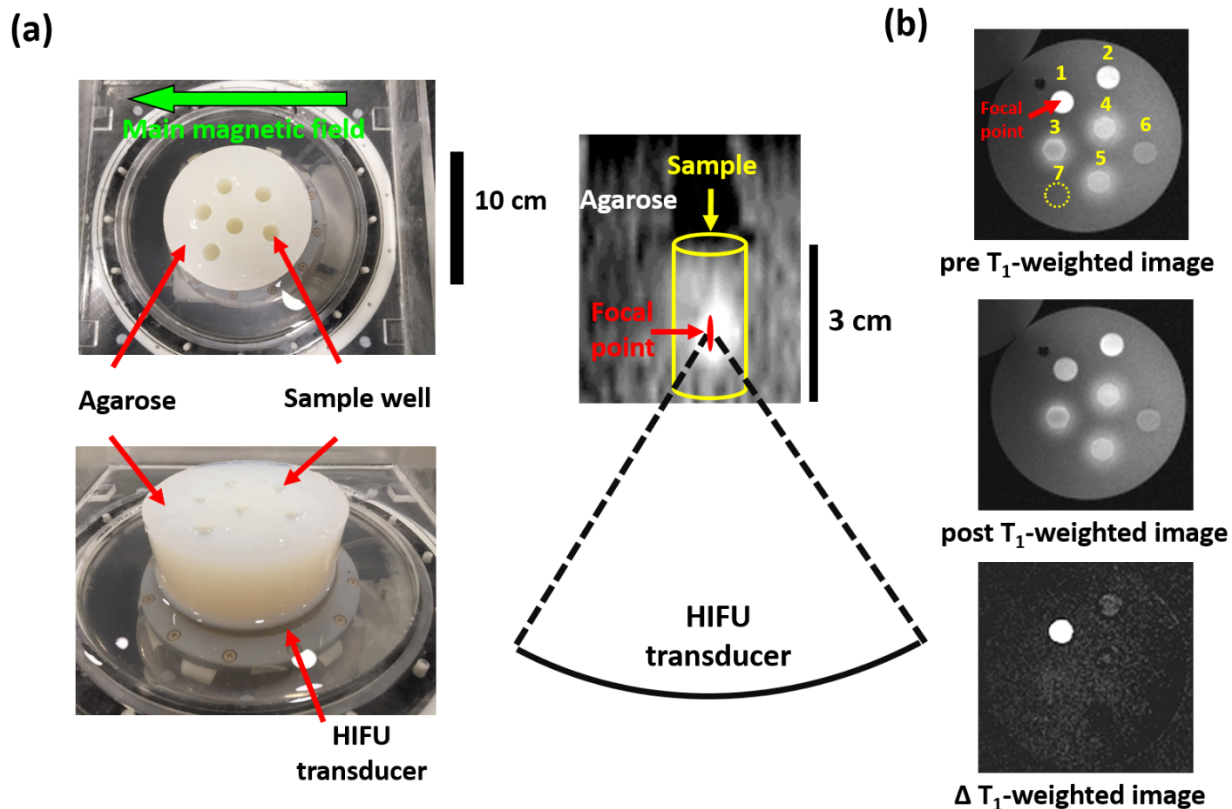


**Figure 4.8.** HIFU-stimulated  $\text{Gd}(\text{DTPA})^{2-}$  release in a tissue-mimicking agarose phantom and the resulting observable MRI contrast changes. (a) Different views of the agarose phantom and the HIFU transducer. The agarose phantom was placed on top of the HIFU transducer. The agarose phantom (10 cm in diameter) was molded with six sample wells (1.3 cm in diameter, 5 cm in height). The cigar-shaped HIFU focal point ( $1 \times 1 \times 7 \text{ mm}^3$  in size) was positioned close to the center of the sample well. (b)  $T_1$ -weighted images before (left) and after (middle) HIFU stimulation (3 cycles of 1 min, 74 W) focused on water-suspended  $\text{Gd}(\text{DTPA})^{2-}$ -loaded MSNs-PEG (sample 1, with the focal point indicated). The  $\Delta T_1$ -weighted image is shown on the right. Unstimulated control groups included: water-suspended  $\text{Gd}(\text{DTPA})^{2-}$ -loaded MSNs-PEG (control 2),  $\text{Gd}(\text{DTPA})^{2-}$ -loaded MSNs-PEG mixed in methylcellulose gel/milk (controls 3-5), and methylcellulose gel/milk (control 6). Control 7 was the agarose phantom.

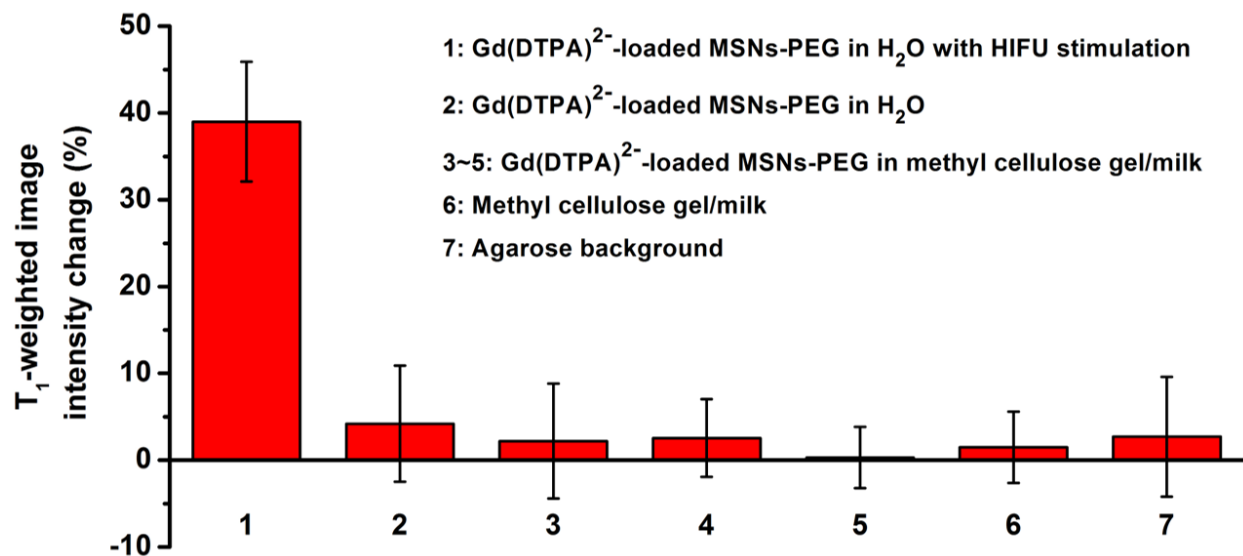


**Figure 4.9.** The percentage of T<sub>1</sub>-weighted image intensity changes of the MRgHIFU-stimulated water-dispersed Gd(DTPA)<sup>2-</sup>-loaded MSNs-PEG (sample 1), unstimulated water-dispersed Gd(DTPA)<sup>2-</sup>-loaded MSNs-PEG (control 2), unstimulated Gd(DTPA)<sup>2-</sup>-loaded MSNs-PEG mixed in methylcellulose (2.5 wt %) and concentrated milk (v/v = 1/1) (controls 3 to 5), the mixture of methylcellulose (2.5 wt %) and concentration milk (v/v = 1/1) (control 6), and agarose phantom background (control 7). The amount of Gd(DTPA)<sup>2-</sup> release of HIFU-stimulated sample 1 was quantified by ICP-OES.

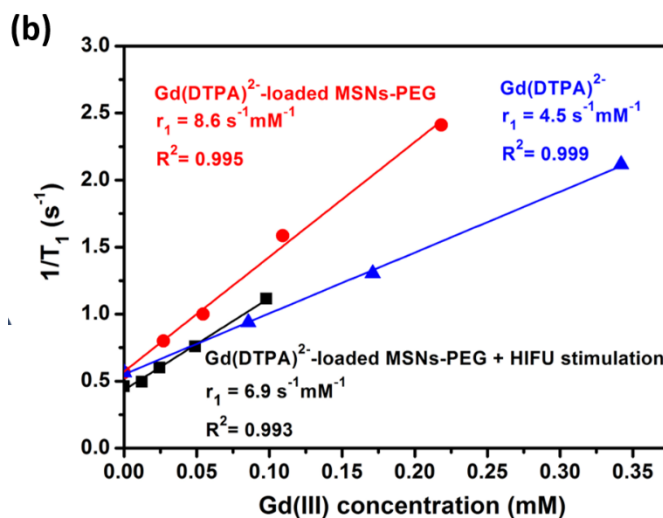
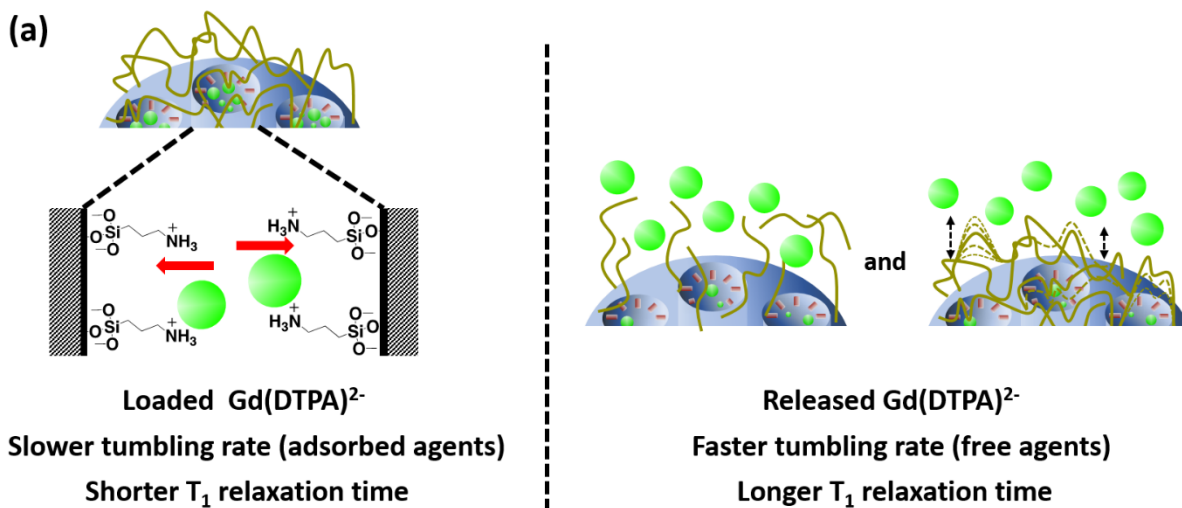
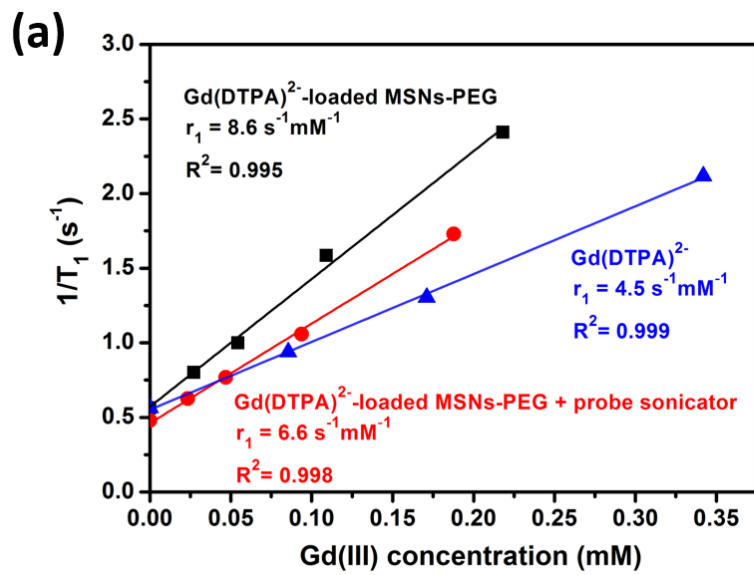


**Figure 4.10.** (a) Schematic illustration showing the shortening and lengthening effect of loaded and released  $\text{Gd}(\text{DTPA})^{2-}$  on  $T_1$  relaxation time. The loaded  $\text{Gd}(\text{DTPA})^{2-}$  inside the pores of MSN-PEG interacts electrostatically with the positively-charged pore wall and acts like an adsorbed agent. This leads to a slower tumbling rate and a shorter  $T_1$  relaxation time of the loaded  $\text{Gd}(\text{DTPA})^{2-}$ . On the contrary, the released  $\text{Gd}(\text{DTPA})^{2-}$  acts like a free agent and leads to a faster tumbling rate and a longer  $T_1$  relaxation time of the released  $\text{Gd}(\text{DTPA})^{2-}$ . (b)  $T_1$  relaxivity ( $r_1$ ) values of free  $\text{Gd}(\text{DTPA})^{2-}$  (blue), and  $\text{Gd}(\text{DTPA})^{2-}$ -loaded MSNs-PEG before (red) and after HIFU stimulation (3 cycles of 1 min, 74 W) (black).



(b)

$\text{Gd(DTPA)}^{2-}$ -loaded MSNs-PEG



$\text{Gd(DTPA)}^{2-}$ -loaded MSNs-PEG + probe sonicator



$\text{Gd(DTPA)}^{2-}$



Gd(III) concentration

**Figure 4.11.** Ultrasound-stimulated  $\text{Gd(DTPA)}^{2-}$  release using a probe sonicator. (a)  $T_1$  relaxivity ( $r_1$ ) values of free  $\text{Gd(DTPA)}^{2-}$  (blue), and  $\text{Gd(DTPA)}^{2-}$ -loaded MSNs-PEG without (black) and with (red) 30 min of ultrasound stimulation by the probe sonicator. (b)  $T_1$ -weighted images of each sample in (a) at different Gd(III) concentrations.

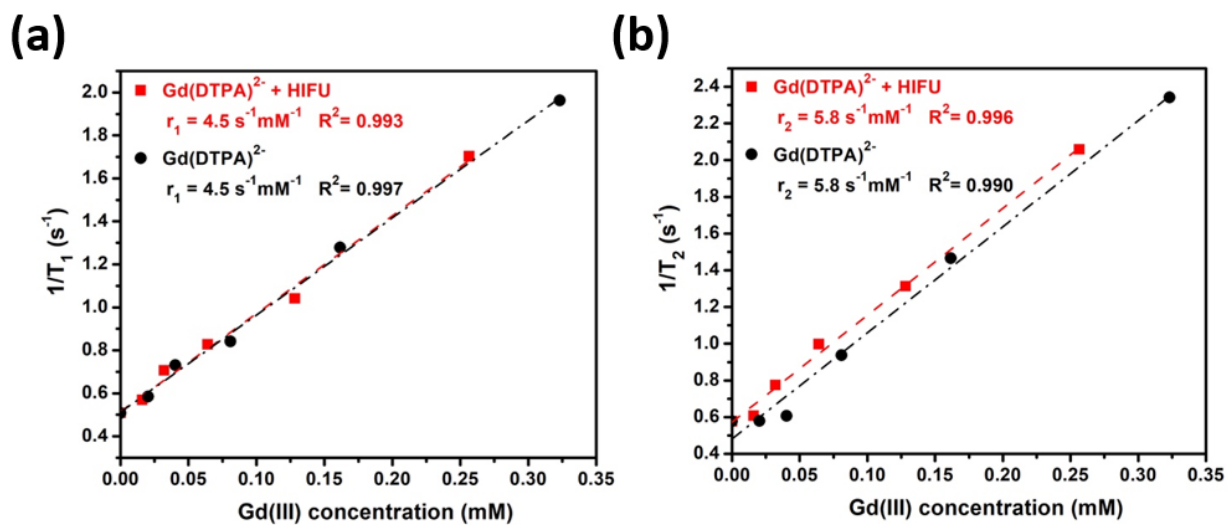


Figure 4.12. (a)  $r_1$  and (b)  $r_2$  values of  $\text{Gd}(\text{DTPA})^{2-}$  with or without HIFU stimulation (3 cycles of 1 min, 74 W).

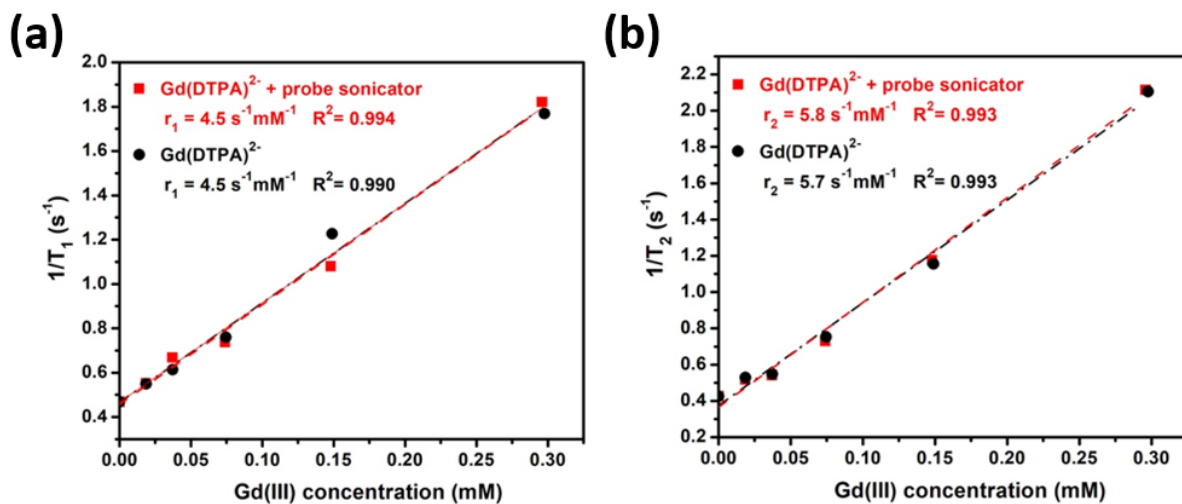
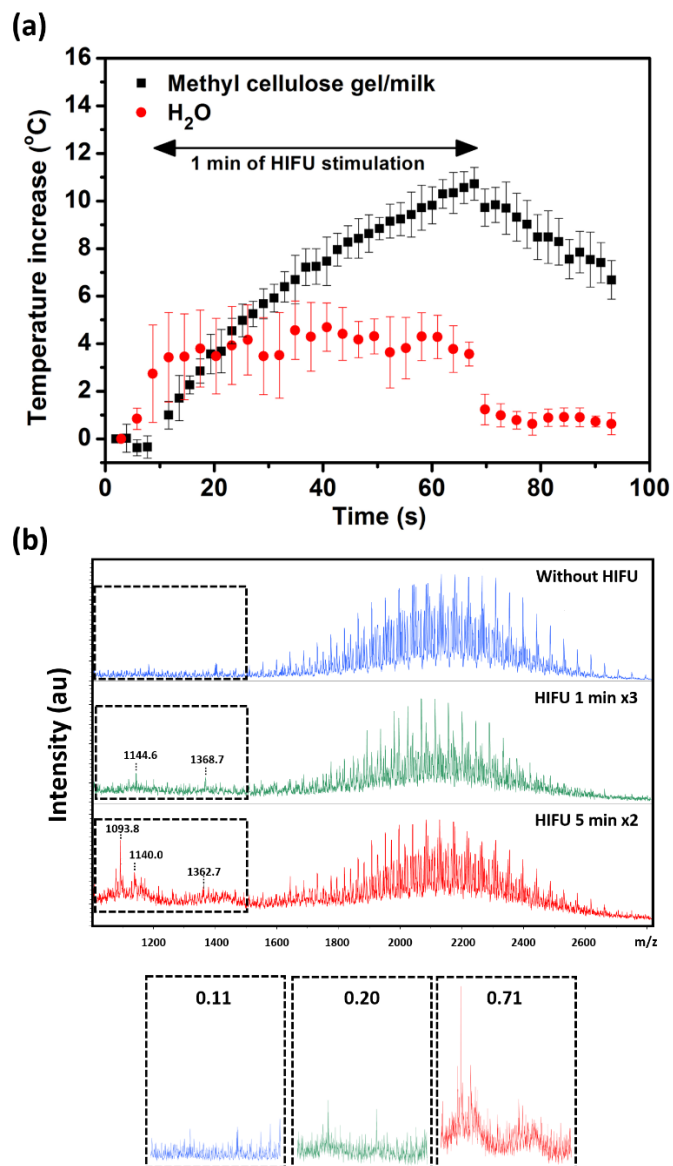
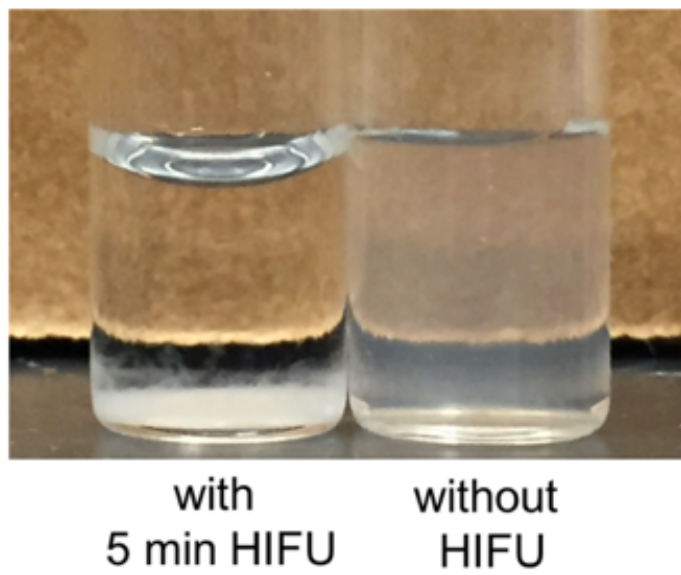


Figure 4.13. (a)  $r_1$  and (b)  $r_2$  values of  $\text{Gd}(\text{DTPA})^{2-}$  with or without 30 min of probe sonication.



**Figure 4.14.** (a) Temperature increase profiles of  $\text{Gd}(\text{DTPA})_2$ -loaded MSNs-PEG in deionized  $\text{H}_2\text{O}$  and in methylcellulose gel/milk mixture during the HIFU stimulation (74 W) measured by dynamic MRI temperature mapping acquired using a 2D gradient-echo protocol (For sample in water: TE= 20 ms, TR= 30 ms, spatial resolution of  $1 \times 1 \times 3 \text{ mm}^3$ , and temporal resolution of 2.8 s; for sample in gel/milk: TE= 10 ms, TR= 20 ms, spatial resolution of  $1 \times 1 \times 3 \text{ mm}^3$ , and temporal resolution of 1.8 s). (b) MALDI-TOF spectra of PEG ( $M_n$  2,000 Da) without HIFU stimulation (top), after 3 cycles of 1 min HIFU stimulation (middle), and 2 cycles of 5 min HIFU stimulation (bottom). The intensity ratios, calculated as the highest intensity of the peak around  $m/z$  1,000/the highest intensity of the peak around  $m/z=2,000$ , were determined to be 0.11, 0.20, and 0.71, respectively.



**Figure 4.15.** The colloidal stability of HIFU-stimulated MSNs-PEG (left tube) and unstimulated MSNs-PEG (right tube) in deionized H<sub>2</sub>O after being kept undisturbed for 30 min. The HIFU-stimulated tube has aggregation at the bottom due to loss of colloidal stability after disruption of PEG caps.



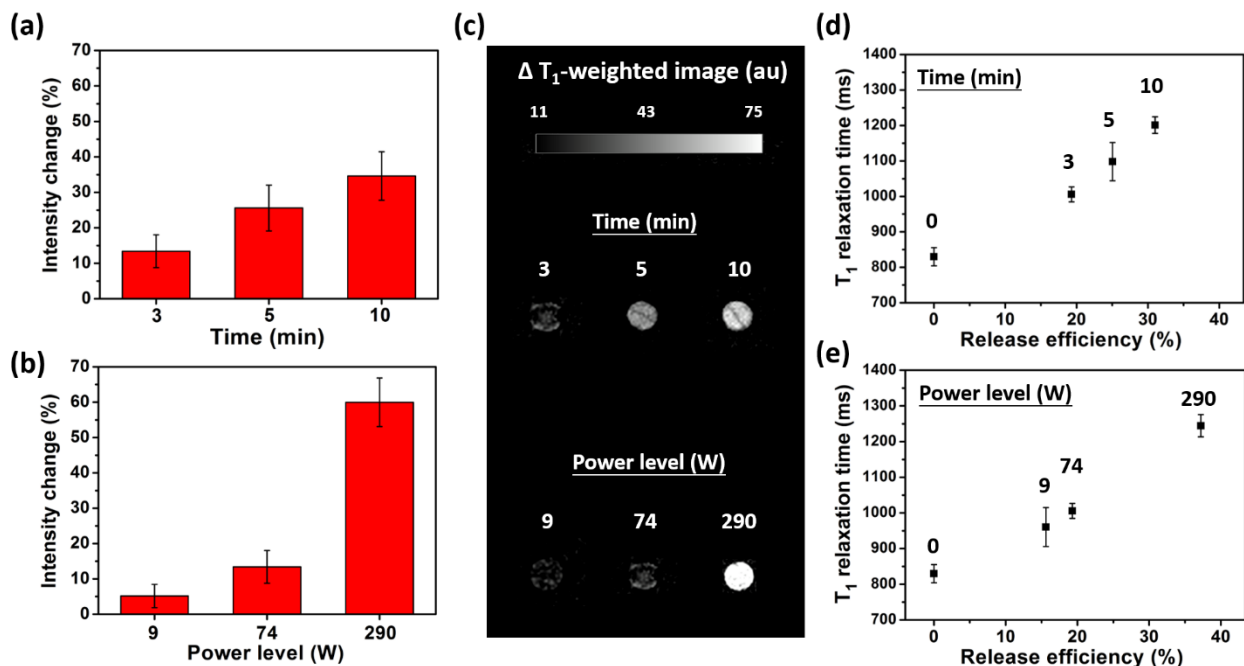


**Figure 4.16.** Dose control of released Gd(DTPA)<sup>2-</sup> and MRI contrast enhancement with different HIFU stimulation parameters. The percentage changes of  $T_1$ -weighted image intensity of Gd(DTPA)<sup>2-</sup>-loaded MSNs-PEG is shown in (a) after 3, 5, or 10 min of HIFU stimulation (1 MHz, 74 W), and in (b) after 3 min of HIFU stimulation at electrical power levels of 9 W, 74 W, or 290 W. (c) The  $\Delta T_1$ -weighted images of each HIFU-stimulated sample in (a) and (b). (d)(e) Correlations between  $T_1$  relaxation times and the release efficiencies of Gd(DTPA)<sup>2-</sup> from HIFU-stimulated samples in (a) and (b), respectively.

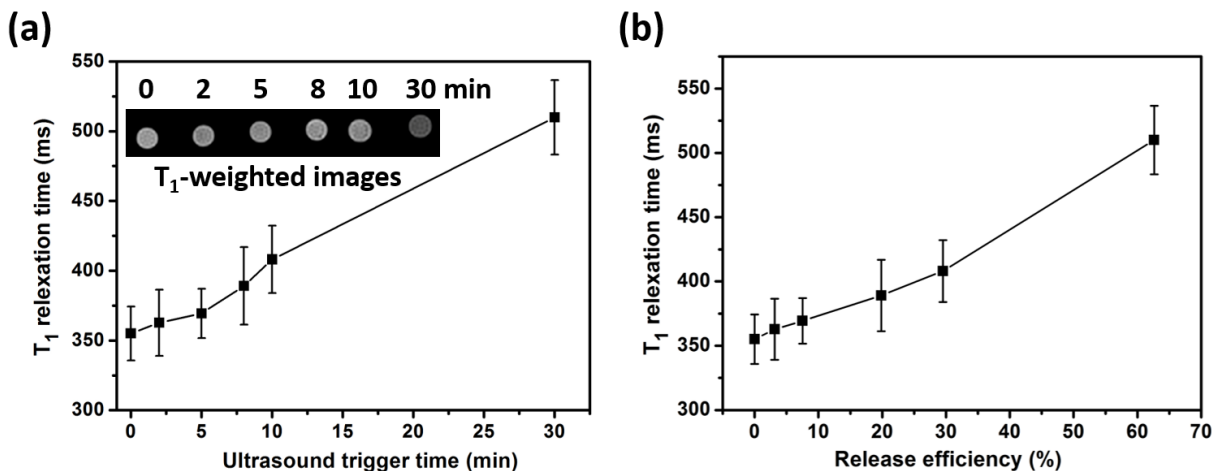


**Figure 4.17.** Ultrasound-stimulated  $\text{Gd}(\text{DTPA})^{2-}$  release using the probe sonicator and the resulting  $T_1$  changes. (a)  $T_1$  of  $\text{Gd}(\text{DTPA})^{2-}$ -loaded MSNs-PEG after 2, 5, 8, 10, and 30 min of probe sonication. Inset shows the corresponding  $T_1$ -weighted images. (b) Positive correlation between  $T_1$  and the release efficiencies of  $\text{Gd}(\text{DTPA})^{2-}$ .

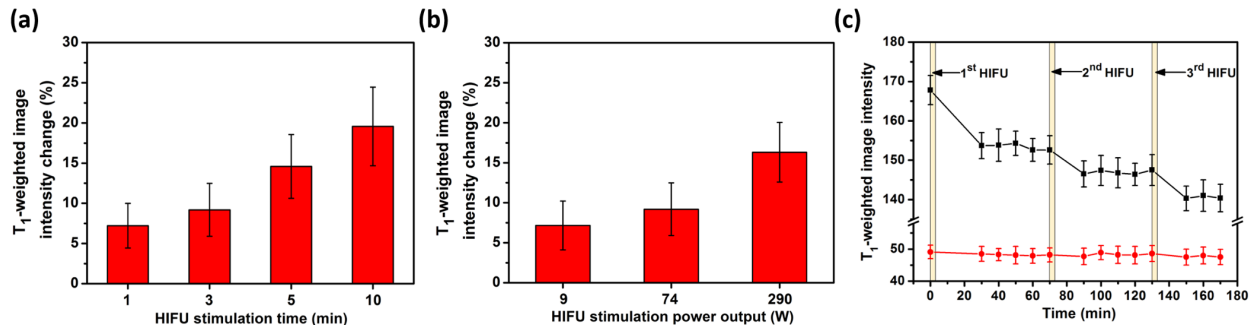


**Figure 4.18.** The percentage of  $T_1$ -weighted image intensity changes of the methylcellulose gel/milk-mixed  $\text{Gd}(\text{DTPA})^{2-}$ -loaded MSNs-PEG (a) after 1, 3, 5, or 10 min of HIFU stimulation (74 W); (b) after 3 min of HIFU stimulation at electrical power levels of 9 W, 74 W, or 290 W. (c) Time-dependent  $T_1$ -weighted image intensity of  $\text{Gd}(\text{DTPA})^{2-}$ -loaded MSNs-PEG with multiple HIFU stimulations (3 cycles of 1 min, 74 W) (shown in black).  $T_1$ -weighted image intensity of agarose background is shown in red. The yellow boxes show the ON time (3 min) of each HIFU stimulation. The OFF times between each ON time were 67 min and 57 min.

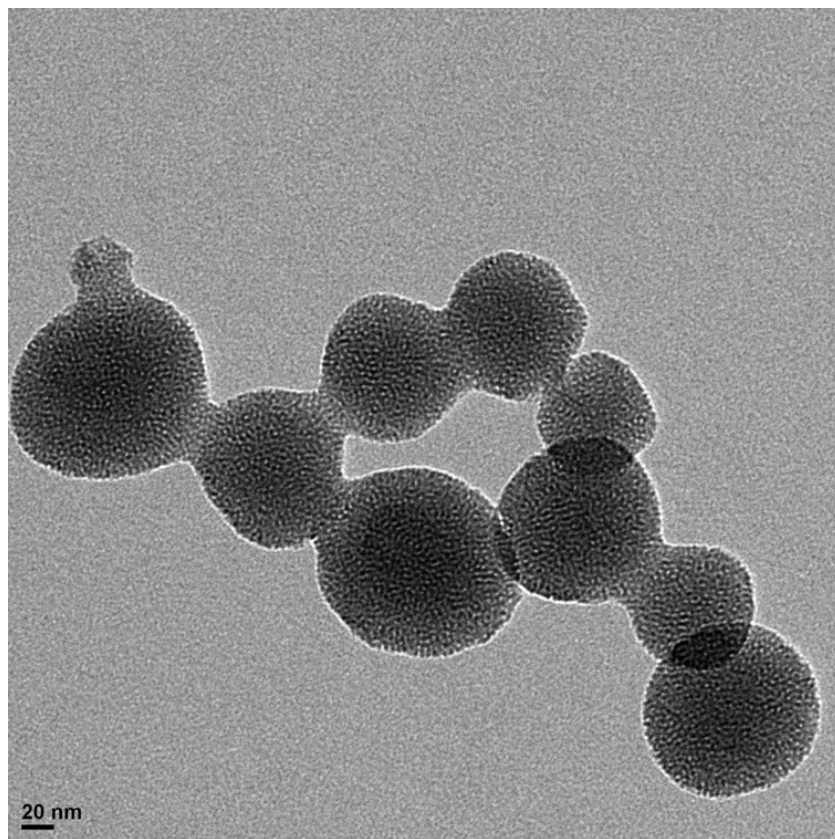


**Figure 4.19.** TEM image of MSNs-PEG after 3 min of HIFU stimulation.

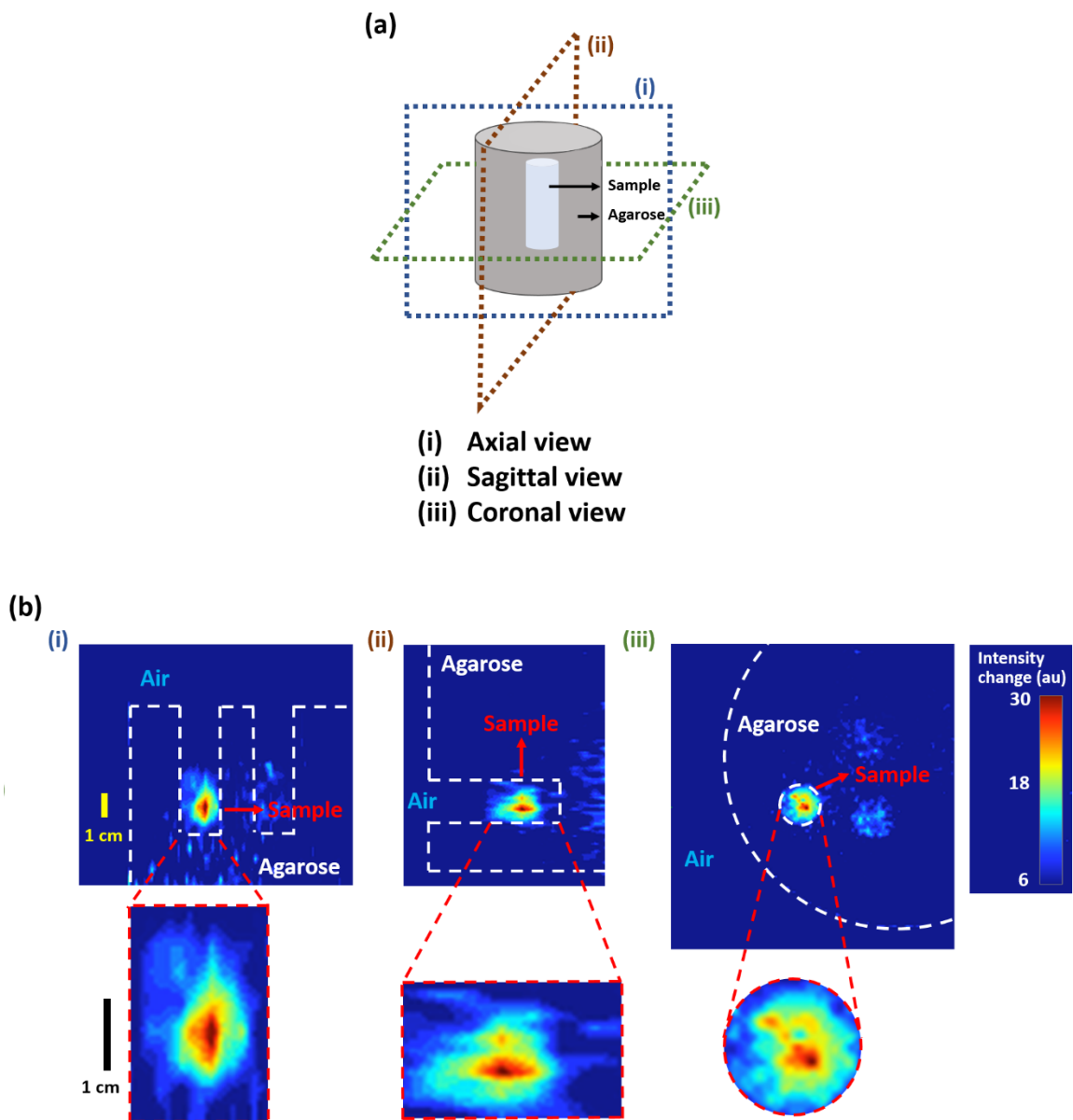


**Figure 4.20.** 3-D control of the MRgHIFU focal point and stimulated cargo release. (a) The axial, sagittal and coronal cross sections of the sample well of interest in the agarose phantom.  $\text{Gd}(\text{DTPA})_2$ -loaded MSNs-PEG were mixed in methylcellulose and placed in a 3 cm-in-depth sample well. The agarose phantom was placed on top of the HIFU transducer and the HIFU beam was focused to a cigar-shaped focal point ( $1 \times 1 \times 7 \text{ mm}^3$ ) near the center of the sample well. The color-coded  $\Delta T_1$ -weighted images in three orientations are shown in (b). The zoomed-in images showed a sharply defined region of image change in 3-D space.

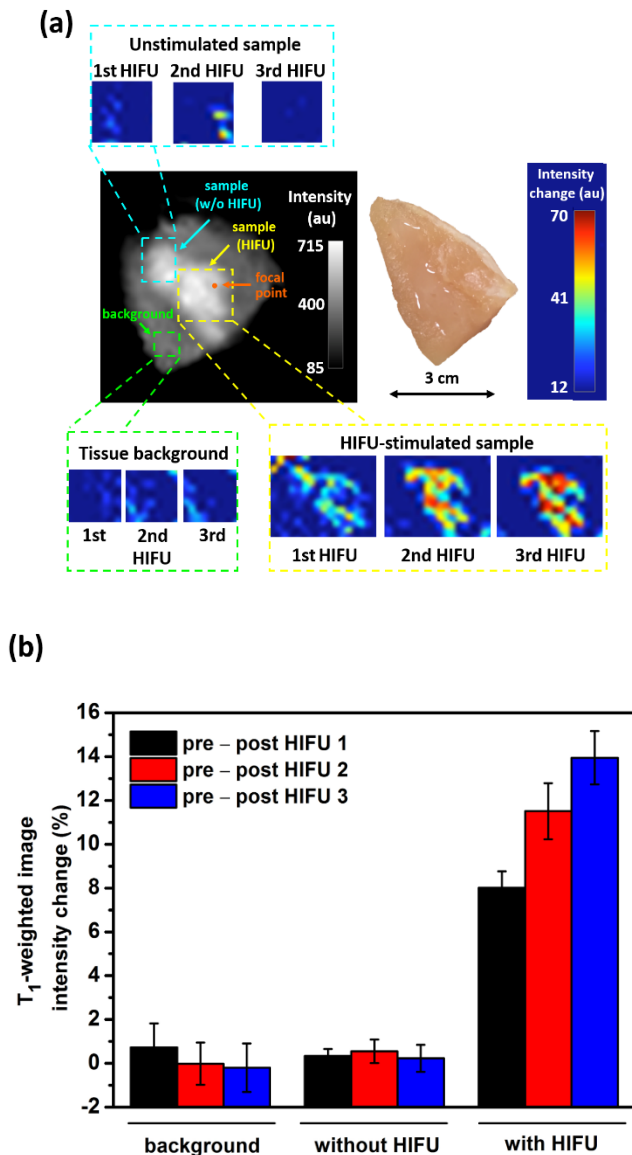


**Figure 4.21.** *Ex vivo* MRgHIFU-stimulated Gd(DTPA)<sup>2-</sup> release and the controllable MRI contrast changes. (a) T<sub>1</sub>-weighted image before HIFU stimulation of the 3 × 6 cm<sup>2</sup> chicken breast tissue injected with methylcellulose gel containing Gd(DTPA)<sup>2-</sup>-loaded MSNs-PEG. The location of the HIFU focal point is indicated by a circle. The color-coded ΔT<sub>1</sub>-weighted images of the HIFU-stimulated sample, unstimulated sample, and tissue background after each cycle of HIFU stimulation (3 min, 2.5 MHz, 8 W) are shown. Total number of cycles= 3. (b) The percentage of T<sub>1</sub>-weighted image intensity changes of the background, unstimulated sample, and HIFU-stimulated sample after each cycle of HIFU stimulation. Error bars were calculated from six analyzed locations within the region of interest. Only the HIFU-stimulated sample showed substantial and progressively increasing T<sub>1</sub>-weighted image intensity change.

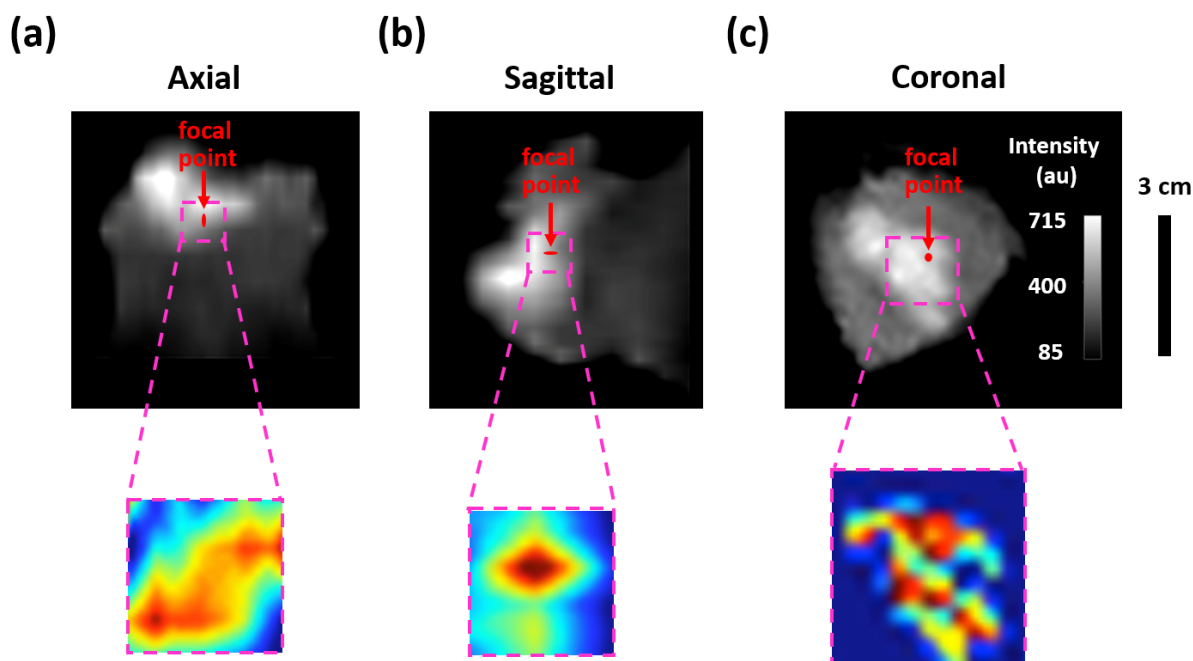


**Figure 4.22.** *Ex vivo* MRgHIFU-stimulated  $\text{Gd}(\text{DTPA})_2^-$  release and the controllable MRI contrast changes in three-dimensional space. A piece of  $3 \times 6 \text{ cm}^2$  chicken breast tissue was injected with methylcellulose gel containing  $\text{Gd}(\text{DTPA})_2^-$ -loaded MSNs-PEG and stimulated with HIFU for 3 cycles of 3 min (2.5 MHz, 8 W). The  $T_1$ -weighted image of the chicken breast before the HIFU stimulation was shown in (a) axial, (b) sagittal, and (c) coronal orientations. The color-coded  $\Delta T_1$ -weighted images, acquired by subtracting the  $T_1$ -weighted images before from the one after 3 cycles of HIFU stimulation, were shown in three-dimensional space.

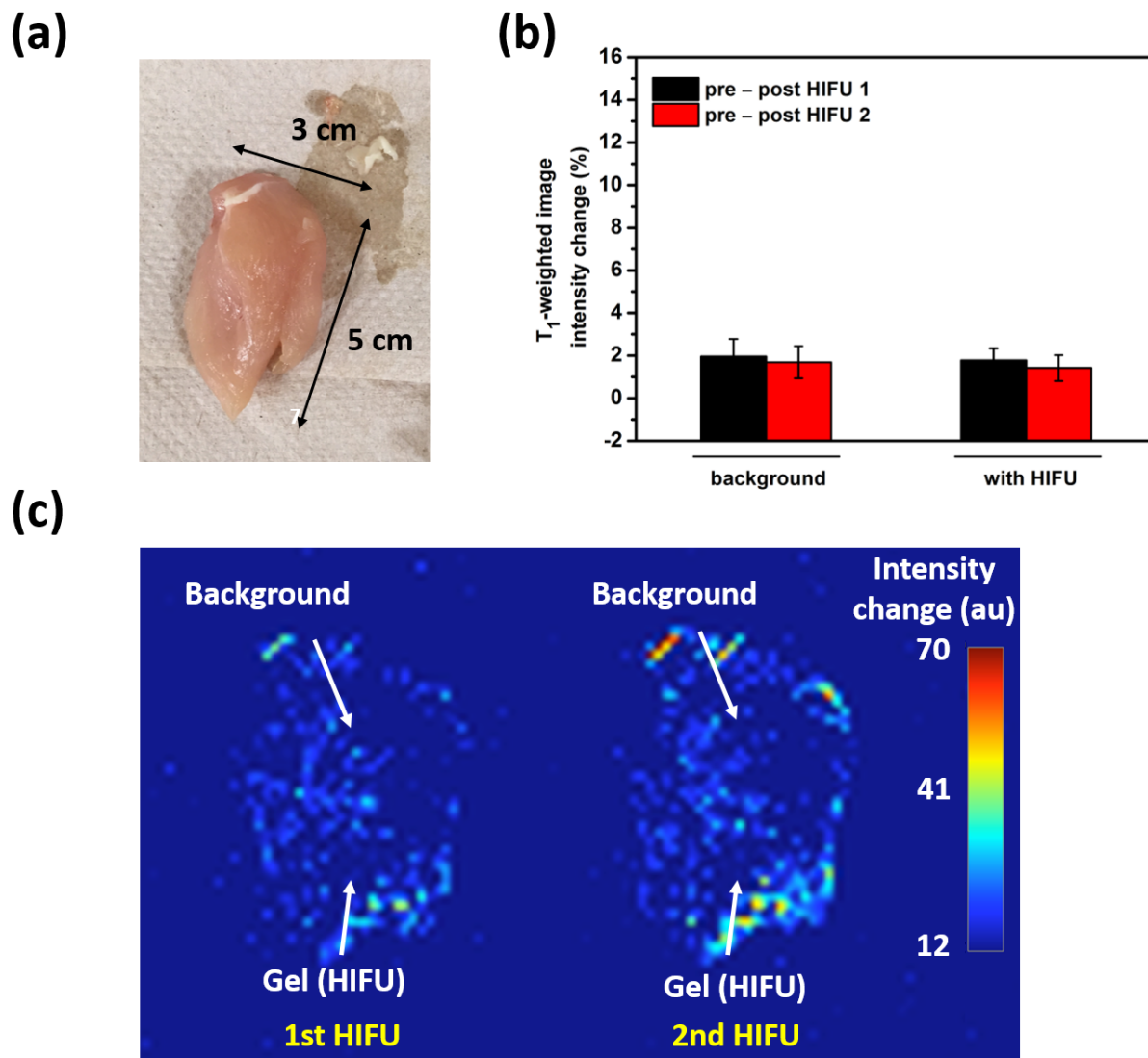


**Figure 4.23.** *Ex vivo* MRgHIFU control experiment. (a) A piece of chicken breast tissue (3 cm × 5 cm) was injected with methylcellulose gel only. (b) The percentage of  $T_1$ -weighted image intensity changes of the tissue background and the HIFU-stimulated gel after each cycle of HIFU stimulation (3 min, 2.5 MHz, 8 W). Total number of cycles= 2. (c) Color-coded  $\Delta T_1$ -weighted images of the chicken tissue after each cycle of HIFU stimulation. The position of HIFU-stimulated gel and tissue background was indicated.

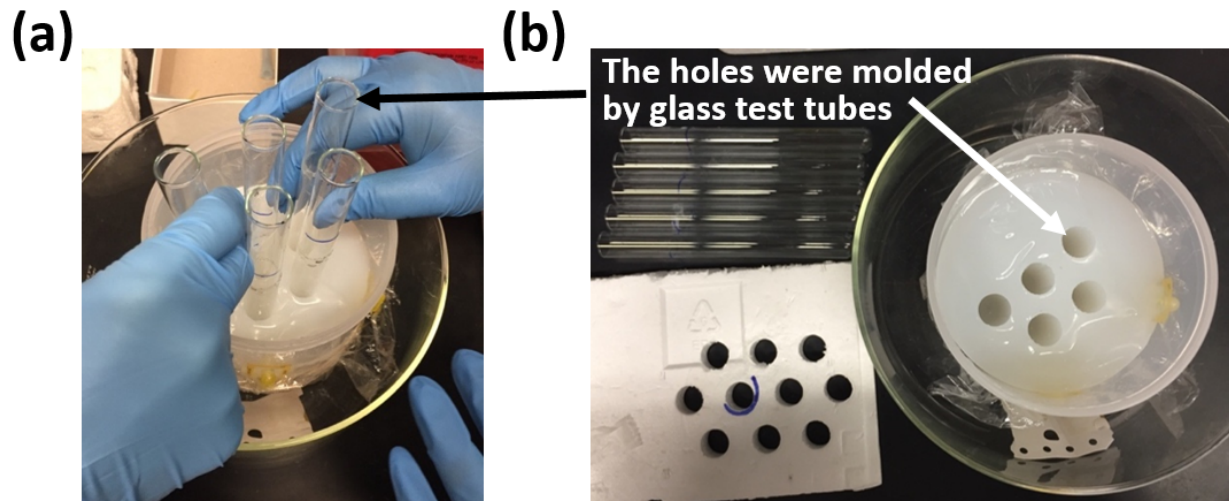


**Figure 4.24.** Preparation of the agarose phantom. (a) Before the removal of the glass test tubes, and (b) after the removal of the glass test tubes. Five sample wells were molded in the agarose phantom.



	MSNs	MSNs-APTS	MSNs-PEG	Gd(DTPA) <sup>2-</sup> -loaded MSNs-PEG
<b>BET surface area (m<sup>2</sup>/g)</b>	1045	595	108	99
<b>Pore volume (cc/g)</b>	1.04	0.52	0.19	0.13
<b>Average pore diameter (nm)</b>	2.9	2.4	N/A	N/A

**Table 4.1.** Brunauer-Emmett-Teller (BET) surface area, total pore volume, and average pore diameter of MSNs, MSNs-APTS, MSNs-PEG, and Gd(DTPA)<sup>2-</sup>-loaded MSNs-PEG analyzed from the N<sub>2</sub> adsorption/desorption isotherms.

<b>HIFU parameters (power level, stimulation time)</b>	<b>Release efficiency</b>	<b>Temperature increase</b>
(9 W, 3 min)	15.61 %	1 °C
(74 W, 3 min)	19.29 %	4 °C
(74 W, 5 min)	25.05 %	7 °C
(74 W, 10 min)	31.01 %	10 °C
(290 W, 3 min)	37.22 %	10 °C

**Table 4.2.** Summary of the Gd(DTPA)<sup>2-</sup> release efficiency and temperature increase using various HIFU parameters (power levels and stimulation times).

## 4.16 References

- (1) Terreno, E.; Castelli, D. D.; Viale, A.; Aime, S. Challenges for Molecular Magnetic Resonance Imaging. *Chem. Rev.* **2010**, *110*, 3019-3042.
- (2) Ahmed, H. U.; Hindley, R. G.; Dickinson, L.; Freeman, A.; Kirkham, A. P.; Sahu, M.; Scott, R.; Allen, C.; Van der Meulen, J.; Emberton, M. Focal Therapy for Localised Unifocal and Multifocal Prostate Cancer: A Prospective Development Study. *Lancet Oncol.* **2012**, *13*, 622-632.
- (3) Hynynen, K. MRI-Guided Focused Ultrasound Treatments. *Ultrasonics* **2010**, *50*, 221-229.
- (4) Hirsch, L. R.; Stafford, R. J.; Bankson, J. A.; Sershen, S. R.; Rivera, B.; Price, R. E.; Hazle, J. D.; Halas, N. J.; West, J. L. Nanoshell-Mediated Near-Infrared Thermal Therapy of Tumors Under Magnetic Resonance Guidance. *Proc. Natl. Acad. Sci. U.S.A.* **2003**, *100*, 13549-13554.
- (5) Medvid, R.; Ruiz, A.; Komotar, R. J.; Jagid, J. R.; Ivan, M. E.; Quencer, R. M.; Desai, M. B. Current Applications of MRI-Guided Laser Interstitial Thermal Therapy in the Treatment of Brain Neoplasms and Epilepsy: A Radiologic and Neurosurgical Overview. *Am. J. Neuroradiol.* **2015**, *36*, 1998-2006.
- (6) Sun, Q.; You, Q.; Wang, J.; Liu, L.; Wang, Y.; Song, Y.; Cheng, Y.; Wang, S.; Tan, F.; Li, N. Theranostic Nanoplatfrom: Triple-Modal Imaging-Guided Synergistic Cancer Therapy Based on Liposome-Conjugated Mesoporous Silica Nanoparticles. *ACS Appl. Mater. Interfaces* **2018**, *10*, 1963-1975.
- (7) Rieke, V.; Pauly, K. B. MR Thermometry. *J. Magn. Reson. Imaging* **2008**, *27*, 376-390.
- (8) Schlesinger, D.; Benedict, S.; Diederich, C.; Gedroyc, W.; Klibanov, A.; Lerner, J. MR-Guided Focused Ultrasound Surgery, Present and Future. *Med. Phys.* **2013**, *40*, 080901.
- (9) Minh Duc, N.; Keserci, B. Emerging Clinical Applications of High-intensity Focused Ultrasound. *Diagn. Interv. Radiol.* **2019**, *25*, 398-409.
- (10) Frenkel, V. Ultrasound Mediated Delivery of Drugs and Genes to Solid Tumors. *Adv. Drug Deliv. Rev.* **2008**, *60*, 1193-1208.
- (11) Centelles, M. N.; Wright, M.; So, P. W.; Amrahli, M.; Xu, X. Y.; Stebbing, J.; Miller, A. D.; Gedroyc, W.; Thanou, M. Image-Guided Thermosensitive Liposomes for Focused Ultrasound Drug Delivery: Using NIRF-Labelled Lipids and Topotecan to Visualise the Effects of Hyperthermia in Tumours. *J. Control. Release* **2018**, *280*, 87-98.
- (12) Tang, H.; Guo, Y.; Peng, L.; Fang, H.; Wang, Z.; Zheng, Y.; Ran, H.; Chen, Y. In Vivo Targeted, Responsive, and Synergistic Cancer Nanotheranostics by Magnetic Resonance Imaging-Guided Synergistic High-Intensity Focused Ultrasound Ablation and Chemotherapy. *ACS Appl. Mater. Interfaces* **2018**, *10*, 15428-15441.
- (13) Ma, M.; Xu, H.; Chen, H.; Jia, X.; Zhang, K.; Wang, Q.; Zheng, S.; Wu, R.; Yao, M.; Cai, X.; Li, F.; Shi, J. A Drug-Perfluorocarbon Nanoemulsion with an Ultrathin Silica Coating for the Synergistic

- Effect of Chemotherapy and Ablation by High-Intensity Focused Ultrasound. *Adv. Mater.* **2014**, *26*, 7378–7385.
- (14) Dromi, S.; Frenkel, V.; Luk, A.; Traughber, B.; Angstadt, M.; Bur, M.; Poff, J.; Xie, J.; Libutti, S. K.; Li, K. C. P.; Wood, B. J. Pulsed-High Intensity Focused Ultrasound and Low Temperature-Sensitive Liposomes for Enhanced Targeted Drug Delivery and Antitumor Effect. *Clin. Cancer Res.* **2007**, *13*, 2722-2727.
- (15) Hijnen, N.; Langereis, S.; Grüll, H. Magnetic Resonance Guided High-Intensity Focused Ultrasound for Image-Guided Temperature-Induced Drug Delivery. *Adv. Drug Deliv. Rev.* **2014**, *72*, 65-81.
- (16) Kheiriloom, A.; Lai, C. Y.; Tam, S. M.; Mahakian, L. M.; Ingham, E. S.; Watson, K. D.; Ferrara, K. W. Complete Regression of Local Cancer Using Temperature-Sensitive Liposomes Combined with Ultrasound-Mediated Hyperthermia. *J. Control. Release* **2013**, *172*, 266-273.
- (17) De Smet, M.; Heijman, E.; Langereis, S.; Hijnen, N. M.; Grüll, H. Magnetic Resonance Imaging of High Intensity Focused Ultrasound Mediated Drug Delivery from Temperature-Sensitive Liposomes: An in vivo Proof-of-Concept Study. *J. Control. Release* **2011**, *150*, 102-110.
- (18) Partanen, A.; Yarmolenko, P. S.; Viitala, A.; Appanaboyina, S.; Haemmerich, D.; Ranjan, A.; Jacobs, G.; Woods, D.; Enholm, J.; Wood, B. J.; Dreher, M. R. Mild Hyperthermia with Magnetic Resonance-Guided High-Intensity Focused Ultrasound for Applications in Drug Delivery. *Int. J. Hyperthermia* **2012**, *28*, 320-336.
- (19) National Institutes of Health - U.S. National Library of Medicine  
<https://clinicaltrials.gov/ct2/show/NCT03749850?term=i-go+feasibility&rank=1>
- (20) Issels, R. D. Hyperthermia Adds to Chemotherapy. *Eur. J. Cancer* **2008**, *44*, 2546-2554.
- (21) Kong, G.; Braun, R. D.; Dewhirst, M. W. Characterization of the Effect of Hyperthermia on Nanoparticle Extravasation from Tumor Vasculature. *Cancer Res.* **2001**, *61*, 3027-3032.
- (22) Thrall, D. E.; LaRue, S. M.; Yu, D.; Samulski, T.; Sanders, L.; Case, B.; Rosner, G.; Azuma, C.; Poulson, J.; Pruitt, A. F.; Stanley, W.; Hauck, M. L.; Williams, L.; Hess, P.; Dewhirst, M. W. Thermal Dose Is Related to Duration of Local Control in Canine Sarcomas Treated with Thermoradiotherapy. *Clin. Cancer Res.* **2005**, *11*, 5206-5214.
- (23) Jones, E.; Thrall, D.; Dewhirst, M. W.; Vujaskovic, Z. Prospective Thermal Dosimetry: The Key to Hyperthermia's Future. *Int. J. Hyperthermia* **2006**, *22*, 247-253.
- (24) Hegewisch-Becker, S.; Braun, K.; Otte, M.; Corovic, A.; Atanackovic, D.; Nierhaus, A.; Hossfeld, D. K.; Pantel, K. Effects of Whole Body Hyperthermia (41.8 Degrees C) on the Frequency of Tumor Cells in the Peripheral Blood of Patients with Advanced Malignancies. *Clin. Cancer Res.* **2003**, *9*, 2079-2084.
- (25) Hegyi, G.; Szigeti, G. P.; Szász, A. Hyperthermia versus Oncothermia: Cellular Effects in Complementary Cancer Therapy. *Evid.-Based Complementary Altern. Med.* **2013**, 672873.

- (26) Yerushalmi, A. Influence on Metastatic Spread of Whole-Body or Local Tumor Hyperthermia. *Eur. J. Cancer* **1976**, *12*, 455-463.
- (27) Zhang, Y.; Yu, J.; Bomba, H. N.; Zhu, Y.; Gu, Z. Mechanical Force-Triggered Drug Delivery. *Chem. Rev.* **2016**, *116*, 12536-12563.
- (28) Kost, J.; Leong, K.; Langer, R. Ultrasound-Enhanced Polymer Degradation and Release of Incorporated Substances. *Proc. Natl. Acad. Sci. U. S. A.* **1989**, *86*, 7663-7666.
- (29) Sirsi, S. R.; Borden, M. A. State-of-the-Art Materials for Ultrasound-Triggered Drug Delivery. *Adv. Drug Deliv. Rev.* **2014**, *72*, 3-14.
- (30) Mura, S.; Nicolas, J.; Couvreur, P. Stimuli-responsive Nanocarriers for Drug Delivery. *Nat. Mater.* **2013**, *12*, 991-1003.
- (31) Liu, Y.; Miyoshi, H.; Nakamura, M. Encapsulated Ultrasound Microbubbles: Therapeutic Application in Drug/Gene Delivery. *J. Control. Release* **2006**, *114*, 89-99.
- (32) Geers, B.; Lentacker, I.; Sanders, N. N.; Demeester, J.; Meairs, S.; De Smedt, S. C. Self-Assembled Liposome-Loaded Microbubbles: The Missing Link for Safe and Efficient Ultrasound Triggered Drug-Delivery. *J. Control. Release* **2011**, *152*, 249-256.
- (33) Wang, J.; Pelletier, M.; Zhang, H.; Xia, H.; Zhao, Y. High-Frequency Ultrasound-Responsive Block Copolymer Micelle. *Langmuir* **2009**, *25*, 13201-13205.
- (34) Xuan, J.; Boissière, O.; Zhao, Y.; Yan, B.; Tremblay, L.; Lacelle, S.; Xia, H.; Zhao, Y. Ultrasound-Responsive Block Copolymer Micelles Based on a New Amplification Mechanism. *Langmuir* **2012**, *28*, 16463-16468.
- (35) Li, F.; Xie, C.; Cheng, Z.; Xia, H. Ultrasound Responsive Block Copolymer Micelle of Poly(Ethylene Glycol)-Poly(Propylene Glycol) Obtained through Click Reaction. *Ultrason. Sonochem.* **2016**, *30*, 9-17.
- (36) Chen, H.; Li, J.; Wan, J.; Weitz, D. A.; Stone, H. A. Gas-Core Triple Emulsions for Ultrasound Triggered Release. *Soft Matter* **2013**, *9*, 38-42.
- (37) Xi, J.; Qian, X.; Qian, K.; Zhang, W.; He, W.; Chen, Y.; Han, J.; Zhang, Y.; Yang, X.; Fan, L. Au Nanoparticle-Coated, PLGA-Based Hybrid Capsules for Combined Ultrasound Imaging and HIFU Therapy. *J. Mater. Chem. B* **2015**, *3*, 4213-4220.
- (38) Wang, T. Y.; Choe, J. W.; Pu, K.; Devulapally, R.; Bachawal, S.; Machtaler, S.; Chowdhury, S. M.; Luong, R.; Tian, L.; Khuri-Yakub, B.; Rao, J.; Paulmurugan, R.; Willmann, J. K. Ultrasound-Guided Delivery of MicroRNA Loaded Nanoparticles into Cancer. *J. Control. Release* **2015**, *203*, 99-108.
- (39) Chumakova, O. V.; Liopo, A. V.; Andreev, V. G.; Cicenaitis, I.; Evers, B. M.; Chakrabarty, S.; Pappas, T. C.; Esenaliev, R. O. Composition of PLGA and PEI/DNA Nanoparticles Improves Ultrasound-Mediated Gene Delivery in Solid Tumors in Vivo. *Cancer Lett.* **2008**, *261*, 215-225.

- (40) Xuan, J.; Boissière, O.; Zhao, Y.; Yan, B.; Tremblay, L.; Lacelle, S.; Xia, H.; Zhao, Y. Advanced Stimuli-responsive Polymer Nanocapsules with Enhanced Capabilities for Payloads Delivery. *Polym. Chem.* **2015**, *6*, 4197–4205.
- (41) Nakanishi, T.; Fukushima, S.; Okamoto, K.; Suzuki, M.; Matsumura, Y.; Yokoyama, M.; Okano, T.; Sakurai, Y.; Kataoka, K. Development of the Polymer Micelle Carrier System for Doxorubicin. *J. Control. Release* **2001**, *74*, 295-302.
- (42) Sun, X.; Wang, G.; Zhang, H.; Hu, S.; Liu, X.; Tang, J.; Shen, Y. The Blood Clearance Kinetics and Pathway of Polymeric Micelles in Cancer Drug Delivery. *ACS Nano* **2018**, *12*, 6179-6192.
- (43) Maeda, H. Macromolecular Therapeutics in Cancer Treatment: The EPR Effect and Beyond. *J. Control. Release* **2012**, *164*, 138-144.
- (44) Maeda, H.; Nakamura, H.; Fang, J. The EPR Effect for Macromolecular Drug Delivery to Solid Tumors: Improvement of Tumor Uptake, Lowering of Systemic Toxicity, and Distinct Tumor Imaging in Vivo. *Adv. Drug Deliv. Rev.* **2013**, *65*, 71-79.
- (45) Maeda, H.; Khatami, M. Analyses of Repeated Failures in Cancer Therapy for Solid Tumors: Poor Tumor-Selective Drug Delivery, Low Therapeutic Efficacy and Unsustainable Costs. *Clin. Transl. Med.* **2018**, *7*, 11.
- (46) Chen, W.; Cheng, C.-A.; Lee, B.-Y.; Clemens, D. L.; Huang, W.-Y.; Horwitz, M. A.; Zink, J. I. A Facile Strategy Enabling Both High Loading and High Release Amounts of the Water-Insoluble Drug Clofazimine Using Mesoporous Silica Nanoparticles. *ACS Appl. Mater. Interfaces* **2018**, *10*, 31870-31881.
- (47) Chen, W.; Cheng, C.-A.; Cosco, E. D.; Ramakrishnan, S.; Lingg, J. G. P.; Bruns, O.T.; Zink, J. I.; Sletten, E.M. Shortwave Infrared Imaging with J-Aggregates Stabilized in Hollow Mesoporous Silica Nanoparticles. *J. Am. Chem. Soc.* **2019**, *141*, 12475–12480.
- (48) Manzano, M.; Vallet-Regí, M. Mesoporous Silica Nanoparticles for Drug Delivery. *Adv. Funct. Mater.* **2019**, 1902634.
- (49) Chen, W.; Glackin, C. A.; Horwitz, M. A.; Zink, J. I. Nanomachines and Other Caps on Mesoporous Silica Nanoparticles for Drug Delivery. *Acc. Chem. Res.* **2019**, *52*, 1531-1542.
- (50) Guardado-Alvarez, T. M.; Chen, W.; Norton, A. E.; Russell, M. M.; Connick, W. B.; Zink, J. I. Analyte-Responsive Gated Hollow Mesoporous Silica Nanoparticles Exhibiting Inverse Functionality and an AND Logic Response. *Nanoscale* **2016**, *8*, 18296-18300.
- (51) Croissant, J. G.; Fatieiev, Y.; Khashab, N. M. Degradability and Clearance of Silicon, Organosilica, Silsesquioxane, Silica Mixed Oxide, and Mesoporous Silica Nanoparticles. *Adv. Mater.* **2017**, *29*, 1604634.
- (52) Chou, C.-C.; Chen, W.; Hung, Y.; Mou, C.-Y. Molecular Elucidation of Biological Response to Mesoporous Silica Nanoparticles in Vitro and in Vivo. *ACS Appl. Mater. Interfaces* **2017**, *9*, 22235-22251.

- (53) Wu, S.-H.; Mou, C.-Y.; Lin, H.-P. Synthesis of Mesoporous Silica Nanoparticles. *Chem. Soc. Rev.* **2013**, *42*, 3862-3875.
- (54) Cheng, C.-A.; Deng, T.; Lin, F.-C.; Cai, Y.; Zink, J. I. Supramolecular Nanomachines as Stimuli-Responsive Gatekeepers on Mesoporous Silica Nanoparticles for Antibiotic and Cancer Drug Delivery. *Theranostics* **2019**, *9*, 3341-3364.
- (55) Chen, W.; Cheng, C.-A.; Zink, J. I. Spatial, Temporal, and Dose Control of Drug Delivery Using Noninvasive Magnetic Stimulation. *ACS Nano* **2019**, *13*, 1292-1308.
- (56) Tarn, D.; Ashley, C. E.; Xue, M.; Carnes, E. C.; Zink, J. I.; Brinker, C. J. Mesoporous Silica Nanoparticle Nanocarriers: Biofunctionality and Biocompatibility. *Acc. Chem. Res.* **2013**, *46*, 792-801.
- (57) Argyo, C.; Weiss, V.; Bräuchle, C.; Bein, T. Multifunctional Mesoporous Silica Nanoparticles as a Universal Platform for Drug Delivery. *Chem. Mater.* **2014**, *26*, 435-451.
- (58) Chen, W.; Lu, F.; Chen, C. C. V; Mo, K. C.; Hung, Y.; Guo, Z. X.; Lin, C. H.; Lin, M. H.; Lin, Y. H.; Chang, C.; Mou, C. Y. Manganese-Enhanced MRI of Rat Brain Based on Slow Cerebral Delivery of Manganese(II) with Silica-Encapsulated  $Mn_xFe_{1-x}O$  Nanoparticles. *NMR Biomed.* **2013**, *26*, 1176-1185.
- (59) Kumar, N.; Chen, W.; Cheng, C.-A.; Deng, T.; Wang, R.; Zink, J. Stimuli-Responsive Nanomachines and Caps for Drug Delivery. *The Enzymes* **2018**, *43*, 31-65.
- (60) Li, Z.; Barnes, J. C.; Bosoy, A.; Stoddart, J. F.; Zink, J. I. Mesoporous Silica Nanoparticles in Biomedical Applications. *Chem. Soc. Rev.* **2012**, *41*, 2590-2605.
- (61) Manzano, M.; Vallet-Regí, M. Ultrasound Responsive Mesoporous Silica Nanoparticles for Biomedical Applications. *Chem. Commun.* **2019**, *55*, 2731-2740.
- (62) Li, X.; Wang, Z.; Xia, H. Ultrasound Reversible Response Nanocarrier Based on Sodium Alginate Modified Mesoporous Silica Nanoparticles. *Front. Chem.* **2019**, *7*, 59.
- (63) Paris, J. L.; Cabanas, M. V.; Manzano, M.; Vallet-Regí, M. Polymer-Grafted Mesoporous Silica Nanoparticles as Ultrasound-Responsive Drug Carriers. *ACS Nano* **2015**, *9*, 11023-11033.
- (64) Paris, J. L.; de la Torre, P.; Cabañas, M. V.; Manzano, M.; Grau, M.; Flores, A. I.; Vallet-Regí, M. Vectorization of Ultrasound-responsive Nanoparticles in Placental Mesenchymal Stem Cells for Cancer Therapy. *Nanoscale* **2017**, *4*, 5528-5537.
- (65) Anirudhan, T. S.; Nair, A. S. Temperature and Ultrasound Sensitive Gatekeepers for the Controlled Release of Chemotherapeutic Drugs from Mesoporous Silica Nanoparticles. *J. Mater. Chem. B* **2018**, *6*, 428-439.
- (66) Li, X.; Xie, C.; Xia, H.; Wang, Z. pH and Ultrasound Dual-Responsive Polydopamine-Coated Mesoporous Silica Nanoparticles for Controlled Drug Delivery. *Langmuir* **2018**, *34*, 9974-9981.

- (67) Kawasaki, H.; Takeda, Y.; Arakawa, R. Mass Spectrometric Analysis for High Molecular Weight Synthetic Polymers Using Ultrasonic Degradation and the Mechanism of Degradation. *Anal. Chem.* **2007**, *79*, 4182-4187.
- (68) Ferrari, M. Nanovector Therapeutics. *Curr. Opin. Chem. Biol.* **2005**, *9*, 343-346.
- (69) Suk, J. S.; Xu, Q.; Kim, N.; Hanes, J.; Ensign, L. M. PEGylation as a Strategy for Improving Nanoparticle-Based Drug and Gene Delivery. *Adv. Drug Deliv. Rev.* **2016**, *99(Pt A)*, 28-51.
- (70) Meng, H.; Xue, M.; Xia, T.; Ji, Z.; Tarn, D. Y.; Zink, J. I.; Nel, A. E. Use of Size and a Copolymer Design Feature To Improve the Biodistribution and the Enhanced Permeability and Retention Effect of Doxorubicin-Loaded Mesoporous Silica Nanoparticles in a Murine Xenograft Tumor Model. *ACS Nano* **2011**, *5*, 4131-4144.
- (71) He, Q.; Zhang, Z.; Gao, F.; Li, Y.; Shi, J. In Vivo Biodistribution and Urinary Excretion of Mesoporous Silica Nanoparticles: Effects of Particle Size and PEGylation. *Small* **2011**, *7*, 271-280.
- (72) Ruehle, B.; Clemens, D. L.; Lee, B.-Y.; Horwitz, M. A.; Zink, J. I. A Pathogen-Specific Cargo Delivery Platform Based on Mesoporous Silica Nanoparticles. *J. Am. Chem. Soc.* **2017**, *139*, 6663-6668.
- (73) Niedermayer, S.; Weiss, V.; Herrmann, A.; Schmidt, A.; Datz, S.; Müller, K.; Wagner, E.; Bein, T.; Bräuchle, C. Multifunctional Polymer-Capped Mesoporous Silica Nanoparticles for pH-Responsive Targeted Drug Delivery. *Nanoscale* **2015**, *7*, 7953-7964.
- (74) Lin, Y. S.; Abadeer, N.; Hurley, K. R.; Haynes, C. L. Ultrastable, Redispersible, Small, and Highly Organomodified Mesoporous Silica Nanotherapeutics. *J. Am. Chem. Soc.* **2011**, *133*, 20444-20457.
- (75) Saint-Cricq, P.; Deshayes, S.; Zink, J. I.; Kasko, A. M. Magnetic Field Activated Drug Delivery Using Thermodegradable Azo-Functionalised PEG-Coated Core-Shell Mesoporous Silica Nanoparticles. *Nanoscale* **2015**, *7*, 13168-13172.
- (76) Berkowski, K. L.; Potisek, S. L.; Hickenboth, C. R.; Moore, J. S. Ultrasound-Induced Site-Specific Cleavage of Azo-Functionalized Poly(Ethylene Glycol). *Macromolecules* **2005**, *38*, 8975-8978.
- (77) Eranki, A.; Mikhail, A. S.; Negussie, A. H.; Katti, P. S.; Wood, B. J.; Partanen A. Tissue-mimicking Thermochromic Phantom for Characterization of HIFU Devices and Applications. *Int. J. Hyperthermia* **2019**, *36*, 518-529.
- (78) de Bever, J. T.; Odéen, H.; Hofstetter, L. W.; Parker D. L. Simultaneous MR Thermometry and Acoustic Radiation Force Imaging Using Interleaved Acquisition. *Magn. Reson. Med.* **2018**, *79*, 1515-1524.
- (79) Farrer, A. I.; Odéen, H.; de Bever, J.; Coats, B.; Parker, D. L.; Payne, A.; Douglas, A. Christensen Characterization and Evaluation of Tissue-mimicking Gelatin Phantoms for Use with MRgFUS. *J. Ther. Ultrasound* **2015**, *3*, 9.



- (80) Lai, C. Y.; Kruse, D.; Seo, J. W.; Kheirrolomoom, A.; Ferrara, K. W. A Phantom for Visualization of Three-Dimensional Drug Release by Ultrasound-Induced Mild Hyperthermia. *Med. Phys.* **2013**, *40*, 083301.
- (81) Pichardo, S.; Kivinen, J.; Melodelima, D.; Curiel, L. Suitability of a Tumour-mimicking Material for the Evaluation of High-intensity Focused Ultrasound Ablation under Magnetic Resonance Guidance. *Phys. Med. Biol.* **2013**, *58*, 2163–2183.
- (82) Dunmire, B.; Kucewicz, J. C.; Mitchell, S. B.; Crum, L. A.; Sekins, K. M. Characterizing an Agar/gelatin Phantom for Image Guided Dosing and Feedback Control of High-intensity Focused Ultrasound. *Ultrasound Med. Biol.* **2013**, *39*, 300–311.
- (83) Choi, M. J.; Guntur, S. R.; Lee, K. I.; Paeng, D. G.; Coleman, A. A Tissue Mimicking Polyacrylamide Hydrogel Phantom for Visualizing Thermal Lesions Generated by High Intensity Focused Ultrasound. *Ultrasound Med. Biol.* **2013**, *39*, 439–448.
- (84) Dabbagh, A.; Abdullah, B. J.; Ramasindarum, C.; Abu Kasim, N. H. Tissue-mimicking Gel Phantoms for Thermal Therapy Studies. *Ultrason Imaging* **2014**, *36*, 291–316.
- (84) Madsen, E. L.; Frank, G. R.; Dong, F. Liquid or Solid Ultrasonically Tissue-Mimicking Materials with Very Low Scatter. *Ultrasound Med. Biol.* **1998**, *24*, 535–542.
- (86) McDonald, M.; Lochhead, S.; Chopra, R.; Bronskill, M. J. Multi-modality Tissue-Mimicking Phantom for Thermal Therapy. *Phys Med Biol.* **2004**, *49*, 2767–2778.
- (87) Jain, R. K. Transport of Molecules, Particles, and Cells in Solid Tumors. *Annu. Rev. Biomed. Eng.* **1999**, *1*, 241-263.
- (88) Salloum, M.; Ma, R. H.; Weeks, D.; Zhu, L. Controlling Nanoparticle Delivery in Magnetic Nanoparticle Hyperthermia for Cancer Treatment: Experimental Study in Agarose Gel. *Int. J. Hyperthmia* **2008**, *24*, 337-345.
- (89) Cao, Y.; Chen, Y.; Yu, T.; Guo, Y.; Liu, F.; Yao, Y.; Li, P.; Wang, D.; Wang, Z.; Chen, Y.; Ran, H. Drug Release from Phase-Changeable Nanodroplets Triggered by Low-Intensity Focused Ultrasound. *Theranostics* **2018**, *8*, 1327–1339.
- (90) Demitri, C.; Sannino, A.; Conversano, F.; Casciaro, S.; Distanto, A.; Maffezzoli, A. *J. Biomed. Mater. Res. B* **2008**, *87B*, 338–345.
- (91) Wu, S. H.; Lin, C. Y.; Hung, Y.; Chen, W.; Chang, C.; Mou C. Y. PEGylated Silica Nanoparticles Encapsulating Multiple Magnetite Nanocrystals for High-Performance Microscopic Magnetic Resonance Angiography. *J. Biomed. Mater. Res. B* **2011**, *99B*, 81–88.
- (92) Culjat, M. O.; Goldenberg, D.; Tewari, P.; Singh, R. S. A Review of Tissue Substitutes for Ultrasound Imaging. *Ultrasound Med. Biol.* **2010**, *36*, 861-873.
- (93) Chen, Z.-J.; Gillies, G. T.; Broaddus, W. C.; Prabhu, S. S.; Fillmore, H.; Mitchell, R. M.; Corwin, F. D.; Fatouros, P. P. A Realistic Brain Tissue Phantom for Intraparenchymal Infusion Studies. *J. Neurosurg.* **2004**, *101*, 314-322.

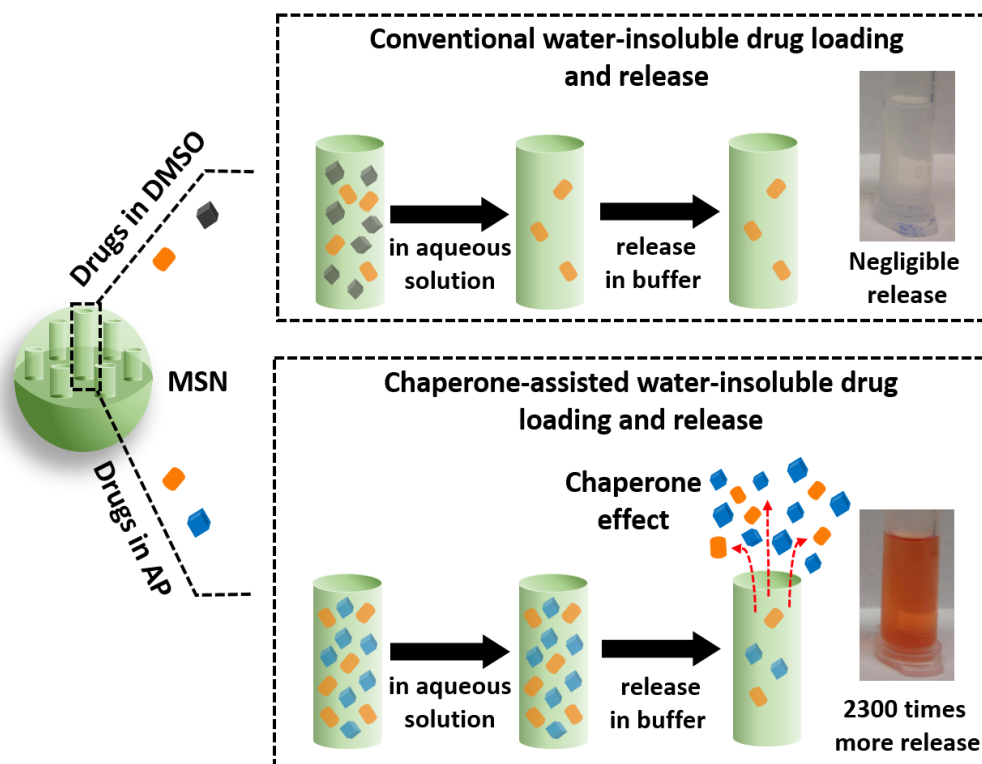
- (94) Tate, M. C.; Shear, D. A.; Hoffman, S. W.; Stein, D. G.; LaPlaca, M. C. Biocompatibility of Methylcellulose-Based Constructs Designed for Intracerebral Gelation Following Experimental Traumatic Brain Injury. *Biomaterials* **2001**, *22*, 1113-1123.
- (95) Madsen, E. L.; Zagzebski, J. A.; Frank, G. R. Oil-in-gelatin Dispersions for Use as Ultrasonically Tissue-mimicking Materials. *Ultrasound Med. Biol.* **1982**, *8*, 277-287.
- (96) Yang, S.; Chen, Y. J.; Cui, R.; Zhao, H. X.; Zhao, Y.; Liu, Z. Q.; Yu, Y.; Shao, X. Y.; Xu, Q. High-Intensity Focused Ultrasound Ablation: An in Vitro Agarose Gel Model. *Int. J. Clin. Exp. Med.* **2017**, *10*, 15302-15308.
- (97) Solomon, I. Relaxation Processes in a System of Two Spins. *Phys. Rev.* **1955**, *99*, 559-565.
- (98) Bloembergen, N.; Morgan, L. O. Proton Relaxation Times in Paramagnetic Solutions. Effects of Electron Spin Relaxation. *J. Chem. Phys.* **1961**, *34*, 842-850.
- (99) Manus, L. M.; Mastarone, D. J.; Waters, E. A.; Zhang, X. Q.; Schultz-Sikma, E. A.; MacRenaris, K. W.; Ho, D.; Meade, T. J. Gd(III)-Nanodiamond Conjugates for MRI Contrast Enhancement. *Nano Lett.* **2010**, *10*, 484-489.
- (100) Caravan, P.; Cloutier, N. J.; Greenfield, M. T.; McDermid, S. A.; Dunham, S. U.; Bulte, J. W. M.; Amedio, J. C.; Looby, R. J.; Supkowski, R. M.; Horrocks, W. D. W.; McMurry, T. J.; Lauffer, R. B. The Interaction of MS-325 with Human Serum Albumin and Its Effect on Proton Relaxation Rates. *J. Am. Chem. Soc.* **2002**, *124*, 3152-3162.
- (101) Bull, S. R.; Guler, M. O.; Bras, R. E.; Venkatasubramanian, P. N.; Stupp, S. I.; Meade, T. J. Magnetic Resonance Imaging of Self-Assembled Biomaterial Scaffolds. *Bioconjug. Chem.* **2005**, *16*, 1343-1348.
- (102) Kanda, T.; Fukusato, T.; Matsuda, M.; Toyoda, K.; Oba, H.; Kotoku, J.; Haruyama, T.; Kitajima, K.; Furui, S. Gadolinium-Based Contrast Agent Accumulates in the Brain Even in Subjects without Severe Renal Dysfunction: Evaluation of Autopsy Brain Specimens with Inductively Coupled Plasma Mass Spectroscopy. *Radiology* **2015**, *276*, 228-232.
- (103) Thomas, C. R.; Farny, C. H.; Coussios, C. C.; Roy, R. A.; Holt, R. G. Dynamics and Control of Cavitation during High-Intensity Focused Ultrasound Application. *Acoust. Res. Lett. Online* **2005**, *6*, 182-187.
- (104) Zhu, C.; He, S.; Shan, M.; Chen, J. Study of a Peak in Cavitation Activity from HIFU Exposures Using TA Fluorescence. *Ultrasonics* **2006**, *44*, e349-e351.
- (105) Nelson, T. R.; Tung, S. M. Temperature Dependence of Proton Relaxation Times in Vitro. *Magn. Reson. Imaging* **1987**, *5*, 189-199.
- (106) Webb, B.; Widek, T.; Neumayer, B.; Bruguier, C.; Scheicher, S.; Sprenger, H.; Grabherr, S.; Schwark, T.; Stollberger, R. Temperature Dependence of Viscosity, Relaxation Times (T1, T2) and Simulated Contrast for Potential Perfusates in Post-Mortem MR Angiography (PMMRA). *Int. J. Legal Med.* **2017**, *131*, 739-749.

## CHAPTER 5

# Facile Strategy Enabling Both High Loading and High Release Amounts of the Water-Insoluble Drug Clofazimine Using Mesoporous Silica Nanoparticles

This chapter of the dissertation was adapted and reprinted with permission from Wei Chen#, Chi-An Cheng#, Bai-Yu Lee, Daniel L. Clemens, Wen-Yen Huang, Marcus A. Horwitz, Jeffrey I. Zink *ACS Applied Materials & Interfaces* **2018**, *10*, 31870-31881. Copyright 2018 American Chemical Society. Co-author contributions: Chen W.#, Cheng C. A.# (co-first authors), and Huang W. Y. designed and performed the synthesis and characterization of material, and all the chemistry related studies. Lee B. Y., and Clemens D. L. performed the cell and bacteria studies. Marcus A. Horwitz, and Jeffrey I. Zink were the P.Is.

### Table of Content Figure



## 5.1 Abstract

The use of nanocarriers to deliver poorly soluble drugs to the sites of diseases is an attractive and general method, and mesoporous silica nanoparticles (MSNs) are increasingly being used as carriers. However, both loading a large amount of drugs into the pores and still being able to release the drug is a challenge. In this work, we demonstrate a general strategy based on a companion molecule that chaperones the drug into the pores and also aids it in escaping. A common related strategy is to use a miscible co-solvent dimethyl sulfoxide (DMSO), but although loading may be efficient in DMSO, this co-solvent frequently diffuses into an aqueous environment, leaving the drug behind. We demonstrate the method by using acetophenone (AP), an FDA-approved food additive as the chaperone for clofazimine (CFZ), a water-insoluble antibiotic used to treat leprosy and multidrug-resistant tuberculosis. AP enables a high amount of CFZ cargo into the MSNs and also carries CFZ cargo out from the MSNs effectively when they are in an aqueous biorelevant environment. The amount of loading and the CFZ release efficiency from MSNs were optimized; 4.5 times more CFZ was loaded in MSNs with AP than that with DMSO and 2300 times more CFZ was released than that without the assistance of the AP. *In vitro* treatment of macrophages infected by *Mycobacterium tuberculosis* with the optimized CFZ-loaded MSNs killed the bacteria in the cells in a dose-dependent manner. These studies demonstrate a highly efficient method for loading nanoparticles with water-insoluble drug molecules and the efficacy of the nanoparticles in delivering drugs into eukaryotic cells in aqueous media.

## 5.2 Introduction

Poor water solubility of drug molecules is a significant problem because almost 40% of the newly discovered drug molecules are hydrophobic which reduces their bioavailability and thus suppresses their efficacy.<sup>1</sup> Great effort has been devoted to solving the problem of getting them to

the site of the disease. One important strategy is to use nanomaterials as carriers to deliver insoluble drugs.<sup>2</sup> Mesoporous silica nanoparticles (MSNs) have aroused much attention in this regard because their properties include high surface area (about 1000 m<sup>2</sup>/g), large pore volume (1 cc/g), tunable pore sizes (2-20 nm), easy surface functionalization, and high biocompatibility.<sup>3-12</sup> These excellent intrinsic properties enable MSNs to carry a wide variety of cargos, including drugs,<sup>13-17</sup> genes,<sup>18-21</sup> proteins,<sup>22,23</sup> and other biomolecules for *in vitro* or *in vivo* biomedical applications.<sup>24,25</sup> Additionally, MSNs can incorporate fluorescence and magnetic properties, and simultaneously serve as image contrast agents by integrating the relevant functional materials for diagnostics and therapeutics.<sup>26-28</sup> Accordingly, these preeminent “theranostic” (therapeutic plus diagnostic) nanoparticles, serving as the excellent nanocarriers, are being broadly explored in biomedical applications.<sup>29-35</sup>

The major challenges are to get the insoluble drug into the pores and then allow the drugs to escape. One of the most widely-used methods to load the poorly water-soluble drugs in MSNs is to dissolve the drugs in dimethyl sulfoxide (DMSO).<sup>14</sup> The loading step is done by soaking MSNs in the DMSO solution which allows the drug molecules to diffuse into the channels of MSNs efficiently. After the loading step, the drug-loaded MSNs are washed with water or buffer solutions thoroughly to remove DMSO from the pores. However, during this washing step, some of drugs may be removed as well considering weak interactions between the hydrophobic drug molecules and the hydrophilic porous surface, thus decreasing the loading weight percent of drugs (defined as (weight of drugs / weight of MSNs) x 100%).<sup>2,14</sup> To attempt to solve this problem of low drug loading, the channels of MSNs were functionalized with hydrophobic groups to increase the hydrophobic interactions between the drugs and the channels.<sup>36,37</sup> However, those further surface modifications complicate the delivery systems and lead to colloidal instability in aqueous environment. Another critical challenge that remains is that the amount of the hydrophobic drug

released from the carriers into an aqueous environment is poor, even though MSNs are able to carry the drugs to the location of a disease.<sup>36–38</sup> Consequently, the bioavailability of the drugs may be reduced to a level insufficient for effective treatment, or an extremely high dosage of the particles may be required to achieve a sufficient local concentration of free drug for it to be effective. Hence, to enhance the bioavailability of the drug, it is essential to improve its release efficiency from the nanocarriers.

Hydrotropy is a technique that increases the water solubility of water insoluble molecules by adding a second solute (*i.e.* hydrotrope).<sup>39,40</sup> Hydrotropes are short chain amphiphilic molecules, usually containing both the hydrophobic and hydrophilic moieties in their chemical structures, in which the hydrophobic part interacts with water-insoluble drugs through hydrophobic interactions, and the hydrophilic part helps solubilize the drug-hydrotropes complexation structure in water. The hydrotrope-assisted solubilization of water-insoluble drugs in water possesses a signature feature of a sigmoidal solubility curve.<sup>41,42</sup> At low concentration of hydrotropes, the solubility of water-insoluble drugs hardly increases. The solubility of water-insoluble drugs significantly increases above a certain hydrotrope concentration, usually called a minimum hydrotrope concentration (MHC), when self-aggregation of the hydrotropes happens.<sup>42,43</sup> Other mechanisms may also involve in the hydrotrope-assisted solubilization of water-insoluble drugs.<sup>44–47</sup> Two advantages of using hydrotropy are that it obviates the need for chemical modification of the drugs, which may interfere with pharmaceutical activity; and it does not require a specific formulation for emulsification. The water solubility of water-insoluble drugs could be enhanced from several folds to several orders of magnitude by the hydrotrope-assisted solubilization especially if the hydrotropes associate well with the drugs.<sup>40,41,48</sup>

In this study, we choose clofazimine (CFZ) as an example of a water-insoluble drug (defined as having water solubility of less than 100 µg/mL) to demonstrate our strategy for hydrophobic

drug delivery. CFZ has an extremely low (0.2  $\mu\text{g/mL}$ ) water solubility. The motivation for improving the delivery of CFZ lies in the fact that it has good efficacy against multidrug-resistant Tuberculosis (TB).<sup>49–52</sup> TB is a serious contagious disease caused by the bacterium *Mycobacterium tuberculosis* (*M. tuberculosis*) and has becoming a global health problem; in 2016, there were approximately 10.4 million new TB cases and 1.3 million TB deaths worldwide.<sup>53</sup> However, the extremely low water solubility of CFZ complicates its delivery by nanoparticles or other novel approaches *e.g. via* inhalation.

In this work, we developed a facile “chaperone-assisted” delivery strategy which improves the loading of CFZ and delivers a large amount of CFZ with MSNs into an aqueous environment (**Figure 5.1**). First, we found acetophenone (AP) is the most promising chaperone among 9 candidate molecules tested. Then, we compared the efficacy of AP and DMSO as non-aqueous solvents for CFZ loading and release. Next, we measured the effect of CFZ loading concentration on CFZ release and AP release and determined the optimized CFZ loading concentration. The effect of the location of AP relative to MSNs on CFZ was also explored. Finally, using the optimized AP/CFZ loaded MSNs, we investigated the antibacterial effect of this hydrotrophy-based delivery strategy on intracellular *M. tuberculosis* to further validate their potential use in medicine and biomedical research. To the best of our knowledge, this is the first work to demonstrate appropriate chaperone for CFZ and to apply the strategy to the construction of nanoparticles with enhanced CFZ loading and release efficiency.

### 5.3 Synthesis and Characterization of MSNs

MSNs were synthesized by a sol-gel synthetic strategy in the presence of cationic surfactant template.<sup>15,55</sup> By transmission electron microscopy (TEM) (**Figure 5.2a**), MSNs have a well-ordered hexagonal mesoporous structure and the average size is 100 nm in diameter. The diameter

of MSNs measured by dynamic light scattering (DLS) is 165.7 nm (**Figure 5.2b**), which implies that MSNs are well-suspended in deionized (D.I.) H<sub>2</sub>O. The zeta potential value of MSNs is -21.2 mV in D.I. H<sub>2</sub>O. Nitrogen adsorption/desorption isotherms of MSNs were measured at 77 K. The surface area, pore volume, and pore size are 1060 m<sup>2</sup>/g, 1.12 cm<sup>3</sup>/g, and 2.8 nm, respectively (**Figure 5.2c and 5.2d**). The high surface area, characteristic of MSNs,<sup>8,18</sup> provides an advantage for loading cargos such as clofazimine (CFZ) and acetophenone (AP).

#### 5.4 Clofazimine Solubility Enhancement

To enhance the water solubility of CFZ, we applied the concept of “hydrotrophy” to the MSNs platform. During the past decades, the successful application of hydrotrophy to the delivery of hydrophobic drugs by nanocarriers has been demonstrated by several research groups. For instance, Koo *et al.* used hydrotropic oligomer-conjugated glycol chitosan nanoparticles for paclitaxel (PTX) delivery.<sup>56</sup> Wang, *et al.* used 70 nm hydrotropic polymer-based nanocarriers to load and deliver PTX in *in vitro* studies.<sup>57</sup> Most of their work involved anticancer drugs, especially PTX, whose water solubility is 5.6 µg/mL.<sup>40,58,59</sup> To the best of our knowledge, no application of hydrotrophy to the delivery of water-insoluble antibiotics from nanocarriers has been demonstrated. It is known that highly effective hydrotropes frequently have either a phenyl ring or pyridine in their structures.<sup>59,60</sup> For example, sodium benzoate and nicotinamide, with either a phenyl ring or pyridine in their structures, are effective hydrotropes for PTX.<sup>60</sup> Therefore, sodium benzoate, nicotinamide, and other molecules with similar structures, including isoniazid, pyrazinamide, 2-hydroxyacetophenone, benzoic acid, and AP were considered candidates for hydrotropes to enhance the water solubility of CFZ. **Figure 5.3** shows the solubility enhancement of CFZ in H<sub>2</sub>O in the presence of the various hydrotropes mentioned above. The solubility of CFZ was determined from UV-Vis spectra where the maximum absorbance is at 490 nm. It is surprising that neither



sodium benzoate nor nicotinamide is a good hydrotrope; compared with the control, the CFZ solubility enhancement is only 1.3- and 1.5-fold in 1 M of sodium benzoate and nicotinamide solution, respectively. The results indicate that isoniazid and pyrazinamide are also not effective hydrotropes for CFZ (1.7-fold in 1 M isoniazid and 1.4-fold in 1 M pyrazinamide solution). The poor hydrotropic performance of these four molecules may be due to their relatively high water solubility (629 mg/mL for sodium benzoate, 500 mg/mL for nicotinamide, 140 mg/mL for isoniazid, and 50 mg/mL for pyrazinamide) as shown in **Table 5.1**. It is very difficult to provide the hydrophobic interaction between the possible hydrotropes and CFZ. In this case, the strong intermolecular force of CFZ (mainly from the hydrophobic interaction of the phenyl rings of CFZ) is much stronger than the interaction between possible hydrotropes and CFZ. Such hydrophilicity of these molecules makes them unable to associate well with the hydrophobic CFZ molecules, and thus the water solubility of CFZ was only slightly enhanced effectively.

On the other hand, the water solubility enhancement of CFZ is 1.6-fold, 1.7-fold, 2.0-fold, and 2.6-fold for 2-hydroxyacetophenone, hexanoic acid, benzoic acid, and 2-heptanone hydrotropes, respectively. Benzoic acid and 2-heptanone have better water solubility enhancement than 2-hydroxyacetophenone or hexanoic acid. This is due to the fact that the water solubility of benzoic acid and 2-heptanone – only 3.4 mg/mL and 4.3 mg/mL, respectively – is lower than that of 2-hydroxyacetophenone and hexanoic acid – 20.0 mg/mL and 10.8 mg/mL, respectively. Thus, these hydrotropes may associate better with the hydrophobic CFZ molecules and enhance the water solubility of CFZ. In addition, the presence of the phenyl rings in the structure of hydrotropes could also contribute to improvement in the water solubility of CFZ because of the hydrophobic interactions that exist between the phenyl rings of the hydrotropes and hydrophobic moiety (phenyl rings) of CFZ. For example, the solubility enhancement of CFZ in the presence of benzoic acid or hexanoic acid is 2.0 or 1.7-fold, respectively. By using benzoic acid, the solubility enhancement is

higher than that of hexanoic acid due to the presence of the phenyl ring in benzoic acid. Additionally, the solubility enhancement of CFZ in the presence of 2-heptanone or AP is 2.6 or 10.1-fold. By using AP as the hydrotrope, the solubility enhancement is about four times greater than that with 2-heptanone. Therefore, the phenyl ring could effectively enhance the water solubility of CFZ because either AP or benzoic acid could provide the hydrophobic interaction between their phenyl ring and the phenyl ring of CFZ.

The hydrogen bonding between water molecules and CFZ is not strong enough to solvate CFZ since the intermolecular hydrophobic interaction between the phenyl rings of CFZ is strong. Therefore, the water solubility of CFZ is low (only 0.2  $\mu\text{g/mL}$ ), or water-insoluble by definition. However, for AP or 2-heptanone, there exists both a hydrophobic phenyl ring or alkyl chain and a polar carbonyl group in their chemical structures. These molecules could provide both the hydrophobic interaction between the hydrophobic phenyl ring or alkyl chain of AP or 2-heptanone and the hydrophobic moiety of CFZ, and hydrogen bonding between the carbonyl group of AP or 2-heptanone and amine hydrogen in CFZ. Therefore, the presence of carbonyl group in AP or 2-heptanone could provide stronger interaction between the possible hydrotropes and CFZ, *e.g.* the CFZ solubility enhancement is 10.1 or 2.6-fold by using AP or 2-heptanone as the hydrotrope, higher than those of benzoic acid (2.0-fold) or hexanoic acid (1.7-fold). In terms of polarity of the possible hydrotropes, a carboxylic acid group has larger polarity than a ketone. Therefore, if we compare 2-heptanone with hexanoic acid, the solubility enhancement of CFZ is 2.6 or 1.7-fold in the presence of 2-heptanone or hexanoic acid, respectively. The higher polarity of hexanoic acid has less hydrotropic effect to increase the water solubility of CFZ. This could also be proved that the solubility enhancement of CFZ is 10.1 or 2.0-fold in the presence of AP or benzoic acid, respectively, since benzoic acid has higher polarity. Based on the above observations, AP, with good association with CFZ and both a phenyl ring and a ketone in its structure, was chosen as a

promising hydrotrope for CFZ in this study. The hydrotropic efficacy of AP was examined in more detail in below Section 5.4.1.

#### 5.4.1 Hydrotropic Efficacy of AP on CFZ Solubility

The hydrotropic efficacy of AP was examined in more detail using UV-Vis spectra to determine the CFZ solubility enhancement as a function of AP concentration in H<sub>2</sub>O (**Figure 5.4a**). When the AP concentration was below 2.2 mM, the absorbance at 490 nm was almost equal to that of the control (0 mM), whereas the absorbance rapidly increased as the AP concentration rose to more than 2.2 mM. The result shows that the water solubility of CFZ dramatically increases when the concentration of AP reaches around 2.2 mM. **Figure 5.4b** displays the fold enhancement of CFZ solubility by AP compared with the control. The maximum solubility enhancement of CFZ reached 12.2-fold at an AP concentration of 60 mM, which is the saturated concentration of AP in H<sub>2</sub>O. Accordingly, the result indicates that the water solubility of CFZ can be enhanced from 0.2 mg/L to about 2.4 mg/L in the presence of AP in H<sub>2</sub>O. From **Figure 5.4a** and **5.4b**, no hydrotropic efficacy was observed at concentrations of AP below 2.2 mM. Below this threshold, the solubility enhancement of CFZ is independent of the AP concentration. In contrast, when the concentration of AP is more than 2.2 mM, the solubility enhancement of CFZ increases significantly with AP concentration. The critical AP concentration may imply that the minimum hydrotropic concentration (MHC) is about 2.2 mM. Above the concentration, the self-aggregation of AP occurred,<sup>41,42</sup> which is similar to that the surfactant molecules form the ordered micelle structure above the critical micelle concentration but not identical.<sup>42</sup> Such self-aggregation of hydrotropes interact the water-insoluble drugs through hydrophobic interaction between the hydrophobic benzene ring of AP and water-insoluble CFZ and simultaneously help the solubilization of CFZ. Therefore, once the concentration of AP is higher than this threshold concentration, the self-

aggregation of AP and its' hydrotropic effect could help the solubilization of CFZ in water. This behavior follows the mechanism of hydrotropy-assisted solubility enhancement of hydrophobic drugs which may be attributed to the preferential interaction between AP and CFZ.<sup>43</sup> A photograph of serial CFZ solutions with different AP concentrations is shown in **Figure 5.4c**. The color of the solutions became darker as the AP concentration increased, indicating that AP helps dissolve CFZ in H<sub>2</sub>O. These results show that the water solubility of CFZ is significantly enhanced by the addition of the AP.

### **5.5 Clofazimine Loading by Using Different Nonaqueous Solvents: AP and DMSO**

To realize whether AP could also facilitate the loading of CFZ in MSNs, we compared the loading amount of CFZ by using AP to that of conventional method using DMSO, a widely-used loading solvent for dissolving poorly water-soluble drugs.<sup>2,14</sup> We called the method of using AP the “chaperone-assisted” method due to the preferential interaction between AP and CFZ, making AP act like a chaperone carrying the CFZ with it (**Figure 5.5a**). CFZ loading into MSNs was achieved by soaking MSNs in CFZ solutions with various concentrations dissolved in AP or DMSO. After 24 h loading of CFZ, the CFZ-loaded MSNs were introduced back to aqueous solution. To calculate the loading capacity, which is defined as (the mass of loaded CFZ/the mass of MSNs) x 100%, the CFZ loaded MSNs with AP or DMSO were respectively washed with AP or DMSO several times until the supernatant after centrifugation was clear. Those supernatants were collected and measured by UV-Vis spectroscopy. The total amount of CFZ loaded in MSNs was calculated based on Beer's law and its calibration curve (**Figure 5.6**). From **Figure 5.5b**, the loading capacity of 0.1, 1, and 10 mM CFZ by using DMSO as the loading solvent were found to be 0.2, 0.9, and 5.9 %, respectively. However, with AP as the loading solvent, the higher loading

capacity were achieved under all loading concentrations of CFZ, which were 0.3, 1.3, 9.6, and 26.8 % for 0.1, 1, 10, and 50 mM CFZ, respectively. The loading capacity of CFZ increased with the loading concentration of CFZ. The higher loading capacity of CFZ by using AP as the loading solvent can be explained by two reasons: (1) the CFZ solubility in AP (>71 mg/mL) is higher than in DMSO (5 mg/mL), so that the saturated concentration of CFZ in AP (more than 150 mM) is much higher than in DMSO (only 10.5 mM); (2) DMSO is miscible with water, so most of the DMSO molecules were removed by water during the washing steps, leading to the release of some CFZ molecules from MSNs together with DMSO. However, the water solubility of AP is only 6.1 mg/mL, so a large amount of AP was still loaded in the pores of MSNs after they were re-dispersed in aqueous solution (**Figure 5.5a**). As will be shown in the next section, the AP in the pores is essential for good CFZ release.

On the basis of the significant enhancement of CFZ loading by AP, it was of interest to investigate the detailed relationship between the loading of AP chaperone and its cargo CFZ. MSNs were loaded with AP itself (no CFZ), or AP with 0.1, 1, 10, and 50 mM solubilized CFZ. The pore volume of MSNs is 1.12 cm<sup>3</sup>/g; hence the maximum volume for cargo loading is 1.12 μL/mg. The density of AP is 1.03 g/cm<sup>3</sup>, and thus the maximum loading capacity would be 115.4%. When AP itself (0 mM CFZ), or AP with 0.1, 1, 10, and 50 mM solubilized CFZ were used as the loading solvents, the loading capacity of AP was found to be 100.9 %, 102.4 %, 101.1%, 97.2 %, and 71.4 %, respectively (**Figure 5.5c**). The amount of loaded AP in MSNs corresponds to 8397.8, 8522.7, 8414.5, 8089.9, and 5942.6 nmole/mg, and the amount of loaded CFZ in MSNs was 6.3, 27.5, 202.8, and 566.1 nmole/mg at those respective CFZ loading concentrations (**Table 5.2**). This implies that when the CFZ loading capacity is low (no higher than 1.3 %, **Figure 5.5b**), regardless of the presence of CFZ, about 88% of the pore volume of MSNs is filled with AP after loading, which is reasonable since the low water solubility of AP (only 6.1 mg/mL) makes a large amount

of AP remain in the pores of MSNs after they are re-dispersed in aqueous solution. The loading capacity of AP is lower at higher CFZ concentrations (10 and 50 mM), at which the loading capacity of CFZ was enhanced (9.6 % and 26.8 %, **Figure 5.5b**). This is because part of the pore volume of MSNs is occupied by CFZ, thus reducing the volume available for AP loading. The mole ratios of AP to CFZ loaded in MSNs with those CFZ loading concentrations was calculated to be 1352.8, 306.0, 39.9, and 10.5, respectively (**Table 5.2**). As CFZ loading concentrations in AP increase, both the amount of loaded CFZ and the mole ratio of CFZ to AP increase.

## **5.6 CFZ Release to Aqueous Solution by Using Different Nonaqueous Solvents: AP and DMSO**

Before applying the methods with AP and DMSO to deliver CFZ to biological systems, we examined their capability for facilitating the release of CFZ into aqueous solution. MSNs loaded with CFZ (1 mM) either by DMSO or AP were dispersed in HEPES buffer solution (pH = 7.4) for 1, 2, 3, or 5 days, respectively (**Figure 5.5a**). **Figure 5.7a** shows the UV-Vis spectra of the supernatant after CFZ released from MSNs in buffer solution with DMSO as the loading solvent. The absorption peak of CFZ at 490 nm is not evident, indicating that the release of CFZ is negligible even after 5 days. This phenomenon could be explained as a result of the water-insoluble property of CFZ, making the drug molecules themselves prefer to stay in the pores of MSNs. On the contrary, with AP as the loading solvent, the release of CFZ could be easily found in the UV-Vis spectra with the apparent peaks at 490 nm (**Figure 5.7b**). The absorbance peaks at 490 nm increased with time between 5 days, and the absorbance is significantly different from those with DMSO. To quantify the release amount of CFZ, the time dependent release efficiency of CFZ using either DMSO or AP was calculated (**Figure 5.5d**) based on Beer's law and its calibration curve (**Figure 5.8**). The release efficiency is defined as (the mass of released CFZ/the mass of

loaded CFZ) x 100%. By using the “chaperone-assisted” strategy with AP, the release efficiency of CFZ achieved 47.2%, which is 2300 times higher than that by the conventional method with DMSO (0.02%) (**Figure 5.5d**). This significant enhancement in the release efficiency of CFZ by AP could also be clearly observed in the photograph of the supernatant (**Figure 5.5e**).

### 5.7 Effect of the CFZ Loading Concentration on CFZ Release

To optimize the release of CFZ in aqueous environment using the “chaperone-assisted” delivery strategy, we explored the effect of CFZ loading concentration on the long-term release behavior of CFZ. The release of CFZ was confirmed by the absorbance peaks at 490 nm in the UV-Vis spectra measured from the supernatants collected after spinning down MSNs after 1, 2, 3, and 5 days (**Figure 5.7b**). The time-dependent release capacity of CFZ was calculated based on Beer’s law and its calibration curve (**Figure 5.8**). Release capacity is defined as: (the mass of released CFZ / the mass of MSNs) x 100%. **Figure 5.9a** shows the time-dependent release capacity of CFZ in HEPES buffer solution (pH = 7.4) with four different CFZ loading concentrations (0.1, 1, 10, and 50 mM) in AP. The absorbance peaks increase with time up to 5 days. Regardless of the CFZ loading concentration, the amount of CFZ released gradually increases with time, until it levels off at about five days. The amount of CFZ released from MSNs loaded with 0.1 mM CFZ in AP is only 0.10 % on day 5, which is mainly due to the tiny amount of CFZ (0.3 % loading capacity) loaded in MSNs. For the MSNs loaded with 1 and 10 mM CFZ in AP, the CFZ release capacity on day 5 was 0.56 % and 0.54 %, respectively. Even though the amount of CFZ loaded with those two samples (1.3 % and 9.6 % CFZ loading capacity, respectively) differed by 7-fold, the amount of CFZ released was nearly the same. However, the CFZ release capacity of the MSNs loaded with 50 mM CFZ in AP on day 5 is only 0.27 %, lower than those loaded with 1 and 10 mM CFZ in AP. This low CFZ release capacity at this high CFZ loading concentration may be due

to a small amount of AP in the pores of MSNs that contain a large amount of CFZ (26.8 % CFZ loading capacity) as referred to **Table 5.2**, which shows the mole ratio of AP/CFZ to be only 10.5. This less amount of AP renders the environment inside the pores much more hydrophobic and thus reducing the “chaperone-assisted” effect or the hydrotropic effect. The time-dependent release efficiency of CFZ with four different CFZ loading concentrations (0.1, 1, 10, and 50 mM) was also calculated (**Figure 5.9b**). Release efficiency is defined as: (the mass of released CFZ / the mass of loaded CFZ in MSNs) x 100%. The time-dependent release efficiency on day 5 for MSNs loaded with 0.1, 1, 10, and 50 mM CFZ in AP is 42.3 %, 47.2 %, 4.6 %, and 0.1%, respectively. The lowest release efficiency, observed when MSNs were loaded with 50 mM CFZ in AP, indicates that most of the loaded CFZ remains in the pores of MSNs, which again may be due to the small amount of loaded AP and the enhanced hydrophobicity in the pores of MSNs as described above.

### **5.8 Effect of the CFZ Loading Concentration on AP Release**

After the “chaperone-assisted” strategy was successfully demonstrated, we studied the effect of CFZ cargo loading concentration on the release of AP chaperone (**Figure 5.9c and 5.9d**). The release efficiency of AP was calculated based on Beer’s law and its calibration curve (**Figure 5.10**). The time-dependent release capacity of AP from MSNs loaded with 0.1, 1, 10, and 50 mM CFZ in AP is lower than from MSNs not loaded with CFZ on day 1 (**Figure 5.9c**). Nevertheless, the release capacity of AP from MSNs loaded with CFZ substantially increases on day 2. Finally, the release capacity of AP on day 5 reaches 94.2, 90.0, 77.8, and 53.6 % from MSNs loaded with 0.1, 1, 10, and 50 mM CFZ in AP, respectively. For the release efficiency of AP from MSNs loaded with 0.1, 1, 10, and 50 mM CFZ, only 22, 11, 12, and 13 % were found on day 1, much lower than without loaded CFZ (33%) (**Figure 5.9d**). However, on day 2, the release efficiency of AP from MSNs loaded with 0.1, 1, 10, and 50 mM CFZ in AP achieves 60, 61, 59, and 57 %, respectively, which



is close to that without loaded CFZ (58%). Finally, on day 5, the release efficiency of AP reaches about 92, 89, 80, and 75 % for MSNs loaded with 0.1, 1, 10, and 50 mM CFZ in AP, respectively, and reaches about 95% for the MSNs loaded with AP itself (0 mM CFZ). Interestingly, the result on day 5 shows that the release efficiency of AP decreases as the loading concentration of CFZ increases. This finding together with the lower loading capacity of AP at 10 and 50 mM CFZ loading concentration (**Figure 5.5c**) adequately explain the much lower release capacity of AP when MSNs are loaded with 10 mM or 50 mM CFZ than when MSNs are loaded with AP without any CFZ (95.9%) (**Figure 5.9c**).

The sigmoidal release profiles of both CFZ and AP loaded in MSNs are characterized by slow release during the first day followed by increased release at later time points, and a final leveling off (**Figure 5.9b and 5.9d**). In the presence of both CFZ and AP in MSNs, almost all of the CFZ (**Figure 5.9b**) as well as the greater part of AP (**Figure 5.9d**) remain inside the pores on day 1, especially for the MSNs loaded with 1, 10, and 50 mM CFZ in AP. This supports that there may exist an interaction between CFZ and AP in the pores of MSNs, and that this association favors most of the AP molecules residing in the pores of MSNs, reducing the AP release on day 1. The loaded CFZ molecules may sterically block the release of AP from MSNs as well. The better AP release compared to that of CFZ on day 1 could be explained by the higher water solubility of AP than CFZ, so that the release of AP in aqueous environment can occur in a short period of time. For MSNs loaded with 0.1 and 1 mM CFZ in AP, the release efficiency of AP increases significantly after day 1 (**Figure 5.9d**), which corresponds to the substantial increase in CFZ release efficiency on day 2 (**Figure 5.9b**). This feature is due to the high mole ratio of AP/CFZ in the pores of MSNs with 0.1 and 1 mM CFZ (**Table 5.2**). The abundant AP chaperone in the pores carry CFZ out of MSNs and thus facilitates CFZ release into an aqueous environment. Interestingly, for particles loaded with 10 and 50 mM CFZ, the CFZ release efficiency shows no significant

increase during those five days compared with the dramatic increase in AP release efficiency after day 1. This is because the mole ratio of AP/CFZ is low at those CFZ loading concentrations (**Table 5.2**), and thus the interaction between AP and CFZ is not strong enough to carry CFZ out of MSNs and into the aqueous environment. In other words, when the mole ratio of AP/CFZ is low, even though the interaction between CFZ and AP in the pores retards the release of AP, the high water solubility of AP dominates such that more AP is released into an aqueous environment as the release time increases.

The “chaperone-assisted” delivery strategy makes use of the interaction between CFZ cargo and AP chaperone which provides the mechanism for the release of CFZ from MSNs, and thus significantly enhances the water solubility of CFZ. By carefully tuning the mole ratio of AP/CFZ, we can control the dosage and the release profile of CFZ over time. This would be favorable in terms of improving the bioavailability and the efficacy of CFZ, as well as reducing the side-effect causing by the overdose of CFZ.

## **5.9 Effect of External AP on CFZ Release**

As the chaperone, AP is supposed to be stayed together with its CFZ cargo in the pores of MSNs to bring its assistance into full play. To further confirm the idea of “chaperone-assisted” delivery, we studied the release of CFZ in a buffer solution with or without the addition of dissolved AP. Instead of using AP as the loading solvent, DMSO was used for loading CFZ to prevent AP from being present in the pores of MSNs. Release buffer with or without the addition of AP was used for CFZ release. With DMSO as the loading solution, the release efficiency of CFZ released in HEPES buffer solution (10 mM, pH = 7.4) without the addition of AP is only 0.02% after 120 h, which indicates that almost all of the CFZ stays in the pores of MSNs (**Figure 5.11**). The release efficiency of CFZ released in HEPES buffer solution with the addition of AP,

on the other hand, is only 4.3% after 120 h. Both of these CFZ release efficiencies are significantly lower than that with AP as the loading solvent and HEPES buffer solution as the release buffer (47.2%). This result suggests that the CFZ release efficiency is significantly enhanced by the AP loaded inside the pores of MSNs together with CFZ, of which the interaction between CFZ cargo and AP chaperone inside the pores contributes substantially to the significant improvement of CFZ release. On the other hand, AP outside of the MSNs that doesn't have good interaction with CFZ only contributes to about 1/10th of the CFZ release. This slightly greater CFZ release could be explained by the increased hydrophobicity of the environment causing by the AP located in solution outside of MSNs. This study further strengthens the idea of “chaperone-assisted” delivery, where MSNs act like a primary vehicle carrying both a secondary vehicle – the AP chaperone – and the CFZ cargo inside. As the chaperone, AP carries the CFZ and brings it out and away from MSNs effectively.

### **5.10 Antibacterial Effect of AP-Assisted CFZ Delivery by MSNs**

To explore the antibacterial effect of the developed “chaperone-assisted” delivery strategy shown in **Figure 5.12a**, we examined the treatment efficacy of the CFZ loaded MSNs using a macrophage model of *Mycobacterium tuberculosis* (*M. tuberculosis*) infection. The mole ratio of AP/CFZ was tuned and the optimized CFZ loading concentration was found to be 10 mM considering both the loading capacity and release capacity of CFZ (**Figure 5.5b and 5.9a**). The *M. tuberculosis*-infected macrophages were treated with MSNs loaded with 10 mM CFZ in AP (AP/CFZ-MSN) for 4 days (**Figure 5.12a**). As controls, the macrophages were untreated or treated with MSNs loaded with AP only (AP-MSN), or with free CFZ dissolved in a mixture of DMSO and H<sub>2</sub>O (CFZ/DMSO). All of the infected macrophages were lysed at day 4 post-infection and the lysates were plated for viable *M. tuberculosis*. The number of *M. tuberculosis* colony forming units (CFUs) recovered

from the macrophages was enumerated to determine bacterial viability under each treatment. As shown in **Figure 5.12b**, treatment with AP-MSN (11 and 22  $\mu\text{g/mL}$ ) for 4 days without CFZ had little effect on *M. tuberculosis* because the number of bacteria in macrophage monolayers (6.29, and 6.25 log CFU, respectively) was similar to and not statistically different from the number in untreated macrophages (6.51 log CFU). In contrast, AP/CFZ-MSN killed the intracellular bacteria in a dose-dependent manner. AP/CFZ-MSN at concentrations of 5.5, 11, and 22  $\mu\text{g/mL}$  correspond to 0.5, 1, and 2  $\mu\text{g/mL}$  of free CFZ dissolved in DMSO. The number of viable bacteria after treatment with those concentrations of AP/CFZ-MSN was 5.97, 5.82, and 5.50 log CFU, respectively, suggesting that 90% of bacteria was killed (the number of bacteria decreased by 1 log CFU) in macrophages treated with 22  $\mu\text{g/mL}$  of AP/CFZ-MSN. We also compared the effect of free CFZ with that of the MSN-encapsulated CFZ. The treatment efficacy of AP/CFZ-MSN dispersed in culture medium was similar to that of an equivalent amount of CFZ dissolved in the mixture of DMSO and culture medium without MSNs. This comparison shows that with the help of the AP chaperone, most of the CFZ loaded inside MSNs is efficiently released in the macrophages and kill the bacteria effectively and selectively (**Figure 5.12a**).

To investigate if the “chaperone-assisted” delivery strategy with AP, an FDA approved food additive, has any cytotoxicity to the macrophages, we examined the viability of the infected macrophages after the treatment with AP-MSN and AP/CFZ-MSN for 4 days. No significant decrease in macrophage viability was detected (**Figure 5.12c**) at the concentrations studied. No adverse effect on the morphological appearance of the macrophages treated with AP-MSN or AP/CFZ-MSN was observed. Taken together, these results show that the “chaperone-assisted” CFZ delivery strategy *via* MSNs has no evident toxicity to macrophages but can selectively and efficiently kill the bacteria residing inside them due to the significant release of CFZ from MSNs.

## 5.11 Summary

In this study, we have developed a novel “chaperone-assisted” strategy based on mesoporous silica nanoparticles (MSNs) to both load water-insoluble drugs into MSN carriers and release them into aqueous biological environment. First, we utilized the concept of “hydrotrophy” to explore the nine candidate small molecules for their utility to enhance the water solubility of a water-insoluble antibiotics — clofazimine (CFZ), who has good efficacy against multidrug-resistant Tuberculosis (TB). Acetophenone (AP) was selected as the most efficacious solvent to enhance 10.1-fold of the water solubility of CFZ. Acting as a chaperone, AP not only brought a great amount of CFZ cargos (26.8% loading capacity of CFZ) into the MSN nanocarriers, but carried a significant amount of CFZ cargos (47.2% release efficiency of CFZ) out from MSNs into the aqueous solution. This release efficiency of CFZ achieved is 2300 times higher than that by conventional method using DMSO (0.02%). This considerable increase in CFZ release is mainly driven by the release of AP chaperone from the chaperone-rich pores of MSNs, which allows CFZ cargo to be carried together into the aqueous solution, and can be supported by our three findings: (1) a lower loading concentration of CFZ (1 mM) gave a higher release efficiency of CFZ (47.2%) compared with a higher loading concentration of CFZ (0.1%); (2) AP in the solution outside of MSNs only minimally increased the release efficiency of CFZ (4.3%); (3) without AP, the release efficiency of CFZ was only 0.02%. We examined this delivery strategy in a macrophage model of *Mycobacterium tuberculosis* (*M. tuberculosis*) infection using MSNs loaded with the optimized ratio of CFZ and AP (10 mM CFZ in AP). *M. tuberculosis* residing inside macrophages were efficiently killed (reduced by 1 log CFU) by the high amount of the released CFZ, which is comparable to that with the same amount of CFZ dissolved in a mixture of DMSO and culture medium. No adverse effect on the morphological appearance of the macrophages treated with either MSNs loaded with AP or MSNs loaded with CFZ and AP was observed. This novel

“chaperone-assisted” delivery strategy for CFZ could also be applied to other hydrophobic drugs with their suitable loading solvents (chaperone), opening up opportunities to apply this drug delivery strategy for further use in medicine and biomedical research.

## **5.12 Methods**

### **5.12.1 Materials and Chemicals**

Hexadecyltrimethylammonium bromide (CTAB, 99+%), tetraethyl orthosilicate (TEOS, 98%), clofazimine (CFZ, 98+%), acetophenone (AP, 99%), 2-heptanone (98%), 2-hydroxyacetophenone (98%), sodium benzoate (99%), pyradinamide (97.5+%), nicotinamide (99.5+%), isoniazid (99+%), hexanoic acid (99+%), benzoic acid (99.5+%), sodium hydroxide (NaOH) (97+%), 4-(2-hydroxyethyl)-1-piperazineethanesulfonic acid (HEPES, 99.5+%), and ammonium nitrate ( $\text{NH}_4\text{NO}_3$ , 98+%) were purchased from Sigma-Aldrich. Dimethyl sulfoxide (DMSO, 99.9+%) was purchased from Fisher Chemical. Absolute ethanol (200 proof) was purchased from Decon Labs, Inc. All chemicals were used without further purification.

### **5.12.2 Characterization**

The size and morphology of mesoporous silica nanoparticles (MSNs) were investigated by transmission electron microscopy (TEM, Tecnai T12). MSNs were dispersed in ethanol at a very low concentration (0.2 mg/mL). Ten microliters of the suspension were dropped onto the carbon-coated copper grid and dried at room temperature. The  $\text{N}_2$  adsorption-desorption isotherms of MSNs were obtained at liquid  $\text{N}_2$  temperature (77K) on a Autosorb-iQ (Quantachrome Instruments) apparatus. MSNs were degassed at 110 °C for 12 h before the measurement. The surface area and pore size distribution of MSNs were determined by Brunauer-Emmett-Teller (BET) and Barrett-Joyner-Halenda (BJH) methods. The dynamic light scattering (DLS) size and zeta potential value

of MSNs were examined by a laser particle analyzer LPA-3100 at room temperature. The loading capacity, release capacity, and release efficiency of CFZ or AP were determined by UV-Vis Spectroscopy (Cary 5000). The absorbance of the peaks was used for quantification by Beer-Lambert Law.

### **5.12.3 Synthesis of MSNs**

CTAB (250 mg) was dissolved in a mixture of deionized water (120 mL) and 2 M NaOH (875  $\mu$ L) under vigorous stirring. The solution was heated to 80 °C and tetraethyl orthosilicate (TEOS) (1.25 mL) was then added dropwise to the solution for about 20 seconds. The reaction was kept at 80 °C for 2 h. Subsequently, the solution was cooled to room temperature and MSNs were centrifuged and washed 3 times with ethanol. MSNs were then dispersed in 100 mL of ethanol containing 2 g of  $\text{NH}_4\text{NO}_3$  and the reaction was refluxed for 1 h to remove the surfactant. The surfactant removal procedures were repeated twice and MSNs were washed thoroughly with ethanol and D.I. water to obtain the surfactant-free MSNs.

### **5.12.4 Screening of Possible Hydrotropes for CFZ**

Nine different small molecules – nicotinamide, sodium benzoate, pyradinamide, isoniazid, 2-hydroxyacetophenone, benzoic acid, hexanoic acid, 2-heptanone, and acetophenone – were screened to investigate their hydrotropic ability for CFZ in  $\text{H}_2\text{O}$ . For the control lacking a hydrotrope, 1  $\mu$ mol of CFZ and 1 mL of  $\text{H}_2\text{O}$  were added into a 20 mL of glass vial and sonicated for 10 min to suspend CFZ in  $\text{H}_2\text{O}$ . The undissolved CFZ was removed by centrifugation at 14000 rpm for 15 min. Then, the supernatant was collected and measured by UV-Vis spectroscopy. For experimental samples with hydrotropes, 1  $\mu$ mol of CFZ, 1 mL of  $\text{H}_2\text{O}$ , and the respective hydrotrope [sodium benzoate (50  $\mu$ mol, 500  $\mu$ mol, or 1 mmol), pyrazinamide (50  $\mu$ mol, 500  $\mu$ mol, or 906  $\mu$ mol), nicotinamide (50  $\mu$ mol, 500  $\mu$ mol, or 1 mmol), isoniazid (50  $\mu$ mol, 500  $\mu$ mol, 1

mmol), 2-hydroxyacetophenone (50  $\mu\text{mol}$ ), hexanoic acid (50  $\mu\text{mol}$ ), benzoic acid (28  $\mu\text{mol}$ ), 2-heptanone (38  $\mu\text{mol}$ ), or acetophenone (50  $\mu\text{mol}$ )] were added into 20 mL glass vials and sonicated for 10 min. The undissolved CFZ was removed by centrifugation as described above. Finally, the supernatant was collected and measured by UV-Vis spectroscopy. The solubility enhancement was determined by the change in absorbance at 490 nm.

#### **5.12.5 Concentration Dependent Hydrotropy Effect of AP**

To investigate the hydrotropic effect of AP in more detail, we prepared concentrations ranging from 0 to 60 mM of AP in  $\text{H}_2\text{O}$  to dissolve CFZ. Similarly, 1  $\mu\text{mol}$  of CFZ, 1 mL of  $\text{H}_2\text{O}$ , and the respective concentration of AP were added into 20 mL glass vials and sonicated for 10 min. The undissolved CFZ was removed by centrifugation as described above. The solubility enhancement was determined by the change in absorbance at 490 nm.

#### **5.12.6 Creation of Calibration Curve of CFZ in AP, CFZ in Ethanol-Water Mixture, and AP in Ethanol-Water Mixture**

To determine the loading capacity, release efficiency, and release capacity of CFZ, the calibration curves were created by dissolving CFZ in AP. The concentration of CFZ in AP ranged from 0 to 50  $\mu\text{M}$ . The absorption spectra of the solutions were measured by UV-Vis spectroscopy, and the absorbance maximum (490 nm for CFZ and 244 nm for AP) was used to plot the calibration curve. The calibration curves ranging from 0 to 25  $\mu\text{M}$  of CFZ dissolved in a mixture of ethanol and HEPES buffer solution (10 mM, pH = 7.4) (v/v = 1/1) were also generated. To determine the release capacity and release efficiency of AP, the calibration curve of AP was generated by dissolving AP in a mixture of ethanol and HEPES buffer solution (10 mM, pH = 7.4) (v/v = 1/1). The concentration of AP ranged from 0.25 to 66  $\mu\text{M}$ .

#### **5.12.7 Loading Capacity Analysis of Clofazimine (CFZ)**



The loading of CFZ was studied using DMSO or AP as loading solvents. In general, 10 mg of MSNs were dispersed in AP or DMSO with 0.1, 1, 10, or 50 mM CFZ, respectively. After 24 h stirring, the CFZ loaded MSNs were centrifuged at 14000 rpm for 10 min and the pellets were washed three times with H<sub>2</sub>O under sonication to remove the excess CFZ. Then, the CFZ loaded MSNs with AP or DMSO were washed with AP or DMSO, respectively, and pelleted by centrifugation. The washing steps were repeated several times until the supernatant was clear. The supernatants were collected and measured by UV-Vis spectroscopy. The loading capacity of CFZ was calculated using the maximum absorbance at 490 nm based on Beer's law, its calibration curve, and the following definition of loading capacity: (mass of loaded CFZ/mass of MSNs) x 100%.

#### **5.12.8 Release of CFZ and AP in HEPES Buffer**

The release of CFZ and AP from MSNs was carried out in HEPES buffer solution (pH = 7.4, 10 mM). In general, 10 mg of MSNs loaded with 0.1, 1, 10, or 50 mM CFZ in AP were dispersed in 1 mL of HEPES buffer solution and stirred for 1, 2, 3, or 5 days, respectively. Afterwards, the CFZ loaded MSNs were spun down at 14000 rpm for 10 min. The supernatant was collected and mixed homogeneously with ethanol, which was then diluted and measured by UV-Vis spectroscopy. The release efficiency of CFZ and AP were calculated using their maximum absorbance at 490 nm and 244 nm, respectively, based on Beer's law, their calibration curves, and the definition of release efficiency: (mass of released CFZ/mass of loaded CFZ) x 100%.

#### **5.12.9 Release of CFZ in HEPES Buffer with Addition of AP**

To gain insight into whether the AP residing outside of the pores of MSNs would affect CFZ release, we added AP into the release buffer. After MSNs were loaded with 1 mM CFZ in DMSO, 10 mg of MSNs were dispersed in 1 mL of HEPES buffer (10 mM, pH = 7.4) with the addition of 10  $\mu$ L of AP. The solution was stirred for 24 h and then centrifuged at 14000 rpm for 10 min. The

supernatant was collected and measured by UV-Vis spectroscopy; the pellet of CFZ loaded MSNs was resuspended by sonication in 1 mL of HEPES buffer with the addition of 10  $\mu$ L of AP and stirred for another 24 h. Again, the supernatant was collected as described above and measured by UV-Vis spectroscopy. The same procedures were repeated and the supernatant was collected and analyzed at 72 h and 120 h as described above.

#### **5.12.10 Assay for killing of *M. tuberculosis* in macrophages**

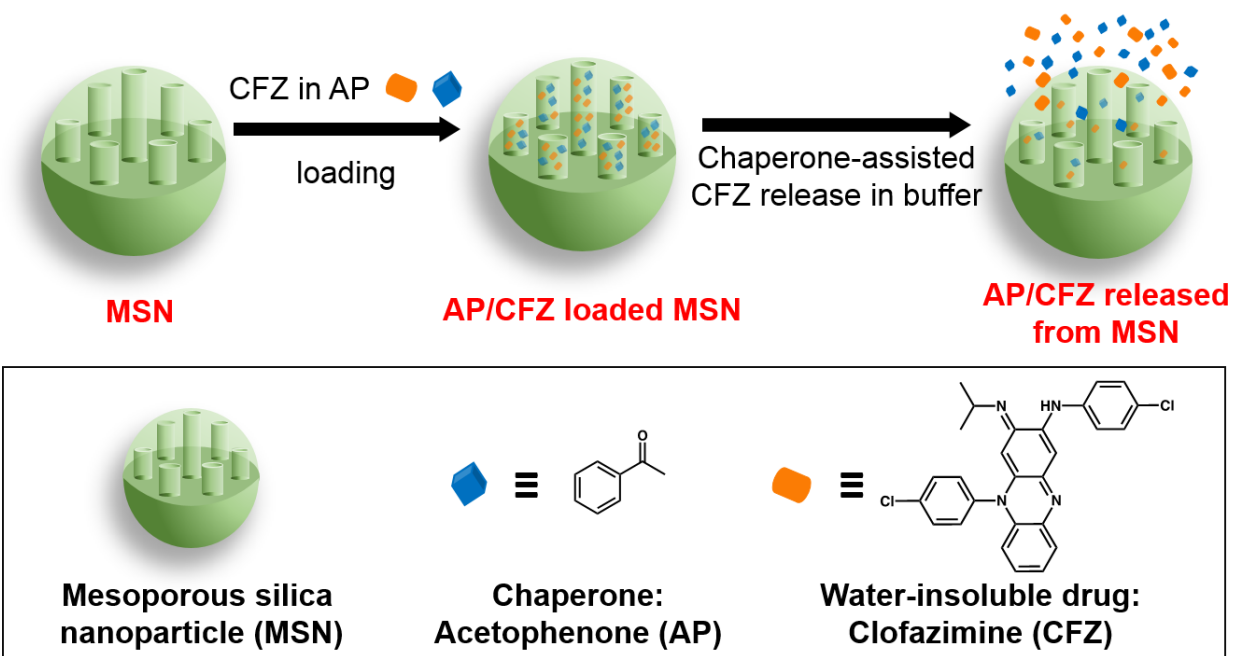
Human monocytic THP-1 cells (ATCC TIB202) were maintained in RPMI-1640 supplemented with 10% fetal bovine serum, GlutaMAX, and Penicillin-Streptomycin (100 IU-100  $\mu$ g/mL). Prior to infection, the cells were treated with phorbol 12-myristate 13-acetate (PMA) for 3 days to differentiate them into macrophage-like cells. *M. tuberculosis* virulent strain Erdman (ATCC 35801) was cultured on Middlebrook 7H11 plates for 10 days. Lawns of bacteria were scraped from the plates, suspended in RPMI with 20 mM HEPES, and a single bacterial suspension was prepared by sonication and repeated centrifugation to remove bacterial clumps. After opsonization with human serum type AB containing active complement, the bacteria were used to infect PMA-differentiated THP-1 macrophages at a multiplicity of infection of 1:1 (bacterium:macrophage). The bacteria were incubated with macrophages for 1 hour at 37 °C, after which MSNs loaded with AP (AP-MSN), MSNs loaded with 10 mM CFZ in AP hydrotrope (AP/CFZ-MSN), or free CFZ were added to the culture of the *M. tuberculosis* infected macrophages. The concentrations of AP-MSN were 11 and 22  $\mu$ g/mL. The concentrations of AP/CFZ-MSN were 5.5, 11, and 22  $\mu$ g/mL, corresponding to 0.5, 1, and 2  $\mu$ g/mL of CFZ, respectively. Free CFZ was dissolved in DMSO first, and then added to *M. tuberculosis* infected macrophages at concentrations of 0.5, 1, and 2  $\mu$ g/mL, those concentrations of free CFZ had 0.005%, 0.01%, and 0.02% DMSO, respectively. The cells were incubated for 4 days at 37 °C, 5%

CO<sub>2</sub>-95% air, lysed with 0.1% SDS, serially diluted in Middlebrook 7H9 broth supplemented with ADC enrichment and 0.05% Tween 80, and plated on Middlebrook 7H11 agar plates. The number of bacterial colonies on the plates was enumerated after incubation for 2.5 weeks at 37 °C, 5% CO<sub>2</sub>-95% air.<sup>32,54</sup>

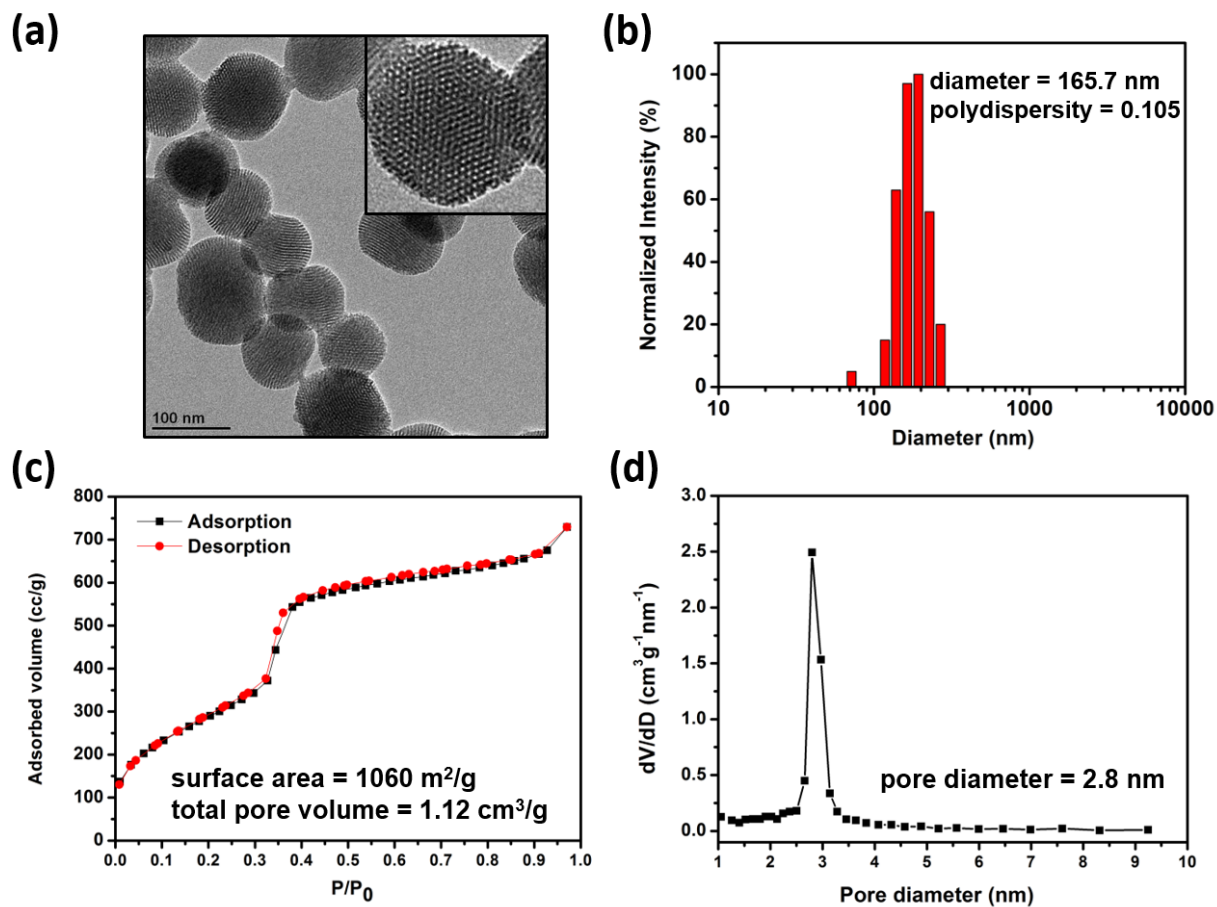
### **5.13 Acknowledgment**

We gratefully acknowledge financial support by Defense Threat Reduction Agency Grant HDTRA1-13-1-0046.

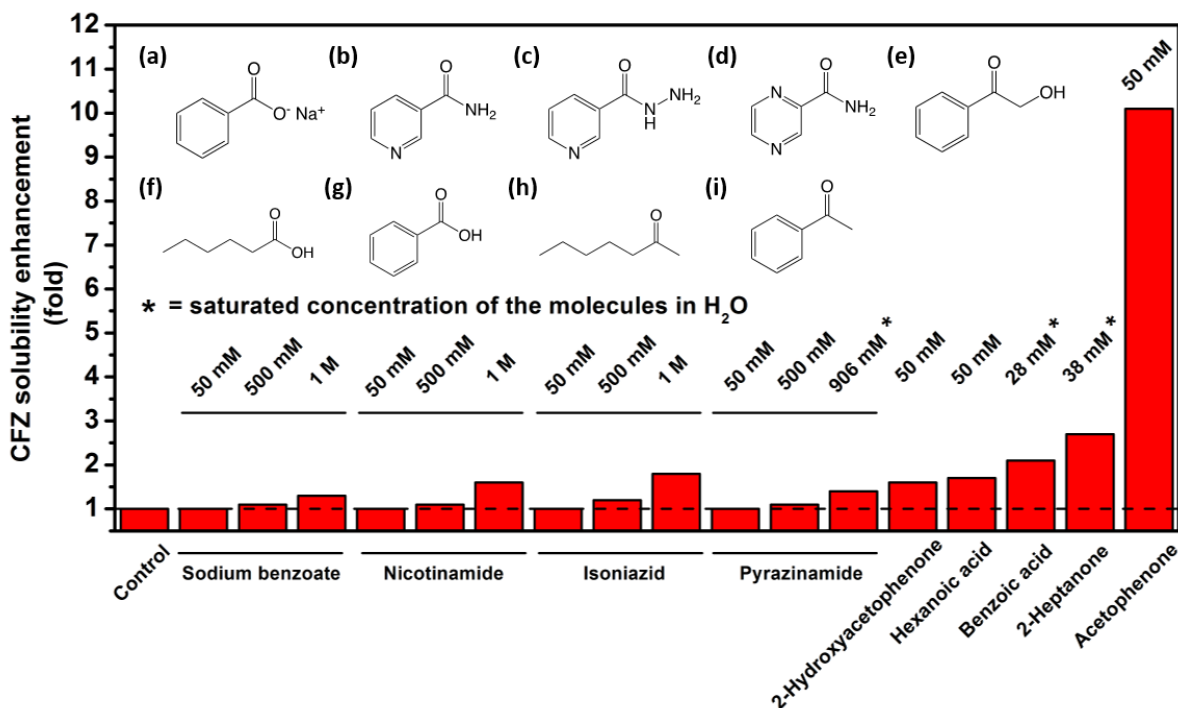
## 5.14 Figures and Tables



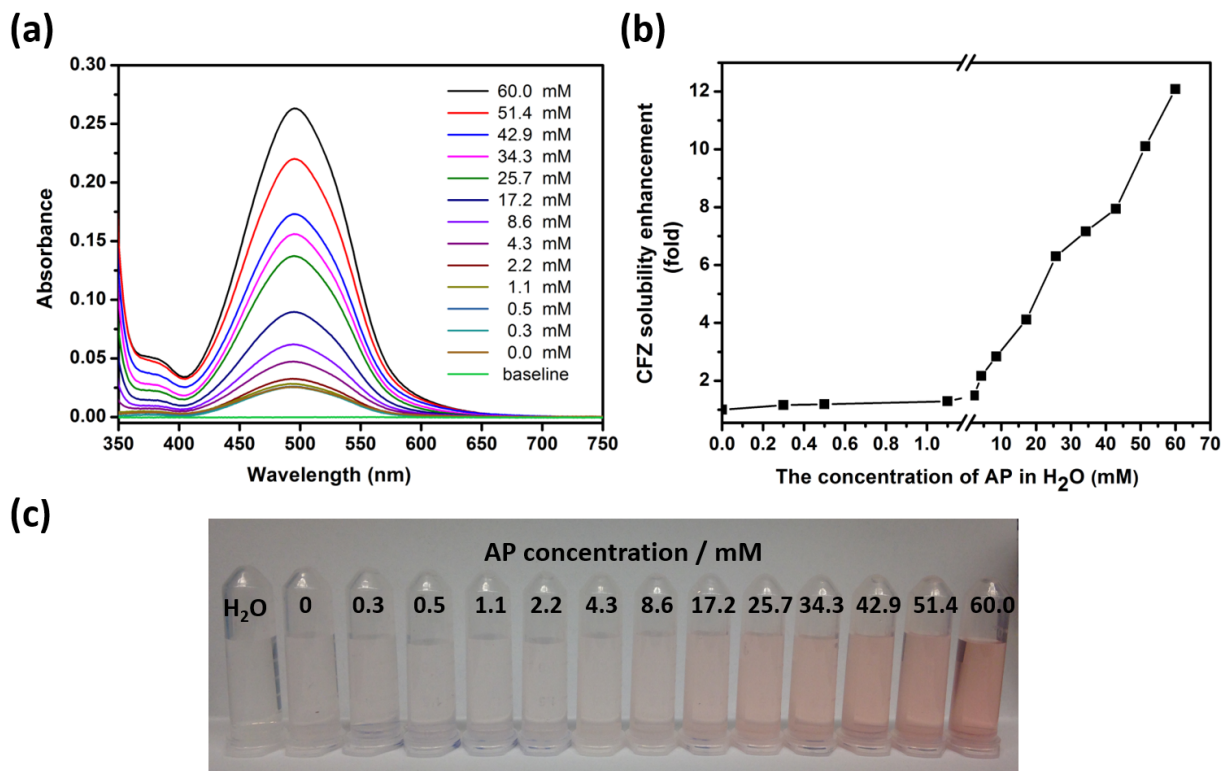
**Figure 5.1.** Chaperone-assisted delivery strategy for water-insoluble drugs. Clofazimine (CFZ) was chosen as an example of a water-insoluble antibiotic. Acetophenone (AP) acts like a chaperone bringing CFZ cargo into the vehicle — mesoporous silica nanoparticles (MSNs) and then carrying CFZ cargo out from the MSNs effectively.



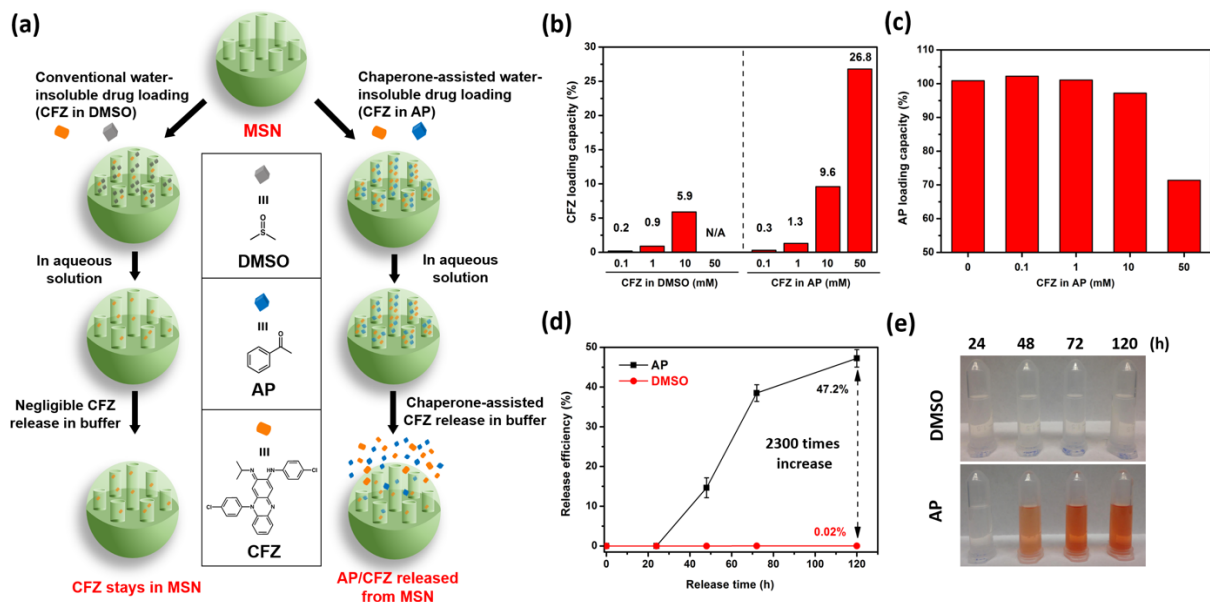
**Figure 5.2.** (a) TEM image of mesoporous silica nanoparticles (MSNs). Inset shows the enlarged image. (b) Dynamic light scattering diameter distribution of MSNs in D.I. H<sub>2</sub>O. The diameter of the MSNs is 165.7 nm. (c) Nitrogen adsorption-desorption isotherms of MSNs at 77 K. BET surface area and pore volume are 1060 m<sup>2</sup>/g and 1.12 cm<sup>3</sup>/g, respectively. (d) Pore diameter distribution of MSNs. Average pore diameter of MSNs is 2.8 nm.



**Figure 5.3.** CFZ solubility enhancement in the presence of (a) sodium benzoate, (b) nicotinamide, (c) isoniazid, (d) pyrazinamide, (e) 2-hydroxyacetophenone, (f) hexanoic acid, (g) benzoic acid, (h) 2-heptanone, and (i) acetophenone. The solubility of CFZ in deionized water without the addition of any molecule served as a control.

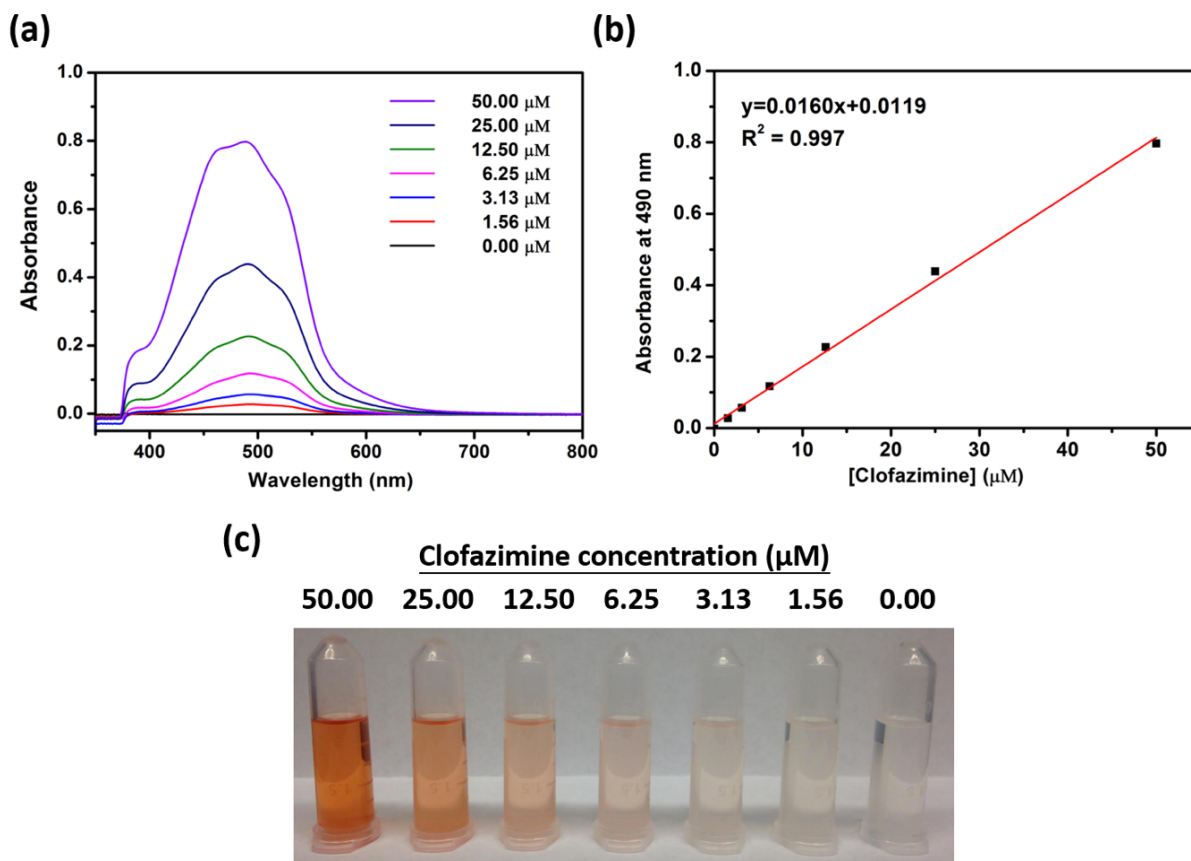


**Figure 5.4.** (a) UV-Vis spectra of CFZ dissolved in H<sub>2</sub>O in the presence of different concentrations of AP. (b) CFZ solubility enhancement (fold increase compared with no AP) in the presence of different concentrations of AP in H<sub>2</sub>O. (c) Photograph of CFZ dissolved in H<sub>2</sub>O in the presence of different concentrations of AP.

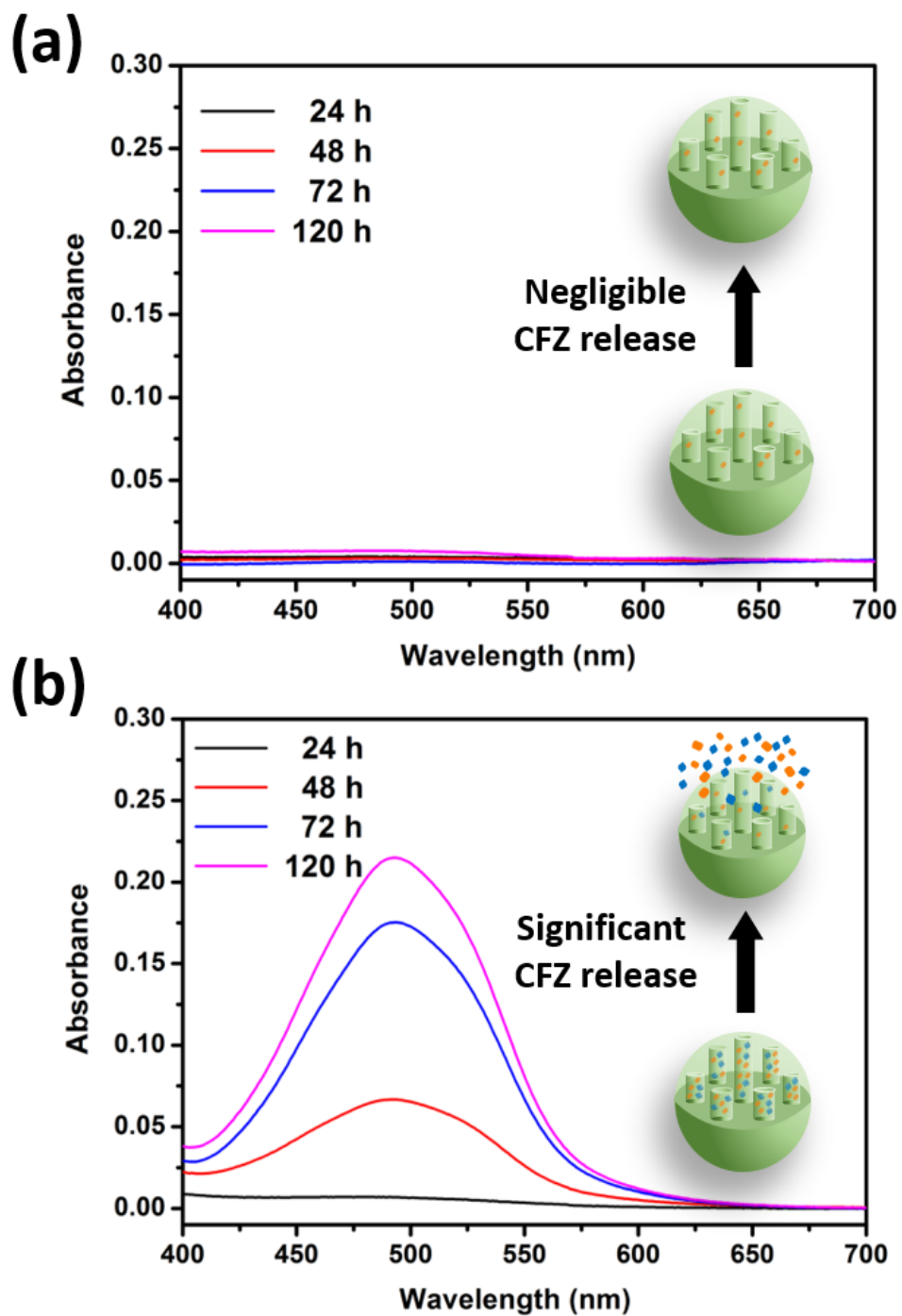


**Figure 5.5.** (a) Schematic illustration of conventional method (CFZ in DMSO) or chaperone-assisted method (CFZ in AP) for water-insoluble CFZ loading in MSN. By using AP as the chaperone, CFZ release from MSNs could be enhanced significantly. Loading capacity of (b) CFZ and (c) AP using 0.1, 1, or 10 mM CFZ in DMSO or 0, 0.1, 1, 10, or 50 mM CFZ in AP as the loading solution. The concentration of MSNs was 10 mg/mL. (d) Time-dependent release efficiency of CFZ in HEPES buffer solution (10 mM, pH = 7.4) with 1 mM CFZ in DMSO or 1 mM CFZ in AP as loading solutions. (e) Photographs of supernatant after CFZ release collected at selected time points. MSNs were loaded with 1 mM CFZ in DMSO or 1 mM CFZ in AP.

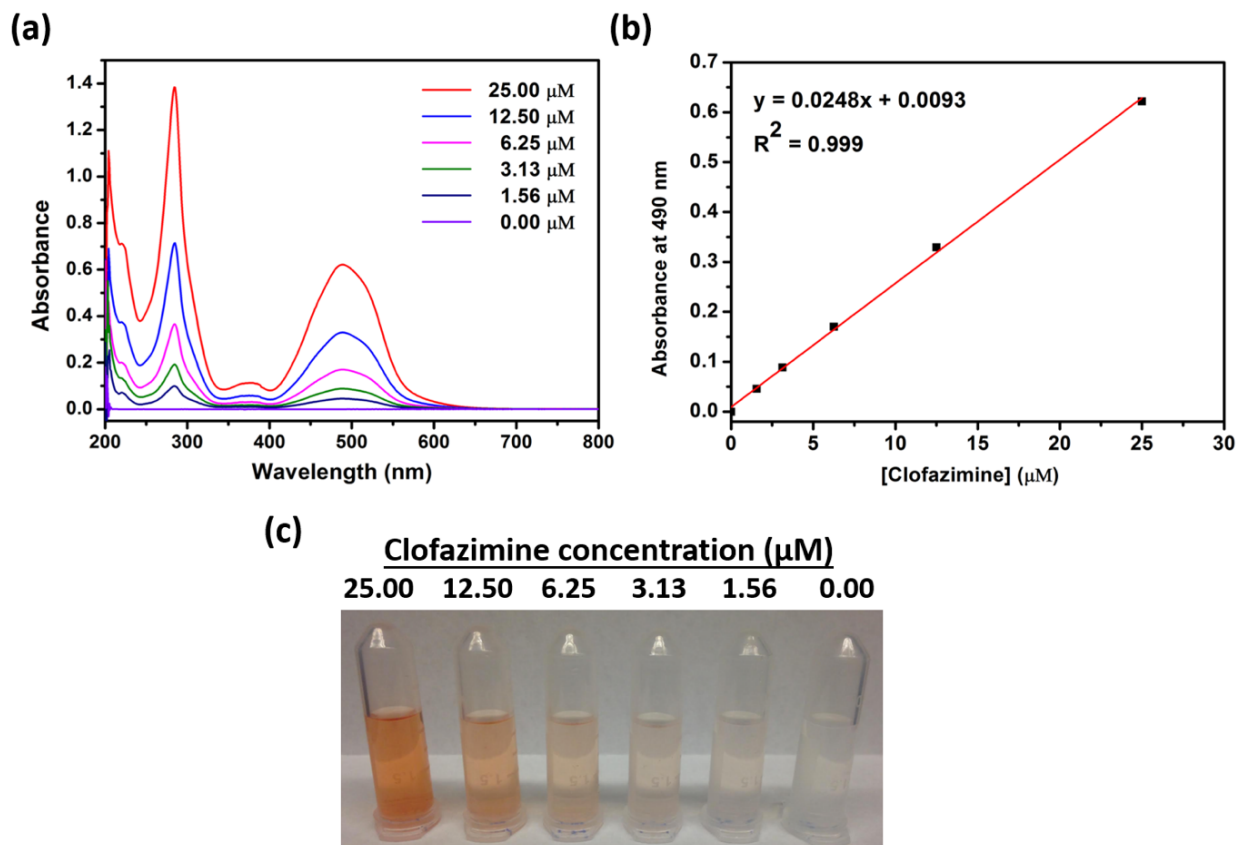




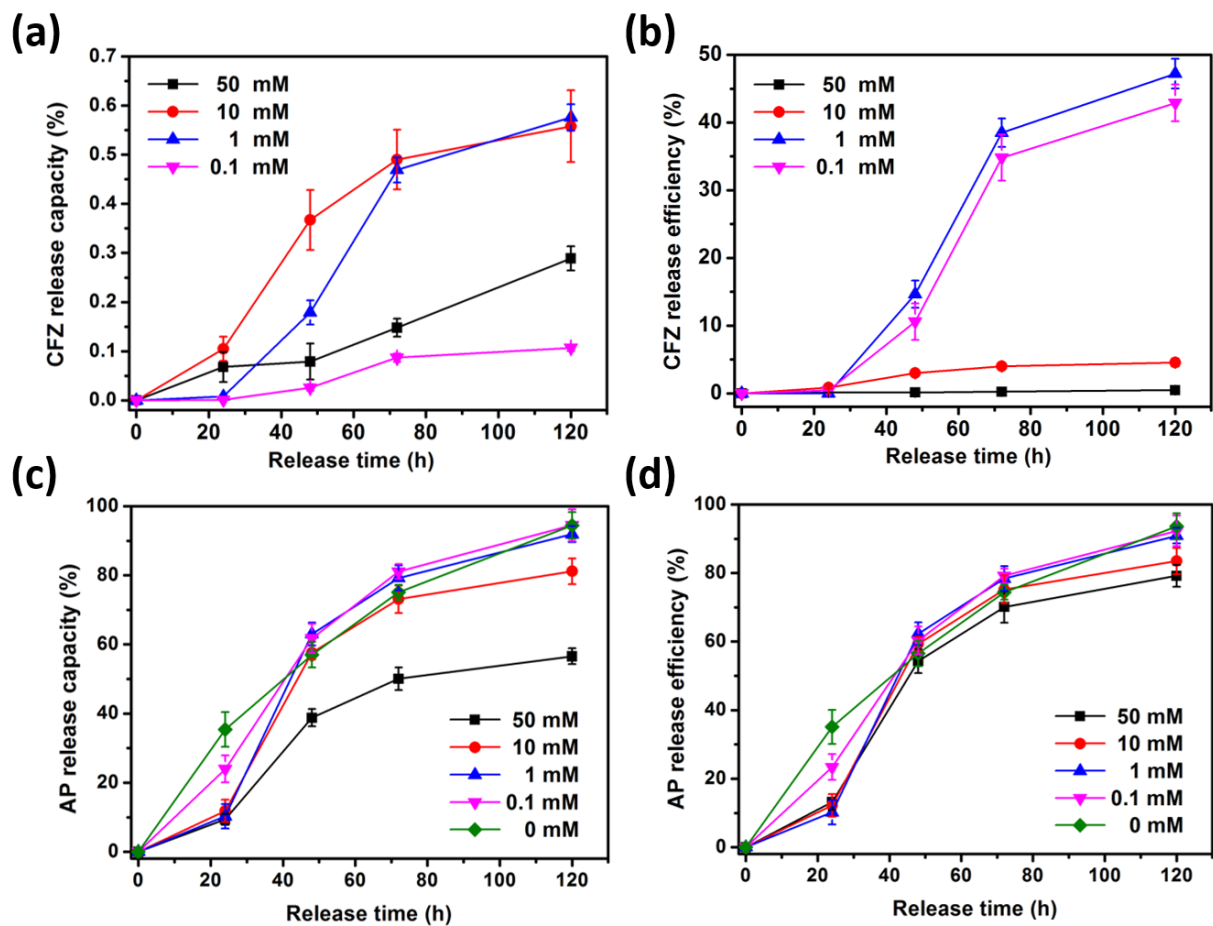
**Figure 5.6.** (a) UV-Vis spectra of CFZ in AP as a function of concentration and (b) calibration curve of CFZ in AP at room temperature. (c) Photograph of CFZ dissolved in AP.



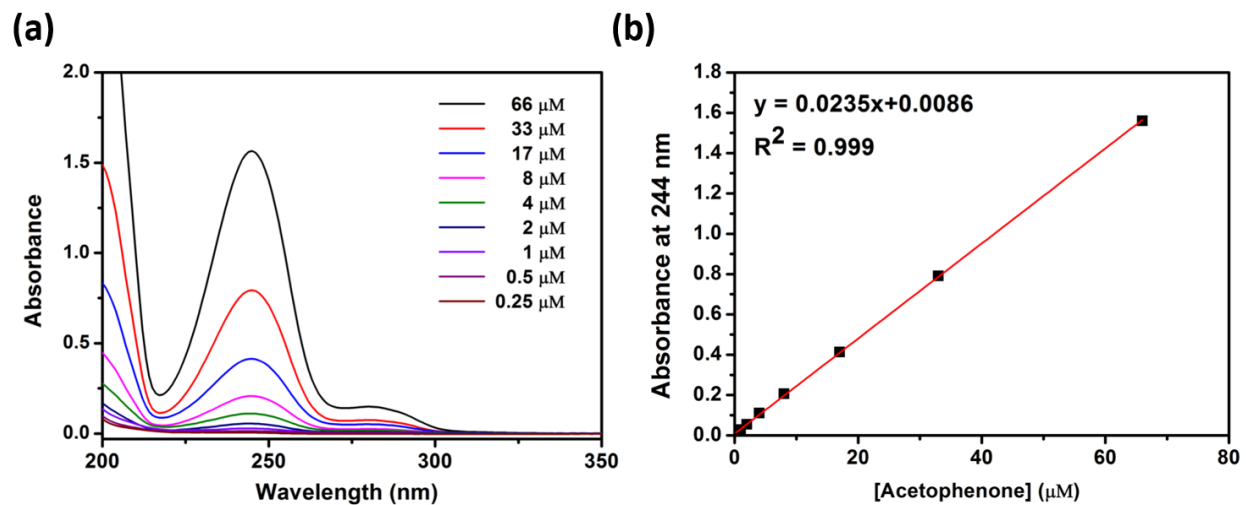
**Figure 5.7** UV-Vis spectra of time-dependent CFZ release in HEPES buffer solution (10 mM, pH = 7.4) by using (a) DMSO or (b) AP as loading solvents. MSNs were loaded with 1 mM CFZ in DMSO or 1 mM CFZ in AP. The concentration of MSNs in both loading solution and release buffer solution were 10 mg/mL.



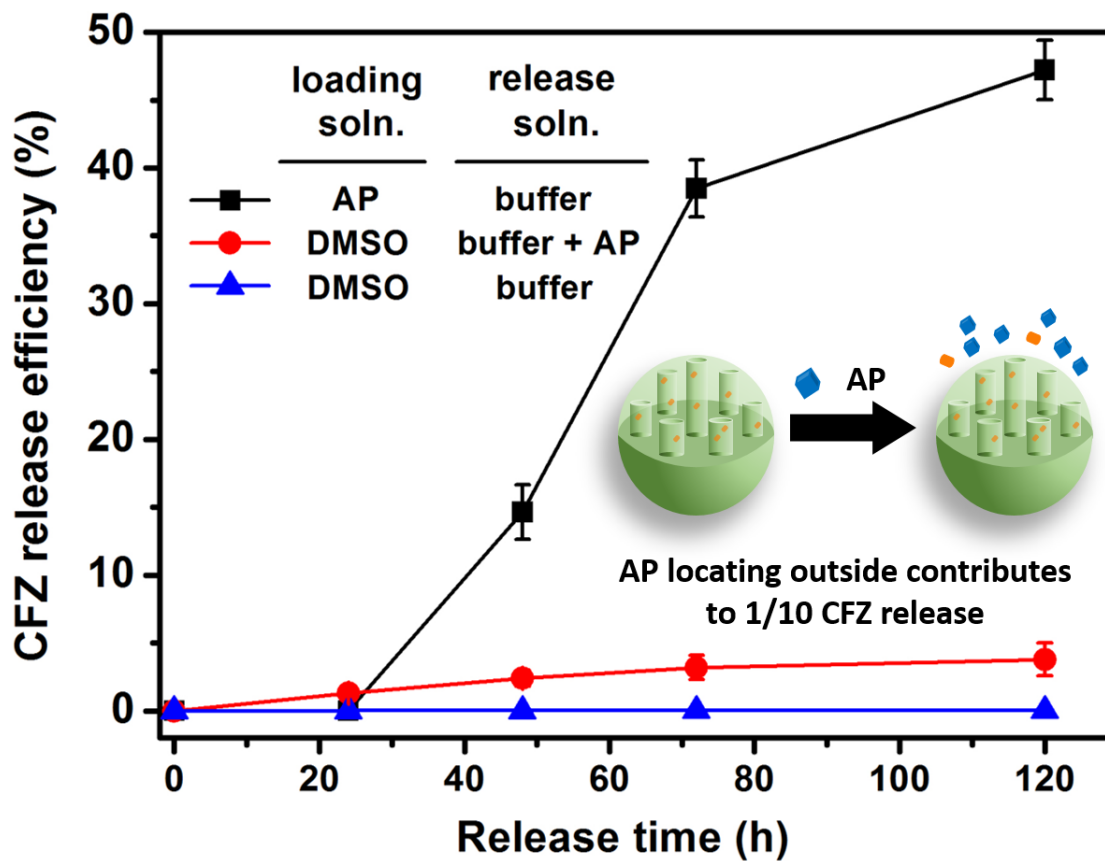
**Figure 5.8.** (a) Concentration dependent UV-Vis spectra and (b) calibration curve of CFZ in EtOH/HEPES buffer (10 mM, pH = 7.4) (v/v=1/1) solution at room temperature. (c) Photograph of CFZ dissolved in EtOH/HEPES buffer solution (10 mM, pH=7.4) (v/v=1/1).



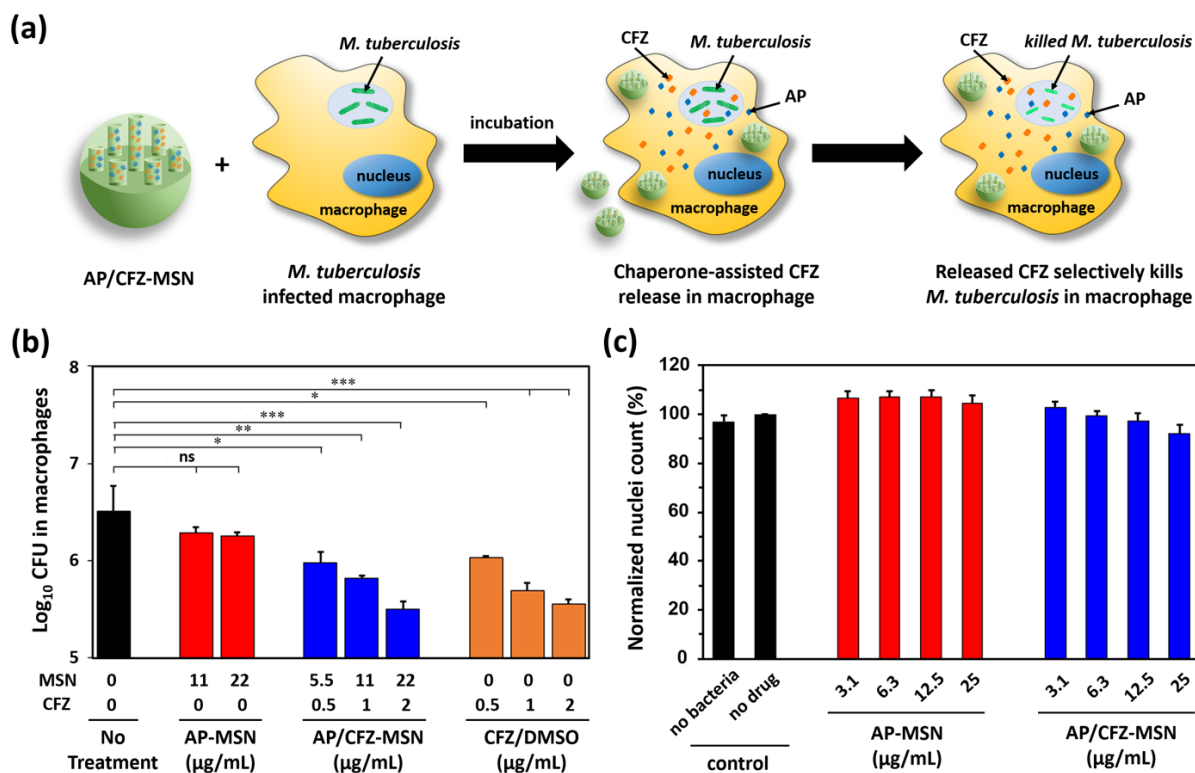
**Figure 5.9.** Time-dependent release capacity of (a) CFZ and (c) AP and release efficiency of (b) CFZ and (d) AP in HEPES buffer solution (10 mM, pH = 7.4) with 0, 0.1, 1, 10, and 50 mM CFZ in AP as loading solutions. The concentration of MSNs in both loading solution and release buffer solution was 10 mg/mL (n=3).



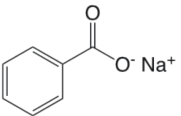
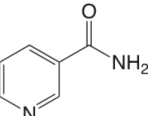
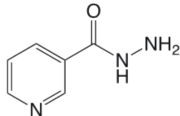
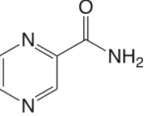
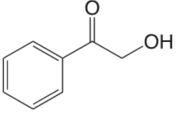
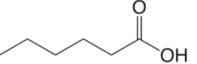
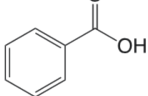
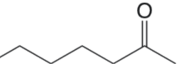
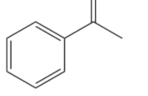
**Figure 5.10** (a) Concentration dependent UV-Vis spectra and (b) calibration curve of AP in EtOH/ HEPES buffer solution (10 mM, pH = 7.4) (v/v=1/1).



**Figure 5.11.** Time-dependent release efficiency of CFZ in HEPES buffer solution (10 mM, pH = 7.4) with or without the addition of AP to the buffer solution. After loading with 1 mM CFZ in DMSO, 10  $\mu$ L of AP was added to the buffer solution (10 mg MSNs/mL, 1 mL) (n=3).



**Figure 5.12.** (a) Schematic illustration of applying chaperone-assisted CFZ delivery strategy to selectively killing *M. tuberculosis* in macrophage. (b) AP/CFZ loaded MSNs kill *M. tuberculosis in vitro* in macrophage cultures. *M. tuberculosis*-infected THP-1 macrophages were untreated, treated with MSN loaded with AP (AP-MSN), treated with MSN loaded with CFZ and AP (AP/CFZ-MSN), or treated with CFZ dissolved in a mixture of DMSO and H<sub>2</sub>O (CFZ/DMSO) for 4 days. Bacterial colony forming units (CFUs) were determined by spreading serially diluted lysates of the infected macrophages on agar plates. CFU data are shown as the mean  $\pm$  standard deviation. Statistical analysis was performed using one-way ANOVA with Tukey's correction for multiple comparisons. ns, not significant; \* $p < 0.05$ ; \*\* $p < 0.01$ ; \*\*\* $p < 0.001$  (c) Count of macrophage nuclei per 10x microscopic field normalized to that of the macrophage control wells without addition of drug. Count of macrophage nuclei per microscopic field is used as a surrogate of macrophage viability, as dead macrophages detach and are lost from the monolayer over the long incubation period. Human THP-1 macrophages were either not infected (no bacteria) or infected with *Mycobacterium tuberculosis* in the absence of nanoparticles (no drug) or in the presence of AP-MSN and AP/CFZ-MSN with serial two-fold increasing concentration ranging from 3.1 to 25  $\mu\text{g/mL}$ , as indicated. At the end of a 4-day incubation, macrophages were fixed with paraformaldehyde and the nuclei were stained with DAPI and imaged with an ImageXpress High Content Screening system using a 10x objective lens. The acquired images were analyzed using the Count Nuclei module of MetaXpress software to quantitate numbers of nuclei per 10x field. Data shown are mean  $\pm$  sem of three biological replicates.

<b>Chemical structure</b>					
<b>Chemical name</b>	Sodium benzoate	Nicotinamide	Isoniazid	Pyrazinamide	2-Hydroxyacetophenone
<b>H<sub>2</sub>O solubility (mg/mL)</b>	629	500	140	50	20
<b>Chemical structure</b>					
<b>Chemical name</b>	Hexanoic acid	Benzoic acid	2-Heptanone	Acetophenone	
<b>H<sub>2</sub>O solubility (mg/mL)</b>	10.8	3.4	4.3	6.1	

**Table 5.1.** Chemical structures of possible hydrotropes for clofazimine (CFZ) and their water solubilities.



CFZ in AP (mM)	0	0.1	1	10	50
loaded CFZ/MSNs (nmole/mg)	0	6.3	27.5	202.8	566.1
loaded AP/MSNs (nmole/mg)	8397.8	8522.7	8414.5	8089.9	5942.6
mole ratio of AP/CFZ	n/a	1352.8	306.0	39.9	10.5

**Table 5.2.** Summary of the amount of loaded CFZ and AP in MSNs (nmole/mg) and the mole ratio of AP/CFZ loaded in MSNs.

## 5.15 References

- (1) Khadka, P.; Ro, J.; Kim, H.; Kim, I.; Kim, J. T.; Kim, H.; Cho, J. M.; Yun, G.; Lee, J. Pharmaceutical Particle Technologies: An Approach to Improve Drug Solubility, Dissolution and Bioavailability. *Asian J. Pharm. Sci.* **2014**, *9*, 304–316.
- (2) Ferris, D. P.; Lu, J.; Gothard, C.; Yanes, R.; Thomas, C. R.; Olsen, J. C.; Stoddart, J. F.; Tamanoi, F.; Zink, J. I. Synthesis of Biomolecule-Modified Mesoporous Silica Nanoparticles for Targeted Hydrophobic Drug Delivery to Cancer Cells. *Small* **2011**, *7*, 1816–1826.
- (3) Wu, S. H.; Mou, C. Y.; Lin, H. P. Synthesis of Mesoporous Silica Nanoparticles. *Chem. Soc. Rev.* **2013**, *42*, 3862–3875.
- (4) Tarn, D.; Ashley, C. E.; Xue, M.; Carnes, E. C.; Zink, J. I.; Brinker, C. J. Mesoporous Silica Nanoparticle Nanocarriers: Biofunctionality and Biocompatibility. *Acc. Chem. Res.* **2013**, *46*, 792–801.
- (5) Ruehle, B.; Saint-Cricq, P.; Zink, J. I. Externally Controlled Nanomachines on Mesoporous Silica Nanoparticles for Biomedical Applications. *Chemphyschem* **2016**, *17*, 1769–1779.
- (6) Tang, F.; Li, L.; Chen, D. Mesoporous Silica Nanoparticles: Synthesis, Biocompatibility and Drug Delivery. *Adv. Mater.* **2012**, *24*, 1504–1534.
- (7) Chou, C. C.; Chen, W.; Hung, Y.; Mou, C. Y. Molecular Elucidation of Biological Response to Mesoporous Silica Nanoparticles in Vitro and in Vivo. *ACS Appl. Mater. Interfaces* **2017**, *9*, 22235–22251.
- (8) Li, Z.; Barnes, J. C.; Bosoy, A.; Stoddart, J. F.; Zink, J. I. Mesoporous Silica Nanoparticles in Biomedical Applications. *Chem. Soc. Rev.* **2012**, *41*, 2590–2605.
- (9) Li, Y.; Shi, J. Hollow-Structured Mesoporous Materials: Chemical Synthesis, Functionalization and Applications. *Adv. Mater.* **2014**, *26*, 3176–3205.
- (10) Wei, J.; Sun, Z.; Luo, W.; Li, Y.; Elzatahry, A. A.; Al-Enizi, A. M.; Deng, Y.; Zhao, D. New Insight into the Synthesis of Large-Pore Ordered Mesoporous Materials. *J. Am. Chem. Soc.* **2017**, *139*, 1706–1713.
- (11) Suteewong, T.; Sai, H.; Hovden, R.; Muller, D.; Bradbury, M. S.; Gruner, S. M.; Wiesner, U. Multicompartment Mesoporous Silica Nanoparticles with Branched Shapes: An Epitaxial Growth Mechanism. *Science* **2013**, *340*, 337–341.
- (12) Zhang, Q.; Wang, X.; Li, P. Z.; Nguyen, K. T.; Wang, X. J.; Luo, Z.; Zhang, H.; Tan, N. S.; Zhao, Y. Biocompatible, Uniform, and Redispersible Mesoporous Silica Nanoparticles for Cancer-Targeted Drug Delivery in Vivo. *Adv. Funct. Mater.* **2014**, *24*, 2450–2461.
- (13) Argyo, C.; Weiss, V.; Bräuchle, C.; Bein, T. Multifunctional Mesoporous Silica Nanoparticles as a Universal Platform for Drug Delivery. *Chem. Mater.* **2014**, *26*, 435–451.
- (14) Lu, J.; Liong, M.; Zink, J. I.; Tamanoi, F. Mesoporous Silica Nanoparticles as a Delivery System for

- Hydrophobic Anticancer Drugs. *Small* **2007**, *3*, 1341–1346.
- (15) Ruehle, B.; Clemens, D. L.; Lee, B.-Y.; Horwitz, M. A.; Zink, J. I. A Pathogen-Specific Cargo Delivery Platform Based on Mesoporous Silica Nanoparticles. *J. Am. Chem. Soc.* **2017**, *139*, 6663–6668.
- (16) Li, Z.; Clemens, D. L.; Lee, B. Y.; Dillon, B. J.; Horwitz, M. A.; Zink, J. I. Mesoporous Silica Nanoparticles with pH-Sensitive Nanovalves for Delivery of Moxifloxacin Provide Improved Treatment of Lethal Pneumonic Tularemia. *ACS Nano* **2015**, *9*, 10778–10789.
- (17) Yan, H.; Teh, C.; Sreejith, S.; Zhu, L.; Kwok, A.; Fang, W.; Ma, X.; Nguyen, K. T.; Korzh, V.; Zhao, Y. Functional Mesoporous Silica Nanoparticles for Photothermal-Controlled Drug Delivery in Vivo. *Angew. Chem. Int. Ed.* **2012**, *51*, 8373–8377.
- (18) Chen, W.; Tsai, P. H.; Hung, Y.; Chiou, S. H.; Mou, C. Y. Nonviral Cell Labeling and Differentiation Agent for Induced Pluripotent Stem Cells Based on Mesoporous Silica Nanoparticles. *ACS Nano* **2013**, *7*, 8423–8440.
- (19) Chang, J. H.; Tsai, P. H.; Chen, W.; Chiou, S. H.; Mou, C. Y. Dual Delivery of siRNA and Plasmid DNA Using Mesoporous Silica Nanoparticles to Differentiate Induced Pluripotent Stem Cells into Dopaminergic Neurons. *J. Mater. Chem. B* **2017**, *5*, 3012–3023.
- (20) Xia, T.; Kovoichich, M.; Liong, M.; Meng, H.; Kabehie, S.; George, S.; Zink, J. I.; Nel, A. E. Polyethyleneimine Coating Enhances the Cellular Uptake of Mesoporous Silica Nanoparticles and Allows Safe Delivery of siRNA and DNA Constructs. *ACS Nano* **2009**, *3*, 3273–3286.
- (21) Wu, M.; Meng, Q.; Chen, Y.; Du, Y.; Zhang, L.; Li, Y.; Zhang, L.; Shi, J. Large-Pore Ultrasmall Mesoporous Organosilica Nanoparticles: Micelle/precursor Co-Templating Assembly and Nuclear-Targeted Gene Delivery. *Adv. Mater.* **2015**, *27*, 215–222.
- (22) Chen, Y. P.; Chen, C. T.; Hung, Y.; Chou, C. M.; Liu, T. P.; Liang, M. R.; Chen, C. T.; Mou, C. Y. A New Strategy for Intracellular Delivery of Enzyme Using Mesoporous Silica Nanoparticles: Superoxide Dismutase. *J. Am. Chem. Soc.* **2013**, *135*, 1516–1523.
- (23) Tu, J.; Boyle, A. L.; Friedrich, H.; Bomans, P. H. H.; Bussmann, J.; Sommerdijk, N. A. J. M.; Jiskoot, W.; Kros, A. Mesoporous Silica Nanoparticles with Large Pores for the Encapsulation and Release of Proteins. *ACS Appl. Mater. Interfaces* **2016**, *8*, 32211–32219.
- (24) Chen, F.; Hong, H.; Zhang, Y.; Valdovinos, H. F.; Shi, S.; Kwon, G. S.; Theuer, C. P.; Barnhart, T. E.; Cai, W. In Vivo Tumor Targeting and Image-Guided Drug Delivery with Antibody-Conjugated, Radiolabeled Mesoporous Silica Nanoparticles. *ACS Nano* **2013**, *7*, 9027–9039.
- (25) Qu, Q.; Ma, X.; Zhao, Y. Anticancer Effect of  $\alpha$ -Tocopheryl Succinate Delivered by Mitochondria-Targeted Mesoporous Silica Nanoparticles. *ACS Appl. Mater. Interfaces* **2016**, *8*, 34261–34269.
- (26) Liong, M.; Lu, J.; Kovoichich, M.; Xia, T.; Ruehm, S. G.; Nel, A. E.; Tamanoi, F.; Zink, J. I. Multifunctional Inorganic Nanoparticles for Imaging, Targeting, and Drug Delivery. *ACS Nano* **2008**, *2*, 889–896.

- (27) Guardado-Alvarez, T. M.; Chen, W.; Norton, A. E.; Russell, M. M.; Connick, W. B.; Zink, J. I. Analyte-Responsive Gated Hollow Mesoporous Silica Nanoparticles Exhibiting Inverse Functionality and an AND Logic Response. *Nanoscale* **2016**, *8*, 18296–18300.
- (28) Kwon, D.; Cha, B. G.; Cho, Y.; Min, J.; Park, E. B.; Kang, S. J.; Kim, J. Extra-Large Pore Mesoporous Silica Nanoparticles for Directing in Vivo M2 Macrophage Polarization by Delivering IL-4. *Nano Lett.* **2017**, *17*, 2747–2756.
- (29) Kamkaew, A.; Cheng, L.; Goel, S.; Valdovinos, H. F.; Barnhart, T. E.; Liu, Z.; Cai, W. Cerenkov Radiation Induced Photodynamic Therapy Using Chlorin e6-Loaded Hollow Mesoporous Silica Nanoparticles. *ACS Appl. Mater. Interfaces* **2016**, *8*, 26630–26637.
- (30) Kempen, P. J.; Greasley, S.; Parker, K. A.; Campbell, J. L.; Chang, H. Y.; Jones, J. R.; Sinclair, R.; Gambhir, S. S.; Jokerst, J. V. Theranostic Mesoporous Silica Nanoparticles Biodegrade after pro-Survival Drug Delivery and Ultrasound/magnetic Resonance Imaging of Stem Cells. *Theranostics* **2015**, *5*, 631–642.
- (31) Rühle, B.; Datz, S.; Argyo, C.; Bein, T.; Zink, J. I. A Molecular Nanocap Activated by Superparamagnetic Heating for Externally Stimulated Cargo Release. *Chem. Commun.* **2016**, *52*, 1843–1846.
- (32) Hwang, A. A.; Lee, B. Y.; Clemens, D. L.; Dillon, B. J.; Zink, J. I.; Horwitz, M. A. Tuberculosis: pH-Responsive Isoniazid-Loaded Nanoparticles Markedly Improve Tuberculosis Treatment in Mice. *Small* **2015**, *11*, 5066–5078.
- (33) Paris, J. L.; Cabanas, M. V.; Manzano, M.; Vallet-Regí, M. Polymer-Grafted Mesoporous Silica Nanoparticles as Ultrasound-Responsive Drug Carriers. *ACS Nano* **2015**, *9*, 11023–11033.
- (34) Li, H.; Tan, L. L.; Jia, P.; Li, Q. L.; Sun, Y. L.; Zhang, J.; Ning, Y. Q.; Yu, J.; Yang, Y. W. Near-Infrared Light-Responsive Supramolecular Nanovalve Based on Mesoporous Silica-Coated Gold Nanorods. *Chem. Sci.* **2014**, *5*, 2804–2808.
- (35) Thomas, C. R.; Ferris, D. P.; Lee, J. H.; Choi, E.; Cho, M. H.; Kim, E. S.; Stoddart, J. F.; Shin, J. S.; Cheon, J.; Zink, J. I. Noninvasive Remote-Controlled Release of Drug Molecules in Vitro Using Magnetic Actuation of Mechanized Nanoparticles. *J. Am. Chem. Soc.* **2010**, *132*, 10623–10625.
- (36) Wang, H.; Wang, K.; Tian, B.; Revia, R.; Mu, Q.; Jeon, M.; Chang, F. C.; Zhang, M. Preloading of Hydrophobic Anticancer Drug into Multifunctional Nanocarrier for Multimodal Imaging, NIR-Responsive Drug Release, and Synergistic Therapy. *Small* **2016**, *12*, 6388–6397.
- (37) Palanikumar, L.; Kim, H. Y.; Oh, J. Y.; Thomas, A. P.; Choi, E. S.; Jeena, M. T.; Joo, S. H.; Ryu, J. H. Noncovalent Surface Locking of Mesoporous Silica Nanoparticles for Exceptionally High Hydrophobic Drug Loading and Enhanced Colloidal Stability. *Biomacromolecules* **2015**, *16*, 2701–2714.
- (38) Jiao, Y.; Sun, Y.; Tang, X.; Ren, Q.; Yang, W. Tumor-Targeting Multifunctional Rattle-Type Theranostic Nanoparticles for MRI/NIRF Bimodal Imaging and Delivery of Hydrophobic Drugs.

- Small* **2015**, *11*, 1962–1974.
- (39) Neuberg, C. Hydrotropic Phenomena. I. *Biochem. Z.* **1916**, *76*, 107–176.
- (40) Kim, J. Y.; Kim, S.; Papp, M.; Park, K.; Pinal, R. Hydrotropic Solubilization of Poorly Water-Soluble Drugs. *J. Pharm. Sci.* **2010**, *99*, 3953–3965.
- (41) Shimizu, S.; Matubayasi, N. The Origin of Cooperative Solubilisation by Hydrotropes. *Phys. Chem. Chem. Phys.* **2016**, *18*, 25621–25628.
- (42) Subbarao, C. V.; Chakravarthy, I. P. K.; Sai Bharadwaj, A. V. S. L.; Prasad, K. M. M. Functions of Hydrotropes in Solutions. *Chem. Eng. Technol.* **2012**, *35*, 225–237.
- (43) Das, S.; Paul, S. Mechanism of Hydrotropic Action of Hydrotrope Sodium Cumene Sulfonate on the Solubility of Di-t-Butyl-Methane: A Molecular Dynamics Simulation Study. *J. Phys. Chem. B* **2016**, *120*, 173–183.
- (44) Booth, J. J.; Omar, M.; Abbott, S.; Shimizu, S. Hydrotrope Accumulation around the Drug: the Driving Force for Solubilization and Minimum Hydrotrope Concentration for Nicotinamide and Urea. *Phys. Chem. Chem. Phys.* **2015**, *17*, 8028–8037.
- (45) Das, S.; Paul, S. Exploring Molecular Insights into Aggregation of Hydrotrope Sodium Cumene Sulfonate in Aqueous Solution: A Molecular Dynamics Simulation Study. *J. Phys. Chem. B*, **2015**, *119*, 3142–3154.
- (46) Shimizu, S.; Booth, J. J.; Abbott, S. Hydrotrope: Binding Models vs. Statistical Thermodynamics. *Phys. Chem. Chem. Phys.* **2013**, *15*, 20625–20632.
- (47) Shimizu, S.; Matubayasi, N. Hydrotropy: Monomer-Micelle Equilibrium and Minimum Hydrotrope Concentration. *J. Phys. Chem. B*, **2014**, *118*, 10515–10524
- (48) Patel, A.; Malinowska, L.; Saha, S.; Wang, J.; Alberti, S.; Krishnan, Y.; Hyman, A. A. Biochemistry: ATP as a Biological Hydrotrope. *Science* **2017**, *356*, 753–756.
- (49) Dalcolmo, M.; Gayoso, R.; Sotgiu, G.; D’Ambrosio, L.; Rocha, J. L.; Borga, L.; Fandinho, F.; Braga, J. U.; Galesi, V. M. N.; Barreira, D.; Sanchez, D. A.; Dockhorn, F.; Centis, R.; Caminero, J. A.; Migliori, G. B. Effectiveness and Safety of Clofazimine in Multidrug-Resistant Tuberculosis: A Nationwide Report from Brazil. *Eur. Respir. J.* **2017**, *49*, 1602445.
- (50) Lechartier, B.; Cole, S. T. Mode of Action of Clofazimine and Combination Therapy with Benzothiazinones against Mycobacterium Tuberculosis. *Antimicrob. Agents Chemother.* **2015**, *59*, 4457–4463.
- (51) Tyagi, S.; Ammerman, N. C.; Li, S.-Y.; Adamson, J.; Converse, P. J.; Swanson, R. V.; Almeida, D. V.; Grosset, J. H. Clofazimine Shortens the Duration of the First-Line Treatment Regimen for Experimental Chemotherapy of Tuberculosis. *Proc. Natl. Acad. Sci. USA* **2015**, *112*, 869–874.
- (52) Cholo, M. C.; Steel, H. C.; Fourie, P. B.; Germishuizen, W. A.; Anderson, R. Clofazimine: Current Status and Future Prospects. *J. Antimicrob. Chemother.* **2012**, *67*, 290–298.
- (53) WHO. *WHO Global Tuberculosis Report 2016*; 2016.

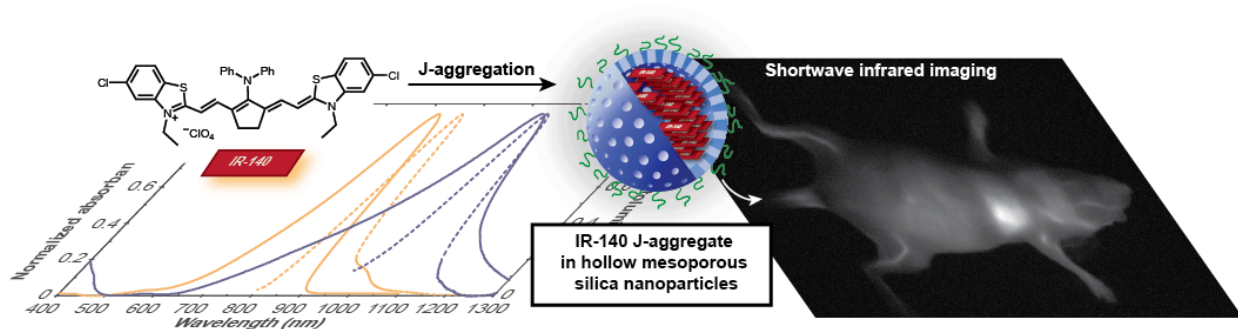
- (54) Clemens, D. L.; Lee, B. Y.; Xue, M.; Thomas, C. R.; Meng, H.; Ferris, D.; Nel, A. E.; Zink, J. I.; Horwitz, M. A. Targeted Intracellular Delivery of Antituberculosis Drugs to Mycobacterium Tuberculosis-Infected Macrophages via Functionalized Mesoporous Silica Nanoparticles. *Antimicrob. Agents Chemother.* **2012**, *56*, 2535–2545.
- (55) Huang, W. Y.; Zink, J. I. Effect of Pore Wall Charge and Probe Molecule Size on Molecular Motion inside Mesoporous Silica Nanoparticles. *J. Phys. Chem. C* **2016**, *120*, 23780–23787.
- (56) Koo, H.; Min, K. H.; Lee, S. C.; Park, J. H.; Park, K.; Jeong, S. Y.; Choi, K.; Kwon, I. C.; Kim, K. Enhanced Drug-Loading and Therapeutic Efficacy of Hydrotropic Oligomer-Conjugated Glycol Chitosan Nanoparticles for Tumor-Targeted Paclitaxel Delivery. *J. Control. Release* **2013**, *172*, 823–831.
- (57) Gao, L.; Gao, L.; Fan, M.; Li, Q.; Jin, J.; Wang, J.; Lu, W.; Yu, L.; Yan, Z.; Wang, Y. Hydrotropic Polymer-Based Paclitaxel-Loaded Self-Assembled Nanoparticles: Preparation and Biological Evaluation. *RSC Adv.* **2017**, *7*, 33248–33256.
- (58) Lee, S. C.; Huh, K. M.; Lee, J.; Cho, Y. W.; Galinsky, R. E.; Park, K. Hydrotropic Polymeric Micelles for Enhanced Paclitaxel Solubility: In Vitro and in Vivo Characterization. *Biomacromolecules* **2007**, *8*, 202–208.
- (59) Huh, K. M.; Lee, S. C.; Cho, Y. W.; Lee, J.; Jeong, J. H.; Park, K. Hydrotropic Polymer Micelle System for Delivery of Paclitaxel. *J. Control. Release* **2005**, *101*, 59–68.
- (60) Lee, J.; Lee, S. C.; Acharya, G.; Chang, C. J.; Park, K. Hydrotropic Solubilization of Paclitaxel: Analysis of Chemical Structures for Hydrotropic Property. *Pharm. Res.* **2003**, *20*, 1022–1030.

## CHAPTER 6

# Shortwave Infrared Imaging with J-aggregates Stabilized in Hollow Mesoporous Silica Nanoparticles

This chapter of the dissertation was adapted and reprinted with permission from Wei Chen#, **Chi-An Cheng**#, Emily D. Cosco#, Shyam Ramakrishnan, Jakob G. P. Lingg, Oliver T. Bruns, Jeffrey I. Zink, Ellen M. Sletten *Journal of the American Chemical Society* **2019**, *141*, 12475–12480. Copyright 2019 American Chemical Society. Co-author contributions: Chen W.#, Cheng C. A.#, and Cosco E. D.# (co-first authors) performed the synthesis and characterization of materials, and photophysics. Cheng C. A. performed the cell studies. Cosco E. D., Ramakrishnan S., and Lingg J. G. P. performed the shortwave infrared imaging and animal studies. Oliver T. Bruns, Jeffrey I. Zink, and Ellen M. Sletten were the P.Is. The texts of introduction, result and discussion were mainly organized and written by Professor Ellen M. Sletten when preparing the manuscript for publication.

### Table of Content Figure



### 6.1 Abstract

Tissue is translucent to shortwave infrared (SWIR) light, rendering optical imaging superior in this region. However, the widespread use of optical SWIR imaging has been limited, in part, by the lack of bright, biocompatible contrast agents that absorb and emit light above 1000 nm. J-aggregation offers a means to transform stable, near-infrared (NIR) fluorophores into red-shifted

SWIR contrast agents. Here we demonstrate that J-aggregates of NIR fluorophore IR-140 can be prepared inside hollow mesoporous silica nanoparticles (HMSNs) to result in nanomaterials that absorb and emit SWIR light. The J-aggregates inside PEGylated HMSNs are stable for multiple weeks in buffer and enable high resolution imaging *in vivo* with 980 nm excitation.

## 6.2 Introduction

Optical imaging with shortwave infrared (SWIR, 1000–2000 nm) light has emerged as a powerful method of fluorescence imaging in animals due to the superior resolution and contrast one can achieve with low energy light (**Figure 6.1A**).<sup>1</sup> A primary challenge with SWIR imaging is the development of bright, biocompatible, SWIR contrast agents.<sup>2</sup> Originally, the advantageous qualities of imaging in the SWIR region were showcased with carbon nanotubes,<sup>3</sup> quantum dots,<sup>4</sup> and rare earth nanomaterials.<sup>5</sup> In efforts to set the stage for clinical translation, the past three years have seen a focus on the synthesis of non-toxic, SWIR-emissive organic fluorophores.<sup>6</sup> This work has significantly expanded the suite of fluorophores that emit above 1000 nm; however, challenges remain in the stability, delivery, and brightness of SWIR dyes. Consequently, we looked to explore an alternative avenue to create SWIR organic materials: J-aggregation.

J-aggregation is the slip-stacked alignment of chromophores that leads to constructive coupling of the excited state transition dipoles (**Figure 6.1B**).<sup>7</sup> The photophysical consequences of J-aggregation are bathochromically-shifted absorption and emission spectra, narrow absorption and emission bands with small Stokes shifts, enhanced absorbance coefficients ( $\epsilon$ ), and shortened fluorescence lifetimes which can result in enhanced quantum yields ( $\Phi_F$ ) and cycling rates. Many J-aggregate characteristics are beneficial qualities for *in vivo* imaging: red-shifted absorption and emission spectra will enable significant depth penetration during both the excitation and image acquisition,<sup>2,8</sup> narrow bands can facilitate multiplexed imaging, and increased  $\epsilon$  will result in bright



materials. Despite the significant photophysical advantages J-aggregates typically have over the monomer, there are few reports of employing J-aggregates for *in vivo* imaging due to the difficulty in obtaining and stabilizing the necessary chromophore alignment in complex settings.<sup>9</sup>

Nanostructures can sequester and protect payloads, rendering nanomaterials a promising approach toward stabilizing J-aggregates *in vivo*. In 2016, Zheng and coworkers performed image-guided surgery with porphyrin lipids that formed J-aggregates upon self-assembly into nanovesicles.<sup>10</sup> The following year, Xu and coworkers prepared pyrrolopyrrole cyanine J-aggregate-containing polymer micelles, which could be visualized after subcutaneous injection.<sup>11</sup> In work recently published, Fan and coworkers reported a squaraine J-aggregate, stabilized in polymeric micelles, for SWIR image-guided photothermal therapy.<sup>12</sup> Each of these reports utilizes self-assembled organic nanomaterials,<sup>13</sup> which are prone to disassembly when diluted in the presence of hydrophobic biomolecules, leading to destabilization of the J-aggregate.<sup>14</sup> Here, we employ robust, biocompatible, hollow mesoporous silica nanoparticles to stabilize and protect SWIR-emissive J-aggregates of IR-140 for *in vivo* imaging (**Figure 6.1C/D**).

Hollow mesoporous silica nanoparticles (HMSNs) have 2–4 nm pores that open into a large, 10–200 nm cavity, allowing these nanostructures to carry significant cargo.<sup>15</sup> The surfaces of the HMSNs can be modified to alter the biodistribution of the nanoparticles.<sup>16</sup> Consequently, there are numerous reports of HMSNs as the core scaffold of multifunctional materials.<sup>15a,16b,17</sup> Included in these studies are the loading or conjugation of visible<sup>18</sup> and near-infrared<sup>15a,19</sup> fluorophores and administering the resulting nanomaterials for imaging. However, the controlled assembly of J-aggregates in HMSNs has yet to be demonstrated.

To realize SWIR-emissive J-aggregates inside HMSNs, we utilized the heptamethine dye IR-140 (1). IR-140 is a commercially available NIR fluorophore ( $\lambda_{\text{max,abs}}=826$  nm,  $\lambda_{\text{max,em}}=875$  nm) that has been applied as a photopolymerization initiator,<sup>20</sup> fluorescent payload,<sup>21</sup> component of

plasmonic arrays,<sup>22</sup> as well as a Raman<sup>23</sup> and two-photon<sup>24</sup> imaging agent. In 2016, Wang and Weiss reported that introduction of IR-140 to glutathione coated quantum dots results in J-aggregate formation with two aggregates observed: J1 ( $\lambda_{\text{max,abs}}=965$  nm, non-emissive), and J2 ( $\lambda_{\text{max,abs}}=1040$  nm,  $\lambda_{\text{max,em}}=1047$  nm).<sup>25</sup> We envisioned that similar IR-140 J-aggregates could be formed on the negatively charged pores and inner surface of HMSNs. Further, once the aggregates were assembled inside the particles, the hydrophobic nature of IR-140 would make them unlikely to disassemble in aqueous environments, rendering J-aggregates stable *in vivo*.

### 6.3 Result and Discussion

We prepared HMSNs by synthesizing a mesoporous silica coating on a Stöber sphere core that was subsequently removed via etching with sodium carbonate (**Scheme 6.1, Figure 6.2**). The HMSNs were treated with varying amounts of IR-140 in different solvents (**Figure 6.3A**). J-aggregate formation was assayed by UV/Vis/NIR spectroscopy evaluating loss of monomeric IR-140 at 826 nm and formation of the J-aggregates at 965 nm (J1) and 1040 nm (J2). Upon optimization, we found that SWIR J-aggregates could be obtained when IR-140 dissolved in dimethyl sulfoxide (DMSO) was combined with HMSNs and washed. The washing procedure proved essential for obtaining the desired J2 aggregate formation (**Figure 6.3B and 6.4**), with gentle PBS washes yielding the largest amount of the desired J2 aggregate (dark blue, **Figure 6.3B**). When these optimized conditions were repeated on Stöber spheres that did not have pores or an inner surface for IR-140 to associate with, only a small J-band was observed (**Figure 6.3B**, gray line, **Figure 6.5**). Similar results were obtained when loading was performed on mesoporous silica coated Stöber spheres (**Figure 6.4**). These control experiment (**Figure 6.6**) suggests that the majority of IR-140 is protected inside the HMSN cavity. Through analysis of IR-140 collected after the washing procedures, we calculated the loading of IR-140 to be  $\sim 10^3$  molecules/particle

**(Figure 6.7, Note 6.5.13.1).**

The HMSNs were further characterized through transmission electron microscopy (TEM), indicating ~85 nm particles with a distinct cavity and pores (**Figure 6.3C**). The pore size was quantified to be 3.2 nm through nitrogen adsorption experiments (**Figure 6.8**). While the pores are clearly visible in the TEM of the empty HMSNs, they are darkened after treatment with IR-140 (**Figure 6.3D**), suggesting the presence of IR-140. Control experiments in which HMSNs were subjected to PBS washing procedures but no IR-140 show no change in contrast of the pores upon TEM analysis (**Figure 6.9**).

After confirming that the HMSNs could facilitate J-aggregation of IR-140, we modified the surface with poly(ethylene glycol) (PEG) such that they could be suspended in aqueous media. This was accomplished by loading HMSNs that had undergone surface silanization with (3-aminopropyl)triethoxysilane (APTS) prior to Stöber sphere and surfactant removal (**Scheme 6.2**). This procedure resulted in HMSNs that were positively charged on the outside but still contained a negatively charged interior to associate with the cationic IR-140.<sup>26</sup> Nitrogen adsorption data (**Figure 6.8**) also suggests that the pores are not modified with APTS.<sup>27</sup> The introduction of IR-140 into the HMSNs-APTS proceeded similarly to the HMSNs, yielding analogous loading of IR-140 and a higher ratio of J2:J1 (**Figure 6.10**). Control experiments performed with Stöber spheres treated with APTS support that IR-140 is protected on the interior of the HMSNs (**Figures 6.5 and 6.6**). After loading, a 23kDa PEG-carboxylate was conjugated to the amines present on the outer surface of the HMSNs-APTS using carbodiimide chemistry (**Scheme 6.2**). Successful PEG conjugation was verified by changes in hydrodynamic diameter and zeta potential (**Figures 6.11 and 6.12**).

We evaluated the photophysical properties of the PEGylated HMSNs (HMSNs-PEG) containing IR-140 in comparison to IR-140 in solution as the monomer and J-aggregate (**Figure**

**6.13A**). Monomeric IR-140 has been well-characterized;<sup>28</sup> however, the solution J-aggregate of IR-140 had previously not been reported.<sup>29</sup> After screening numerous conditions (**Figure 6.14**), we found that 35% DMSO/0.9% NaCl in water afforded formation of the desired SWIR J-aggregate with a  $\lambda_{\text{max,abs}}=1042$  nm,  $\lambda_{\text{max,em}}=1043$  nm,  $\epsilon=3.9 \times 10^5 \text{ M}^{-1}\text{cm}^{-1}$ , and  $\Phi_{\text{F}}=0.01\%$  (**Table 6.1, Notes 6.5.13.2 and 6.5.13.3**). The IR-140-containing HMSNs-PEG had similar spectral properties with a  $\lambda_{\text{max,abs}}=1038$  nm,  $\lambda_{\text{max,em}}=1047$  nm, although the absorbance was considerably broader, which we attribute to the presence of other non-emissive aggregate states. When solutions of IR-140 in DMSO, IR-140 in 35% DMSO/0.9% NaCl in water, and IR-140 loaded HMSNs-PEG in PBS were excited with a 980 nm laser, the wavelength to be used for *in vivo* imaging experiments, the IR-140 J-aggregate in solution and in the particles were similarly emissive, while the monomer was not excited by 980 nm light (**Figures 6.13B and 6.15**).<sup>30</sup> Thus, J-aggregation is essential for SWIR imaging with low energy excitation.

Next, we analyzed the role of the HMSNs in stabilizing IR-140 J-aggregates. Over two weeks in PBS at room temperature, we observed only a ~10% decrease in absorbance from the IR-140 loaded HMSNs-PEG and no evidence that the packing of the IR-140 within the nanoparticles was changing (**Figures 6.13C**, blue; **Figure 6.16**). Comparatively, only ~8% of the J-aggregate in solution remained after 1 day (**Figure 6.13C**, red; **Figure 6.16**). Not only do the HMSNs stabilize the assembly of the J-aggregate, but they also enhance the photostability. The fluorescence of solutions containing IR-140 J-aggregate in 35% DMSO/0.9% NaCl in water and HMSNs-PEG containing IR-140 J-aggregate in PBS were continually irradiated with a 980 nm laser (97 mW/cm<sup>2</sup>) and the fluorescence intensity was measured with an InGaAs camera. The photostability of monomeric IR-140 in DMSO was also evaluated via excitation at 785 nm (97 mW/cm<sup>2</sup>). As shown in **Figure 6.13D**, the J-aggregates within the HMSNs-PEG are 4-fold more stable than the J-aggregates in solution and ~60-fold more stable than the monomer (**Table 6.2, Note 6.5.13.4**). This

result is consistent with the use of silica shells to overcome the poor photostability that is characteristic of J-aggregates by limiting the amount of reactive oxygen species that can access the aggregate.<sup>31</sup> Photobleaching experiments in deoxygenated solvents support that the HMSNs protect the IR-140 J-aggregate from reactive oxygen species (**Figure 6.17**). Taken together, our data show that the HMSNs are critical for stabilizing J-aggregates to light and solution.

Finally, with bright SWIR-emissive nanoparticles prepared and characterized, we evaluated their biocompatibility and *in vivo* imaging performance. *In vitro* studies showed no cytotoxicity of the IR-140 loaded HMSNs-PEG over 6 h at concentrations up to 200 µg/mL (**Figure 6.18**). These data are consistent with other studies regarding mesoporous silica, which is generally considered non-toxic to animals.<sup>26,32</sup> We performed *in vivo* imaging experiments using the IR-140 loaded HMSNs-PEG with excitation at 980 nm and collection from 1000–1700 nm. The SWIR-emissive HMSNs-PEG were intravenously injected into nude mice and the mice were immediately imaged (**Figure 6.19**). The HMSNs-PEG rapidly clear from the blood stream and intense signal can be seen in the lungs, liver, and spleen. Fifty minutes after injection, the signal intensity within these organs remained constant (**Figure 6.20**).

## 6.4 Summary

In summary, we have presented J-aggregation as an approach to prepare biocompatible, SWIR contrast agents and demonstrated this concept by stabilizing J-aggregates of the NIR fluorophore IR-140 inside HMSNs. The bathochromically-shifted absorption and emission and small Stokes shifts of the IR-140 J-aggregate allow imaging with 980 nm excitation and 1000–1700 nm acquisition, providing high resolution *in vivo* images. The modularity of the HMSNs will enable facile exchange of the imaging agent as well as the addition of targeting agents and/or therapeutics, poising these materials to become SWIR theranostics.<sup>33</sup> While we did not observe an

enhanced  $\Phi_F$  with the IR-140 J-aggregate, likely due to disorder or intermolecular vibrations,<sup>34</sup> work is ongoing to access a SWIR J-aggregate that exhibits the superradiance phenomena predicted by Kasha.<sup>35</sup> Collectively, the use of J-aggregates stabilized in HMSNs as SWIR imaging agents has the potential to overcome the stability, toxicity, and brightness challenges of contrast agents for this compelling region of the electromagnetic spectrum.

## 6.5 Methods

### 6.5.1 Materials and Chemicals

IR-140 (95%), cetyltrimethylammonium chloride (CTAC, 25 wt% in water), cetyltrimethylammonium bromide (CTAB, 99+%), tetraethyl orthosilicate (TEOS, 98%), (3-aminopropyl)triethoxysilane (APTS, 99%), ammonium nitrate (NH<sub>4</sub>NO<sub>3</sub>, 98+%), triethanolamine (TEA, 99+%), 2-(*N*-morpholino)ethanesulfonic acid hydrate (MES hydrate, 99.5+%), and phosphate buffer saline (X10) were purchased from Sigma-Aldrich. Sodium carbonate anhydrous (99.5+%) was purchased from EMD Millipore. Alpha-methoxy-omega-carboxylic acid poly(ethylene glycol) (MeO-PEG-COOH, M<sub>w</sub> = 23,000 Da) was purchased from Iris Biotech GmbH. Ethanol (200 proof) was purchased from Decon Laboratories, Inc. 1-Ethyl-3-(3-dimethylaminopropyl) carbodiimide hydrochloride (EDC-HCl, 99+%), and *N*-hydroxysulfosuccinimide sodium salt (sulfo-NHS, 99+%) were purchased from CovaChem. Dimethyl sulfoxide (DMSO, 99.9+%), sodium hydroxide (NaOH, 97+%), and ammonium hydroxide (NH<sub>4</sub>OH) purchased from Fisher Scientific. Dulbecco's modified Eagle's medium (DMEM) with high glucose, fetal bovine serum (FBS), antibiotics (10,000 U/mL penicillin, 10,000 μg/mL streptomycin, and 29.2 mg/mL L-glutamine), trypsin-ethylenediaminetetraacetic acid (trypsin-EDTA) (0.05 %), and Dulbecco's phosphate-buffered saline (DPBS) were purchased from Gibco. Cell counting kit-8 (CCK-8) was purchased from Dojindo Molecular Technologies, Inc.

All chemicals were used without further purification.

### **6.5.2 Instrumentation**

Bath sonication was performed using a Branson 3800 ultrasonic cleaner or an Elma S15 Elmasonic. Masses for analytical measurements were taken on a Sartorius MSE6.6S-000-DM or MSA6.6S-000-DM Cubis Micro Balance. Absorbance spectra were collected on a JASCO V-770 UV-Visible/NIR spectrophotometer with a 2000 nm/min scan rate after blanking with the appropriate solvent, on a Cary 5000 UV-Vis-NIR spectrophotometer or on a Shimadzu UV-1800 UV-Visible Scanning Spectrophotometer. Photoluminescence spectra were obtained on a Horiba Instruments PTI QuantaMaster Series fluorometer. Quartz cuvettes (10 mm, 3 mm and 2 mm) were used for absorbance and photoluminescence measurements. The dynamic light scattering (DLS) measurements were performed on a ZETAPALS instrument with a 660 nm red diode laser (Brookhaven Instruments Corporation). Zeta potential value was measured on a Malvern Zetasizer Nano at room temperature. Nitrogen adsorption/desorption isotherms were acquired at 77 K on a Autosorb-iQ, Quantachrome Instruments. Transmission electron microscopy was performed on a Tecnai T12 instrument with an operating voltage of 120 kV. Animal imaging was performed on custom instrumentation described below.

### **6.5.3 Synthesis of Stöber Silica Spheres**

Stöber silica spheres were synthesized by a sol-gel reaction in basic solution as reported previously.<sup>36</sup> Briefly,  $\text{NH}_4\text{OH}$  (1.6 mL) was dissolved in a mixture of ethanol (71.4 mL) and D.I. water (10 mL) in a 250 mL flask with vigorous stirring. After stirring for 10 min at room temperature, TEOS (2 mL) was rapidly added to the solution which was further stirred for 1 h at room temperature for the formation of Stöber silica nanoparticles. Afterwards, the solution containing Stöber silica spheres was centrifuged (7830 rpm, 7197 g, 20 min) and washed with

ethanol and D.I. water twice, respectively. The Stöber silica spheres were finally dispersed in 40 mL of D.I. water for further use.

#### **6.5.4 Synthesis of Hollow Mesoporous Silica Nanoparticles (HMSNs)**

The synthesis of hollow mesoporous silica nanoparticles (HMSNs) was carried out by using Stöber silica spheres as the hard templates which were later removed by selective etching in a basic solution. First, CTAC (2 g, 25 wt% in water solution) and TEA (20 mg) were dissolved in D.I. water (20 mL) in a 100 mL round-bottom flask with vigorous stirring at 80 °C. The reaction mixture was stirred for 5 min followed by the addition of 10 mL of Stöber silica sphere solution prepared as described above, and stirred for 20 min. To coat mesoporous silica on the surface of Stöber silica spheres, TEOS (150 µL) was added dropwise to the solution with vigorous stirring. The nanoparticles were designated as dSiO<sub>2</sub>@MSNs (Scheme 4.1). After 1 h, the solution was cooled to 50 °C and sodium carbonate (1.89 g) dissolved in D.I. water (3 mL) was added to selectively etch the Stöber silica sphere template in the mesoporous silica shell. The etching process was carried out at 50 °C for 2 h. Afterwards, the solution containing HMSNs were centrifuged (7830 rpm, 7197 g, 15 min) and washed with ethanol 3 times (3 x 50 mL) to remove the unreacted impurities. To remove the CTAC surfactant templates, HMSNs were dispersed in 50 mL of ethanol containing NH<sub>4</sub>NO<sub>3</sub> (1 g). The solution was brought to 60 °C with vigorous stirring. After 1 h, the solution was cooled to room temperature, centrifuged (7830 rpm, 7197 g, 15 min), and washed once with ethanol (50 mL). The surfactant removal process was repeated two more times. Finally, surfactant free HMSNs were washed with D.I. water (2 x 50 mL) and ethanol (2 x 50 mL) twice, respectively and stored in 10 mL of absolute ethanol for further use.

#### **6.5.5 Synthesis of APTS Functionalized HMSNs (HMSNs-APTS)**

APTS functionalized HMSNs (HMSNs-APTS) were synthesized by procedures similar to



those of HMSNs. First, CTAC (2 g, 25 wt% in water solution) and TEA (20 mg) were dissolved in D.I. water (20 mL) in a 100 mL round-bottom flask with vigorous stirring at 80 °C. The reaction solution was stirred for 5 min followed by the addition of 10 mL of Stöber silica sphere solution prepared as described above. After stirring for 20 min, TEOS (150  $\mu$ L) was added dropwise to the solution with vigorous stirring. After 1 h, a mixture of APTS (40  $\mu$ L) and ethanol (120  $\mu$ L) was added to the solution followed by stirring for another 1 h at 80 °C to conjugate APTS on the surface of HMSNs. The Stöber silica sphere etching and surfactant removal processes were the same as described in the synthesis of HMSNs section. The resulting nanoparticles were dispersed in ethanol and designated as HMSNs-APTS.

#### **6.5.6 Synthesis of APTS Functionalized Stöber Silica Spheres**

The Stöber silica spheres (80 mg) were dispersed in a mixture of ethanol (20 mL) and APTS (10  $\mu$ L). The solution was stirred at room temperature for 5 min and was brought to 78 °C. Then, the solution was refluxed for 12 h with vigorous stirring. Subsequently, the solution was cooled to room temperature, and APTS functionalized Stöber silica spheres (Stöber silica spheres-APTS) were washed twice (2 x 20 mL) with ethanol and stored in 10 mL of absolute ethanol for further use.

#### **6.5.7 Loading of IR-140 in HMSNs, HMSNs-APTS, or dSiO<sub>2</sub>@MSNs**

HMSNs, HMSNs-APTS, or dSiO<sub>2</sub>@MSNs (2 mg) dispersed in ethanol were centrifuged (14000 rpm, 16873 g, 15 min) and washed with DMSO (3 x 1 mL) before IR-140 loading. HMSNs or HMSNs-APTS were then dispersed in 200  $\mu$ L of a DMSO solution containing 5, 10, or 20 mM IR-140 by sonication in a bath sonicator for 10 min. For dSiO<sub>2</sub>@MSNs, the nanoparticles were dispersed in 200  $\mu$ L of a DMSO solution containing 5, or 20 mM IR-140 by sonication in a bath sonicator for 10 min. After stirring the solution for 20 h to make IR-140 diffuse into the pores and

cavity of HMSNs, HMSNs-APTS, or dSiO<sub>2</sub>@MSNs, the solution containing the particles was centrifuged (14000 rpm, 16873 g, 15 min) and the supernatant was kept for loading capacity calculations. Then, IR-140 loaded HMSNs were washed with three different methods: (a) washed with PBS (1 mL) using a water bath sonication, (b) gently washed with PBS (1 mL) by using plastic transfer pipettes, and (c) washed with water (1 mL) by using plastic transfer pipettes, respectively, to remove free DMSO and DMSO loaded in the pores. IR-140 loaded HMSNs-APTS, or IR-140 loaded dSiO<sub>2</sub>@MSNs were washed only by method (b). Afterwards, IR-140 loaded nanoparticles were centrifuged (8000 rpm, 5510 g, 3 min) to remove the supernatant. The washing steps were repeated 5 times. Finally, IR-140 loaded HMSNs, HMSNs-APTS, or dSiO<sub>2</sub>@MSNs were re-dispersed in PBS (1 mL) solution by sonication.

#### **6.5.8 PEG Conjugation on the Surface of IR-140 Loaded HMSNs-APTS**

To increase the colloidal stability, PEG was conjugated on the surface of IR-140 loaded HMSNs-APTS via amide bond formation. After IR-140 was loaded in HMSNs-APTS, the nanoparticles were gently washed with PBS (5 x 1 mL), D.I. water (2 x 1 mL), and MES buffer solution (pH = 6.0, 10 mM) (1 x 1 mL), respectively. Finally, IR-140 loaded HMSNs-APTS (2 mg) were dispersed in MES buffer (1 mL) by sonication. Alpha-methoxy-omega-carboxylic acid poly(ethylene glycol) (MeO-PEG-COOH, CAS No. 92450-99-2) (10 mg) was dissolved in MES buffer (200 µL) followed by the addition of EDC-HCl (5 mg) and sulfo-NHS (2.5 mg) pre-dissolved in MES buffer (300 µL). The solution was stirred for 30 min. Then, the MES buffer solution containing the activated MeO-PEG-COOH (500 µL) was added to 1 mL of 2 mg/mL IR-140 loaded HMSNs-APTS MES solution. The solution was further mixed and stirred for 20 h to conjugate PEG on the surface of IR-140 loaded HMSNs-APTS. Then, IR-140 loaded HMSNs-PEG were centrifuged (10000 rpm, 8609 g, 10 min) and washed with D.I. water (2 x 1 mL) and

PBS (1 x 1 mL) to remove the excess MeO-PEG-COOH, EDC-HCl, sulfo-NHS, and MES buffer solution. Finally, IR-140 loaded HMSNs-PEG were dispersed in PBS buffer (1 mL) solution for UV-Vis-NIR or photoluminescence measurements.

### **6.5.9 Cell Culture Procedures**

HeLa cells, a cervical cancer cells line, were cultured in T-75 flasks (Corning) with vented caps in a high glucose Dulbecco's modified Eagle's medium (DMEM) supplemented with 10 % fetal bovine serum (FBS), and 1 % antibiotics (100 U/mL penicillin and 100 µg/mL streptomycin) in a humidity-controlled incubator at 37 °C with 5% CO<sub>2</sub>. The HeLa culture media were daily changed and the cells were harvested by trypsinization with 0.05% trypsin-ethylenediaminetetraacetic acid (EDTA) for passaging every 2–3 days.

### **6.5.10 Animal Procedures**

Animal experiments were conducted in accordance with the approved institutional protocols of Helmholtz Zentrum München. Non-invasive whole mouse imaging was performed on two six-week old female CD-1 nude mice (22.4 g, 19.1 g), purchased from Charles River Laboratories. Mice were anesthetized with an i.p. injection of a ketamine/xylazine mixture. Tail vein injections were performed with a catheter assembled from a 30 ga needle connected through plastic tubing to a second 30 ga needle with syringe prefilled with isotonic saline solution. The bevel of the needle was then inserted into the tail vein and secured using tissue adhesive.

### **6.5.11 SWIR imaging apparatus**

For whole mouse imaging, we used a custom-built setup. A 35 W 980 nm laser (Lumics LU0980D350-D30AN) was coupled in a fiber (600 µm core, Thorlabs BF46LS01) The output from the fiber was fixed in an excitation cube and reflected off of a mirror (Thorlabs BBE1-E03), and passed through a positive achromat (Thorlabs AC254-050-B), 1000 nm shortpass filter

(Thorlabs FESH 1000), and an engineered diffuser (Thorlabs ED1-S20-MD) to provide uniform illumination over the working area. The excitation flux at the object was adjusted to be close to  $100 \text{ mWcm}^{-2}$  with an error of  $\pm 3\%$  (power density used is defined separately in each experiment). The working area was covered by a heating mat coated with blackout fabric (Thorlabs BK5). A 4-inch square first-surface silver mirror (Edmund Optics, 84448) was used to direct the emitted light through a custom filter set (Thorlabs NF980-41, 3x FELH1000, 2x FGL1000) to an Allied Vision Goldeye G-032 Cool TEC2 camera at  $-30 \text{ }^{\circ}\text{C}$ , equipped with a C-mount camera lens (Navitar, SWIR-35). The assembly was partially enclosed to avoid excess light while enabling manipulation of the field of view during operation. The image acquisition toolbox of MATLAB programming environment is used in combination with a custom MATLAB script to preview and collect the required image data. The prepared MATLAB script allows users to access basic functionalities of the image acquisition device by establishing a packet jitter free data streaming link between the desktop computer and the acquisition device.

### **6.5.12 Experimental Procedures of Figures**

#### **Figure 6.2**

Stöber silica spheres,  $\text{dSiO}_2\text{@MSNs}$ , or HMSNs were dispersed in ethanol at a concentration of  $0.1 \text{ mg/mL}$ . The suspension ( $5 \text{ }\mu\text{L}$ ) of the nanoparticles was dropped onto the carbon-coated copper grid and dried at room temperature. Transmission electron microscopy was measured on a Tecnai T12 instrument with an operating voltage of  $120 \text{ kV}$ .

#### **Figure 6.3 B**

Refer to 6.5.7 “Loading of IR-140 in HMSNs, HMSNs-APTS, or  $\text{dSiO}_2\text{@MSNs}$ ”.  $10 \text{ mM}$  IR-140 was used as the loading solution. Then, IR-140 loaded HMSNs were washed by methods (a), (b), or (c) to compare the extent of IR-140 aggregate by using the above washing methods.

The washing steps were repeated 5 times and finally IR-140 loaded HMSNs were re-dispersed in 1 mL of PBS solution by sonication.

Stöber silica spheres dispersed in ethanol were centrifuged (14000 rpm, 15 min) and washed with DMSO 3 times before IR-140 loading. Afterwards, Stöber silica spheres were dispersed in 200  $\mu$ L of DMSO solution containing 10 mM IR-140 by sonication in a bath sonicator for 10 min. Then, the solution was stirred for 20 h. After the IR-140 loading, the solution containing the particles was centrifuged (14000 rpm, 15 min) to get IR-140 loaded Stöber silica spheres. Then, IR-140 loaded Stöber silica spheres were washed with 1 mL of PBS by gently washing with plastic transfer pipettes to remove free DMSO. After each washing step, IR-140-loaded Stöber silica spheres were centrifuged (8000 rpm, 3 min) to remove the supernatant. The washing steps were repeated for 5 times and finally IR-140-loaded Stöber silica spheres were re-dispersed in PBS solution (1 mL) by sonication. The absorbance spectra of IR-140 loaded HMSNs or IR-140 loaded Stöber silica spheres were measured with 10 mm quartz cuvettes at a concentration of 0.25 mg nanoparticles/mL PBS on a Cary 5000 UV-Vis-NIR spectrophotometer at room temperature. Absorbance traces were corrected for the non-linearity between gratings. Absorbance traces were corrected for the non-linearity between gratings.

For the prewash spectrum: after the IR-140 (10 mM) loading, the particles solution (10 mg/mL) was diluted 1:350 with DMSO for measurement. The absorbance spectrum of the prewash sample was measured with 3 mm quartz cuvettes on a JASCO V-770 UV-Vis-NIR spectrophotometer at room temperature.

### **Figure 6.3 C/D**

HMSNs and IR-140 loaded HMSNs were dispersed in ethanol and D.I. water, respectively at a concentration of 0.1 mg/mL. The suspension (5  $\mu$ L) of the nanoparticles was dropped onto the carbon-coated copper grid and dried at room temperature. Transmission electron microscopy was

measured on a Tecnai T12 instrument with an operating voltage of 120 kV.

#### **Figure 6.4**

Refer to 6.5.7 “Loading of IR-140 in HMSNs, HMSNs-APTS, or dSiO<sub>2</sub>@MSNs”. 5 or 20 mM IR-140 was used as the loading solution. Then, IR-140 loaded HMSNs were washed by methods (a), (b), or (c). In addition, IR-140 loaded dSiO<sub>2</sub>@MSNs were washed by method (b). The washing steps were repeated 5 times and finally IR-140 loaded HMSNs or IR-140 loaded dSiO<sub>2</sub>@MSNs were re-dispersed in 1 mL of PBS solution by sonication. The absorbance spectra of IR-140 loaded HMSNs or IR-140 loaded dSiO<sub>2</sub>@MSNs were measured with 10 mm quartz cuvettes at a concentration of 0.25 mg nanoparticles/mL PBS on a Cary 5000 UV-Vis-NIR spectrophotometer at room temperature. Absorbance traces were corrected for the non-linearity between gratings.

#### **Figure 6.5**

Stöber silica spheres or Stöber silica spheres-APTS were prepared and described in synthetic procedures. Stöber silica spheres or Stöber silica spheres-APTS (2 mg for each) dispersed in ethanol were centrifuged (14000 rpm, 16873 g, 15 min) and washed with DMSO 3 times before IR-140 loading. Afterwards, Stöber silica spheres or Stöber silica spheres-APTS were dispersed in 200  $\mu$ L of DMSO solution containing 20, 10, or 5 mM IR-140 by sonication in a bath sonicator for 10 min. Then, the solution was stirred for 20 h. After the IR-140 loading, the solution containing the particles was centrifuged (14000 rpm, 16873 g, 15 min) to get IR-140 loaded Stöber silica spheres or Stöber silica spheres-APTS. Then, IR-140 loaded Stöber silica spheres or Stöber silica spheres-APTS were washed with 1 mL of PBS by gently washing with plastic transfer pipettes to remove free DMSO and DMSO loaded in the pores. After each washing step, IR-140 loaded Stöber silica spheres or Stöber silica spheres-APTS were centrifuged (8000 rpm, 5510 g, 3 min) to remove the supernatant. The washing steps were repeated for 5 times and finally IR-140 loaded Stöber

silica spheres or Stöber silica spheres-APTS were re-dispersed in PBS solution (1 mL) by sonication. The absorbance spectra of Stöber silica spheres or Stöber silica spheres-APTS were measured with 10 mm quartz cuvettes at a concentration of 0.25 mg nanoparticles/mL PBS on a Cary 5000 UV/Vis/NIR Spectrophotometer at room temperature. Absorbance traces were corrected for the non-linearity between gratings.

For zeta potential measurement, Stöber silica spheres or Stöber silica spheres-APTS were dispersed in D.I. water (2 mL) at a concentration of 50 µg/mL. The measurement was performed on a Malvern Zetasizer Nano at room temperature.

### **Figure 6.6**

HMSNs, Stöber silica spheres, Stöber silica spheres-APTS, or dSiO<sub>2</sub>@MSNs (2 mg for each) dispersed in ethanol were centrifuged (14000 rpm, 16873 g, 15 min) and washed with DMSO 3 times before IR-140 loading. Afterwards, HMSNs, Stöber silica spheres, Stöber silica spheres-APTS, or dSiO<sub>2</sub>@MSNs were dispersed in 200 µL of DMSO solution containing 10 mM IR-140 by sonication in a bath sonicator for 10 min. Then, the solution was stirred for 20 h. After the IR-140 loading, the solution containing the particles was centrifuged (14000 rpm, 16873 g, 15 min) to get IR-140 loaded nanoparticles. Then, IR-140 loaded nanoparticles were washed with 1 mL of PBS by gently washing with plastic transfer pipettes to remove free DMSO and DMSO loaded in the pores. After each washing step, IR-140 loaded nanoparticles were centrifuged (8000 rpm, 5510 g, 3 min) to remove the supernatant. The washing steps were repeated for 5 times and finally IR-140 loaded nanoparticles were re-dispersed in PBS solution (1 mL) by sonication. The absorbance spectra of IR-140 loaded HMSNs, Stöber silica spheres, Stöber silica spheres-APTS, or dSiO<sub>2</sub>@MSNs were measured with 10 mm quartz cuvettes at a concentration of 0.25 mg nanoparticles/mL PBS on a Cary 5000 UV/Vis/NIR Spectrophotometer at room temperature. Absorbance traces were corrected for the non-linearity between gratings.

### **Figure 6.7**

The loading capacity of IR-140 in HMSNs or HMSNs-APTS was calculated based on the absorbance difference between the IR-140 DMSO solution before and after loading. After loading with IR-140 for 20 h, HMSNs or HMSNs-APTS were centrifuged (14000 rpm, 16873 g, 15 min) and the supernatant was collected for absorbance measurements. The loading capacity of IR-140 was calculated using the difference of maximum absorbance at 831 nm and the following definition of loading capacity (%): (mass of loaded IR-140/mass of particles) x 100.

### **Figure 6.8**

HMSNs (A/B) and HMSNs-APTS (C/D), and dSiO<sub>2</sub>@MSNs (E/F) were prepared as described in the synthetic procedures and degassed at 120 °C under vacuum for 16 h before the measurement. The surface area and pore diameter distribution of HMSNs, HMSNs-APTS, and dSiO<sub>2</sub>@MSNs were determined by Brunauer-Emmett-Teller (BET) and Barrett-Joyner-Halenda (BJH) methods, respectively.

### **Figure 6.9**

(A) HMSNs were dispersed in ethanol at a concentration of 0.1 mg/mL. (B) The control HMSNs were subjected to washing by method (b) in the Section II “Loading of IR-140 in HMSNs, HMSNs-APTS, or dSiO<sub>2</sub>@MSNs” but without the loading of IR-140. The particles were dispersed in PBS at a concentration of 0.1 mg/mL. (C) Refer to Section II “Loading of IR-140 in HMSNs, HMSNs-APTS, or dSiO<sub>2</sub>@MSNs”. 10 mM IR-140 was used as the loading solution. IR-140 loaded HMSNs were dispersed in PBS at a concentration of 0.1 mg/mL. (D) The mixed samples were prepared by mixing 50 µL of HMSNs in PBS solution (0.2 mg/mL) and 50 µL of IR-140 loaded HMSNs in PBS solution (0.2 mg/mL) and were sonicated in a water bath sonicator for 20 s. The suspension (5 µL) of each of the nanoparticles was dropped onto the carbon-coated copper grid and dried at room temperature. Transmission electron microscopy was measured on a Tecnai



T12 instrument with an operating voltage of 120 kV.

### **Figure 6.10**

HMSNs-APTS (2 mg) dispersed in ethanol were centrifuged (14000 rpm, 16873 g, 15 min) and washed with DMSO (3 x 1 mL) before IR-140 loading. Afterwards, HMSNs-APTS was dispersed in 200  $\mu$ L of DMSO solution containing 5, 10, or 20 mM IR-140 by sonication in a bath sonicator for 10 min. Then, the solution was stirred for 20 h to let IR-140 diffuse into the pores and cavity of HMSNs-APTS. After the IR-140 loading, the solution containing the particles was centrifuged (14000 rpm, 16873 g, 15 min) to get IR-140 loaded HMSNs-APTS. Then, IR-140 loaded HMSNs-APTS were washed with PBS (1 mL) by gently washing with plastic transfer pipettes to remove free DMSO and DMSO loaded in the pores. After each washing step, IR-140 loaded HMSNs-APTS were centrifuged (8000 rpm, 5510 g, 3 min) to remove the supernatant. The washing steps were repeated 5 times and finally IR-140 loaded HMSNs-APTS were re-dispersed PBS (1 mL) by sonication. The absorbance spectra of IR-140 loaded HMSNs-APTS were measured with 10 mm quartz cuvettes at a concentration of 0.25 mg nanoparticles/mL PBS on a Cary 5000 UV/Vis/NIR Spectrophotometer at room temperature. Absorbance traces were corrected for the non-linearity between gratings.

### **Figure 6.11**

Refer to 6.5.7 “Loading of IR-140 in HMSNs, HMSNs-APTS, or dSiO<sub>2</sub>@MSNs”. 20 mM IR-140 was used as the loading solution. The loading concentration of HMSNs-APTS was 10 mg/mL. Then, IR-140 loaded HMSNs-APTS were washed by method (b). The washing steps were repeated 5 times and finally IR-140 loaded HMSNs-APTS were re-dispersed in PBS (1 mL) by sonication. The synthetic procedures of PEGylation of IR-140 loaded HMSNs-APTS can be referred to Section II “PEG conjugation on the surface of IR-140 loaded HMSNs-APTS”. For dynamic light scattering size measurement, HMSNs-APTS, HMSNs-APTS containing IR-140,

and HMSNs-PEG containing IR-140 were dispersed in PBS (2 mL) at a concentration of 50  $\mu\text{g/mL}$ . The measurement was performed on a ZETAPALS instrument with a 660 nm red diode laser at room temperature.

### **Figure 6.12**

Refer to 6.5.7 “Loading of IR-140 in HMSNs, HMSNs-APTS, or  $\text{dSiO}_2\text{@MSNs}$ ”. 20 mM IR-140 was used as the loading solution. The loading concentration of HMSNs-APTS was 10 mg/mL. Then, IR-140 loaded HMSNs-APTS were washed by method (b). The washing steps were repeated 5 times and finally IR-140 loaded HMSNs-APTS were re-dispersed in 1 mL of PBS solution by sonication. The synthetic procedures of PEGylation of IR-140 loaded HMSNs-APTS can be referred to Section II “PEG conjugation on the surface of IR-140 loaded HMSNs-APTS”. For zeta potential measurement, HMSNs, HMSNs-APTS, HMSNs-APTS containing IR-140, and HMSNs-PEG containing IR-140 were dispersed in D.I. water (2 mL) at a concentration of 50  $\mu\text{g/mL}$ . The measurement was performed on a Malvern Zetasizer Nano at room temperature.

### **Figure 6.13A**

All absorbance and emission traces were baseline corrected and normalized. Absorbance traces were acquired on a JASCO V-770 UV-Visible/NIR spectrophotometer. The slit widths used in fluorescence spectra were 5.76 mm for excitation and 11.52 mm for emission. The step size was 1.0 nm, integration time 0.1 s, and traces were acquired after an automatic detector background subtraction.

IR-140 monomer was dissolved in DMSO and diluted to an O.D. of  $\sim 0.7$  for absorbance and less than 0.1 for fluorescence spectroscopy (ex. 785 nm) in a 1 cm path length cuvette. The monomer absorption trace was corrected for the non-linearity between gratings before baseline subtraction and normalization.

The IR-140 J-aggregate in 35% DMSO/0.9% NaCl was prepared by dissolving 0.02 mg of

IR-140 in 350  $\mu$ L DMSO, vortexing briefly, adding 650  $\mu$ L 0.9% aqueous NaCl, and shaking briskly. The solution becomes warm and immediately loses the blue color. Absorbance and emission traces of the J-aggregate in solution were obtained with a 2 mm path length cuvette. For the fluorescence trace, a 10 mm path length was used on the excitation side and a 2 mm path length on the emission side. A reabsorption correction was performed on the emission trace analogous to that described in **Note 6.5.13.2**.

The IR-140 loaded HMSNs-PEG were prepared as described in the synthetic procedures, section VI. The absorbance was collected without dilution in a 10 mm cuvette. The fluorescence spectrum was obtained by diluting the sample to an O.D. of less than 0.1 in a 3 mm path length square quartz cuvette, and exciting at 885 nm with a shortpass filter (Thorlabs, FES0900).

### **Figure 6.13B**

Samples consisted of IR-140 monomer: 0.01 mg/mL IR-140 in DMSO (left); IR-140 J-aggregate in solution: 0.01 mg/mL IR-140 in 35% DMSO/0.9% NaCl in water (center); IR-140 HMSNs-PEG: 1 mg/mL in PBS (right). Vials were excited with 980 nm light (with Thorlabs FESH1000) with an average power density of  $99 \pm 3$  mWcm<sup>-2</sup>. Power densities over the three samples were not identical due to varying distance from the excitation cube. See Figure 4.15 for images with consistent distances from the excitation cube. Collection was from 1000–1700 nm (1000 nm LP, Edmund Optics 84-776). The custom lens system consists of a 4f configuration with a  $f=750.0$ mm lens (Thorlabs LB1247-C) and two  $f=200.0$ mm lenses (Thorlabs LB1199-C). For ergonomic reasons a 2” protected silver-coated elliptical mirror (PFE20-P01) mounted to a kinematic mount (Thorlabs KCB2EC/M) was used. Images were acquired at 35 ms exposure time, 16.65 fps. Displayed image was background subtracted and averaged over 6 frames.

### **Figure 6.13C**

Stability of IR-140 in HMSNs-PEG over time. IR-140 loaded HMSNs-PEG were dispersed

in PBS at 0.25 mg/mL. The absorbance spectra were taken in a 3 mm path length cuvette immediately (day 0) and after 14 days (day 14) on a JASCO V-770 UV-Visible/NIR spectrophotometer. The absorbance was normalized, relative to spectrum (1). Results of the triplicate experiment are presented in Figure 4.16.

Stability of IR-140 in solution over time. IR-140 J-aggregate was prepared in DMSO as described in **Figure 6.11A**. The aggregate absorbance in a 2 mm path length cuvette was obtained immediately (day 0) and after 17 h storage in the dark (day 1) on a JASCO V-770 UV-Visible/NIR spectrophotometer. The absorbance was normalized, relative to spectrum at day 0. Results are reproduced in triplicate in **Figure 6.16**.

#### **Figure 6.13D**

Three solutions were prepared: (a) 1 mg/mL solution of HMSNs-PEG containing IR-140 (b) 0.01 mg/mL IR-140 in 35% DMSO/0.9% NaCl solution, and (c) 0.01 mg/mL IR-140 in DMSO. Each solution (400  $\mu$ L) was irradiated with  $97 \pm 3$  mWcm<sup>-2</sup> of 980 nm (a and b) and 785 nm (c) light and their emission was monitored by a SWIR camera. Acquisition settings were 2 fps and (a) 25 ms, (b) 15 ms, and (c) 0.3 ms. Excitation and emission settings were identical to **Figure 6.13B**. Error represents the standard deviation of three measurements.

#### **Figure 6.14**

Samples were prepared as by dissolving 0.02 mg IR-140 in DMSO, and then adding to the appropriate aqueous phase (either MilliQ water, 1x PBS, or 0.9% NaCl in water) and shaking vigorously. The appropriate volumes of DMSO and aqueous phase were used to sum to 2.0 mL for each listed percentage. For the 0% DMSO traces, IR-140 is at its solubility limit, after sonicating 0.02 mg IR-140 in 1.0 mL of the appropriate solvent for 4 hours. Absorbance traces were measured in a 3.0 mm cuvette with blanking to the appropriate solvent mixture on a JASCO V-770 UV-Visible/NIR spectrophotometer.

### **Figure 6.15**

Samples were prepared and excitation and acquisition was performed as described in **Figure 6.13B**. Absorbance traces were acquired on a Shimadzu UV-1800 UV-Visible Scanning Spectrophotometer.

### **Figure 6.16**

IR-140 loaded HMSNs-PEG, obtained as described in 6.5.8 “PEG conjugation on the surface of IR-140 loaded HMSNs-APTS,” were dispersed in PBS (0.25 mg/mL). The absorbance spectra were taken in a 3 mm path length cuvette immediately (day 0) and after 14 days storage in the dark. IR-140 J-aggregate in solution was prepared by dissolving 0.02 mg IR-140 in 700  $\mu$ L DMSO, and subsequently adding 1.3 mL 0.9% NaCl and briskly shaking. The aggregate absorbance in a 2 mm path length cuvette was obtained immediately and after 24 h storage in the dark.

### **Figure 6.17A**

Deoxygenated IR-140 solution J-aggregates were prepared by adding 1.4 mL DMSO to 0.04 mg IR-140 in a purged dram vial, followed by 2.6 mL 0.9% NaCl solution in water and shaking. Solvents were deoxygenated by purging with N<sub>2</sub> for at least one hour. Oxygenated IR-140 solution J-aggregates were prepared analogously, but with solvents which had been exposed to air. Solutions (4 mL), sealed with septa, were irradiated for 20 min. The optical parameters for experiment in (A) consisted of the following: a 4-inch square first-surface silver mirror (Edmund Optics, 84448) was used to direct the emitted light through a custom filter set (Edmund optics #84-776, TL) to an Allied Vision Goldeye G-032 Cool TEC2 camera at -20 °C, equipped with a C-mount camera lens (Navitar, SWIR-35). Excitation light was passed through a positive achromat (Thorlabs AC254-050-B), 1000 nm shortpass filter (Thorlabs FESH 1100), and an engineered diffuser (Thorlabs ED1-S20-MD) to provide uniform illumination over the working area. Exposure time used was 100 ms, with 2 fps.

### **Figure 6.17B**

IR-140 containing HMSNs-PEG were prepared according to 6.5.7 “Loading of IR-140 in HMSNs, HMSNs-APTS, or dSiO<sub>2</sub>@MSNs” and 6.5.8 “PEG conjugation on the surface of IR-140 loaded HMSNs-APTS”. Deoxygenated solutions were purged with N<sub>2</sub> for at least 30 min, while oxygenated were left open to air. Both sample types (1 mg/L, 0.40 mL), sealed with septa, were irradiated for 20 minutes. The optical parameters for experiment in (B) consisted of the following: a 4-inch square first-surface silver mirror (Edmund Optics, 84448) was used to direct the emitted light through a custom filter set (Edmund optics #84-776, 3x FELH1000,) to an Allied Vision Goldeye G-032 Cool TEC2 camera at -20 °C, equipped with a C-mount camera lens (Navitar, SWIR-35). Excitation light was passed through a positive achromat (Thorlabs AC254-050-B), 1000 nm shortpass filter (Thorlabs FESH 1000), and an engineered diffuser (Thorlabs ED1-S20-MD) to provide uniform illumination over the working area. Exposure time used was 200 ms, with 2 fps.

Data were analyzed analogous to that discussed in **Note 6.5.13.4**, however only the relative rates between oxygenated and deoxygenated experiments were calculated and evaluated.

### **Figure 6.18**

The viabilities of HeLa cells after the treatment of IR-140 loaded HMSNs-PEG were examined by using a cell counting kit-8 (CCK-8) assay. The cells were seeded in 96-well plates at a density of  $5 \times 10^3$  cells per well in 200  $\mu$ L DMEM supplemented with 10% FBS and 1% antibiotics in a humidity-controlled incubator at 37 °C for 24 h attachment. After the attachment, the medium was removed and the cells were incubated in 200  $\mu$ L fresh DMEM containing 0, 2, 5, 10, 15, 20, and 40  $\mu$ g of IR-140 loaded HMSNs-PEG (*i.e.* 0, 10, 25, 50, 75, 100, and 200  $\mu$ g/mL) for 3 or 6 h in an incubator at 37 °C. After incubation, the medium was removed and the treated cells were washed with DPBS 1 time (200  $\mu$ L). To measure the cell viability, 100  $\mu$ L of DMEM

and 10  $\mu\text{L}$  of CCK-8 cellular cytotoxicity reagent were added to each well. Then, the plates were put in the incubator for 2 h at 37  $^{\circ}\text{C}$ . To measure the number of the viable cells in each condition, a plate reader (Tecan M1000) was used to measure the absorbance at 450 nm and 650 nm (as a reference). The DMEM (100  $\mu\text{L}$ ) mixed with CCK-8 reagent (10  $\mu\text{L}$ ) served as a background control.

### **Figure 6.19**

The IR-140 HMSNs-PEG in PBS were sonicated (Elma S15 Elmasonic) for 30 mins prior to injection and filtered through a 40  $\mu\text{m}$  nylon filter. 200  $\mu\text{L}$  of the IR-140 HMSNs-PEG in PBS were injected via the tail vein and immediately imaged. The excitation flux (980 nm) had an average power density of  $91 \pm 3 \text{ mWcm}^{-2}$  over the field of view. Images were acquired at 60 ms exposure time and 16.65 fps, in 8-bit format. Displayed images were background subtracted with an average of 10-frames from the pre-injection time points, outliers were removed, and the stills were averaged over 5 frames.

### **Figure 6.20**

Refer to **Figure 6.19** experimental procedures.

## **6.5.13 Supplementary Notes**

### **Note 6.5.13.1: Estimation of The Amount of Dye Molecules in a Single HMSN and HMSN-PEG**

In order to calculate how many IR-140 molecules loaded in a single HMSN or HMSN-APTS, we need to estimate the mass of a single HMSN or HMSN-APTS using the equation:

$$m_{\text{amorphous silica}} = V_{\text{amorphous silica}} \times \rho_{\text{amorphous silica}} \quad (1)$$

Amorphous silica is defined as the silica in HMSNs shell excluding mesopores. The density ( $\rho$ ) of amorphous silica is known to be 2.5 ( $\text{g/cm}^3$  amorphous silica). There are several ways to

estimate the volume of a single MSNs, as we have published previously.<sup>37</sup> Here, we started to determine the shell volume of a single HMSN ( $V_{shell}$ ) from the equation below:

$$V_{shell} = \frac{4\pi}{3} \times (R_1^3 - R_2^3) = V_{mesopore} + V_{amorphous\ silica} \quad (2)$$

$V_{shell}$  of the HMSNs used here (**Figure 6.21**) was calculated to be 141961 nm<sup>3</sup> based on equation (2).  $V_{mesopore}$  was determined to be 0.94 (cm<sup>3</sup>/g amorphous silica) from N<sub>2</sub> adsorption-desorption isotherm analysis.

Although we cannot directly calculate  $V_{amorphous\ silica}$  from the equation (2) at this point because  $V_{mesopore}$  is a function of the mass of amorphous silica, we can first determine the ratio ( $a$ ) between  $V_{mesopore}$  and  $V_{amorphous\ silica}$  which would facilitate determination of  $V_{amorphous\ silica}$ .

$$V_{mesopore} \div V_{amorphous\ silica} = a \quad (3)$$

From the density of amorphous silica, 1 g of amorphous silica has a volume of 0.4 cm<sup>3</sup>, and thus  $a = 2.35$ , which is derived from  $V_{mesopore}/V_{amorphous\ silica} = 0.94 \text{ cm}^3/0.4 \text{ cm}^3$ . Now, plug the ratio in equation (2):

$$\begin{aligned} V_{shell} &= V_{mesopore} + V_{amorphous\ silica} = 2.35 V_{amorphous\ silica} + V_{amorphous\ silica} \\ &= 3.35 V_{amorphous\ silica} \end{aligned} \quad (4)$$

From above, we determine that the percentage ( $b$ ) of  $V_{amorphous\ silica}$  occupying  $V_{shell}$  is:

$$(V_{amorphous\ silica} \div V_{shell}) \times 100 \% = b \quad (5)$$

$b$  was calculated to be 30%. Since we already calculated  $V_{shell}$  to be 141961 nm<sup>3</sup>,  $V_{amorphous\ silica}$  was then determined to be 42446 nm<sup>3</sup> from (5). The mass of a single HMSN ( $m_{amorphous\ silica}$ ) was then calculated by plugging in  $V_{amorphous\ silica}$  in the equation (1), which was determined to be  $1.06 \times 10^{-16}$  (g).



To estimate the amount of dye molecules in a single HMSN, the average loading capacities of IR-140 in HMSNs ( $5.9 \pm 1.2$  %,  $8.9 \pm 1.1$  %, and  $22.9 \pm 2.8$  % with 5 mM, 10 mM, and 20 mM IR-140 as the loading solution, respectively) were used to determine the mass of IR-140 loaded in a single HMSN. Then, the number of IR-140 molecules loaded in a single HMSN could be calculated as:

$$\text{number of IR-140 molecules loaded in a single HMSN} = [(\text{the loading capacity of IR-140 in HMSNs}) \times m_{\text{amorphous silica}} \div \text{molecular weight of IR-140}] \times N_A \quad (6)$$

where  $N_A$  is the Avogadro's constant. For example, using equation (6), with 5 mM IR-140, the number of IR-140 molecules loaded in a single HMSN was then determined to be  $4.87 \times 10^3 \pm 0.99 \times 10^3$  molecules. The number of IR-140 molecules loaded in a single HMSN with 10 and 20 mM IR-140 were  $7.35 \times 10^3 \pm 0.91 \times 10^3$  and  $1.89 \times 10^4 \pm 0.23 \times 10^4$ , respectively.

By applying the above calculation to HMSNs-APTS, we can also estimate how many IR-140 molecules were loaded in a single HMSN-APTS. Given that  $V_{\text{mesopore}}$  of HMSNs-APTS is  $0.73 \text{ cm}^3/\text{g}$ , the mass of a single HMSN-APTS is calculated to be  $1.26 \times 10^{-16} \text{ g}$ .

Given that the loading capacity of IR-140 in HMSN-APTS is  $6.6 \pm 2.5$  %,  $10.2 \pm 1.8$  %, and  $21.6 \pm 1.5$  % with 5, 10, and 20 mM IR-140, respectively, the number of IR-140 molecules loaded in a single HMSN-APTS were estimated to be  $6.43 \times 10^3 \pm 2.44 \times 10^3$ ,  $9.94 \times 10^3 \pm 1.76 \times 10^3$ , and  $2.10 \times 10^4 \pm 0.15 \times 10^4$ , respectively.

#### **Note 6.5.13.2: Absorption Coefficients**

Absorption coefficients were calculated according to the Lambert - Beer-Lambert law,

$$A = \epsilon lc \quad (7)$$

where A represents absorbance (unitless),  $\epsilon$  the absorption coefficient ( $\text{M}^{-1}\text{cm}^{-1}$ ),  $l$  the path length (cm), and c the concentration (M). Masses were determined on a microbalance and diluted

using Hamilton microsyringes to concentrations within the linear range of the UV-Vis-NIR spectrophotometer. Four concentrations were obtained for each experiment and the reported error represents the standard deviation of three measurements.

The monomer absorption coefficient was straightforward as only one species is present in solution. These data were collected using a 10 mm quartz cuvette in DMSO. The raw data was corrected for non-linearity between gratings, and baseline corrected to 478 nm. The absorption coefficient at all relevant wavelengths is displayed below in **Figure 6.22**. The absorption coefficient at  $\lambda_{\text{max,abs}} = 826 \text{ nm}$  was  $1.7 \pm 0.1 \times 10^5 \text{ M}^{-1}\text{cm}^{-1}$ .

The J-aggregate absorption coefficient is more complex due to the requirement of high concentrations for selective formation of the J-aggregate over the monomer. As a result, to use higher concentrations, yet stay in the linear range of the spectrometer, these data were collected using a 3 mm cuvette. The raw data were baseline corrected to 449 nm and are included below in **Figure 6.23**. The uncorrected absorption coefficient ( $\epsilon_{\text{raw}}$ ) at  $\lambda_{\text{max,abs}} = 1043 \text{ nm}$  was  $3.3 \pm 0.3 \times 10^5 \text{ M}^{-1}\text{cm}^{-1}$ .

Despite the higher concentrations, some monomer remained in solution. The uncorrected data can be corrected for the remaining monomer in solution using the absorption coefficient of the monomer at its  $\lambda_{\text{max,abs}}$  and making the assumption that the absorption coefficient of the monomer does not change significantly between 100% DMSO and 35% DMSO/0.9% NaCl in water. We used the equation:

$$\alpha_m + a_j = 1 \quad (8)$$

where  $\alpha_m$  represents the mole fraction of monomer and  $\alpha_j$  the mole fraction of J-aggregate. The value  $\alpha_m$  for each absorbance trace was obtained using the Beer-Lambert law from the absorption coefficient of the monomer and the known concentration of total dye. The value  $a_j$  was then used

as a multiplicative factor to correct the concentration of J-aggregate in solution. The absorption coefficient was then recalculated with the corrected concentration values. The corrected absorption coefficient at  $\lambda_{\text{max,abs}} = 1043 \text{ nm}$  was  $3.9 \pm 0.4 \times 10^5 \text{ M}^{-1}\text{cm}^{-1}$ . Error was taken as the standard deviation of the three replicates. The corrected absorption coefficient is displayed below in **Figure 6.24**.

### **Note 6.5.13.3: Quantum Yield**

The photoluminescence quantum yield ( $\Phi_F$ ) of a molecule or material is defined as follows,

$$\Phi_F = \frac{P_E}{P_A} \quad (9)$$

where  $P_E$  and  $P_A$  are the number of photons absorbed and emitted, respectively. To determine the quantum yield, we either use a relative method with a known standard in the same region of the electromagnetic spectrum, or an absolute method, in which the number of photons absorbed and emitted are measured independently. Here, due to the limits of our petite integrating sphere (Horiba KSPHERE-Petite with InGaAs detector Horiba Edison DSS IGA 020L), we use a relative method, with IR-26 as the known standard.

The quantum yield was measured at three different excitation wavelengths, 885 nm, 900 nm, and 915 nm and the results were averaged to obtain the value reported.

To compare an unknown to a reference with a known quantum yield, the following relationship was used:

$$\Phi_{F,x} = \Phi_{F,r} (m_x/m_f) (\eta_x^2/\eta_r^2) \quad (10)$$

Where  $m$  represents the slope of the line ( $y = mx + b$ ) obtained from graphing integrated fluorescence intensity versus optical density across a series of samples,  $\eta$  is the refractive index of the solvent, and the subscripts  $x$  and  $r$  represent values of the unknown and reference, respectively.

The ( $\Phi_{F,r}$ ) of IR-26 was taken to be  $0.05 \pm 0.03\%$ , as we have previously measured<sup>38</sup>, and which agrees with several recent measurements.<sup>[6,9]</sup>

To obtain a plot of integrated fluorescence intensity versus absorbance for the reference and unknown, five solutions and a solvent blank were prepared and their absorbance and emission spectra were acquired. IR-26 was diluted in dichloroethane to concentrations with optical densities less than 0.1 to minimize effects of reabsorption. The baseline corrected (to 1500 nm) fluorescence traces were integrated from 950 – 1500 nm, and the raw integrals were corrected by subtracting the integral over an identical range from fluorescence traces of the blank solvent (**Figure 6.25A**). The methods employed here were validated with comparison of IR-26 to IR-1061, giving a  $\Phi_F$  value of  $0.3 \pm 0.2 \%$ , which is in agreement with our prior absolute quantum yield measurement,<sup>[8]</sup> but with lower precision due to the uncertainty in IR-26 absolute  $\Phi_F$ .

The IR-140 J-aggregate was prepared as described in **Figure 6.13A**, in 35% DMSO/0.9% NaCl in water. Due to the necessity of using concentrated samples for IR-140 to remain in the J2 aggregate state, high concentrations of IR-140 J-aggregate were used for quantum yield measurements (the OD with a 2 mm path length at the relevant excitation wavelengths ranged from 0.07 – 0.16). The baseline corrected (to 1400 nm) fluorescence traces of the optically dense IR-140 J-aggregate samples were corrected for reabsorption by the relationship,

$$I(\lambda) = I_o(\lambda)[- \ln (10^{-OD(\lambda)}) / (1 - 10^{-OD(\lambda)})] \quad (11)$$

where  $I(\lambda)$  and  $I_o(\lambda)$  are the corrected and experimental fluorescence intensities at each wavelength, and  $OD(\lambda)$  is the optical density of the sample at the corresponding wavelength. The corrected fluorescence traces were then integrated from 965 nm – 1400 nm, and the raw integrals were corrected by subtracting the integral over an identical range from fluorescence traces of the blank solvent.

The integrated fluorescence intensities were then plotted against the baseline corrected absorbance values at the relevant wavelength, and the slope and error in slope were obtained ( $R^2 > 0.95$  for all traces) (Figure 6.25B).

The refractive index for DCE was taken as 1.440<sup>39</sup>, while that of the 35% DMSO/0.9% NaCl solution in water was approximated as a binary mixture of 35% DMSO in water and taken to be 1.383.<sup>40</sup> Both values were designated to have a precision to  $\pm 0.001$ .

The average quantum yield value (over 885 nm, 900 nm, and 915 nm excitations) was calculated to be  $0.012 \pm 0.007$ . Errors were propagated from the error in IR-26  $\Phi_F$  ( $\pm 0.03$ )<sup>[8]</sup>, slope of the integrated fluorescence intensity versus optical density plot (unique for each trace, but ranged from 7-10% of the slope value), and refractive indices ( $\pm 0.001$ ).

For quantum yield measurements, fluorescence traces were acquired with ex. 885 nm, 900 nm, and 915 nm with a 950 nm shortpass filter (Thorlabs FESH0950) and collection from 950–1400 nm for IR-140 J-aggregate and 950–1500 for IR-26. The slits were 5.76 mm for excitation and 11.52 mm for emission. The step size used was 1.0 nm, integration time 0.1 s, and traces were acquired after an automatic detector background subtraction, and with the default excitation correction. All absorbance and fluorescence traces were taken in a 10 mm x 2 mm path length cuvette. For absorbance traces, the 2 mm path length was used, while emission traces were acquired with 10 mm at the excitation side and 2 mm on the emission side, with emission detection occurring at 90° from excitation.

#### Note 6.5.13.4: Photobleaching Rates

All photobleaching data were fit to a mono-exponential decay and the rate constants were obtained from the first order reaction equation:

$$\ln[A] = -kt + \ln [A]_o \quad (12)$$

where  $A$  and  $A_o$  represent the emission collected at time  $t$  and the initial emission collected, respectively. All  $R^2$  values were  $> 0.96$ . Error bars represent the standard deviation of three measurements. If a change in slope occurred in the  $\ln[A]$  values (*i.e.* in the IR-140 J-aggregate bleaching in 35% DMSO/0.9% NaCl in water solution), the rate was taken as the initial rate and the lines were fit only to the linear region (**Figure 6.26**). This analysis conservatively estimates the photobleaching rate of the solution phase aggregate as slower than it appeared in subsequent time points (see **Figure 6.13D**).

To compare photobleaching rates between samples irradiated at distinct wavelengths, it is necessary to consider the relative number of photons absorbed by each species. This requires corrections for (1) the difference in photon energy between the two wavelengths, and (2) the difference in photons absorbed by the two samples.

To account for photons of different energy, we go back to the common unit of number of photons per second per surface unit  $N_p$ , ( $\text{cm}^{-2}\text{s}^{-1}$ ). This value can be obtained by first calculating energy of a photon  $E_p$ , (J) at the wavelength of irradiation:

$$E_p = \frac{hc}{\lambda} \quad (13)$$

where  $h$  is Planck's constant, and  $c$  the speed of light. The  $N_p$  can then be found from the irradiance  $I$  ( $\text{Wcm}^{-2}$ ) and  $E_p$  by the following equation:

$$N_p = \frac{I}{E_p} \quad (14)$$

The  $N_p$  for 980 nm and 785 nm light is  $4.8 \times 10^{17}$  and  $3.8 \times 10^{17} \text{ cm}^{-2}\text{s}^{-1}$ , respectively.

To account for the difference in photons absorbed, we use the absorption coefficients at the wavelength of irradiation,  $\lambda_{\text{ex}}$ . For the IR-140 J-aggregate, the corrected absorption value was used. The absorption coefficient of IR-140 in HMSNs-PEG was taken to be that of the J-aggregate

in solution. The relative values of  $N_p \times \varepsilon$  can then be compared to obtain a ratio,  $X$  for each wavelength,

$$X_{785} = (N_{p,785} \times \varepsilon_m) / (N_{p,980} \times \varepsilon_j) \quad (15)$$

$$X_{980} = (N_{p,980} \times \varepsilon_j) / (N_{p,980} \times \varepsilon_j) \quad (16)$$

where  $\varepsilon_m$  and  $\varepsilon_j$  represent the absorbance coefficient of the monomer and J-aggregate, respectively, at their appropriate excitation wavelength,  $\lambda_{ex}$ . The ratio  $X_{785}$  was calculated to be 0.998, providing a correction factor for the relative number of photons absorbed per second in the 785 nm experiment compared to the 980 nm experiments, while the ratio  $X_{980}$  is 1.000. These values can be related to the relative rate,  $k_{rel}$  by the equation:

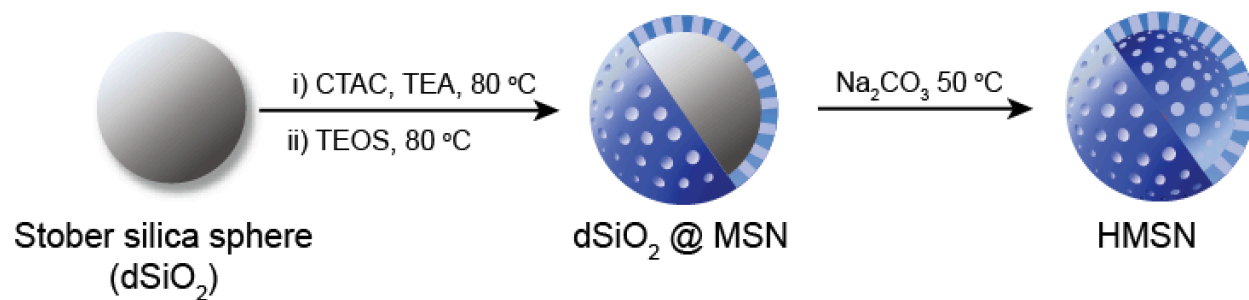
$$k_{rel} = \frac{k_{raw}}{X} \quad (17)$$

The relative rates with intermediate values used in the calculations are listed below in **Table 6.3**.

## 6.6 Acknowledgment

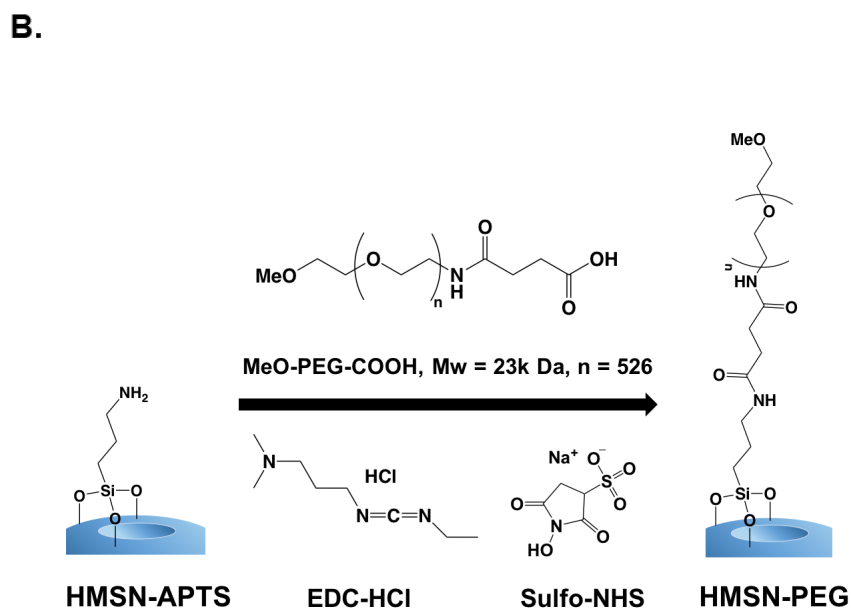
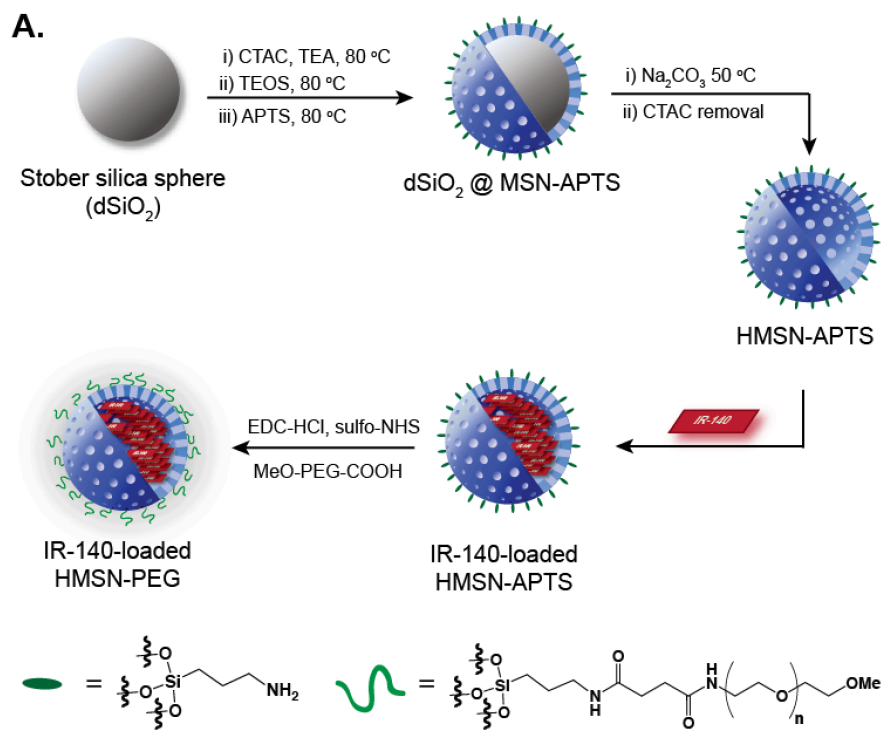
We thank Prof. Matthias Tschöp, Prof. Vasilis Ntziachristos, Dr. Thomas Schwarz-Romond, Uwe Klemm and all members of the Helmholtz Pioneer Campus and Institute for Biological and Medical Imaging for their support. No competing financial interests have been declared. This work was supported by grants to E.D.C (NSF GRFP DGE-1144087, Christopher S. Foote Fellowship), O.T.B. (Emmy-Noether-Programm of DFG BR 5355/2-1, Helmholtz Pioneer Campus Institute for Biomedical Engineering), J.I.Z. (Zink student research fund), and E.M.S. (UCLA, Sloan Research Award FG-2018-10855, NIH 1R01EB027172-01).

## 6.7 Schemes, Figures and Tables



**Scheme 6.1.** Synthesis of hollow mesoporous silica nanoparticles (HMSNs).





**Scheme 6.2.** Synthesis of IR-140-loaded HMSN-PEG. A) Overall synthesis starting from Stöber spheres. B) Detailed schematic of conjugation of PEG to the surface of HMSN-APTS. Note that we believe the APTS modification is only on the outer surface due to the Stöber silica sphere blocking the inner surface and the CTAC surfactant blocking the pores.

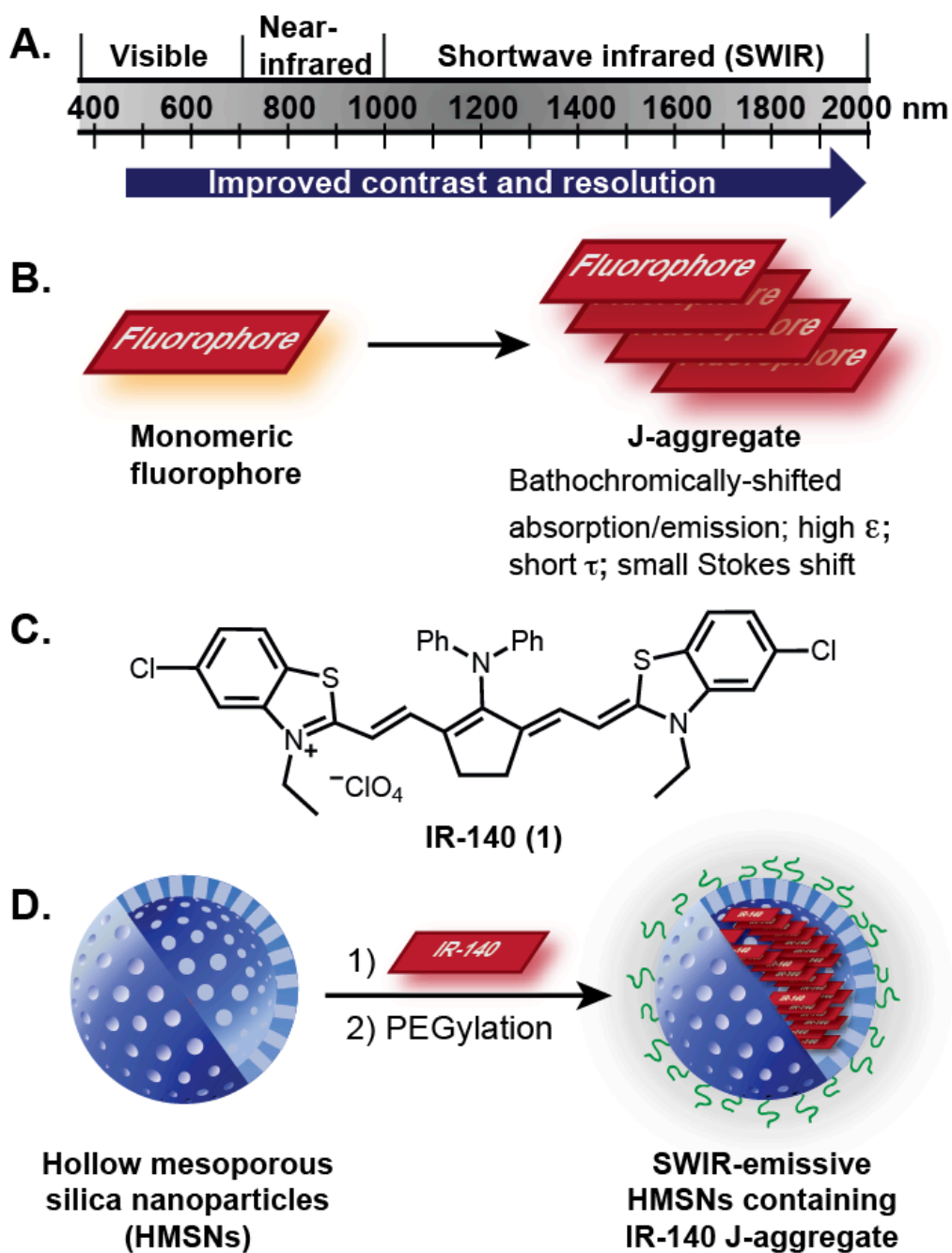


**Figure 6.1.** (A) Regions of the electromagnetic spectrum employed for optical imaging. For further details on contrast and resolution within regions of the SWIR see references 1bc; 8b-c. (B) J-aggregation and characteristic photophysical properties. (C) IR-140. (D) Work reported herein: the stabilization of IR-140 J aggregates in hollow mesoporous silica nanoparticles (HMSNs) to result in biocompatible SWIR-emissive contrast agents.

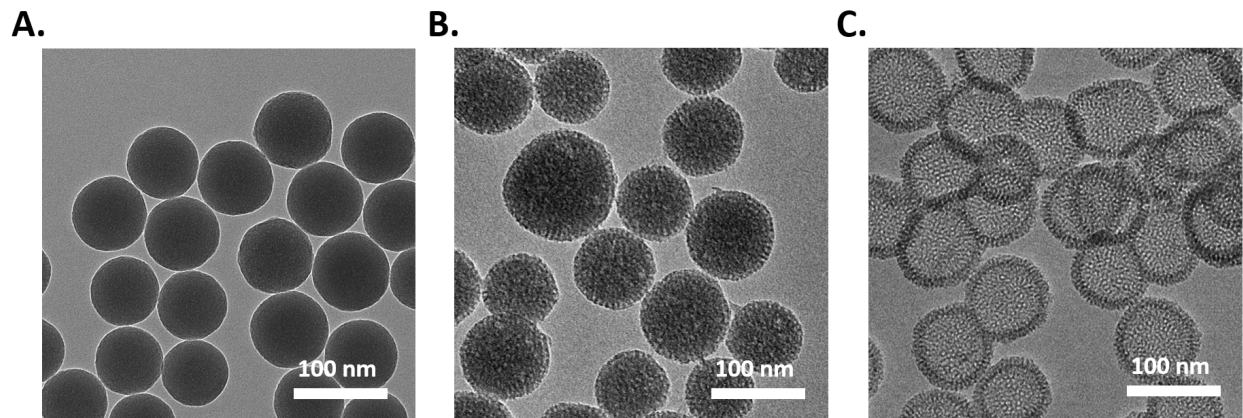


**Figure 6.2.** TEM images of (A) Stöber silica spheres, (B) dSiO<sub>2</sub>@MSNs, and (C) HMSNs. The nanoparticles were dispersed in ethanol at a concentration of 0.1 mg/mL. TEM images were measured on a Tecnai T12 instrument with an operating voltage of 120 kV.

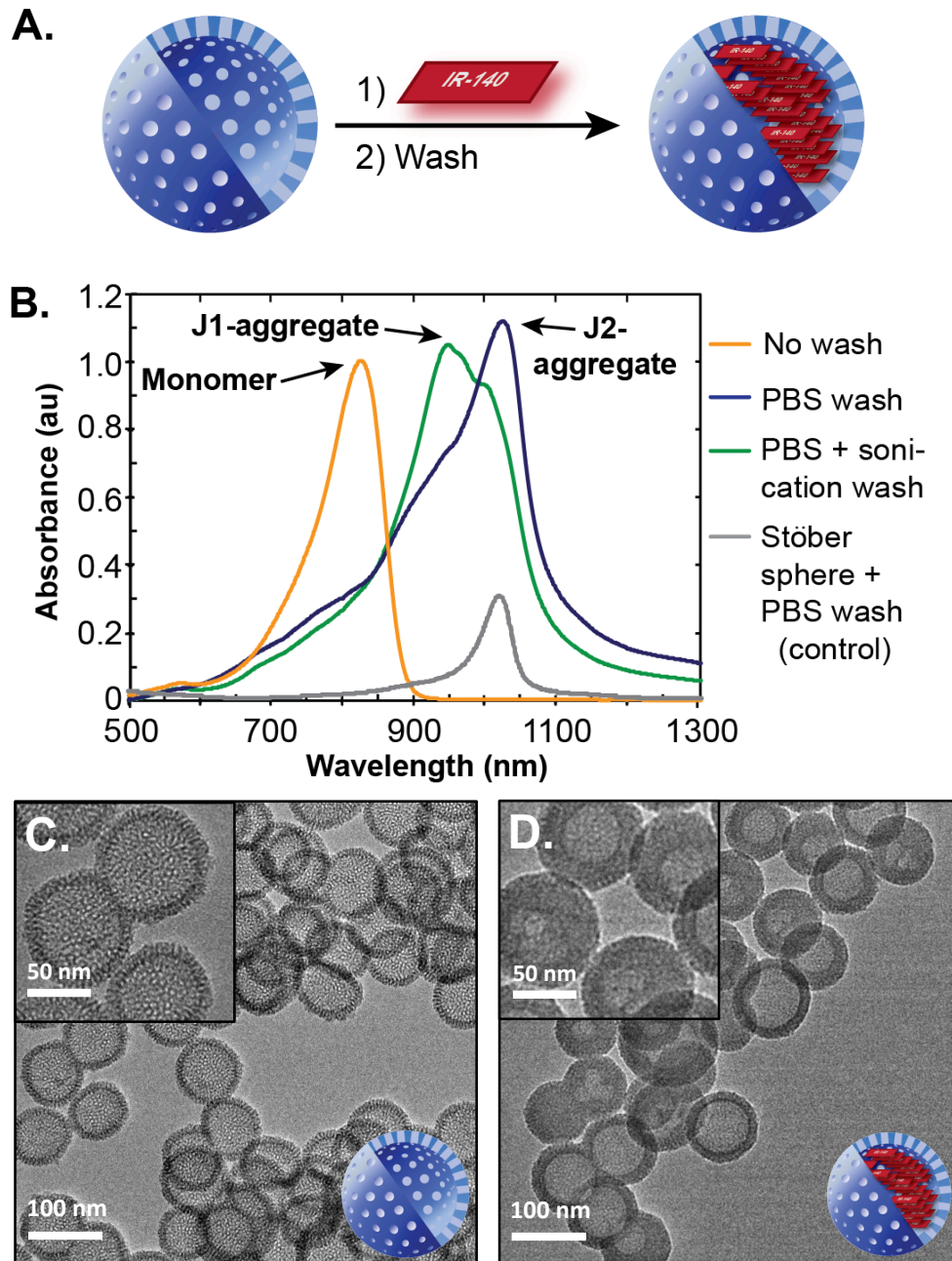


**Figure 6.3.** (A) Schematic of loading IR-140 into HMSNs. (B) Washing conditions facilitate J-aggregation. 10 mg/mL HMSNs were combined with 10 mM IR-140 in DMSO and washed with PBS with (green) and without (dark blue) sonication. Pre-wash spectrum, diluted 1:350 is shown in orange. Loading control for solid, non-porous Stöber spheres is shown in gray. (C/D) Transmission electron microscopy images of HMSNs with (D) and without (C) IR-140 treatment.

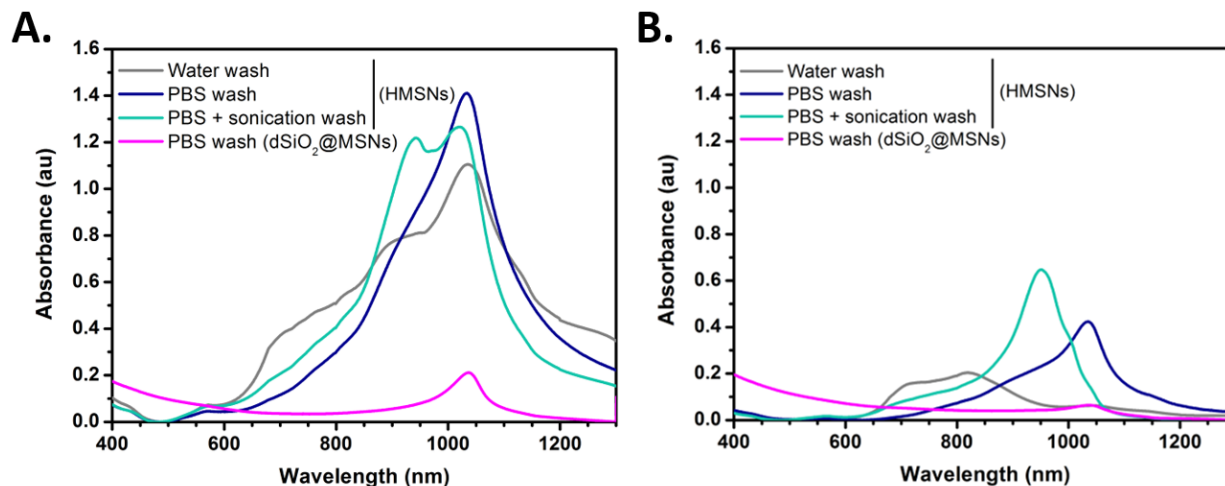


**Figure 6.4.** UV/Vis/NIR spectra of HMSNs or dSiO<sub>2</sub>@MSNs containing IR-140. The loading concentrations of IR-140 were (A) 20 mM and (B) 5 mM; HMSNs or dSiO<sub>2</sub>@MSNs were loaded at 10 mg/mL. The HMSNs particles were washed by methods (a, PBS with sonication, teal), (b, PBS, blue), or (c, water, gray) (5x, 1 mL), or the dSiO<sub>2</sub>@MSNs were washed by method (b, PBS, magenta) (see Section II, synthetic procedures). The absorbance spectra were measured with 10 mm quartz cuvettes at 0.25 mg nanoparticles/mL in PBS.

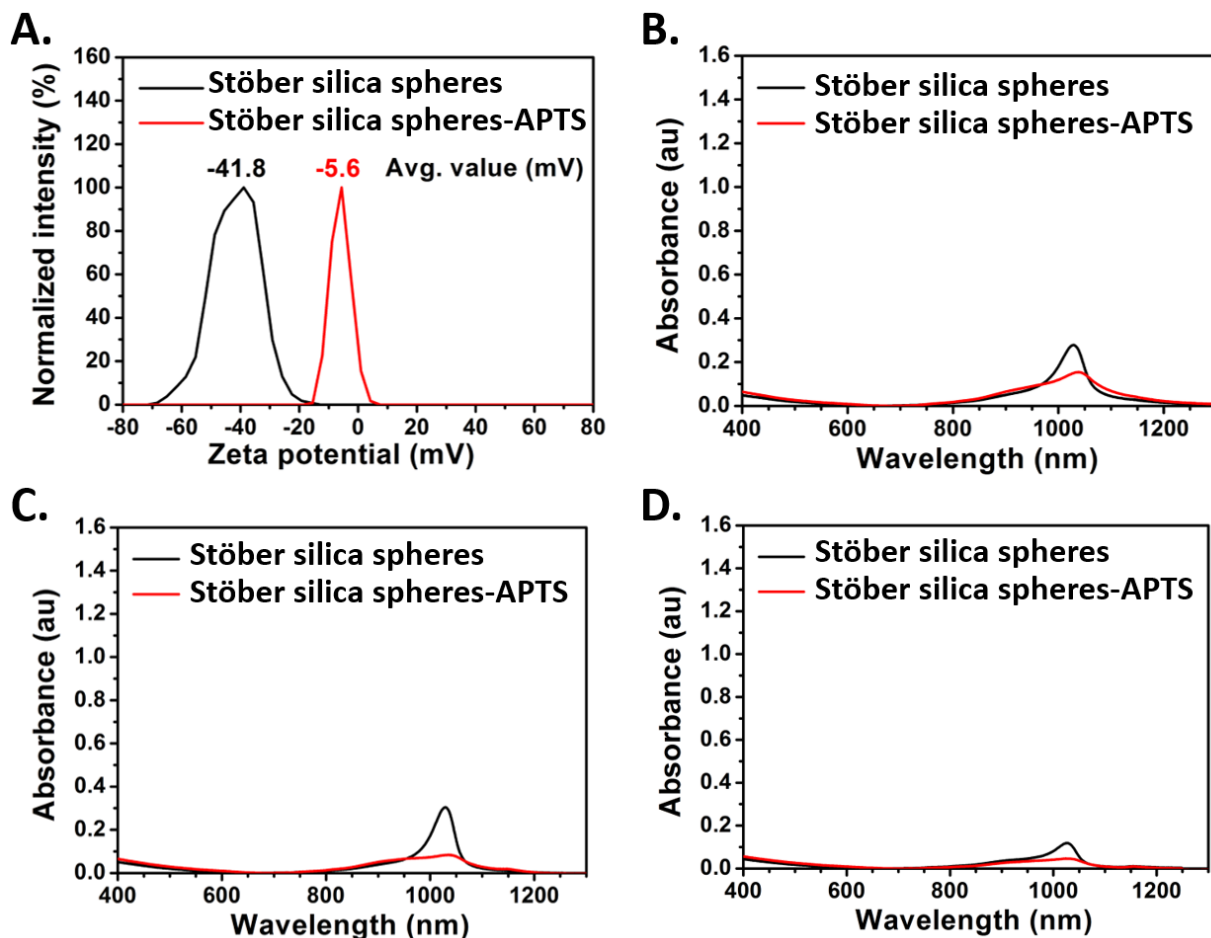


**Figure 6.5.** Control experiment with Stöber silica spheres. (A) The zeta potential of Stöber silica spheres (black), and Stöber silica spheres-APTS (red) in D.I. water at 0.05 mg/mL at room temperature. In the case of the APTS-modified Stöber spheres, we believe the surface is saturated with APTS as higher concentrations of APTS did not significantly change the zeta potential. (B/C/D) UV/Vis/NIR spectra of Stöber silica spheres (black) or Stöber silica spheres-APTS (red) containing IR-140. The loading concentrations of IR-140 were (B) 20 mM, (C) 10 mM, or (D) 5 mM; Stöber silica spheres or Stöber silica spheres-APTS were loaded at 10 mg/mL. After the loading, the particles were washed with PBS (5x, 1 mL). The absorbance spectra were measured with 10 mm quartz cuvettes at 0.25 mg nanoparticles/mL PBS.

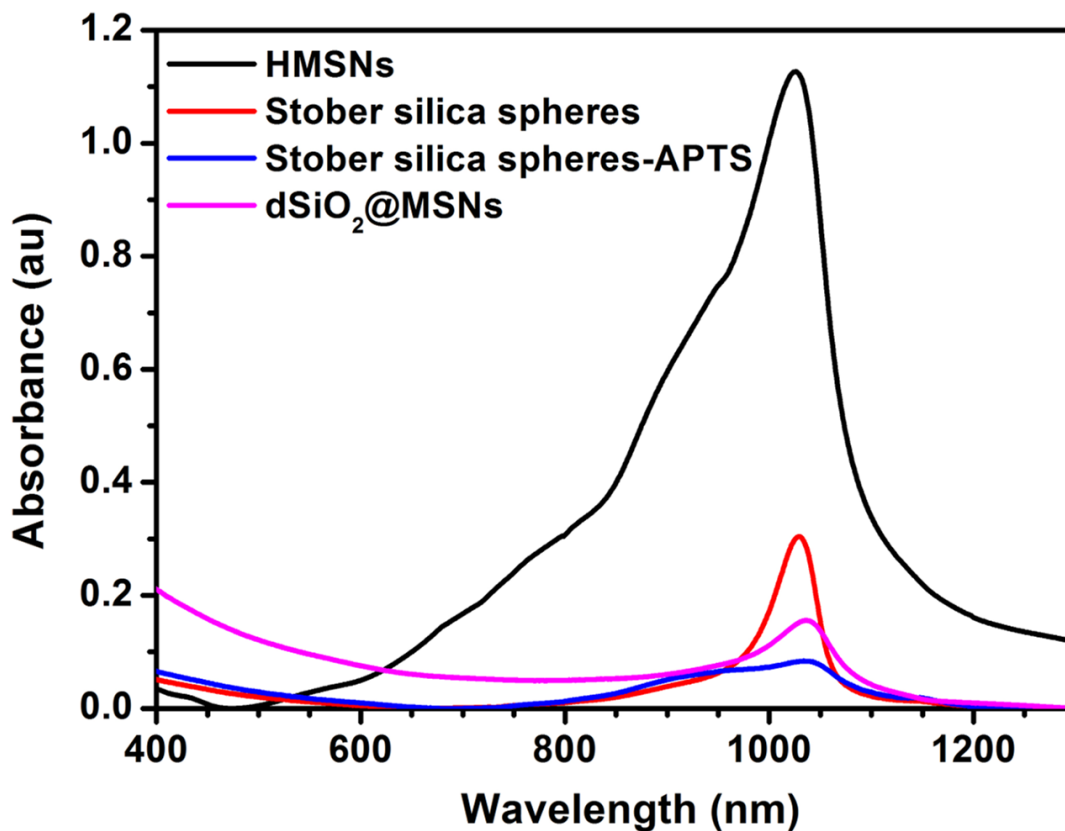


**Figure 6.6.** UV/Vis/NIR spectra of IR-140 loaded HMSNs, Stober silica spheres, Stober silica spheres-APTS, or dSiO<sub>2</sub>@MSNs. The loading concentrations of IR-140 were 10 mM; HMSNs, Stober silica spheres, Stober silica spheres-APTS, or dSiO<sub>2</sub>@MSNs were loaded at 10 mg/mL. After the loading, the particles were gently washed with PBS (5x, 1 mL). The absorbance spectra were measured with 10 mm quartz cuvettes at 0.25 mg nanoparticles/mL in PBS.

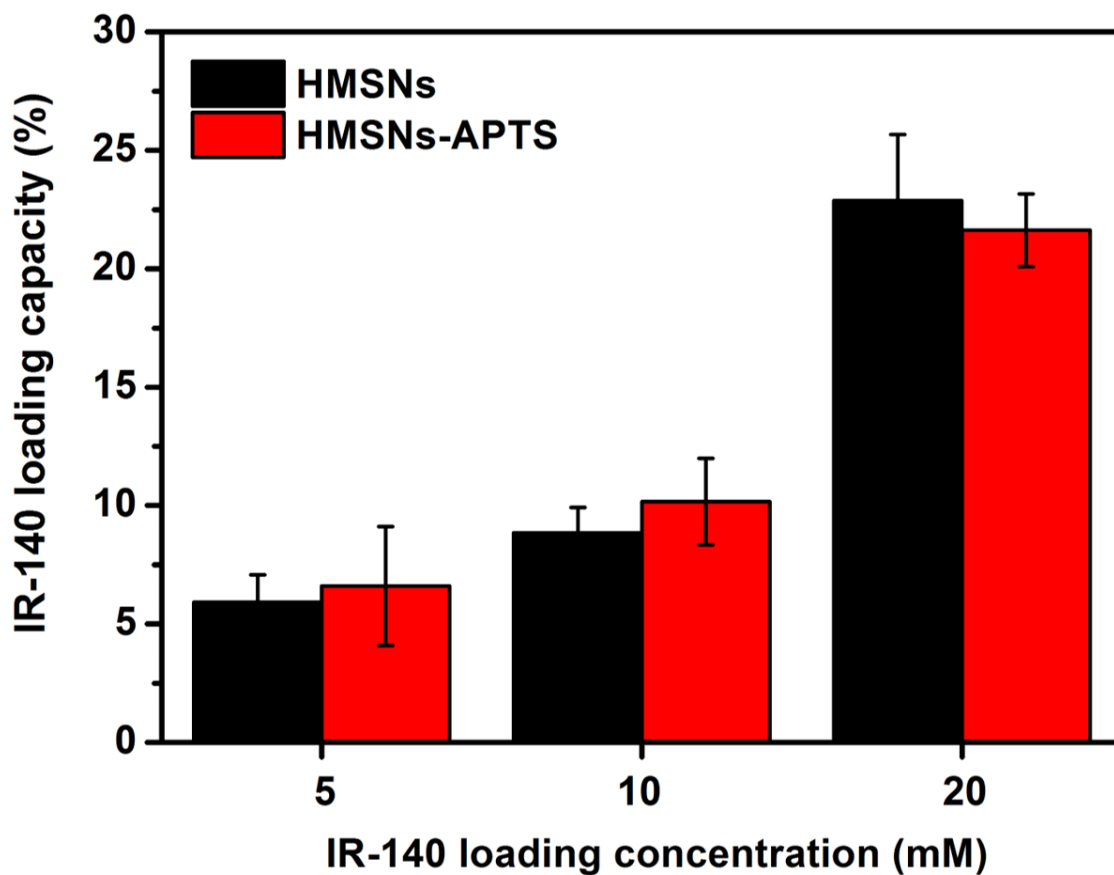


**Figure 6.7.** The loading capacity, defined as (grams IR-140/grams HMSNs or HMSNs-APTS) x 100%, of IR-140 in HMSNs (black) or HMSNs-APTS (red) at different IR-140 loading concentrations. The loading concentration of HMSNs or HMSNs-APTS was 10 mg/mL. Error represents the standard deviation of three replicates.



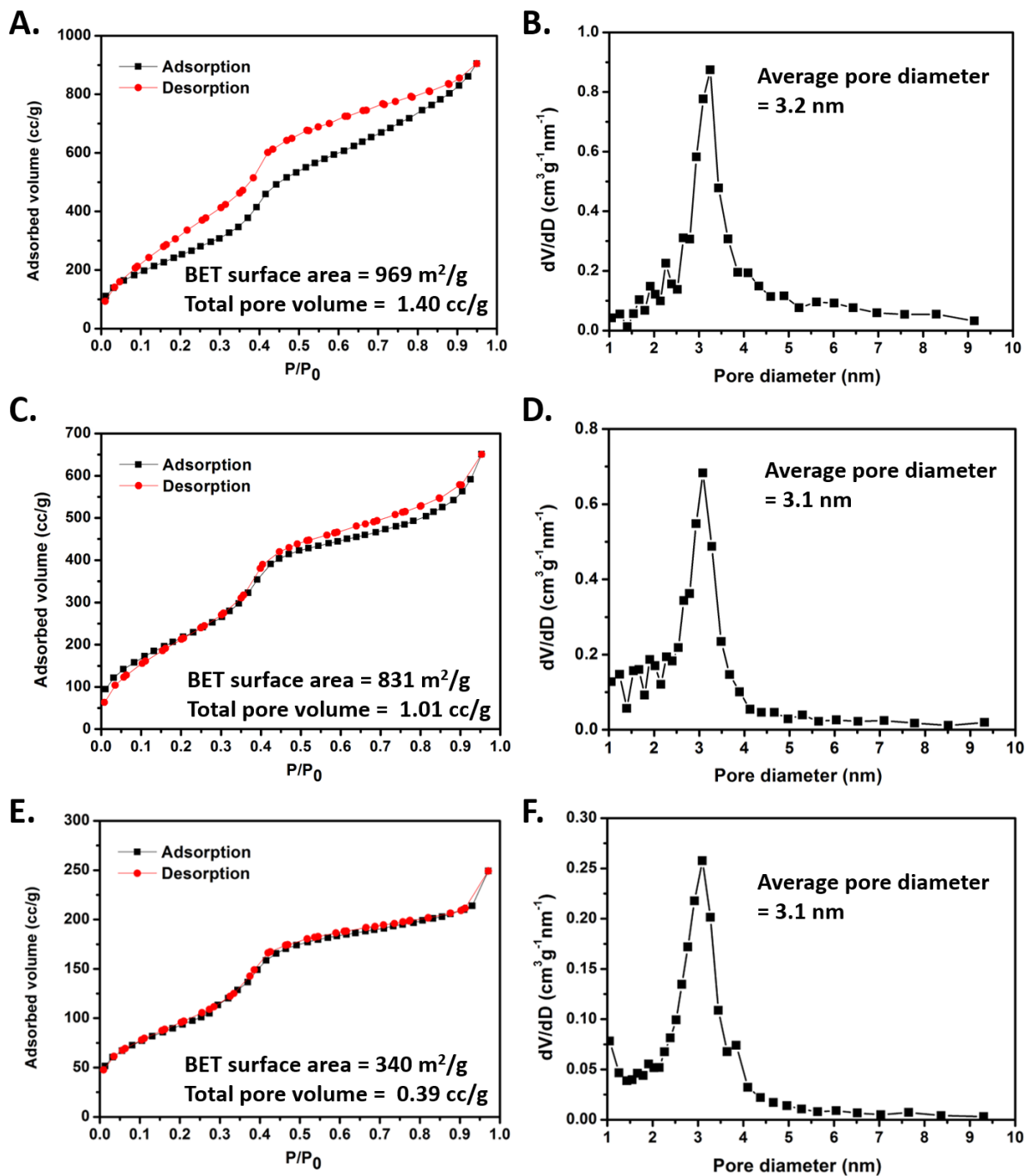


**Figure 6.8.** Nitrogen adsorption (black)/desorption (red) isotherms of (A) HMSNs, (C) HMSNs-APTS, and (E) dSiO<sub>2</sub>@MSNs. The BET surface areas of HMSNs, HMSNs-APTS, and dSiO<sub>2</sub>@MSNs are 969 m<sup>2</sup>/g, 831 m<sup>2</sup>/g, and 340 m<sup>2</sup>/g, respectively. The total pore volumes of HMSNs, HMSNs-APTS, and dSiO<sub>2</sub>@MSNs are 1.40 cc/g, 1.01 cc/g, and 0.39 cc/g, respectively. Pore diameter distributions of (B) HMSNs, (D) HMSNs-APTS, and (F) dSiO<sub>2</sub>@MSNs. The average pore diameters are 3.2 nm, 3.1 nm, and 3.1 nm, respectively.

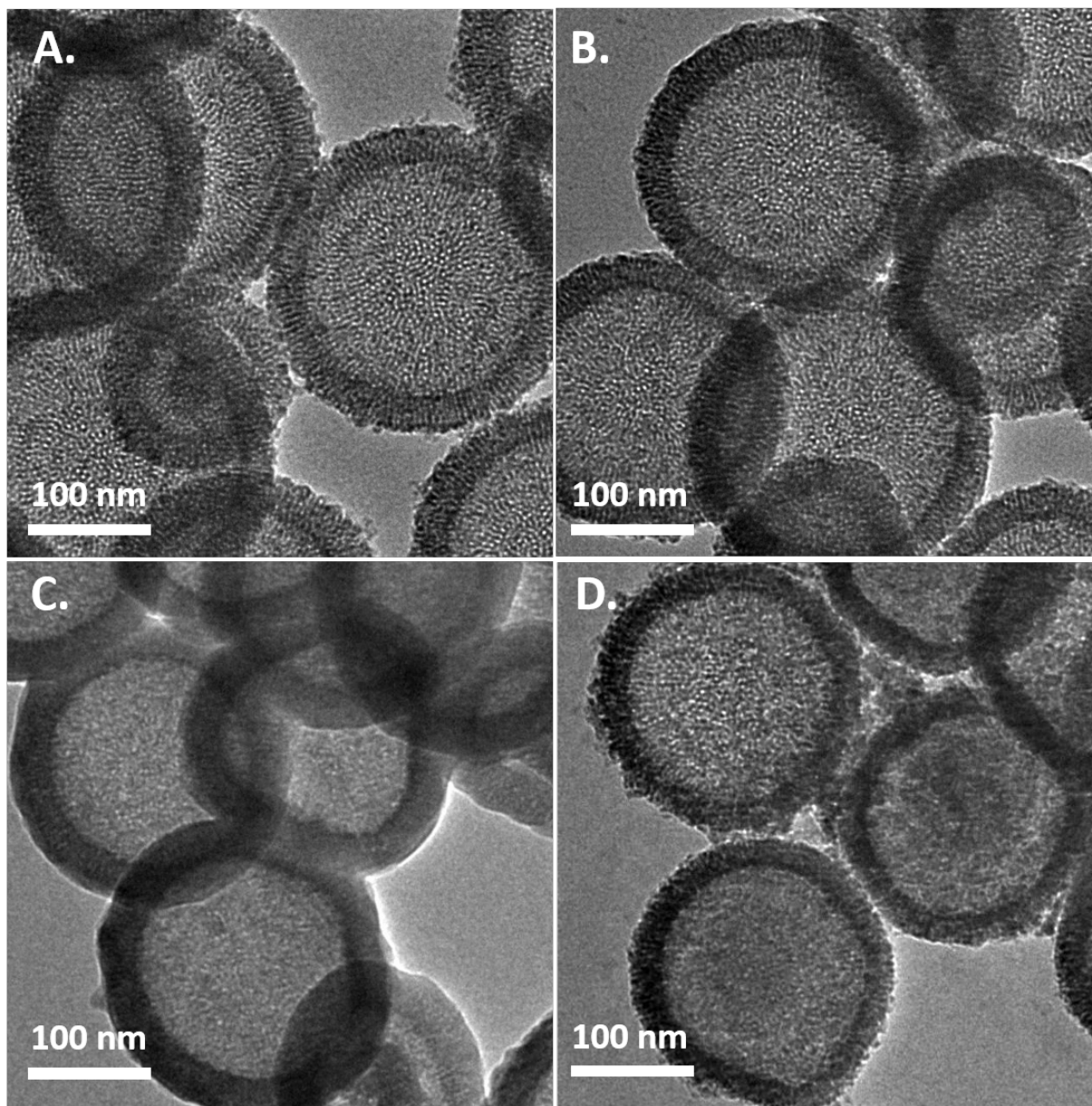


**Figure 6.9.** TEM images of HMSNs with (C) and without (A) IR-140 treatment. (A) HMSNs were dispersed in ethanol at a concentration of 0.1 mg/mL. (C) The loading concentration of IR-140 was 10 mM; HMSNs were loaded at 10 mg/mL. After loading, the particles were washed with PBS (5x, 1 mL) and dispersed in PBS at a concentration of 0.1 mg/mL. (B) As a control, HMSNs were washed with PBS (5x, 1 mL) but without the loading of IR-140. After washing, HMSNs were dispersed in PBS at a concentration of 0.1 mg/mL. (D) Mixture of HMSNs with and without IR-140 treatment. The mixed particles were prepared by mixing HMSNs in PBS solution (50  $\mu$ L, 0.2 mg/mL) with IR-140 loaded HMSNs in PBS solution (50  $\mu$ L, 0.2 mg/mL) at the mass ratio of 1:1. TEM images were measured on a Tecnai T12 instrument with an operating voltage of 120 kV.

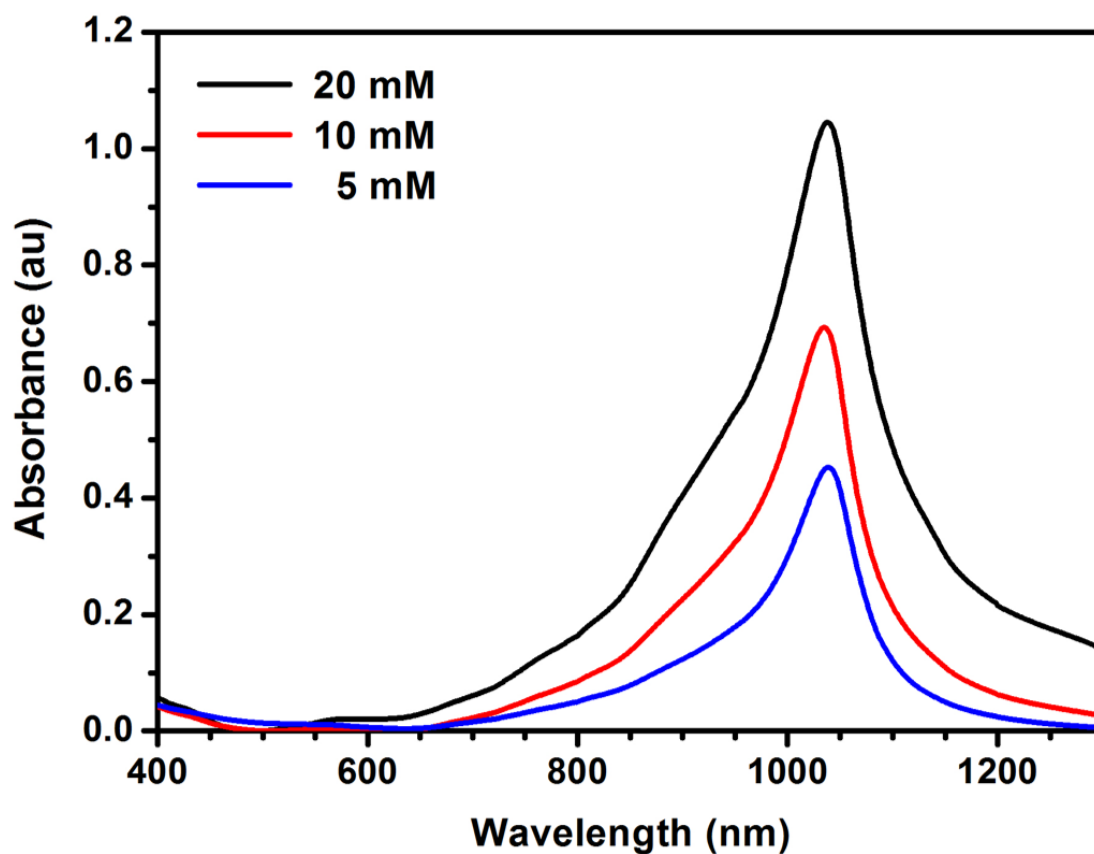


**Figure 6.10.** UV/Vis/NIR spectra of HMSNs-APTS containing IR-140 for dye loading concentrations of 20 mM (black), 10 mM (red), or 5 mM (blue) in PBS, after washing the particles with PBS (5 x 1 mL). The loading concentration of HMSNs-APTS was 10 mg/mL. The absorbance spectra were measured with 10 mm quartz cuvettes at 0.25 mg nanoparticles/mL.

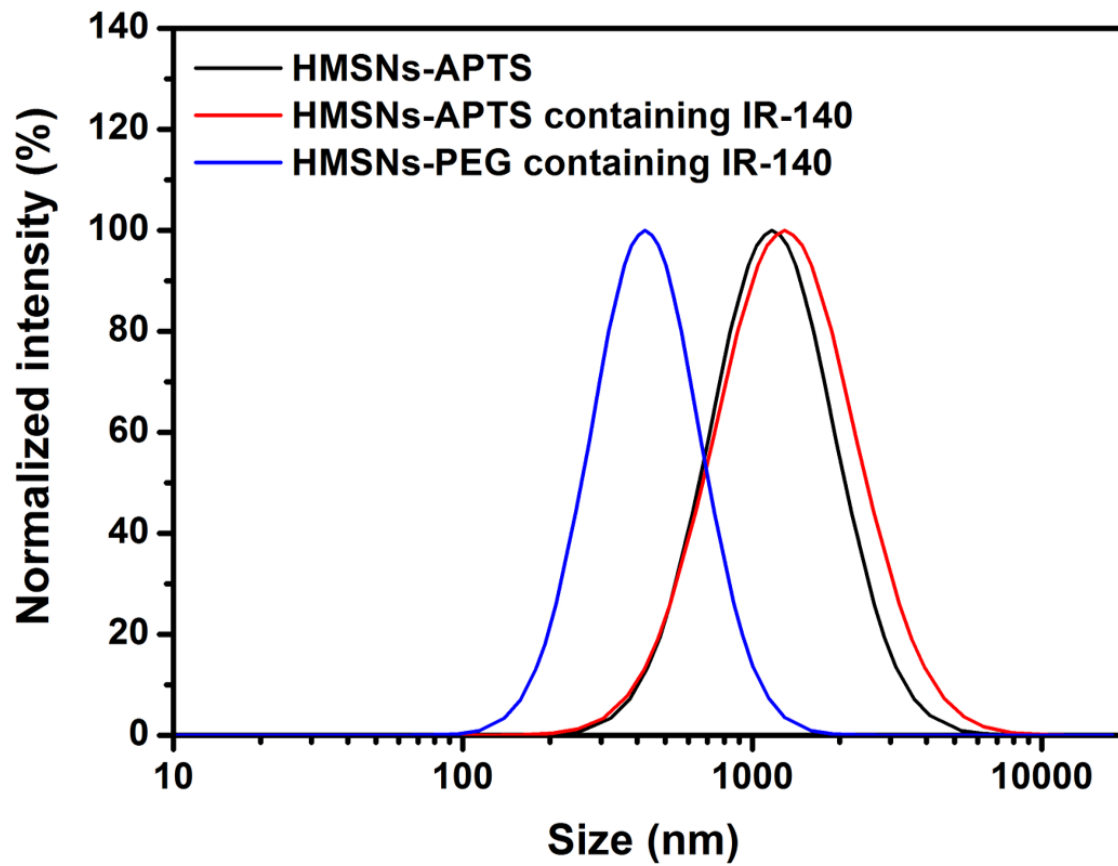


**Figure 6.11.** The dynamic light scattering size distribution of HMSNs-APTS (black), HMSNs-APTS containing IR-140 (red), and HMSNs-PEG containing IR-140 in PBS (blue) measured at 0.05 mg/mL at room temperature in PBS. Note that the HMSNs-APTS are not soluble in water and significant aggregation is observed in the DLS until after conjugation of PEG.

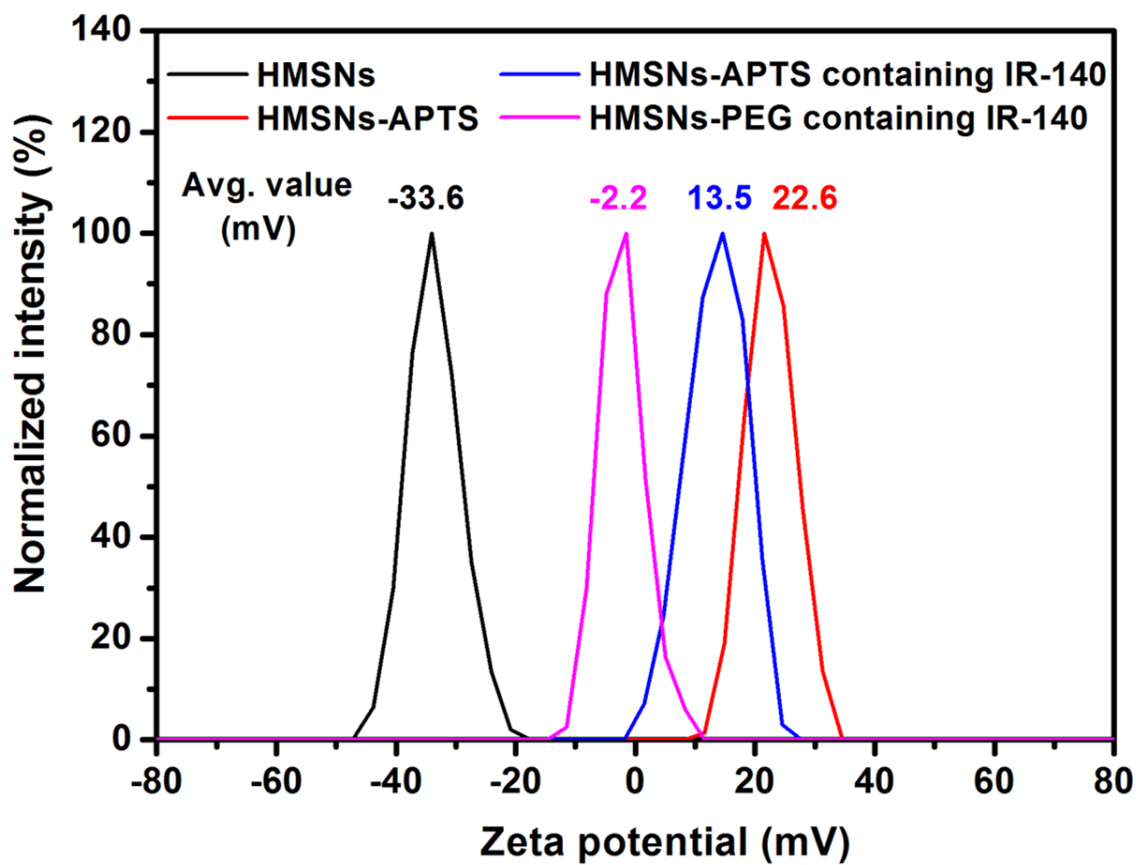


**Figure 6.12.** The zeta potential of HMSNs (black), HMSNs-APTS (red), HMSNs-APTS containing IR-140 (blue), and HMSNs-PEG containing IR-140 (pink) in D.I. water at 0.05 mg/mL at room temperature.

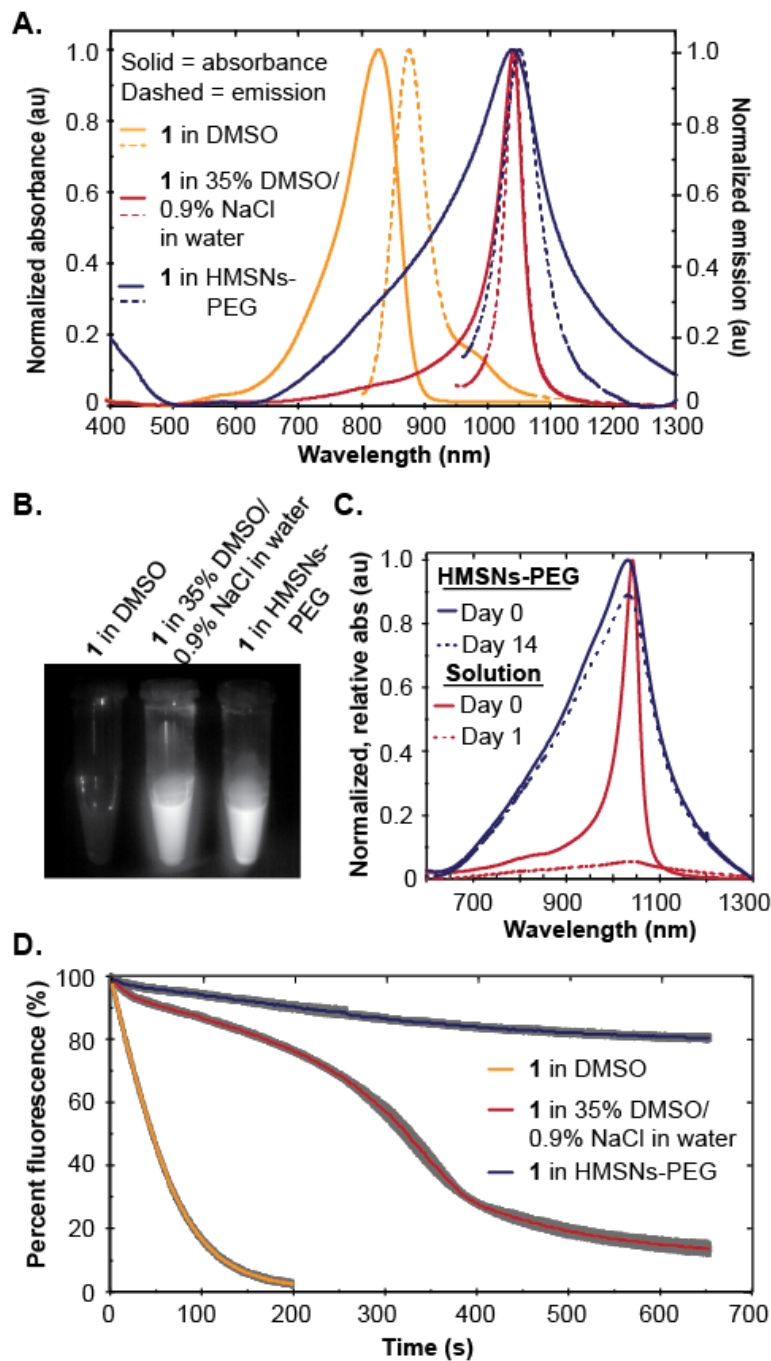


**Figure 6.13.** (A) Normalized absorption and emission of IR-140 J-aggregate in HMSNs-PEG (blue), J-aggregate in solution (red), and monomer (yellow). (B) Emission (1000–1700 nm) of IR-140 monomer (left), J-aggregate in solution (middle) and J-aggregate in HMSNs-PEG (right) upon 980 nm excitation. (C) Normalized relative absorption of IR-140 J-aggregate in 35% DMSO/0.9% NaCl in water (red) and in HMSNs-PEG in PBS (blue) on day zero (solid) and day 1 or 14 (dotted). (D) Photostability under laser irradiation ( $97 \text{ mW/cm}^2$ ) at 980 nm for IR-140 J-aggregate in HMSNs-PEG (blue) and IR-140 J-aggregate in 35% DMSO/0.9% NaCl in water (red), and at 785 nm for monomer in DMSO (yellow).

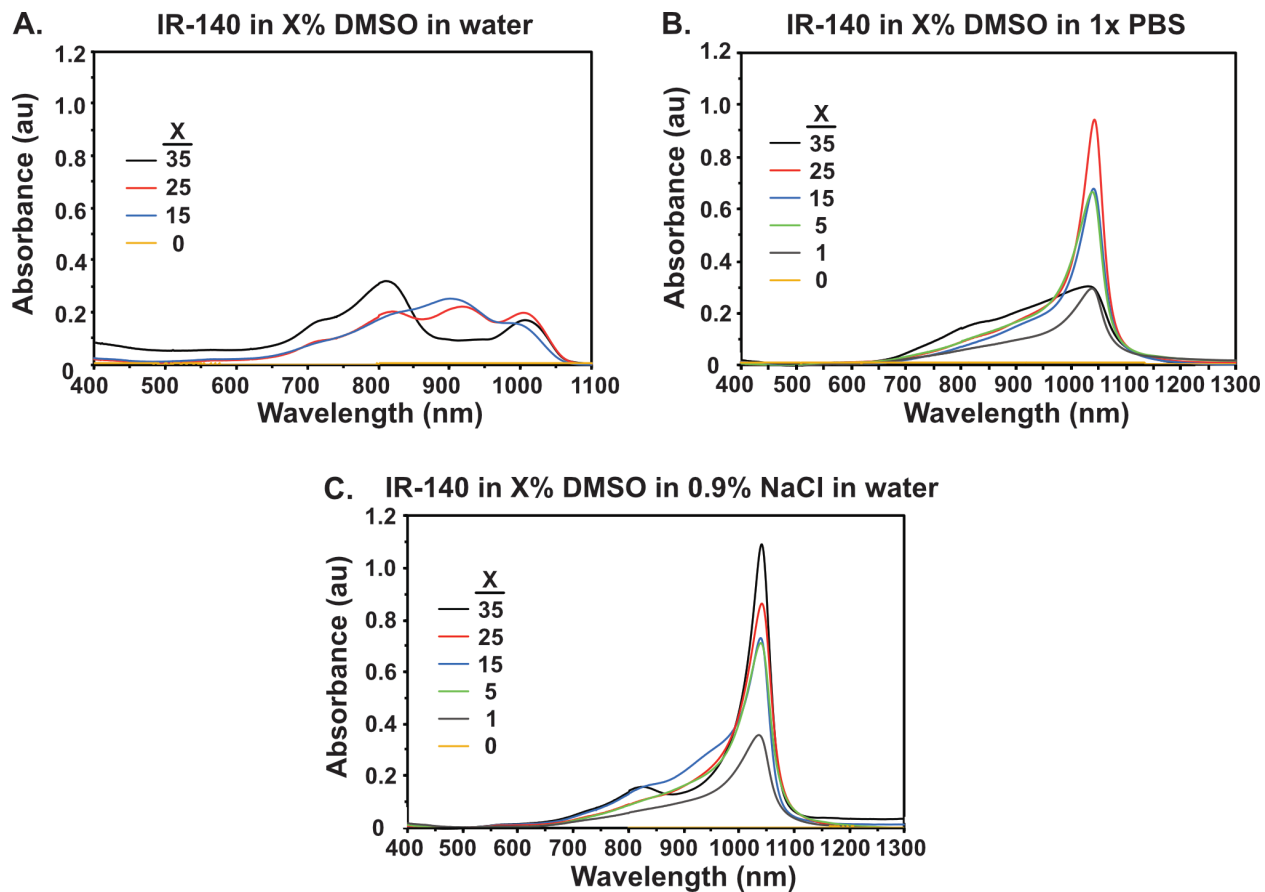


**Figure 6.14.** UV-Vis-NIR characterization of IR-140 J-aggregate formation in solution at 0.01 mg/mL in (A) DMSO/water, (B) DMSO/1xPBS, and (C) DMSO/0.9% NaCl in water.

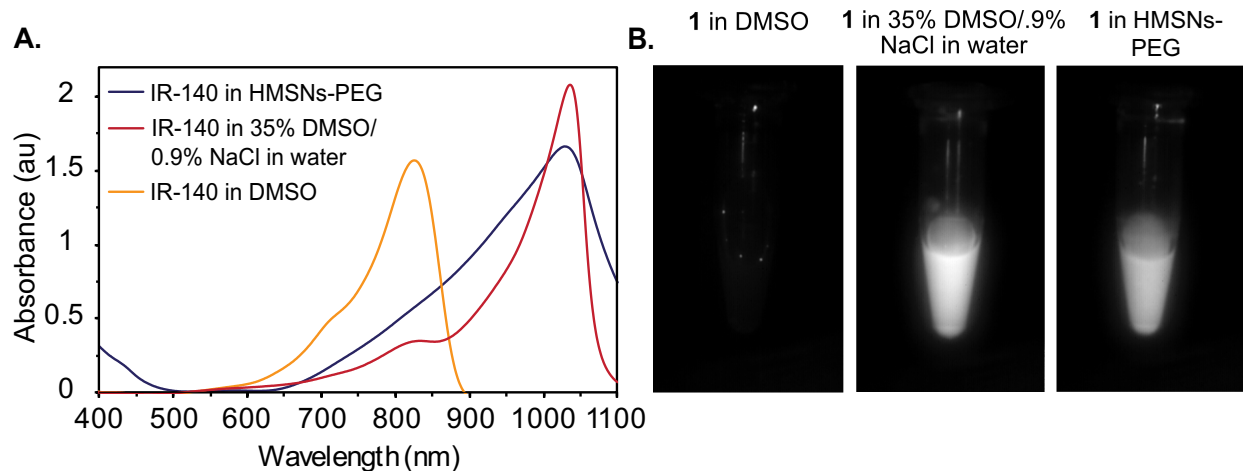


**Figure 6.15.** Emission of monomer and J-aggregate states of IR-140 under 980 nm excitation. (A) Absorbance traces of samples (10 mm path length) used in vial images in B and in Figure 4.13B, baseline corrected to 521 nm. (B) Images of IR-140 monomer in DMSO (left), IR-140 J-aggregate in solution (center) and J-aggregate in HMSNs-PEG (right) under 980 nm irradiation ( $99 \pm 3 \text{ mWcm}^{-1}$ ). All Eppendorf tubes are placed in the same location, such that laser intensity across all samples is identical. See Figure 4.13B experimental procedure for sample preparation and acquisition settings. Displayed images were background subtracted, averaged over 10 frames and the contrast was set to identical values for comparison.



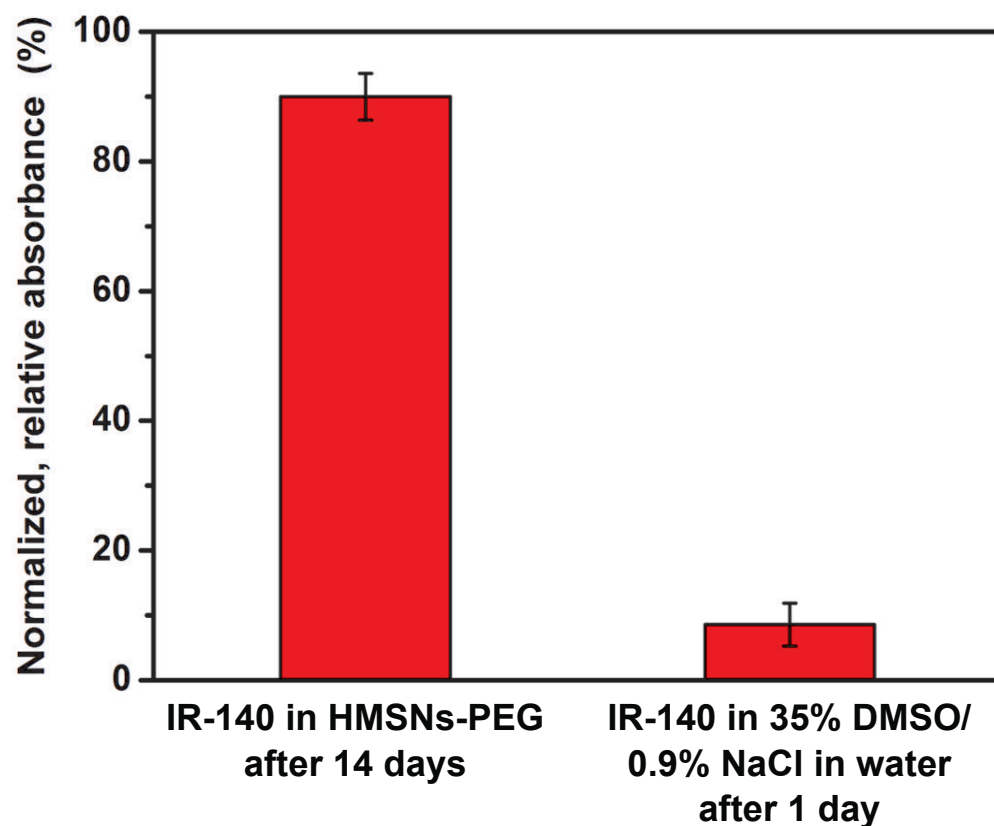


**Figure 6.16.** Stability of J-aggregates over time, displayed as the normalized, relative absorbance remaining for IR-140 in HMSNs-PEG after 14 days, and IR-140 in solution after 1 day. IR-140 loaded HMSNs-PEG were dispersed in PBS (0.25 mg/mL), and IR-140 J-aggregate was composed of 0.01 mg/mL IR-140 in 35% DMSO/0.9% NaCl in water. Error represents the standard deviation of three replicates.

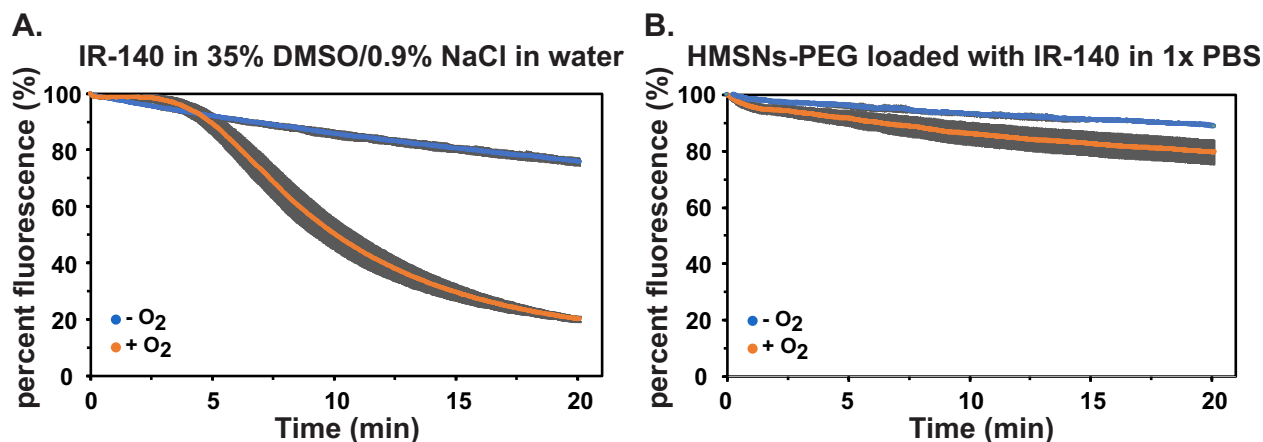


**Figure 6.17.** Photostability of J-aggregates in the presence and absence of oxygen. (A) Raw data of IR-140 J-aggregate in 35 % DMSO/0.9% NaCl at 0.01 mg/mL under 980 nm irradiation with 79 mWcm<sup>-2</sup> power density. The relative rates of oxygenated to deoxygenated photobleaching is 7.1 to 1. (B) Raw data of HMSNs-PEG loaded with IR-140 at 1.0 mg/mL in 1x PBS under 980 nm irradiation with 101 mWcm<sup>-2</sup> power density. The relative rates of oxygenated to deoxygenated photobleaching is 1.9 to 1. Error bars represent the standard deviation of three replicate experiments in (A) and (B) oxygenated and two replicate experiments in (B) deoxygenated. Deoxygenated samples were prepared by purging with N<sub>2</sub> for 30-60 min; oxygenated samples were not purged with N<sub>2</sub>. **Note:** The photobleaching rate of the solution IR-140 aggregate is substantially attenuated by the removal of oxygen, (~7x) while the photobleaching of the HMSNs IR-140 is improved by only ~2x. These data indicate that the IR-140 loaded inside the HMSNs are less affected by the presence of oxygen, which may be due to a shielding of reactive oxygen species by the dense silica shells, as suggested previously.<sup>41</sup>

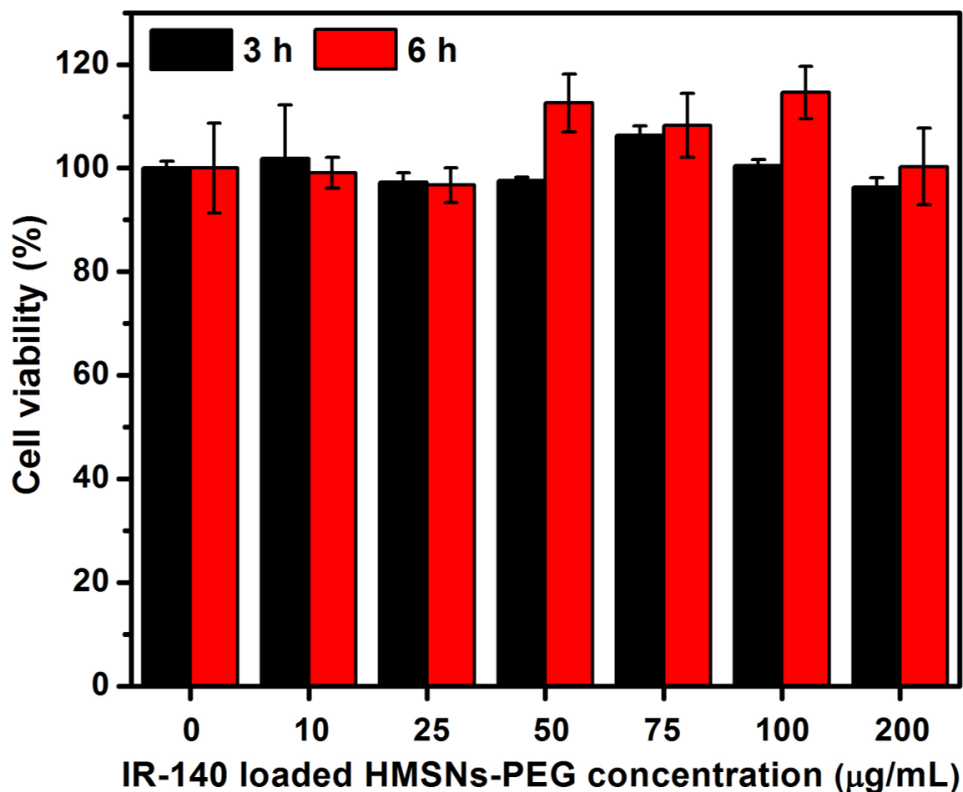


**Figure 6.18.** Cytotoxicity study of IR-140 loaded HMSNs-PEG examined by a CCK-8 assay. HeLa cells were incubated in 200 µL fresh DMEM containing 0, 2, 5, 10, 15, 20, and 40 µg of IR-140 loaded HMSNs-PEG (*i.e.* 0, 10, 25, 50, 75, 100, and 200 µg/mL) for 3 (black) or 6 (red) hours at 37 °C. The viable cells in each condition was determined by the absorbance at 450 nm and 650 nm (as a reference). The DMEM (100 µL) mixed with CCK-8 reagent (10 µL) served as a background. Error bars represent the standard deviation of three replicate experiments.

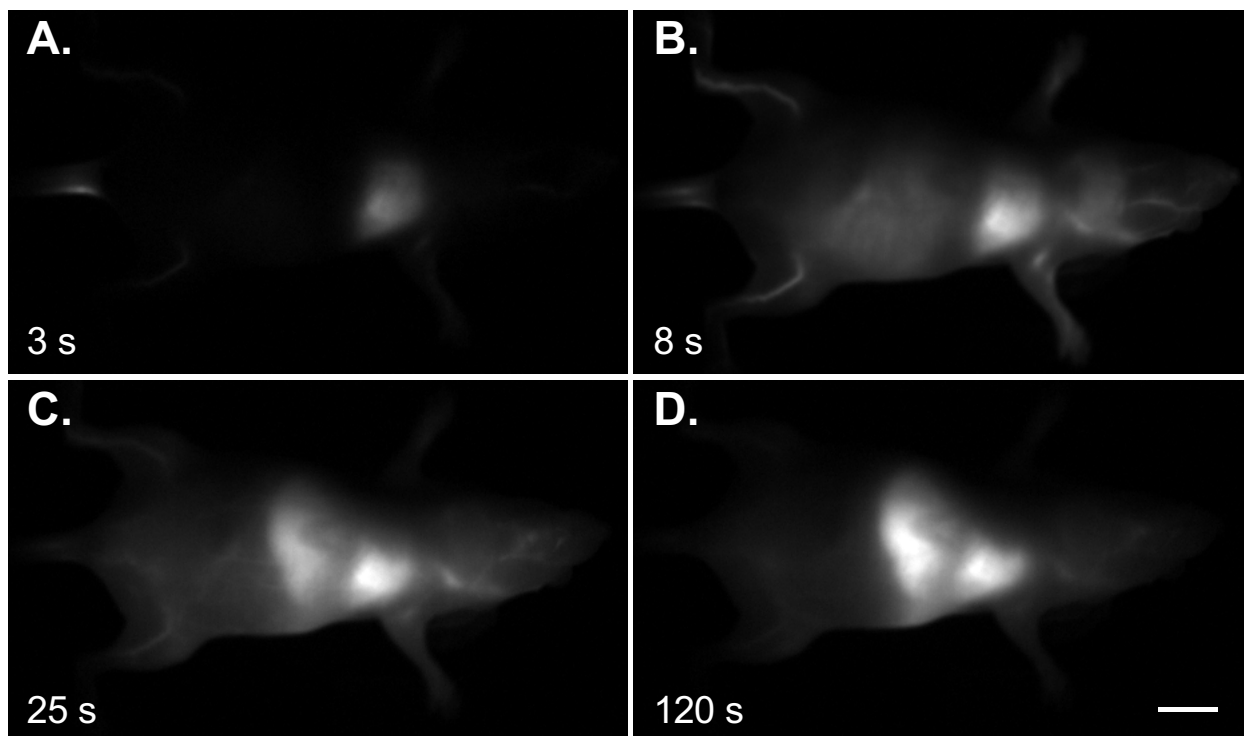


**Figure 6.19.** Whole-mouse imaging at 16 fps (980 nm, 91 mW/cm<sup>2</sup> excitation; 1000–1700 nm collection) upon i.v. delivery of IR-140 HMSNs-PEG. Background subtracted stills were averaged over 5 frames at 3 s (A), 8 s (B), 25 s (C), and 120 s (D) post injection. Scale bar represents 1 cm. Data are representative of two replicate experiments.

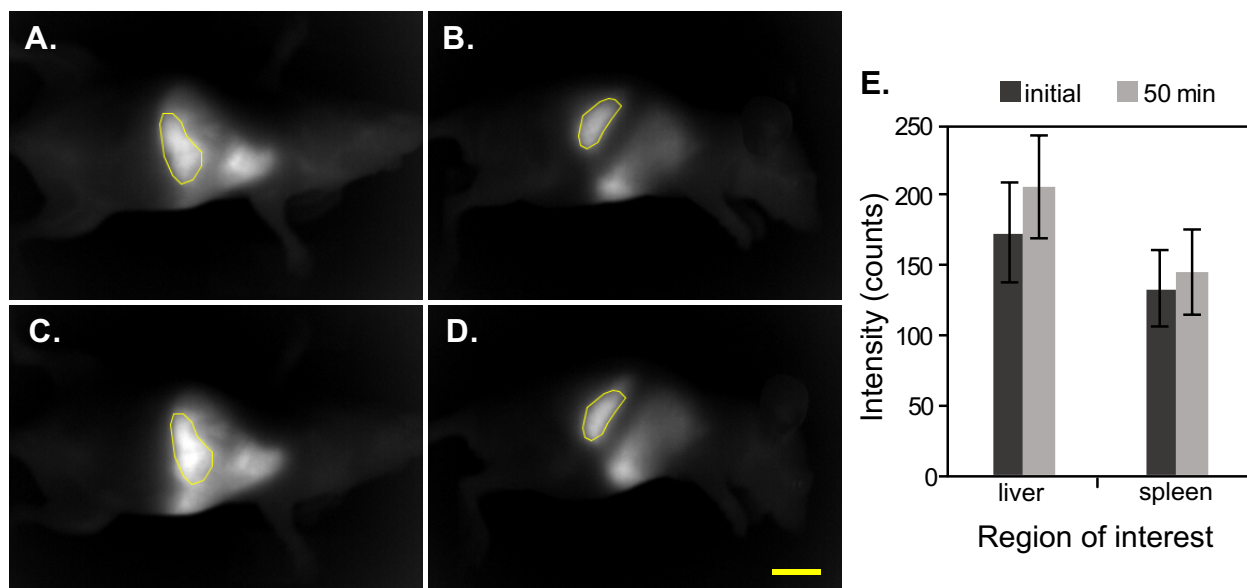


**Figure 6.20.** Images from the front (A/C) and left side (B/D) of a nude mouse directly after vascular clearance (>2 m post injection) (A/B), and after 50 minutes (C/D), showing uptake of IR-140 loaded HMSNs-PEG in the liver and spleen. Images were acquired with 60 ms exposure time at 16.65 fps with 980 nm ex. ( $91 \pm 3 \text{ mW/cm}^2$ ) and 1000–1700 nm detection (see general experimental procedures, section I, for details of optical set up). Displayed images were background subtracted, averaged over 5 frames, outliers were removed, and the contrast was set to identical values for comparison. Regions of interest were defined and applied to quantify the intensity in the liver (A/C) and spleen (B/D) over time. Scale bar represents 1 cm. (E) Quantification of signal for liver and spleen showing no significant change in signal over 50 minutes. Error bars represent the standard deviation over the regions of interest. Data are representative of two replicate experiments.

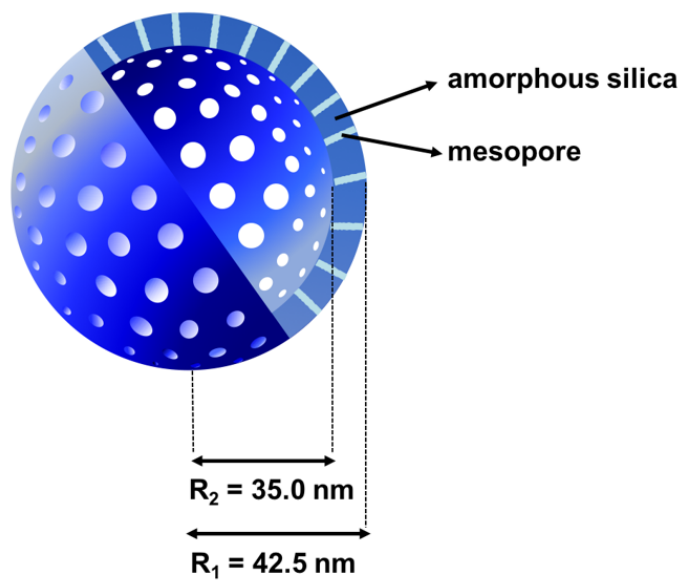


**Figure 6.21.** HMSN or HMSN-APTS used in this work.  $R_1$  and  $R_2$  are the outer radius and inner radius of HMSN or HMSN-APTS, respectively.  $V_{shell}$  is the shell volume of a single HMSN.  $V_{mesopore}$  is the volume of the mesopores in the shell.  $V_{amorphous\ silica}$  is the volume of silica in the shell excluding mesopores.

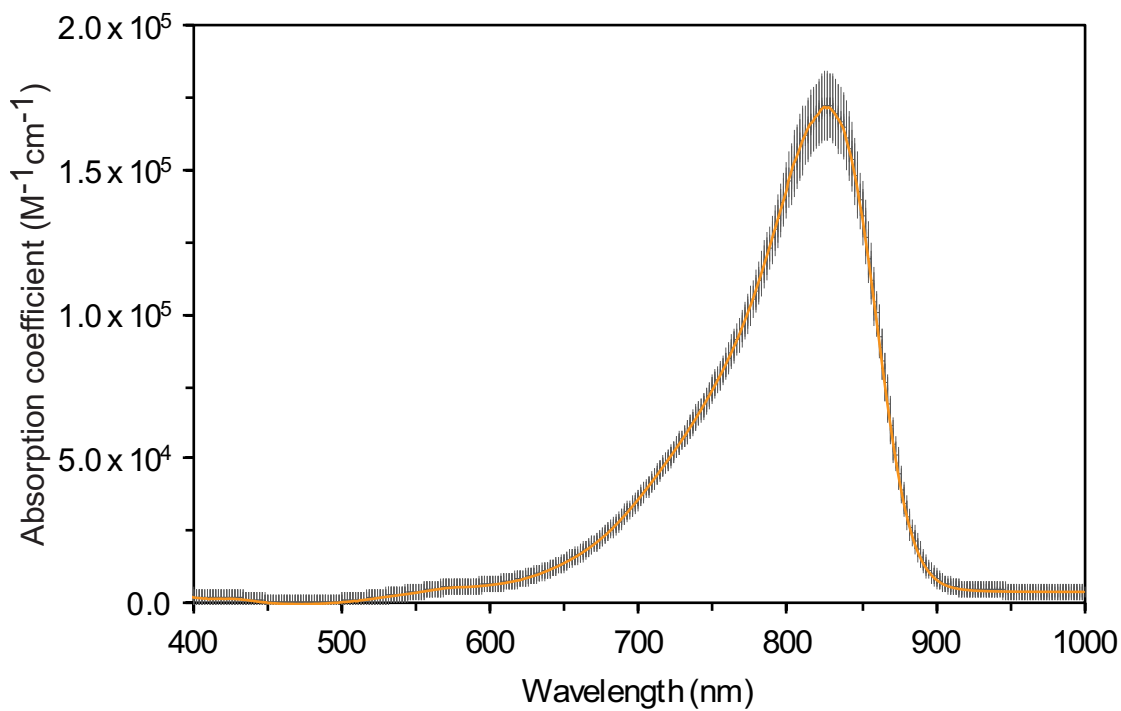


**Figure 6.22.** Absorption coefficient of IR-140 monomer in DMSO.

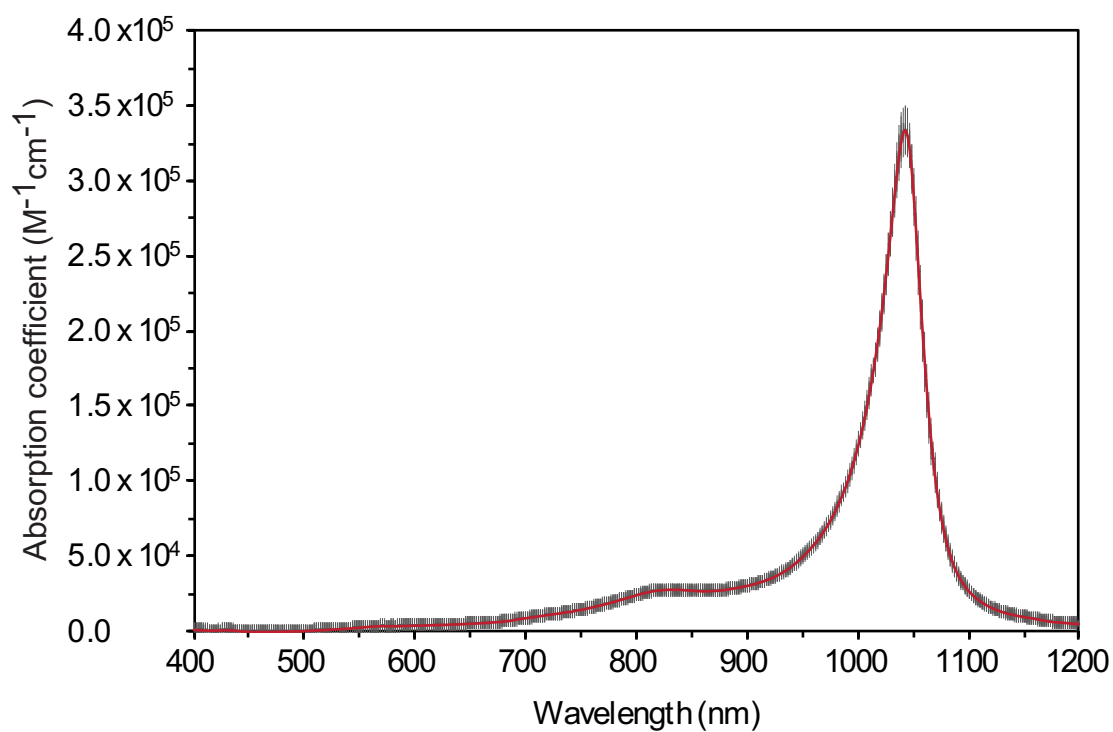


**Figure 6.23.** Uncorrected absorption coefficient of IR-140 J-aggregate in 35% DMSO/0.9% NaCl in water.

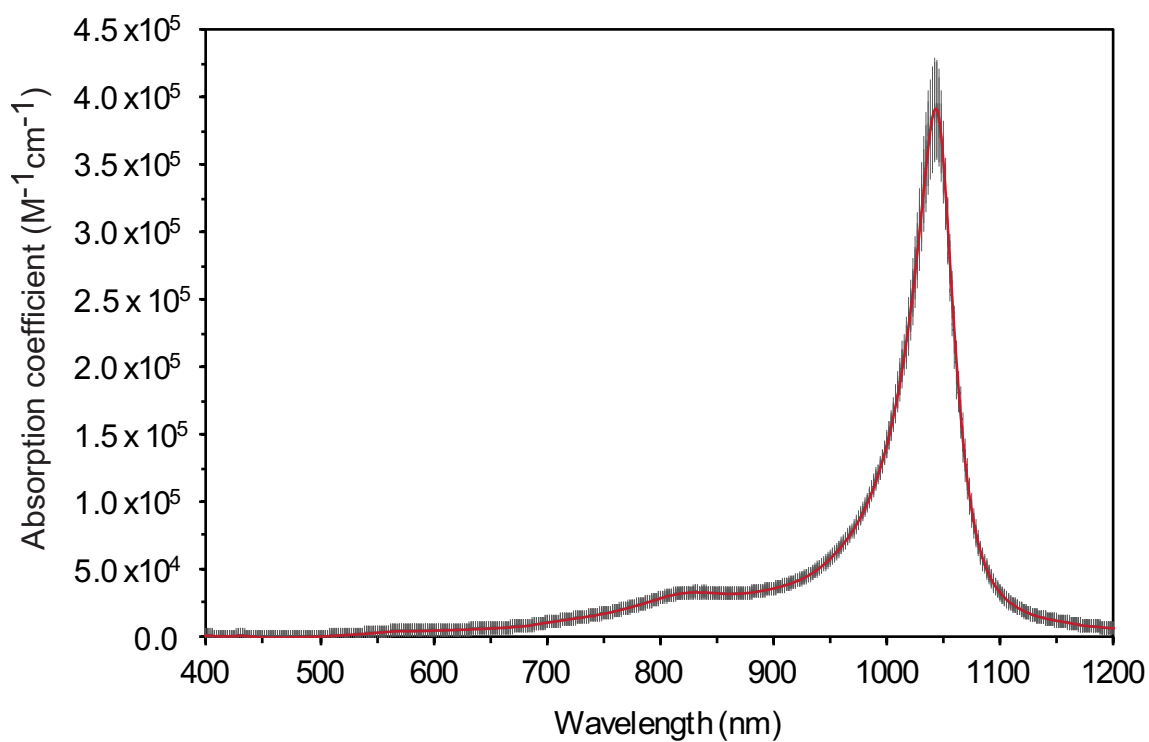


**Figure 6.24.** Corrected absorption coefficient of IR-140 J-aggregate in 35% DMSO/0.9% NaCl in water.

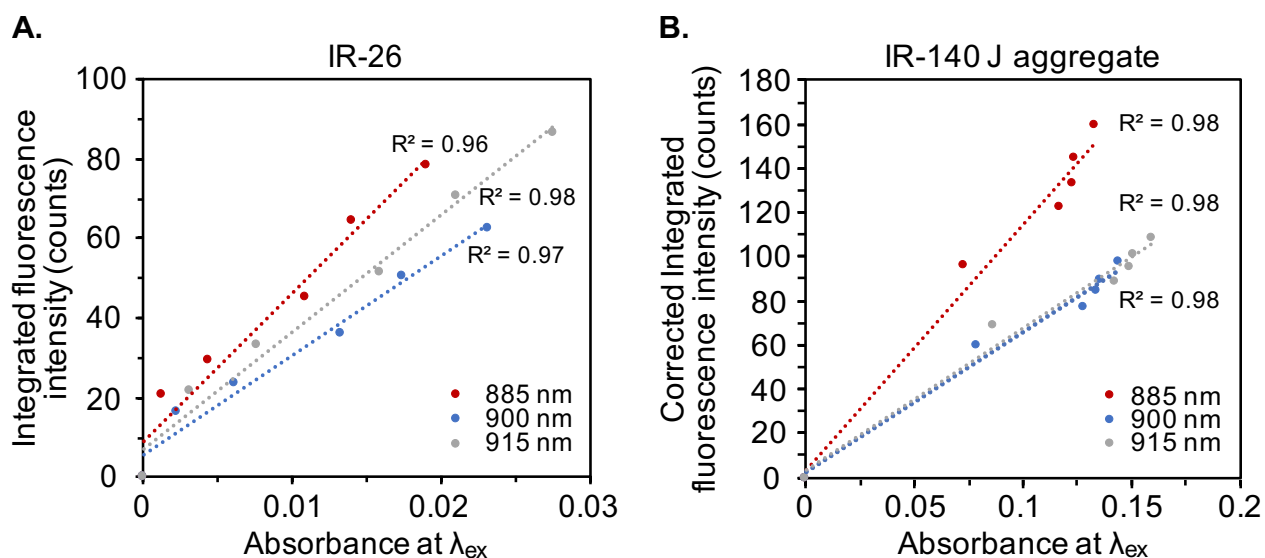


**Figure 6.25.** Solvent corrected integrated fluorescence intensity versus absorbance plots for (A) IR-26 and (B) IR-140 J-aggregate, also corrected for reabsorption.

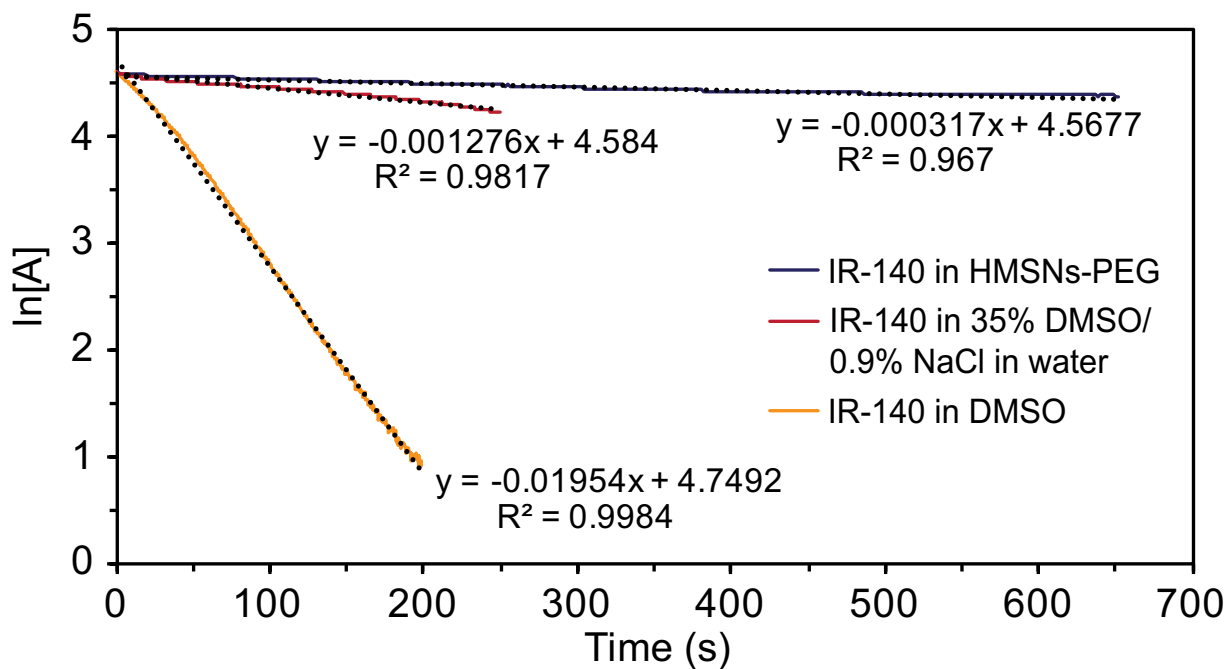


**Figure 6.26.** Photobleaching data plotted as the  $\ln[A]$  vs time and the corresponding linear fits.



**Table 6.1.** Photophysical characterization of **1** (IR-140)

Species	$\lambda_{\max, \text{abs}}$ (nm)	$\epsilon$ ( $\text{M}^{-1}\text{cm}^{-1}$ )	$\lambda_{\max, \text{em}}$ (nm)	$\Phi$ (%)
<b>1</b> monomer <sup>a</sup>	826	$1.7 \pm 0.1 \times 10^5$	875	20 <sup>42</sup>
<b>1</b> J-aggregate <sup>b</sup>	1042	$3.9 \pm 0.4 \times 10^5$	1043	$0.012 \pm 0.007$

<sup>a</sup> in DMSO<sup>b</sup> in 35% DMSO/0.9% NaCl in water**Table 6.2.** Photobleaching rates of IR-140 (**1**)

Species	$\lambda_{\text{ex}}$ (nm)	$k_{\text{raw}}$ ( $\text{s}^{-1}$ ) $\times 10^3$	$k_{\text{rel}}$ ( $\text{s}^{-1}$ ) $\times 10^3$	Relative stability
<b>1</b> monomer	785	$19.54 \pm 0.04$	$19 \pm 1$	1
<b>1</b> J-aggregate	980	$1.276 \pm 0.008$	$1.28 \pm 0.05$	$15 \pm 1$
<b>1</b> in HMSNs-PEG	980	$0.317 \pm 0.002$	$0.32 \pm 0.01$	$62 \pm 5$

**Table 6.3.** Photobleaching rates and values used in calculations and corrections

Sample	$\lambda_{\text{ex}}$ (nm)	Fluence ( $\text{mWcm}^{-2}$ )	$k_{\text{raw}}$ ( $\text{s}^{-1}$ ) $\times 10^3$	$\epsilon$ at $\lambda_i$ ( $\text{M}^{-1}\text{cm}^{-1}$ ) $\times 10^{-5}$	$N_p$	$k_{\text{rel}}$ ( $\text{s}^{-1}$ ) $\times 10^3$	Relative stability
<b>1</b> monomer	785	$97 \pm 3$	$19.54 \pm .04$	$1.18 \pm 0.07$	$3.83 \times 10^{17}$	$19 \pm 1$	1
<b>1</b> J-aggregate	980	$97 \pm 3$	$1.276 \pm 0.008$	$0.95 \pm 0.04$	$4.79 \times 10^{17}$	$1.28 \pm 0.05$	$15 \pm 1$
<b>1</b> in HMSNs-PEG	980	$97 \pm 3$	$0.317 \pm 0.002$	$0.95 \pm 0.04$	$4.79 \times 10^{17}$	$0.32 \pm 0.01$	$62 \pm 5$

## 6.8 References

- (1) (a) Hong, G.; Antaris, A.L.; Dai, H. Near-infrared fluorophores for biomedical imaging. *Nat. Biomed. Eng.* **2017**, *1*, 0010. (b) Carr, J.A.; Aellen, M.; Franke, D.; So, P.T.C.; Bruns, O.T.; Bawendi, M.G. Absorption by water increases fluorescence image contrast of biological tissue in the shortwave infrared. *Proc. Natl. Acad. Sci. U.S.A.* **2018**, *37*, 9080–9085. (c) Smith, A.M.; Mancini, M.C.; Nie, S.M. Second window for in vivo imaging. *Nat. Nanotechnol.* **2009**, *4*, 710–711.
- (2) Thimsen, E.; Sadtler, B.; Berezin, M.Y. Shortwave-infrared (SWIR) emitters for biological imaging: a review of challenges and opportunities *Nanophotonics* **2017**, *6*, 1043–1054.
- (3) Welsher, K.; Liu, Z.; Sherlock, S.P.; Robinson, J.T.; Chen, Z.; Daranciang, D.; Dai, H. A route to brightly fluorescent carbon nanotubes for near-infrared imaging in mice. *Nat. Nanotechnol.* **2009**, *4*, 773–780.
- (4) (a) Hong, G.; Tobinson, J.T.; Zhang, Y.J.; Diao, S.; Antaris, A.L.; Wang, Q.B.; Dai, H. In vivo fluorescence imaging with Ag<sub>2</sub>S quantum dots in the second near-infrared window. *Angew. Chem. Int. Ed.* **2012**, *24*, 9818–9821. (b) Bruns, O.T.; Bischof, T.S.; Harris, D.K.; Franke, D.; Shi, Y.; Riedemann, L.; Bartelt, A.; Jaworski, F.B.; Carr, J.A.; Rowlands, C.J.; Wilson, M.W.B.; Chen, O.; Wei, H.; Hwang, G.W.; Montana, D.M.; Coropceanu, I.; Achorn, O.B.; Kloepper, J.; Heeren, J.; So, P.T.C.; Fukumura, D.; Jensen, K.F.; Jain, R.K.; Bawendi, M.G. Next-generation in vivo optical imaging with short-wave infrared quantum dots. *Nat. Biomed. Eng.* **2017**, *1*, 0056.
- (5) (a) Chen, G.; Ohulchanskyy, T.Y.; Liu, S.; Law, W.-C.; Wu, F.; Swihart, M.T.; Agren, H.; Prasad, P.N. Core/shell NaGdF<sub>4</sub>:Nd<sup>3+</sup>/NaGdF<sub>4</sub> nanocrystals with efficient near-infrared to near-infrared downconversion photoluminescence for bioimaging applications. *ACS Nano* **2012**, *6*, 2969–2977. (b) Naczynski, D.J.; Tan, M.C.; Zevon, M.; Wall, B.; Kohl, J.; Kulesa, A.; Chen, S.; Roth, C.M.; Riman, R.E.; Moghe, P.V. Rare-earth doped biological composites as in vivo shortwave infrared reporters. *Nat. Commun.* **2013**, *4*, 2199.
- (6) (a) Yang, Q.; Ma, Z.; Wang, H.; Zhou, B.; Zhu, S.; Zhong, Y.; Wang, J.; Wan, H.; Antaris, A.; Ma, R.; Zhang, X.; Yang, J.; Zhang, X.; Sun, H.; Liu, W.; Liang, Y.; Dai, H. Rational design of molecular fluorophores for biological imaging in the NIR-II window. *Adv. Mater.* **2017**, *29*, 1605497. (b) Cosco, E.D.; Caram, J.R.; Bruns, O.T.; Franke, D.; Day, R.A.; Farr, E.P.; Bawendi, M.G.; Sletten, E.M. Flavylium polymethine fluorophores for near- and shortwave infrared imaging. *Angew. Chem. Int. Ed.* **2017**, *56*, 13126–13129. (c) Xu, G.; Yan, Q.; Lv, X.; Zhu, Y.; Xin, K.; Shi, B.; Wang, R.; Chen, J.; Gao, W.; Shi, P.; Fan, C.; Zhao, C.; Tian, H. Imaging of colorectal cancers using activatable nanoprobe with second near-infrared window emission. *Angew. Chem. Int. Ed.* **2018**, *57*, 3626–3630. (d) Li, B.; Lu, L.; Zhao, M.; Lei, Z.; Zhang, F. An efficient 1064 nm NIR-II excitation fluorescent molecular dye for deep-tissue high-resolution dynamic bioimaging. *Angew. Chem. Int. Ed.* **2018**, *57*, 7483–7487. (e) Yang, Q.; Hu, Z.; Zhu, S.; Ma, R.; Ma, H.; Ma, Z.; Wan, H.; Zhu, T.; Jiang, Z.; Liu,

- W.; Jiao, L.; Sun, H.; Liang, Y.; Dai, H. Donor engineering for NIR-II molecular fluorophores with enhanced fluorescent performance. *J. Am. Chem. Soc.* **2018**, *140*, 1715–1724. (f) Sheng, Z.H.; Guo, B.; Hu, D.H.; Xu, S.D.; Wu, W.B.; Liew, W.H.; Yao, K.; Jiang, J.Y.; Liu, C.B.; Zheng, H.R.; Liu, B. Bright aggregation-induced emission dots for targeted synergetic NIR-II fluorescence and NIR-I photoacoustic imaging of orthotopic brain tumors. *Adv. Mater.* **2018**, 1800766.
- (7) (a) Wuerthner, F.; Kaiser, T.E.; Saha-Moeller, C.R. J-aggregates: From serendipitous discovery to supramolecular engineering of functional dye materials. *Angew. Chem. Int. Ed.* **2011**, *50*, 3376–3410. (b) Kobayashi, T. *J-aggregates*; World Scientific: Singapore, **1996**. (c) Jelley, E.E. Spectral absorption and fluorescence of dyes in the molecular state. *Nature* **1936**, *138*, 1009–1010. (d) Scheibe, G. Über die veränderlichkeit der absorptionsspektren in lösungen und die nebenvalezen als ihre ursache. *Angew. Chem.* **1937**, *50*, 51. (e) Hestand, N.J.; Spano, F.C. Molecular aggregate photophysics beyond the Kasah Model: Novel design principles for organic materials. *Acc. Chem. Res.* **2017**, *50*, 341–350.
- (8) (a) Bashkatov, A. N.; Genina, E. A.; Kochubey, V. I.; Tuchin, V. V. Optical properties of human skin, subcutaneous and mucous tissues in the wavelength range from 400 to 2000 nm. *J. Phys. D. Appl. Phys.* **2005**, *38*, 2543–2555. (b) Lim, Y.T.; Kim, S.; Nakayama, A.; Stott, N.E.; Bawendi, M.G.; Frangioni, J.V. Selection of quantum dot wavelengths for biomedical assays and imaging. *Mol. Imaging*, **2003**, *2*, 50–64. (c) Won, N.; Jeon, S.; Kim, K.; Kwag, J.; Park, J.; Kim, S.G.; Kim, S. Imaging depths of near-infrared quantum dots in first and second optical windows. *Mol. Imaging* **2012**, *11*, 338–352.
- (9) Bricks, J.L.; Slominskii, Y.L.; Panas, I.D.; Demchenko, A.P. Fluorescent J-aggregates of cyanine dyes: basic research and applications review. *Methods Appl. Fluoresc.* **2018**, *6*, 012001.
- (10) Shakiba, M.; Ng, K.K.; Huynh, E.; Chan, H.; Charron, D.M.; Chen, J.; Muhanna, N.; Foster, F.S.; Wilson, B.C.; Zheng, G. Stable J-aggregation enabled dual photoacoustic and fluorescence nanoparticles for intraoperative cancer imaging. *Nanoscale* **2016**, *8*, 12618–12625.
- (11) Yang, C.; Wang, X.; Wang, M.; Xu, K.; Xu, C. Robust colloidal nanoparticles of pyrrolopyrrole cyanine J-aggregates with bright near-infrared fluorescence in aqueous media: From spectral tailoring to bioimaging applications. *Chem. Eur. J.* **2017**, *23*, 4310–4319.
- (12) Sun, P.; Wu, Q.; Sun, X.; Miao, H.; Deng, W.; Zhang, W.; Fan, Q.; Huang, W. J-aggregate squaraine nanoparticles with bright NIR-II fluorescence for imaging guided photothermal therapy. *Chem. Commun.* **2018**, *54*, 13395–13398.
- (13) Two other J-aggregates have been employed *in vivo* for photothermal therapy and photoacoustic imaging. (a) Song, X.; Gong, H.; Liu, T.; Cheng, L.; Wang, C.; Sun, X.; Liang, C.; Liu, Z. J-aggregates of organic dye molecules complexed with iron oxide nanoparticles for imaging-guided photothermal therapy under 915 nm light. *Small* **2014**, *10*, 4362–4370. (b) Dumani, D.S.; Brecht, H.-P.; Ivanov, V.; Deschner, R.; Harris, J.T.; Homan, K.A.; Cook, J.R.; Emelianov, S.Y.; Ermilov, S.A.

- Co-registered photoacoustic and fluorescent imaging of a switchable nanoprobe based on J-aggregates of indocyanine green. *Proc. SPIE 10494, Photons Plus Ultrasound: Imaging and Sensing* **2018**, 104942W.
- (14) Kim, S.; Shi, Y.; Kim, J.Y.; Park, K.; Cheng, J.X. Overcoming the barriers in micellar drug delivery: Loading efficiency, in vivo stability, and micelle-cell interaction. *Expert Opin. Drug. Deliv.* **2010**, *7*, 49–62.
- (15) (a) Chen, F.; Hong, H.; Shi, S.; Goel, S.; Valdovinos, H.F.; Hernandez, R.; Theuer, C.P.; Barnhart, T.E.; Cai, W. Engineering of hollow mesoporous silica nanoparticles for remarkably enhanced tumor active targeting efficacy. *Sci. Rep.* **2014**, *4*, 5080. (b) Guardado-Alvarez, T.M.; Chen, W.; Norton A.E.; Russell M.M.; Connick, W.B.; Zink, J.I. Analyte-responsive gated hollow mesoporous silica nanoparticles exhibiting inverse functionality and an AND logic response. *Nanoscale* **2016**, *8*, 18296–18300.
- (16) (a) He, Q.; Zhang, Z.; Gao, F.; Li, Y.; Shi, J. In vivo biodistribution and urinary excretion of mesoporous silica nanoparticles: Effects of particle size and PEGylation. *Small* **2011**, *7*, 271–280. (b) Liu, J.; Luo, Z.; Zhang, J.; Luo, T.; Zhou, J.; Zhao, X.; Cai, K. Hollow mesoporous silica nanoparticles facilitated drug delivery via cascade pH stimuli in tumor microenvironment for tumor therapy. *Biomaterials* **2016**, *83*, 51-65.
- (17) (a) Li, Y.; Li, N.; Pan, W.; Yu, Z.; Yang, L.; Tang, B. Hollow mesoporous silica nanoparticles with tunable structures for controlled drug delivery. *ACS Appl. Mater. Interfaces* **2017**, *9*, 2123–2129. (b) Chakravarty, R.; Goel, S.; Hong, H.; Chen, F.; Valdovinos, H. F.; Hernandez, R.; Barnhart, T. E.; Cai, W. Functionalized hollow mesoporous silica nanoparticles for tumor vasculature targeting and PET image-guided drug delivery. *Nanomedicine (Lond)* **2015**, *10*, 1233–1246. (c) Luo, Z.; Hu, Y.; Cai, K.; Ding, X.; Zhang, Q.; Li, M.; Ma, X.; Zhang, B.; Zeng, Y.; Li, P.; Li, J.; Liu, J.; Zhao, Y. Intracellular redox-activated anticancer drug delivery by functionalized hollow mesoporous silica nanoreservoirs with tumor specificity. *Biomaterials* **2014**, *35*, 7951-7962. (d) Du, L.; Liao, S.; Khatib, H.A.; Stoddart, J.F.; Zink, J.I. Controlled-access hollow mechanized silica nanocontainers. *J. Am. Chem. Soc.* **2009**, *131*, 15136–15142.
- (18) (a) Singh, R.K.; Kim, T.H.; Mahapatra, C.; Patel, K.D.; Kim, H.W. Preparation of self-activated fluorescence mesoporous silica hollow nanoellipsoids for theranostics. *Langmuir* **2015**, *31*, 11344–11352. (b) Yang, S.; Chen, D.; Li, N.; Xu, Q.; Li, H.; Gu, F.; Xie, J.; Lu, J. Hollow mesoporous silica nanocarriers with multifunctional capping agents for in vivo cancer imaging and therapy. *Small* **2016**, *12*, 360–370. (c) Huang, C.C.; Huang, W.; Yeh, C.S. Shell-by-shell synthesis of multi-shelled mesoporous silica nanospheres for optical imaging and drug delivery. *Biomaterials* **2011**, *32*, 556–564. (d) Fan, Z.; Li, D.; Yu, X.; Zhang, Y.; Cai, Y.; Jin, J.; Yu, J. AIE luminogen-functionalized hollow mesoporous silica nanospheres for drug delivery and cell imaging. *Chem. Eur. J.* **2016**, *22*, 3681–3685.

- (19) Hong, S.; Kim, H.; Choi, Y. Indocyanine green-loaded hollow mesoporous silica nanoparticles as an activatable theranostic agent. *Nanotechnology* **2017**, *28*, 185102.
- (20) (a) Soppera, O.; Turck, C.; Lougnot, D.J. Fabrication of micro-optical devices by self-guiding photopolymerization in the near IR. *Opt. Lett.* **2009**, *34*, 461–463. (b) Bonardi, A.H.; Dumar, F.; Grant, T.M.; Noirbent, G.; Gigmes, D.; Lessard, B.H.; Fouassier, J.-P.; Lalevee, J. Higher performance near-infrared (NIR) photoinitiating systems operating under low light intensity and in the presence of oxygen. *Macromolecules* **2018**, *51*, 1314–1324.
- (21) Leung, K.C.F.; Nguyen, T.D.; Stoddart, J.F.; Zink, J.I. Supramolecular nanovalves controlled by proton abstraction and competitive binding. *Chem. Mater.* **2006**, *18*, 5919–5928.
- (22) (a) Zhou, W.; Dridi, M.; Suh, J.Y.; Kim, C.H.; Co, D.T.; Wasielewski, M.R.; Schatz, G.C.; Odom, T.W. Lasing action in strongly coupled plasmonic nanocavity arrays. *Nat. Nanotechnol.* **2013**, *8*, 506–511. (b) Yang, A.; Hoang, T.B.; Dridi, M.; Deeb, C.; Mikkelsen, M.H.; Schatz, G.C.; Odom, T.W. Real-time tunable lasing from plasmonic nanocavity arrays. *Nat. Commun.* **2015**, *6*, 6939.
- (23) Oseledchyk, A.; Andreou, C.; Wall, M.A.; Kircher, M.F. Folate-targeted surface-enhanced resonance Raman scattering nanoprobe ratiometry for detection of microscopic ovarian cancer. *ACS Nano* **2017**, *11*, 1488–1497.
- (24) Berezin, M.Y.; Zhan, C.; Lee, H.; Joo, C.; Akers, W.J.; Yazdanfar, S.; Achilefu, S. Two-photon optical properties of near-infrared dyes at 1.55  $\mu\text{m}$  excitation. *J. Phys. Chem. B.* **2011**, *115*, 11530–11535.
- (25) Wang, C.; Weiss, E.A. Sub-nanosecond resonance energy transfer in the near-infrared within self-assembled conjugates of PbS quantum dots and cyanine dye J-aggregates. *J. Am. Chem. Soc.* **2016**, *138*, 9557–9564.
- (26) Modification of pores with APTS is predicted to have a size change of 0.5 nm, whereas we didn't observe pore size change. See: (a) Chen, W.; Tsai, P.H.; Hung, Y.; Chiou, S.H.; Mou, C.Y. Nonviral cell labeling and differentiation agent for induced pluripotent stem cells based on mesoporous silica nanoparticles. *ACS Nano* **2013**, *7*, 8423–8440. (b) Chou, C.C.; Chen, W.; Hung, Y.; Mou, C.Y. Molecular elucidation of biological response to mesoporous silica nanoparticles in vitro and in vivo. *ACS Appl. Mater. Interfaces* **2017**, *9*, 22235–22251. (c) Chen, W.; Cheng, C.A.; Zink, J.I. Spatial, temporal, and dose control of drug delivery using noninvasive magnetic stimulation. *ACS Nano* **2019**, *13*, 1292–1308. (d) Zhang, Y.; Ang, C.Y.; Li, M.; Tan, S.Y.; Qu, Q.; Luo, Z.; Zhao, Y. Polymer-coated hollow mesoporous silica nanoparticles for triple-responsive drug delivery. *ACS Appl. Mater. Interfaces* **2015**, *7*, 18179–18187.
- (27) Modification of pores with APTS is predicted to have a size change of 0.5 nm, whereas we didn't observe pore size change. See ref 26.
- (28) (a) Rurack, K.; Spieles, M. Fluorescence quantum yields of a series of red and near-infrared dyes emitting at 600–1000 nm. *Anal. Chem.* **2011**, *83*, 1232–1242. (b) Hatami, S.; Würth, C.; Kaiser, M.;

- Leubner, S.; Gabriel, S.; Bahrig, L.; Lesnyak, V.; Pauli, J.; Gaponik, N.; Eychmüller, A.; Resch-Genger, U. Absolute photoluminescence quantum yields of IR-26 and IR-emissive Cd<sub>1-x</sub>Hg<sub>x</sub>Te and PbS quantum dots- method and material-inherent challenges. *Nanoscale* **2015**, *7*, 133–143.
- (29) A sulfonated variant of the IR-140 chromophore has been characterized to J-aggregate in solution. See ref 27b.
- (30) NIR fluorophores have emission that extends into the SWIR. (a) Carr, J.A.; Franke, D.; Caram, J.R.; Perkinson, C.F.; Askoxylakis, V.; Datta, M.; Rukumura, D.; Jain, R.K.; Bawendi, M.G.; Bruns, O.T. Shortwave infrared fluorescence imaging with the clinically-approved near-infrared dye indocyanine green. *Proc. Natl. Acad. Sci. U.S.A.* **2018**, *115*, 4465-4470. (b) Starosolski, Z.; Bhavane, R.; Ghaghada, K.B.; Vasudevan, S.A.; Kaay, A.; Annapragada, A. Indocyanine green fluorescence in second near-infrared (NIR-II) window. *PLoS ONE* **2017**, *12*, e0187563. (c) Zhu, S.; Hu, Z.; Tian, R.; Yung, B.C.; Yang, Q.; Zhao, S.; Kiesewetter, D.O.; Niu, G.; Sun, H.; Antaris, A.L.; Chen, X. Repurposing cyanine NIR-I dyes accelerates clinical translation of near-infrared-II (NIR-II) bioimaging. *Adv. Mater.* **2018**, *30*, 1802546.
- (31) Qiao, Y.; Polzer, F.; Kirmse, H.; Kirstein, S.; Rabe, J.P. Nanohybrids from nanotubular J-aggregates and transparent silica nanoshells. *Chem. Commun.* **2015**, *51*, 11980–11982.
- (32) (a) Ruhle, B.; Saint-Cricq, P.; Zink, J.I. Externally controlled nanomachines on mesoporous silica nanoparticles for biomedical applications. *ChemPhysChem* **2016**, *17*, 1769–1779. (b) Chen, W.; Cheng, C.A.; Lee, B.Y.; Clemens, D.L.; Huang, W.Y.; Horwitz M.A.; Zink, J.I. Facile strategy enabling both high loading and high release amounts of the water-insoluble drug Clofazimine using mesoporous silica nanoparticles. *ACS Appl. Mater. Interfaces* **2018**, *10*, 31870–31881. (c) Chen, W.; Glackin, C.A.; Horwitz, M.A.; Zink, J.I. Nanomachines and other caps on mesoporous silica nanoparticles for drug delivery. *Acc. Chem. Res.* **2019**, *52*, 1531–1542. (d) Cheng, C.A.; Deng, T.; Lin, F.C.; Cai, Y.; Zink, J.I. Supramolecular nanomachines as stimuli-responsive gatekeepers on mesoporous silica nanoparticles for antibiotic and cancer drug delivery. *Theranostics* **2019**, *9*, 3341–3364.
- (33) (a) Sumer, B.; Gao, J. Theranostic nanomedicine for cancer. *Nanomedicine* **2008**, *3*, 137–140. (b) Chakravarty, R.; Goel, S.; Hong, H.; Chen, F.; Valdovinos, H.F.; Hernandez, R.; Barnhart, T.E.; Cai, W. Functionalized hollow mesoporous silica nanoparticles for tumor vasculature targeting and PET image-guided drug delivery. *Nanomedicine* **2015**, *10*, 1233–1246. (c) Ni, D.; Jiang, D.; Ehlerding, E.B.; Huang, P.; Cai, W. Radiolabeling silica-based nanoparticles via coordination chemistry: basic principles, strategies, and applications. *Acc. Chem. Res.* **2018**, *51*, 778–788. (d) Zhao, N.; Yan, L.; Zhao, X.; Chen, X.; Li, A.; Zheng, D.; Zhou, X.; Dai, X.; Xu, F.J. Versatile types of organic/inorganic nanohybrids: From strategic design to biomedical applications. *Chem. Rev.* **2019**, *119*, 1666–1762.
- (34) (a) Brixner, T.; Hildner, R.; Kohler, J.; Lambert, C.; Würthner, F. Exciton transport in molecular aggregates– from natural antennas to synthetic chromophore systems. *Adv. Energy Mater.* **2017**, *7*,

1700236. (b) Doria, S.; Sinclair, T.S.; Klein, N.F.; Bennett, D.I.G.; Chuang, C.; Freyria, F.S.; Steiner, C.P.; Foggi, P.; Nelson, K.A.; Cao, J.; Aspuru-Guzik, A.; Llyod, S.; Caram, J.R.; Bawendi, M.G. Photochemical control of exciton superradiance in light-harvesting nanotubes. *ACS Nano* **2018**, *12*, 4556–4564.
- (35) Kasha, M.; Rawls, H. R.; El-Bayoumi, M. A. The exciton model in molecular spectroscopy. *Pure Appl. Chem.* **1965**, *11*, 371–392.
- (36) Chen, F.; Hong, H.; Shi, S.; Goel, S.; Valdovinos, H.F.; Hernandex, R.; Theuer, C.P.; Barnhart, T.E.; Cai, W. Engineering of hollow mesoporous silica nanoparticles for remarkably enhanced tumor active targeting efficacy *Sci. Rep.* **2014**, *4*, 5080.
- (37) Xue, M.; Zink, J.I. Probing the Microenvironment in the Confined Pores of Mesoporous Silica Nanoparticles. *J. Phys. Chem. Lett.* **2014**, *5*, 839–842.
- (38) Cosco, E. D.; Caram, J. R.; Bruns, O. T.; Franke, D.; Day, R. A.; Farr, E. P.; Bawendi, M. G.; Sletten, E. M. Flavylum Polymethine Fluorophores for Near- and Shortwave Infrared Imaging. *Angew. Chem. Int. Ed.* **2017**, *56*, 13126–13129.
- (39) Ali, A.; Tariq, M. Deviations in Refractive Index Parameters and Applicability of Mixing Rules in Binary Mixtures of Benzene+1,2-Dichloroethane at Different Temperatures. *Chem. Eng. Commun.* **2008**, *195*, 43–56.
- (40) LeBel, R. G.; Goring, D. A. I. Density, Viscosity, Refractive Index, and Hygroscopicity of Mixtures of Water and Dimethyl Sulfoxide. *J. Chem. Eng. Data* **1962**, *7*, 100–101.
- (41) Qiao, Y.; Polzer, F.; Kirmse, H.; Kirstein, S.; Rabe, J.P. Nanohybrids from nanotubular J-aggregates and transparent silica nanoshells. *Chem. Commun.* **2015**, *51*, 11980–11982.
- (42) Hatami, S.; Würth, C.; Kaiser, M.; Leubner, S.; Gabriel, S.; Bahrig, L.; Lesnyak, V.; Pauli, J.; Gaponik, N.; Eychmüller, A.; Resch-Genger, U. Absolute photoluminescence quantum yields of IR26 and IR-emissive Cd<sub>1-x</sub>Hg<sub>x</sub>Te and PbS quantum dots—method- and material-inherent challenges. *Nanoscale* **2015**, *7*, 133–143.